Koji Sugioka
Michel Meunier
Alberto Piqué
Editors

SPRINGER SERIES IN MATERIALS SCIENCE 135

Laser Precision Microfabrication

Springer Series in
MATERIALS SCIENCE 135

Springer Series in

MATERIALS SCIENCE

Editors: R. Hull C. Jagadish R.M. Osgood, Jr. J. Parisi Z. Wang H. Warlimont

The Springer Series in Materials Science covers the complete spectrum of materials physics, including fundamental principles, physical properties, materials theory and design. Recognizing the increasing importance of materials science in future device technologies, the book titles in this series reflect the state-of-the-art in understanding and controlling the structure and properties of all important classes of materials.

Please view available titles in *Springer Series in Materials Science* on series homepage http://www.springer.com/series/856

Koji Sugioka
Michel Meunier
Alberto Piqué
Editors

Laser Precision Microfabrication

With 158 Figures

Editors
Dr. Koji Sugioka
RIKEN
Advanced Science Institute
Laser Technology Laboratory
Hirosawa 2-1
351-0198Wako-shi, Saitama, Japan
E-mail: ksugioka@riken.jp

Professor Michel Meunier
Canada Research Chair in Laser
Micro/Nanoengineering of materials
Laser Processing Laboratory
Department of Engineering Physics
École Polytechnique Montréal
Montreal, QC, Canada
E-mail: michel.meunier@polymtl.ca

Dr. Alberto Piqué
Naval Research Laboratory
Overlook Ave. SW., 4555, Washington,
DC 20375, USA
E-mail: pique@nrl.navy.mil

Series Editors:
Professor Robert Hull
University of Virginia
Dept. of Materials Science and Engineering
Thornton Hall
Charlottesville, VA 22903-2442, USA

Professor Jürgen Parisi
Universität Oldenburg, Fachbereich Physik
Abt. Energie- und Halbleiterforschung
Carl-von-Ossietzky-Straße 9–11
26129 Oldenburg, Germany

Professor Chennupati Jagadish
Australian National University
Research School of Physics and Engineering
J4-22, Carver Building
Canberra ACT 0200, Australia

Dr. Zhiming Wang
University of Arkansas
Department of Physics
835 W. Dicknson St.
Fayetteville, AR 72701, USA

Professor R.M. Osgood, Jr.
Microelectronics Science Laboratory
Department of Electrical Engineering
Columbia University
Seeley W. Mudd Building
New York, NY 10027, USA

Professor Hans Warlimont
DSL Dresden Material-Innovation GmbH
Pirnaer Landstr. 176
01257 Dresden, Germany

Springer Series in Materials Science ISSN 0933-033X
ISBN 978-3-642-10522-7 e-ISBN 978-3-642-10523-4
DOI 10.1007/978-3-642-10523-4
Springer Heidelberg Dordrecht London New York

Library of Congress Control Number: 2010931868

© Springer-Verlag Berlin Heidelberg 2010
This work is subject to copyright. All rights are reserved, whether the whole or part of the material is concerned, specifically the rights of translation, reprinting, reuse of illustrations, recitation, broadcasting, reproduction on microfilm or in any other way, and storage in data banks. Duplication of this publication or parts thereof is permitted only under the provisions of the German Copyright Law of September 9, 1965, in its current version, and permission for use must always be obtained from Springer. Violations are liable to prosecution under the German Copyright Law.
The use of general descriptive names, registered names, trademarks, etc. in this publication does not imply, even in the absence of a specific statement, that such names are exempt from the relevant protective laws and regulations and therefore free for general use.

Typesetting and Production: Data prepared by SPi using a Springer TEX macro package
Cover concept: eStudio Calamar Steinen
Cover production: SPi Publisher Services

Printed on acid-free paper

Springer is part of Springer Science+Business Media (www.springer.com)

Preface

The use of lasers in materials processing, machining, diagnostics, and medical applications is a rapidly growing area of research. The main driving force behind this research is that lasers can provide unique solutions in materials processing, offer the ability to manufacture otherwise unattainable devices, and yield cost-effective solutions to complex manufacturing processes. In particular, recent advances in short-pulse and short-wavelength beams have stimulated research into laser precision microfabrication (LPM) in the fields of electronics, optoelectronics, micro- and nanomachining, new materials synthesis, and medical and biological applications.

In view of the impact of LPM, The Japan Laser Processing Society (JLPS) organized the inaugural International Symposium on Laser Precision Microfabrication (LPM 2000) in 2000 in Omiya, Saitama, Japan. The aim of this symposium was to provide a forum where leading experts, end users, and vendors can congregate to discuss both fundamental and practical aspects of LPM. It has grown in strength through successive conferences held annually in Singapore (2001), Osaka, Japan (2002), Munich, Germany (2003), Nara, Japan (2004), Williamsburg, USA (2005), Kyoto, Japan (2006), Vienna, Austria (2007), Quebec, Canada (2008), Kobe, Japan (2009), and Stuttgart, Germany (2010) and it is now recognized as one of the biggest and most important events in the field of laser microprocessing. The numbers of participants as well as papers presented continue to increase year by year due to expansion of the range of laser applications in both fundamental and practical research.

This book was primarily planned to introduce key papers presented at recent LPM symposia. However, we felt that its scope should be broadened to provide readers with more comprehensive information on the state of the art and future prospects of LPM. The book consists of 13 chapters covering a broad range of topics in LPM, introduced by internationally recognized experts in the field, most of whom are involved in the committee of the LPM symposia. It includes an overview of LPM (Chap. 1), theory and simulation (Chaps. 2 and 8), laser devices and optical systems for LPM (Chap. 3), fundamentals of laser–matter interaction (Chap. 4), beam shaping techniques (Chap. 5), biomedical applications (Chap. 6), nanotechnology (Chaps. 7 and 8), relevant processing techniques such as surface modification, micromachining, and laser-induced forward transfer (LIFT) (Chaps. 4, 9, and 10–12), and practical applications (Chap. 13).

We believe that this book offers a comprehensive review of LPM, which will be used not only by researchers and engineers already working in the field, but also by students and young scientists who plan to work in this area of research in the future. Last but not least, we would like to thank all of the chapter contributors for their great efforts and kind cooperation in editing this book.

Saitama, Montréal, Washington
April 2010

Koji Sugioka
Michel Meunier
Alberto Piqué

Contents

1 Process Control in Laser Material Processing for the Micro and Nanometer Scale Domains 1
Henry Helvajian
1.1 Introduction 1
1.2 Laser Processing 5
1.2.1 Laser Wavelength 7
1.2.2 Laser Power 11
1.2.3 Laser Dose 13
1.2.4 Laser Beam 16
1.2.5 Laser Pulse Temporal Profile 19
1.2.6 Pattern Generation 23
1.3 Possible Steps Forward 26
1.4 Conclusions 29
References 30

2 Theory and Simulation of Laser Ablation – from Basic Mechanisms to Applications 35
Laurent J. Lewis and Danny Perez
2.1 Introduction 35
2.2 Basic Physics 37
2.2.1 Light-Matter Interaction 37
2.2.2 Material Removal from the Target: The Basics of Ablation 37
2.3 Ablation in the Thermal Regime 38
2.3.1 Thermodynamics 38
2.3.2 Conventional Wisdom: Early Theories 39
2.3.3 A New Understanding 41
2.3.4 Computer Models 41
2.3.5 The Femtosecond Regime 44
2.3.6 Picosecond Pulses and Beyond 49
2.3.7 Molecular Solids 50
2.4 Materials Processing 53
2.4.1 Nanoparticle Production in Solvents 53
2.4.2 Damages and Heat Affected Zones 55

2.5 Conclusions and Perspectives 58
References 59

3 **Laser Devices and Optical Systems for Laser Precision Microfabrication** 63
Kunihiko Washio
3.1 Introduction 63
3.2 Laser Devices 64
3.2.1 Various Laser Devices from Deep UV and Mid-IR Spectral Region 64
3.2.2 Diode-Pumped High-Brightness Continuous Wave Solid-State Lasers 67
3.2.3 Q-Switching and Cavity Dumping 70
3.2.4 Picosecond and Femtosecond, Ultrafast Pulsed Laser Oscillators and Amplifiers 72
3.3 Optical Systems 77
3.3.1 Optical Components for Modification and Control of Laser Beams 77
3.3.2 Optical Systems for Beam Shape Transformation 78
3.3.3 Galvanometer-Based Optical Scanners 81
3.3.4 Spatial Light Modulators 82
3.3.5 Nonlinear-Optical Systems for Harmonic Generation 83
3.3.6 Optical Systems for Beam Characterization and Process Monitoring 84
3.4 Summary 86
References 86

4 **Fundamentals of Laser-Material Interaction and Application to Multiscale Surface Modification** 91
Matthew S. Brown and Craig B. Arnold
4.1 Introduction 91
4.2 Fundamentals of Laser Surface Processing 92
4.2.1 Light Propagation in Materials 92
4.2.2 Energy Absorption Mechanisms 94
4.2.3 The Heat Equation 96
4.2.4 Material Response 98
4.3 Laser Surface Processing Applications 101
4.4 Case Study I: Surface Texturing for Enhanced Optical Properties 104
4.5 Case Study II: Surface Texturing for Enhanced Biological Interactions 110
4.6 Conclusions 116
References 117

5 Temporal Pulse Tailoring in Ultrafast Laser Manufacturing Technologies 121
Razvan Stoian, Matthias Wollenhaupt, Thomas Baumert, and Ingolf V. Hertel
5.1 Introduction 121
5.2 Fundamental and Technical Aspects of Pulse Shaping 123
5.2.1 Basics of Ultrashort Laser Pulses 123
5.2.2 Frequency Domain Manipulation (Mathematical Formalism) 123
5.2.3 Analytical Phase Functions Relevant to Material Processing 127
5.2.4 Pulse Shaping in the Spatial Domain 130
5.2.5 Experimental Implementations for Temporal Pulse Shaping 130
5.2.6 Optimization Strategies 132
5.3 Material Interaction with Temporally Shaped Pulses 133
5.3.1 Control of Laser-Induced Primary Excitation Events 133
5.3.2 Engineered Thermodynamic Phase-Space Trajectories 135
5.3.3 Refractive Index Engineering by Temporally Tailored Pulses 139
5.4 Conclusion and Perspectives 141
References 142

6 Laser Nanosurgery, Manipulation, and Transportation of Cells and Tissues 145
Wataru Watanabe
6.1 Introduction 145
6.2 Laser Direct Surgery 146
6.2.1 Nanosurgery with a Focused Laser Beam in the Ultraviolet and Visible Region 146
6.2.2 Femtosecond Laser Surgery 147
6.3 Nanoparticles and Chromophore-Assisted Manipulation and Processing 153
6.3.1 Chromophore-Assisted Laser Inactivation 153
6.3.2 Plasmonic Nanosurgery 154
6.4 Laser Manipulation and Transport of Cells and Tissues 154
6.4.1 Optical Tweezers 154
6.4.2 Laser Transport of Cells 155
6.5 Application of Laser-Induced ShockWaves and Mechanical Waves 155
6.5.1 Targeted Gene Transfection by Laser-Induced Mechanical Waves 155
6.5.2 Femtosecond Laser-Induced ShockWave in Liquid 156
6.6 Laser-Induced Stimulation 157

6.7 Fabrication of Microfluidic Channels and Scaffolds 158
6.8 Summary and Conclusions 159
References 159

7 Laser Synthesis of Nanomaterials 163
Sébastien Besner and Michel Meunier
7.1 Introduction 163
7.2 General Principles of Laser Based Synthesis of Nanomaterials 164
7.2.1 Nanosecond Pulsed Laser Ablation 165
7.2.2 Ultrafast Laser Ablation 166
7.3 Synthesis of Nanomaterials Based on Laser Ablation of a Bulk Target ...168
7.4 Laser Ablation in Vacuum/Gas Environment 171
7.5 Laser Ablation in Liquids: Formation of Colloidal Nanoparticles ...173
7.5.1 Ablation Mechanisms 173
7.5.2 Effect of Laser Parameters 176
7.5.3 Effect of Stabilizing Agents 177
7.5.4 Process Model 179
7.6 Synthesis of Nanomaterials Based on Laser Interaction with Micro/Nanomaterials ...180
7.7 Conclusions and Perspective 182
References 183

8 Ultrafast Laser Micro- and Nanostructuring 189
Wolfgang Kautek and Magdalena Forster
8.1 Introduction 190
8.2 Theoretical Background 190
8.2.1 Dielectrics 191
8.2.2 Metals 194
8.2.3 Thermodynamic Approach 195
8.3 Recent Results 198
8.3.1 Top-Down Approaches to Nanostructures 198
8.3.2 Thin Film Ablation 199
8.3.3 Incubation Phenomena 201
8.3.4 Bottom-Up Approaches to Nanostructures 203
8.3.5 Biogenetic Materials 204
8.4 Outlook 206
8.4.1 Recent Instrumental Developments 206
8.4.2 Nanostructuring in the Nearfield 208
8.5 Summary 209
References 209

9 3D Fabrication of Embedded Microcomponents 215
Koji Sugioka and Stefan Nolte
9.1 Introduction 215
9.2 Principles of Internal Processing 216
9.3 Refractive Index Modification 217
9.3.1 Advantages of Femtosecond Laser in Photonic Device Fabrication 217
9.3.2 Optical Waveguide Writing 218
9.3.3 Fabrication of Photonic Devices 220
9.3.4 Fabrication of Fiber Bragg Gratings (FBGs) 223
9.4 Formation of 3D Hollow Microstructures 225
9.4.1 Direct Ablation in Water 225
9.4.2 Internal Modification Followed by Wet Etching 226
9.5 3D Integration of Microcomponents 228
9.6 Beam Shaping for Fabrication of 3D Microcomponents 231
9.7 Summary 233
References 234

10 Micromachining and Patterning 239
Jürgen Ihlemann
10.1 Introduction 239
10.2 Direct Writing 240
10.3 Micro Fluidics 241
10.4 Gratings 243
10.5 Diffractive Optical Elements 245
10.6 Micro Lenses/Lens Arrays 246
10.7 Patterning of Layers 249
10.8 Dielectric Masks 252
10.9 Two Step Processing of Layers: Ablation + Oxidation 253
10.10 Summary and Outlook 255
References 256

11 Laser Transfer Techniques for Digital Microfabrication 259
Alberto Piqué
11.1 Introduction 259
11.2 Lasers in Digital Microfabrication 261
11.3 Origins of Laser Forward Transfer 262
11.3.1 Early Work in Laser-Induced Forward Transfer 262
11.3.2 Transferring Metals and Other Materials with LIFT 264
11.3.3 Fundamental Limitations of the Basic LIFT Approach 265
11.4 Evolution of Laser Forward Transfer Techniques 265
11.4.1 The Role of the Donor Substrate 266
11.4.2 Development of Multilayered Ribbons and Dynamic Release Layers 267

11.4.3 LIFT with Ultra-Short Laser Pulses 269
11.4.4 Laser Transfer of Composite or Matrix-Based Materials 270
11.4.5 Laser Transfer of Rheological Systems 271
11.4.6 Jetting Effects 273
11.4.7 Laser Transfer of Entire Devices 274
11.4.8 Recent Variations of the Basic LIFT Process 276
11.5 Applications 277
11.5.1 Microelectronics 277
11.5.2 Sensor and Micropower Generation Devices 278
11.5.3 Biomaterials 281
11.5.4 Embedded Electronic Circuits 283
11.6 The Future of Laser-Based Digital Microfabrication 284
11.6.1 Laser Forward Transfer vs. Other Digital Microfabrication Processes 285
11.7 Summary 286
References 287

12 Hybrid Laser Processing of Transparent Materials 293
Hiroyuki Niino
12.1 Introduction 293
12.2 Multiwavelength Excitation Process 294
12.2.1 Principle of Multiwavelength Excitation Process 294
12.2.2 Microfabrication of Transparent Materials by Multiwavelength Excitation Process 295
12.3 Media Assisted Process 297
12.3.1 Classification of Media Assisted Processes 297
12.3.2 LIPAA Process 299
12.3.3 LIBWE Process 302
12.4 Conclusions 306
References 307

13 Drilling, Cutting, Welding, Marking and Microforming 311
Oliver Suttmann, Anas Moalem, Rainer Kling, and Andreas Ostendorf
13.1 Parameter Regimes 311
13.1.1 Pulse Duration 312
13.1.2 Wavelength 314
13.1.3 Beam Quality 315
13.1.4 Output Power 315
13.2 Drilling 316
13.2.1 Laser Drilling Without Relative Movement Between Laser Spot and Workpiece 316
13.2.2 Laser Drilling with Relative Movement Between Laser Spot and Workpiece 318

13.2.3 Trepanning Head 320
13.2.4 Further Trends and Outlook 320
13.3 Cutting 321
13.3.1 Melt Cutting 321
13.3.2 Laser Ablation Cutting 323
13.3.3 Laser Scribing 326
13.3.4 Laser Induced Stress Cutting 326
13.4 Microjoining 327
13.4.1 Welding 327
13.4.2 Soldering 330
13.5 Marking 331
13.5.1 Laser Marking by Material Removal or Addition 331
13.5.2 Laser Marking by Material Modification 332
13.6 Microforming 333
13.7 Summary 333
References 334

Index 337

Contributors

Craig B. Arnold Department of Mechanical and Aerospace Engineering, Princeton Institute for Science and Technology of Materials, Princeton University, Princeton, NJ 08544, USA, cbarnold@princeton.edu

Thomas Baumert Institut für Physik and CINSaT, Universität Kassel, 34132 Kassel, Germany, baumert@physik.uni-kassel.de

Sébastien Besner Laser Processing Laboratory, Canada Research Chair in Laser Micro/nano Engineering of Materials, Department of Engineering Physics, École Polytechnique de Montréal, CP6079, Succ. Centre-ville, Montréal, QC, H3C 3A7, Canada, sebastien.besner@polymtl.ca

Matthew S. Brown Department of Mechanical and Aerospace Engineering, Princeton Institute for Science and Technology of Materials, Princeton University, Princeton, NJ 08544, USA, msbrown@princeton.edu

Magdalena Forster Department of Physical Chemistry, University of Vienna, Währinger Strasse 42, A-H1090 Vienna, Austria, magdalena.forster@univie.ac.at

Henry Helvajian Physical Sciences Laboratory, The Aerospace Corporation, MS:M2/241, P.O. Box 92957, Los Angeles, CA 90009, USA, Henry.Helvajian@aero.org

Ingolf V. Hertel Max Born Institute for Nonlinear Optics and Short Pulse Spectroscopy, 12489 Berlin, Germany, hertel@mbi-berlin.de
and
Fachbereich Physik, Freie Universität Berlin, 14195 Berlin, Germany

Jürgen Ihlemann Laser-Laboratory Goettingen, Germany, juergen.ihlemann@llg-ev.de

Wolfgang Kautek Department of Physical Chemistry, University of Vienna, Währinger Strasse 42, A-H1090 Vienna, Austria, wolfgang.kautek@univie.ac.at

Rainer Kling Laser Zentrum Hannover e.V, Germany, r.kling@lzh.de

Laurent J. Lewis Département de Physique et Regroupement Québécois sur les Matériaux de Pointe (RQMP), Université de Montréal, C.P. 6128, Succursale Centre-Ville, Montréal, (Québec), Canada H3C 3J7, Laurent.Lewis@UMontreal.CA

Michel Meunier Laser Processing Laboratory, Canada Research Chair in Laser Micro/nano- Engineering of Materials, Department of Engineering Physics, École Polytechnique de Montréal, CP6079, Succ. Centre-ville, Montréal, QC, H3C 3A7, Canada, michel.meunier@polymtl.ca

Anas Moalem Laser Zentrum Hannover e.V, Germany, a.moalem@lzh.de

Hiroyuki Niino National Institute of Advanced Industrial Science and Technology (AIST), Tsukuba, Ibaraki 305-8565 Japan, niino.hiro@aist.go.jp

Stefan Nolte Institute of Applied Physics, Friedrich-Schiller-University Jena, Max-Wien-Platz 1, 07743 Jena, Germany, stefan.nolte@uni-jena.de

Andreas Ostendorf Lehrstuhl für Laseranwendungstechnik und Meßsysteme, Ruhr-Universität Bochum, Germany, Andreas.Ostendorf@ruhr-uni-bochum.de

Danny Perez Theoretical Division T-1, Los Alamos National Laboratory, MS B-268, Los Alamos, NM 87545, USA, danny_perez@lanl.gov

Alberto Piqué Materials Science and Technology Division, US Naval Research Laboratory, Washington, DC 20375, USA, pique@nrl.navy.mil

Razvan Stoian Laboratoire Hubert Curien, UMR 5516 CNRS, Université de Lyon, Université Jean Monnet, 42000 Saint Etienne, France, razvan.stoian@univ-st-etienne.fr

Koji Sugioka Laser Technology Laboratory, RIKEN – Advanced Science Institute, Wako, Saitama 351-0198, Japan, ksugioka@riken.jp

Oliver Suttmann Laser Zentrum Hannover e.V, Germany, o.suttmann@lzh.de

Kunihiko Washio Paradigm Laser Research Limited, Machida, Tokyo, 195-0072 Japan, k-washio@paradigm-laser-research.jp

Wataru Watanabe Photonics Research Institute, National Institute of Advanced Science and Technology (AIST), Higashi 1-1-1, Tsukuba, Ibaraki, 305-8565 Japan, wataru.watanabe@aist.go.jp

Matthias Wollenhaupt Institut für Physik and CINSaT, Universität Kassel, 34132 Kassel, Germany, wollenhaupt@physik.uni-kassel.de

Chapter 1
Process Control in Laser Material Processing for the Micro and Nanometer Scale Domains

Henry Helvajian

Abstract An array of laser material processing techniques is presented for fabricating structures in the micro and nanometer scale length domains. For the past 20 years, processes have been demonstrated where the use of the inherent properties of lasers has led to increased fidelity in the processing of materials. These demonstrated processes often use inventive approaches that rely on derivative aspects of established primary principles that govern laser/material interaction phenomena. The intent of this overview is to explore the next generation of processes and techniques that could be applied in industry because of the need for better precision, higher resolution, smaller feature size, true 3D fabrication, and higher piece-part fabrication throughput.

1.1 Introduction

This is an overview of the possible laser material processing techniques that could be implemented in future industrial applications to realize process control. Lasers have been used in materials processing for over 50 years. In the early days, the focus was more on mitigating laser damage in the materials that were exposed rather than utilizing the laser light to process material itself. Nonetheless, the application of lasers to controllably alter materials was recognized early, and it has become an industry that now leads laser sales world wide [1]. The calendar 2005 sales totals for laser process tooling shows nearly $6.0 B USD [2]. The world market in 2007 is $8.6 B USD if sales of excimer lasers ($2.5 B USD) are also included. Excimer lasers are now mostly used in photolithography applications. Europe leads the world in the use of industrial lasers for manufacturing followed by the USA and Japan. Marking and engraving lead the industrial applications with 43% of the market followed by metal cutting (23%) and micro processing (13%).

H. Helvajian (✉)
Physical Sciences Laboratory, The Aerospace Corporation, MS:M2/241, P.O. Box 92957, Los Angeles, CA 90009, USA
e-mail: Henry.Helvajian@aero.org

K. Sugioka et al. (eds.), *Laser Precision Microfabrication*,
Springer Series in Materials Science 135, DOI 10.1007/978-3-642-10523-4_1,
© Springer-Verlag Berlin Heidelberg 2010

Modern lasers are now manufactured in clean rooms similar to those used in the microelectronics fabrication industry and are delivered as a sealed system with minimal user serviceable parts. Current lasers also include health and status monitoring subsystems, and these are used not only to help diagnose faults but also help maintain the laser output at the design level. Consequently, the reliability of laser systems has increased manifold in the past two decades, and it is one reason why there have been giant strides in laser based manufacturing. A second reason why lasers have been able to make inroads into manufacturing is because of the development of the all solid state and fiber lasers. These lasers can offer KW of laser power in a desktop footprint or watts of power that can be held in your hands. A final reason could be that industry is willing to accept laser based processing tools because it can conform to a twenty-first-century manufacturing vision; all tooling is under computer control for automation, designs "travel" to processing stations on the Intranet via computer-assisted-design/computer-assisted-manufacturing (CAD/CAM) software, and the machine tooling of choice is one that is adaptable and can produce a range of parts or conduct a series of manufacturing processes based on a common platform. Lasers and laser process tooling can reinforce/fit/enable this vision because as a directed energy source it can enable the deposition, the removal, and alteration of material primarily through changes in configuration (i.e., wavelength, power, dose, etc.). China, a global powerhouse in commodity manufacturing, has recognized the value of lasers and laser material processing in advanced materials development. It has identified lasers and advanced manufacturing (i.e., automation technology and advanced materials) as two of the eight frontier technologies warranting special support in the 15 year, medium-to-long-term, national plan called the 863 Program. China's industrial laser market in 2006 is estimated at 5.5 billion RMB ($800 M USD).

Given the manufacturing refinements that have been applied to lasers in the past few decades, the near global use of lasers to manufacture new commodities, and the recent trend of national rulers to identify lasers as a strategic tool, it is safe to conclude that laser material processing can no longer be considered a niche industry. Commensurate with this view is the fact that the number of conferences devoted to laser material processing continues to grow along with the number of journals that publish laser materials processing science and technology. Figure 1.1 shows a graph that depicts the number of worldwide publications per year that mention laser material processing in the title or the abstract. The data span nearly 40 years. The results represent a lower value to the total number of publications because there could be publications that discuss laser material processing research or development but fail to mention it in the title or abstract. The data are from an assembled series of databases that includes not only journal articles but also government sponsored research articles from the USA, Japan (e.g., MITI), Germany (e.g., BMFT), France (e.g., CNRS), Canada (e.g., NRC), UK (e.g., Department of Industry) and others. Furthermore, the data do not distinguish applications of laser material processing between the micro or macro domains. The figure shows that laser material processing, at least in terms of publications, began to grow in the early 1970s presumably with the first experimental observation of $Xe_2{}^*$ excimer laser emission in liquid by Basov et al. [3]. However, the publication rate does not grow in earnest until the mid

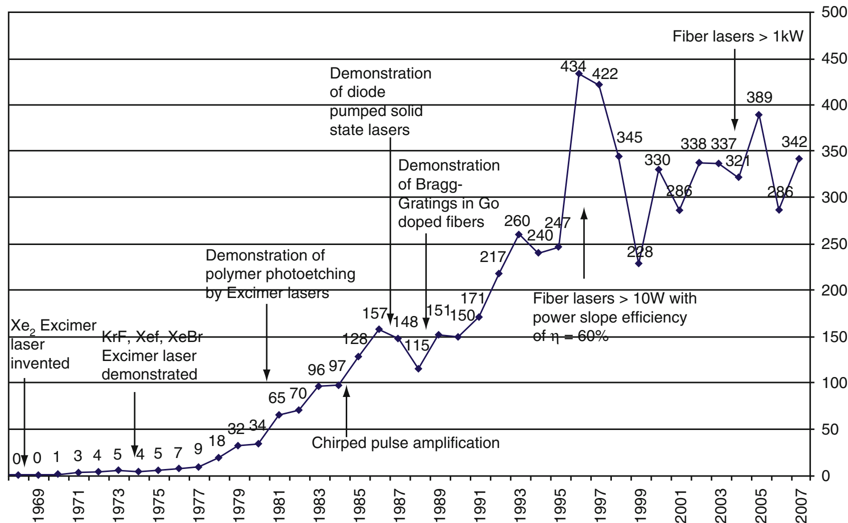

Fig. 1.1 The number of worldwide publications per year that mention laser material processing in the title or abstract with relevant developments noted

to late 1970s again presumably with demonstration of all the common excimer laser wavelengths [4–9]. In 1982, the observation of photoetching of polymers by excimer laser irradiation by Srinivasan et al. [10] and Kawamura et al. [11] demonstrated the usefulness of UV lasers in precision machining. With further developments and near simultaneous research, initially at Siemens Corporation [12], then at the IBM Corporation, IBM was successful in developing the laser microvia fabrication tool for electronics packaging which enabled high throughput circuit fabrication on a near 24/7 schedule [13, 14]. During the 1980s, several other technical innovations were demonstrated that would have major impacts for laser microfabrication. These innovations included: exploring Ti:Al_2O_3 as a laser medium by Moulton [15, 16] starting in 1982, understanding the behavior of solitons in fibers by Mollenauer et al. [17] in 1984, chirped pulse amplification by Strickland et al. [18] in 1985, and the demonstration of a femtosecond laser in 1989 by Ippen et al. [19] (for details see Chap. 3). Another relevant technological breakthrough in the 1980s was the US patent issued to Baer et al. at Spectra Physics Inc. [20] in 1987 for the feasibility of developing a diode pumped solid state laser. The patent and subsequent demonstrations showed that laser rods could be optically pumped by laser diodes instead of flashlamps. This enabled the development of higher repetition rate solid state lasers [21] with increasing average powers. In 1989 Meltz et al. [22] demonstrated the fabrication of Bragg gratings in Ge-doped fibers using excimer lasers and holography. The work was based on an earlier observation of laser induced index changes reported in 1978 by Hill et al. [23]. Progress in diode pumped solid state laser technology was significantly enhanced by the development of photosensitive cladding at Polaroid Corporation (USA), University of Southampton (UK) and other research institutions in the 1980s [24–26]. These breakthroughs enabled the development of diode pumped fiber lasers that crossed the 10W output power (and power slope

efficiency of 60%) mark around 1997 [27] and the 1 KW CW output power barrier, less than 10 years later, in 2004 [28, 29]. Finally, one notable event which does not appear in the selected database supporting the figure is the demonstration and development of optical coherent tomography (OCT) and its variants. As an imaging technology rather than a processing tool, OCT has allowed the biological and biophysical research communities to invest in laser sources for their research and development. OCT has its roots in the late 1980s [30, 31] but was demonstrated in medicine in the early 1990s [32–36] and now provides exceptionally high-resolution 3D cross sectional images and video of microstructures in biological materials including tissue. The OCT technology was transferred to industry in 1996 and is becoming a standard clinical instrument in ophthalmology. The consequence of all these developments is the establishment of laser processing applications in industry. A selected list relevant to the goal of this report is given in Table 1.1.

In this paper, we explore a small segment of the overall laser material processing industry, namely the use and application of lasers in micro and nanofabrication, an application area that in 2007 supported nearly 13% of the industrial laser sales. By their very nature of being a directed energy source, lasers have been the processing tool of choice when site-specific processing was desired. However, beyond just being able to deliver energy to a spot, much more sophisticated techniques and processes have been demonstrated for micro and nanofabrication. This has earned the laser the moniker, *the multifunctional tool*.

The goal of this paper is to present, by example, a select number of processes and techniques that enable the controlled fabrication/processing in micro/nano dimensions, with the stipulation that the chosen examples are conceivably scalable to the industrial environment. By the abbreviated set of applications presented in Table 1.1, it is clear that many processes and techniques have found their way into the industrial realm already. Therefore, the focus of this paper is to explore the *next possible generation of processes and techniques* that could find their way into the market place as a consequence of the need for better precision, higher resolution, smaller feature size, true 3D fabrication, and higher piece part fabrication throughput. This report does not place emphasis on a particular type of laser or a particular application, as for example, the two recent and excellent reviews on the application of femtosecond lasers to bulk modification of transparent materials [37, 38]. This report casts a broader net over the possible techniques that have been developed to gain advantage in fabricating/processing in the micro/nano scale domain. As a conceptual framework, the overview employs the commonly known laser processing parameters (i.e., wavelength, power, dose, etc.) as an inventory of possible control *knobs* and describes the techniques in terms of these *control parameters*.

All reviews have the fundamental shortcoming of not being able to capture all the important research in one document. Furthermore, in presenting certain technical results that now appear to show potential, the author is judging and assuming that all the remaining technical barriers will be solvable. It is a simple fact that a process with a demonstrated technical advantage is by itself not a sufficient condition that it will be successfully implemented in industry. Finally, this report places more emphasis in the development and application of laser processing to nonbiological applications; a fundamental decision made by the author.

Table 1.1 Relevant established laser processing examples in industry [13, 42, 163, 164]

Major process	Application examples
Micromachining	Micro via hole drilling in circuit interconnection packages
	Inkjet printer nozzle drilling (>600 dpi)
	Micro drilling in catheter probes for analyzing arterial blood gases
	Trimming of electronic passive elements
	Cleaning of semiconductor wafers
	Cutting for automotive combustion applications
	Glass cutting
	Photovoltaics (e.g., edge isolation and backside drilling for contacts)
	Microfluidic bio devices (e.g., travelling-wave dielectrophoresis systems)
Texturing	Surface texturing of landing zone in hard disk manufacturing
Irradiating	Sintering
	Recrystallization for displays
	Volumetric lithography
Shaping	Micro-cladding
	Micro nanobending
Joining	Sealing of glass, polymers, ceramics
	Electronics packaging in final step sealing
	Soldering (e.g., lead free solder and on laminates)
Separating	Dicing
	Insulation stripping in wires or fibers
Rapid Prototyping	Stereolithography
Scribing	Marking of silicon wafers and electronics packaging
	General marking applications
	Thin film solar cells (e.g., cell segregation)
	Flat panel display manufacturing (e.g., defining interconnect electrode circuitry)
Repair	Microelectronic circuits (open and shorted circuit elements)
Annealing	Micromechanical components
Holding	Optical tweezers
Photodynamic therapy	Treatment of cancer tumors in urinary tract and esophagus
Imaging	Flow cytometry for cell sorting and analysis
	Optical coherent tomography
	Two photon confocal microscopy in biological systems

1.2 Laser Processing

The basic intent of laser material processing is to use the energy/force of the laser electromagnetic radiation to alter a material property in a desirable and controllable manner. This action entails the delivery of the energy to the material at the right time and place to ensure the desired light/matter interaction (for details see Chap. 4). The fundamental initial interaction can be via an absorber present in/on the material (e.g., dopant or chromophore) or via an induced or transient excitation because of the high intensities achievable with lasers. Regardless, the initial light/matter interaction is always via an electronic excitation that quickly decays by electron-phonon

coupling to result in local heating. Therefore, the physics/chemistry of laser material processing is nearly always a coupled phenomenon of electronic and thermal events. To produce a predominantly electronic process requires the exercising of experimental controls that have high fidelity. Ironically, this is easier to do in the nanometer scale, less so in the micrometer scale, and even more difficult in larger dimension scales. A common approach to minimize thermally mediated processes is to utilize the time dimension to advantage (i.e., short pulse or femtosecond laser processing) or to employ a specific photochemical/physical process (e.g., bond scission). The use of a short pulse to minimize thermal excitation has been successfully applied in the scission of living biological samples without the need for sensitizing agents [39, 40] (for details see Chap. 6). Vogel et al. [40, 41] in a detailed investigation on the relevant mechanisms of femtosecond laser interaction with transparent biological media show that free electrons are generated over a large irradiance range *below* the optical breakdown threshold. As they rightly argue, this low density of plasma can be used to tune the nature of the light matter interaction (i.e., chemical and physical processes) by deliberately varying the irradiance. The proposed approach could serve to be a very powerful tool if the irradiance could be controlled with high fidelity. While this is possible albeit difficult in controlling chemical and physical processes, the use of the irradiance parameter to "tune" the physical outcome of a thermally mediated process has been applied and with some degree of success.

High precision materials processing via a thermally mediated action is feasible because such processes can be calibrated more easily and over larger dimensional areas (e.g., controlled stress-induced bending). Thermally mediated processes can also be modeled more easily using heat transfer modules found in most commercially available physics based software tools (e.g., COMSOL™, MEMCAD™). The European Union AMULET (Accurate Manipulation Using Laser Technology) project was designed to use lasers to make sub-micron precision adjustments with multiple degrees of freedom by controlled laser heating [42]. The laser induced stress-bending technique enables precise tolerances to be achieved where accessibility by humans or other tooling is not feasible. The AMULET test device was a microoptical system designed for digital audio/video recording systems where sub micron accuracy in multiple dimensions must be simultaneously achieved. Hoving et al. have argued that accurate positioning and fixation of delicate components is currently done by use of expensive *external* actuators or tooling which is costly, takes time, and cannot easily hold tolerances in multiple dimensions [42]. They further explain that in the future, the actuator tooling will be incorporated as part of the product. Therefore, laser induced manipulation could be used to provide submicron accuracy movements through short time scale local heating at tension points. In the AMULET project, both in plane and out of plane bending adjustments have been demonstrated in stainless steel and aluminum alloys with deformation control ranging from 0.1 to 5.0 mrad/pulse. A more recent investigation by Bechtold et al. uses a short pulse laser (100 fs) to ablate the actuator surface and using the ensuing recoil energy produces a calibrated tensile stress bend in the material [43]. Accurate bends were obtained not only in metals (steel, copper) but also in silicon and Pyrex glass. The latter materials have technological significance in the

development of microelectromechanical systems (MEMS) and micro-optic electromechanical system (MOEMS) where nanometer scale precision is commonly desired. Finally, using laser thermally mediated physics very recent work by Chou et al. [44] show that it is possible to utilize controlled laser liquefaction of patterned metal structures to fabricate more refined nanostructures in a post processing step. Using this technique, the 3σ line-edge roughness of a 70 nm wide chromium grating line was reduced from 8.4 nm to less than 1.5 nm. Intriguing is the observation that the height of the patterned line increases. The physics of this latter process is not yet well understood, but this author believes that an important factor could be the fluid dynamics of charged liquids or more specifically, Taylor cones [45].

Over the years, the realized improvements in laser material processing technology have come because the attributes of the laser light, the features of the beam delivery system, and the inherent properties in propagating coherent light have been used to advantage. These aspects can be categorized in terms of a controllable property that is commonly used in the processing of materials. A list is given below.

- Wavelength.
- Energy, power fluence, irradiance.
- Dose (e.g., number of applied laser shots).
- Processing beam character and spatial, temporal properties.
- Laser pulse "train".
- Pattern generation approach.

1.2.1 Laser Wavelength

In early industrial applications, the established laser material processing approach was to choose the closest available laser wavelength that achieved the intended process with most effectiveness. Discounting optically pumped dye lasers as impractical for most industrial applications, only a handful of fixed wavelengths were available from lasers deemed reliable. As the industry matured, there has been an increase in the number of available laser wavelengths. Consequently, in contemporary research, there is more emphasis in exploring laser material processing with multiple laser wavelengths in a pump-probe configuration. For the specific case of micromachining, experiments have demonstrated that processing with multiple laser wavelengths results in better micromachining if one of the wavelengths is able to generate a strong transient absorption. For example, in experiments in the late 1990s conducted by Sugioka et al. in Japan demonstrated the power of multi-wavelength laser processing on wide band gap materials. Both fused silica [46], SiC and GaN [47] were tried (for details see Chap. 12). Figure 1.2 shows the scanning probe microscopy results for 6H-SiC and molecular beam epitaxy (MBE) grown GaN samples.

The experiments in Fig. 1.2 used a combination of UV and VUV laser sources that were co-aligned and where the higher power UV laser photon energy was below

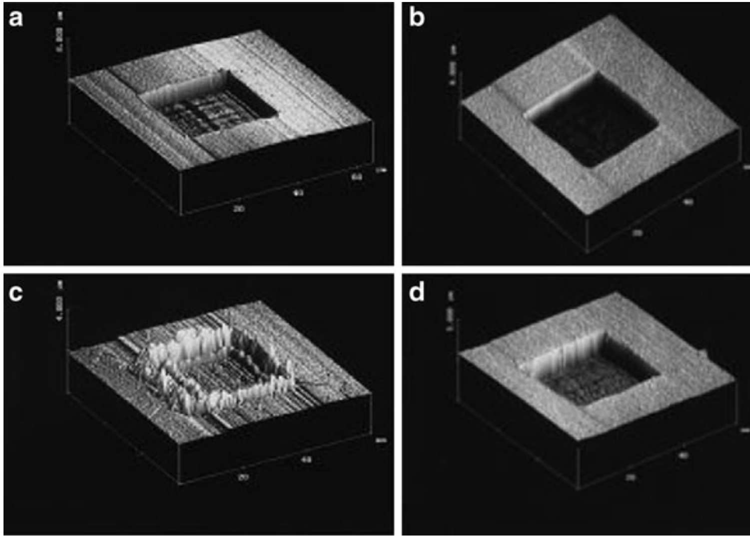

Fig. 1.2 Scanning probe microscopy images of two color laser machining of SiC (6H-SiC) (*left*) and MBE grown GaN (*right*). The top figures show the results with UV and VUV (133, 141, 150, 160, 171, and 184 nm) pulses present while the bottom figures show with only UV (i.e., 266 nm). Used with permission [47]

the material bandgap energy. A portion of the 266 nm Nd:YAG laser was antiStokes Raman shifted to generate VUV light with antiStokes components up to 6 measured (i.e., 160 nm) for the fused silica studies and up to 9 (133 nm) for the SiC and GaN studies. Clearly, the technique applies a nuance to the standard laser machining approach, but it is a nuance that enhances the process, and it can be applied in the industrial environment because it only requires one laser. The authors conclude that the multi wavelength ablation approach yielded a better surface finish in the ablated material [46] when compared to the 266 nm only irradiated samples. In the case of fused silica and from dynamic absorption experiments, the authors further concluded that it is not the steady state increase in the absorption generated by the VUV (i.e., scission of Si-0 bonds and creation of SiO_x, ($x < 2$)) that enhances the absorption. The amount of this absorption is deduced to be approximately 1% per laser pulse. The major effect is the transient change in the absorption which was measured to be nearly 60%. In a more recent systematic study by Zoppel et al. on silicon <100> using nanosecond and picosecond lasers, similar conclusions were reached in that multicolor ablation provided a higher ablation yield and left a better surface finish [48]. The experiments, as performed, required a small fraction of the fundamental IR pulse to be converted to the second harmonic wavelength (i.e., 532 nm). In the case of ns ablation (1,064 nm + 532 nm), the results show an enhancement of approximately 160% over the ablation results when only the fundamental IR laser is used with equivalent intensity. In the case of ps laser (Nd:Vanadate) ablation, the authors report a 70% enhancement in the ablation rate when 532 nm is present

and time synchronous with the IR 1,064 nm pulse. In all cases, the fluence of the harmonic laser light was kept well below the multipulse ablation threshold of the sample. These results can be understood by examining the fundamental photophysical light/matter interaction; if the initial laser pulse (i.e., pump) dynamically alters the material absorption properties to enhance the absorption of the second laser wavelength, then more energy can be controllably deposited in the material via two color processing approach. The dynamic absorption changes need not necessarily be via an electronic excitation but can also be via other processes (e.g., thermal, phase change). In the case of the silicon experiments, both the 1,064 nm (1.16 eV) and 532 nm (2.33 eV) excitation wavelengths are above the band gap of silicon (1.14 eV at 300 K), but because the band gap is indirect, there is no direct excitation possible without coupling to phonon modes. Therefore, it is difficult to argue, at least on first order principles that the enhancement is due to electronic excitation and excited state absorption. An alternative explanation for the enhancement in the ablation could be that after a single ablation event, the surface of the silicon is nominally covered with silicon nanocrystalline "debris". Recent experiments show that silicon nanocrystals have strong nonlinear absorptions at 532 nm [49, 50]. Given that the experiment utilized multiple laser pulses to measure the effect, nanocrystalline debris on the surface could possibly explain the observed enhancements with two colors. Regardless of the explanation, the fact remains that with two colors the results were more promising with regard to micro/nanofabrication.

Multicolor processing, if based on harmonics of the primary laser light, offers an exceptionally practical approach to realizing laser processing enhancements in the industrial environment. A simple alternative to two-color processing is tuning the laser wavelength beam at a very high speed. In some materials processing, the absorbed energy can be very long lived (e.g., $\mu s \rightarrow s$) allowing this approach to prove useful. Recent technical developments show that it is possible to electronically tune the wavelength of a soliton laser with very high speed [51]. Hori et al. show that the wavelength of their soliton fs pulses can be tuned from 1.61 to 1.94 μm at 2.5 μs intervals by merely altering the voltage of the acousto-optic modulator.

A potential extension of two color processing is chirp-pulse processing where there is a temporal distribution to the wavelengths in the band. Chirp-pulse processing requires a large optical bandwidth that is commonly present in femtosecond (fs) lasers. In a recent experiment, Louzon et al. show that chirp can enhance the ablation in wide band dielectrics (fused silica, MgF_2) [52]. A 20% reduction in the damage threshold was measured for negative chirp (high frequencies arrive first) at pulse durations ranging from 60 fs to 1 ps. Figure 1.3 shows the data. This dependence of damage on chirp direction was not observed in semiconductors (silicon, GaAs). Based on a model that includes electron generation and Joule heating, the authors conclude that the observed effect is related to the dominant role that multiphoton ionization plays in wide gap materials. A more recent experiment in support of chirp-pulse material processing is the fabrication of embedded optical waveguides of circular cross section in phosphate glass [53]. The fabrication intent was to create an index change without inducing damage. Ferrer et al. show that a positive chirp (i.e., low frequencies arrive first) on a 100 fs laser pulse (6.4 μJ) produces the most

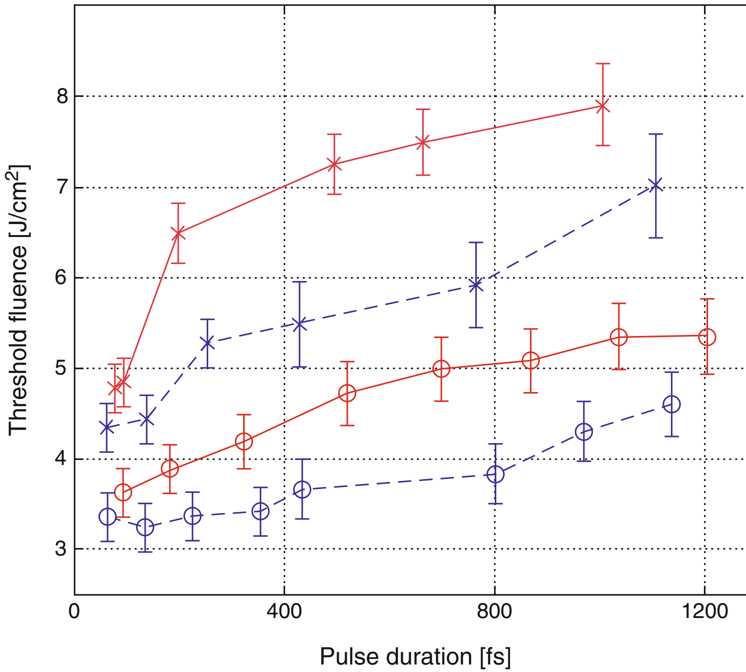

Fig. 1.3 The threshold damage fluence as a function of pulse duration in fused silica (*circles*) and MgF_2 (*crosses*), for positive (*solid red*) and negative (*dashed blue line*) chirp. Used with permission [52]

circular embedded waveguide. This result complements the earlier work of Louzon et al. where a negative chirp was shown to enhance damage. Of a more practical consequence is the conclusion drawn by Ferrer et al. that the use of chirp can be used as an optimization tool in the fabrication of embedded guided modes.

As more laser media and nonlinear optical materials are discovered, there will be more possible wavelengths for materials processing. Terahertz (THz) sources are becoming more powerful, and MASERS have been available longer than the LASER. These sources have wavelengths ranging from many micrometer (μm) to centimeter (cm), and it is not yet clear how they could directly lead to better material processing in the nano/micro dimensions. In the case of THz, the wavelength dimension should help in the manipulation or processing of macrobiological systems because the wavelength is on the order of a macro-molecular length and therefore a more "uniform" field interaction with the molecular dipole moment may be possible. For example, resonant frequencies of mammalian somatic cells are near 2.39 THz, chromosomes of different genic activity have resonances in the range 0.75–15 THz, and calculations show that lung alveoli should have resonances in the band from 0.3 to 0.5 THz [54]. In the case of inorganic material processing, the THz wavelength makes feasible a more uniform electric field interaction across a micron scale device. Furthermore, given that the condition for constructive interference is

related to the wavelength (i.e., $d \sin(\theta_n) = n\lambda$, where d is the distance between two emitters and θ is the interfering angle in between) and interference effects have been a bane in laser material processing, then processing of material in the micron or less dimensions could be freed from such interference effects by merely setting the incident angle θ.

In the past 15 years, free electron lasers (FELs) have made significant gains in both increasing the average output power (>10 KW) and in providing a source with a wide tuning range in wavelength (UV to far IR) [55]. Consequently, modern FELs have become research enabling tools [56]. These advancements have been realized because of two major innovations in FEL technology that surpassed all the development work that was conducted in the 1980s. These are the development of superconducting RF accelerator technology and a means for recovering the beam energy upon each recirculation. The consequence is that the estimated cost of delivering photons drops significantly and is predicted to be $0.02/KJ USD for a 100 KW class machine [57]. The practical consequence of this cost figure for micro/nanofabrication is the ability to process square km of material (e.g., surface texturing of material for antimicrobial applications) to exacting standards but on a very large scale. Finally, assuming that nonlinear optics technology continues to develop robust materials for sum and difference frequency mixing, a unique kind of laser processing *factory* could be developed given a high average power pulsed FEL. Imagine the FEL as a separate entity delivering light at low cost into a laser processing factory building much like electricity is delivered at any desired location. The FEL light would be distributed to numerous processing stations, and at each station an optical module would be present to convert the FEL light to a desired wavelength via nonlinear scheme. Locally, at each station, the FEL light is "processed" to suit the type of material processing being conducted. Unlike other material processing factories where lasers are used, in this scheme, the factory floor does not house power supplies to support each laser head. There is an additional capability that is realized with an FEL based factory. The FEL itself could be tuned to allow scheduled operation of specific laser processing stations where both resonance excitation and high average power are necessary.

1.2.2 Laser Power

A major processing control parameter is the on-target laser power (W), which can also be represented in terms of fluence (J/m^2)] or radiance (W/m^2) depending on the application. The established approach has been to maintain this parameter constant and within a prescribed *processing window*. Even though this common approach will continue to be of use in laser material processing, technologies now exist for controlling the laser pulse repetition rate and amplitude at the fidelity of individual laser pulses. Recent efforts have shown that the controlled variation of this parameter could enable processing advantages where different functional properties of the exposed base material are realized by mere consequence of the irradiation

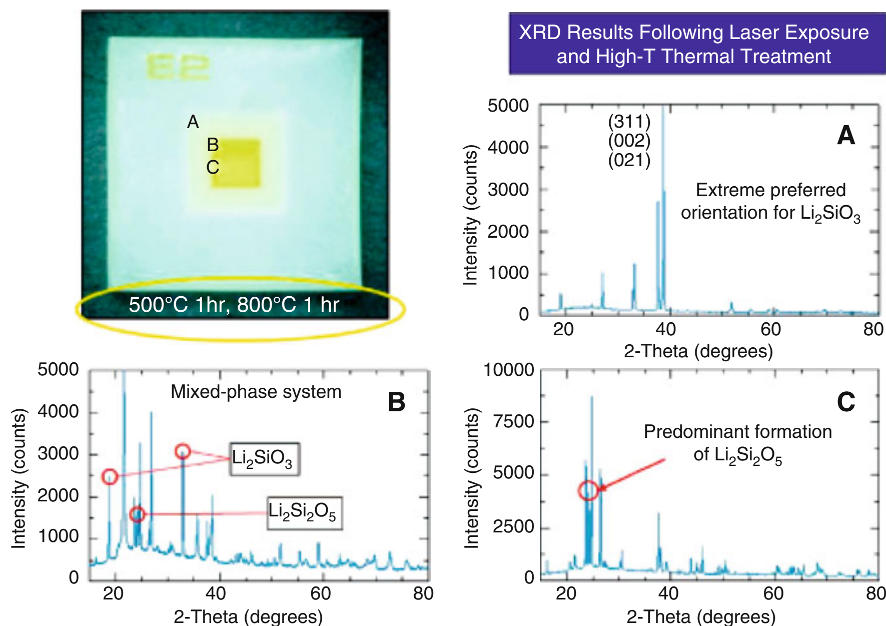

Fig. 1.4 Optical microscope photography of an exposed/baked photostructurable glass ceramic sample (*upper left*) in which each area received the same photon dose but with different distribution. Region A received 29 pulses for every spot size, region B received 153 laser pulses, and region C 305 laser pulses. XRD 2-θ data show that a chemical soluble crystalline phase has grown (*upper right*) while in region C a high temperature compatible (∼850 C) crystalline phase has grown (*lower right*). Region B shows both crystalline phases present (*lower left*) [59]

conditions [58]. In a series of experiments on photostructurable glass ceramics, Livingston et al. have been able to demonstrate that by keeping the total photon dose constant, but altering the irradiated photon distribution, two different crystals can be grown as a consequence of the different exposures. Figure 1.4 presents these results. The exposure was done using a UV 355 nm Nd:Vanadate laser operating at a 10 KHz repetition rate. A pulse delivery control system was developed to guarantee that each laser spot size (∼2 μm dia) during the direct-write patterning process (∼1 mm/sec) received the prescribed photon dose, no more, no less [59].

In laser material processing, the power can be controlled either internally to the laser using the inherent excitation and light amplification characteristics to advantage, or externally by use of a light valve and modulator (e.g., Pockels or acousto optic device). In the past and for pulsed lasers, the attempt to vary the laser power through internal schemes would always be at the expense of increasing the pulse-to-pulse instability. With the advent of the all solid state laser and with particular care in the design of thermal management, it is now possible for lasers to vary the laser power without incurring much loss in pulse-to-pulse stability. In fact, the current generation of pulsed lasers that are entering the market have the capability to create any pulse amplitude profile and controllably alter it on a pulse to pulse level.

In a recent publication, Murison et al. [60] discuss the development of a fiber laser system where the pulse width can be varied over a range from 1–250 ns with the temporal shape of each pulse arbitrarily tailored at 1 ns resolution. This type of control is achievable while the laser runs at a repetition rate of 500 KHz. The design uses optical modulators that have been integrated into the input and output of a double-pass amplifier which is driven by digital pulse shaping electronics. Another approach for controlling the laser power is the application of the techniques used for coherent laser beam combining [61], but with the additional feature that the individual laser beams are amplitude modulated. There continue to be strong technological advancements in the coherent combining of individual laser beams as an efficient method of providing high powers on a target. The reasons are that even though single mode fibers currently exist to produce low to medium power lasers, the fibers will ultimately be power limiting because of nonlinear effects and damage. Coherent beam combining obviates this problem by allowing for power scale-up by many orders of magnitude without degrading either spectral purity or beam quality. This technique may also be adaptable to power modulation (over a limited range) that is useful in laser material processing. In a recent paper, Liang et al. have demonstrated, in a proof-of-concept experiment, the coherent combining of two 100 mW 1,064 nm semiconductor lasers with an efficiency of 94% [62]. To achieve this extraordinary efficiency, the authors have implemented optical phase locked loops (OPLL) in their system. The OPLL enable very subtle control in beam combining and therefore could enable very high fidelity control of the total output power.

It has been evident from research [63] and now there appears to be commercial developments (e.g., the Pyroflex^{TM} from Pyrophotonics Inc. [60]) which point to laser processing approaches that could synchronously adapt to the time varying photophysical interaction. If this approach is to be the modus operandi in future laser processing, then the parameter, laser power on target, has less meaning. Similarly, concepts such as average laser power, irradiance, and fluence also loose meaning in conveying critical aspects of a photophysical interaction. Apart from intensity (photon flux(cnts/(cm^2-s))), parameters such as single pulse fluence (J/cm^2) and radiance (W/cm^2) also do not convey enough information. However, there are other parameters such as energy flux (J/(cm^2-s), energy transfer rate per mass (J/(g-s)), energy transfer rate per volume (J/(cm^3-s)) and for multiple wavelength excitations, irradiance (flux/wavelength(ergs/(cm^2-s-nm))), spectral irradiance (photon flux/wavelength (photons/(cm^2-sec-nm))), and photon number intensity (cnts/(cm^2-ster-s)) which take on a more meaningful role. Ultimately, the necessary information will be the profile of the photon distribution on target along with the integrated sum that represents the total energy deposited [64].

1.2.3 Laser Dose

In current laser material processing, the process dose is a parameter associated with the laser power. It is commonly defined as the number of laser shots for pulsed lasers and the exposure duration length for CW lasers. For a particular laser material

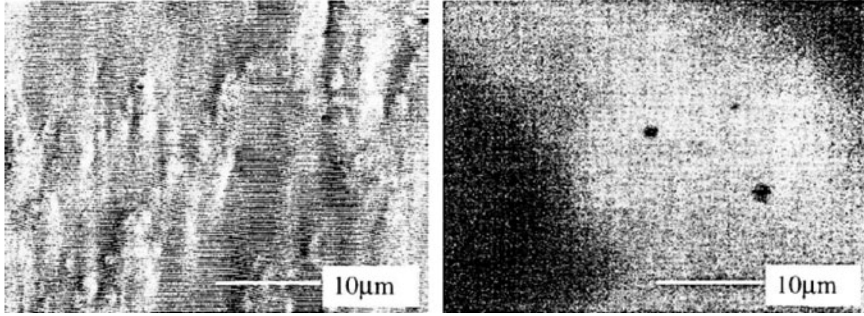

Fig. 1.5 Scanning electron microscopy images of laser chemically assisted etched areas in high quality sulfur doped <001> InP. The left image shows a surface irradiated at a fluence of 114 mJ/cm^2. The image at right was measured after laser irradiation at 73 mJ^2/cm^2. Used with permission [65]

process and over a select range of laser powers, there exists, in general, a tradeoff between applying a smaller number of pulses with high per pulse fluence or higher number of pulses at lower per pulse fluence. For micro and nanofabrication, it has been found that better results, in terms of surface finish and morphology, are possible with lower laser fluences and large number of laser pulses (or for CW laser processing, short duration with repeated exposures). These conclusions were made clear in the late 1990s by work in Canada on the laser chemical assisted etching of InP [65] as shown in Fig. 1.5. In developing a UV laser (308 nm) etching process for InP in the presence of chlorine and helium, Moffitt et al. found that at fluences for ablation and photodesorption (>114 mJ/cm^2), deposits of InCl compound remained. Furthermore, the surface took on a rough morphology with particulates around the etched areas. However, when the process was conducted at a lower fluence (73 mJ/cm^2), selective etching could be observed without inducing contamination. The authors conclude that a thermally mediated process is active but argue for the existence of a photochemical induced channel as well because the mixture of Cl/He does not spontaneously react with InP. An interesting result from this work is that when the low fluence irradiated samples were analyzed under high resolution SEM, the authors were able to document that with increasing laser shot number the surface morphology changed from exhibiting small ripple structures ($\sim$25 nm dia at 600 shots) to larger structures ($\sim$100 nm at 2,400 shots). This last observation has also been seen in the UHV low fluence laser desorption of crystalline aluminum <111> [66]. The general conclusion to be derived is that reducing laser fluence and increasing the number of laser shots *ad infinitum* do not necessarily lead to smoother and smoother surface morphologies. For optimum morphology, the photo induced surface electronic excitations which lead to organized structures, must be offset by a thermally mediated process.

Just 10 years ago, most pulsed laser repetition rates were well below the MHz capabilities that are currently available today. From an industrial perspective, applications that required a large number of low fluence pulses would have been

impractical (i.e., not cost effective). That perspective may no longer hold. At the present, MHz laser repetition rates are possible with tabletop systems delivering 10s of watts. Furthermore, more recent experiments have supported the notion that the application of a large number of pulses produces better processed material as opposed to small number of laser shots and higher fluences. The intuitive conclusion is that with higher fluences the destructive thermal effects cannot easily be mitigated through engineering. A particularly interesting example with large scale industrial applications is the laser synthesis of TiN_x functional coatings on pure titanium, by a high repetition rate free electron (FEL) laser. Following the pioneering work of Katayama et al. in the 1980s [67], Carpene et al. [68, 69] demonstrate that δ-TiN_x ($x \sim 1.0$) could be formed under pure nitrogen conditions as thick as 15 μm with an FEL. The FEL beam consisted of a series of 0.5–0.6 ps pulses at a laser repetition rate of 37.4 MHz with average pulse energy of 20 μJ. The authors had the ability to modify the irradiation conditions by controlling the length and repetition rate of the macropulses (i.e., a duration of time containing micropulses at 37 MHz). Figure 1.6 shows a SEM of the surface under different irradiation conditions with the surface roughness being reduced with increasing laser pulse number. Under experimental conditions with a specific laser dose, the nitride δ-TiN_x (200) crystallographic direction is aligned parallel to the irradiated surface with the aligned dendrites growing normal to the surface. In conclusion, the authors point out that

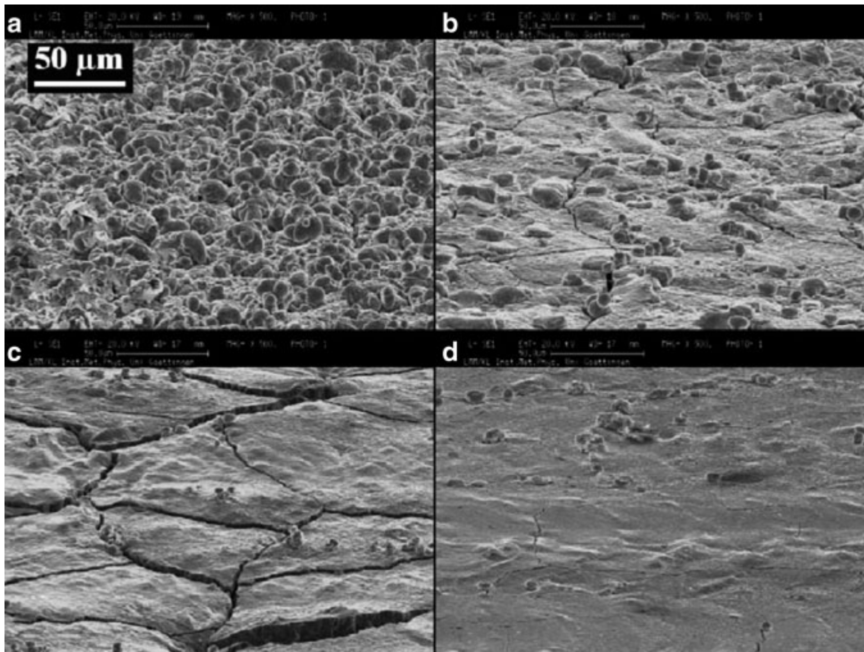

Fig. 1.6 SEM images of surface morphology of grown TiN under different experimental conditions. The images (**a**), (**b**), (**c**), and (**d**) essentially represent the surface morphology with increase in the number of micropulses (increasing macropulse duration). Used with permission [69]

other technologically interesting compounds (e.g., TiC, TiC_xN_{1-x}, ZrN, ZrC, TaN) with crystallographic and thermodynamic properties similar to TiN could be similarly grown.

A number of laser processing research studies have pointed to the use of more pulses and lower fluences. Consequently, this has generated interest on exploring the effects of tailored photon fluxes on materials processing. How might a desired photon flux be expressed for an application? One approach could be in the form of prescribed information scripts in which relevant processing parameters are defined and can be implemented by appropriate light valve devices on demand [64]. For the system to operate efficiently, the light valves must be integrated with in situ feedback from the photophysical event. This is likely to come via spectroscopic signatures that are sensed and analyzed for deciding the next course of action. The practical question is whether a photon flux control system, such as described, could be realized when operating at near real time processing speeds. The analysis is easier to do for a direct-write patterning tool. Assume a processing laser with 50 MHz repetition rate (pulses separated by 20 ns) that is brought to a 1 μm (dia) focus on a target. Assume also that the patterning tool can move at a hefty speed of 1 m/sec (e.g., Aerotech Corp. ABL8000 air bearing stage) which means that the patterning tool can service 10^6 spot-sizes/sec. At the maximum velocity, the average time the patterning tool spends over a single spot-size is 1 μs. There are now optical sensors with subnanosecond response times and typical electrical signal transfer times in common cabling run about 3 ns/m. Microprocessor speeds have significantly evolved in the past 15 years with the 2007 PC CPU tests showing the Intel CORE 2 Extreme QX6800 processor capable of over 37 GFLOPS (Giga FLoating point Operations Per Second). Finally, in the early 1990s, there was literature on acousto-optic modulators (e.g., Ti:$LiNbO_3$) with bandwidths near 20 GHz [70] and current analog to digital convertors (ADCs) can operate up to 2 G samples per sec (e.g., Delphi Engineering ADC3244: 2GSPS, 10 bit accuracy and an integral field programmable gate array). Given this information and the fact that for this example the average duration of time spent over a single spot-size is 1 μs, it becomes possible to assemble a control system whereby information from a sensor is analyzed by the microprocessor (e.g., for GO/NO-GO or via a complex decision tree), and this information is sent to a light switch which either adds or subtracts extra laser pulses accordingly.

1.2.4 Laser Beam

The size and shape of the laser processing beam can also serve as processing parameters. Typical processing approaches use single laser beams, Gaussian optics, and processing in the far field with diffraction effects as the limitation with regard to resolution. Contemporary techniques have displayed quite a bit of variety with regard to circumnavigating diffraction limitations. For example, there has been ample research in the use of multiple laser beams and the use of interference effects to fabricate true three dimensional periodic structures that appear to violate diffraction laws [71]; The primary driving application being the desire to develop

artificial crystals that have programmed photonic bandgaps [72, 73]. In the work of Seet et al. [71], photonic bandgap nanostructures have been fabricated in both polymethylacrylate (PMMA) and the negative epoxy based photoresist, SU8, using both laser direct-write patterning and multiple laser beam interference approaches (i.e., 5 laser beamlets at 34° half angle). The structures in PMMA were fabricated by dielectric breakdown, while in SU8 material photoinduced cross-linking was used. A variety of photonic crystal structures (woodpile and spiral arm) were fabricated with the lateral dimension of the repeating structure on the order of 230 nm. The Steet et al. work demonstrates that it is possible to fabricate complicated structures with extended depth via laser direct-write processing. While the use of multiple lasers and interfering beams have been used to make complex 3D structures, there are at least two advantages when using laser direct write patterning. First, it enables the fabrication of complex shapes that are not easily possible via simple interference. Second, and more importantly it simplifies the fabrication of defects. In the fabrication of photonic crystals, defect-engineering is important because it imbues them with functionality (e.g., waveguiding, reflection). Figure 1.7 shows an SEM perspective view of a spiral photonic crystal fabricated in SU8 with two interconnected L-shaped line defects patterned via laser direct write. Several novel processing features were employed in the direct write and multiple beam interference fabrication to circumvent the limitations of linear Gaussian optics. First, the authors implement multiphoton absorption by the use of an ultrafast laser. This technique has been utilized in much prior work and has its roots well over 20 years ago [74, 75]. Second, the experimental arrangement to induce interference among 5 pulsed laser beams is not trivial when each 150 fs optical pulse has a spatial length of 45 μm and all pulses must arrive at the same time. Just maintaining the optical alignment would be impractical for an industrial application. To realize this complex arrangement, the authors used a single laser source and a diffractive beam-splitter to form an annular array of transmitted beams. Then by simple masking, they could select the desired beamlets for refocusing on the sample. The consequence is that no relative

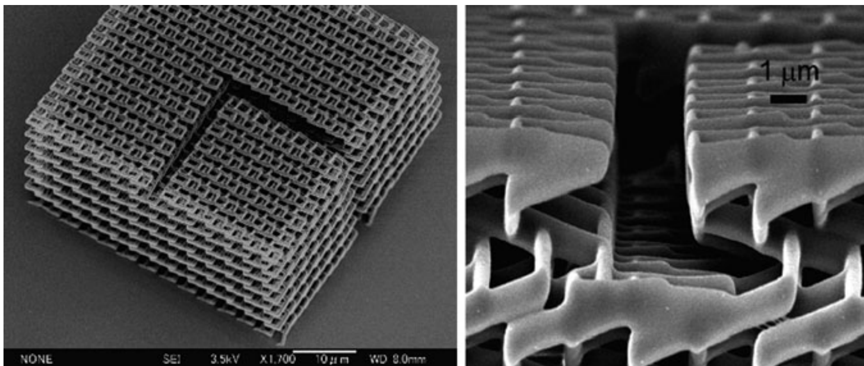

Fig. 1.7 An SEM image of a spiral shape photonic crystal fabricated by laser direct write processing. The lattice period is 1.2–1.8 μm. The figure also shows two interconnected L-shaped line defects also fabricated by direct-write. Used with permission [71]

delays are introduced and the approach becomes amenable to industrial use. Third, to further circumvent the limitations posed by the laser beam and Gaussian optics, the authors alter the properties of the SU8 material to advantage. By tailoring the pre-processing conditions (i.e., varying solvent content to match the exposure) and the bake protocols (multiple bake cycles), features with lateral dimensions on the order of 230 nm are realized using a laser wavelength of 800 nm. The calculated diffraction-limited beam diameter for 800 nm wavelength is 720 nm; $1/e^2$ level.

Other approaches have been used to circumvent the limits imposed by Abbé diffraction both for laser direct write and for mask based (i.e. lithography) laser processing. One is the implementation of techniques that allow optical radiation to be harnessed and used in the near field. Material characterization using the optical near field has been very successful from the point of microscopy (i.e., scanning near field optical microscopy; SNOM) [76–78], but it is still a spectroscopic probe and not a material processing tool. The SNOM technique integrates an optical near field sensor/source with an AFM tip to form a single unit where the AFM is used to establish and maintain distance. This single unit could be further integrated with a laser direct write tool that is intended for nanometer scale material processing (also see Chap. 8). The capabilities of SNOM and AFMs have continued to advance offering the possibility for "material processing" truly on the molecular scale. For example, in the work of Kaupp et al. [76], SNOM is used to probe surface hydration processes of crystalline phthalimide by monitoring the hydrolytic ring opening to generate phthalimide acid. Direct "imaging" after photochemical excitation could be envisioned in this experiment. Similarly, the work of Rangelow [78] demonstrates that the resolution of the surface topology near 0.1 nm is feasible with advanced AFM designs.

Photolithography is a critical element in the production of microelectronics devices and accounts for over a third of manufacturing costs in a typical wafer fabrication facility. Consequently, there has been extensive worldwide research to find means for circumventing the effects of diffraction or pushing the limits of diffraction while developing optical sources at shorter and shorter wavelengths. There is a strong commercial drive because reducing the half pitch from 65 nm (ca 2005) to 32 nm yields 4 times more memory on the same footprint and it is believed that processors could half in size while doubling speed. Currently, 193 nm sources (i.e., ArF laser) and immersion optics technologies (e.g., water) are extending use down to 45 nm half pitch where some form of EUV (extreme UV) source will be required at 13.5 nm for soft X-ray lithography. An alternative approach to further extend the usefulness of the 193 nm source is the application of Fourier masks and the use of multiple exposures or to take into consideration the etching properties of the exposed material. In the former case, two approaches are possible and both have been tried by the Brueck et al. group. The first approach uses laser interference exposure on the photoresist but with each exposure the phase, period and orientation are varied [79]. As a consequence of the multiple exposures, complex shapes are possible that scale as $\lambda/4$ instead of $\lambda/2$. A second approach uses two separate lithography masks instead of one. Each mask then selectively collects and images either the low or high spatial frequencies separately [80]. Using this approach, Chen et al. [80] were able to enhance the spatial frequency coverage of an optical system from

∼NA/λ (λ is the wavelength and NA is the numerical aperture) to ∼3 NA/λ. In 1998 Chen et al. produced an array of 90 nm dia dense holes using UV laser light (355 nm, Nd:YAG) [81]. Recently, Raub et al. [82] has developed an alternative approach that extends optical lithography by utilizing the anisotropic properties of crystalline silicon <100> to advantage. They first apply a protective layer mask in parallel to the <110> direction and chemically etch the silicon to form 57° grooves that are terminated at the <111> plane. The metal mask is stripped revealing the <100> surface, and the silicon is etched in KOH again. The result is a pattern at twice the spatial frequency of the original exposure. Using this technique with a 193 nm source (water immersion optics), they were able to achieve 22 nm half-pitch lines.

An interesting technique in very preliminary development stages is the conversion of the incident laser electromagnetic field to surface plasmon modes, enabling nanometer scale resolution processing. Plasmon modes have also been used to extend photolithography to sub wavelengths. Shao et al. have shown enhanced patterning resolution by exciting surface plasmons in a metallic mask that is in near contact with a substrate [83]. Finally, even though Gaussian beams and optics continue to dominate laser material processing at micro/nanometer dimensions, there is an increasing use of Bessel beams to enable long depth of field exposures in laser direct write processing [84] (also see Chap. 3). A recent development shows that Bessel beams need not have static focal properties. Mermillod-Blondin et al. have demonstrated a tunable acoustic gradient (TAG) index lens that is capable of dynamically altering the spatial intensity profile of an incident laser beam [85]. The TAG lens is fast, scalable in aperture, and nonpixilated. A variety of Bessel beams have been produced, and consequently this device opens the door for novel micromachining where the "scalpel" shape can be altered at will.

1.2.5 Laser Pulse Temporal Profile

Until the advent of femtosecond lasers, the natural temporal profiles of pulsed lasers were not altered except to remove temporal spikes resulting from mode beating. Dictated by material processing applications, the recent trend has been to develop lasers that are widely variable in pulse width; for example, there are laser systems that can be tuned from 4–20 ns [86] or from 40 to 300 ns while maintaining constant energy [87]. The development of the Pyroflex laser by Pyrophotonics, as discussed above, provides even more flexibility to the user; namely that each laser pulse shape can be tailored with 1 ns resolution [60]. The advent of femtosecond lasers has enabled a more profound scheme for controlling temporal profiles. Through selective filtering of the laser bandwidth (e.g., 40 fs pulse laser ∼25 nm bandwidth), the temporal profile can be altered at a level that is amenable to controlling molecular reactions. The capability has been applied to control the branching ratios of organometallic (e.g., $CpFe(CO)_2Cl$) photodissociation reactions [88] in the selective formation of molecules (e.g., CH_3CO from $(CH_3)_2CO$ acetone) [89] and to the control of matter in general [90,91]. As might be expected, pulse shaping also affects micromachining

quality. Stoian et al. [92] proved this in an experiment on dielectric materials, for example, a-SiO_2, CaF_2 (for details see Chap. 5). The nonintuitive result from that experiment is that a single uniform pulse profile may not necessarily yield the best machined surface. The results show that a pulse profile spanning nearly 2 ps yields a better hole than a single uniform fs pulse. The authors conclude and there is evidence to support their claim that shaped or articulated pulses work best for brittle materials with strong electron to phonon coupling because, in essence, the shaped pulses allow for controlled heating and therefore the potential for relaxing the induced stresses. In a more recent experiment on fused silica and using a spectral phase modulation technique to shape the pulse, Wollenhaupt et al. [93] demonstrated that hole diameters on the order 100 nm could be fabricated by a 790 nm wavelength fs laser (i.e., 35 fs FWHM) that was focused to a 1.4 μm spot size ($1/e^2$ level) (see Chap. 5). The intriguing aspect is that the diameter of the hole is one order of magnitude below the diffraction limited diameter of the focused laser. Unlike the pulse shape used by Stoian et al., the shaped pulse in the Wollenhaupt et al. experiment resembles an asymmetric series of pulses with decreasing amplitude over time. Both the Stoian et al. and Wollenhaupt et al. experiments reveal a second conclusion. The best quality machining is achieved using a train of laser pulses. This conclusion echoes prior work that laser pulse trains result in better quality machining over single shot events. This concept was demonstrated in a systematic study in 1999 on fused silica. Herman et al. [94] demonstrated that a burst of mode locked pulses (i.e., ∼400 identical 1 ps pulses with 7.5 ns pulse to pulse separation) produced a higher quality ablation (i.e., less microcracking and shock induced effects) in comparison to a single high fluence laser pulse. Very smooth and deep (∼30 μm) holes on the order of 7–10 μm in dia were produced. Furthermore, when the samples were viewed under a Nomarski microscope, no evidence of fractures, cracks, or surface swelling could be measured. In a more recent investigation on steel, Pivovarov et al. [95] demonstrated that pairs of ns pulses also result in higher ablation rates over single pulses given the same energy density. The data show that there is a factor of 2 increase in ablation rate for pairs of laser pulses where the first (i.e., pump) is the lower fluence pulse. The factor of 2 increase is only accomplished if the single pulse ablation is conducted in vacuum (1 mbar). If the double pulse data are compared to the single pulse ablation rate at 1,000 mbar (i.e., the preferred industrial processing condition), the ablation rate increase is a factor of nearly 50. The observed differences of multiple pulse versus single pulse ablation have been referred to in the laser material processing lexicon as *incubation* effects [96]. Even though incubation or the increase concentration of defects does play a role, it could very well be that it is the dynamics of the localized heating/cooling under multiple pulses that drive the more efficient process for some materials.

Recently, there has been a development that enables the modulation of the amplitude, number of pulses, and polarization of each delivered laser pulse to generate a modulation script (i.e., a concatenated series of amplitude and polarization settings) that can be seamlessly mapped to the prescribed toolpath pattern. It is applicable for a direct write tool. Livingston et al. [97] have demonstrated a technology that uses commercial off the shelf translation stages with commercially available CAD/CAM

software that allows a design engineer to choose appropriate modulation scripts during the design phase (i.e., CAD). The choices are integrated into the G-Code tool-path program and implemented during the run. A similar technology can be developed where the laser pulse shape is chosen during the product design phase to realize a particular type of processing. Technologies as described above will be necessary, if direct write laser processing is to make further inroads into the industrial market.

Laser pulse shaping and polarization control will find its nexus in the area of nanofabrication and molecular quantum control. Even though laser polarization has been a controllable parameter for many decades [98], the ability to change the polarization on a molecular dynamics time scale was not possible. Light matter interaction is described by the vectorial quantities $\boldsymbol{\mu}\cdot\mathbf{E}(t)$, where $\boldsymbol{\mu}$ represents the transition dipole moment vector and $\mathbf{E}(t)$ is the time varying electric field vector of the laser. Conventional laser pulse shaping techniques alter the amplitude of the electric field as a function of time but leave the direction of the electric field vector untouched. The need to control the laser polarization vector arises because in a quantum system, the polarization state generally follows the temporal evolution of the molecular dynamics to maximize population transfer. Recent developments show that both pulse shape and polarization could be controllably varied on ultrafast time scales [99]. These techniques are sure to be important in biophysical and photophysical investigations, but they may also find use in nanometer scale laser material processing; for example, in surface texturing where structures on the surface form in specific directions related to the laser polarization vector.

In most pulsed laser processing applications, the irradiated material in the focal plane is commonly examined as the result of a single causal event; namely the laser pulse. There is no differentiation in the regions within the focal plane of separately evolving dynamical processes. However, the speed of light is determinate and there can be circumstances where viewing the focal plane from the perspective of multiple causal events becomes an advantage. These circumstances become probable for some short pulse width ultrafast lasers. Consider this gedanken experiment. Assume a 10 fs laser that is focused to a submicron spot size defined as region A (the Ti:Sapphire laser medium has a fluorescence bandwidth that supports the direct generation of sub-10 fs pulses centered at 800 nm). To further simplify the example, we assume that region A absorbs some of the light but does not fluoresce and merely scatters the balance. Therefore, at the end of the laser pulse the scattered light from region A will have traveled 3 μm. Species located in a region defined as B that is 6 μm from the focal spot center will not yet be affected from the event that occurred in region A. The scattered light will require 20 fs more time before it reaches and effects region B. In the cases where region A does not only scatter light but emits other forms of energy (i.e., heat, shock), region B would feel these effects much later and perhaps for a much longer duration of time. Why is this realization important? Region B, the area near the exposure, is typically called the "heat affect zone". Now consider the following circumstance and further realization.

- Assume a 10 fs laser pulse is focused to a 9 μm diameter laser spot.
- We define Region A as a 3 μm diameter circle in the center and Region B anything outside this circle.

- For a finite but practical duration of time
  (a) The exposed material on the left side of Region A will not sense the ongoing effects on the exposed right side.
  (b) This is also similarly true for all regions outside Region A.
- The experimentalist (i.e., overall observer) knows, a priori, an event will occur in region A and that only after a finite time will region B "feel" the effects of the event in region A.

Question: Can the observer/experimentalist set in motion events in region B in anticipation of the upcoming effects? For example, temporarily "softening" the surface in region B to mitigate the effects of shock induced damage from the intense pulse to be deposited in region A. This capability will require the generation of different pulse shapes (or scripts) that affect different regions within the focal area differently. This requires the control of femtosecond pulse shapes in two spatial dimensions. This technology has been developed and is used to investigate structural changes in condensed matter and the collective modes of motion through which it occurs. The first reported results were by the Nelson group at MIT (USA) in 2002 [102]. Figure 1.8 shows data from the Nelson group. The image is a 2D assembly of second harmonic generated cross correlation signals (i.e., measuring the pulse shape/delay) as a function of spatial position on the 2D liquid crystal spatial light modulator (i.e., used to imprint phase modulation on the laser to pulse shape). A β-barium borate (BBO) crystal is used to generate the second harmonic signals and spatial recording is done with a CCD camera. As the authors point out, because a 2D pulse shaper can irradiate a sample with different pulse shapes at different locations, it can permit the manipulation of propagating excitations. As an application tool, this technology makes attainable the suggestion of using spatial-temporal control to "guide" the flow of excess deposited energy away from a laser irradiated zone and possibly into a local energy "sink".

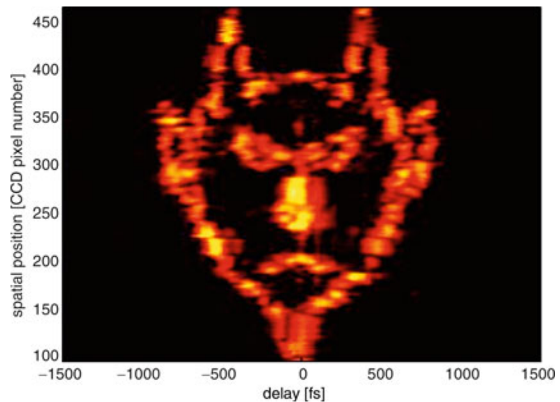

Fig. 1.8 A CCD image of a cross correlation signal in two dimensions. For example, at pixel location 200 the fs pulse shape has intensity at $\sim\pm$ 500 fs from zero delay, while at pixel location 100 all the laser energy is concentrated near zero delay. Used with permission [162]

1.2.6 Pattern Generation

In laser material processing, patterns are generated either via lithography (masks and imaging) or via direct write processing, for example, use of a multi axis motion stage or galvanometers (for details, see Chap. 10). Patterning with masks and lithography tends to be costly at high resolution, while direct write patterning being a serial process is generally slower. A novel but practical extension to the traditional fixed mask lithography technique has been the use of spatial light modulators to realize a dynamic mask [100]. The technique does reduce cost by enabling the ability to make rapid design changes. An alternative extension has been the use of fixed masks that move synchronously with the laser pulse (i.e., mask-dragging) [101]. Using this technique, Holmes et al. have been able to fabricate structures that have a graded exposure. For example, turbines with slanted blades have been fabricated by using laser ablation and mask dragging techniques. Patterning via mask lithography can be low cost if the desired patterns can be formed from an assembly of diffraction effects. The use of optical diffraction around structures has been used as a natural patterning source [102]. Pattern generation has also been reported and used via a self organization process that occurs after multiple overlapping laser pulses irradiate a chromium thin film on a glass substrate [103]. These ad hoc maskless patterning approaches currently remain as research efforts until means are found to generate more complex patterns. However, techniques have been developed that borrow heavily from traditional phase mask technology and holography, and these do show promise. Two techniques in this realm are the novel use of phase Fresnel lenses and holographic exposure techniques to make patterns of arbitrary features on a large scale [104].

In the specific area of direct-write patterning where the substrate or the laser beam is moved, there have been novel extensions to the basic idea also. One primary development that appears to have wide applicability is patterning via laser induced forward transfer (LIFT) [105] (for details see Chap. 11). Tóth et al. first demonstrated this technique where a transfer tape holds the desired species to be transferred and the absorbed laser energy within the transfer tape forces the transfer of the material to a substrate. This technique is reminiscent of old typewriters but has been demonstrated in the transfer of metal [106], electronic circuit elements [107], liquid droplets [108] and biological materials [109]. Many of the recent advances in LIFT with regard to the transfer of circuit elements and biological materials have been developed and refined by the Naval Research Laboratory group (USA). LIFT has the potential capability to replace traditional pick and place machines used in microelectronics. In contrast to the traditional machines, LIFT has the added feature that following the transfer of circuit elements to specific locations on a circuit board, the elements can be wired or miniature batteries (super-capacitors) can be locally deposited all using the same tool. In a recent publication, Piqué et al. [107] used a high viscosity metallic nanoparticle suspension ink as the transfer "tape" to pattern conductive silver lines with resistivity as low as $3.4\,\mu\Omega$ cm (i.e., 2.1 times the resistivity of bulk silver metal). LIFT is used to transfer the ink and a second

laser is used to cure and harden it. The ink has sufficiently high viscosity that a 3D suspended bridge can be fabricated by using LIFT. In this technique, LIFT is used to transfer the two landing segments (2 laser pulses), and this is followed by the transfer of the bridge section (one laser pulse) with the bridge ends supported by the landings leaving a suspended bridging section in between.

Because laser direct write processing is more versatile than the use of masks and lithography, it has engendered a more variety of fabrication processes, much like when laser chemical vapor deposition (laser CVD) came into existence in the early 1980s [110, 111]. Three of the more recent processes that appear to have practical applications are laser induced plasma assisted ablation (LIPAA) [112] (for details see Chap. 12), laser induced backside wet etching (LIBWE) [113] (for details, see Chap. 12), and volumetric exposure 3D patterning (3DVEP) [114–116] (also see Chap. 9). LIPPA and LIBWE were developed in Japan by the Sugioka et al. and Niino et al. groups, respectively, while 3DVEP is a development from our laboratories. In the case of LIPPA, the substrate to be patterned is "assisted" by the inclusion of an adjacent metallic surface, while for LIBWE the surface is placed in contact with a laser absorbing chemical reagent. The 3DVEP technique is merely an exposure technique that relies on the properties of a photosensitized glass ceramic. All three techniques share an important point that makes these processes practical. In all three cases, the first step is a serial process (i.e., laser direct write), but the subsequent steps are a batch process and can be done in parallel. The important idea is that the key step of the patterning can be done via serial mode at relatively high speed. In LIPPA, the goal is to deposit a seed metal layer on the substrate in the shape of a pattern via plasma assisted ablation. Different metal seed layers (e.g., Cu, Al) have been deposited allowing for a single substrate to have multiple pattern metallization. In LIBWE, the goal is to fabricate trenches and holes in a transparent medium. The process uses the intense laser light at the reagent substrate interface to induce chemical etching. The chemical etching rates can be relatively high (15 nm/pulse at 1 J/cm^2, $\lambda = 248$ nm), very deep trenches can be fabricated (>300 μm) with high aspect ratio (∼33–50). Even though 3DVEP is an exposure process, it differs from traditional lithography and photoresist material. The exposed pattern can have complicated true 3D shapes with embedded cavities if a coordinated motion three axis direct write tool is used. Furthermore, depending on the choice of the processing steps following the exposure, the exposed regions can either be converted to a crystalline phase that is soluble in hydrofluoric (HF) acid or to an alternative crystalline phase that is not soluble but is high temperature compatible (∼850 C). In addition, the conversion to the soluble phase and chemical etching not only allows for the selective removal of material but it also enables the back filling of the host with other materials. Using this technique, an eight wafer device has been fabricated that includes multi wafer fluidic vias, nozzles, micro/macro cavities, and microstructures that separate the gas from a high pressure liquid. The device with electronics and 3D metallization is a prototype propulsion unit for a mass producible small 1 kg class spacecraft [117]. All three techniques, LIPPA, LIBWE, and 3DVEP, operate most efficiently in the micrometer dimension.

A complementary set of techniques is also being developed that show pattern resolution capability in the sub micron to nanometer dimensions. One example is the work of Burmeister et al. where molecular self-assembly techniques are used to pattern surfaces using a nanoparticle contact mask that can be washed after exposure [118]. Although this approach has the capability to pattern 2D structures with resolution near 100 nm, it cannot achieve resolution down to the molecular level. The potential for near molecular level patterning was revealed by the recent demonstration from Denmark [119]. Duroux et al. have developed a photonic technique whereby UV light is used to sterically orient and immobilize a large variety of protein molecules onto either a thiolated quartz, gold, or silicon surfaces. The immobilized proteins can be further functionalized to serve as molecular scaffolding for further growth by chemical reaction. Therefore, it is conceivable that by utilizing a combination of high resolution mask lithography, control of the dose at or near the exposure threshold level and, controlling the protein concentration, large scale patterning near the molecular limit could be achieved. Figure 1.9 shows a microscope image with fluorescent tagging of UV-immobilized and patterned cutinase. The protein was immobilized, but not destroyed (i.e., de-natured), in a 4×4 pattern by focusing a frequency tripled Ti-Sapphire laser ($\lambda = 280$ nm) onto a moving stage. The technique has applications in allowing the coupling of drugs, proteins, bioactive peptides, nucleic acids, and other molecules to nano scale dimension structures such as nanoparticles.

A variant of this concept has recently been demonstrated on the micron size scale by a group in Greece. The technique uses photo polymerization of an organic/inorganic glass (OCMOCER) to form a scaffolding on which biologically active systems can be patterned by biotin photolysis [120]. Farsari et al. employed 3-photon polymerization to fabricate a 3D structure (e.g., woodpile shape) that shows minimum feature sizes on the order of 2 μm. The complete 50×50 μm area was made bioactive by attaching biotin/streptavidin (with Atto 565 fluorescent label).

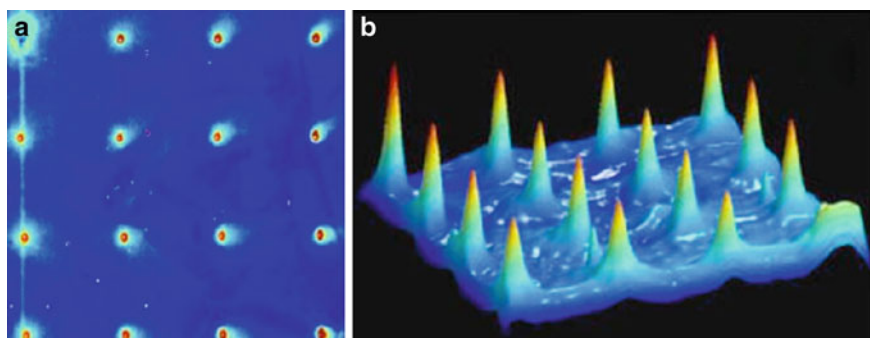

Fig. 1.9 MATLAB processed microscope fluorescent image of a 4×4 array of UV-immobilized cutinase labeled with Alexa Fluor 488 without micro dispensing. (**a**) A 2D view of the array. (**b**) A 3D view of the same array with integrated fluorescence intensity information on the z axis. Images have different scale. With permission [119]

1.3 Possible Steps Forward

Several interesting experiments have recently come to light where the use of laser processing could yield new application areas. For example, there is always the desire to develop novel alloys or composite phase materials in order to better adapt materials to applications. However, the development of new material formulations using traditional methods can be costly. There is an increasing need to develop specific alloys that are not to be used in bulk form but more as surface treatments (i.e., on the micro/nanometer scales); an example is the nitriding of metals for creating corrosion resistant surfaces. A recent technique labeled as laser interference metallurgy by Lasagni et al. [121] could be used in the development of new alloys. Lasagni et al. use a multilayered metallic thin films (i.e., Fe/Cu/Al) and laser interference heating/ablation to melt and generate a periodic surface microstructure. Upon closer examination, the microstructures appear to be an array of possible metal alloys. These intermetallic alloys (e.g., $CuAl_2$, Al_2Cu) have dimensions on submicron scales. They are first partitioned by focused ion beam (FIB) and then characterized by TEM, EDX, and STEM spectroscopy. This technique presents the possibility of quickly investigating a range of alloys. For example, the authors give examples of the many possible intermetallic phases that Al and Cu can form (e.g., Al_4Cu_9, Al_2Cu_3, AlCu). In this research, scale up is the real issue, however the technique could at least expand the development of novel alloy materials. A variant of this technique has been used to produce metal nanoparticles on desired substrates by the controlled laser nanostructuring of a single very thin metallic film (i.e., 6–10 nm) [122]. Henley et al. demonstrate that metal nanoparticles can be produced on a range of oxide substrates including indium tin oxide (ITO) by pulsed laser irradiation/melting. The nanoparticles form on the surface by self organization. Even though, the goal was to investigate the photonic properties of nanoparticles (e.g., Ni particles on 100 nm ITO/glass), the potential for applying this technique to the in situ and local fabrication of chemically catalytic surfaces is evident. Catalytically active surfaces can be patterned on a post assembled part making follow on chemical treatments easier. In another recent experiment, lasers have been used to fabricate novel micro/nanostructures in thermally confined spaces [123]. Dogaev et al. use substrates that have micro patterned surface structures that have been prior machined. These structures are on the micron scale and are physically separated to minimize heat transfer between the structures. The researchers then use laser irradiation to apply heat to these micro scale features to grow submicron and possibly nanometer scale structures. The types of submicron structures that can grow or be fabricated are strongly affected by the dynamics of laser heating and cooling in confined spaces. The technique has merit beyond just an investigation on thermal confinement physics. In many applications the desired nanometer scale or submicron structure has to physically reside on a larger micron size feature usually called a pedestal. With this technique, it becomes possible to develop processes for the fabrication of small structures that reside on pedestals. Furthermore, because the structural boundaries are well delineated, thermal modeling maybe simplified.

Notwithstanding the fact that nearly all laser fabrication processes are ultimately thermally mediated, there is the hope that at some future time where there is better understanding of the fundamental processes and the delivery of laser photons reaches a sufficiently high fidelity, it would be possible to modify solid state materials by direct electronic excitation. Material modification by electronic excitation naturally lends itself to nanofabrication at the atomic scale. Evidence for the viability of this kind of processing extends back over twenty years with work from many researchers being compiled in the book by Itoh and Stoneham [124]. The process was labeled photon stimulated desorption (PSD) which followed even prior work on electron stimulated desorption (ESD). The conclusion from many investigations including that of Itoh and Stoneham demonstrate that desorption induced by electronic transition (DIET) is possible and for some applications (i.e., nanofabrication), even practical. In PSD experiments, the photon energy required must be commensurate with the atomic core shell energy of the desorbing species. Traditional DIET requires photons at very high energies ($\gg 10\,\text{eV}$), and this is typically generated by x-ray sources with its consequent low fluxes. However, a number of experiments have been done with pulsed lasers (photon energies 3–5 eV) where species desorption was attributed to a DIET-like (i.e., nonthermal) mechanism [125–131]. In these experiments, the ion species desorbed flux shows a highly nonlinear dependence with the incident photon flux. Furthermore, the kinetic energy (KE) of the desorbed species does *not* depend on the laser fluence. DIET-like processes have been invoked because the desorbed species yield distinct KEs and the yields are well below any laser induced plasma process. Nevertheless, the photophysics of laser DIET is still controversial and not yet very well understood. However, what is evident is the key role of surface defects. The evidence for this comes from the work of Dickinson et al. in the USA, that covers a 15 year investigative effort on many systems but which started with MgO and NaCl [132, 133]. Given that defects play a significant role in laser desorption, consider the fact that defects can be patterned a priori into a material by FIB or laser techniques to enable the removal of selected species at critical processing steps. From an applications perspective, if pulsed laser desorption processes could be better controlled, then it is conceivable to realize atomic level processing [130]. However, this author believes that for some systems, such as metals, an alternative mechanism could be harnessed to yield nanofabrication at the near atomic level. When laser photons irradiate a nonsmooth metal surface both surface and volume plasmons [134, 135] are excited contrary to the laws that dictate the impossibility of the event. Both surface and volume plasmons propagate, releasing their energy upon annihilation at defect sights. The generation of surface and bulk plasmons by laser excitation could be utilized to induce atomic level material processing at pre-patterned defect sites. The use of plasmon excitation for material modification has already been demonstrated most recently in the nanometer domain by a Japanese group [136]. In a simple experiment, Atanasov et al. demonstrate the fabrication of nanoholes ($\sim$150 nm dia, 30 nm deep) on silicon by femtosecond laser ($\lambda = 820\,\text{nm}$) pulses below the damage threshold of silicon. The nanoholes appear only when gold nanoparticles (e.g., 200 nm dia) are placed on the surface.

The authors imply that the formation of the hole is mediated by localized surface plasmon polariton excitation in the gold nanoparticles (also see Chaps. 8 and 12).

In the nearer term and a growing application area is the use of lasers, mostly pulsed, to selectively induce phase transformation in an amorphous material. The process entails the use of a laser to provide a transient heating/cooling profile which enables the growth of crystalline matter or the precipitation of a particular material phase within a host. Recent experiments that have shown the applicability of the technique comes from the work of Yonesaki et al. [137]. Using a focused IR femtosecond pulsed laser (120 fs, $\lambda = 800$ nm), the authors were able to demonstrate the site-selective precipitation of crystals with large second-order nonlinear optical susceptibilities. Various nonlinear crystals were grown in their respective glass hosts; For example, $LiNbO_3$ crystals in Li_2O–Nb_2O_5–SiO_2, $BaTiO_3$ in Na_2O–BaO–TiO_2–SiO_2, and Ba_2Ti–Si_2O_8 in BaO–TiO_2–SiO_2, respectively. The existence of the nonlinear crystals could be directly measured via second harmonic emission at 400 nm from the 800 nm laser pump. In a similar experiment, the laser induced phase transformation of the perovskite structure $BaTiO_3$ thin film from the non-pyroelectric cubic polymorph to the pyroelectric tetragonal polymorph has been demonstrated and shows the promise that laser techniques with direct write control can open a new generation of sensor development [138]. The ability to directly pattern *active* material simplifies the development of integrated systems as for example where a nonactive material is first assembled into the unit then activated. For optical applications where the alignment of the optical axis is crucial, this approach obviates the need for additional alignment. However, the ability to transform a material between two phases repeatedly enables other applications. For example, optical recording and for some material systems, the ability to develop very complex shape 3D MEMS. As discussed above, the family of photostructurable glass ceramics has the property that a particular material phase is soluble in hydrofluoric acid. Using a CW CO_2 laser, Veiko et al. [139] have recently demonstrated the reversible phase transformation in the lithium aluminosilicate glass system which is a photostructurable glass ceramic. The authors conclude that the structural modifications can be orders of magnitude faster (e.g., 10^2–10^3) than conventional heating approaches. While the transformation speed may not be as important a factor in the development of MEMS, it is in optical recording. In the early 1990s, Afonso et al. demonstrated ultrafast reversible phase change in thin films of the chalcogenide GeSb [140]. The authors then pointed to the large application area for erasable optical storage. The work was continued in the same group and Solis et al. [141] demonstrated the need for optimizing Sb concentration to meet the demands of optical data storage applications. Further investigations by this group have included crystallization kinetics (e.g., Sb_x-$Se_{100\text{-}x}$ [142, 143] with the forethought that to gain the most benefit, both the material and the laser process conditions must be optimized together. A somewhat similar conclusion has been reached in a more recent experiment on VO_2. Vanadium dioxide is a nonmagnetic compound that is known to undergo an insulator/metal phase transition at a critical temperature ($T_c = 340$ K). The transfer to the metallic phase has been measured to be within 70 fs [144] while the recovery to the insulating phase is much longer (∼ns) because it is driven by diffusion [145].

Recent experimental results by Rini et al. [146] using femtosecond laser excitation show that upon reaching the metallic state, the absorption spectrum exhibits a surface plasmon resonance at telecommunication wavelengths. The authors make the argument that this resonance could be further shifted into better resonance by altering the shape of the embedded VO_2 nanoparticles. Perhaps true coherent control within a material could be exercised by utilizing the near field effects of shaped embedded nanosystems within a host. This kind of "processing" or control was recently put forth by Stockman et al. [147].

There is ample evidence in the literature that for laser material processing to further advance, material developers must be engaged to help design and tailor materials for the specific laser/material interaction process that is desired. This idea was aptly demonstrated, now over a decade ago, by Lippert in collaboration with polymer scientists. The experiments proved that by chemically altering the chromophore group in the polymer backbone, the micromachining of triazenopolymers could be radically improved [148]. Despite the desire and necessity of developing tailored materials, there is an ultimate challenge that can be placed on material developers. The challenge is to develop protean (i.e., variable, mutable, adjustable) materials that can be light activated. Then by choosing the laser wavelength, photon flux, pulse shape, and exposure dose, the protean material can be imbued with various desired properties that are commensurate with the application at hand [149]. This author believes the glassy/amorphous material state is a good starting place to demonstrate protean behavior.

1.4 Conclusions

In summary, the laser material processing community now supports a worldwide industry with sales measured in $B USD. A number of textbooks, spanning over 20 years, now document the research and technology developments in precision micro and nanofabrication [71, 107, 124, 150–161]. Over the same time duration, there have been dramatic strides in laser technology with smaller footprint, pulse stability, and reliability being the current hallmarks and the controllable delivery of a prescribed photon flux being a capability on the horizon. Commensurate with this progress, there has been the development of a vast array of laser processing techniques that utilize the unique properties of the laser to evident advantage and thereby add value to the manufactured unit. There are many "possible steps that point forward". However, to further advance into realms not yet reached, this author believes a closer collaboration with material scientists will be required.

Acknowledgments The author acknowledges The Aerospace Corporation's Independent Research and Development Program for providing funding to write this review. The author also acknowledges the support from The Air Force Office of Scientific Research (Dr. Howard Schlossberg, Program Manager Physics). All trademarks, service marks, and trade names are the property of their respective owners.

References

1. D.A. Belforte, Laser Technik J. **5**(3), 10 (2008)
2. A. Mayer, Laser Technik J. **3**(3), 16 (Wiley, Weinheim, 2006)
3. N.G. Basov, V.A. Danilychev, Y. Popov, D.D. Khodkevich, Zh. Eksp. Fiz. i Tekh. Pis'ma. Red. **12**, 473 (1970)
4. S.K. Searles, G.A. Hart, Appl. Phys. Lett. **27**, 243 (1975)
5. E.R. Ault, R.S. Bradford, M.L. Bhaumilk, Appl. Phys. Lett. **27**, 435 (1975)
6. J.J. Ewing, C.A. Brau, Appl. Phys. Lett. **27**, 350 (1975)
7. C.A. Brau, J.J. Ewing, Appl. Phys. Lett. **27**, 435 (1975)
8. J.A. Mangano, J.H. Jacob, Appl. Phys. Lett. **27**, 495 (1975)
9. G.C. Tisone, A.K. Hays, J.M. Hoffman, Opt. Commun. **15**, 188 (1975)
10. R. Srinivasan, V. Mayne-Banton, Appl. Phys. Lett. **41**, 576 (1982)
11. Y. Kawamura, K. Toyoda, S. Namba, Appl. Phys. Lett. **40**, 374 (1982)
12. F. Bachmann, Chemtronics **4**, 149 (1989)
13. J. Brannon, Proc. SPIE **4637**, 474 (2002)
14. J.R. Lankard Sr., G. Wolbold, Appl. Phys. A **54**, 355 (1992)
15. P.F. Moulton, Presented at the 12th International Quantum Electronics Conference, Munich, Germany, (unpublished) (1982)
16. P.F. Moulton, J. Opt. Soc. Am. B **3**(1), 125 (1986)
17. L.F. Mollenauer, R.H. Stolen, Opt. Lett. **9**(1), 13 (1984)
18. D. Strickland, G. Morou, Opt. Commun. **56**, 221 (1985)
19. J. Mark, L.Y. Liu, K.L. Hall, H.A. Haus, E.P. Ippen, Opt. Lett. **14**, 48 (1989)
20. T.M. Baer, M.S. Keirstead, USA Patent No. 4,701,929, 1987
21. R.L. Byer, Science **239**, 742 (1988)
22. G. Meltz, W.W. Morey, W.H. Glenn, Opt. Lett. **14**(15), 823 (1989)
23. K.O. Hill, Y. Fujii, D.C. Johnson, B.S. Kawasaki, App. Phys. Lett. **32**(10), 647 (1978)
24. S.B. Poole, D.N. Payne, M.E. Fermann, Electron. Lett. **21**(17), 737 (1985)
25. R.J. Mears, L. Reekie, I.M. Jauncey, D.N. Payne, Electron. Lett. **23**(19), 1026 (1987)
26. P. Urquhart, IEE Proc. **135**(6), 385 (1988)
27. B. Rossi, Laser Focus World **33**(5), 143 (1997)
28. Y. Jeong, J.K. Sahu, D.N. Payne, J. Nilsson, Electron. Lett. **40**, 470 (2004)
29. A. Liem, J. Limpert, H. Zellmer, A. Tunnermann, V. Reichel, K. Morl, S. Jetschke, S. Unger, H.R. Muller, J. Kirchhof, T. Sandrock, A. Harschak, in *Proc. Conference on Lasers and Electro-Optics*, CLEO, San Francisco, CA, Vol. Post deadline paper, pp. CPDD2 (2004)
30. R.C. Yougquist, S. Carr, D.E.N. Davies, Opt. Lett. **12**, 158 (1987)
31. K. Takada, I. Yokohama, K. Chida, J. Noda, Appl. Opt. **26**, 1603 (1987)
32. D. Huang, E.A. Swanson, C.P. Lin, J.S. Schuman, W.G. Stinson, G. Fujimoto, Science **254**, 1178 (1991)
33. A.F. Fercher, C.K. Hitzenberger, W. Drexler, G. Kamp, H. Sattmann, Amer. J. Ophthalmol. **116**, 113 (1993)
34. J.M. Schmitt, A. Knuttel, M. Yadlowsky, R.F. Bonner, Phys. Med. Biol. **42**, 1427 (1994)
35. J.M. Schmitt, M. Yadlowsky, R.F. Bonner, Dermatology **191**, 93 (1995)
36. J.G. Fujimoto, M.E. Brezinski, G.J. Tearney, S.A. Boppart, B.E. Bouma, M.R. Hee, J.F. Southern, E.A. Swanson, Nature Med. **1**, 970–972 (1995)
37. K. Itoh, W. Watanabe, S. Nolte, C.B. Schaffer, MRS Bull. **31**, 620 (2006)
38. R.R. Gattass, E. Mazur, Nat. Photonics **2**, 219 (2008)
39. W. Watanabe, N. Arakawa, S. Matsunaga, T. Higashi, K. Fukui, K. Isobe, K. Itoh, Opt. Express **12**(18), 4205 (2004)
40. A. Vogel, J. Noack, G. Huttman, G. Paltauf, Appl. Phys. B **81**, 1015 (2005)
41. A. Vogel, J. Noack, G. Huttermann, G. Paltauf, J. Phys. Conf. Ser. **59**, 249 (2007)
42. W. Hoving, Proc. SPIE **3097**, 248 (1997)
43. P. Bechtold, M. Schmidt, JLMN **2**(3), 183 (2007)
44. S.Y. Chou, Q. Xia, Nat. Nanotechnol. **3**(5), 295 (2008)

45. J.F. de la Mora, Annu. Rev. Fluid Mech. **39**, 217 (2007)
46. K. Sugioka, S. Wada, Y. Ohnuma, A. Nakamura, H. Tashiro, K. Toyoda, Appl. Surf. Sci. **96–98**, 347 (1996)
47. J. Zhang, K. Sugioka, S. Wada, H. Tashiro, K. Toyoda, K. Midorikawa, Appl. Surf. Sci. **127–129**, 793 (1998)
48. S. Zoppel, J. Zehetner, G.A. Reider, Appl. Surf. Sci. **253**, 7692–7695 (2007)
49. S.B. Korovin, A.N. Orlov, A.M. Prokhorov, V.I. Pustovoi, M. Konstantaki, S. Couris, E. Koudoumas, Quantum Electron. **31**(9), 817 (2001)
50. P. Cheng, H. Zhu, Y. Bai, Y. Zhang, T. He, Y. Mo, Opt. Commun. **270**, 391 (2006)
51. T. Hori, N. Nishizawa, H. Nagai, M. Yoshida, T. Goto, IEEE Photonics Technol. Lett. **13**, 13–15 (2001)
52. E. Louzon, Z. Henis, S. Pecker, Y. Ehrlich, D. Fisher, M. Fraenkel, App. Phys. Lett. **87**, 241903 (2005)
53. A. Ferrer, V. Diez-Blanco, A. Ruiz, J. Siegel, J. Solis, Appl. Surf. Sci. **254**(4), 1121–1125 (2007)
54. O.V. Betskiy, V.V. Kislov, V.F. Kirichuk, A.P. Krenitskiy, A.V. Majborodin, A.P. Rytik, V.D. Tupikin, D.A. Usanov, Joint 30th International Conference on Infrared and Millimeter Waves & 13th Intl. Conference on Terahertz Electronics, 305 (2005)
55. S.V. Benson, G.R. Neil, C. Bohn, G. Biallas, D. Douglas, F. Dylla, J. Fugitt, K. Jordan, G. Krafft, L. Merminga, J. Preble, M. Shinn, T. Siggins, R. Walker, B. Yunn, Proc. SPIE **3889**, 309–314
56. G.S. Edwards, Proc. SPIE **5725**, 210 (2005)
57. G.R. Neil, DOE/ER/40150–345 Report No. CONF-950512–383 (1995)
58. E.F. Livingston, H. Helvajian, J. Photochem. Photobiol. A Chem. **182**, 310–318 (2006)
59. F.E. Livingston, L.F. Steffeney, H. Helvajian, Appl. Phys. A **93**(1), 75 (2008)
60. R. Murison, B. Reid, R. Boula-Picard, R. Larose, and T. Panarello, in *9th International Symposium on Laser Precision Microfabrication*, Vol. #08–73, ed. by K. Sugioka (JLPS, Quebec, Canada, 2008), pp. 1
61. B. Lei, Y. Feng, Opt. Commun. **281**, 739–743 (2008)
62. W. Liang, N. Satyan, F. Aflatouni, A. Yariv, A. Kewitsch, G. Rakuljic, H. Hashemi, J. Opt. Soc. Am. B **24**(12), 2930 (2007)
63. F.E. Livingston, L.F. Steffeney, H. Helvajian, Appl. Surf. Sci. **253**, 8015 (2007)
64. F.E. Livingston, H. Helvajian, in *Laser Processing of Materials: Fundamentals, Applications, and Developments* ed. by P. Schaaf (Springer, Berlin Heidelberg, 2009), Vol. Materials Science
65. C.E. Moffitt, J.M. Wrobel, D.M. Wieliczka, J.J. Dubowski, J.W. Fraser, Proc. SPIE **274**, 121 (1998)
66. D.P. Taylor, H. Helvajian, Proc. SPIE **3618**, 171 (1999)
67. S. Katayama, A. Matsunawa, A. Morimoto, S. Ishimoto, Y. Arata, J. Metals **35**, 85 (1983)
68. E. Carpene, M. Shinn, P. Schaaf, Appl. Phys. A **80**, 1707 (2005)
69. E. Carpene, M. Shinn, P. Schaaf, Appl. Surf. Sci. **247**, 307 (2005)
70. R.L. Jungerman, C. Johnsen, D.J. Mcquate, K. Salomaa, M.P. Zurakowski, R.C. Bray, G. Conrad, D. Cropper, P. Hernday, J. Lightwave Technol. **8**(9), 1363 (1990)
71. K.K. Seet, T. Kondo, V. Mizeikis, V. Jarutis, S. Juodkazis, H. Misawa, Proc. SPIE **6161**, 616103 (2005)
72. J.D. Joannopoulos, P.R. Villeneuve, S. Fan, Solid State Commun. **102**(2–3), 165 (1997)
73. E. Yablonovitch, Phys. Rev. Lett. **58**(20), 2059 (1987)
74. N. Bloembergen, *Nonlinar Optics*, 4th edn. (W. A. Benjamin, Inc., Reading, 1982)
75. V.S. Letokhov, *Nonlinear laser chemistry: Multiple-photon excitation*. (Springer, Berlin, 1983)
76. G. Kaupp, A. Herrmann, J. Schmeyers, J. Boy, J. Photochem. Photobiol. A Chem. **139**, 93096 (2001)
77. D. Bäuerle, G. Wysocki, L. Landström, J. Klimstein, K. Piglmayer, J. Heitz, Proc. SPIE, 8 (2003)

78. I.W. Rangelow, Microelectronic Eng. **83**, 1449 (2006)
79. S.H. Zaidi, S.R.J. Brueck, J. Vac. Sci. Technol. B **11**, 658 (1993)
80. X. Chen, S.R.J. Brueck, Proc. SPIE **3331**, 214 (1998)
81. X. Chen, A. Frauenglass, S.R.J. Brueck, Proc. SPIE **3331**, 496 (1998)
82. A.K. Raub, D. Li, A. Frauenglass, S.R.J. Brueck, J. Vac. Sci. Technol. B **25**(6), 2224 (2007)
83. D.B. Shao, S.C. Chen, App. Phys. Lett. **86**, 253107 (2005)
84. J. Amak, K. Yoshimura, D. Sawaki, T. Shimoda, Proc. SPIE, 497 (2005)
85. A. Mermillod-Blondin, E. McLeod, C.B. Arnold, Appl. Phys. A **93**, 231 (2008)
86. R. Patel, M.L. Stock, Z. Sartania, J. Bovatsek, A. Arai, H. Endert, Proc. SPIE **4830**, 352 (2003)
87. W. Wiechmann, L. Eyres, J. Morehead, J. Gregg, D. Richard, W. Grossman, in Proceedings of 4th International Conference LAMP, 1 (2006)
88. A. Assion, T. Baumert, M. Bergt, T. Brixner, B. Kiefer, V. Seyfried, M. Strehle, G. Gerber, Science **282**(5390), 919 (1998)
89. R.J. Levis, G.M. Menkir, H. Rabitz, Science **292**(5517), 709 (2001)
90. S.A. Rice, M. Zhao, *Optical control of molecular dynamics*. (Wiley, New York, 2000)
91. M. Shapiro, P. Brumer, *Principles of the quantum control of molecular processes*. (Wiley, New Jersey, 2003)
92. R. Stoian, M. Boyle, A. Thoss, A. Rosenfeld, G. Korn, I.V. Hertel, Proc. SPIE **4830**, 435 (2003)
93. M. Wollenhaupt, L. Englert, A. Horn, T. Baumert, *Proceedings of LPM2008-the 9th International Symposium on Laser Precision Microfabrication* (JLPS, Quebec City, Canada, 2008)
94. P.R. Herman, A. Oettle, K.P. Chen, R.S. Marjoribanks, Proc. SPIE **3616**, 148 (1999)
95. P.A. Pivovarov, S.M. Klimentov, V.I. Konov, F. Dausinger, Proc. SPIE **6606**, 66060Y1 (2006)
96. S. Preuss, H.C. Langowski, T. Damm, M. Stuke, Appl. Phys. A **65**(4), 360 (1992)
97. F. Livingston, H. Helvajian, Proceedings of the 6th International Symposium on Laser Precision Microfabrication (LPM2005) (2005)
98. J.I. Steinfeld, *Molecules and Radiation: An Introduction to Modern Molecular Spectroscopy*, 2nd edn. (MIT, Cambridge, Massachusetts, 1979)
99. T. Brixner, T. Pfeifer, G. Gerber, M. Wollenhaupt, T. Baumert, in *Femtosecond Laser Spectroscopy*, ed. by P. Hannaford (Kluwer, 2004), Vol. Progress in Lasers, p. 229
100. W.G. Oldham, Y. Shroff, Microelectronic Eng. **73–74**, 42 (2004)
101. A.S. Holmes, M.E. Heaton, G. Hong, K.R. Pullen, P.T. Rumsby, Proc. SPIE **5063**, 152 (2003)
102. O. Van Overschelde, G. Guisbiers, M. Wautelet, Appl. Surf. Sci. **253**, 7890–7894 (2007)
103. M. Gedvilas, G. Raciukaitis, K. Regelskis, P. Gecys, J. Laser Micro/Nanoeng. **3**(1), 58 (2008)
104. S. Hasegawa, Y. Hayasaki, N. Nishida, Opt. Lett. **31**(11), 1705 (2006)
105. Z. Tóth, T. Szörényi, A.L. Tóth, Appl. Surf. Sci. **69**(1–4), 317 (1993)
106. Z. Kántor, Z. Tóth, T. Szörényi, Appl. Surf. Sci. **86**(1–4), 196 (1995)
107. A. Pique, R.C.Y. Auyeung, H. Kim, K.M. Metkus, S.A. Mathews, in *Proceedings of LPM2008-the 9th International Symposium on Laser Precision Microfabrication* (JLPS, Quebec City, Canada, 2008)
108. M. Duocastella, P. Serra, J.M. Fernandez-Pradas, M. Colina, J.L. Morenza, in *4th International Congress LAMP* (JLPS, Kyoto, Japan, 2006)
109. C.Z. Dinu, V. Dinca, J. Howard, D.B. Chrisey, Appl. Surf. Sci. **253**, 8119–8124 (2007)
110. D.J. Ehrlich, R.M. Osgood Jr., T.F. Deutsch, App. Phys. Lett. **39**, 957 (1981)
111. M. Meunier, T.R. Gattuso, D. Adler, J.S. Haggerty, App. Phys. Lett. **43**(3), 273 (1983)
112. Y. Hanada, K. Sugioka, I. Miyamoto, K. Midorikawa, Proc. SPIE **5713**, 445 (2005)
113. Y. Kawaguchi, H. Niino, T. Sato, A. Narazaki, R. Kurosaki, J. Phys. **59**, 380–383 (2007)
114. K.M. Davis, K. Miura, N. Sugimoto, K. Hirao, Opt. Lett. **21**(21), 1729 (1996)
115. E.N. Glezer, M. Milosavljevic, L. Huang, R.J. Finlay, T.H. Her, J.P. Callan, E. Mazur, Opt. Lett. **2023** (1996)
116. W.W. Hansen, S.W. Janson, H. Helvajian, Proc. SPIE **2991**, 104 (1997)
117. S. Janson, P.H. Huang, W. Hansen, L. Steffeney, H. Helvajian, in *Space 2005* (AIAA, Long Beach, CA, 2005), Vol. AIAA-2005–3650

118. F. Burmeister, W. Badowsky, T. Braun, S. Wieprich, J. Boneberg, P. Leiderer, Appl. Surf. Sci. **144–145**, 461–466 (1999)
119. M. Duroux, L. Duroux, M.T. Neves-Petersen, E. Skovsen, S.B. Petersen, Appl. Surf. Sci. **253**, 8125 (2007)
120. M. Farsari, G. Filippidis, T.S. Drakakis, K. Sambani, S. Georgiou, G. Papadakis, E. Gizeli, C. Fotakis, Appl. Surf. Sci. **253**, 8115–8118 (2007)
121. A. Lasagni, C. Holzapfel, T. Weirich, F. Mucklich, Appl. Surf. Sci. **253**, 8070 (2007)
122. S.J. Henley, J.D. Carey, S.R.P. Silva, Appl. Surf. Sci. **253**, 8080 (2007)
123. S.I. Dogaev, N.A. Kirichenko, A.V. Simakin, G.A. Shafeev, Appl. Surf. Sci. **253**, 7987 (2007)
124. N. Itoh, A.M. Stoneham, *Materials modification by electronic excitation*. (Cambridge University Press, Cambridge, UK, 2001)
125. N. Itoh, K. Hattori, Y. Nakai, J. Kanasaki, A. Okano, R.F. Haglund Jr, in *Laser Ablation: Mechanisms and Applications*, Vol. 389, ed. by J.C. Miller, R.F. Haglund Jr (Springer, Berlin, 1991), p. 213
126. E. Matthias, H.B. Nielsen, J. Reif, A. Rosen, E. Westin, J. Vac. Sci. Technol. B **5**(5), 1415 (1987)
127. H. Helvajian, S. Welle, J. Chem. Phys. **91**, 2616 (1989)
128. S. Kano, S.C. Langford, J.T. Dickinson, J. Appl. Phys. **89**, 2950–2957 (2001)
129. H.S. Kim, H. Helvajian, J. Phys. Chem. **95**, 6623 (1991)
130. L. Wiedeman, H.S. Kim, H. Helvajian, Adv. Mat. for Opt. Electr. **2**, 31 (1993)
131. L. Wiedeman, H.S. Kim, H. Helvajian, in *Laser Ablation Mechanisms and Applications*, Vol. 389, ed. by J.C. Miller, R.F. Haglund Jr (Springer, Berlin, 1991), p. 350
132. R.L. Webb, L.C. Jensen, S.C. Langford, J.T. Dickinson, J. Appl. Phys. **74**(4), 2323 (1993)
133. R.L. Webb, L.C. Jensen, S.C. Langford, J.T. Dickinson, J. Appl. Phys. **74**(4), 2338 (1993)
134. H. Helvajian, Proc. SPIE **2403**, 2 (1995)
135. D.P. Taylor, H. Helvajian, Phys. Rev. B **79**(1), 075411 (2009)
136. P.A. Atanasov, H. Takada, N.N. Nedyalkov, M. Obara, Appl. Surf. Sci. **253**, 8304 (2007)
137. Y. Yonesaki, K. Miura, R. Araki, K. Fugita, K. Hirao, J. Non-Crystalline Solids **351**, 885 (2005)
138. F.E. Livingston, W.L. Sarney, K. Niesz, T. Ould-Ely, A.R. Tao, D.E. Morse, Proc. SPIE **7321**, 732101 (2009)
139. V.P. Veiko, G.K. Kostyuk, N.V. Nikonorov, A.N. Rachinskaya, E.B. Yakovlev, D.V. Orlov, Proc. SPIE **6606**, 66060Q (2007)
140. C.N. Afonso, J. Solis, F. Catalina, C. Kalpouzos, Appl. Phys. Lett. **60**, 3123 (1992)
141. J. Solis, C.N. Afonso, J.F. Trull, M.C. Morilla, J. Appl. Phys. **75**(12), 7788 (1994)
142. D. Dimitrov, M.A. Ollacarizqueta, C.N. Afonso, N. Starbov, Thin solid films **280**, 278 (1996)
143. N. Starbov, T. Missana, C.N. Afonso, K. Starbova, M.A. Ollacarizqueta, Appl. Phys. A **63**(2), 161 (2004)
144. A. Cavalleri, T. Dekosy, H.H. Chong, J.C. Kieffer, R.W. Schoenlein, Phys. Rev. B **70**(16), 161102 (2004)
145. M.F. Becker, A.B. Buckman, R.M. Walser, T. Lepine, P. Georges, A. Brun, J. Appl. Phys. **79**(5), 2404 (1996)
146. M. Rini, A. Cavalleri, R.W. Schoenlein, R. Lopez, L.C. Feldman, R.F.H. Jr, L.A. Boatner, T. Haynes, Opt. Lett. **30**(5), 558 (2005)
147. M.I. Stockman, S.V. Faleev, D.J. Bergman, Phys. Rev. Lett. **88**(6), 067402 (2002)
148. T.K. Lippert, Proc. SPIE **3274**, 204 (1998)
149. F.E. Livingston, H. Helvajian, in *MRS Bulletin*, Vol. 32, (2007), p. 40
150. D. Bäuerle, *Laser Processing and Chemistry*. (Springer, Heidelberg, 1986)
151. L.D. Laude, D. Bäuerle, M. Wautelet (eds.), *Interfaces Under Laser Irradiation*, Vol. 134 (Martinus Nijhoff, Boston, 1987)
152. M. von Allmen, A. Blatter (eds.), *Laser Beam Interactions with Materials*, (Springer, Heidelberg, 1987)
153. D.J. Ehrlich, J.Y. Tsao (eds.), *Laser Microfabrication: Thin Film Processes and Lithography*, (Academic, London, 1989)

154. W.M. Steen, *Laser Material Processing*. (Springer, London, 1991)
155. D.B. Chrisey, G.K. Hubler (eds.), *Pulsed Laser Deposition of Thin Films*, (Wiley, New York, 1994)
156. J.C. Miller (ed.), *Laser Ablation: Principles and Applications*, (Springer, Heidelberg, 1994)
157. L. Migliore (ed.), *Laser Materials Processing*, (Marcel Dekker, New York, 1996)
158. H.G. Rubahn, *Laser Applications in Surface Science and Technology*. (Wiley, New York, 1999)
159. J.F. Ready, D.F. Farson (eds.), *LIA Handbook of Laser Materials Processing*, (Magnolia, Orlando, FL, 2001)
160. J.J. Dubowski, S. Tanev (eds.), *Photon-based Nanoscience and Nanobiotechnology NATO ASI, Vol 239*, (Springer, Heidelberg, 2006)
161. N.B. Dahotre, S.P. Harimkar, *Laser Fabrication and Machining of Materials*. (Springer, Heidelberg, 2008)
162. T. Feurer, J.C. Vaughan, R.M. Koehl, K.A. Nelson, Opt. Lett. **27**(8), 652 (2002)
163. R.E. Slusher, Rev. Mod. Phys. **71**(2), S471 (1999)
164. M.C. Gower, Opt. Exp. **7**(2), 56 (2000)

Chapter 2
Theory and Simulation of Laser Ablation – from Basic Mechanisms to Applications

Laurent J. Lewis and Danny Perez

Abstract Numerical simulations have provided significant insights into the physics of ablation. In this chapter, we briefly review the progresses that we have accomplished using a simple two-dimensional molecular-dynamics (MD) model, insisting on the importance of considering the thermodynamics pathways in order to understand ablation. We also illustrate how theory and simulations help in understanding the physics relevant to materials processing applications.

2.1 Introduction

Computer simulations have provided, and are still providing, essential information about the physical processes taking place in a solid target following irradiation by ultrashort, intense laser pulses, in particular the mechanisms that lead to the ejection of matter (atoms, clusters, nanoparticles, etc.), i.e., ablation, and the damages caused by the absorption of the energetic photons (heat affected zone (HAZ), extended defects, etc). The chain of events that leads to ablation is indeed so complex that analytical or phenomenological approaches are unable to account for the whole spectrum of relevant processes; to make things worse, these occur on a wide range of length and time scales, making the problem even more untractable. Nevertheless, significant progress has been achieved using numerical models [1–11] which adequately complement experiment [12–14].

As can evidently be assessed by the present book (and others), laser ablation is a technology widely used in many applications such as thin film deposition and

L.J. Lewis (✉)
Département de Physique et Regroupement Québécois sur les Matériaux de Pointe (RQMP), Université de Montréal, C.P. 6128, Succursale Centre-Ville, Montréal (Québec), Canada H3C 3J7
e-mail: Laurent.Lewis@UMontreal.CA

D. Perez
Theoretical Division T-1, Los Alamos National Laboratory, MS B-268, Los Alamos, NM 87545, USA
e-mail: danny_perez@lanl.gov

K. Sugioka et al. (eds.), *Laser Precision Microfabrication*,
Springer Series in Materials Science 135, DOI 10.1007/978-3-642-10523-4_2,
© Springer-Verlag Berlin Heidelberg 2010

cleaning, surface micro-machining (see Chap. 10), laser surgery, mass spectrometry, etc. [15], as well as the controlled production of nanoparticles, either in vacuum, in a gaseous environment, or in a liquid (e.g., water – see Chap. 7 and [16, 17]). While direct connection with experiment remains challenging given the complexity of the physics involved, knowledge of the basic physical mechanisms that lead to material modification, and the identification of trends in the materials' response, is invaluable for experimentalists and engineers using laser ablation as a tool for materials processing.

In this chapter, we review the recent progresses in the understanding of the mechanisms that cause ablation by short, intense laser pulses. We focus on the processes that take place *within* the irradiated materials; there is a great deal of interest in the physics of the ablation plume, whose evolution is complex and proceeds over very long timescales (compared to ablation), but this problem is still largely open and probably not yet ripe for a comprehensive review. Further, we are concerned here with the problem of ablation in the thermal regime, for which the relevant physics sits on firmer grounds.

We begin in Sect. 2 by reviewing the basics of light-matter interactions and the "visible" effects on materials – how light is absorbed, how the energy is transferred to the lattice, etc. Because they are central to the physics of the problem, we also discuss to an extent the excitations and timescales that determine the energy transfers, in particular the electron "cooling time".

The central theme of this review – the physics of ablation – is addressed in Sect. 3. We first discuss early models and theories, particularly the influential description of ablation proposed by Miotello and Kelly [18, 19]. We then discuss the paradigm shift initiated by the experimental observation of a *universal behavior* in a wide range of (strongly-absorbing) materials, following the absorption of ultrashort pulses of light. Mainly drawing from our own studies, we move on to review the abundant results from molecular-dynamics (MD) simulations. We discuss the "generic" features of ablation in terms of universality and thermodynamics, focussing on the results we have obtained using a simple, generic 2D Lennard–Jones model and also using the more precise 3D Stillinger–Weber model for silicon. By exploiting the thermodynamic information provided by the MD trajectories, these provide, in a simple yet powerful manner, a rigourous classification of the mechanisms that operate in the target following the arrival of the laser pulse, eventually leading to the collective ejection of matter. We highlight the novel aspects of the ablation physics that have been revealed by the simulations, in particular fragmentation. Finally, we discuss how the physics evolves as the pulse duration is stretched to the picosecond (ps) and nanosecond (ns) regimes. We also briefly examine the peculiarities of ablation in molecular solids where the optical penetration depth is so large that inertial confinement plays an essential role in regulating the ablation process.

Section 4 is concerned with a discussion of some materials processing issues as viewed from the perspective of computer simulations. This is a vast field; we selected two applications that are particularly relevant to the general theme of this book, namely damages and the HAZ, and nanoparticle production in solvents. In

these two cases, we show how the knowledge of the basic physical processes involved has shed new light on the behavior of materials in technologically relevant situations.

In the course of the last decade, much efforts have been devoted to the study of laser ablation, in particular using theoretical models and computer simulations. The large body of literature on the subject is such that an exhaustive review is impossible. We therefore concentrate on our own work which has provided a comprehensive understanding of the basic mechanims behind ablation; we apologize to all authors whose work cannot be covered in full or even cited.

2.2 Basic Physics

2.2.1 Light-Matter Interaction

The nature of the phenomena induced by the laser irradiation of solids is determined, for the most part, by the coupling of the laser parameters – pulse duration τ_L, wavelength λ_L, and energy per unit area (fluence) F – with the optical, mechanical, and thermal properties of the target material (also see Chaps. 4 and 8). *Grosso modo*, incoming photons are absorbed by the electronic degrees of freedom of the target, leading to the formation of a gas of hot carriers (electrons or electron-hole pairs) which eventually transfer their energy to the ions through repeated emission of phonons; ionic and electronic degrees of freedom eventually achieve equilibrium on a timescale $\tau_E = 10^{-12} - 10^{-11}$ s [20]. This timescale is crucially important as it sets the boundary between strictly thermal and possible nonthermal routes, and a separation between "long" and "short" pulses [21]: if $\tau_L \gg \tau_E$, equilibrium between electrons and phonons prevails throughout the heating stage (i.e., $T_e \approx T$) and phase changes can be regarded as slow thermal processes involving quasiequilibrium thermodynamics. In contrast, for ultrashort pulses ($\tau_L \leq 10^{-12}$ s), the material is driven into a highly nonequilibrium state and $T_e \gg T$ [22]: in this case, the time with which structural modifications take place, τ_M, determines whether thermal mechanisms are involved ($\tau_M \gg \tau_E$) or not ($\tau_M < \tau_E$) [21]. Figure 2.1 summarizes the most important processes involved in the absorption of the laser energy, its redistribution and transport throught the target, and the resulting structural and thermal consequences, together with their typical timescales; full details can be found in many publications, e.g., the excellent book of Bäuerle [15].

2.2.2 Material Removal from the Target: The Basics of Ablation

The removal of macroscopic amounts of matter from a laser-irradiated surface, i.e., laser ablation, reveals an additional battleground where thermal and nonthermal pathways collide. In transparent materials, on the one hand, the high intensities commonly delivered by femtosecond (fs) pulses are normally required to excite

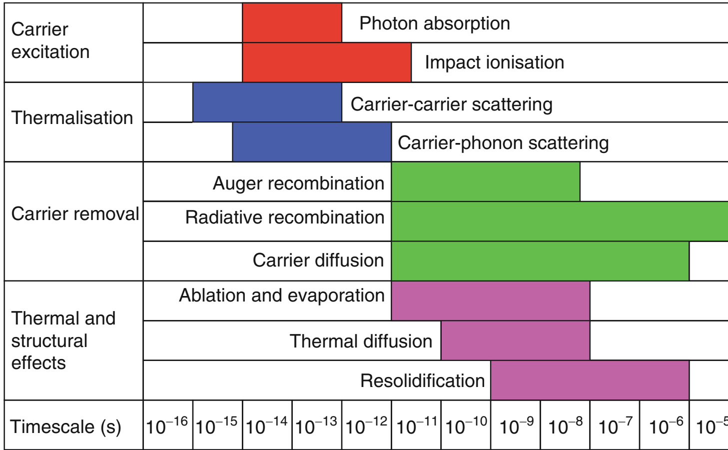

Fig. 2.1 Processes (and associated timescales) taking place in the target following the absorption of the laser pulse. Ablation typically takes place on a timescale of ps (onset) to a fraction of a ns (complete). (Adapted from [23])

the electrons across the large band gap. At irradiances above a certain threshold $I_{\mathrm{break}} \sim 10^{13}\,\mathrm{W.cm}^{-2}$, a direct solid-to-plasma transition follows by optical breakdown [21, 24–26]: the dielectric material is fully ionized into a very dense ($N \sim 10^{23}\,\mathrm{cm}^{-3}$) and hot ($T_e \sim 10^6\,\mathrm{K}$) plasma. In absorbing materials, on the other hand, the strong coupling with the laser field is such that ablation can be achieved with fs [12–14, 21, 25, 27], ps [27–30], and ns [27, 31–34] pulses at irradiances well below I_{break}. In this case, the process is mostly thermal and belongs to either one of the following two broad classes of mechanisms: (a) *photothermal*, where changes in the state of aggregation of the molten material arise from a phase transition to the vapor; possible outcomes include homogeneous nucleation of gas bubbles in a metastable liquid, i.e., phase explosion or explosive boiling [4–8, 10, 13, 18, 29, 32–36], phase separation of a mechanically unstable liquid by spinodal decomposition [37], and normal vaporization of the outer surface [7, 31, 38]; (b) *photomechanical*, whereby the breakup of the material is driven by strong, tensile pressure waves – spallation [4, 5, 39] in solids and cavitation [40,41] in liquids – or involves the dissociation of a homogeneous, supercritical fluid into clusters upon dilution in vacuum – i.e., fragmentation [5–8, 10, 42]. These different processes will be described in some detail below.

2.3 Ablation in the Thermal Regime

2.3.1 Thermodynamics

Given the enormous complexity of modeling the dynamics of strongly excited carriers and their coupling with ions, most of the theoretical effort has been

dedicated to understanding the so-called thermal regime, where $\tau_M \gg \tau_E$. In this case, the details of the complex excitation and relaxation processes are washed out by the local equilibrium that electrons and ions achieve long before ablation proceeds. Thus, despite the extremely short timescale on which the laser couples with the material, carriers play only a secondary role in this case. In absorbing solids, this regime usually extends from F_{th} to about $5F_{\text{th}}$, where F_{th} is the threshold fluence for ablation.

As is now well established – and this will be discussed at some length in the pages that follow –, much of the physics of laser ablation in the thermal regime can be understood by following the thermodynamic evolution of various portions of the target in the appropriate phase diagram – either density-temperature or temperature-pressure. Note that this does not imply that the target as a whole reaches thermodynamic equilibrium but, rather, that thermodynamic equilibrium can be assumed to take place locally, i.e., on scales smaller than the optical penetration depth of the laser light. Figure 2.2a shows, in a schematic way, the density-temperature phase diagram of a binary (liquid-vapor) mixture which derives from the stability condition for the Gibbs free energy of mixing. The stable one-phase fluid becomes metastable at the binodal line where the free energy of the gas becomes smaller than that of the liquid. Gas bubbles may thus nucleate and eventually grow within the metastable liquid: the nucleation barrier decreases exponentially upon reaching deeper into this zone, and the system may go into a state of homogenous boiling, decomposing by a so-called phase explosion process. The nucleation barrier vanishes at the spinodal line, which is the metastability limit: when pushed past this limit, the system becomes mechanically unstable and decomposes spontaneously, a process called spinodal decomposition. The corresponding picture in the temperature-pressure plane is represented in Fig. 2.2b, which we discuss next so as to introduce the ablation model of Miotello and Kelly [18, 19].

2.3.2 *Conventional Wisdom: Early Theories*

In order to explain ablation in metals irradiated by long (ns) pulses, Miotello and Kelly [18, 19, 43], following Martynyuk [36, 44, 45], have proposed a picture in which matter removal essentially results from phase explosion; this scenario, which was further adopted by numerous authors for fs [46] and ps [4, 28, 29, 47] pulses, can be summarized as follows [cf. Fig. 2.2b]: (a) If $\tau_L \gg \tau_{\text{LV}}$ – where $\tau_{\text{LV}} \sim 10^{-9}$ – 10^{-8} s is the time required for a liquid to achieve equilibrium with its vapor [32] – the expanding molten material is stable and heating takes place along the liquid-vapor coexistence line, i.e., the binodal. If $\tau_L \leq \tau_{\text{LV}}$, however, a significant fraction of the energy is stored in the liquid before it can be consumed as latent heat of vaporization. In this case, the liquid attempts to equilibrate with its undersaturated vapor and heats up, instead, below the binodal, i.e., is pushed into the liquid-gas regime upon rapid heating [19, 29, 32, 33, 44]. (b) At sufficiently high fluences, the molten material is superheated near the spinodal [48] to a temperature $\approx 0.9T_c$ (with T_c the critical temperature) [18, 32, 33, 36]. (c) Nucleation and growth of gas bubbles

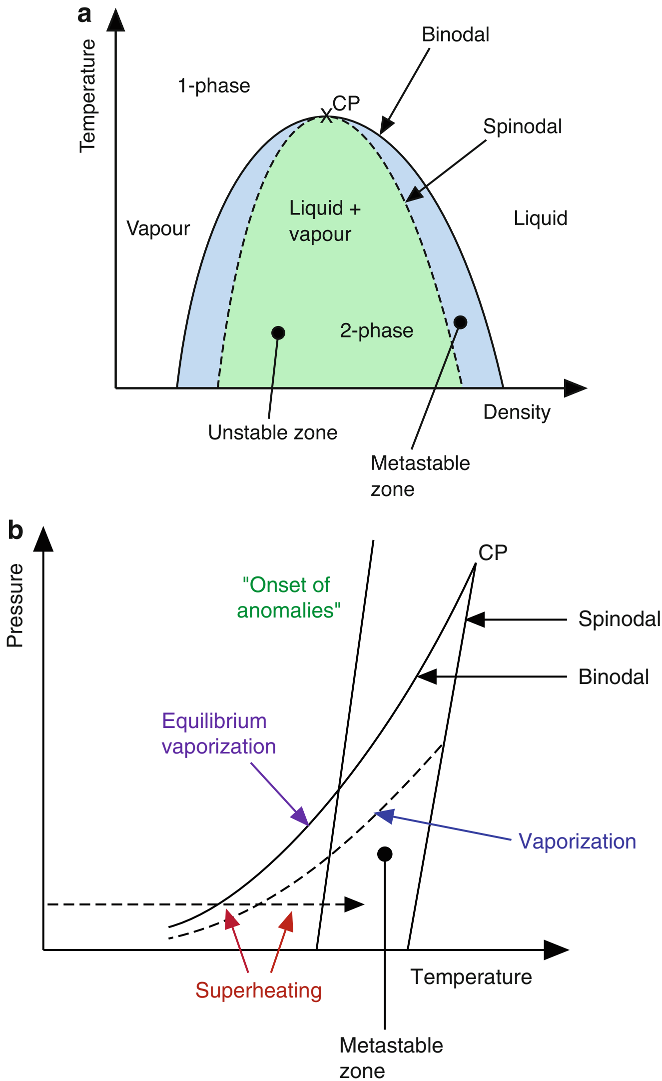

Fig. 2.2 (**a**) Density-temperature phase diagram of a binary (liquid-vapor) mixture and (**b**) Miotello–Kelly model in the temperature-pressure plane. (Adapted from [43])

sets in on a time scale $\tau_{\text{NUC}} \sim 10^{-9}$–$10^{-7}$ s [18,36,44,45] and the metastable mother phase is converted into a heterogeneous mixture of liquid and gas, i.e., explosive boiling occurs. To complete the picture, the ablation threshold, evidenced by a sharp increase in the total ablated mass [12,34,49,50] and the onset of large liquid-droplet ejection [34], has often been ascribed to an abrupt rise in the bubble nucleation rate as the metastable liquid heats up toward the spinodal line [4, 18, 32, 33, 43, 51, 52].

2.3.3 A New Understanding

This picture, however simple (and thus appealing) it may be, is not supported by the remarkable time-resolved microscopy experiments of Sokolowski-Tinten et al. [12–14, 25], nor is it by various analytical models [35, 53, 54]. Indeed, for an extremely fast laser, one expects the material to initially heat up without being structurally affected because the characteristic time for the transfer of the excitation energy from the carriers to the lattice is of the order of ps (cf. Fig. 2.1), while the target is inertially confined on such short timescales. As a consequence, the material should instead first heat up isochorically and thus be pulled *away* from the binodal line and into a near-critical or supercritical state from which the strongly pressurized matter adiabatically cools during its subsequent dilution in vacuum, possibly reaching the metastable zone. Theoretical investigations [35, 53, 54] of this process indicate that the expanding material should develop a bubblelike structure – more precisely a low-density, heterogeneous, two-phase mixture between two optically flat interfaces (the nonablated matter and a thin, moving liquid shell) – as it expands through the liquid-vapor metastable region of the phase diagram. The observation of Newton rings in the time-resolved femtosecond laser excitation and imaging of numerous metal and semiconductor surfaces fully supports this view [12–14, 25]. This novel "universal" picture – isochoric heating followed by adiabatic relaxation – resulted in renewed interest on the subject from the theoretical side and, largely through the use of computer simulations, quickly yielded a rich portrait of the dynamics of materials following ultra-short laser irradiation. This is discussed in the following sections where we examine in detail the case of fs pulses, then more succintly the problem of longer pulses. Again, because space is limited, we focus on our own work which, we believe, has provided a comprehensive picture of the mechanisms behind ablation in strongly-absorbing materials. We begin by discussing briefly the methodology.

2.3.4 Computer Models

Our approach for simulating the interaction of a laser pulse with a target, and the subsequent evolution of both the target and the plume, is based on the MD simulation technique, which consists in integrating the equations of motion of an ensemble of particles whose interactions are described by a proper potential energy function (see e.g. [55] for a review of MD). In practice, we have considered two different, complementary models: (a) a *generic* two-dimensional system of particles interacting via the Lennard–Jones (LJ) potential, and (b) a *realistic* three-dimensional system of Si atoms interacting via the Stillinger–Weber (SW) potential [56]. The laser pulse, Gaussian in time and of duration (standard deviation) τ_L, is modeled as a sequence of discrete photons absorbed by the target according to the Beer–Lambert law, $I(z) = I_0 e^{-z\alpha}$, where the depth z is measured from the surface of the target and α is the absorption coefficient (i.e., $1/\alpha$ is the

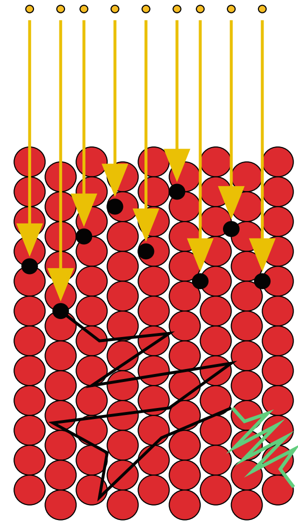

Fig. 2.3 Schematic illustration of the 2d/LJ model: the atoms are represented by *red circles* and the photons by *yellow arrows*. Upon absorption of a photon by the target, a carrier (*black circle*) is created and subsequently undergoes a Drude-like dynamics (*black line*), transferring its energy to the lattice in the form of phonons (*green wavy line*)

penetration depth). The energy of the photons is transferred to carriers which obey a Drude-like dynamics, eventually giving up their energy to atoms via carrier-phonon interactions. This is illustrated in Fig. 2.3; full details can be found in the original references [5, 7].

The two models – 2d/LJ and 3d/SW – describe the same physics and provide the same "answers" at least as far as the nature of the ablation mechanisms is concerned; minor differences between the two systems can be traced back to the specifics of their phase diagrams. The "universality" of the ablation mechanisms is well documented experimentally and was further rationalized by a description of the ablation process in terms of the thermodynamic pathways followed by the material after irradiation [57]. In fact, this is precisely the rationale behind the success of our simple 2d/LJ model, which has become a very powerful tool for investigating ablation in a variety of situations and has actually led to the discovery of a new mechanism for ablation, viz. fragmentation [5, 7]. The 3d/SW model, in contrast, while recovering the mechanisms found using the 2d/LJ model, has provided detailed information on the behavior of the prototypical material Si; in particular, it has led to the demonstration that, at variance with earlier studies (see e.g., [4, 28, 29, 32, 47]), phase explosion is not relevant to ablation in the ps regime, nor is it in the ns regime. Because the LJ model offers the enormous advantage (over SW) of being able to deal with much larger systems over longer timescales, it is the method of choice for investigating, for example extended damage in the target and the dynamics of the plume. One obvious limitation is that neither model can account for plasma formation. We are thus only concerned here with the low-fluence thermal regime, that is below $\sim 5F_{\mathrm{th}}$ [12].

In what follows, we focus on the 2d/LJ model with which we have obtained a consistent and comprehensive set of results. The LJ system is entirely defined in terms of two parameters: the hard-sphere diameter σ and the bonding energy ϵ; the

contact with real materials can be made by assigning some specific values to σ and ϵ. All quantities in the problem can be expressed in terms of those two fundamental "units", or in terms of units derived from them. Thus, for example, we may have $\alpha = 0.002\sigma^{-1}$ and $\tau_L = \tau$, where $\tau = \sqrt{m\sigma^2/\epsilon}$ is the unit of time (and m is the mass of the atoms). Setting $\sigma = 2.284$ Å and $\epsilon = 0.74$ eV, which are appropriate for Cu, these translate into a penetration depth of $1/\alpha = 1{,}140$ Å and a pulse duration of $\tau_L = \tau = 215$ fs (i.e., FWHM = 360 fs). It should however be noted that, given the generic nature of the model, parameters are not tuned to particular materials but are used as free variables to delineate the different regimes and identify the corresponding physics.

The target configurations are constructed in a slab geometry, typically containing a few hundred atomic planes in each direction. Periodic boundary conditions are imposed in the direction perpendicular to the pulse, while absorbing boundary conditions are used at the bottom of the solid to eliminate the reflection of pressure waves generated by the pulse and traveling toward the bulk [47]. All samples are equilibrated properly before light impinges on their surface (initially at $z = 0$).

MD simulations have a long and productive history of significant contributions to laser ablation understanding. Its powerful predictive ability has allowed key insights into the mechanisms that lead to material ejection upon excitation by short, intense laser pulses. In particular, the early studies by Zhigilei and collaborators, using the "breathing-sphere model", have been extraordinarily useful in elucidating the physics of ablation in molecular solids (see [47] for a review). For metals, the same group has developed a model in which the gas of carriers excited by the laser field is described using a continuum approach; the gas evolves and connects to the atomic degrees of freedom by way of a two-temperature model [58]. Other examples of laser ablation by MD can be found in, for example, [59–61].

While powerful, MD has limitations, the most notable being the finite length and timescales it can cover, typically tens of nm (i.e., a million atoms or so) and ns, respectively. Thus, it is not possible to study the progression of shockwaves over macroscopic scales, to follow the evolution of the ablated material on experimental timescales, or to simulate microstructural changes on lengthscales typical of experimental laser spot sizes. Such problems can be addressed for instance using continuum hydrodynamics (HD) models [37, 62–64] whereby the evolution of the system is obtained from a hydrodynamic description based on its equation of state (EOS). Because the system is locally described in terms of macroscopic variables, HD models are relatively "inexpensive" and thus allow macroscopic time and length scales to be covered. The HD approach, further, is ideally suited to a description of the carrier gas [63] and can in fact be generalized to describe such complex electronic effects as plasma formation [64]. However, because they are based on an EOS description of the dynamics of the target, these models are unable to account for some non-equilibrium effects, for example, the decay of metastable phases. Great care must therefore be taken when interpreting HD results. With their complementary strengths and weaknesses, MD and HD models provide the tools necessary for a comprehensive understanding of the physics of ablation.

2.3.5 *The Femtosecond Regime*

We examine first the case of ultrashort fs pulses ($\tau_L = 0.5\tau \sim 100\,\text{fs}$), which study has provided key insights into the mechanisms behind ablation. After qualitatively describing the response of a target to the absorption of a pulse, we show how the ablation processes can be unambiguously identified by way of an analysis of the thermodynamic evolution of the target. Longer pulses will be examined in the next section.

2.3.5.1 Visual Analysis

A visual inspection of the evolution of the target following the arrival of the laser pulse provides useful information for identifying the regions and mechanisms of interest. Figure 2.4 shows a few snapshots of a 2d/LJ system with 400,000 atoms at different moments during the simulations, for an absorption coefficient $\alpha = 0.002\sigma^{-1}$ and for two values of the fluence – close to the threshold for ablation, $F = 1.2F_{\text{th}}$, and somewhat above, $F = 2.8F_{\text{th}}$. By about $t = 5\tau$, the pulse is essentially over in both cases and, in spite of the considerable heating which occurs

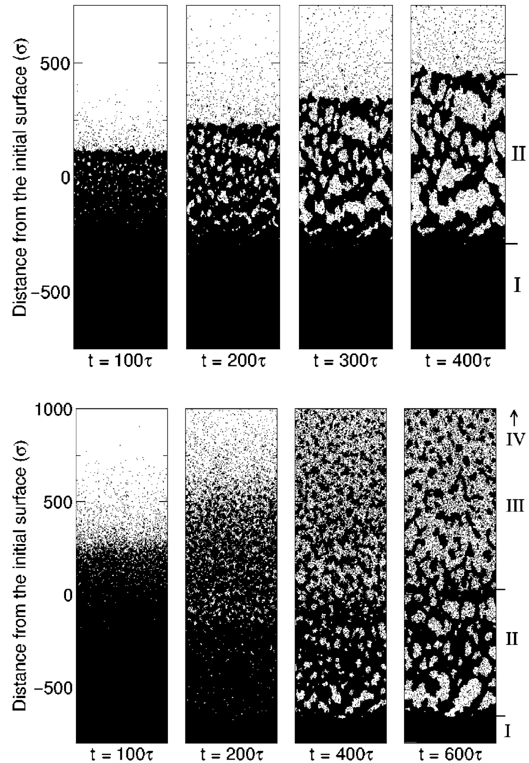

Fig. 2.4 Snapshots of a simulation at fluences $F = 1.2F_{\text{th}}$ (*top*) and $F = 2.8F_{\text{th}}$ (*bottom*) for a pulse with $\alpha = 0.002\sigma^{-1}$ and $\tau_L = 0.5\tau$. Roman numerals identify different regions of the target (see text); region IV is the gaseous region (out of the range of the last snapshot). (Reprinted with permission from [7])

during the relaxation of the carrier gas, the target does not react much. From this moment on, the important pressure build-up generated by the isochoric heating relaxes by the emission of a pressure wave and the expansion of the target starts; the ejection of monomers from the surface has also begun by then.

At low fluence (top panel of Fig. 2.4), at $t \sim 100\tau$, the nucleation of small pores is clearly visible in the surface region. At $t = 200\tau$, the pores have grown in size, becoming voids, which are evidently filled with gas. During the following 200τ, intense growth and coalescence occur so that the size of the voids increases rapidly. This finally leads to the ablation of large liquid droplets from the topmost 300σ portion of the target. An interesting feature of the plume in this case is that the matter-vacuum interface progresses slowly and stays relatively sharp for a long period of time. These results, we have established, confirm the Newton-ring model proposed by Sokolowski et al. to explain the optical interference patterns in fs pump-probe experiments [13]. Despite the exponential temperature profile initially imposed by the laser pulse, the reaction of the system is remarkably homogeneous: the size of the pores and their gas content do not seem to depend strongly on depth. In this case, only two regions are distinguishable: the non-ablated solid region and the porous region, numbered I and II, respectively.

The situation is somewhat more complex at higher fluence – cf. bottom panel of Fig. 2.4. The expansion and emission of monomers from the surface is now much more intense, as can be clearly seen from the $t = 100\tau$ snapshot; again, small voids are present near the surface. However, by $t = 200\tau$, the coalescence of these voids causes the fast-expanding surface region to decompose into an ensemble of small clusters. Evaporation from the surface of the clusters quickly fills the surrounding area with gas. By then, the front matter-vacuum interface is already destroyed, that is, the density varies continuously with position. One important consequence of this observation is that Newton rings can no longer develop; this corresponds precisely to the results of pump-probe experiments at high fluences [13]. One may therefore already anticipate that the mechanism for ablation here is different than for the lower-fluence case. At $t = 400\tau$, many gas-filled pores develop in the bottom section of the target; the morphology of this section very much resembles the surface region of the low-fluence case. Finally, at $t = 600\tau$, the pores coalesce and induce the ejection of this part of the target. At this moment, the cluster creation process in the top part of the target is complete. Thus, in this case, four distinct regions can be identified: the non-ablated solid region (I), the porous region (II), the cluster-filled region (III), and a purely gaseous region (IV – out of the range of the last snapshot). By comparing the four snapshots, we see that regions II and III expand at different velocities – the latter faster than the former, which behaves the same as in the case of near-threshold fluences.

The strongly-varying morphologies and expansion speeds of the different regions in the high-fluence case suggest that the ablation mechanisms are specific to the effective amount of energy locally absorbed, that is, the energy density, so that several mechanisms are actually operating at the same time, depending on depth below the surface; we will return to this point below.

The general features of the morphological evolution of the targets following irradiation are robust. Indeed, similar results have been obtained for a wide range of materials using different models [4, 11, 46, 61]. This is not surprising in view of the universal behavior of materials observed in experiments, and its rationalization in terms of the thermodynamical pathways along which rapidly-heated materials evolve, as we discuss next.

2.3.5.2 Thermodynamic Trajectories

While the above visual analysis is useful, it is not sufficient for a rigorous identification of the ablation mechanisms. These are best understood in terms of the thermodynamic analysis method introduced in [5] and [7] (and described in detail therein). In brief, the system is first partioned into thin slices perpendicular to the pulse's direction. Three "thermodynamic trajectories" are then computed for each of these slices: a so-called average trajectory, which corresponds to the usual thermodynamic average, and two phase-resolved trajectories where the contribution of gaseous and dense regions of the slice are individually evaluated. The results of this analysis for portions of the target typical of regions II and III in Fig. 2.4 are presented in Fig. 2.5.

Region II undoubtedly bears the thermodynamic signature of phase explosion: it is heated at constant volume up to a very high, super-critical temperature, after which a quasi-adiabatic relaxation process begins, moving through the solid-liquid coexistence region before the material melts upon entering the one-phase liquid region. The system then proceeds to the liquid-vapor metastable region, where the liquid is under tension. Note that no voids are present before entering the metastable zone: the gas branch is absent, and the average and dense branches are superimposed. The separation of the average and dense branches, and the concomitant appearance of the gas branch, occurs *in* the metastable zone, indicating that

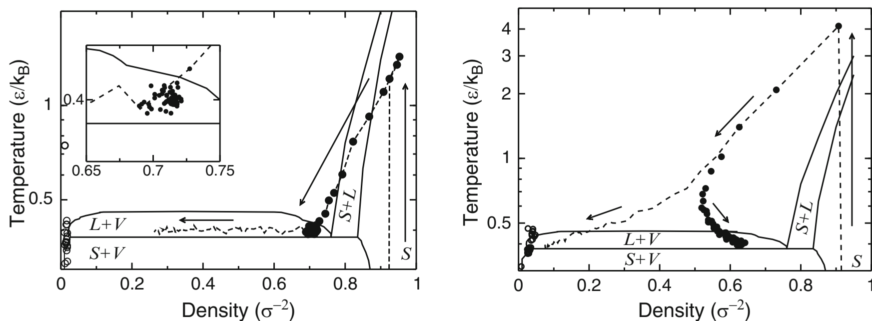

Fig. 2.5 Typical thermodynamic trajectories for regions of the target where ablation proceeds by homogeneous nucleation (region II, *left*) and fragmentation (region III, *right*). *Dashed line*: average branch; *filled circles*: dense branch; *empty circles*: gas branch. *Inset* to *left panel*: zoom on the trajectory upon entering the metastable region. (Reprinted with permission from [7])

gas-filled bubbles begin to nucleate after the binodal is crossed. A phase separation process then sets in: the dense phase gradually converts into gas by nucleation and growth of gas bubbles. Because the free-energy barrier for the nucleation of gas bubbles is very low for any significant incursion into the metastable region (actually vanishes at the spinodal line) [65], nucleation proceeds at a very large rate. The growth and coalescence of the gas-filled bubbles eventually cause the ablation of large liquid droplets. This type of thermodynamic trajectories corresponds exactly to the thermodynamical pathway that was proposed to explain the formation of Newton rings [12–14, 25, 35, 53, 54].

In region III, now, the heating rate is so intense that the material is pushed into a strongly superheated solid state. Melting occurs at the very beginning of the relaxation process and the material then expands in a super-critical fluid state. Soon after, voids begin to appear. The split between the average and dense branches – signaling the onset of the creation of pores – now occurs way *above* the binodal line, implying that the system has already decomposed by the time the metastable region is reached. This very simple observation leads to the following important conclusion: *ablation cannot result from homogeneous nucleation in this case*; further, because large clusters are present in the plume, vaporization must also be excluded. Through an analysis of the distribution of cluster sizes in this region of the plume, we have demonstrated that ablation was caused here by fragmentation – a structural rearrangement occuring to compensate for inhomogeneities associated to the strains caused by the rapid thermal expansion [66, 67]. Fragmentation was independently proposed as a possible ablation mechanisms by Glover [42].

While phase explosion and fragmentation are the dominant ablation mechanisms in most situations (see below), complete vaporization is also observed in regions of the target that absorb very large amounts of energy, for example, region IV. Here vaporization should not be understood as a thermal desorption process but, rather, as the rapid decomposition of the solid following the absorption of energy exceeding the cohesive energy of the material. Finally, at the other end of the energy spectrum, we have shown that near-threshold ablation could occur directly through the solid phase following the expansion of the surface region of the target up to the instability point where the homogeneous solid becomes mechanically unstable against the growth of gas-filled voids; this is spallation. This is akin to the thermo-mechanical ablation mechanisms proposed by Zhigilei and Garrison for organic solids [4, 47]. Note, however, that this mechanism does not take place in Si where ablation always occurs from the liquid phase [11].

One other mechanism – critical point phase separation, or spinodal decomposition – is sometime invoked in the literature [37, 46]. It corresponds to situations where the material decomposes in the *unstable* liquid-vapor region of the phase diagram (located within the spinodal line) following an expansion passing in the neighborhood of the critical point. While our simulations indicate that the fast expanding material is likely to have fragmented before it reaches the critical point, the occurence of spinodal decomposition as a possible (and significant) ablation mechanism remains to be established.

These observations suggest that materials irradiated by low-fluence, ultra-short laser pulses exhibit a universal behavior that can be entirely understood in terms of general features of their phase diagrams; taken together with a rigourous thermodynamic description of the phenomenon, our simulations have provided a clear and concise picture of the different physical processes involved in ablation. They have also provided unambiguous evidence that the popular Miotello and Kelly model [18, 19], whereby phase explosion is assumed to occur during the rapid heating phase of the target, is not an appropriate description of the thermodynamics of ablation.

2.3.5.3 Ablation Mechanisms vs Depth

Our calculations clearly demonstrate that different sections of the target ablate via different mechanisms depending on the local energy density received from the laser pulse. For a material with linear absorption, the energy density at a given depth varies logarithmically with fluence and, therefore, the portion of the target which ablates by a given mechanism depends on fluence. This is illustrated in Fig. 2.6: deep into the target, where the energy density is smallest, ablation proceeds by spallation; upon increasing energy, the system undergoes phase explosion, fragmentation, and vaporization. In turn, this implies that, while spallation and phase explosion dominate the ablation yield at low fluences, fragmentation becomes increasingly dominant as the fluence increases.

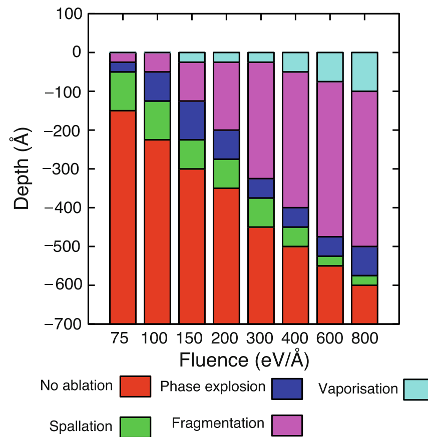

Fig. 2.6 Breakup of the ablated region in terms of the mechanisms ablation arises from for a laser pulse with $\tau_L = 200$ fs at various fluences. For illustration purposes, we have set $\epsilon = 0.74$ eV and $\sigma = 0.228$ nm, appropriate for Cu; the photons have an energy of 3.34 eV (i.e., $\lambda = 370$ nm) and the absorption coefficient is $\alpha = 0.01\sigma^{-1}$ (i.e., $\alpha^{-1} = 100\sigma = 22.8$ nm). The initial target extends from −2,700 to 0 Å. For this system, $F_{\text{th}} \sim 50$ eV/Å

2.3.6 Picosecond Pulses and Beyond

While the Miotello and Kelly model of phase explosion [18, 19] can definitively be excluded as far as fs pulses are concerned, there have been speculations that phase explosion during heating was nevertheless possible for longer, ps pulses. Indeed, while heating is closely isochoric for fs pulses (thus the heated target is pushed *away* from the metastable region of the phase diagram, cf. Fig. 2.5), expansion can occur concomitantly with heating for ps pulses. Early simulations using the 3d/SW model [6] have, however, demonstrated that this scenario is also unfounded: already for pulse durations of 50 ps, phase explosion is totally inhibited. Rather, ablation proceeds by *trivial fragmentation* [68], whereby a slowly expanding super-critical fluid adopts an inhomogeneous equilibrium structure as its density decreases. This problem was revisited using our generic 2d model [8] and similar conclusions were reached. As Fig. 2.7 shows, already for pulses of about 100 ps, the thermodynamic trajectories corresponding to the ablated regions always expand super-critically, crossing the liquid-vapor binodal line far off on the vapor side of the phase diagram. Phase explosion therefore has to be excluded here also as a possible route to ablation. In this case, since expansion is slow, fragmentation is also irrelevant. As mentioned above, this mechanism is referred to as trivial fragmentation in the expanding fluid literature. These results underline the fact that the system does not fail in response to an overwhelming external stimulus, but simply adopts the equilibrium inhomogeneous structure corresponding to moderate density super-critical fluids.

It is interesting to note that some regions of the material located deeper into the target do actually reach the binodal line (cf. inset of Fig. 2.7). However, instead of progressing into the metastable region, their expansion stops, and they subsequently relax *along* the binodal. Combined with the 3d simulations for Si mentioned above, these results indicate that it is exceedingly difficult to push a material into a state of liquid-vapor metastability *during* the fast heating stage, if at all possible, and this certainly does not constitute a universal pathway for ablation with pulses shorter than the nanosecond, as used to be "generally believed".

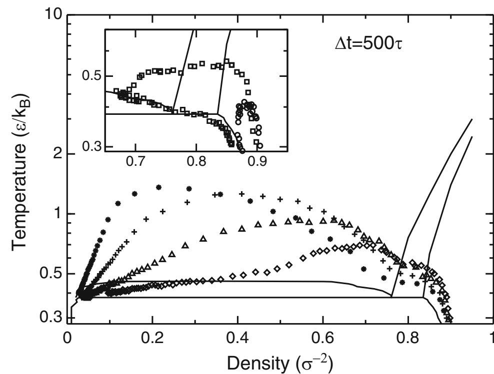

Fig. 2.7 Typical thermodynamic trajectories for ablation under ps pulses ($\tau_L = 500\tau$) with $\alpha = 0.06\sigma^{-1}$ for a fluence of $F = 900\,\epsilon/\sigma$. Average trajectories are shown for different depths under the surface. *Inset*: subthreshold trajectories for deeper, non-ablated portions of the target. (Reprinted with permission from [8])

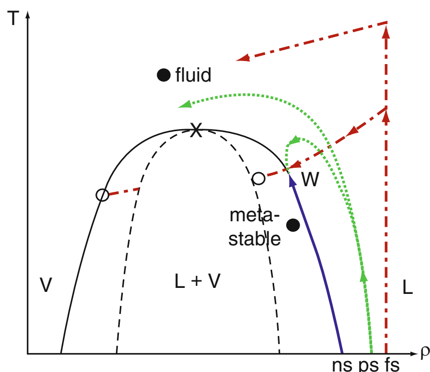

Fig. 2.8 Schematic illustration of the typical thermodynamic pathways followed by the target as a function of pulse duration – *dash-dotted*, *dotted*, and *continuous lines* correspond to fs, ps, and ns pulses, respectively – in a typical strongly-absorbing solid (e.g., metal or semiconductor)

In spite of the simplicity of our generic 2d/LJ model, our simulations have provided a wealth of information on the nature of the thermal ablation mechanisms in different conditions, ranging from ultra-short fs to much longer ns pulses; this is summarized schematically in Fig. 2.8 for strongly-absorbing solids.

2.3.7 Molecular Solids

We have been concerned so far with the case of strongly-absorbing materials where the penetration of light is limited to a few tens of nanometers. The problem of laser ablation in weakly-absorbing organic or molecular solids is of utmost interest and has been addressed by a number of authors (e.g., see [69]), notably Zhigilei et al. [4, 47] using the breathing-sphere model. Because the deposition of the laser energy extends over much larger distances than with "hard" materials, the physics is expected to be different. In particular, inertial confinement is expected to play a very significant role since the expansion dynamics of material far away from the surface will be hampered by material on top of it. Also, as we have demonstrated above, the ablation of a particular portion of the target depends on the effective amount of energy it receives. The combination of the two effects leads to a very different behavior in molecular solids, as we discuss below. Finally, the Miotello–Kelly model has often been invoked to explain ablation not only in strongly-absorbing solids but also in materials having a relatively large optical penetration depth (see for example [70] and references therein). Thus, a clear reassessment of the situation is necessary and, again, thermodynamic trajectories provide invaluable insights into this problem.

Our generic LJ model can be used to study weakly-absorbing solids provided the potential parameters are adequately chosen. Indeed, for a typical molecular solid (see, e.g., [47]), $\epsilon \simeq 0.2\,\text{eV}$, $\sigma \simeq 2\,\text{nm}$, and $m \simeq 100\,\text{amu}$; hence, $\tau \simeq 5\,\text{ps}$. Here we present results for a pulse duration (FWHM) $\tau_p = 500\tau$ ($\approx 2.5\,\text{ns}$) and an optical penetration depth $\delta = 2{,}000\sigma$ ($\approx 4\,\mu\text{m}$).

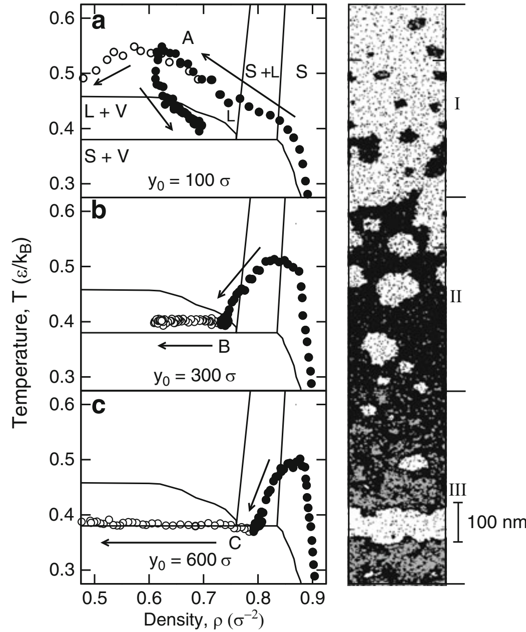

Fig. 2.9 *Left*: Time evolution of the irradiated system in the density-temperature plane for different depths y_0 below the original surface (as indicated). *White circles*: macroscopic branch; *black circles*: dense branch; the gas branch is out of range. *Arrows* indicate the flow of time. *S*: solid; *L*: liquid; *V*: vapor. Other capital letters refer to locations in the phase diagram. *Right*: Snapshot of the corresponding simulations at a fluence $F = 1.25F_{\text{th}} = 2000\,\epsilon/\sigma$ and time $t = 2500\tau$. *Gray*: locally crystalline structure; *black*: locally disordered structure. Note that only the near-surface, ablating region is shown. (Reprinted with permission from [9])

The results of our simulations are summarized in Fig. 2.9 for a fluence slightly above threshold ($F_{\text{th}} = 1{,}600\epsilon/\sigma$). Three regions, associated with different removal mechanisms, can be identified in the ablating material: (a) in the topmost region (I), the system is composed of a rapidly expanding mixture of liquid droplets and gas; (b) further down into the plume (II), homogeneously nucleating gas bubbles in a slowly expanding melt are observed; (c) cavities are found to grow heterogeneously in the underlying solid-liquid region (III). Note that regions III ($F \geq 0.95F_{\text{th}}$), II ($F \geq 1.05F_{\text{th}}$), and I ($F \geq 1.1F_{\text{th}}$) appear sequentially as a function of increasing fluence. The nucleation of gas bubbles at fluences starting slightly below F_{th} and the ejection of liquid droplets above F_{th} are features in qualitative agreement with experiments on molecular solids using ns pulses [70].

A typical trajectory for region I is displayed in Fig. 2.9a. As a consequence of the weak inertial confinement near the surface, the irradiated solid expands almost freely into vacuum; the solid-liquid coexistence region is eventually reached and melting takes place. The liquid is further heated to a supercritical state where void nucleation causes the breakup of the initially homogeneous fluid into clusters. Clearly, matter removal cannot be attributed to the phase explosion (or spinodal

decomposition) of a subcritical, metastable liquid; instead it results from "trivial" fragmentation, a process already encountered above.

The thermodynamic pathway is fundamentally different further down into the expanding target where inertial confinement operates [II; Fig. 2.9b]: heating is nearly isochoric and expansion occurs upon cooling rather than heating (recall that the pulse duration is ≈ 2.5 ns). In the process, the system melts and ultimately enters the liquid-vapor coexistence region where homogeneous nucleation of gas bubbles takes place (B), that is, the system phase explodes. This is evidently analogous to the behaviour found in strongly-absorbing materials under near-threshold fs pulses [7,11,13], but fundamentally different from the predictions of the MK model.

Finally, in regions located deep into the ablating plume, a third mechanism operates [III; Fig. 2.9c]. As in region II, the system is first heated at nearly constant volume. However, owing to the increased confinement, mechanical expansion is now slow enough that thermal diffusion becomes an additional, effective cooling process. As a result, the material expands almost entirely within the solid-liquid region where it only partially melts before reaching the metastable solid-vapor region. Shortly after, the heterogeneous nucleation of gas bubbles takes place at the solid-liquid boundaries (C); the cavities eventually coalesce, causing the ejection of a relatively large (few-hundred-nanometer-thick) piece of material. This ejection mechanism is observed at all fluences above F_{th}.

The MK model predicts the superheated liquid to undergo phase explosion as it is rapidly heated into the liquid-vapor region at nearly constant pressure under long (ns) pulses. This is certainly not supported by the thermodynamic trajectories in region II, of which a typical illustration is displayed (in the temperature-pressure plane) in Fig. 2.10 along with the MK scenario. Here, the inertially-confined irradiated matter is heated *away* from the metastability region; the latter is accessed, instead, as the pressure buildup is gradually released upon subsequent expansion and cooling.

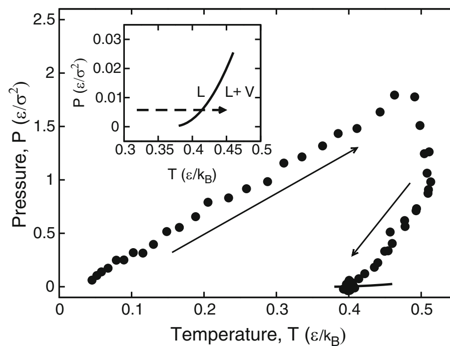

Fig. 2.10 Time evolution of the irradiated system in the temperature-pressure plane for a depth $y_0 = 300\sigma$ below the original surface (region II). The *solid line* is the binodal; the spinodal is not shown. *Inset*: thermodynamic trajectory (*dashed arrow*) of the heated system under ns irradiation, as predicted by the MK model. (Reprinted with permission from [9])

2.4 Materials Processing

Armed with a detailed understanding of the physical nature of the ablation processes, the scope of computer models can be extended to situations that are of direct relevance to materials processing. It is not possible to exhaustively review the field; we focus on two applications taken from our own work, namely the ablation of targets immersed in solvents to produce nanoparticles and the conformation of nanoscale features produced by laser writing.

2.4.1 Nanoparticle Production in Solvents

At the root of the nanotechnology revolution of the last decade lies the fact that nanoscale materials, nanoparticles in particular, exhibit novel and tunable properties, be they optical, electronic, or structural (see Chap. 7). It is thus of utmost importance to develop reliable methods for mass-producing such materials. While "conventional" laser ablation can be used to produce nanoparticles, this method is rather ineffective as it is not very size-selective – the nanoparticles are usually widely distributed in size. Control over the size distribution can, however, be improved dramatically if the targets are immersed [16, 17, 72], for example, in water. This offers the additional advantage that the particles can then easily be manipulated or functionalized while in solution. In order to qualitatively understand the impact of solvents on ablation and nanoparticle formation, and to elucidate the origin of the increased selectivity, we have adapted our simple 2d/LJ model to simulate this technologically relevant process. To our knowledge, this is the first MD investigation of ablation of solvated solids. See [73, 74] for a discussion of the wetting layer dynamics under subthreshold irradiation.

We have examined the problem of laser ablation of targets immersed in both a low-density liquid (e.g., water) and a high-density liquid (e.g., a metallic melt) in order to understand the role of inertial confinement on the ablation process and the formation of nanoparticles. The results are summarized in Fig. 2.11 and briefly discussed below; full details can be found in the original reference [71].

We start with the case of wetting by a low-density liquid. One immediate difference with the dry target is the slower expansion rate of the ablated material, roughly by a factor of 5: monomers and small clusters, while having been ejected from the target, tend to remain confined to a small region near the liquid-solid interface. The evolution of the dry and wetted targets are otherwise similar, and both the formation of clusters in the topmost region and the growth of gas bubbles deeper into the target can be observed. Late in the process, however, a very significant difference appears: the gas bubbles within the target have completely collapsed while cluster formation proceeds; note that the liquid has now been almost completely expelled from the interface region. Once ablation is complete, the majority of clusters, which have been slowed down by the liquid, remain close to the target, in contrast to the dry case where only very large clusters remain. Thus, the presence of a low-density

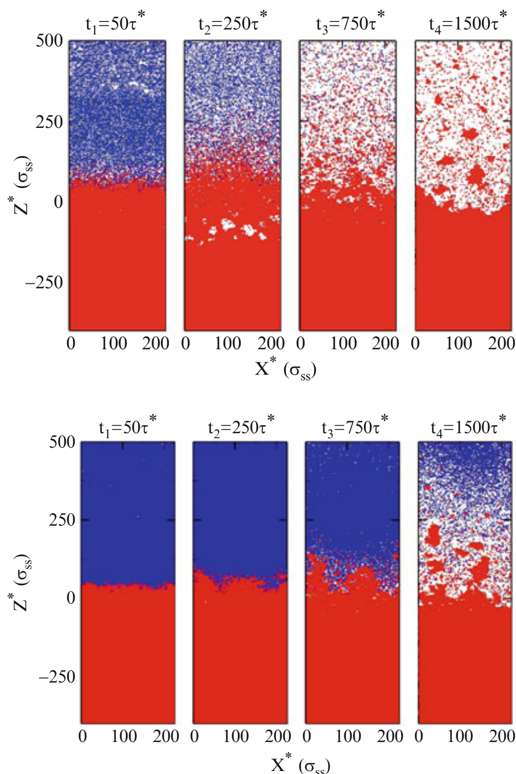

Fig. 2.11 Snapshots of the simulation of a solid target wetted by a low-density (*top*) and a high-density (*bottom*) liquid, at a fluence of 560 ϵ/σ; the *red* and *blue dots* correspond to the solid and the liquid phases, respectively. (Reprinted with permission from [71])

liquid film causes the expansion of the target to slow down. This is sufficient to stop the gas bubbles from growing until coalescing inside the target, hence inhibiting ablation by phase explosion; in contrast, ablation by fragmentation may still occur, and this leads to the ejection of a significant number of clusters.

This behavior is amplified in the case of wetting by a high-density liquid. As can be seen in Fig. 2.11, the early ejection of monomers now is totally suppressed, but later on takes place with the concomitant formation of a few clusters. Very late in the process, these are finally ejected from the target, following the formation of a low-density layer in the fluid. In this case, the formation of gas bubbles within the target is totally inhibited and only the topmost section of the target undergoes structural modifications.

The presence of a wetting layer confining the solid affects considerably the formation of nanoparticles as can be appreciated from Fig. 2.12 where the composition of the plume is analyzed. For the dry target, most of the atoms in the plume belong to large clusters (containing more than 1,000 atoms) which have been produced through phase explosion. As the fluence increases, fragmentation becomes more important and leads to a larger proportion of atoms within moderate-size clusters (between 11 and 1,000 atoms). The proportion of monomers (mainly produced by vaporization) is also seen to increase a bit with fluence; the rest of the plume

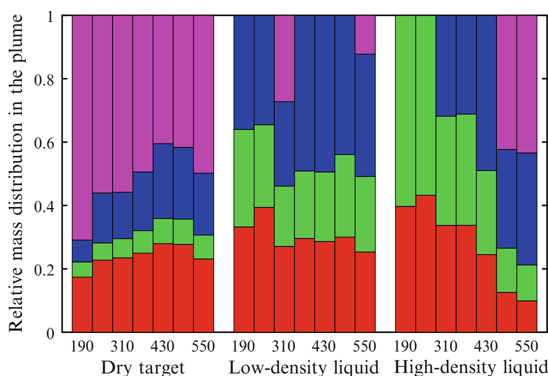

Fig. 2.12 (Color online) Relative mass distribution in the plume for the dry, low-density, and high-density cases, as a function of fluence. From *bottom to top*: (*red*) monomers; (*green*) atoms in clusters of size between 2 and 10; (*blue*) atoms in clusters of size between 11 and 1,000; (*magenta*) atoms in clusters larger than 1,000 atoms. (Reprinted with permission from [71])

consists of small clusters (between 2 and 10 atoms); the range of cluster sizes in our simulations is certainly typical of experimental observations [75, 76]. For the target wetted by a dense liquid, now, the situation is reversed: at low fluence, the plume contains mostly monomers and small clusters; as the fluence increases, these become less popular, with more and more large clusters being produced by fragmentation. This observation is coherent with experiments on wet gold targets [17, 77]. The two effects seem to balance out in the low-density liquid: the plume mostly consists of monomers and moderate-size clusters, and this is essentially independent of fluence. These differences are principally due to the complete inhibition of phase explosion in the wet targets, thus suppressing the formation of large clusters in favor of smaller ones produced through fragmentation. The liquid environment thus provides one way of controlling the morphology of the ablations plume, that is, the distribution in size of the clusters, as it allows the expansion dynamics of the plume to be fine-tuned.

2.4.2 Damages and Heat Affected Zones

Another area where laser ablation shows great promises is micro-machining. Indeed, lasers can be used to "write", "cut", or "dig" structures on the surfaces of materials (see Chaps. 10 and 13). In a variety of these applications, the damages inflicted to the targets by the laser pulses must evidently be minimized in order to optimize the quality of the features [27, 78–83]. There is therefore a need to understand the formation of damage – in particular the so-called HAZ – at a fundamental level. Given its critical technological importance, the problem received surprisingly little attention from the MD community, probably because of the rather severe length-scale limitations. However, as the power of modern computers increases, the gap

is gradually filling-in [84–87]. We have examined this problem using our LJ model and provide here a brief summary of our findings [88]. In the present case, the laser pulse adopts a Gaussian shape in space, so that ablation is confined to a subsection of the target.

In the top panel of Fig. 2.13, we show a "movie" of the ablation crater formation in a typical sample for a fs laser pulse at relatively high fluence. At low deposited energy (which depends on depth), ablation occurs mainly by the growth and coalescence of gas bubbles inside the liquefied portion of the target, that is, phase explosion, and the plume is composed of relatively large liquid droplets. As the energy of the laser increases, ablation results from the decomposition of the target into small clusters during the rapid expansion of the material, that is, fragmentation. Finally, at high energy, vaporization is observed. It is important to note that, as can be appreciated from Fig. 2.13, the three mechanisms occur simultaneously inside the target since the nature of the ablation mechanism is mainly determined by the local deposited energy as we have seen earlier. Since phase explosion is the

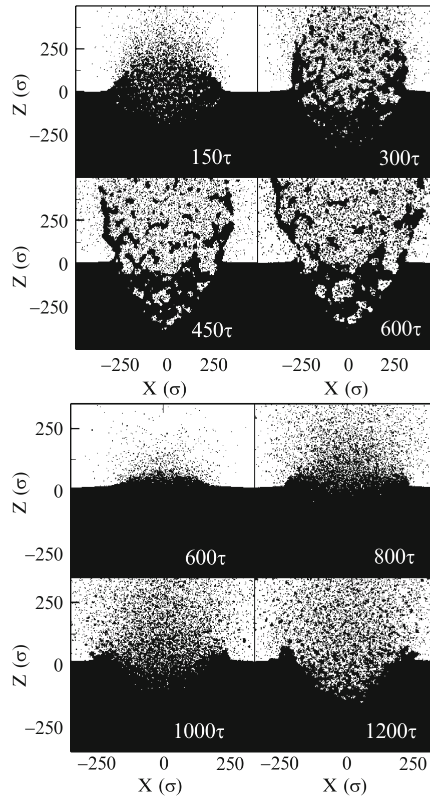

Fig. 2.13 Snapshots of the formation of craters as a function of time for a fs pulse (*top*) and a ps pulse (*bottom*), at fluences of 1,500 and 1,250 ϵ/σ, respectively. (Reprinted with permission from [88])

ablation mechanism which requires the least amount of energy, it follows that the material found near the crater's edge has received an energy close to the ablation threshold, and thus has suffered phase explosion at some point during the evolution of the target.

In the bottom panel of Fig. 2.13, now, we present corresponding results for irradiation with a ps laser, exhibiting significant differences with the fs laser. Here, the ejection of matter begins while the laser is still shining and takes place continuously by the emission of monomers and small clusters till after the end of the pulse. Also, large clusters are not seen. This is coherent with our earlier observation that phase explosion (which leads to large clusters) is inhibited for long pulses and ablation occurs when the heated material slowly expands within the super-critical region of the phase diagram via "trivial fragmentation". This is the only mechanism which operates in the ps regime (for strongly-absorbing materials), in contrast to fs pulses where other routes to ablation are possible.

One interesting difference between fs and ps pulses is the formation of a sizeable rim around the crater in the later case; this results from sub-threshold liquid being dragged along the crater walls by the expanding material or pushed out by the recoil pressure. In the thermal fs regime, the amount of material that melts without ablating is minuscule, and the rims are consequently small. In the ps regime, in contrast, extensive melting does occur before ablation, so that rim formation is favored. This is fully consistent with experiment which shows the formation of a rim and the redeposition of various debris on the target to occur preferentially with ps pulses, while fs pulses lead to cleaner craters in the thermal regime [27, 81].

The damages and the HAZ can in fact be seen quite clearly in Fig. 2.14 where we plot, for the same samples as before, those atoms which have been disrupted by the laser pulse (more precisely, atoms whose neighbourhood has changed with respect to the initial state). Here also differences emerge between the fs and ps pulses: while, as discussed above, the regions affected by melting and recrystalization is rather small for fs pulses, it is much more extended in the ps case, because of the longer time available for thermal diffusion into the target. However, in the latter case, the material is left in rather good shape after recrystallization: only small vacancy clusters remain in an otherwise perfect crystal. In the former case, however, larger pores (remnants of near-threshold phase explosion) are found close the crater's wall

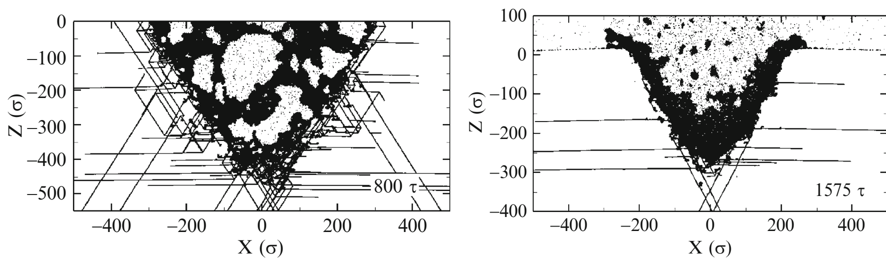

Fig. 2.14 Damage and the heat affected zone (HAZ) for the same two simulations as in Fig. 2.13 – fs pulse (*left*) and ps pulse (*right*). (Reprinted with permission from [88])

while an extensive network of dislocations extends deep into the target. Thus, while thermal damage to the target is indeed limited with fs pulses, mechanical damage mediated by dislocations is more important because of the high pressure created in the irradiated region following the absorption of the pulse. A complete discussion and analysis of the defect formation processes can be found in [88].

2.5 Conclusions and Perspectives

In spite of the simplicity of our generic 2d/LJ model, our simulations have provided a wealth of information on the nature of the thermal ablation mechanisms in different conditions, ranging from ultra-short fs to much longer ns pulses. As confirmed from a comparison with a more realistic model for silicon, the behavior of materials following short-pulse irradiation is essentially universal and best understood in terms of the thermodynamic pathways along which the materials evolve. We have notably established that different ablation mechanisms correspond to different classes of pathways. In the fs regime, the exact mechanism is closely related to the regions of the phase diagram that the system encounters when evolving from high to low temperatures and densities: trajectories crossing the solid-vapor line, the liquid-vapor line, or expanding entirely within the super-critical fluid region, ablate via spallation, phase explosion and fragmentation, or vaporization, respectively. In contrast, ablation results exclusively from trivial fragmentation as the pulse duration is stretched to ps durations. In these conditions, the sub-threshold material is unable to penetrate into the liquid-vapor metastable region but, rather, relaxes along the binodal line back toward the solid state. Phase explosion can, however, be restored for longer pulses in weakly-absorbing solids because of inertial confinement effects [9]. When the pulse duration is pushed to the ns regime, the expansion occurs increasingly close to the binodal line [8], but the behavior of the material as it reaches the critical point is still uncertain.

It appears therefore that the picture is essentially complete inasmuch as the thermal regime is concerned. It remains a challenging objective to understand the non-thermal regime; work in this direction is already under way.

Acknowledgments We are grateful to many people who have contributed to our research efforts in this area over the years, in particular Patrick Lorazo and Michel Meunier; thanks also go to Delphine Bouilly, Laurent Karim Béland, Delphine Deryng, Vincent Mijoule, Danahé Paquin-Ricard, and Élisabeth Renaud. It is a pleasure also to acknowledge numerous discussions and exchanges with several researchers in the field, including Salvatore Amoruso, Riccardo Bruzzese, Savas Georgiou, Tatiana Itina, Klaus Sokolowski-Tinten, Alfred Vogel, and Leonid V. Zhigilei. This work has been supported by grants from the Natural Sciences and Engineering Research Council of Canada (NSERC) and the *Fonds Québécois de la Recherche sur la Nature et les Technologies* (FQRNT). We are immensely grateful to the *Réseau Québécois de Calcul de Haute Performance* (RQCHP) for generous allocations of computer resources. D.P. gratefully acknowledges Director's Funding at Los Alamos National Laboratory. Los Alamos National Laboratory is operated by Los Alamos National Security LLC, for the National Nuclear Security Administration of the U.S. Department of Energy under contract DE-AC52-O6NA25396.

References

1. D.S. Ivanov, L.V. Zhigilei, Phys. Rev. Lett. **91**, 105701 (2003)
2. V.V. Zhakhovskiĭ, K. Nishihara, S.I. Anisimov, N.A. Inogamov, JETP Lett. **71**, 167 (2000)
3. N.M. Bulgakova, R. Stoian, A. Rosenfeld, I.V. Hertel, E.E.B. Campbell, Phys. Rev. B **69**, 054102 (2004)
4. L.V. Zhigilei, B.J. Garrison, J. Appl. Phys. **88**, 1281 (2000)
5. D. Perez, L.J. Lewis, Phys. Rev. Lett. **89**, 255504 (2002)
6. P. Lorazo, L.J. Lewis, M. Meunier, Phys. Rev. Lett. **91**, 225502 (2003)
7. D. Perez, L.J. Lewis, Phys. Rev. B **67**, 184102 (2003)
8. D. Perez, L.J. Lewis, Appl. Phys. A **79**, 987 (2004)
9. D. Perez, L.J. Lewis, P. Lorazo, M. Meunier, Appl. Phys. Lett. **89**, 141907 (2006)
10. P. Lorazo, D. Perez, L.J. Lewis, M. Meunier, in *High Power Laser Ablation V*, ed. by C.R. Phipps. Proceeding of SPIE, vol. 5448 (SPIE, Bellingham, 2004), pp. 520–531,
11. P. Lorazo, L.J. Lewis, M. Meunier, Phys. Rev. B **73**, 134108 (2006)
12. A. Cavalleri, K. Sokolowski-Tinten, J. Bialkowski, M. Schreiner, D. von der Linde, J. Appl. Phys. **85**, 3301 (1999)
13. K. Sokolowski-Tinten, J. Bialkowski, A. Cavalleri, D. von der Linde, A. Oparin, J. Meyer ter Vehn, S.I. Anisimov, Phys. Rev. Lett. **81**, 224 (1998)
14. D. von der Linde, K. Sokolowski-Tinten, Appl. Surf. Sci. **154–155**, 1 (2000)
15. D. Bauërle, *Laser Processing and Chemistry* (Springer, Berlin, 2000)
16. G.W. Yang, Progr. Mater. Sci. **52**, 648 (2007)
17. A.V. Kabashin, M. Meunier, in *Recent Advances in Laser Processing of Materials*, eds. by J. Perrière, E. Milon, E. Fogarassy (Elsevier, Amsterdam, 2006)
18. A. Miotello, R. Kelly, Appl. Phys. Lett. **67**, 3535 (1995)
19. A. Miotello, R. Kelly, Appl. Phys. A **69**, S67 (1999)
20. Y. Siegal, E.N. Glezer, L. Huang, E. Mazur, Ann. Rev. Mat. Sci. **25**, 223 (1995)
21. D. von der Linde, K. Sokolowski-Tinten, J. Bialkowski, Appl. Surf. Sci. **109–110**, 1 (1997)
22. S. I. Anisimov, B.L. Kapeliovich, T.L. Perel'man, Sov. Phys. JETP **39**, 375 (1974)
23. S.K. Sundaram, E. Mazur, Nat. Mater. **1**, 217 (2002)
24. D. von der Linde, H. Schüler, J. Opt. Soc. Am. B **13**, 216 (1996)
25. K. Sokolowski-Tinten, J. Bialkowski, A. Cavalleri, M. Boing, H. Schüler, D. von der Linde, in *High Power Laser Ablation*, ed. by C.R. Phipps, Proceedings of SPIE, vol. 3343 (SPIE, Bellingham, 1998) pp. 46–57
26. D. von der Linde, private communication.
27. B.N. Chichkov, C. Momma, S. Nolte, F. von Alvensleben, A. Tünnermann, Appl. Phys. A **63**, 109 (1996)
28. D.A. Willis, X. Xu, Appl. Surf. Sci. **197–198**, 118 (2002)
29. D.A. Willis, X. Xu, Int. J. Heat Mass Transf. **45**, 3911 (2002)
30. J. Jandeleit, G. Urbasch, H.D. Hoffmann, H.-G. Treusch, E.W. Kreutz, Appl. Phys. A **63**, 117 (1996)
31. V.A. Batanov, F.V. Bunkin, A.M. Prokhorov, V.B. Fedorov, Sov. Phys. JETP **36**, 311 (1973)
32. N.M. Bulgakova, A.V. Bulgakov, Appl. Phys. A **73**, 199 (2001)
33. K.H. Song, X.Xu, Appl. Surf. Sci. **127–129**, 111 (1998)
34. J.H. Yoo, S.H. Jeong, X.L. Mao, R. Greif, R.E. Russo, Appl. Phys. Lett. **76**, 783 (2000)
35. N.A. Inogamov, Yu.V. Petrov, S.I. Anisimov, A.M. Oparin, N.V. Shaposhnikov, D. von der Linde, J. Meyer ter Vehn, JETP Lett. **69**, 310 (1999)
36. M.M. Martynyuk, Sov. Phys. Tech. Phys. **21**, 430 (1976)
37. F. Vidal, T.W. Johnston, S. Laville, O. Barthélemy, M. Chaker, B. Le Drogoff, J. Margot, M. Sabsabi, Phys. Rev. Lett. **86**, 2573 (2001)
38. P.P. Pronko, S.K. Dutta, D. Du, R.K. Singh, J. Appl. Phys. **78**, 6233 (1995)
39. S.I. Anisimov, V.V. Zhakhovskiĭ, N.A. Inogamov, K. Nishihara, A.M. Oparin, Yu.V. Petrov, JETP Lett. **77**, 606 (2003)
40. A.A. Oraevsky, S.L. Jacques, F.K. Tittel, J. Appl. Phys. **78**, 1281 (1995)

41. O.Yavas, P. Leiderer, H.K. Park, C.P. Grigoropoulos, C.C. Poon, A.C. Tam, Phys. Rev. Lett. **72**, 2021 (1994)
42. T.E. Glover, J. Opt. Soc. Am. B **20** 125 (2003)
43. R. Kelly, A. Miotello, Phys. Rev. E **60**, 2616 (1999)
44. M.M. Martynyuk, Russ. J. Phys. Chem. **57**, 494 (1983)
45. M.M. Martynyuk, Sov. Phys. Tech. Phys. **19**, 793 (1974)
46. J.K. Chen, J.E. Beraun, J. Opt. A **5**, 168 (2003)
47. L.V. Zhigilei, E. Leveugle, B.J. Garrison, Y.G. Yingling, M.I. Zeifman, Chem. Rev. **103**, 321 (2003)
48. V.P. Carey, *Liquid-Vapor Phase-Change Phenomena* (Hemisphere, New York, 1992)
49. A. Cavalleri, K. Sokolowski-Tinten, J. Bialkowski, D. von der Linde, Appl. Phys. Lett. **72**, 2385 (1998)
50. X. Xu, Appl. Surf. Sci. **197–198**, 61 (2002)
51. Q. Lu, S.S. Mao, X. Mao, R.E. Russo, Appl. Phys. Lett. **80**, 3072 (2002)
52. B.J. Garrison, T.E. Itina, L.V. Zhigilei, Phys. Rev. E **68**, 041501 (2003)
53. S.I. Anisimov, N.A. Inogamov, A.M. Oparin, B. Rethfeld, T. Yabe, M. Ogawa, V.E. Fortov, Appl. Phys. A **69**, 617 (1999)
54. N.A. Inogamov, S.I. Anisimov, B. Retfeld, J. Exp. Theor. Phys. **88**, 1143 (1999)
55. D. Frenkel, B. Smit, Understanding Molecular Simulations – from Algorithms to Applications (Academic, San Diego, 1992)
56. F.H. Stillinger, T.A. Weber, Phys. Rev. B **31**(8), 5262–5271 (1985)
57. K. Sokolowski-Tinten, C. Blome, C. Dietrich, A. Tarasevitch, M. Horn von Hoegen, D. von der Linde, A. Cavalleri, J. Squier, M. Kammler, Phys. Rev. Lett. **87**, 225701 (2001)
58. D.S. Ivanov, L.V. Zhigilei, Phys. Rev. B **68**, 064114 (2003)
59. V. Zhakhovskii, N. Inogamov, K. Nishihara, J. Phys. Conf. Ser. **112**(4), 042080 (2008)
60. C. Cheng, X. Xu, Phys. Rev. B **72**, 165415 (2005)
61. N.N. Nedialkov, S.E. Imamova, P.A. Atanasov, J. Phys. D: Appl. Phys. **37**, 638 (2004)
62. M.E. Povarnitsyn, T.E. Itina, M.Sentis, K.V. Khishchenko, P.R. Levashov, Phys. Rev. B **75**(23), 235414 (2007)
63. J.P. Colombier, P. Combis, F. Bonneau, R. Le Harzic, E. Audouard, Phy. Rev. B 71(16), 165406 (2005)
64. K. Eidmann, J. Meyer-ter Vehn, T. Schlegel, S. Hüller, Phys. Rev. E **62**(1), 1202–1214 (2000)
65. V.K. Shen, P.G. Debenedetti, J. Chem. Phys. **114**, 4149–4159 (2001)
66. B.L. Holian, D.E. Grady, Phys. Rev. Lett. **60**, 1355 (1988)
67. Wm.T. Ashurst, B.L. Holian, Phys. Rev. E **59**, 6742 (1999)
68. S. Toxvaerd, Phys. Rev. E **59**, 6742 (1999)
69. A. Vogel, V. Venugopalan, Chem. Rev. **103**, 577 (2003)
70. S. Georgiou, A. Koubenakis, Chem. Rev. **103**, 349 (2003)
71. D. Perez, L.K. Béland, D. Deryng, L.J. Lewis, M. Meunier, Phys. Rev. B **77**(1), 014108 (2008)
72. J.-P. Sylvestre, A.V. Kabashin, E. Sacher, M. Meunier, Appl. Phys. A **80**, 753–758 (2005)
73. X. Gu, H.M. Urbassek, Appl. Phys. B **81**, 675 (2005)
74. X. Gu, H.M. Urbassek, Appl. Surf. Sci. **253**, 4142 (2007)
75. S. Amoruso, R. Bruzzese, N. Spinelli, R. Velotta, M. Vitiello, X. Wang, Europhys. Let. **67**, 404–410 (2004)
76. S. Eliezer, N. Eliaz, E. Grossman, D. Fisher, I. Gouzman, Z. Henis, S. Pecker, Y. Horovitz, M. Fraenkel, S. Maman, Y. Lereah, Phys. Rev. B **69**, 144119 (2004)
77. A.V. Kabashin, M. Meunier, J. Appl. Phys. **94**, 7941–7943 (2003)
78. R. Le Harzic, D. Breitling, M. Weikert, S. Sommer, C. Föhl, F. Dausinger, S. Valette, C. Donnet, E. Audouard, Appl. Phys. A **80**, 1589 (2005)
79. Q. Feng, Y.N. Picard, H. Liu, S.M. Yalisove, G. Mourou, T.M. Pollock, Scr. Mater. **53**, 511 (2005)
80. S. Valette, E. Audouard, R. Le Harzic, N. Huot, P. Laporte, R. Fortunier, Appl. Surf. Sci. **239**, 381 (2005)
81. A. Borowiec, D.M. Bruce, D.T. Cassidy, H.K. Haugen, Appl. Phys. Lett. **83**, 225 (2003)
82. A. Borowiec, M. Mackenzie, G.C. Weatherly, H.K. Haugen, Appl. Phys. A **77**, 411 (2003)

83. A. Borowiec, M. Mackenzie, G.C. Weatherly, H.K. Haugen, Appl. Phys. A **76**, 201 (2003)
84. N.N. Nedialkov, P.A. Atanasov, Appl. Surf. Sci. **252**, 4411 (2005)
85. X. Wang, J. Phys. D Appl. Phys. **38**(11), 1805–1823 (2005)
86. Z. Lin, R.A. Johnson, L.V. Zhigilei, Phys. Rev. B **77**(21), 214108 (2008)
87. L. Huang, J.P. Callan, E.N. Glezer, E. Mazur, Phys. Rev. Lett. **80**, 185 (1998)
88. D. Bouilly, D. Perez, L.J. Lewis, Phys. Rev. B **76**(18), 184119 (2007)

Chapter 3
Laser Devices and Optical Systems for Laser Precision Microfabrication

Kunihiko Washio

Abstract This chapter provides introductory explanation on various laser devices and optical systems for laser precision microfabrication regarding their basic operation principles and examples of performance capability. Emphasis is placed on compact and efficient diode-pumped high-brightness solid-state lasers capable of a variety of lasing operations from continuous wave to ultrafast pulse generation. The following optical systems are discussed: beam shaping optics, beam scanning optics, spatial light modulators, optical frequency convertors, and optics for beam characterization and process control.

3.1 Introduction

Today, almost all the functional key components used in high-end electronic appliances or medical equipment, etc., are composed of numerous elegant materials with sophisticated structures having fine feature sizes and demand sophisticated leading-edge microfabrication technologies. These microfabrication technologies must meet the requirements for device performance, processing quality, throughput and yield, among other tough specifications. Given the availability of laser devices of diversified types and operation modes and their integration with various types of advanced optical systems, flexible laser precision microfabrication technologies can often provide the best solution for the above complicated requirements.

The goal of this chapter is to provide an introductory explanation on various laser devices and optical systems regarding their basic operation principles and examples of performance capability. For further detailed explanation, the reader should consult the references given in the text.

K. Washio (✉)
Paradigm Laser Research Limited, Machida, Tokyo, 195-0072 Japan
e-mail: k-washio@paradigm-laser-research.jp

K. Sugioka et al. (eds.), *Laser Precision Microfabrication*,
Springer Series in Materials Science 135, DOI 10.1007/978-3-642-10523-4_3,

© Springer-Verlag Berlin Heidelberg 2010

3.2 Laser Devices

Laser radiation is characterized by an extremely high degree of monochromaticity, coherence, directionality, brightness, and emission capability in short pulse duration [1]. Various types of laser devices with wide range of physical and operating parameters have been so far developed for different diversified applications. Laser devices can be characterized by various categories, such as physical states of the active material, emission wavelengths, etc. Important parameters for high precision microfabrication application are wavelength, pulse duration, pulse energy, pulse repetition frequency, polarization, irradiating beam spot size and profile at the workpieces, etc. This section introduces various high-power laser devices having distinct features in emission wavelengths or operation modes for industrial use. Although semiconductor diode lasers can operate at high wall-plug efficiency, they are not so predominantly used by themselves for microfabrication purposes due to the lack of enough brightness or power density. Therefore, this chapter omits discussion of semiconductor diode lasers. However, semiconductor diode lasers are becoming very important and are predominantly used as pump sources for realizing efficient and compact diode-pumped solid-state lasers (DPSSLs) and fiber lasers.

3.2.1 Various Laser Devices from Deep UV and Mid-IR Spectral Region

In macro processing such as cutting or welding of sheet metal, two types of lasers, namely, 10.6-μm CO_2 lasers and 1,064-nm Nd:YAG lasers in CW or not-so-short pulsed operation modes (with pulse duration longer than 1 μs), have been predominantly utilized [2]. However, for microfabrication applications, various kinds of lasers are being utilized to satisfy the wide range of different requirements. Table 3.1 shows some representative laser devices for microfabrication applications capable of operating in the wavelength range from deep UV to mid-IR. Harmonic wave generation using nonlinear crystals with high power IR pump lasers is nowadays more preferably used in the UV and visible region than using low-efficiency and bulky gas lasers such as Ar ion lasers or copper vapor lasers.

3.2.1.1 Excimer Lasers

The name "excimer" comes from "*exc*ited d*imer*." There are wide variety of excimer lasers, including F_2 (157 nm), ArF (193 nm), KrF (248 nm), XeCl (308 nm), and XeF (351 nm, 354 nm, etc.) lasers. Laser action in rare gas halogen excimers was reported for the first time in 1975 for XeBr (281.8 nm) and XeF (354 nm). The first experimental study with excimer lasers was performed by electron beam excitation of high-pressure gas. Although electron beam excitation has some attractive

Table 3.1 Some representative laser devices for microfabrication applications capable of operating in the wavelength range from deep UV to mid-IR

Physical states	Active medium or species (Center wavelengths)	Excitation methods	Features
Gas (excimer)	ArF (193 nm) KrF (248 nm) XeCl (308 nm)	Electric discharge	High energy, nanosecond pulses with relatively low-repetition rate (less than several kHz)
Solid state	Nonlinear crystals (Typically visible or UV)	Pumping by high power IR lasers	Harmonic generation with nonlinear optics
Solid state	Ti:sapphire (800 nm)	Optical pumping	Capable of ultrafast pulse emission
	Nd:YAG (1,064 nm)		Wide variety of operation modes
	Nd:YVO_4 (1,064 nm)		Wide variety of operation modes
	Yb:YAG (1,030 nm)		Wide variety of operation modes
	Yb:glass fiber (∼1.07 μm)		Efficient and high beam quality
Gas (molecular)	CO_2 (10.6 μm or 9.4 μm)	Electric discharge	Efficient and high power in mid-IR

features such as possibility of studying laser kinetics process for various gas compositions, its complexity, high costs and limited repetition rate are not suitable for practical applications. The more practical excitation technology is based on the self-sustained discharge in a laser gas [3]. Operation of high-pressure gas lasers in a self-sustained discharge regime demands a proper preionization technique to obtain a uniform glow discharge. UV radiation or X-rays can be used for preionization. Industrial excimer lasers, however, are generally adopting UV preionization by either spark discharge or surface corona discharge for ease of operation [4].

Depending on the material, practical wavelengths and fluences are recommended to achieve best results [5]. For many polymers and ceramics, 308 nm or 248 nm lasers are good choices for ablation processes. However, materials which are transparent or weakly absorbing at 308 nm or 248 nm wavelength may require 193 nm or 157 nm laser radiation, as for example fused silica or polytetrafluoroethylene (PTFE).

Pulse durations of typical discharge pumped excimer lasers used for material processing are in the range of 5–100 ns. The repetition rates of industrial excimer lasers capable of generating large energy per pulse are generally less than 1 kHz. For example, a recently developed high energy XeCl excimer laser capable of delivering up to 900 mJ pulse energy is designed to operate at 600 Hz [6]. For microlithography applications, however, high repetition rate lasers as high as 6 kHz with up to a 90 W average power have became now commercially available.

3.2.1.2 Solid-State Lasers

Following the advent of the first laser operation by a ruby laser in 1960, a variety of solid-state laser materials have been investigated [7, 8]. Most solid-state lasers emit radiation in the spectral region ranging from 400 nm to 3 μm that is based

on 4f–4f transitions of rare-earth ions or 3d–3d transitions of transition-metal ions. Solid-state host materials may be broadly grouped into crystalline solids and glasses. Fiber lasers are special cases of glass lasers and are usually separately classified from bulk-based solid-state lasers due to their distinct features such as flexible wave-guiding structures. Among many rare-earth-doped solid-state lasers, neodymium-doped lasers such as Nd:YAG ($Nd{:}Y_3Al_5O_{12}$) and $Nd{:}YVO_4$ lasers and ytterbium-doped lasers such as Yb:YAG and Yb:silica fiber lasers are of high importance because of their excellent lasing properties in terms of laser efficiency, maximum output power, and pulsed operation capability.

Solid-state lasers can be pumped optically by utilizing either artificial high intensity light sources such as flashlamps, arc lamps, diode lasers, etc., or collimating natural solar light. DPSSLs are more efficient than lamp-pumped ones and becoming very important due to their excellent laser properties and are explained in more detail in the following subsection.

Ti:sapphire (Ti: Al_2O_3) lasers have a broad emission band capable of emitting tunable output between 670 and 1,070 nm, and they are most widely used in the scientific research fields in which leading-edge high-peak power, ultrafast pulses are particularly required. Due to the lack of suitable high power green diode lasers for pumping Ti:sapphire lasers, non-diode-based, inefficient high power green lasers are required as pump sources, and therefore Ti:sapphire lasers tend to be expensive for industrial use. Therefore, development of diode-pumped rare-earth solid-state lasers is being extensively pursued for realizing more practical ultrashort light sources to replace Ti:sapphire lasers.

3.2.1.3 CO_2 Lasers

Compact, RF-excited waveguide CO_2 lasers [9] are well suited for microprocessing of ceramics, polymers, etc., and large number of such lasers are commercially utilized such as for alumina ceramics scribing, drilling of print circuit boards (PCBs), and marking on plastic packages. The usual operating wavelength of high power CO_2 lasers is 10.6 μm. For RF-excited waveguide CO_2 lasers, however, commercial models with laser output at 9.4 μm are also available by controlling waveguide loss in the laser resonator. There are many materials such as polyimide (also known as Kapton^{TM}), which exhibit higher absorption at 9.4 μm than 10.6 μm wavelength and can be processed with better quality and faster speed.

Large peak power enhancement and reduction in pulse width for planar waveguide RF-excited CO_2 lasers have been realized by gain modulation through RF discharge [10]. A peak power enhancement of 38 times the CW power level, with pulse duration as short as 10 μs, has been obtained. Such an enhanced peak power planar waveguide CO_2 laser was found to be very effective for microvia drilling of resin-coated copper (RCC) layers of laminated circuit boards [11]. Planar waveguide RF-excited CO_2 lasers also enable to operate in a pseudo-CW, burst mode with duty cycles that momentarily could reach 60% while being below the overall 20%

limit [12]. The intraburst repetition could exceed 40 kHz at 100% modulation. Clean scribe holes have been produced using a 200 μs pseudo-CW pulse with a 6 μs high energy tail pulse to eject residual molten material before it solidifies.

3.2.2 Diode-Pumped High-Brightness Continuous Wave Solid-State Lasers

Solid-state laser development has paralleled the improvement and discovery of pump sources and advanced device design for excellent heat management. In 1985, Sipes reported that 80 mW CW power in a single mode was achieved from a Nd:YAG laser with only 1 W of electrical power input to a single semiconductor laser array pump [13]. This corresponds to an overall efficiency of 8%, the highest reported CW efficiency for Nd:YAG laser at that time. The pump source used was a GaAlAs laser diode array operating at about 220 mW CW output at 810 nm with about 22% electrical to optical efficiency. Diode laser-pumped solid-state lasers are efficient, compact, all solid-state sources of coherent radiation. The recent and rapid advances in power and efficiency of diode lasers and their aggressive applications to the pumping of solid-state lasers have led to a renaissance in solid-state laser development [14].

The optical pumping process in a solid-state laser material is associated with the generation of heat for a number of reasons [15]. The volumetric heating of the laser material by the absorbed pump radiation and surface cooling required for heat reduction leads to a nonuniform temperature distribution in the material. This results in a distortion of the laser beam due to a temperature- and stress-dependent variation of the index of refraction. Thermal stress induced birefringence and thermal lensing effects caused in rod-shaped materials have been a big issue for realizing high performance solid-state lasers. The advent of diode-laser-based pump sources has enabled drastic reductions in heat generation from flash lamps, and it also has enabled the exploration of more sophisticated laser designs by shifting the rod-laser configuration to such as disk laser or fiber laser designs. In the following subsections, the state of the art of advanced diode-pumped lasers is briefly introduced.

3.2.2.1 Diode-Pumped Neodymium-Doped Solid-State Lasers

Neodymium-doped yttrium aluminum garnet (Nd:YAG) possesses a combination of properties uniquely favorable for laser operation. The YAG host is mechanically hard, of good optical quality, and has a high thermal conductivity. Furthermore, the cubic structure of YAG favors narrow fluorescent linewidth, which results in high gain and low threshold for laser operation [7]. Neodymium-doped yttrium vanadate (Nd:YVO_4) has several spectroscopic properties that are particularly relevant to laser diode pumping. The two outstanding features of vanadate are a large stimulated emission cross-section which is five times higher than Nd:YAG, and a

strong broadband absorption at 809 nm. Its high gain coefficient and short fluorescent lifetime enable high repetition-rate Q-switching operation which is very favorable for high-speed direct-write microfabrication. The crystal Nd:YLF (Nd: $LiYF_4$) has a number of attributes that offer an advantage over Nd:YAG in certain applications. The natural birefringence of this uniaxial crystal dominates thermally induced birefringence and the polarized output eliminates the thermal depolarization losses of optically isotropic hosts such as YAG. The material also has advantages for diode pumping since the fluorescence lifetime in Nd:YLF is twice as long as in Nd:YAG, enabling efficient energy storage with a number of pump diodes.

888 nm Pumping of Nd:YVO_4 Lasers

Nd:YVO_4 (vanadate) has favorable material properties for high repetition rate and short pulse operations in nanosecond (ns) Q-switched and picosecond (ps) mode-locked regimes. It has been demonstrated recently that optimized pumping of vanadate at 888 nm results in favorable system performance for extending the benefits of vanadate in the higher power range, benefiting from polarization-independent absorption, reduced quantum defect, and very low absorption coefficients compared to the common pump wavelength of 808 nm [16]. A series of systems, such as a compact 60 W high-efficiency TEM_{00} CW oscillator and a CW intracavity-frequency-doubled system capable of providing 62 W of power at 532 nm, have been developed based on this pumping technique.

3.2.2.2 Diode-Pumped Ytterbium-Doped Solid-State Lasers and Fiber Lasers

Owing to the recently made substantial progress in the development of efficient and high-brightness semiconductor diode lasers in the wavelength range from 910 to 980 nm, ytterbium-based DPSSLs and fiber lasers have emerged as novel important high-power lasers for material processing [17]. As can be seen from the spectroscopic data comparison between Nd:YAG and Yb:YAG shown in Table 3.2, the Yb ion has some advantages over Nd ion as laser emitting center. The broad absorption spectral width and long fluorescent life time enable efficient utilization of pump power from pump diodes, and broad emission spectral width enables generating shorter pulse width in mode-locked operation. The small Stokes shift between absorption and emission reduces the thermal loading in the laser material during laser operation. Since Yb ion has a very simple energy level scheme, there is no excited state absorption deteriorating the laser performance. The disadvantage for the Yb ion is that the final laser level is thermally populated and the lasing threshold becomes high due to quasi-three-level operation. Spectroscopic studies have been made for various host crystals in search for efficient ytterbium-doped crystalline laser material [18]. According to the evaluation studies, KYW ($KY(WO_4)_2$), KGdW ($KGd(WO_4)_2$), and Sc_2O_3 are much more efficient than YAG as host materials for ytterbium-doped crystalline lasers.

Table 3.2 Spectroscopic laser parameter values for Nd:YAG and Yb:YAG [17]

Parameter (units)	Nd:YAG	Yb:YAG
Pump transition wavelength, λ_p, (nm)	808	941
Pump transition peak cross-section, σ_p, (E-20 cm^2)	6.7	0.7
Pump transition line-width, $\Delta\lambda_p$, (nm)	<4	18
Pump transition saturation intensity, φ_p, (kW/cm^2)	12	28
Minimum pump intensity, I_{min}, (kW/cm^2)	∼0	2.8
Laser transition wavelength, λ_l, (nm)	1,064	1,030
Laser transition peak cross-section, σ_l, (E-20 cm^2)	2.8	2.1
Laser transition line-width, $\Delta\lambda_l$, (nm)	∼0.6	∼6
Laser transition saturation fluence, $\Gamma_{l,sat}$, (J/cm^2)	0.6	9.0
Laser transition saturation intensity, φ_l, (kW/cm^2)	2.6	9.5
Upper state manifold lifetime, τ, (ms)	0.26	0.97
Quantum defect fraction	0.24	0.11
Chi (specific heat fraction per excited state), X	0.37	∼0.11
Specific waste heat @ 0.05 cm^{-1} gain, (W/cm^3)	∼51	∼55

Diode-Pumped-Thin-Disk Yb:YAG Lasers

The core concept of the thin-disk laser principle is the usage of a thin, disk-shaped active medium that is cooled through one of the flat faces; simultaneously, the cooled face is used as folding or end mirror of the resonator. This face-cooling minimizes the transversal temperature gradient and the phase distortions transversal to the direction of the beam propagation. This, in fact, is the basis of one of the outstanding features of the thin-disk laser: the excellent beam quality [19].

The laser crystal has a diameter of several millimeters (depending on the output power/energy) and a thickness of 100–200 μm depending on the laser-active material, the doping concentration, and the pump design. The crystal can be pumped in a quasi-end-pumped scheme. In this case, the pump beam hits the crystal under an oblique angle. Depending on the thickness and the doping level of the crystal, only a small fraction of the pump radiation is absorbed in the laser disk. Most of the incident pump power leaves the crystal after being reflected at the backside. By successive redirecting and imaging of this part of the pump power again onto the laser disk, the absorption can be increased.

Very high laser output power can be achieved from one single disk, by increasing the pump spot diameter while keeping the pump power density constant. More than 5.3-kW power has been achieved with a maximum optical efficiency of more than 65% with a beam propagation ratio M^2 of less than 24. Excellent fundamental mode operation has also been achieved with more than 225-W laser power and an M^2 better than 1.2.

Diode-Pumped Ceramic Lasers

Ceramic laser materials fabricated by the vacuum sintering technique and nanocrystalline technology have gained more attentions as potential solid-state materials in

recent years because they have remarkable advantages compared with single crystal materials, such as easy fabrication of high concentration and large-sized ceramic samples, multilayer and multifunctional ceramic laser materials, low cost, and mass production [20]. Both Nd-doped and Yb-doped ceramic materials have been intensively studied. Slope efficiency of 79% and optical-to-optical efficiency of 60% have been obtained at 1,030 nm for a 1-mm-thick Yb:YAG ceramic plate ($C_{Yb} = 9.8$ at%) under CW diode-laser pumping [20].

High-Power Diode-Pumped Fiber Lasers

The high-power diode-pumped fiber lasers are operated with cladding-pumping technique using double-clad fiber structure [21]. The pump light is launched into an inner cladding which surrounds the active core and acts as a waveguide for the pump light. The pump light propagates in the inner cladding and is absorbed in the active core over the entire fiber length, enabling high gain and efficiency. Fiber lasers can generate high quality output beam without significant adverse effects from thermo-optical effects as thermally-induced lens formation or stress-induced birefringence even at high-power levels [21]. An all-fiber format, 10-mJ energy and a 200 W average power, Yb-doped laser has been developed with wall plug efficiency of 25% [22]. Based on a seed that utilizes first relaxation peaks and 65-μm multimode fiber amplifier, the laser produces 300 ns pulses at 1–50 kHz variable repetition frequencies. The cladding-pumping technologies have several variations. In the GTWave™ cladding-pumping technology [23], one signal and two pump fibers are placed in a common low-index coating for efficient pump power coupling.

3.2.3 Q-Switching and Cavity Dumping

Both Q-switching and cavity dumping are techniques to obtain laser pulses having high peak power. For laser mediums having long fluorescent lifetime, generally higher peak power can be obtained by Q-switching than cavity dumping. As for Q-switching methods, there are two kinds: namely, active and passive Q-switching. In active Q-switching, either acousto-optic modulators or electro-optic modulators are incorporated in the laser resonators. In passive Q-switching, saturable absorbers are used in the laser resonators. For material processing, active Q-switching is more dominantly used than passive Q-switching because of the ease of high average power operation and on-demand pulse emission capability.

3.2.3.1 Acousto-Optic Q-Switching

Since an acousto-optic modulator having very low insertion loss is easily obtainable, acousto-optic Q-switching is well suited for use in a CW-pumped low gain laser.

An acousto-optic loss modulator made by bonding an X-cut quartz transducer to a fused silica scattering medium offers a practical means for repetitively Q-switching continuously pumped Nd:YAG lasers at repetition rates up to 50 kHz [24]. The peak power output of a multi-transverse mode laser is typically enhanced by a factor of about 500 or more relative to CW operation at low (much less than 5 kHz) repetition rates and by larger factors when the transverse mode structure is suitably restricted. At high repetition rates, the peak power becomes smaller and the average power output approaches the CW level.

Q-switched lasers are well suited for efficient frequency conversion with nonlinear crystals. Vanadate lasers are well suited to obtain very high-repetition Q-switched pulses exceeding 50 kHz. With an end-pumped vanadate MOPA configuration, UV average power of 36 W with TEM_{00} mode has been realized at repetition rates around 100 kHz [25].

3.2.3.2 Electro-Optic Q-Switching and Pulse Slicing

Unlike the acousto-optic Q-switches in which the total turn-off time is limited by the duration of sound wave propagation (110–220 ns/mm) across the beam diameter, the electro-optic devices provide a short (less than 10 ns) response needed for minimum losses. Extinction ratios of better than 100:1 for electro-optic crystals ensure their reliable hold-off. By contrast, acousto-optic devices are characterized by single-pass dynamic losses of approximately 40%, which hinders their use in high-gain lasers. A new generation of oxide crystals, such as rubidium titanyl phosphate $RbTiOPO_4$ (RTP) and barium metaborate (BBO), is emerging for electro-optic Q-switching or control of high-power pulsed lasers [26]. Especially, RTP stands out in their ability to provide Q-switching at extremely high repetition rates up to 200 kHz [26].

Electro-optic devices can also be used to generate short pulses by slicing longer pulses. Achieving subnanosecond optical switching using a Pockels cell requires an electrically optimized cell design and a compatible fast driver. The design and operation of a high voltage, high speed switching circuit have been demonstrated by achieving an optical switching time of 238 ps when used in conjunction with a 6 mm aperture Pockels cell [27]. The driver uses a Marx-configured avalanche-transistor design to deliver up to 4 kV pulses into a 50 Ω load with approximately 12 ps jitter and an output pulse length of 7 ns.

3.2.3.3 Cavity Dumping

Cavity dumping is a method to obtain short pulses with duration close to roundtrip transit time in the cavity by coupling out entire laser energy circulating in the cavity with an optical switch. The actually obtainable pulse duration depends on the switching time of the optical switch used.

Both acousto-optic and electro-optic switches can be used depending on the applications. Faster switching is possible with electro-optic switches than acousto-optic switches, but higher laser gain is necessary to allow their larger insertion loss. Since 100% reflective mirrors can be used in the cavity, the laser build-up time

can be very short and pulse repetition rate can be much higher than that obtainable by using Q-switching. In early cavity dumping experiments with an intracavity acousto-optic modulator made of fused silica in the CW-pumped Nd:YAG laser, the repetition rate of the light pulses could be controlled from 125 kHz to several MHz [28]. To achieve a high power at high repetition rate of 1 MHz or so, the cavity length is critical [29]. If the cavity length is too long, the pulse has not enough time to build up and extract significant amount of energy from laser crystals. High speed, high-voltage driving technologies also become important to obtain high-repetition operation with short light pulses. In tests with a Yb:YAG thin-disk laser and a Pockels cells containing two BBO crystals, the pulse width obtained was 19 ns at 1 MHz, whereas the cavity round-trip time was 4.5 ns [29]. The pulse duration was found to be primary dependent on the switching time of the Pockels cells and independent on the repetition rate. Cavity dumping can be incorporated into mode-locked laser oscillators to obtain picosecond- or femtosecond ultrashort light pulses [30].

3.2.4 Picosecond and Femtosecond, Ultrafast Pulsed Laser Oscillators and Amplifiers

Ultrafast pulses having high peak power are increasingly used for various precision microfabrication applications such as ablative surface microstructuring or localized, three-dimensional bulk material modification by utilizing multiphoton absorption processes. Mode locking is an elegant and powerful technology to obtain ultrafast pulses with pulse duration much shorter than the cavity roundtrip transit time. However, due to the high repetition rate of the mode-locked oscillation, the peak power obtainable from the laser oscillator alone is usually not strong enough for material processing and sophisticated pulse amplification schemes are necessary for practical microfabrication applications. This section introduces some key technologies for obtaining ultrafast pulsed laser oscillators and amplifiers.

3.2.4.1 Mode Locking

In the free-running, non-mode-locked lasers having broad gain spectrum, many axial modes oscillate independent of the others, and the total intensity has thermal noise-like characteristics due to the superposition of the randomly oscillating axial modes. Mode locking is a scheme to enforce the oscillating modes to maintain a fixed-phase relationship to each other, so that the output will vary in a well-defined manner as a function of time [31].

There are two kinds of mode locking schemes, namely, passive mode locking and active mode locking [31, 32]. In active mode locking, intracavity optical modulators such as acousto-optic modulators are used. In passive mode locking, some kinds of nonlinear materials such as saturable absorbers or Kerr lens (virtual component) are

used. In certain systems, dynamic gain saturation is combined. With passive mode locking, shorter pulses are obtainable than with active mode locking. Sophisticated techniques have been often required to reliably self start passive mode locking for gain materials having long upper state fluorescent lifetime. SESAM's (semiconductor saturable absorber mirrors) have successfully solved this problem in mode locking of solid-state lasers [33].

As for gain materials for ultrafast lasers for micro processing, two types of materials, namely, Ti:sapphire with very wide gain bandwidth and rare-earth doped (Nd-or Yb-doped) materials capable of pumping with diode lasers are of practical importance and are discussed next.

3.2.4.2 Ultrafast Ti:Sapphire Laser Systems

The fluorescence of Ti:sapphire (Ti:Al_2O_3) peaks at 780 nm and has a wide bandwidth of about 180 nm (FWHM) [7], enabling broadband mode locking for generating extremely short femtosecond pulses. The Ti:sapphire has an absorption band in the blue/green spectral region which enables pumping with high-power Ar ion lasers or frequency-doubled Nd-doped solid state lasers such as Nd:YAG.

Chirped-Pulse Amplification in Ti:Sapphire Regenerative Amplifiers

Because typical output energies obtainable from Ti:sapphire ultrafast laser oscillators are in the range of 1–10 nJ, several orders of magnitude amplification are necessary for applications in materials processing. Chirped-pulse amplification (CPA) in a regenerative amplifier is a powerful technique by which the energy of ultrafast pulses can be increased significantly [34]. This method makes possible the production of energetic femtosecond (fs) pulses without damage or unwanted nonlinear effects in the amplifier material. In an early experimental setup [34], 40-fs pulses were stretched to 372 ps by all-reflective-optics stretches with 1,200-line/mm holographic gratings and were then injected and amplified to energies of 0.7 mJ with 17 round trips in a regenerative amplifier. After cavity dumping with a Pockels cell and compression with a grating-pair compressor, 0.35-mJ, 55-fs transform-limited pulses were produced with 1 kHz repetition rate.

The regenerative amplifiers can be repetitively injected and cavity-dumped either with electro-optic switches or acousto-optic switches. Typical high-repetition-rate Ti:sapphire amplification systems using electro-optic pulse selection methods operate in the range from 10 Hz to 20 kHz with an energy of ∼mJ, whereas those using acousto-optic pulse selection methods can operate in the range from 100–250 kHz with an energy range of ∼μJ [35, 36]. Recently, 28 μJ, 39 fs pulses with a peak power as high as 0.7 GW at a repetition rate of 100 kHz have been obtained from a downchirped-pulse amplification (DPA) Ti:sapphire laser amplification system [36]. In DPA configuration, the laser pulse is stretched with negative dispersion elements (down-chirp), such as prism pair and grating pair, and then compressed by a positive

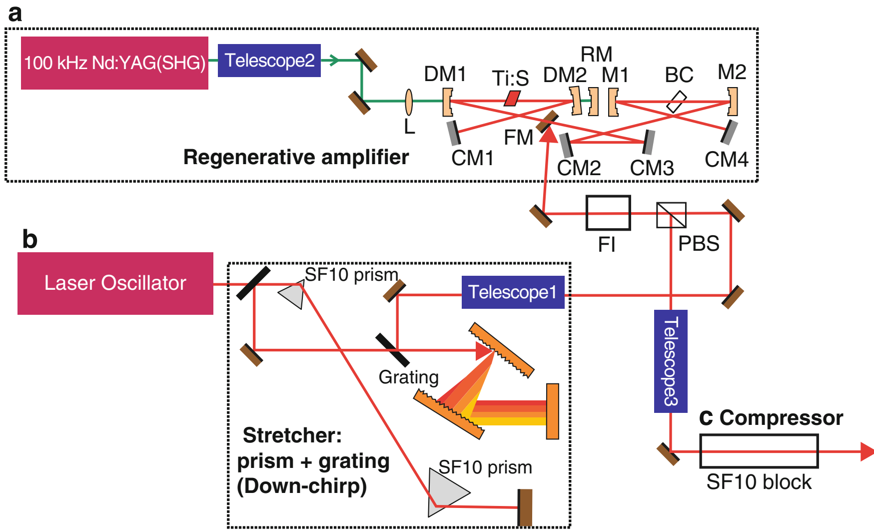

Fig. 3.1 Schematic diagram of a 100 kHz DPA Ti:sapphire amplification system. Regenerative amplifier (**a**), pulse stretcher (**b**), and pulse compressor (**c**). L, lens; DMs dichroic mirrors; Ms, dielectric mirrors; RM, re-focusing mirror; FM, folding mirror; CMs, chirped mirrors; FI, Faraday isolator; PBS, polarizing beam splitter; Ti:S, Ti:sapphire crystal

dispersion element which is just an optical glass block. The main advantage of DPA is high compression efficiency (larger than 95%) and simple compressor alignment. Figure 3.1 shows the schematic diagram of the 100 kHz DPA Ti:sapphire amplification system.

Water-Cooled Ti:Sapphire Femtosecond Laser System

The main challenge to overcome in a high repetition-rate, high pulse energy femtosecond Ti:sapphire laser system is the thermal load of the Ti:sapphire crystal [37]. Although 20 W compressed output power has been obtained at 10 kHz operation with cryogenic cooling at 100 K, simple water cooling would be more attractive for industrial microfabrication application. A compact and reliable water-cooled femtosecond all solid-state laser running at a repetition rate of 10 kHz with a nearly diffraction limited beam (having M^2 value of less than 1.2) has been recently demonstrated [37]. Average power of 3.5 W with pulse duration of 60 fs after compression has been obtained with a delivered pump power of 31 W.

3.2.4.3 Rare-Earth-Doped and Diode-Pumped Ultrafast Laser Systems

Neodymium- or Ytterbium-doped laser mediums have strong absorption bands in the near infrared spectral region and can be pumped efficiently with high-power diode lasers available in those spectral regions, enabling very compact laser systems

as compared with Ti:sapphire-based laser systems. Although pulse widths are much broader than those available with Ti:sapphire-based laser systems, complex chirped-amplification systems are generally not required as for ps pulse generation and overall system configuration can be very simple and compact. Ytterbium-doped lasers have generally much broader spectral widths and enable production of much shorter pulses than available with neodymium-doped lasers. However, much stronger pump intensity is required for ytterbium-doped lasers than neodymium-doped lasers for efficient laser operation. For ytterbium lasers, thin disk or fiber designs are more favored than rod-based designs for excellent heat management and efficient operation.

Neodymium-Doped Vanadate Picoseconds Laser Systems

Neodymium vanadate lasers such as Nd:YVO_4 lasers and Nd:$GdVO_4$ lasers can produce high-power ps pulses in the 10 ps range, a few times shorter than those available with Nd:YAG lasers because of their wider gain bandwidths. With a diode-pumped ps Nd:$GdVO_4$ regenerative amplifier system designed for micromachining applications, an average output power of 13 W has been obtained at 200 kHz repetition rate with pulse duration as short as 6.8 ps and with a pulse energy of 65 μJ [38]. By utilizing a diode-pumped rod-based Nd:YVO_4 regenerative amplifier, more than 25 W of average power has been obtained at 200 kHz with a pulse duration of 10 ps at 1,064 nm [39]. The seed laser used in this experiment was a mode-locked fiber laser generating around 3 mW average power at 40 MHz. The average power of the amplifier has been increased further using a single pass linear amplifier to produce 54 W at 200 kHz. The advanced oscillator-amplifier (MOPA) laser design, based on reliable Nd:YVO_4-systems, enables power scaling of IR-pulses and leads to a series of laser systems with a repetition rate as high as 1 MHz and average power levels ranging from 10 W to well above 50 W [40].

Yb:YAG Thin-Disk Picosecond Regenerative Amplifiers

As compared to conventional, end-pumped amplifiers in rod geometry, thin disk lasers have the advantage of power scalability without sacrificing beam quality. Figure 3.2 shows a schematic view of a thin-disk ps regenerative amplifier [41]. High-power ps pulses with duration of about 7 ps and with an average power of about 80 W have been obtained corresponding to a pulse energy of 400 μJ at 200 kHz, and an optical to optical efficiency with respect to the launched power close to 50%.

Yb:YAG Thin-Disk, Long-Cavity Ultrafast Laser Oscillators

The pulse energy can be scaled by increasing the cavity length by utilizing, for example, multipass Herriot cells [42]. As compared to laser systems using regenerative amplifiers, ultrafast oscillators are very attractive owing to their simplicity and

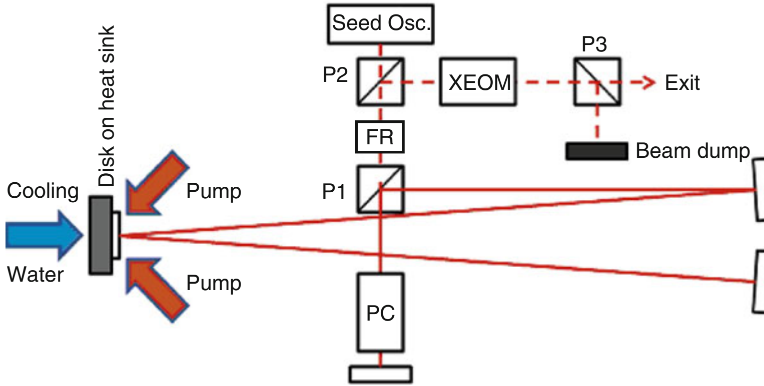

Fig. 3.2 A schematic view of a thin-disk ps regenerative amplifier. PC: Pockels cell; P1, P2, and P3: Polarizers; FR: Faraday rotator; XEOM: external modulator comprising a half-wave Pockels cell

compactness. By employing a self-imaging active multipass geometry in a Yb:YAG thin-disk laser oscillator, stable single-pulse-operation has been obtained with an average power in excess of 50 W at a repetition rate of 3.8 MHz [43]. The maximum pulse energy was 13.4 μJ at pulse duration of 1.36 ps with a time-bandwidth product of 0.34 (within 10% of the transform limit of 0.315 for soliton pulse). In an another experimental setup with the cavity length extended to 37 m using a Herriot-type multipass cell and operating the laser in a helium atmosphere in order to eliminate the air nonlinearity, 11.3-μJ pulses with pulse duration of 791 fs have been obtained at a repetition rate of 4 MHz [42]. The obtained peak power of 12.5 MW is very attractive for many laser microfabrication applications.

Fiber Chirped Amplification Systems

Fiber lasers have some attractive features as light sources for ultrafast pulse generation. The well-known advantages of fiber lasers in the continuous regime, the excellent heat dissipation characteristics along with the high efficiencies and power-independent excellent beam quality, can be transferred to the short pulse regime [44]. Furthermore, the laser transition spectra are significantly broadened in the glass host than crystalline host, enabling the amplification of ultrafast laser pulses in fibers. The high single-pass gain of a rare-earth-dope fiber enables a compact laser system by omitting the needs for the complex amplification schemes such as regenerative or multipass amplification. However, peak power scaling of ultrafast single-mode fiber amplifiers is restricted due to nonlinear pulse distortions, which are enforced by the large product of intensity and the interaction length inside the fiber core. Therefore, adoption of chirped amplification schemes is necessary for high-power ultrafast fiber amplifier systems. Recently, by utilizing a large-mode-ytterbium-doped photonic crystal fiber (PCF), a CPA system delivering

100 μJ pulse energy at a repetition rate of 900 kHz, corresponding to an average power of 90 W, has been obtained [44]. The emitted pulses are as short as 500 fs.

A robust and very compact fiber chirped pulse amplifier (FCPA) has been recently realized by adopting a fiber stretcher in place of conventional free-space gratings and linking the all critical components with fiber-optics [45]. Ultrafast pulses with pulse duration of 500 fs and pulse energy of 10 μJ have been obtained at a repetition rate of 100 kHz.

3.3 Optical Systems

Various kinds of optical components for modification and control of laser beams are needed to realize practical laser processing equipment. The following sections describe the most important of these.

3.3.1 Optical Components for Modification and Control of Laser Beams

For the purpose of explaining in this subsection the various optical components, they are grouped into the following two categories:

1. Basic beam delivery optics
   Mirrors, lenses, optical fibers, beam splitters, polarization optics, isolators, apertures, optical switches, etc
2. Advanced functional optics

Beam shaping optics, beam scanning optics, spatial light modulators (SLM), optical frequency convertors, optics for beam characterization and process control.

The following subsections describe the above mentioned advanced functional optics. Explanations on the basic beam delivery optics are mostly omitted except on radial and azimuthal polarization optics as an example of recent hot topics on polarization optics for laser microfabrication. For further general explanation on the basic beam delivery optics, readers are advised to refer to the relevant literatures [46, 47].

3.3.1.1 Optics for Generating Radially-Polarized and Azimuthally-Polarized Laser Beams

Recently, application of a radially polarized UV laser beam for interconnect via drilling was investigated [48]. Microvias drilled with a p-polarized beam were compared to those drilled with a radially polarized beam. Results revealed that a radially

polarized laser beam significantly improves the performance of laser drilling in all aspects, including feature size, efficiency, the cross-section profile, and cleanness of the finishing. Some interesting features of radially polarized beams are improved radiation energy coupling with the irradiated materials and the availability of sharper focus [49].

There are several intracavity techniques for generating radial or azimuthal polarization states from laser oscillators [50]. Examples of specially developed optical components for generating radial polarization are multilayer polarizing grating mirrors [51] and segmented half-wave plates [52]. A segmented half-wave plate can be used for polarization conversion external to the lasers. A high power, radially-polarized laser beam of 110 W has been produced from a single-transverse-mode, linearly-polarized Yb fiber laser by using a segmented half-wave plate made of 12 segments of differently oriented 2D photonic crystals [53].

3.3.2 Optical Systems for Beam Shape Transformation

Although Gaussian shaped laser beams are widely used, they do not necessarily have the best properties in terms of the beam profiles and phases, depending on particular applications. Therefore, beam shaping becomes necessary to realize optimum irradiation condition. Beam shaping is the process of redistributing the irradiance and the phase of a beam of optical radiation [54]. The irradiance distribution defines the profile of the beam, such as Gaussian, circular, rectangular, annular, or multimode. The phase of the shaped beam determines its propagation properties to a large extent. The beam shaping techniques can be divided into the following three categories.

1. Aperturing of the beam
2. Field mapping
3. Beam integrators

Aperturing is trivial, but useful. Field mapping realizes transformation of the input field into the desired output fields in a controlled manner by utilizing reflective, refractive, or diffractive optics.

3.3.2.1 Beam Homogenizers for Mask Imaging Systems

Beam homogenizers are indispensable optical components in mask-based imaging systems using multimode lasers such as excimer lasers [55]. There are several beam integrator type beam homogenizers such as biprism homogenizers, fly's eye beam homogenizers, etc. There are four issues to be considered when evaluating the quality of the beam at the homogenized plane. They are large-scale homogeneity, diffraction effects, coherence length effects, and astigmatism [55].

3.3.2.2 Gaussian to Flat-Top Beam Shaping for Laser Microfabrication

The drilling of microvia holes in high-density electronic packages has recently entered broad industrial use for high-volume production [56]. In such applications, process stability and throughput are key drivers of commercial success. When Gaussian irradiance with an aperture is used, a tradeoff between quality and speed emerges in this so-called Clipped-Gaussian configuration. On the contrary to this, it has been demonstrated that with the shaped beam imaging configuration using a field-mapping-based beam shaping optics to transform the Gaussian profile to a super Gaussian, near tophat profile at the plane of the aperture, the tradeoffs between process speed and quality are less severe, and throughput is about 25% higher than achieved without the beam shaping optics.

Gaussian profile to tophat profile conversion can be accomplished by refractive or diffractive optics. The main advantages of refractive optics are higher transmission and efficiency as well as better homogeneities of the generated light field [57]. The main advantages of diffractive optics are extended design flexibility for generating light patterns of any shape, such as circular, rectangular, line shape or multispots and design capability to extend process stability against such as input variations [58].

One of the most demanding micro-welding applications is the welding of thin stainless steel for hard disk head assemblies. An off-axis diffractive beam shaper has been successfully applied to produce focused spots less than 50 μm in diameter from a TEM_{00} single-mode 200 W fiber laser [59]. The tophat spots have found to be effective not only to improve weld quality and repeatability, but also to reduce the process sensitivity to small fluctuations in pulse energy.

3.3.2.3 Anamorphic Beam Transformation System for a Very Thin and Long Line

A line-shaped green laser beam is required for high-throughput thermal annealing of Si by phase transition from amorphous to polycrystalline Si for flat panel display (FPD) production. For such an application, an extremely anamorphic beam transformation system having an aspect ratio as high as about 10,000 has been developed to be used with a laser source with a symmetrical beam parameter product [60]. In this system, at first, the symmetrical laser beam is expanded by a telescope to illuminate several lenslets of the beam transformation unit (BTU) for beam asymmetrization. The BTU divides and transforms the original beam into several beamlets which are then reimaged onto the microlens homogenizing unit (HOM) for the long axis. Finally, an anamorphic focusing system generates the long line with a length of 60 mm and a width of only 10 μm (FWHM) on the target. The key components of this beam line generator are the BTU and the homogenizing unit (HOM) and both can be realized by micro-optics-only subsystems.

3.3.2.4 Beam Shaping for Parallel Material Processing

For high speed patterning of large numbers of microstructures, parallel processing with a multispot generator and a high-power laser is often a better solution than using several lasers in parallel. Multispot generators using micro-optics [61] and diffractive optical element (DOE) [62] (see Chap. 3) have been developed. A uniform field having $5 \times 3\,\text{mm}^2$ has been transformed into 5×3 square uniform spots having dimensions of $0.2 \times 0.2\,\text{mm}^2$ by using a micro-optics-based multispot generator [61]. Nonuniformity below 5% and an efficiency (i.e., energy fluence inside the region of interest divided by the total fluence on the target plane) greater than 80% have been achieved.

A DOE is thin and light and enables to realize very compact parallel processing equipment. In order to obtain better performance than digitized elements, non-digitized beam splitters have been developed [62]. An efficiency of 95% with uniformity of exceeding 90% and SN of about 38% has been experimentally obtained for 13-beam non-digitized splitters. Figures 3.3 and 3.4 show the intensity distributions of the diffracted beams from a non-digitized element and a binary digitized element, respectively.

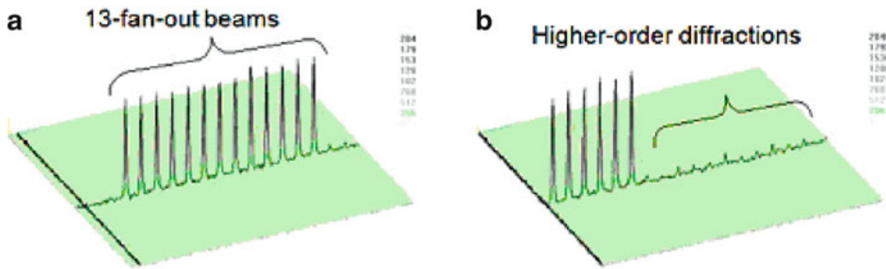

Fig. 3.3 Diffracted intensity distributions from a non-digitized element [62]. (**a**) The 13-fan-out beams and (**b**) higher-order diffraction beams in close-up

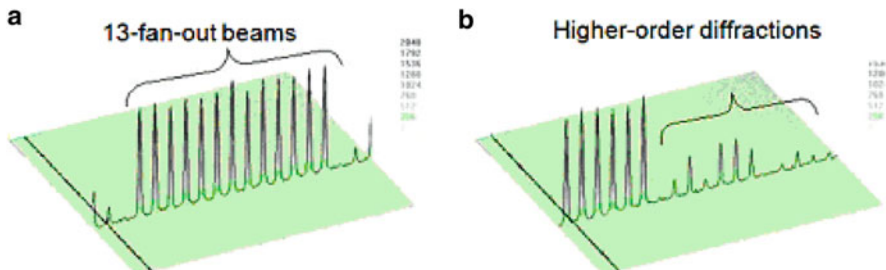

Fig. 3.4 Diffracted intensity distributions from a binary digitized element [62]. (**a**) The 13-fan-out beams and (**b**) higher-order diffraction beams in close-up

3.3.2.5 Beam Shaping to Generate Nondiffractive Bessel Beams

A Bessel beam is suitable for laser microfabrication because it possesses both a micron-sized focal spot and a deep focal depth (also see Chap. 1). As the influence of focusing aberrations is much smaller than that of a convex lens, the generation of a Bessel beam is very practical. Bessel beams can be generated by using an axicon lens [63] or diffractive optics [64]. A through hole with a diameter smaller than 10 μm has been made on a stainless steel sheet of 20 μm thickness by using a Bessel beam [63]. The taper angle of the hole drilled with Bessel beam has been found to be smaller than that with the focused beam from the convex lens.

3.3.3 Galvanometer-Based Optical Scanners

Galvanometer-based optical scanners have been used in laser-based system applications for many years. The popularity of the closed loop galvanometers stems from its unique combination of position accuracy, speed, control flexibility, ease of integration, and cost for optical scanning applications [65].

3.3.3.1 Basics of Galvanometer-Based Optical Scanners

There are three elements to a closed loop galvanometer system: the positioning actuator, the position detector, and the closed loop servo control electronics. For each of the three elements, there are several different design topologies and technologies that provide unique levels of position accuracy, speed, and cost [65].

There are three types of laser scanning: preobjective, objective, and postobjective scanning [66]. Among them, objective scanning or trepanning involves moving the large mass of the objective lens to produce a scan and is not well suited to high-speed scanning. Typically, a pair of galvanometer scanners is used to deflect the incident beam in two axes to create the x–y vector. The preobjective system uses a flat-field scan lens (f-θlens) in the optical path after the beam is deflected. The postobjective system uses a simple on-axis objective in the optical path before the beam is deflected, and for large field coverage, a z-axis galvanometer translator is used for dynamic field-focusing [66]. Preobjective scan lenses can be an inexpensive and simple solution, whereas postobjective systems can provide a very flexible scanning system.

Scanning operations can be performed in three different modes: in “step” mode, the galvanometers are moved from a start to a stop angle as quick as possible with maximum acceleration [67]. This mode is particularly used for rapid laser beam positioning. Exact trajectories are achieved in “vector” mode when individual vectors are processed with control speed at output rate of 8–10 kHz. A line-by-line scanning is done in “raster” mode: the first galvanometer deflects the laser beam in straight lines at a constant speed, while the second galvanometer is incrementing the beam position between lines.

Although universally accepted and highly advanced, limitations in analog servo electronics has lead to newly developed digital servo electronics for control of galvanometer scanner-based scan heads, providing numerous advantages to the user of laser systems [68]. Based on a digital servo board with a DSP system for each galvanometer axis, these scan heads feature highly advanced control algorithms achieving performance far superior to the fastest analog driven systems.

3.3.4 Spatial Light Modulators

Parallel processing with a SLM having large number of pixels array is a powerful approach to realize variable laser patterning faster than available by using a laser beam scanner. Two types of SLMs are currently used for computer-controlled high speed laser pattering. The one is based on a MEMS technology with a large number of micromirror arrays. The other is based on a liquid crystal SLM (LC-SLM) technology.

3.3.4.1 Laser Pattern Generator with a MEMS-Based Spatial Light Modulator

A revolutionary laser pattern generator as a mask writer has been developed by using a MEMS-based SLM, consisting of one million pixel micromirror array fabricated onto a CMOS substrate [69]. The SLM functions as a dynamic mask which is illuminated by a 1 kHz DUV excimer laser. A new pattern is calculated and downloaded into the SLM for each laser pulse, and the resultant SLM image is then projected onto the mask substrate.

The typical MEMS-based SLM developed is a $512 \times 2{,}048$ array of torsional $16 \times 16\,\mu$m micromirrors fabricated on a CMOS substrate. The micromirror pixels are demagnified by the $160\times$ imaging lens to yield a $0.1 \times 0.1\,\mu$m spot grid on the mask blank. The 64 levels of gray scale results in a virtual address grid of 100 nm/64 or 1.56 nm in single pass writing.

3.3.4.2 Parallel Processing Using Liquid-Crystal Spatial Light Modulators

There are two types in LC-SLMs namely, PAL-SLM (parallel aligned nematic crystal spatial light modulators) and LCOS-SLM (liquid-crystal-on-silicon SLM). Both types can be used for phase-only modulation. The PAL-SLM is an older version of LCSLM and is optically addressed with an LCD, an illuminating LD and collimating optics for the LD [70]. The LCOS-SLM is an advanced version of LC-SLM and is controlled, pixel by pixel, by using a CMOS backplane and can be very compact by eliminating optical addressing [71].

An early variable patterning experiment using LC-SLM has been performed by using a femtosecond laser and a PAL-SLM displaying a computer-generated hologram with a 2 Hz repetition rate [72,73]. Recently, high throughput laser processing for high precision surface microstructuring on silicon and Ti_6Al_4V has been demonstrated by creating multiple beams using a LCOS-SLM with $1,024 \times 768$ pixels [74]. Real time processing has been carried out at 50 Hz refresh rate.

3.3.5 Nonlinear-Optical Systems for Harmonic Generation

For extending the frequency range of available laser sources, nonlinear optical devices, such as harmonic generators are often utilized in laser precision microfabrication. Harmonic generation is achieved by sum frequency mixing in birefringent crystals which possess a second-order nonlinear optical susceptibility [75]. Phase matching (PM) is required for efficient frequency conversion. There are two types for PM processes. In type I process, the two input waves have the same polarization, and in the type II process, the waves are orthogonally polarized.

3.3.5.1 Second Harmonic Generation

Second harmonic generation (SHG) is the case of three-wave interaction where the two of the waves have equal frequencies. Frequency doubling of neodymium lasers is one of the major applications of SHG. For efficient frequency doubling of high-power neodymium lasers, lithium triborate, LiB_3O_5 (LBO), is commonly utilized. Although frequency-doubling efficiencies in excess of 65% are now routinely obtained from potassium titanyl phosphate, $KTiOPO_4$ (KTP), KTP is known to suffer from gradual photochemical degradation (gray tracking) [75]. LBO is a nonlinear crystal characterized by good UV transparency, a high-damage threshold, and a moderate nonlinear optical coefficient. Therefore, LBO is an attractive alternative to KTP for frequency doubling of high-power pulsed neodymium lasers. For example, 93 W green light at 10 kHz with a pulse width of 10.7 ns has been obtained from a diode end-pumped high-power Q-switched double Nd:YAG slab laser by imaging the 1,064 nm beam to LBO with type I PM. Efficient external SGH with conversion efficiency up to 57% has been achieved [76].

3.3.5.2 Third Harmonic Generation

Efficient conversion of the output of a laser to the third harmonic is an example of sum frequency generation via the process of three-wave mixing [75]. LBO is commonly used also for the third harmonic generation (THG) of neodymium lasers. For example, efficient picoseconds laser operation at 355 nm is readily achieved by using extracavity conversion by employing noncritically phase-matched LBO for

SHG and critically phase-matched LBO for THG. Over 3 W at 355 nm at 100 kHz with smaller than 20 ps pulses was achieved with an input of 8.5 W at 1,064 nm [77].

Recently, efficient 355 nm generation in CsB_3O_5(CBO) crystals has been achieved by use of a type II CBO crystal as a sum frequency of the fundamental light and the second harmonic of a nanosecond Nd:YVO_4 laser [78]. A 3.0-W output of the third-harmonic was obtained at a repetition rate of 31 kHz. The conversion efficiency from the fundamental light to the third harmonic reached 30%, which was 1.5 times higher than that obtained with a type II LBO crystal under the same experimental conditions.

3.3.6 Optical Systems for Beam Characterization and Process Monitoring

In the following subsection, various optical systems and techniques for beam characterization and process monitoring will be introduced.

3.3.6.1 Beam Characterization

Measurement of laser beam propagation parameters and focus characterization is very important to realize reliable and high quality microfabrication. For the case using ultrafast lasers, an all optical measurement system becomes necessary for temporal profile and phase characterization.

Laser Beam Propagation Parameter Measurement

The ISO standard 11146-1 describes beam diameter definitions, procedures for power-/energy-density measurements, and beam propagation ratios ${M_x}^2$ and ${M_y}^2$ for noncircular stigmatic and simple astigmatic beams (M^2 for circular beam and $M^2 = 1$ for the Gaussian beam). The beam propagation ratios are the ratios of the beam parameter product of the beam of interest to the diffraction limit of a perfect Gaussian beam of the same wavelength and can be used to characterize the degree of imperfection of a laser beam or the beam quality. The main part of calculating the beam parameter is the determination of the beam width based on the second order moments of the power distribution. The second order moments are sensitive to incorrect determination of the zero level of the detector. The constraints between the demands of the standard and practical application have been discussed in [79]. Since the beam propagation parameter measurement according to ISO11146 series is not a simple procedure and might take a long time, an alternative method based on Shack–Hartmann wavefront sensor has been proposed, and comparison of the two methods have been discussed in [80].

Laser beam profilers using CCDs have been used extensively throughout the laser industry to enable users the evaluation of the quality of their laser beam with ease.

Profilers have made many technological strides recently, including new cameras having high resolution, megapixel arrays, digital CCDs, new beam sampling optics, new calculation algorithms, and new profile displays. Beam profile displays in both 2D and 3D have been improved to provide intuitive insight such as for beam shaping [81].

Focus Characterization for Laser Micromachining Under Real Process Conditions

The product of laser material processing is controlled mainly by the properties of the focused laser beam. Special requirements have to be taken into account to characterize such a focused laser beam, which is finally used for laser micromachining. Based on a CCD-camera concept, care has to be taken to magnify and to attenuate the beam properly. Specially designed electronics and algorithms are necessary to optimize the performance and finally to realize such a technical measuring system [83].

Characterization of Ultrashort Laser Pulses

All optical methods such as second-order autocorrelation methods have to be used for ultrashort pulses for which pure electronic methods cannot be used directly [83]. Although these autocorrelation techniques have been widely used in all the diagnostics approaches, they are far from qualifying unambiguously the laser pulse electric field (amplitude and phase). A more rigorous approach can be found in the simultaneous measurement of the amplitude and phase of the laser pulse, by techniques such as frequency-resolved optical gating (FROG), and spectral-phase for direct electric-field reconstruction (SPIDER). [84].

3.3.6.2 Process Monitoring

Various phenomena occurring during pulsed laser processing can be observed optically for in situ, real-time process monitoring.

Emission Diagnostics for Real-Time Monitoring of Pulsed Laser Ablation

There is rich signal emission in the laser ablation. Optical emission spectrum analyzer and high-speed ICCD photography are used to study laser-ablation induced plasma dynamics such as for diagnostics and real-time monitoring during pulsed laser ablation of solid materials (silicon, metal, IC molding component, etc.) [85].

Coupled Photo-Thermal and Time Resolved Reflectivity Measurement

A new method to plot the thermal history of the surface by using a combination of the time resolved reflectivity (TRR) and the pulsed photo-thermal (PPT) or infrared

radiometry (IR) methods has been proposed [86]. Surface temperature, melting kinetics, threshold of melting, and threshold of plasma formation have been determined in the case of KrF laser spot in interaction with several materials including monocrystalline silicon and metallic surfaces (Cu, Mo, Ni, Stainless steel, Sn, Ti).

Real-Time Monitoring and Evaluation of Surface Profile Deformation

The real-time monitoring/evaluation of laser processing performance in-situ is needed to prevent the excessive deformation of the material and to determine optimal processing conditions. Optical coherence tomography (OCT) has advantages such as capability of high resolution and noninvasive investigation for evaluation of laser processing performance. OCT images of pit formation on biological samples at different irradiation conditions have been investigated [87].

3.4 Summary

This chapter provided an introductory explanation on various laser devices and optical systems for laser precision microfabrication regarding their basic operation principles and examples of performance capability. Emphasis was placed on compact and efficient diode-pumped high-brightness solid-state lasers such as rare-earth-doped solid-state lasers and fiber lasers capable of a variety of lasing operations from continuous wave to ultrafast pulse generation. Optical systems described here comprise various advanced functional optics including beam shaping optics, beam scanning optics, SLMs, optical frequency convertors, and optics for beam characterization and process control.

References

1. O. Svelto, in *Principles of Lasers*, 4th edn. (translated from Italian), ed. by D.C. Hanna (Plenum Press, New York, 1998) pp. 1–15
2. T.R. Kugler, in *LIA Handbook of Laser Materials Processing*, ed. by J.F. Ready, D.F. Farson (Laser Institute of America, Orland, FL, 2001), pp. 27–44
3. W.J. Witterman, in *Handbook of Laser Technology and Applications*, ed. by C. Webb, J. Jones. Laser Design and Laser Systems, vol. 2 (Institute of Physics Publishing, Bristol, Philadelphia, 2004), p. 791
4. H. von Bergmann, U. Rebhan, U. Stamm, in *Excimer Laser Technology*, ed. by D. Basting, G. Marowsky (Springer, Berlin, Heidelberg, New York, 2005), p. 47
5. M. Wehner, J. Ihlemann, in *Excimer Laser Technology*, ed. by D. Basting, G. Marowsky (Springer, Berlin, Heidelberg, New York, 2005), p. 155
6. L. Herbst, I. Klaft, K. Schmidt, I. Bragin, H.-S. Albrecht, Proc. SPIE **6459**, 64590I (2007)
7. W. Koechner, *Solid-State Laser Engineering*, 6th edn. (Springer, Berlin, Heidelberg, New York, 2006), pp. 38–101

8. R. Iffländer, *Solid-State Lasers for Materials Processing* (Springer, Berlin, Heidelberg, New York, 2001), pp. 257–318
9. D.R. Hall, in *Handbook of Laser Technology and Applications*, ed. by C. Webb, J. Jones. Laser Design and Laser Systems, vol. 2 (Institute of Physics Publishing, Bristol, Philadelphia, 2004), p. 751
10. F. Villarreal, P.R. Murray, H.J. Baker, D.R. Hall, Appl. Phys. Lett. **78**, 2276 (2001)
11. C.J. Moorhouse, F. Villarreal, J.J. Wendland, H.J. Baker, D.R. Hall, D.P. Hand, Proc. SPIE, **5339**, 276 (2004)
12. C.J. Moorhouse, F. Villarreal, J.J. Wendland, H.J. Baker, D.R. Hall, D.P. Hand, Proc. SPIE, **5827**, 438 (2005)
13. D.L. Sipes, Appl. Phys. Lett. **47**, 74 (1985)
14. R.L. Byer, Science **239**, 742 (1988)
15. W. Koechner, *Solid-State Laser Engineering*, 6th edn. (Springer, Berlin, Heidelberg, New York, 2006), pp. 423–487
16. L. McDonagh, R. Knappe, A. Nebel, R. Wallenstein, Proc. SPIE **6451**, 64510F (2007)
17. W.F. Krupke, IEEE J. Sel. Top. Quant. Electron. **6**, 1287 (2000)
18. A. Brenier, G. Boulon, J. Alloy. Comp. **323–324**, 210 (2001)
19. A. Giesen, J. Speiser, IEEE J. Sel. Top. Quant. Electron. **13**, 598 (2007)
20. J. Dong, A. Shirakawa, K. Ueda, H. Yagi, T. Yanagitani, A.A. Kaminskii, Proc. SPIE **6451**, 645118 (2007)
21. A. Tünnermann, H. Zellmer, in *Handbook of Laser Technology and Applications*, ed. by C. Webb, J. Jones. Laser Design and Laser Systems, vol. 2 (Institute of Physics Publishing, Bristol, Philadelphia, 2004), p. 977
22. S. Maryashin, A. Unt, V.P. Gapontsev, Proc. SPIE **6102**, 61020O (2006)
23. R. Horley, S. Norman, M.N. Zervas, Proc. SPIE **6738**, 67380K (2007)
24. R.B. Chesler, M.A. Karr, J.E. Geusic, Proc. IEEE **58**, 1899 (1970)
25. C.X. Wang, G.Y. Wang, A.V. Hicks, D.R. Dudley, H.Y. Pang, N. Hodgson, Proc. SPIE **6100**, 610019 (2006)
26. M. Roth, M. Tseitlin, N. Angert, Glass Phys. Chem. **31**, 86 (2005)
27. A.I. Bishop, P.F. Barker, Rev. Sci. Instrum. **77**, 044701 (2006)
28. D. Maydan, R.B. Chesler, J. Appl. Phys. **42**, 1031 (1971)
29. C. Stolzenburg, A. Voss, T. Graf, M. Larionov, A. Giesen, Proc. SPIE **6871**, 68710H (2008)
30. A. Killi, J. Dörring, U. Morgner, M. Lederer, J. Frei, D. Kopf, Optic. Express **13**, 1916 (2005)
31. W. Koechner, *Solid-State Laser Engineering*, 6th edn. (Springer, Berlin, Heidelberg, New York, 2006), pp. 534–586
32. D.T. Reid, in *Handbook of Laser Technology and Applications*, ed. by C. Webb, J. Jones. Laser Design and Laser Systems, vol. 2 (Institute of Physics Publishing, Bristol, Philadelphia, 2004), p. 1273
33. U. Keller, K.J. Weingarten, F.X. Kärtner, D. Kopf, B. Braun, I.D. Jung, R. Fluck, C. Hönninger, N. Matuschek, A. Aus der Au, IEEE J. Sel. Top. Quant. Electron. **2**, 435 (1996)
34. J.V. Rudd, G. Korn, S. Kane, J. Squier, G. Mourou, Opt. Lett. **18**, 2044 (1993)
35. T.B. Norris, Opt. Lett. **17**, 1009 (1992)
36. K.-H. Hong, S. Kostritsa, T.J. Yu, J.H. Sung, I.W. Choi, Y.-C. Noh, D.-K. Ko, J. Lee, Optic. Express **14**, 970 (2006)
37. G. Matras, N. Huot, E. Baubeau, E. Audouard, Optic. Express **15**, 7528 (2007)
38. J. Kleinbauer, R. Knappe, R. Wallenstein, Appl. Phys. B **81**, 163 (2005)
39. D.A. Clubley, A.S. Bell, G. Friel, Proc. SPIE **6871**, 68711D (2008)
40. R. Knappe, A. Nebel, Proc. SPIE **6871**, 687121 (2008)
41. J. Kleinbauer, D. Eckert, S. Weiler, D.H. Sutter, Proc. SPIE **6871**, 68711B (2008)
42. S.V. Marchese, C.R.E. Baer, A.G. Engqvist, S. Hashimoto, D.J.H.C. Maas, M. Golling, T. Südmeyer, U. Keller, Optic. Express **16**, 6397 (2008)
43. J. Neuhaus, J. Kleinbauer, A. Killi, S. Weiler, D. Sutter, T. Dekorsy, Opt. Lett. **33**, 726 (2008)
44. F. Röser, D. Schimpf, O. Schmidt, B. Ortac, K. Rademaker, J. Limpert, A. Tünnermann, Opt. Lett. **32**, 2230 (2007)

45. A. Arai, J. Bovatsek, F. Yoshino, Z. Liu, G.C. Cho, L. Shah, M.E. Fermann, Y. Uehara, Proc. SPIE **6343**, 63430S (2006)
46. J.C. Ion, *Laser Processing of engineering materials* (Elsevier Butterworth-Heinemann, Burlington, MA, 2005), pp. 104–138
47. J. Jones, in *Handbook of Laser Technology and Applications*, ed. by C. Webb, J. Jones. Laser Design and Laser Systems, vol. 2 (Institute of Physics Publishing, Bristol, Philadelphia, 2004), p. 1165
48. K. Venkatakrishnan, B. Tan, J. Micromech. Microeng. **16**, 2603 (2006)
49. R. Dorn, S. Quabis, G. Leuchs, Phys. Rev. Lett. **91**, 233901 (2003)
50. M.A. Ahmed, M.M. Vogel, A. Austerschulte, F. Sterns, A. Voss, T. Schoder, M. Ubl, M. Pritschow, T. Graf, Proc. SPIE **6998**, 69980H (2008)
51. M.A. Ahmed, A. Voss, M.M. Vogel, T. Graf, Opt. Lett. **32**, 3272 (2007)
52. H. Kawauchi, Y. Kozawa, S. Sato, T. Sato, S. Kawakami, Opt. Lett. **33**, 399 (2008)
53. P.B. Phua, W.J. Lai, Y.L. Lim. B.S. Tan, R.F. Wu, K.S. Lai, H.W. Tan, Technical Digest of CLEO/QELS 2008, CMO4 (2008)
54. F.M. Dickey, S.C. Holswade, in *Laser Beam Shaping Applications*, ed. by F.M. Dickey, S.C. Holswade, D.L. Shealy (CRC Press, Taylor & Francis Group, Boca Raton, FL, 2006), p. 269
55. J.P. Sercel, M. von Dadelszen, in *Laser Beam Shaping Applications*, ed. by F.M. Dickey, S.C. Holswade, D.L. Shealy (CRC Press, Taylor & Francis Group, Boca Raton, FL, 2006), p. 113
56. C. Dunsky, Proc. SPIE **4443**, 135 (2001)
57. O. Homburg, F. Toennissen, T. Mitra, V. Lissotschenko, Proc. SPIE **6880**, 68800R (2008)
58. Y. Chen, D. Li, Y. Sheng, Appl. Opt., **36**, 568 (1997)
59. K. Kanzler, A. Hoult, Proc. SPIE **6663**, 66630B (2007)
60. O. Homburg, D. Hauschild, P. Harten, L. Aschke, V. Lissotschenko, Proc. SPIE **6663**, 66630D (2007)
61. J. Fruendt, M. Jarczynski, T. Mitra, Proc. SPIE **7062**, 70620S (2008)
62. J. Amako, E. Fujii, Y. Yamazaki, T. Shimoda, Proc. SPIE **6107**, 61070D (2006)
63. Y. Matsuoka, Y. Kizuka, T. Inoue, Appl. Phys. A **84**, 423 (2006)
64. J. Amako, D. Sawaki, E. Fujii, J. Opt. Soc. Am. B **20**, 2562 (2003)
65. R.P. Aylward, Proc. SPIE **3787**, 158 (1999)
66. J.S. Ehrmann, Proc. SPIE **1454**, 245 (1991)
67. M. Muth, Proc. SPIE **2774**, 535 (1996)
68. D.A. Sabo, D. Brunner, A. Engelmayer, Proc. SPIE **5873**, 113 (2005)
69. T. Sandström, T. Fillion, U. Ljungblad, M. Rosling, Proc. SPIE **4409**, 270 (2001)
70. T. Hara, N. Fukuchi, Y. Kobayashi, N. Yoshida, Y. Igasaki, M.H. Wu, Proc. SPIE **4470**, 114 (2001)
71. T. Inoue, H. Tanaka, N. Fukuchi, M. Takumi, N. Matsumoto, T. Hara, N. Yoshida, Y. Igasaki, Y. Kobayashi, Proc. SPIE **6487**, 64870Y (2007)
72. Y. Hayasaki, T. Sugimoto, A. Takita, N. Nishida, Appl. Phys. Lett. **87**, 031101 (2005)
73. Y. Hayasaki, Proc. SPIE **6831**, 683205 (2007)
74. Z. Kuang, W. Perrie, J. Leach, M. Sharp, S.P. Edwardson, M. Padget, G. Dearden, K. G. Watkins, Appl. Surf. Sci. **255**, 2284 (2008)
75. W. Koechner, *Solid-State Laser Engineering*, 6th edn. (Springer, Berlin, Heidelberg, New York, 2006), pp.587–679
76. P. Zhu, D. Li, B. Qi, A. Schell, P. Shi, C. Haas, S. Fu, N. Wu, K. Du, Opt. Lett. **33**, 2248 (2008)
77. J.A. Albelo, P.Y. Pirogovsky, J.N. O'Brien, B.W. Baird, Proc. SPIE **6871**, 687122 (2008)
78. H. Kitano, T. Matsui, K. Sato, N. Ushiyama, M. Yoshimura, Y. Mori, T. Sasaki, Opt. Lett. **28**, 263 (2003)
79. R. Kramer, H. Swede, V. Brandl, S. Wolf, O. Märten, Proc. SPIE **5962**, 59622H (2005)
80. J.V. Sheldakova, A.V. Kudryashov, V.Y. Zavalova, T.Y. Cherezova, Proc. SPIE **6452**, 645207 (2007)
81. C.B. Roundy, L. Green, Proc. SPIE **5876**, 587604 (2005)
82. H. Schwede, O.W. Märten, R. Kramer, S. Wolf, V. Brandl, Proc. SPIE **6872**, 687208 (2008)
83. L. Sarger, J. Oberlé in *Femtosecond Laser Pulses*, ed. by C. Rullière (Springer, Berlin, Heidelberg, New York, 2003), p. 195

84. X. Gu, S. Akturk, P. Gabolde, Q. Cao, A.P. Shreenath, R. Trebino, Proc. SPIE **6108**, 61080A (2006)
85. M.H. Hong, Y.F. Lu, T.C. Chong, Proc. SPIE **4426**, 51 (2002)
86. N. Semmar, J. Martan, O. Cibulka, E. Le Menn, C. B-Leborgne, Proc. SPIE **6261**, 626123 (2006)
87. E.S. Choi, W. Kwak, Y. Shin, Y. Kim, W. Jung, Y.-C. Ahn, Z. Chen, E.J. Jeong, C.-S. Kim, Proc. SPIE **6847**, 68470W (2008)

Chapter 4
Fundamentals of Laser-Material Interaction and Application to Multiscale Surface Modification

Matthew S. Brown and Craig B. Arnold

Abstract Lasers provide the ability to accurately deliver large amounts of energy into confined regions of a material in order to achieve a desired response. For opaque materials, this energy is absorbed near the surface, modifying surface chemistry, crystal structure, and/or multiscale morphology without altering the bulk. This chapter covers a brief introduction to the fundamental principles governing laser propagation and absorption as well as the resulting material responses. We then highlight two case studies of improving efficiency in photovoltaic and optoelectronic devices as well as optimizing cell-surface interactions in biological interfaces.

4.1 Introduction

Modification of surface properties over multiple length scales plays an important role in optimizing a material's performance for a given application. For instance, the cosmetic appearance of a surface and its absorption properties can be controlled by altering its texture [1, 2] and presence of chemical impurities in the surface [3]. A material's susceptibility to wear and surface damage can be reduced by altering its surface chemistry, morphology, and crystal structure [4]. Also, one can consider the frictional, adhesive, and wetting forces acting at a material interface as being strongly influenced by the size and shape of the micro and nanoscale features present [5]. As such, multiscale surface modifications are a critical factor in the development of new material structures and in engineering the detailed interactions that occur at surfaces and interfaces.

From the earliest work with pulsed ruby lasers, it has been understood that the unique interaction of laser light with a material can lead to permanent changes in the material's properties not easily achievable through other means. Laser irradiation

M.S. Brown and C.B. Arnold (✉)
Department of Mechanical and Aerospace Engineering, Princeton Institute for Science and Technology of Materials, Princeton University, Princeton, NJ 08544, USA
e-mail: msbrown@princeton.edu; cbarnold@princeton.edu

K. Sugioka et al. (eds.), *Laser Precision Microfabrication*,
Springer Series in Materials Science 135, DOI 10.1007/978-3-642-10523-4_4,
© Springer-Verlag Berlin Heidelberg 2010

has been shown to induce changes to the local chemistry, the local crystal structure, and the local morphology, all of which affect how the material behaves in a given application. A number of fine books and review articles have been written on this subject [6–9]. The main issue here is the ability to precisely deposit a large amount of energy into a material over a short time scale and in a spatially confined region near the surface. This allows control of local surface properties relative to the bulk and relative to other regions on the surface. But perhaps more importantly, the effect of this incident energy, the interaction time scale, and other laser parameters can lead to material responses and changes that span multiple length scales, from the atomic to the macroscale.

Clearly, a complete treatment of all laser surface modifications and applications is beyond the scope of a single book chapter, so we will primarily focus on two specific case studies in which new applications are actively being developed. Before delving into these case studies, we start with a short review of the underlying principles and equations governing the absorption of laser light and the transport of heat inside the material. We discuss the fundamental material responses that can occur as well as some of the established applications of laser surface modification. We then turn to the first case study where we examine the multiscale morphological and chemical changes to the surfaces of laser irradiated metals and semiconductors, which allow optimized optical properties for such emerging applications as high efficiency solar cells, security, or microfluidics. In the second case study, we discuss how laser processing can be used to produce multiscale changes to the surface morphology and chemistry of biomaterials to enhance the adhesion of proteins and cells for applications such as biomedical implants and lab-on-a-chip type sensors.

4.2 Fundamentals of Laser Surface Processing

One of the major advantages of the laser as a tool for material processing is the ability to precisely control where in the material and at what rate energy is deposited. This control is exercised through the proper selection of laser processing parameters to achieve the desired material modification. In this section, we discuss the principles and equations that describe the propagation and absorption of laser energy and heat flow (also see Chaps. 2 and 8).

4.2.1 Light Propagation in Materials

Confinement of deposited energy to desired regions on a material's surface can be achieved by controlling the laser's spatial intensity profile. The predominant methods for control include beam steering by fixed or galvanometric scanning mirrors, beam focusing through telescoping or converging optics, and beam shaping with homogenizers [10], amplitude masks, refractive elements [11], and diffractive optical

elements (DOE) [12] (see Chaps. 3 and 10). However, one can also use more advanced optical devices such as spatial light modulators [13], deformable mirrors [14], and tunable acoustic gradient index (TAG) lenses [15] allowing real-time modulation of the beam's intensity profile on the surface (see Chaps. 1 and 3). There has been extensive work in the area of beam shaping with a number of articles and books [16, 17] as well as a chapter in this book devoted to the subject (Chap. 5).

When light strikes the surface of a material, a portion will be reflected from the interface due to the discontinuity in the real index of refraction and the rest will be transmitted into the material. The fraction of the incident power that is reflected from the surface R depends on the polarization and angle of incidence θ_i of the light as well as the index of refraction of the atmosphere n_1 and the material n_2. The reflection coefficients for the s-polarized and p-polarized components of the light can be calculated from the well known Fresnel equations [18]:

$$R_s = \left[\frac{E_r}{E_i}\right]^2 = \left[\frac{n_1 \cos(\theta_i) - n_2 \cos(\theta_t)}{n_1 \cos(\theta_i) + n_2 \cos(\theta_t)}\right]^2 \tag{4.1}$$

$$R_p = \left[\frac{E_r}{E_i}\right]^2 = \left[\frac{n_1 \cos(\theta_t) - n_2 \cos(\theta_i)}{n_1 \cos(\theta_t) + n_2 \cos(\theta_i)}\right]^2 \tag{4.2}$$

and are related to the transmission coefficients through $T_s = 1 - R_s$ and $T_p = 1 - R_p$. For the case of normally incident light on a flat surface, the above equations reduce to the more familiar form:

$$R = R_s = R_p = \left(\frac{n_1 - n_2}{n_1 + n_2}\right)^2 \tag{4.3}$$

The reflectivity of a given material will depend on the frequency of the light source through the dispersion relation of its index of refraction. For instance in the case of normal incidence, values for reflectivity of metals in the near UV and visible spectral range are typically between 0.4 and 0.95, and between 0.9 and 0.99 for the IR [7]. In addition, the reflectivity of a surface will depend on the temperature of the material through changes in the permittivity, band structure, plasma oscillations, or material phase [19]. For instance, upon melting, the reflectivity of silicon increases by a factor of about 2 [20], while that of a metal such as Ni changes by only a few percent [21]. In the case of small scale or structured materials, additional optical resonances are possible, such as surface and bulk plasmons and polaritons, which can lead to enhanced absorption or reflection due to the details of the photon–electron interactions [22].

Once inside the material, absorption causes the intensity of the light to decay with depth at a rate determined by the material's absorption coefficient α. In general, α is a function of wavelength and temperature, but for constant α, intensity I decays exponentially with depth z according to the Beer–Lambert law,

$$I(z) = I_0 e^{-\alpha z} \tag{4.4}$$

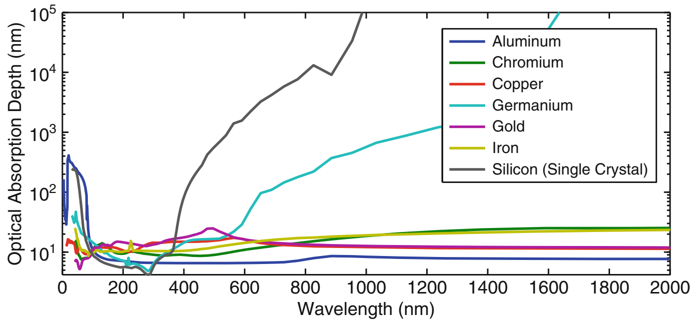

Fig. 4.1 Optical absorption depths for several materials over a range of wavelengths [23]

where I_0 is the intensity just inside the surface after considering reflection loss. The magnitude of the gradient of intensity yields the volumetric energy deposition rate $\alpha I_0 e^{-\alpha z}$.

It is convenient to define the optical penetration or absorption depth, $\delta = 1/\alpha$, which is the depth at which the intensity of the transmitted light drops to $1/e$ of its initial value at the interface. Figure 4.1 shows optical absorption depths as a function of wavelength for a variety of metals and semiconductors. The important thing to note from Fig. 4.1 is that the absorption depths are short relative to bulk material dimensions. For instance, in the case of most metals undergoing UV illumination, the absorption depth is on the order of 10 nm. Although the interpretation of absorption depth was developed for a plane wave, the fact that energy absorption is approximately confined within the absorption depth still holds for more general beam profiles. Therefore, choosing wavelength with short absorption depths can allow local modification of surface properties without altering the bulk of the material.

The above treatments considered only linear optical phenomena; however, this is not necessarily the case in all materials, nor for all incident laser conditions. Some materials such as glasses exhibit strong non-linearities in their index of refraction [24], which can lead to a number of interesting effects such as self-focusing, defocusing, or soliton propagation [25]. When dealing with CW or nanosecond duration laser pulses, it is typically assumed that most of the absorption is due to single photon interactions. However, for picosecond (ps) and femtosecond (fs) lasers, the extremely high instantaneous intensity enables phenomena such as optical breakdown and multiphoton absorption which can significantly decrease absorption depths [26]. Effects such as these will change the fundamental material interactions and are discussed in more detail in Chaps. 8 and 9.

4.2.2 Energy Absorption Mechanisms

The absorption coefficient, which can be derived from the material's dielectric function and conductivity, determines the absorption of light as a function of depth.

However, the specific mechanisms by which the absorption occurs will depend on the type of material. In general, photons will couple into the available electronic or vibrational states in the material depending on the photon energy. In insulators and semiconductors, the absorption of laser light predominantly occurs through resonant excitations such as transitions of valence band electrons to the conduction band (interband transitions) or within bands (intersubband transitions) [7]. These excited electronic states can then transfer energy to lattice phonons. Photons with energy below the material's band gap will not be absorbed (unless there are other impurity or defect states to couple to or if there is multiphoton absorption). Such energies typically correspond to light frequencies below vacuum ultraviolet for insulators and below the visible to infrared spectrum for semiconductors. However, resonant coupling to high-frequency optical phonons in the near-infrared region is possible in some cases [27].

In metals, optical absorption is dominated by the free electrons through such mechanisms as inverse bremsstrahlung [28]. Energy is subsequently transferred to lattice phonons by collisions. An important parameter relating the electron density of a metal N_e to its optical properties is the plasma frequency $\omega_p = \sqrt{N_e e^2/m_e\varepsilon_0}$, where m_e is the mass of an electron and ε_0 the permittivity of free space. Reflectivity and absorptance for light frequencies below the plasma frequency are high because electrons in the metal screen the electric field of the light. However, above the plasma frequency, reflectivity and absorptance drop off drastically because the electrons cannot respond fast enough to screen it [29]. Additionally, electronic or vibrational states that are associated with defects, impurities, or surface phenomenon such as diffuse electron scattering, plasmons, and polaritons can be excited [22].

The time it takes for the excited electronic states to transfer energy to phonons and thermalize depends on the specific material and the specific mechanisms within the materials. For most metals, this thermalization time is on the order of 10^{-12}–10^{-10} s, whereas in non-metals, there is significantly more variation in the absorption mechanisms and the thermalization time can be as long as 10^{-6} s [7]. Polymers and dielectric materials are typically on the slower end of this range. Defects and quantum confined electronic states can play a significant role in slowing down this thermalization time.

When the laser-induced excitation rate is low in comparison to the thermalization rate, the details of the transient electronically excited states are not significant. Rather, one can consider the absorbed laser energy as being directly transformed into heat. Such processes are called photothermal (pyrolytic) and the material response can be treated in a purely thermal way. For instance, laser processing of metals or semiconductors with laser pulse times that are slow ($> ns$) is typically characterized by photothermal mechanisms.

When the laser induced excitation rate is high in comparison to the thermalization rate, large excitations can build up in the intermediary states. These excitation energies can be sufficient to directly break bonds (photo-decomposition). This type of non-thermal material modification is typically referred to as photochemical (photolytic) processing. During purely photochemical processing, the temperature of the system remains relatively unchanged. Irradiation of polymers with short

wavelength laser light, where the photon energy is on the order of the chemical bond energy, is an example of a photochemical processing. Similarly, ultrafast femtosecond laser pulses can enable photochemical processing of metals and semiconductors [28]. However, even in these cases, it is possible for thermal modifications to occur after the excited states thermalize with lattice phonons [30]. Material responses that exhibit both thermal and non-thermal mechanisms are typically referred to as photophysical [7].

4.2.3 The Heat Equation

For photothermal processing, the material response can be explained as a result of elevated temperatures. Therefore, it is important to be able to model the flow of heat inside a material. The temporal and spatial evolution of the temperature field inside a material are governed by the heat equation. The heat equation is derived from the conservation of energy and Fourier's law of heat conduction, which states that the local heat flux is proportional to the negative of the gradient of the temperature. In a coordinate system that is fixed with the laser beam, the heat equation can be written as [7]:

$$\begin{aligned} \rho\left(\mathbf{x},T\right)c_{\rho}\left(\mathbf{x},T\right)\frac{\partial T\left(\mathbf{x},t\right)}{\partial t} &- \nabla\left[\kappa\left(\mathbf{x},T\right)\nabla T\left(\mathbf{x},t\right)\right] \\ &+ \rho\left(\mathbf{x},T\right)c_{\rho}\left(\mathbf{x},T\right)\mathbf{v}_s\nabla T\left(\mathbf{x},t\right) = Q\left(\mathbf{x},t\right) \end{aligned} \tag{4.5}$$

where ρ is the mass density, c_p is the specific heat at constant pressure, κ is the thermal conductivity, and $\mathbf{v}_s$ is the velocity of the substrate relative to the heat source. The left hand side describes the evolution of temperature due to heat conduction as well as the convective term $\mathbf{v}_s$ to account for the shift in reference frame. In many laser processing applications, a laser beam is rastered across the work piece or some form of motion control is utilized to move the substrate relative to the beam. Therefore, this form yields a convenient transformations with which to deal with these issues. The right side incorporates the contribution of heat sources and sinks through the volumetric heating rate $Q\left(\mathbf{x},t\right)$.

The evolution of the temperature inside the material is initially driven by the volumetric heating term $Q\left(\mathbf{x},t\right)$ as well as the boundary conditions of the particular problem. Heat exchanges due to convection and radiation at the surface can be accounted for in the boundary conditions of the particular problem. In most cases, laser irradiation is the main source of volumetric heating. In general, for complex beam profiles, one would first have to solve the wave equation for the entire spatial intensity distribution of the light within the material, then take the magnitude of the gradient of intensity as the volumetric heating rate due to laser absorption as input into the heat equation. However, for the case of shallow surface absorption, this contribution can approximately be separated into a spatial shape $g\left(x,y\right)$ determined by the beam's profile, an attenuation term $f\left(z\right)$ determined from (4.4), as well as a

temporal shape $q(t)$, which could be a constant for CW, a pulse, or even a train of temporally shaped pulses. Phase changes or chemical reactions can be accounted for by $U(\mathbf{x}, t)$ and the volumetric heating term becomes,

$$Q(\mathbf{x}, t) = g(x, y) f(z) q(t) + U(\mathbf{x}, t) \tag{4.6}$$

In general, the heat equation (4.5) is a non-linear partial differential equation, which makes finding an analytic solution difficult. The situation is further complicated in real material systems due to changes in the optical properties (and hence the volumetric heating term) as a function of temperature and laser intensity. Thus, quantitative information generally requires methods such as finite difference or finite element numerical analysis. In some cases of extremely rapid material heating or very small material dimensions, the continuum assumptions of (4.5) may break down during the initial laser-material interaction requiring alternative modeling such as molecular dynamic simulations [31]. However, in most cases, shortly after the initial interaction, the heat equation regains its validity. In certain cases, there are simplifying assumptions that can be applied to enable analytic solutions, such as treating material properties as constants, incorporating laser heating through the boundary conditions for the case of surface absorption, or treating the laser shape term as a delta function for the case of a tightly focused laser spot. Solutions of this type can be found in standard textbooks on the subject [7, 8].

An important quantity that comes out of these simplified treatments is the thermal diffusion length $l_T \approx \zeta\sqrt{D\tau}$, where $D = \kappa/\rho c_p$ is the thermal diffusivity of the material. The thermal diffusion length characterizes the distance over which temperature changes propagate in some characteristic time τ. The prefactor ζ is a geometric constant on the order of unity, which depends on the particular geometry of the problem (i.e., bulk versus thin film absorption). Typically, τ is considered to be the laser beam dwell time or temporal pulse width, in which case we can consider the thermal diffusion length as a measure of how far the energy spreads during the laser irradiation. Following this initial interaction, further thermal propagation leads to elevated temperatures at distances beyond this length. The spread in energy during the laser pulse combined with the spread in energy after the pulse can lead to changes in the material properties. The region over which these changes occur is denoted the heat affected zone (HAZ), as discussed in the next section, and can exhibit a number of significant differences relative to the bulk material.

Given the preceding treatment of laser absorption, yielding the optical absorption depth, and the heat transport equations, yielding the thermal diffusion length, we can begin to clearly see the importance of lasers for surface modifications and the ways in which to control these interactions. For opaque materials, optical absorption depths are very small. With short laser dwell times, the thermal diffusion length is similarly small. In such a case, we are in a regime for which we may consider all of the optical energy as absorbed at the surface with a spatial profile matching that of the beam and without significant thermal diffusion out of this region during the initial interaction. Additionally, this confinement can be relaxed by increasing the absorption and diffusion lengths through the appropriate choice

of laser wavelength and increased dwell time. In this way, there is a great deal of flexibility in designing laser processes in order to achieve the exact desired material outcome.

4.2.4 Material Response

The details of the material response will depend on the particular material system and the laser processing conditions. As was mentioned earlier, if laser induced excitation rates are slow compared to the thermalization time, then the process is denoted as photothermal, and one can consider the absorbed laser energy as being directly transformed into heat. In this case, the material response will be a function of the local material heating and cooling rates, maximum temperatures reached, and temperature gradients, all of which can be determined from the solution to the heat equation for the given irradiation conditions. Because material heating rates can be so extreme, reaching as high as 10^9 K/s for nanosecond (ns) pulses and even higher for femtosecond lasers, significant changes to the material can occur.

In this section, we will discuss some of the fundamental material responses that can occur as a result of laser irradiation. The focus will be placed on photothermal responses, but attention will be drawn to photochemical aspects when necessary.

4.2.4.1 Thermally Activated Processes

Laser heating with fluences below the threshold of melting can activate a variety of temperature dependent processes within the solid material. The high temperatures generated can enhance diffusion rates promoting impurity doping, the reorganization of the crystal structure [32], and sintering of porous materials [33]. Energy barriers for chemical reactions can be overcome as well, increasing their reaction kinetics far beyond room temperature rates. Rapid transformations to high-temperature crystal phases can occur. The large temperature gradients achieved with localized laser heating can lead to rapid self-quenching of the material, trapping in highly non-equilibrium structures. Also, the rapid generation of large temperature gradients can induce thermal stresses and thermoelastic excitation of acoustic waves [34]. These stresses can contribute to the mechanical response of the material such as work hardening, warping, or cracking.

4.2.4.2 Surface Melting

Fluences above the threshold of melting can lead to the formation of transient pools of molten material on the surface. The molten material will support much higher atomic mobilities and solubilities than in the solid phase, resulting in rapid material homogenization. High self-quenching rates with solidification front velocities up to

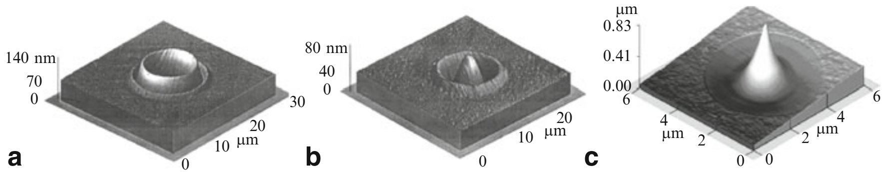

Fig. 4.2 AFM images of the surface deformations recorded on Ni-P hard-disk substrate at (**a**) high energy and (**b**) intermediate energy [38] and (**c**) 0.8 μm nanotips formed on Si SOI [39]

several m/s can be achieved by rapid dissipation of heat into the cooler surrounding bulk material [8, 9]. Such rapid quenching can freeze in defects and supersaturated solutes [35] as well as form metastable material phases. Slower resolidification rates can allow recrystallization of larger grains than the original material. Use of shaped beam profiles has also been shown to allow control of the recrystallization dynamics [36].

At temperatures far above the melting temperature, hydrodynamic motion can reshape and redistribute material. Radial temperature gradients on the order of 10^2-10^4 K/mm can develop in melt pools, causing convective flows to circulate material [9]. For most materials, the liquid's surface tension decreases with increasing temperature and the liquid is pulled from the hotter to the cooler regions (Marangoni effect) [37]. Convective and thermocapillary forces can cause significant deformations that are frozen in during solidification. As can be seen in Fig. 4.2, a variety of shapes can form such as rimmed indentations, sombrero shaped craters, and even nanometer scale tips [38, 39].

4.2.4.3 Ablation

Laser ablation is the removal of material from a substrate by direct absorption of laser energy. Laser ablation is usually discussed in the context of pulsed lasers; however, it is also possible with intense CW irradiation. The onset of ablation occurs above a threshold fluence, which will depend on the absorption mechanism, particular material properties, microstructure, morphology, the presence of defects, and on laser parameters such as wavelength and pulse duration. Typical threshold fluences for metals are between 1 and 10 J/cm^2, for inorganic insulators between 0.5 and 2 J/cm^2, and for organic materials between 0.1 and 1 J/cm^2 [7]. With multiple pulses, the ablation thresholds may decrease due to accumulation of defects. Above the ablation threshold, thickness or volume of material removed per pulse typically shows a logarithmic increase with fluence according to the Beer–Lambert law (4.4).

A variety of mechanisms for material removal may be active during laser ablation depending on the particular material system and laser processing parameters such as wavelength, fluence, and pulse length [40]. At low fluences, photothermal mechanisms for ablation include material evaporation and sublimation. For multi-component systems, the more volatile species may be depleted more rapidly,

changing the chemical composition of the remaining material [41]. With higher fluence, heterogeneous nucleation of vapor bubbles leads to normal boiling. If material heating is sufficiently rapid for the material to approach its thermodynamic critical temperature, rapid homogenous nucleation and expansion of vapor bubbles lead to explosive boiling (phase explosion) carrying off solid and liquid material fragments [42]. These thermal mechanisms can be understood as thermodynamic phase changes in response to the high temperatures.

When the excitation time is shorter than the thermalization time in the material, non-thermal, photochemical ablation mechanisms can occur. For instance, with ultrafast pulses, direct ionization and the formation of dense electron-hole plasmas can lead to athermal phase transformations, direct bond-breaking, and explosive disintegration of the lattice through electronic repulsion (Coulomb explosion) [43]. In certain nonmetals such as polymers and biological materials with relatively long thermalization times, photochemical ablation can still occur with short wavelength nanosecond lasers, producing well defined ablated regions with small HAZs [44].

In all cases, material removal is accompanied by a highly directed plume ejected from the irradiated zone. The dense vapor plume may contain solid and liquid clusters of material. At high intensities, a significant fraction of the species may become ionized, producing a plasma. Also, with pulses longer than ps, interaction of the laser light with the plume may be significant. The plume can absorb and scatter radiation, changing the actual flux received by the surface. Recoil from the plume can generate shockwaves in the material, causing plastic deformation and work hardening [45]. The recoil can also cause further expulsion of any remaining molten material as well as initiate shock waves. Resolidification of expelled liquid and condensation of plume material into thin films and clusters of nanoparticles [46] can alter the topography at the rim and surrounding areas of the ablated region (Fig. 4.3c, d).

The laser's temporal pulse length can have a significant effect on the dynamics of the ablation process. In general, as the pulse length is shortened, energy is more rapidly deposited into the material leading to a more rapid material ejection. The volume of material that is directly excited by the laser has less time to transfer energy to the surrounding material before being ejected. Therefore, the ablated volume becomes more precisely defined by the laser's spatial profile and optical penetration depth, and the remaining material has less residual energy, which reduces the

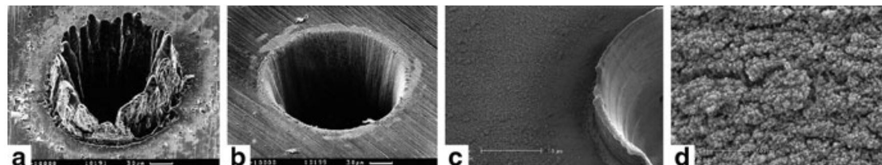

Fig. 4.3 Laser ablation of holes drilled in a 100 μm thick steel foil with (**a**) 200 fs, 120 μJ, $F = 0.5$J/cm^2 laser pulses at 780 nm; and (**b**) 3.3 ns, 1 mJ, and $F = 4.2$ J/cm^2 laser pulses at 780 nm [28]. (**c**) Excimer laser ablation (300 pulses at 193-nm) of zirconium silicate (**d**) producing vapor-condensed aggregates of nanoparticles in the surrounding regions [47]

HAZ [48]. The effect of short pulses (fs to ps) is most apparent in the ablation of metals, which due to their large thermal diffusivities and low melting temperatures will exhibit large HAZs and molten regions when ablated with ns laser pulses. Figure 4.3 shows the relatively large molten layer present in the (a) ns irradiation of steel, in contrast to the precise ablation with (b) fs irradiation showing no trace of molten material [28]. The ablation threshold fluence for a material reduces at shorter pulse lengths and becomes more sharply defined. However, even for these ultrashort pulses, there is excess energy remaining in the material that can still cause thermal effects in the surrounding material after the pulse has ended [30]. Additionally, fs pulses can cause optical breakdown, which reduces the optical absorption depth and can even cause strong absorption in otherwise transparent wide-bandgap materials. Another distinction of fs and ps ablation is that the laser–material interaction is separated in time from material response and ejection. During ns ablation, shielding of the surface by the ejected ablation plume can reduce the amount of energy absorbed by the material.

Material responses often involve a combination of ablation, surface melting, and thermally activated processes, which can lead to cumulative changes in the material's surface texture, morphology, and chemistry. For instance, residual heat left after ablating material from a surface can lead to further melting or other thermally activated processes in the remaining surface and surrounding volume of material. These collective effects can result in complex multiscale material modifications, which can be utilized by various laser material processing applications. These applications will be discussed in the subsequent sections.

4.3 Laser Surface Processing Applications

In the previous section, we discussed some of the fundamental material responses that can occur in a material due to laser irradiation. These responses typically result in permanent changes to the material's surface chemistry, composition, crystal structure, and morphology. By choosing the appropriate laser parameters, precise control of the final material properties can be achieved. This enables processing procedures to be designed and optimized to provide the best material functionality for its desired application. In this section, we briefly discuss some examples of established applications for laser processing. For a more thorough treatment of the details and applications of these laser surface processes as well a mathematical models describing behavior and dependence on processing parameters, the reader is encouraged to follow references [6–9].

One of the first production applications for lasers in surface material processing was the selective heat treatment of metallic parts for reduced wear [4]. Traditionally, heat treatment of metals involved heating in an oven, flame, by induction, or electric arc above a critical temperature to achieve a crystal phase transformation and then subsequently quenching in a gas or liquid to rapidly cool to room temperature and

freeze in a non-equilibrium phase. The rate of cooling from the high temperature crystal phase determines the resulting room-temperature crystal morphology and mechanical properties. Such heat treatments are commonly used to harden or temper load-bearing surfaces for reduced wear, decreased friction, and increased part lifetime [49]. However, in many cases, it is undesirable to treat the entire part as it may be prone to distortion or cracking. By using a laser, rapid heating of the surface can be achieved with little thermal penetration. Subsequent self-quenching into the cooler bulk enables modification that is limited to a thin layer of surface material. The heating and quench rates, and thus resulting material properties, can be precisely controlled by adjusting laser parameters such as pulse time (or scan speed for CW lasers) and intensity [32]. The major advantages of laser surface heat treatment include high processing speeds, precise hardening depth control, minimization of part distortion and cracking, elimination of separate quenching medium, and the ability to selectively harden small hard to reach areas (e.g., inside surface of small holes).

Much like laser hardening, non-melt laser annealing (NLA) utilizes rapid surface heating to enhance atomic mobilities and reorganize the crystal structure. NLA is commonly used to activate the diffusion of ion implanted dopants in silicon wafers to disperse undesirable clustering and repair the lattice damage created during the implantation process [50]. The short thermal penetration and lack of melting allow processing of shallow junctions while preserving composition gradients. On the other hand, excimer laser annealing (ELA) utilizes melting in a thin layer of material at the surface, which then rapidly recrystallizes to relieve internal stresses, remove defects, and enhance crystallinity. ELA is crucial to the production of high-performance, large-area polycrystalline silicon (poly-Si) thin-film transistor (TFT) devices such as active-matrix-driven flat panel displays [26]. ELA is used to recrystallize poorly conducting amorphous silicon to produce larger grain sizes and reduce defects. ELA has also been used in the production of poly-Si thin films for solar cells.

Laser surface melting can also be used to incorporate new material into an existing surface. In laser cladding and hardfacing, new material is fed in by wire feedstock or as a blown powder and bonded, ideally without dilution, to an underlying substrate to create a new surface with little to no porosity and enhanced resistance to wear, high temperature, and corrosive environments (Fig. 4.4a). It provides coatings with a more consistent thickness, better surface finish, smaller HAZs, less cracking, and reduced part distortion than traditional thermal spraying and welding techniques. With higher laser power, complete mixing of the new material into the molten surface can form a homogenously alloyed layer. Rapid resolidification ensures minimal segregation, allowing many materials to be alloyed regardless of their mutual solubility [8]. Materials can be alloyed to increase their hardness and corrosion resistance or reduce friction wear properties of the part surface.

Laser cleaning utilizes intense laser radiation to selectively remove contaminants from a solid surface while leaving the underlying substrate largely unaffected. The technique exploits differences in the optical and thermal properties of the underlying substrate and the contaminant layer as well as the ability to precisely control

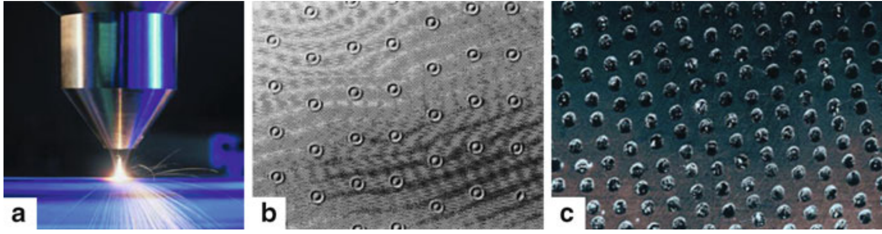

Fig. 4.4 (**a**) Laser surface cladding (MTU Maintenance). (**b**) Micrograph of laser-textured bumps on a super-smooth disk as observed in a phase-contrast microscope [51]. (**c**) Laser surface texturing of micro-dimples for enhanced tribology [52]

material heating depths and removal rates by controlling laser beam parameters such as pulse time (or scan rate), wavelength, and fluence (or intensity). Laser cleaning has become a cost effective alternative to water jet, abrasive blasting, or chemical based cleaning methods. Typical industrial applications include oxide and coating removal, tool cleaning, removal of grease and paint, as well as adhesion promoting pre-treatments for welding, gluing, and painting. Laser cleaning can also be used to efficiently remove very small particles from delicate substrates such as silicon wafers and photolithographic masks [7, 53].

Finally, one of the most important and technologically relevant laser surface processing applications is surface texturing. Laser surface texturing has historically been used to enhance the tribological properties of material interfaces. For instance, magnetic disk drives require surface texturing to overcome stiction problems and reduce friction (Fig. 4.4b) [54]. Also, laser surface texturing of microscopic dimples can improve material tribology by serving as micro-hydrodynamic bearings, micro-reservoirs for lubricant, or micro-traps for wear debris (Fig. 4.4c) [5]. In other cases, texturing can be used to improve adhesion of mating surfaces. Laser textured rollers are commonly used in the manufacturing and processing of flat-rolled steels in the automobile industry to increase the grip on the steel sheet and impart a matte finish to enhance formability and improve the adhesion and appearance of paint [2, 8].

A more recent development in surface texturing involves the creation of super-hydrophobic surfaces ($\theta_c > 150°$) for applications such as self-cleaning surfaces, biological scaffolds, microfluidics, and lab-on-chip devices [56–59]. The process is inspired by several examples from nature, most notably that of the lotus leaf, where natural surface textures result in exceptional water repelling properties (Fig. 4.5a) [60]. The effectiveness of these natural textures is due to the multiscale nature of the features that ranges from the nano- to the microscale [61]. Figure 4.5b shows a close-up image of the surface of a lotus leaf indicating nanotexture on microscale-pillars. Laser texturing can mimic these multiscale structures (Fig. 4.5c) and their superhydrophobic properties (Fig. 4.5d) with a large degree of control through the choice of processing parameters [59]. For example, by varying laser fluence, surface wettability gradients can be generated to drive microfluidic flows [58].

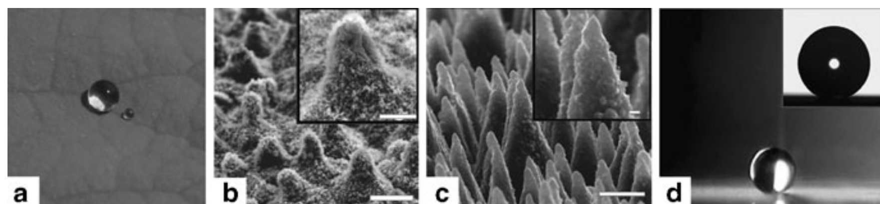

Fig. 4.5 (**a**) A bead of water on a lotus leaf [55]. (**b**) SEM image of the microscale (scale bar 10 μm) and *inset*: nanoscale structures (scale bar 5 μm) on the surface of a lotus leaf [56]. (**c**) SEM images of femtosecond laser textured Si surface showing microscale (scale bar 5 μm) and *inset*: nanoscale (scale bar 1 μm) structures [56]. (**d**) Image of a water droplet on a laser-structured, silane-coated, Si surface with a static contact angle of $\theta = 154 \pm 1°$ [57]

Laser surface processing excels over mechanical (e.g., shot or grit blasting), chemical, and electric discharge texturing because it allows localized modifications with a large degree of control over the shape and size of the features that are formed and a greater range of sizes that can be produced. It is generally cheaper than e-beam texturing and more flexible in that it does not require vacuum. Various textures can be accurately produced (Figs. 4.2, 4.3 and 4.4 b, c) by controlling processing parameters such as beam intensity, spatial and temporal profile, wavelength, and processing environment (background gas or liquid). The primary dimensions of the surface features (e.g., width of the melted or ablation region) are generally defined by the shape and size of the beam. However, secondary microscale and even nanoscale features can form in and around the irradiated region due to a variety of mechanisms including post-ablation melting and resolidification or splashing of a liquid surface due to the recoil pressure as discussed above. These secondary characteristics can be just as important as the primary dimensions in determining material functionality in its desired application.

In the next sections, we present two case studies where laser processing has been used to control the multiscale texture of a material surface as well as influence its surface chemistry and composition in order to optimize material performance. The first application utilizes laser surface texturing to enhance the absorption of light by semiconductor devices for improved efficiency. The second looks at the use of laser texturing to modify the cellular response and adhesion to biological implants.

4.4 Case Study I: Surface Texturing for Enhanced Optical Properties

A large number of important applications rely on semiconductor devices to convert light into an electrical response. For instance, photovoltaic arrays are used to convert solar radiation into renewable electricity, mitigating our reliance on fossil fuels. Photodiodes are widely used in optical communication, optical data storage, or chemical sensing to transduce an optical signal into an electrical one. Digital

imaging sensors have continued to replace film in consumer cameras and have enabled machine vision to automate many industrial operations. Optimum performance in all of these applications requires the optical device to capture as much of the incident light as possible. In this case study, we will discuss how laser texturing of semiconductor surfaces can be utilized to decrease reflections and increase absorption for enhanced device performance without altering bulk properties.

At the heart of the optical to electronic energy conversion in a semiconductor device is the absorption of light by the mechanisms discussed in the earlier sections. Light enters through the air–material interface, where a discontinuity in the index of refraction causes a portion of the wave to reflect and carry off a fraction of the incident power equal to the reflectivity (4.3). Because of the high index of refraction of most semiconductors, this parasitic Fresnel reflection (e.g., 30% for silicon and 25% for CdTe) can significantly reduce the optical power available for transduction into an electrical response.

The most common solution is to apply a single-layer, thin-film antireflection coating [62]; however, such coatings are effective only in a narrow spectral range and at normal incidence. Broadband reduction in reflectivity over a larger range of incidence angles can be achieved with multilayer and graded index (GRIN) thin films. However, their application tends to be costly and the availability of coating materials with the appropriate physical and optical properties is limited [63].

An alternative method for the reduction of reflections is to texture the existing semiconductor surface. Because no additional material is added, these textured surfaces are inherently more stable and do not suffer from material compatibility issues that plague thin films such as weak adhesion, thermal expansion mismatch, and interdiffusion.

Multiscale texturing of a surface can cause significant deviations in how light is reflected and scattered, leading to enhanced absorption over that of a flat smooth surface. For surface features with dimensions greater than several wavelengths of light, this enhancement can most easily be described using the principles of ray optics. A portion from a ray of light will specularly reflect from a flat surface, as shown in Fig. 4.6a, and have no further interaction with the material. On the other hand, protruding features can reflect and scatter light back onto the surface, as seen in Fig. 4.6b. Light can effectively become trapped in crevices and holes where multiple reflections enhance the coupling into the material. Once inside these protruded structures, multiple internal reflections can guide the light into the bulk. Refraction at the surface of these structures also leads to transmission at oblique angles, effectively increasing the optical path length, enhancing absorption. The degree of enhancement depends on the particular geometry and dimension of the surface features [1].

The creation of features at or near the surface with dimensions on the order of a wavelength (e.g., cracks, voids, surface roughness) can also affect the surface reflectivity by scattering light in the material and increasing the optical path length, leading to enhanced absorption. This is especially important for enhancing absorption in thin-film devices where the thickness of the film is on the order of the optical wavelength [64].

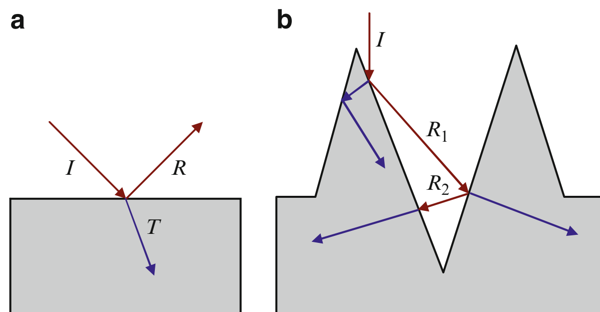

Fig. 4.6 (**a**) Light specularly reflecting from a flat surface. (**b**) Multiple reflections from protruding structures enhance coupling into the material, and refraction causes the light to prorogate at oblique angles, increasing the optical path length

Table 4.1 Multiple length scales over which reflectivity and absorption is determined by surface features

Feature size	Influence on reflectivity
$\gg \lambda$	Light trapping due to multiple reflections enhances coupling into the material. Light refracted at oblique angles increases the effective optical path length
$\approx \lambda$	Small features can successively scatter light, increasing the effective optical path length and enhancing absorption
$\ll \lambda$	Subwavelength structures (SWS) can reduce reflections through the moth-eye effect

Moving still smaller, surface features with dimensions much smaller than a wavelength are not individually resolved by the light, yet periodic arrays of subwavelength structures (SWS) can contribute significantly to the optical response. This is commonly known as the "moth-eye effect," as it was first discovered by Bernhard [65], who found that tapered nanostructures were responsible for the antireflection camoflauge of a moth's eye. A simple explanation for this phenomenon is that the medium takes on a volumetric average of the optical properties between that of the material and the surrounding medium [63, 66]. The tapered nanostructures therefore cause the effective optical properties to continuously change from that of air to that of the material, essentially acting as a GRIN antireflecting layer.

The breadth of length scales over which surface texture affects reflectivity, as summarized in Table 4.1, indicates that surface texturing over multiple length scales can lead to significant reductions in reflectivity and can enhance the absorption of light by the material.

A variety of techniques have been utilized to texture a material's surface to enhance its absorption. Most commercial single crystalline solar cells are etched with potassium hydroxide to enhance light trapping [67], but the texture is limited to random pyramidal structures and the anisotropic etching does not apply to polycrystalline materials. Lithographic techniques combined with isotropic etching have been used to accurately define arbitrary nanoscale patterns to engineer opaque materials such as "black silicon" [68]; however, these processes would be too costly

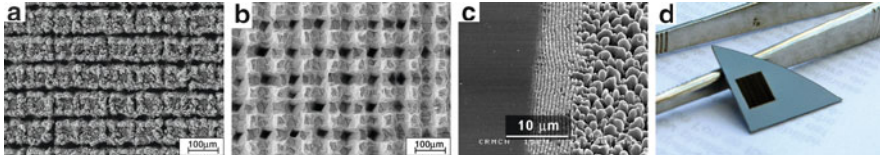

Fig. 4.7 SEM images of multicrystalline silicon direct-write surface textured with a rastered beam (**a**) before and (**b**) after etching to remove laser-induced damage [72]. (**c**) SEM image of silicon processed in vacuum with 800 nm, 100 fs pulses. The remnants of LIPSS with periodicity equal to the laser wavelength can be seen at the edge of the irradiated region (*center*) which transitions to beads approximately 2 μm in width (*right*) [73]. (**d**) Square region of a silicon wafer textured with spontaneously forming quasi-periodic microstructures appears black in contrast to the unprocessed regions [73]

to apply to mass production [66]. Other techniques such as mechanical scribing [69] and solution based pattern deposition [63] have been investigated but may be difficult to integrate into certain manufacturing processes. In contrast, laser texturing is a non-contact technique which can be utilized on both crystalline and polycrystalline material.

There are two distinct methodologies which have been investigated for laser texturing surfaces to enhance absorption. The first is direct-write micromachining where a focused beam is scanned across a surface in a pattern to selectively ablate material and define the structures [21] (Chaps. 10 and 11). It has been used to texture pits, grooves, and pyramidal structures in mono and polycrystalline silicon to enhance absorption (Fig. 4.7a, b) [70–72]. Laser direct write allows a great deal of flexibility in defining surface texture; however, feature dimensions are limited by the focus size of the beam. The second laser texturing methodology is based on spontaneously forming quasi-periodic microstructures, which have been observed on laser exposed surfaces. Under the right conditions, arrays of high-aspect-ratio features such as cones or pillars will fill the irradiated regions of the surface. Surfaces textured in this manner exhibit some of the highest increases in absorptance over a wider spectral band than surfaces textured by the other techniques. And unlike direct writing, large areas can be textured at once by using an unfocused beam. Therefore, there has been a lot of interest in understanding how these structures form and their dependence on processing parameters in order to optimize the processing for cost effective integration into the commercial mass production of semiconductor devices.

The spontaneous formation of laser-induced periodic surface structures (LIPSS) has been studied extensively since the 1960s. Shallow surface rippling with a period close to that of the laser wavelength was first reported by Birnbaum [74] using a ruby laser and has since been identified as a universal phenomenon observed on a variety of materials irradiated above their melting threshold [75]. These ripples, now referred to as low spatial frequency LIPSS (LSFL), are generally well understood and are attributed to interference between the incident beam and a surface scattered wave resulting in an inhomogeneous energy deposition [76, 77]. Recently, structures with subwavelength spatial periods as small as $\lambda/6$ have been observed on

material surfaces irradiated with multiple ultrashort laser pulses. These high spatial frequency LIPPS (HSFL) are generally observed for fs excitation in the transparency range of the material; however, they have also been reported for above-band gap fs excitation of semiconductors and metals. The formation mechanisms of the HSFL remain a topic of debate in the current literature and explanations include nonlinear interactions, transient optical properties during irradiation, self-organization, and Coulombic explosion [78, 79].

The effects of LIPSS on surface optical properties have been noted as acting like a surface grating and have been shown to exhibit dispersive reflections [80]. However, due to their shallow height, they do not significantly contribute to the material's absorptance. Irradiation with a higher fluence near or above the ablation threshold, such as that during pulsed-laser deposition, has been found to lead to surface roughening with larger scale features such as mounds or small mountains [81]. For instance, Fig. 4.7c shows LIPSS at the edge of a laser irradiated region of silicon which transitions into larger bead-like structures. With a large number of additional pulses, reflections from the sides of these features will concentrate light into the surrounding valleys, activating a positive feedback mechanism where material is removed from the valleys and partially deposited onto the peaks. This can lead to the formation of high-aspect-ratio features such as cones or columns [82]. These structures are highly efficient at trapping light and suppressing reflections. Figure 4.7d shows the laser-textured square region of a silicon wafer, which appears black in contrast to the highly reflecting unprocessed regions. In addition, these surfaces have a profound effect on the hydrophobicity of the surface as discussed in the previous section (Fig. 4.5). These structures have been observed on a variety of materials including Ge, W, Ti, Ta, Mo, Pt, steel, and NiTi alloy [83–86]. However, most systematic studies have focused on silicon because of its technological importance.

There is still debate over the mechanism by which these initial undulations form and subsequently transform into cones or columns [87–93]. However, the nature of the process and the details of the final microstructure, such as the shape of the cones or columns, their regularity and density on the surface, chemical composition, and presence of nanostructure, depend strongly on the variables involved in the processing such as the number of incident laser pulses, laser fluence, wavelength, pulse duration, as well as the ambient environment. The structures align with the direction of laser-beam propagation with little dependence on the surface normal and crystallographic orientations. The use of linearly polarized light causes the base of the structures to be elongated perpendicular to the axis of polarization which is consistent with the greater reflectivity and decreased absorption of s-polarized light. Also, the size, aspect ratio, and spacing of the microstructures increase with increasing laser fluence. Figure 4.8a, b show SEM images of silicon irradiated with a Gaussian beam producing microstructures with local density and size reflecting the variation of fluence across the laser profile [94].

Processing atmosphere plays an important role in determining the formation mechanisms and microstructure of the silicon surface. Her et al. found that silicon processed in vacuum, He, and N_2 produced blunted structures as shown in Fig. 4.8a, whereas SF_6 and Cl_2 environments produce conical or triangular sharp spikes with

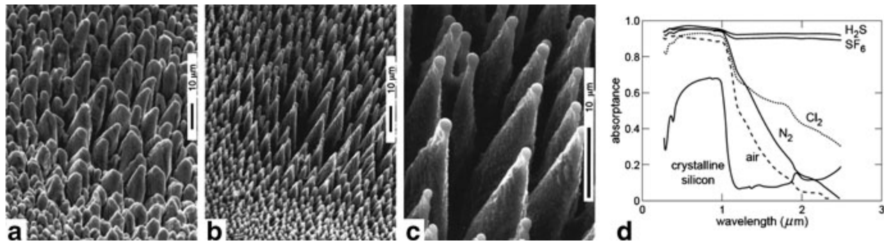

Fig. 4.8 SEM images of the surface microstructuring of Si(100) by 500 laser pulses of a 200 mm diameter, nearly Gaussian beam (100-fs, 800 nm, 10 kJ/m^2) (**a**) processed in vacuum and (**b**,**c**) in a 500 Torr atmosphere of SF_6. Images viewed at an angle of 45° from the surface normal [94]. (**d**) Absorptance of femtosecond laser microstructured silicon in a variety of gases [95]

spherical caps (Fig. 4.8b, c) [94]. The difference was attributed to laser-induced plasma etching by the halogen-containing gases. Nearly identical spiked structures were produced with H_2S indicating the importance of sulfur in the etching process [95]. Younkin et al. found that the number density of structures created was greatest in SF_6, slightly more than Cl_2, but approximately twice that of N_2 and air. Processing in water with 400 nm irradiation produced submicrometer spikes while 800 nm irradiation only resulted in roughening and holes [96]. This strong dependence on wavelength is not observed for gaseous atmosphere or vacuum processing.

Processing environment also has a major impact on the optical properties of the microstructured surface. Figure 4.8d shows absorptance measurements of silicon microstructured in a variety of atmospheres. All of the gases show significant enhancement over the unstructured sample for light above the band gap (250 nm to 1.1 μm). This can be attributed to the microstructure's ability to trap light and reduce reflections. Beyond the band edge (1.1 μm–2.5 μm), the absorptance of N_2-, Cl_2-, and air-processed samples decreased continuously while SF_6- and H_2S-processed samples remained at about 90% absorbing [95]. It was suggested that damage to the lattice and alteration of the band structure through the incorporation of sulfur was responsible for the near unity absorptance in the infrared. Processing with other chalcogens, such as selenium and tellurium, also led to near-unity broadband absorption [3].

The temporal laser pulse width also has a noticeable effect on the formation mechanisms and resulting morphology. Crouch et al. found that despite similar near-unity broadband absorption, processing in SF_6 with fs pulses produced significantly different structures on the surface of silicon than ns pulses [97]. The fs-formed structures are about 8 μm tall with their tips level with the original surface, indicating that ablation and etching dominate the formation. They are also covered with nanoscale particles and features. The ns-formed structures are smoother, stand five times taller at 40 μm, and protrude from the original surface indicating that material deposition played a part in the growth process. Both cases produced structures with a crystalline silicon core covered with a highly disordered layer of nanocrystallites, nanopores,

and sulfur impurities. However, this layer was much thinner and more sparse on the ns-formed structures. They also concluded that the below-band gap enhancement in absorptance is due to an optically active sulfur configuration in the silicon, which degrades upon annealing.

In summary, multiscale texturing plays an important role in a material's optical properties, and such behavior can be exploited for applications such as photovoltaics or electron emitters. At the cutting edge of this is the laser structuring of silicon to produce a variant often referred to as black silicon. Such a structure has been shown to absorb 95% of incident radiation with energy above its bandgap [250–1,100 nm] [98]. Below the bandgap, in which unprocessed silicon is essentially transparent, the microstructured silicon absorbs 90% of incident radiation for wavelengths [1,100–2,500 nm]. This enhanced absorbance has resulted in high-sensitivity infrared photodetectors [99, 100], high-quantum-efficiency avalanche photodiodes (APDs) [101], and has even spawned a company taking advantage of the processing technology (SiOnyx).

4.5 Case Study II: Surface Texturing for Enhanced Biological Interactions

Biological implants are often utilized to reinforce or replace diseased or damaged tissue in the human body. For example, the implantation of a prosthetic joint or the replacement of a tooth are standard orthopedic surgical procedures used to relieve pain and regain functionality in order to improve the quality of life for the patient. Although these procedures are common and generally have a high success rate, fears about the limited implant lifetime have prevented the procedures from being fully utilized in all potential cases. For instance, the typical lifetime of a hip implant can be as short as 10–15 years requiring complex and costly retrieval and revision surgery to reattach the implant [102]. While recent advances in biomaterials engineering have limited the number of failures due to wear or fracture of the implant itself, loosening of the load bearing surfaces of the implants from the supporting hard tissue can still lead to malfunction [102, 103]. Abrasion between the loose implant and the bone surface can cause pain and further wear. Accumulation of debris particles can trigger a macrophage-induced inflammatory response that can lead to bone loss (osteolysis) and further implant loosening [104]. This damage can make future revisions of the implant more difficult and dangerous. Therefore, much of the current implant research has focused on engineering biomaterials that allow for rapid integration with the supporting hard tissue, resist loosening, and shorten the recovery period.

The difficulty faced by biomaterials engineers when designing load bearing implants is that there are a limited number of naturally biocompatible materials with the appropriate mechanical properties to sustain unencumbered, long-term loading in a biological environment. For example, Ti-6Al-4V (Ti64) is one of a few completely biocompatible materials and is the most common metal used in dental

and hip implants because of its excellent fracture toughness, fatigue resistance, and Young's Modulus near that of bone. With such exceptional bulk material properties, researchers now focus on implant surface engineering as a means to enhance the physiological response to existing biomaterials without degrading their bulk strength and weight properties. Biological cells and tissues mainly interact with the outermost atomic layers of an implant [105]. Therefore, modifying only the surface morphology and chemistry is sufficient to elicit novel biological responses from existing materials [102]. Laser processing is ideally suited to such an endeavor.

Current attempts to enhance implant longevity have focused on the initial stages of cell adhesion and osseointegration. Osseointegration is the process by which a direct structural and functional bond is formed between living bone and the surface of the artificial implant without intervening soft tissue. Initially, the surface of a newly fixed implant becomes conditioned by the adsorption of proteins (fibronectin, actin, vinculin, and integrins), which are active in cell adhesion, growth, and differentiation [106, 107]. Osseointegration is then initiated by the osteoblast cells, which migrate to the conditioned implant surface and proliferate in the voids that exist between the implant and the existing bone. The early activities of these osteoblast cells lay the groundwork for mature bone cells that will eventually be formed in that region [108]. It has been seen that surface texture and chemistry greatly influence the adsorption of protein and modify how the osteoblast and other cells attach and interact with the implant surface environment [102, 107, 109, 110]. Thus, optimizing these surface properties can increase the chances of successful osseointegration.

There are several relevant length scales over which modified surface topography and chemistry of a processed implant can influence cell adhesion and behavior, enhance osseointegration, and improve the resulting bond to existing bone [111, 112]. Modifying implant surface energy through chemical processing increases adhesion at the atomic scale and has been shown to improve bonding of proteins and cells [113]. Nanoscale surface features can affect protein interactions associated with cell signaling, which regulates cell adhesion, proliferation, and differentiation. Also, nanoscale surface features can influence the interactions of individual cell microfilaments and microtubules that form focal adhesion complexes (the protein complex that attaches the cell to the surface). Figure 4.9a shows osteoblast-like cells adhering to a surface with the focal adhesion points visible in green. Texturing with micron-sized features such as grooves, ridges, craters, and mountains can increase surface area and provide more opportunities for focal attachment. It can also cause cells to mechanically stretch or contract to align and organize with the features, a phenomenon known as 'contact guidance' (Fig. 4.9b) [111, 114, 115]. This alignment can be utilized to promote healthy regeneration of bone. Since bone consists of sheets of parallel cells, initiating bone healing with parallel cells may improve the healing process [116]. Also, cells grown on substrates with linear grooves exhibit organized regrowth, possibly decreasing scar tissue formation during healing [117]. Finally, macroscopic features textured on the surface of the implant such as vents, slots, dimples, and threads can physically interlock the implant with the bone, increasing longevity [118–121].

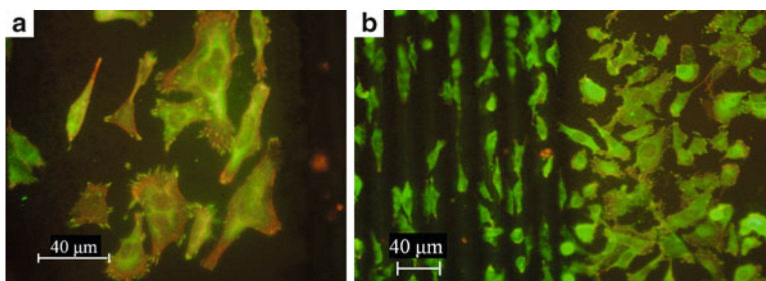

Fig. 4.9 (**a**) Osteoblast-like human osteosarcoma cells. Their vinculin and focal adhesion points are stained *green* and their actin stained *red*. (**b**) Contact guidance by linear grooves causes elongation of the cells (*left*) as compared to the adherance to a polished surface (*right*). (Images by Lara Ionescu)

Table 4.2 Multiple length scales over which the adhesion of bone to the implant is determined

Length scale	Influence on cell adhesion
Atomic scale	Surface energy controls the atomic bonding of proteins and cells
Nanoscale	Nanoscale surface features affect interactions of protein, cell microfilaments, and microtubules, which form focal adhesion complexes and cell signaling, which regulates cell adhesion, proliferation, and differentiation
Microscale	Micron-sized features such as grooves, ridges, craters, and mountains can increase surface area, provide more opportunities for focal attachment, and cause cells to mechanically stretch or contract to align and organize with the features (contact guidance)
Macroscale	Macroscopic features such as vents, slots, dimples, and threads can physically interlock the implant with the bone

Table 4.2 shows a breakdown of the relevant length scales and the biological–material interactions that occur on that scale. As we can see, osseointegration is inherently a multiscale issue, requiring control and understanding of surface properties over many different size scales. Laser surface texturing gives researchers a tool with which to rapidly and conveniently modify surfaces over these scales without the need for subsequent processing.

Various methods to modify biomaterial surface properties have been investigated. Chemical treatments and ion beam implantation have been used to alter surface composition and functionalization. Microprinting of patterned thiols, proteins, silanes, and polymers have also been demonstrated to modify biological adhesion and cellular response. Various biomaterial coating techniques such as liquid immersion, thermal spray, plasma spray, electrocrystallization, electrophoretic processes, and laser-assisted surface coating have been utilized to deposit thin layers of highly biocompatible yet brittle material onto a more rigid supporting material [122]. Such coatings have been shown highly effective at enhancing biocompatibility; however, they tend to require complicated preparation processes and still have problems with coating homogeneity and adhesion to the substrate. Alternatively, laser heat treatments do not share these difficulties associated with coatings as no additional

material is added to the surface. Yet at the same time, these methods allow for similar changes in wetting characteristics of the existing surface by changing roughness, microstructure, and surface chemistry of Ti-6Al-4V [123, 124], positively affecting corrosion resistance and biological adhesion.

Additionally, various techniques have been employed to texture the surface of implants. Currently, implant surfaces are roughened through randomized processes such as sand blasting (Al_2O_3 or SiC particles) or acid etching to encourage cell growth and improve osseointegration [125]. Such techniques are relatively inexpensive and easy to perform on complex surfaces, but cells that grow on these surface typically do so equiaxially leading to the development of random bone cell orientations [126]. Also imbedded blasting particles can contaminate the surface with increased concentrations of cytotoxic elements [127]. Other techniques such as ion beam and electron beam texturing have enabled precise control of complex features but require vacuum, which adds to the cost and limits the dimensions of implants that can be textured. Photolithography has also been used but requires complicated preparation processes and is limited in the implant geometries it can handle and in its ability to produce multiscale features [115].

Alternatively, laser surface texturing provides a fast, non-contact, and clean alternative for microstructuring in ambient conditions. Unlike lithographic techniques, it can handle irregular implant shapes. A number of studies have investigated laser machining of surface features to enhance cellular adhesion to biomaterial surfaces and improve resistance to implant loosening [116, 117, 122, 128–130]. However, most have focused on optimizing cellular response as a function of primary feature dimensions (groove width and depth, dimple diameter, etc.). As was discussed in the background section and previous case study, one of the key benefits of laser processing is the ability to modify surfaces over multiple lengths scales. For instance, Fig. 4.10a, b show a dental implant that was laser micro-patterned using a kinoform producing a regular array of dimples directly on its threads. Figure 4.10c shows a close up of an individual patterned dimple which reveals secondary features such as the presence of material redeposited on the rim and splattered into the surrounding area. This multiscale modification to the surface is critically important in determining the overall interaction between the cells and the surface. Different

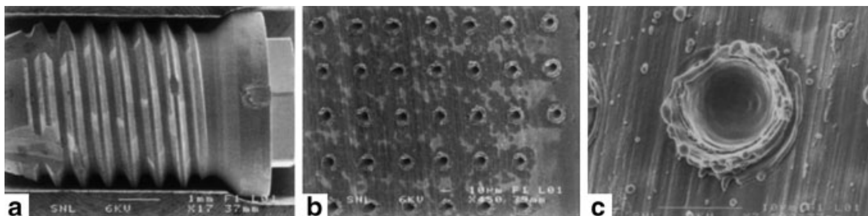

Fig. 4.10 (**a**) SEM image of a dental implant that was laser micro-patterned using a kinoform with (**b**) a regular array of dimples patterned directly onto its threads. (**c**) A close up of one of the 10 μm pits showing remnants of material resolidified on the rim and ejected into the surrounding region [128]

combinations of processing parameters (e.g., number of pulses, pulse energy, pulse time, spot size, laser frequency) can achieve the same primary feature dimensions but with different secondary features.

Ulerich et al. investigated the effects of multiscale laser texturing of a Ti-6Al-4V substrate on the adhesion of osteoblast cells [129]. They rastered a focused beam from a ns pulsed UV laser across the surface to pattern linear grooves. By manipulating processing parameters such as pulse energy, translation distance between pulses, number of passes over the same groove, and machining environment (air, water, or silicon oil), they were able to exercise a large degree of control over the groove properties. They found that groove width was not significantly affected by the number of passes or the distance between pulses. However, they found that they could accurately manipulate groove width by controlling the pulse energy. This control is explained by the fact that as pulse energy increases, a larger fraction of the Gaussian beam exceeded the ablation threshold. Groove depth, on the other hand, was affected by the translation distance and the number of passes as well as the laser pulse energy. Decreasing the distance between pulses or making multiple passes would increase groove depth without affecting the width. This allowed further control of the grove wall slope through selection of processing parameters. These findings are illustrated in Fig. 4.11, which shows cross sectional SEM images of the grooves obtained with different translation distance between pulses.

In addition to the primary groove characteristics, they found that processing conditions also affected the roughness and sub-micron features created on the surface. Small-scale features would form on the surface of the grooves depending on the specific nature of the material ablation and redeposition. Lower surface heating rates had the tendency to merely melt the surface with thermocapillarity causing a net change in the surface morphology, resulting in a smooth surface. As heating rates

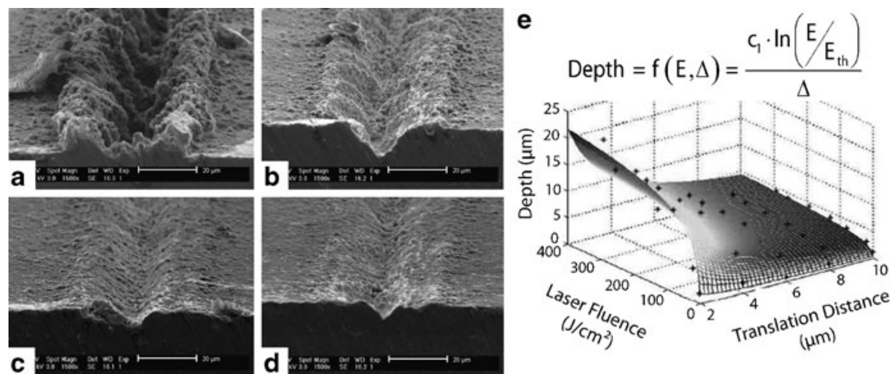

Fig. 4.11 Cross-sectional SEM images (scale bars are 20 µm) of the laser-machined (56 J/cm^2) surfaces shows decreasing size and slope of groove walls with increasing translation distance: (**a**) 2 µm, (**b**) 4 µm, (**c**) 6 µm, and (**d**) 8 µm. (**e**) Groove depth measurement as a function of translation distance and laser fluence [129]

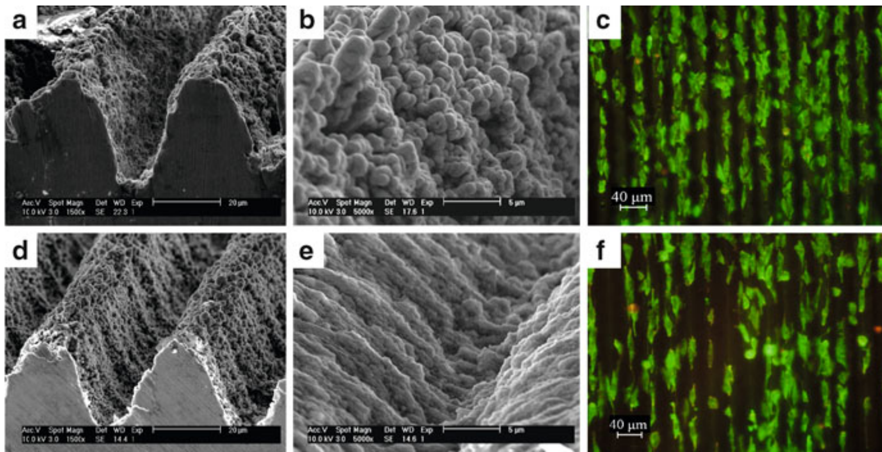

Fig. 4.12 The top (**a,b,c**) and bottom (**d,e,f**) structures have the same groove width and depth but different secondary features (**b** and **e**) resulting in different cellular adhesion behavior (**c** and **f**)

increased, recoil from ejected material would splatter material from the molten pool, which would recast in the surrounding regions with splatter patterns largely affected by the force with which they were expelled. Decreasing the translation distance between laser pulses had the tendency to increase surface roughness due to the increased interaction with the residual heat left from previous pulses. Using a dynamic set of machining parameters, they were able to intentionally create many sub-micron features including nodules, ripples, ledges, and nano-textures (Fig. 4.12b, e) [129].

Surface texturing of the Ti-6Al-4V substrate was also done in liquid environments (water and silicon oil), which enhanced the quenching rate of the laser heated material. Grooves machined in liquid environments tended to contain other types of features such as bubbles where pockets of liquid vaporized during the process. Cracking was also apparent on the surface of the liquid-machined grooves due to additional thermal stresses induced from the high quench rate.

Ulerich et al. found that the surface chemical composition was also affected by the laser texturing process. For instance, they found that with a small translation distance between pulses, there was a measurable depletion of aluminum in the valleys of the grooves and an enrichment of aluminum on the ridges. This effect is consistent with a transient molten pool at the bottom of the grove that preferentially evaporates aluminum due to its higher vapor pressure. In contrast, they found that the depletion of aluminum did not occur under liquid environments. Surface chemical composition can influence how cells attach and react to a metal by changing the way that proteins adsorb or by activating different cellular pathways with nearby cells. Additionally, when dealing with alloy materials, shifts in the surface chemistry can lead to an overabundance of cytotoxic elements on the surface or changes in the mechanical properties of the surface. Therefore consideration of chemical composition changes is important when designing implant processing procedures.

To probe the effects of surface structure and chemistry on the adhesion of cells, Ulerich et al. conducted fluorescent studies of live osteoblast cells cultured on the Ti-6Al-4V surfaces. Results such as these (Fig. 4.12) demonstrate that the direct-write laser-machined grooves led to contact guidance (cell alignment) as well as enhanced cell density with respect to the original surface when structured in an optimal fashion [131]. Also, through such studies, it is possible to probe the importance of secondary groove textures on the cell growth and adhesion. Grooves were textured with equivalent primary dimensions (Fig. 4.12a, d) but different secondary texture (Fig. 4.12b, e). Grooves cut with a final pass of higher energy yielded a greater roughness (Fig. 4.12b) and tended to have a much larger number of cells spanning multiple grooves (Fig. 4.12c) due to the presence of favorable attachment sites near the tops of the grooves. Other more complex patterns and interactions can be probed in this fashion.

Multiscale texturing of surfaces can have a profound impact on the growth and adhesion of cells on surfaces for such applications as structural implants or other medical devices. In these cases, it is not just the overall roughness or large scale morphology but also the detailed features on all length scales that affect the resulting material interaction. The unique laser-induced structures can modify the morphology and local chemistry of the surface making it more beneficial for cells to grow in certain patterns or to grow at a certain density depending on the features at various size scales. Using newer laser processing approaches opens the door to greater optimization in these important applications.

4.6 Conclusions

In this chapter, we have shown some of the versatile capabilities of laser processing to modify the surface properties of materials in order to enhance their performance for a variety of applications. The laser is a flexible tool that allows precise deposition of energy into the material at a controlled rate and within a confined area. A variety of different material responses can be achieved depending on the material system and the laser parameters, allowing processes to be designed and optimized to permanently alter the material's surface chemistry, crystal structure, and morphology to suite its desired function. The unique aspect of this for many applications is that the material modifications can occur over many different length scales, adding complexity to the surface and a new dimension to surface optimization. Laser surface processing has been a key element in a number of large-scale industrial manufacturing operations, yet at the same time it continues to reinvent itself and find ever new uses in emerging areas. As lasers continue to be developed with an ever broadening range of capabilities, laser surface processing will continue to improve the performance of materials in existing applications and will open the door to new materials and novel applications that would not be possible without these unique processing capabilities.

References

1. P. Campbell, J. Opt. Soc. Am. B **10**(12) (1993)
2. V. Semak, N. Dahotre, in *Lasers in Surface Engineering*, *Surface Engineering Series*, vol. 1, ed. by N. Dahotre (ASM International, Materials Park, OH, USA, 1998), pp. 35–67
3. M. Sheehy, B. Tull, C. Friend, E. Mazur, Mat. Sci. Eng. B **137**, 289 (2006)
4. V. Gregson, *Laser Material Processing* (Holland Publishing Company, Holland, 1984)
5. I. Etsion, J. Tribol. Trans. ASME **127**(1), 248 (2005)
6. N. Dahotre, *Lasers in Surface Engineering*, *Surface Engineering Series*, vol. 1 (ASM International, Materials Park, OH, USA, 1998)
7. D. Bäuerle, *Laser Processing and Chemistry* (Springer, Berlin, 2000)
8. W.M. Steen, *Laser Material Processing*, 3rd edn. (Springer, London, 2003)
9. J.C. Ion, *Laser Processing of Engineering Materials: Principles, Procedure and Industrial Applications* (Elsevier Butterworth-Heinemann, Oxford, 2005)
10. S.Y. Zhang, Y.H. Ren, G. Lupke, Appl. Opt. **42**(4), 715 (2003)
11. L.A. Romero, F.M. Dickey, J. Opt. Soc. Am. A: **13**(4), 751 (1996)
12. C. Momma, S. Nolte, G. Kamlage, F. von Alvensleben, A. Tunnermann, Appl. Phys. A Mater. Sci. Process. **67**(5), 517 (1998)
13. N. Sanner, N. Huot, E. Audouard, C. Larat, J.P. Huignard, B. Loiseaux, Opt. Lett. **30**(12), 1479 (2005)
14. K. Nemoto, T. Nayuki, T. Fujii, N. Goto, Y. Kanai, Appl. Opt. **36**(30), 7689 (1997)
15. E. McLeod, A.B. Hopkins, C.B. Arnold, Opt. Lett. **31**(21), 3155 (2006)
16. S. Heinemann, Opt. Commun. **119**(5–6), 613 (1995)
17. F.M. Dickey, S.C. Holswade (eds.), *Laser Beam Shaping: Theory and Techniques* (Marcel Dekker, New York, 2000)
18. E. Hecht, *Optics*, 4th edn. (Addison Wesley, San Francisco, 2002)
19. J. Heller, J.W. Bartha, C.C. Poon, A.C. Tam, Appl. Phys. Lett. **75**(1), 43 (1999)
20. M. Toulemonde, S. Unamuno, R. Heddache, M.O. Lampert, M. Hageali, P. Siffert, Appl. Phys. A Mater. Sci. Process. **36**(1), 31 (1985)
21. C.B. Arnold, M.J. Aziz, M. Schwarz, D.M. Herlach, Phys. Rev. B **59**(1), 334 (1999)
22. J.C. Weeber, J.R. Krenn, A. Dereux, B. Lamprecht, Y. Lacroute, J.P. Goudonnet, Phys. Rev. B **64**(4) (2001)
23. D.R. Lide, *CRC Handbook of Chemistry and Physics*, 82nd edn. (CRC, Boca Raton, 2001)
24. R.E. Slusher, B.J. Eggleton, *Nonlinear Photonic Crystals*, 1st edn. (Springer, Berlin, 2004)
25. N. Ghofraniha, C. Conti, G. Ruocco, S. Trillo, Phys. Rev. Lett. **99**(4) (2007)
26. W. Staudt, S. Borneis, K.D. Pippert, Phys. Status Solidi A Appl. Res. **166**(2), 743 (1998)
27. N. Mori, T. Ando, Phys. Rev. B **40**(9), 6175 (1989)
28. B.N. Chichkov, C. Momma, S. Nolte, F. vonAlvensleben, A. Tunnermann, Appl. Phys. A Mater. Sci. Process. **63**(2), 109 (1996)
29. M. von Allmen, A. Blatter, *Laser-Beam Interactions with Materials: Physical Principles and Applications*. Springer Series in Materials Science (Springer, Berlin, 1995)
30. Y. Hirayama, M. Obara, Appl. Surf. Sci. **197**, 741 (2002)
31. L.V. Zhigilei, P.B.S. Kodali, B.J. Garrison, J. Phys. Chem. B **101**(11), 2028 (1997)
32. A.J. Hick, Heat Treat. Met. **10**(1), 3 (1983)
33. D.L. Bourell, H.L. Marcus, J.W. Barlow, J.J. Beaman, Int. J. Powder Metall **28**(4), 369 (1992)
34. X. Wang, X. Xu, Appl. Phys. A Mater. Sci. Process. **73**(1), 107 (2001)
35. M.J. Aziz, J.Y. Tsao, M.O. Thompson, P.S. Peercy, C.W. White, Phys. Rev. Lett. **56**(23), 2489 (1986)
36. J.S. Im, M.A. Crowder, R.S. Sposili, J.P. Leonard, H.J. Kim, J.H. Yoon, V.V. Gupta, H.J. Song, H.S. Cho, Phys. Status Solidi A Appl. Res. **166**(2), 603 (1998)
37. T.D. Bennett, D.J. Krajnovich, C.P. Grigoropoulos, P. Baumgart, A.C. Tam, J. Heat Transfer **119**(3), 589 (1997)
38. S.C. Chen, D.G. Cahill, C.P. Grigoropoulos, J. Heat Transfer **122**(1), 107 (2000)
39. J. Eizenkop, I. Avrutsky, D.G. Georgiev, V. Chaudchary, J. Appl. Phys. **103**(9), 094311 (2008)

40. D.B. Chrisey, G.K. Hubler (eds.), *Pulsed Laser Deposition of Thin Films* (Wiley-Interscience, New York, 1994)
41. X.L. Mao, A.C. Ciocan, R.E. Russo, Appl. Spectrosc. **52**(7), 913 (1998)
42. N.M. Bulgakova, A.V. Bulgakov, Appl. Phys. A Mater. Sci. Process. **73**(2), 199 (2001)
43. R. Stoian, D. Ashkenasi, A. Rosenfeld, E.E.B. Campbell, Phys. Rev. B **62**(19), 13167 (2000)
44. B.J. Garrison, R. Srinivasan, J. Appl. Phys. **57**(8), 2909 (1985)
45. A.H. Clauer, B.P. Fairand, B.A. Wilcox, Metall. Mater. Trans. B **8**(12), 1871 (1977)
46. N.G. Semaltianos, W. Perrie, V. Vishnyakov, R. Murray, C.J. Williams, S.P. Edwardson, G. Dearden, P. French, M. Sharp, S. Logothetidis, K.G. Watkins, Mater. Lett. **62**(14), 2165 (2008)
47. J. Woodhead, J. Hergt, M. Shelley, S. Eggins, R. Kemp, Chem. Geol. **209**(1–2), 121 (2004)
48. X. Liu, D. Du, G. Mourou, IEEE J. Quantum Electron. **33**(10), 1706 (1997)
49. D.W. Zhang, T.C. Lei, J.G. Zhang, J.H. Ouyang, Surf. Coat. Technol. **115**(2–3), 176 (1999)
50. X.G. Wang, S.S. Li, C.H. Huang, S. Rawal, J.M. Howard, V. Craciun, T.J. Anderson, O.D. Crisalle, Sol. Energy Mater. Sol. Cells **88**(1), 65 (2005)
51. P. Baumgart, D.J. Krajnovich, T.A. Nguyen, A.C. Tam, IEEE Trans. Magn. **31**(6), 2946 (1995)
52. I. Etsion, Tribol. Lett. **17**(4), 733 (2004)
53. A.C. Tam, W.P. Leung, W. Zapka, W. Ziemlich, J. Appl. Phys. **71**(7), 3515 (1992)
54. R. Ranjan, D.N. Lambeth, M. Tromel, P. Goglia, Y. Li, J. Appl. Phys. **69**(8), 5745 (1991)
55. R. Blossey, Nat. Mater. **2**(5), 301 (2003)
56. V. Zorba, E. Stratakis, M. Barberoglou, E. Spanakis, P. Tzanetakis, C. Fotakis, Appl. Phys. A Mater. Sci. Process. **93**(4), 819 (2008)
57. M. Barberoglou, V. Zorba, E. Stratakis, E. Spanakis, P. Tzanetakis, S. Anastasiadis, C. Fotakis, Appl. Surf. Sci. **255**(10), 5425 (2009)
58. V. Zorba, P.D. Persano, L., A. Athanassiou, E. Stratakis, R. Cingolani, P. Tzanetakis, C. Fotakis, Nanotechnology **17**(13), 3234 (2006)
59. T.O. Yoon, H.J. Shin, S.C. Jeoung, Y.I. Park, Opt. Express **16**(17), 12715 (2008)
60. J. Wang, H. Chen, T. Sui, A. Li, D. Chen, Plant Science **176**(5), 687 (2009)
61. N.A. Patankar, Langmuir **20**(19), 8209 (2004)
62. D. Bouhafs, A. Moussi, A. Chikouche, J.M. Ruiz, Sol. Energy Mater. Sol. Cells **52**(1–2), 79 (1998)
63. W. Zhou, M. Tao, L. Chen, H. Yang, J. Appl. Phys. **102**(10) (2007)
64. O. Kluth, B. Rech, L. Houben, S. Wieder, G. Schope, C. Beneking, H. Wagner, A. Loffl, H.W. Schock, Thin Solid Films **351**(1–2), 247 (1999)
65. S.J. Wilson, M.C. Hutley, Opt. Acta **29**(7), 993–1009 (1982)
66. S.A. Boden, D.M. Bagnall, Appl. Phys. Lett. **93**(13), 133108 (2008)
67. J.H. Zhao, A.H. Wang, P. Campbell, M.A. Green, IEEE Trans. Electron Devices **46**(7), 1495 (1999)
68. H. Jansen, M. Deboer, R. Legtenberg, M. Elwenspoek, J. Micromech. Microeng. **5**(2), 115 (1995)
69. H. Nakaya, M. Nishida, Y. Takeda, S. Moriuchi, T. Tonegawa, T. Machida, T. Nunoi, Sol. Energy Mater. Sol. Cells **34**(1–4), 219 (1994)
70. J.C. Zolper, S. Narayanan, S.R. Wenham, M.A. Green, Appl. Phys. Lett. **55**(22), 2363 (1989)
71. M. Abbott, J. Cotter, Prog. Photovoltaics Res. Appl. **14**(3), 225 (2006)
72. L. Dobrzański, A. Drygała, K. Gołombek, P. Panek, E. Bielańska, P. Zięba, J. Mater. Process. Technol. **201**(1–3), 291 (2008)
73. M. Halbwax, T. Sarnet, P. Delaporte, M. Sentis, H. Etienne, F. Torregrosa, V. Vervisch, I. Perichaud, S. Martinuzzi, Thin Solid Films **516**(20), 6791 (2008)
74. M. Birnbaum, J. Appl. Phys. **36**(11), 3688 (1965)
75. H.M. van Driel, J.E. Sipe, J.F. Young, Phys. Rev. Lett. **49**(26) (1982)
76. Z. Guosheng, P.M. Fauchet, A.E. Siegman, Phys. Rev. B **26**, 5366 (1982)
77. J.E. Sipe, J.F. Young, J.S. Preston, H.M. van Driel, Phys. Rev. B **27**, 1141 (1983)
78. E.M. Hsu, T.H.R. Crawford, C. Maunders, G.A. Botton, H.K. Haugen, Appl. Phys. Lett. **92**(22) (2008)
79. D. Dufft, A. Rosenfeld, S.K. Das, R. Grunwald, J. Bonse, J. Appl. Phys. **105**(3) (2009)

80. A.Y. Vorobyev, G. Chunlei, J. Appl. Phys. **103**(4), 043513 (2008)
81. S.R. Foltyn, *Pulsed Laser Deposition of Thin Films* (Wiley-Interscience, New York, 1994)
82. F. Sánchez, J.L. Morenza, R. Aguiar, J.C. Delgado, M. Varela, Appl. Phys. Lett. **69**(5) (1996)
83. Y. Kawakami, E. Ozawa, Appl. Surf. Sci. **218**(1–4), 175 (2003)
84. A. Bensaoula, C. Boney, R. Pillai, G.A. Shafeev, A.V. Simakin, D. Starikov, Appl. Phys. A Mater. Sci. Process. **79**(4–6), 973 (2004)
85. Y. Yang, J.J. Yang, C.Y. Liang, H.S. Wang, Opt. Express **16**(15), 11259 (2008)
86. A.Y. Vorobyev, C. Guo, J. Appl. Phys. **104**(5) (2008)
87. D.H. Lowndes, J.D. Fowlkes, A.J. Pedraza, Appl. Surf. Sci. **154–155**, 647 (2000)
88. V.V. Voronov, S.I. Dolgaev, S.V. Lavrishchev, A.A. Lyalin, A.V. Simakin, G.A. Shafeev, Quantum Electron. **30**, 710 (2000)
89. A.J. Pedraza, J.D. Fowlkes, S. Jesse, C. Mao, D.H. Lowndes, Appl. Surf. Sci. **168**(1–4), 251 (2000)
90. S. Dolgaev, S. Lavrishev, A. Lyalin, A. Simakin, V. Voronov, G. Shafeev, Appl. Phys. A **73**(2), 177 (2001)
91. J. Bonse, S. Baudach, J. Krüger, W. Kautek, M. Lenzner, Appl. Phys. A **74**(1) (2002)
92. B.R. Tull, J.E. Carey, E. Mazur, J.P. McDonald, S.M. Yalisove, MRS Bull. **31**(8), 626 (2006)
93. X.Y. Chen, J. Lin, J.M. Liu, Z.G. Liu, Appl. Phys. A (2008)
94. T.H. Her, R.J. Finlay, C. Wu, S. Deliwala, E. Mazur, Appl. Phys. Lett. **73**(12) (1998)
95. M.A. Sheehy, L. Winston, J.E. Carey, C.M. Friend, E. Mazur, Chem. Mater. **17**, 3582 (2005)
96. M. Shen, C.H. Crouch, J.E. Carey, E. Mazur, Appl. Phys. Lett. **85**, 5694 (2004)
97. C.H. Crouch, J.E. Carey, J.M. Warrender, M.J. Aziz, E. Mazur, F.Y. Génin, Appl. Phys. Lett. **84**, 1850 (2004)
98. C. Wu, C.H. Crouch, L. Zhao, J.E. Carey, R. Younkin, J.A. Levinson, E. Mazur, R.M. Farrell, P. Gothoskar, A. Kager, Appl. Phys. Lett. **78**(1850) (2001)
99. J.E. Carey, C.H. Crouch, M. Shen, E. Mazur, Opt. Lett. **30**, 1773 (2005)
100. Z. Huang, J.E. Carey, M. Liu, X. Guo, E. Mazur, J.C. Campbell, Appl. Phys. Lett. **89** (2006)
101. R.A. Myers, R. Farrell, A.M. Karger, J.E. Carey, E. Mazur, Appl. Opt. **45**, 8825 (2006)
102. B. Ratner, A. Hoffman, F. Schoen, J. Lemons, *Biomaterials Science: An Introduction to Materials in Medicine* Second Edition (Elsevier Acedemic Press, Sand Diego, CA, 2004)
103. D. Brunette, *Titanium in Medicine: Material Science, Surface Science, Engineering, Biological Responses, and Medical Applications* (Springer, New York, 2001)
104. S.K. Gupta, A. Chu, A.S. Ranawat, J. Slamin, C.S. Ranawat, J. Arthroplast. **22**(6), 787 (2007)
105. B. Kasemo, J. Lausmaa, CRC Critical Reviews in Biocompatibility **2**(4), 335 (1986)
106. D.A. Puleo, A. Nanci, Biomaterials **20**(23–24), 2311 (1999)
107. K. Anselme, Biomaterials **21**(7), 667 (2000)
108. U. Meyer, A. Büchter, H. Wiesmann, U. Joos, D. Jones, European Cells and Materials **9**, 39 (2005)
109. M. Wong, J. Eulenberger, R. Schenk, E. Hunziker, J. Biomed. Mater. Res. **29**(12), 1567 (1995)
110. J. Park, J. Bronzino, Y. Kim, *Biomaterials: Principles and Applications* (CRC Press, Boca Raton, USA, 2003)
111. A. Curtis, C. Wilkinson, Biomaterials **18**(24), 1573 (1997)
112. J. Tan, W.M. Saltzman, Biomaterials **25**(17), 3593 (2004)
113. T.G. Vankooten, J.M. Schakenraad, H.C. Vandermei, H.J. Busscher, Biomaterials **13**(13), 897 (1992)
114. D.M. Brunette, Int. J. Oral Maxillofac. Implants **3**(4), 231 (1988)
115. R.G. Flemming, C.J. Murphy, G.A. Abrams, S.L. Goodman, P.F. Nealey, Biomaterials **20**(6), 573 (1999)
116. A. Khakbaznejad, B. Chehroudi, D.M. Brunette, J. Biomed. Mat. Res. A **70A**(2), 206 (2004)
117. W.O. Soboyejo, B. Nemetski, S. Allameh, N. Marcantonio, C. Mercer, J. Ricci, J. Biomed. Mater. Res., Part A **62**(1), 56 (2002)
118. M.D. Ward, D.A. Hammer, Biophys. J. **64**, 936 (1993)
119. N. Wang, J.P. Butler, D.E. Ingber, Science **260**(5111), 1124 (1993)
120. E.T. den Braber, J.E. de Ruijter, H.T.J. Smits, L.A. Ginsel, A.F. von Recum, J.A. Jansen, Biomaterials **17**(11), 1093 (1996)

121. E.T. den Braber, J.E. de Ruijter, L.A. Ginsel, A.F. von Recum, J.A. Jansen, J. Biomed. Mater. Res. **40**(2), 291 (1998)
122. A. Kurella, N.B. Dahotre, J. Biomater. Appl. **20**(1), 5 (2005)
123. J. Lawrence, L. Hao, H.R. Chew, Surf. Coat. Technol. **200**(18–19), 5581 (2006)
124. R. Singh, S.G. Chowdhury, S.K. Tiwari, N.B. Dahotre, J. Mater. Sci. Mater. Med. **19**(3), 1363 (2008)
125. D.L. Cochran, D. Buser, C.M. ten Bruggenkate, D. Weingart, T.M. Taylor, J.P. Bernard, F. Peters, J.P. Simpson, Clin. Oral Implants Res. **13**(2), 144 (2002)
126. J.H.C. Wang, E.S. Grood, J. Florer, R. Wenstrup, J. Biomech. **33**(6), 729 (2000)
127. K. Anselme, B. Noel, P. Hardouin, J. Mater. Sci. Mater. Med. **10**(12), 815 (1999)
128. C. Hallgren, H. Reimers, D. Chakarov, J. Gold, A. Wennerberg, Biomaterials **24**(5), 701 (2003)
129. J.P. Ulerich, L.C. Ionescu, J. Chen, W.O. Soboyejo, C.B. Arnold, in *Photon Processing in Microelectronics and Photonics VI*, ed. by C.B. Arnold, T. Okada, M. Meunier, A.S. Holmes, D.B. Geohegan, F. Träger, J.J. Dubowski (San Jose, 2007)
130. A.Y. Fasasi, S. Mwenifumbo, N. Rahbar, J. Chen, M. Li, A.C. Beye, C.B. Arnold, W.O. Soboyejo, Mater. Sci. Eng. C **29**(1), 5 (2009)
131. J. Chen, J. Ulerich, E. Abelev, A. Fasasi, C.B. Arnold, W.O. Soboyejo, Mater. Sci. Eng. C **29**(4), 1442 (2009)

Chapter 5
Temporal Pulse Tailoring in Ultrafast Laser Manufacturing Technologies

Razvan Stoian, Matthias Wollenhaupt, Thomas Baumert, and Ingolf V. Hertel

Abstract Ultrafast lasers have gained momentum in material processing technologies in response to requirements for higher accuracy. Minimal energy diffusion and high nonlinearity of interaction indicate the possibility of confining energy on the smallest scales. The possibility of temporal beam manipulation allows adapting the incoming energy rate to the material individual reaction. Optimal energy coupling gives thus the possibility to guide the material response towards user-designed directions, offering extended flexibility for quality material processing.

5.1 Introduction

The demand for precision in laser material processing requires the development of irradiation tools that are able to localize the energy on small temporal and spatial scales. Ultrashort laser pulses have therefore become instruments of choice for material structuring on a micro- or even nanometer scale. The high nonlinearity of the interaction, good energy confinement, and limited heat diffusion offer challenging perspectives for judiciously designed direct structuring processes, as well as for applications in nanosurgery, generation of nanoparticles, or minimally invasive ablation for spectroscopic purposes (see, e.g., Chaps. 6, 7 and 9).

R. Stoian (✉)
Laboratoire Hubert Curien, UMR 5516 CNRS, Université de Lyon, Université Jean Monnet, 42000 Saint Etienne, France
e-mail: razvan.stoian@univ-st-etienne.fr

M. Wollenhaupt and T. Baumert
Institut für Physik and CINSaT, Universität Kassel, 34132 Kassel, Germany
e-mail: wollenhaupt@physik.uni-kassel.de; baumert@physik.uni-kassel.de

I.V. Hertel
Max Born Institute for Nonlinear Optics and Short Pulse Spectroscopy, 12489 Berlin, Germany
and
Fachbereich Physik, Freie Universität Berlin, 14195 Berlin, Germany
e-mail: hertel@mbi-berlin.de

K. Sugioka et al. (eds.), *Laser Precision Microfabrication*,
Springer Series in Materials Science 135, DOI 10.1007/978-3-642-10523-4_5,
© Springer-Verlag Berlin Heidelberg 2010

However, new laser machining requirements are imposing higher standards for optimal processing, envisaging possibly reconfigurable technologies that are matter- and shape-adaptable in a self-improving manner. This goal may be achieved by smart manipulations of the laser beam in the spatio-temporal domain and by complex monitoring of the ablation products for optimizing irradiation parameters. Light modulation as a function of the materials reaction implies that a synergetic type of interaction occurs between radiation and material which offers the possibility to regulate and actively improve the energy delivery. Recent technologies allow flexible manipulation of laser pulse characteristics, including its temporal form, spatial distribution, spectral content, and polarization state. The energy delivery can be adaptively controlled to guide the material response towards a designed processing objective. Higher accuracy and novel material states may be obtained in this way that involves a radical change in the materials standard response. The tailored interaction has an engineering aspect, related to a precise definition of the excitation geometry, as well as a phenomenological one, associated with controlling laser-induced physical phenomena. With the focus on the latter, the present review summarizes several concepts of pulse manipulation, emphasizing ultrafast pulse tailoring in the temporal domain, and explores its potential in applications to material processing.

Primary processes induced by ultrafast laser radiation involve nonlinear electronic excitation, energy transfer to vibration modes, and phase transitions that occur on fast but material dependent time scales. Temporal laser control may thus facilitate synchronization between light and material response, thus leading to efficient coupling of laser energy. In addition, new insights become available concerning the physical effects of irradiation. However, due to the complexity of interaction, optimal exposure conditions require optimal search procedures which allow to explore complicated and often only moderately sensitive parameter topologies. Parameter landscapes can be built in this way to determine relevant processing protocols and to collect information on the control mechanisms. The capacity to predict best irradiation conditions is paramount to smart laser processing technologies that can accommodate dynamic material reactions, thus responding to a maximum of user demands.

After this introduction, Sect. 5.2 will review basic laser pulse properties together with practical concepts of pulse manipulation in the spectral Fourier domain. Specifically, the possibility to control pulse characteristics in a programmable way using present light-modulator devices will be discussed in Sect. 5.2.5. Optimization strategies will be indicated in Sect. 5.2.6. Section 5.3 will then present selected aspects of application of these techniques in material processing, starting in Sect. 5.3.1 with a discussion of the primary physical factors prone to play a fundamental role in controlling energy coupling and the time evolution of excited matter. Electronic excitation aspects as well as the possibility to drive specific thermodynamic trajectories in metals and semiconductors upon relaxation (Sect. 5.3.2) will be discussed. Insights will be given into the generation of electron–hole plasmas in band-gap materials or electronic heating in metals, emphasizing the consequences for the

subsequent transient states of matter, including the possibility to adaptively achieve specific thermodynamic and mechanical states. Advances in surface texturing will be indicated, pointing out the potential for nanoscale processing. The presentation will follow how the dynamic light regulation creates the premises to upgrade the degree of process control. Finally, Sect. 5.3.3 will consider practical implementation for processing bulk dielectrics.

5.2 Fundamental and Technical Aspects of Pulse Shaping

5.2.1 Basics of Ultrashort Laser Pulses

With very few exceptions, the generation of ultrashort pulses relies on the technique of mode locking and is described in detail in several textbooks devoted to ultrashort laser pulses [1–3]. An ultrashort laser pulse can be viewed as a Fourier-synthesized object with a large spectral bandwidth containing on the order of 10^6 longitudinal laser modes. In a Fourier-transformed pulse, all frequencies are locked. Manipulation of these frequencies in phase and amplitude constitutes the key tool for changing the temporal structure.

5.2.2 Frequency Domain Manipulation (Mathematical Formalism)

Assuming a linearly polarized light field, the temporal dependence of the real electric field $E(t)$ of an optical pulse may be written as a rapidly oscillating scalar quantity (with a time dependent overall phase $\Phi(t)$) which is multiplied by a real valued temporal envelope function $A(t)$:

$$E(t) = A(t)\cos[\Phi(t)] = A(t)\cos[\zeta(t) + \omega_0 t]\,.$$

Here, ω_0 is the carrier frequency and $\zeta(t)$ a temporal phase. Changes of the instantaneous frequency $\omega(t)$ are described by the derivative of the temporal phase $\zeta(t)$, i.e., $\Delta\omega(t) = \frac{\mathrm{d}}{\mathrm{d}t}\zeta(t)$. The real-valued electric field $E(t)$ of an ultrashort optical pulse at a fixed point in space and its equivalent in frequency space $\tilde{E}(\omega)$ (possibly complex-valued) are related by the Fourier transform which we write as [1, 3, 4]

$$\tilde{E}(\omega) = \int_{-\infty}^{\infty} E(t)\,\mathrm{e}^{-\mathrm{i}\omega t}\mathrm{d}t\,.$$

The knowledge of the spectrum for positive frequencies is sufficient for a full characterization, and in the following we consider $\tilde{E}^+(\omega) = \tilde{E}(\omega)$ for $\omega > 0$. Inverse Fourier transform of $\tilde{E}^+(\omega)$ delivers the analytic signal

$$E^+(t) = \frac{1}{2\pi} \int_0^\infty \tilde{E}^+(\omega)\, \mathrm{e}^{\mathrm{i}\omega t} \mathrm{d}\omega,$$

which is decomposed into the complex-valued pulse envelope $\mathcal{E}^+(t)$ and the carrier oscillation by $E^+(t) = \mathcal{E}^+(t)\, \mathrm{e}^{\mathrm{i}\omega_0 t}$. Fourier transform of the temporal envelope $\mathcal{E}^+(t)$ yields the spectrum of the envelope $\tilde{\mathcal{E}}^+(\omega) = \tilde{E}^+(\omega + \omega_0)$ and its power spectral density $I(\omega) \propto |\tilde{\mathcal{E}}^+(\omega)|^2$. This is displayed along with the temporal intensity $I(t) \propto |\mathcal{E}^+(t)|^2$ for various modulated pulses in Figs. 5.1–5.5.

In order to describe changes in the temporal pulse shape due to spectral manipulations, it is convenient to characterize the passage of an ultrashort pulse through a linear optical system by a complex optical transfer function [5]

$$\tilde{M}(\omega) = \tilde{R}(\omega)\, \mathrm{e}^{-\mathrm{i}\varphi(\omega)},$$

connecting the incident electric field envelope $\tilde{\mathcal{E}}^+_{\mathrm{in}}(\omega)$ with the modulated one:

$$\tilde{\mathcal{E}}^+_{\mathrm{mod}}(\omega) = \tilde{M}(\omega)\, \tilde{\mathcal{E}}^+_{\mathrm{in}}(\omega) = \tilde{R}(\omega)\, \mathrm{e}^{-\mathrm{i}\varphi(\omega)}\, \tilde{\mathcal{E}}^+_{\mathrm{in}}(\omega)\,.$$

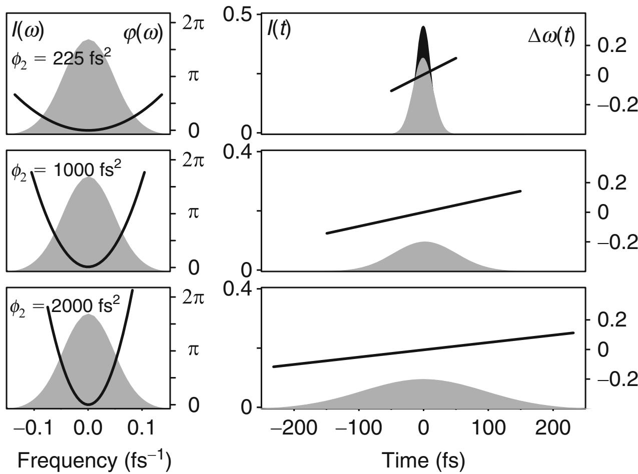

Fig. 5.1 *Left*: Quadratic spectral phase modulation with $\varphi(\omega) = \phi_2/2! \cdot \omega^2$ for increasing GDD ϕ_2 applied to the spectrum $I(\omega)$ of a Gaussian input pulse of $\Delta t = 25$ fs (the carrier frequency is subtracted). *Right*: temporal intensity envelope $I(t)$ of the modulated pulse and change of the instantaneous frequency $\Delta\omega(t)$. The GDD increases from 225 to 2,000 fs^2. For comparison, the unmodulated pulse (in the background) is depicted in the upper panel

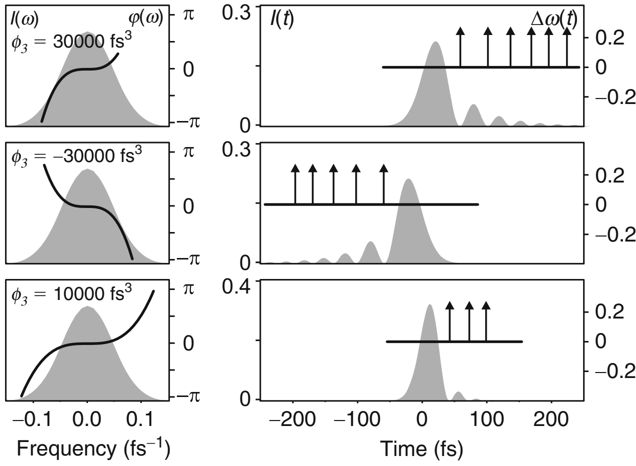

Fig. 5.2 TOD spectral phase functions $\varphi(\omega) = \phi_3/3! \cdot \omega^3$ (*left*) and temporal intensities (*right*) for positive and negative ϕ_3. The *arrows* indicate a change of sign in the temporal envelope, corresponding to a jump of the temporal phase by π

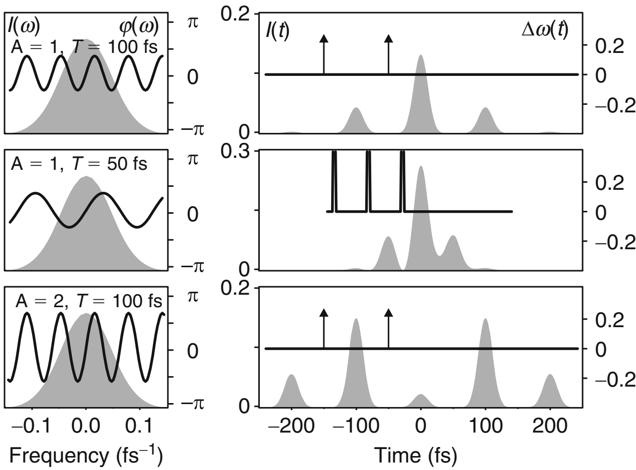

Fig. 5.3 *Upper panel*: sinusoidal spectral phase modulation with $A = 1$; $T = 100\,\text{fs}$, $\phi = 0$. *Middle*: lowering the modulation frequency to $T = 50\,\text{fs}$ merges the sub-pulses. Increasing the amplitude A results in a higher number of sub-pulses. The *arrows* indicate again a phase change by π

Here, $\tilde{R}(\omega)$ is the real valued spectral amplitude response and $\varphi(\omega)$ the so called spectral phase transfer function. This is the phase accumulated by the spectral component of the pulse at frequency ω upon propagation through the optical system.

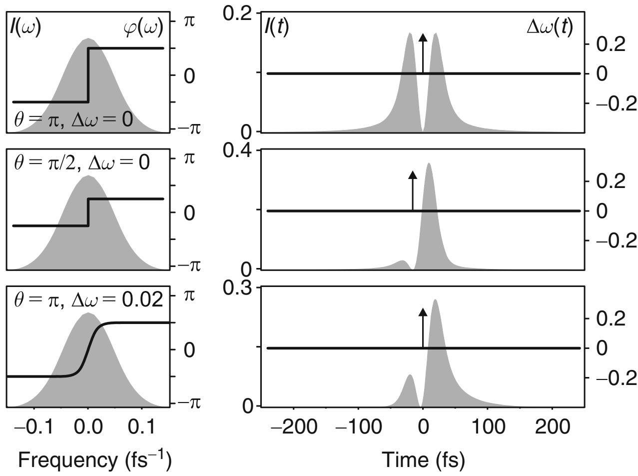

Fig. 5.4 Spectral phase function with a θ-step at the central frequency. *Upper panel*: $\theta = \pi$ leads to symmetric picosecond double pulses, *middle*: $\theta = \pi/2$ results in a weak pre-pulse and an intense post-pulse, lower trace: blurring the π-step reduces the pulse duration

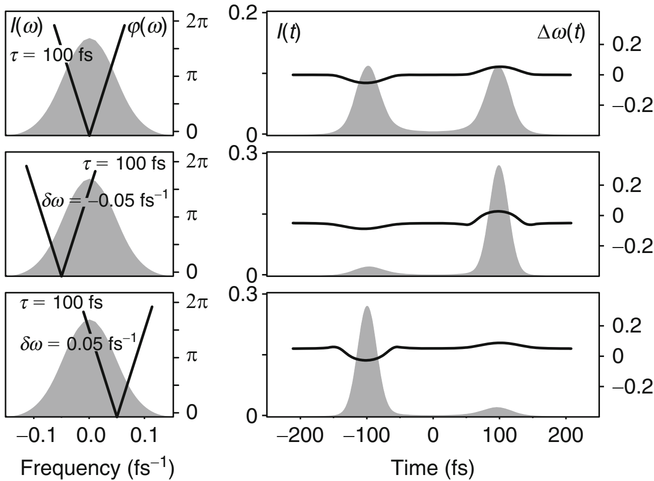

Fig. 5.5 An upright V-shaped spectral phase $\varphi(\omega) = \tau\,|\omega - \delta\omega|$ creates a sequence of a red-detuned pre-pulse and a blue-detuned post-pulse: each portion of the spectrum where the phase is linear corresponds to a longer pulse shifted by $\pm\tau$

Due to the properties of the Fourier transform, the multiplication in the frequency domain corresponds to a convolution in time domain:

$$\mathcal{E}^{+}_{\mathrm{mod}}(t) = \frac{1}{2\pi}\int_{-\infty}^{\infty} \tilde{M}(\omega)\,\tilde{\mathcal{E}}^{+}_{\mathrm{in}}(\omega)\,\mathrm{e}^{\mathrm{i}\omega t}\mathrm{d}\omega = \int_{-\infty}^{\infty} M(t-t')\,\mathcal{E}^{+}_{\mathrm{in}}(t')\,\mathrm{d}t'.$$

In the following, we will concentrate mainly on pure phase modulation and therefore set $\tilde{R}(\omega) = 1$ for all frequencies. For quantitative comparison of experimental results obtained by temporal modulated pulses with those obtained using unmodulated pulses, pure phase modulation guarantees that the sample is exposed to the same pulse energy and the same spectrum, the only difference being the temporal distribution of the laser radiation.

5.2.3 Analytical Phase Functions Relevant to Material Processing

5.2.3.1 Polynomial Phase Functions

A simple approach to understand the physical significance of a spectral phase function $\varphi(\omega)$ with respect to the temporal pulse shape is based on its Taylor expansion resulting in a sum of polynomial phase functions:

$$\varphi(\omega) = \phi_0 + \phi_1\omega + \frac{\phi_2}{2!}\omega^2 + \frac{\phi_3}{3!}\omega^3 + \dots . \tag{5.1}$$

The absolute phase, which relates the carrier oscillation to the envelope, is modulated if the first term ϕ_0 is non-zero. Although this type of modulation can be important for coherent control experiments [6], it does not influence the pulse envelope and is therefore not considered here. In accordance with the Fourier shift theorem, the linear term in the spectral modulation function $\phi_1\omega$ is responsible for a time shift of the pulse envelope of $t = \phi_1$.

Quadratic phase modulation, the so called Group Delay Dispersion GDD $= \phi_2$ with a spectral phase function $\varphi(\omega) = \phi_2/2! \cdot \omega^2$ plays a major role in many applications (see, e.g., [7]). GDD modifies the laser pulse duration and introduces a linear frequency sweep. Figure 5.1 shows the influence of GDD on a Gaussian input pulse. With increasing chirp parameter ϕ_2, the pulse duration increases while the pulse intensity decreases correspondingly.

Third Order Dispersion TOD $= \phi_3$ is given by a spectral phase function $\varphi(\omega) = \phi_3/3! \cdot \omega^3$ and results in asymmetric pulses described by a damped Airy function [3, 8]. Figure 5.2 shows examples for TOD spectral phase modulation for positive and negative values of the parameter ϕ_3, as well as a variation of the absolute value of ϕ_3. The pulse shape is characterized by an intense initial pulse followed or preceded by a pulse sequence with decaying amplitudes. At the zeros of the damped Airy function, the temporal phase jumps by π lead to the (immaterial) delta discontinuities in the instantaneous frequency. Applying the anti-symmetric phase function of TOD results in a constant instantaneous frequency. With respect to material processing, the remarkable features of TOD are (a) temporal symmetry-breaking of the envelope implying control on the time-dependent energy flux onto the sample and (b) the ability to produce a short intense pulse accompanied by a weak long pulse train.

5.2.3.2 Pulse Sequences

Pulse sequences are a common tool to study dynamical properties of light matter interactions and have also found applications to ultrafast material processing [9]. Using an interferometric setup is conceptually the simplest way to produce a sequence of pulses. However, practical considerations, such as the stability and alignment issues, but most importantly the unavoidable spectral modulations introduced by the interferometer, suggest alternative approaches based on pulse shaping techniques. We discuss here three different types of phase functions leading to pulse sequences [10].

Periodic spectral phase functions applied to modulate the spectrum of an ultrafast laser pulse deliver pulse sequences of controllable intensity, phase, and temporal separation. It has been shown [3, 10–15] that a sinusoidal spectral phase modulation $\varphi(\omega) = A\sin(\omega T + \phi)$ leads to a sequence of sub-pulses with a temporal separation T and controllable relative temporal phases determined by the absolute phase ϕ:

$$\mathcal{E}^{+}_{\mathrm{mod}}(t) = \sum_{n=-\infty}^{\infty} J_n(A)\,\mathcal{E}^{+}_{\mathrm{in}}(t - nT)\,\mathrm{e}^{-\mathrm{i}n\phi}.$$

The amplitude of the n-th sub-pulse is given by Bessel functions $J_n(A)$ of the first kind and order n and can be controlled by the modulation parameter A. Provided the individual sub-pulses are temporally separated, the envelope of each sub-pulse is a replica of the unmodulated pulse envelope (Fig. 5.3 upper and lower panel). The arrows between the sub-pulses indicate a change-of-sign in the pulse envelope. For smaller delay times T, the sub-pulses interfere to yield a more structured pulse shape (Fig. 5.3 middle panel).

Spectral phase jumps based on discontinuous functions of the type $\theta\,\mathrm{sgn}/2$ were realized [10] to produce a sequence of two pulses. Such pulses have, for example, been used to manipulate coherent atomic dynamics [6, 16, 17]. An example for a discontinuity of π at the central frequency in the spectral phase function is shown in the upper panel of Fig. 5.4. This so-called π-step results in two pulses with larger duration and delayed with respect to each other. A slight generalization of this spectral phase is introduced by the variation of the step-height. A phase jump of $\pi/2$ breaks the temporal symmetry and is associated with a weak pre-pulse and an intense post-pulse (middle panel of Fig. 5.4). Due to this structure, generalized jumps might be suitable candidates for materials processing similar to TOD. Blurring the phase discontinuity is an alternative approach to deliver asymmetric pulses. In addition, blurred phase functions deliver much shorter pulses (reduced tails) – a property which is required to manipulate ultrafast dynamics on the sub-picosecond (ps) level. Cycling the phase jump can also generate multiple pulses of variable spacing [18], however, with considerable spatio-temporal distortions [19, 20].

V-shaped function impose linear phase relations on chosen spectral domains [21]. The phase function $\varphi(\omega) = \tau\,|\omega - \delta\omega|$ shown in Fig. 5.5 can generate a sequence of two pulses separated by 2τ. This type of modulation can be understood in terms of the shifting property of linear phase functions. In the upper panel of

Fig. 5.5, half the spectrum is shifted by $t = -\tau$ whereas the other half of the spectrum is moved to $t = +\tau$. This procedure results in two detuned coloured pulses with longer durations. The relative intensity ratio is determined by the cusp position. By mirroring the spectral phase function with respect to the central frequency, the temporal envelope is reversed and the temporal phase is conjugated.

5.2.3.3 Linear Combinations of the Above Phase Masks

If a sum of multiple spectral phase functions $\varphi_i(\omega)$ is applied, the combined action of the linear combination can be decomposed into subsequent execution of the corresponding individual phase functions:

$$\tilde{M}(\omega) = \mathrm{e}^{-\mathrm{i}[\varphi_1(\omega)+\varphi_2(\omega)]} = \mathrm{e}^{-\mathrm{i}\varphi_1(\omega)}\mathrm{e}^{-\mathrm{i}\varphi 2(\omega)} = \tilde{M}_1(\omega)\,\tilde{M}_2(\omega)$$

For example, combining sinusoidal phase modulation with quadratic phase function yields a sequence of chirped pulses [22]. Double pulses can also be implemented with the help of amplitude modulation [23, 24]. The spectral transfer function reduces to a real valued spectral amplitude response [23]. In general, the outcome of combinations of spectral phase functions on the temporal pulse shape is not always easy to predict due to interference effects among the subsequent modulations.

5.2.3.4 Iterative Fourier Approaches for Designing Pulse Shapes

In the situation that required pulse shapes are not readily accessible by the above methods, an accurate solution can only be based on a combined phase and amplitude modulation procedure. However, if a phase-only result is preferred, techniques have emerged were approximate solutions to the desired shape can be found. Based on phase modulation, they use iterative transformations between the temporal and the spectral domains in the presence of constraints related to the incident pulse spectrum and the desired shape. An intuitive description of the Gerchberg–Saxton technique is given in [25, 26].

5.2.3.5 Polarization-Shaped Pulses in the Temporal Domain

Since light is a transverse electromagnetic wave, it can be linearly, circularly, or in general elliptically polarized. The same holds of course for an ultrashort optical pulse. Pulse shaping allows for the creation of light pulses where at each instant of time a different state of polarization can be realized [27, 28]. So far these possibilities have not been exploited in material processing, but might open up interesting perspectives for future use. Specifically, this may involve controlling nanoscale phenomena, near-field and plasmon coupling, with extended possibilities for novel processing techniques.

5.2.4 Pulse Shaping in the Spatial Domain

Tailoring of spatial intensities has also acquired a significant attention, and consequences are obvious in material processing, microscopy, imaging, and nonlinear optics. The application field will only be briefly reminded, with implications in control of wavefront distortions and corrective approaches for beam delivery, point-spread-function engineering, and design of excitation geometries, as well as concepts for beam partition for parallel processing.

5.2.5 Experimental Implementations for Temporal Pulse Shaping

In practice, the creation of complex shaped laser pulses with respect to phase, amplitude, and polarization relies on programmable pulse shaping techniques [3, 5, 18] to generate the optical transfer function $\tilde{M}(\omega)$. One way to realize a pulse modulation unit is the Fourier transform pulse shaper. Its operation principle is based on optical Fourier transformation between time and frequency domains. In Fig. 5.6a, a standard design of such a Fourier synthesis pulse shaper is sketched. The incoming ultrashort laser pulse is spectrally dispersed, and the frequency components are back collimated by a focusing optical element with a focal distance f. By this means, the spectral components can be modulated individually by placing a linear mask into the Fourier plane. The laser pulse is reconstructed by performing an inverse Fourier transformation back into the time domain [29].

A popular linear mask for computer controlled pulse shaping in such setups is the liquid crystal spatial light modulator (LC-SLM). The relative retardation of spatially dispersed frequencies can be conveniently manipulated by placing a pixelated liquid crystal array in the Fourier plane and applying voltages at the separate pixels leading to changes of the refractive index. By virtue of the Fourier transform properties, spectral phase changes result in modulated pulse temporal profiles as

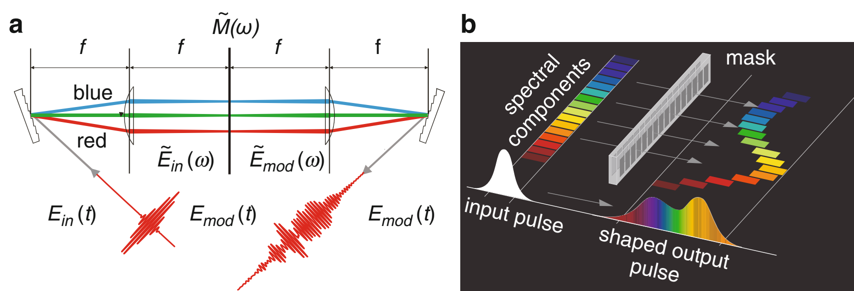

Fig. 5.6 (**a**) Basic layout for Fourier transform femtosecond pulse shaping. (**b**) Schematic illustration of shaping the temporal profile of an ultrashort laser pulse by retardation of the spectrally dispersed individual wavelength components in a phase only Liquid crystal spatial light modulator (LC-SLM). The LC-SLM is located in the Fourier plane

depicted schematically in Fig. 5.6b. Exploiting the LC orientation with respect to the polarization, amplitude modulation may be obtained as well based on the induced birefringence [18, 30].

Another possibility to realize phase only pulse shaping is based on deformable mirrors (DM) [31] placed in the Fourier plane. They usually consist of a small number of control degrees of freedom. The use of a micro mirror array with 240×200 pixels in reflection and a waveform update rate larger than 1 kHz was also demonstrated [32].

Acousto optic modulators (AOMs) can be used for programmable pulse shaping within $4f$ setups in various spectral domains [33–35]. The AOM crystal oriented at Bragg angle is placed in the Fourier plane of a zero dispersion compressor. A programmable radio frequency (RF) signal driving the piezoelectric transducer of the AOM creates an acoustic wave that propagates through the crystal. The photoelastic effect induces a modulated grating where the amplitude and phase of the acoustic wave determine the diffraction efficiency and phase shift at each point in space. Another AOM approach is based on an acousto-optic programmable dispersive filter (AOPDF) which does not need insertion in the Fourier plane of a $4f$ device [36, 37] but relies instead on the time convolution. Again, a programmable RF signal creates an acoustic wave that propagates in the crystal and reproduces spatially the temporal shape of the RF signal. Two optical modes can be coupled by acousto-optic interaction only in the case of phase matching. If there is locally a unique spatial frequency in the acoustic grating, then only one optical frequency can be diffracted at that position from the fast ordinary axis to the slow extraordinary axis. Various groups of optical frequency components travel a different distance before they encounter phase matched spatial frequencies in the acoustic grating where the energy is diffracted from one axis to the other. The modulated pulse will be made of all spectral components that have been diffracted at the various positions, with amplitudes controlled by the acoustic power and retardation given by the velocity difference.

In general, pulse shapers based on LC-SLMs or on DMs have low transmission losses, do not impose additional chirp, and have a low waveform update rate on the order of 10 Hz. Setups based on AOMs have high transmission losses, they do impose additional chirp, but they have a waveform update rate in the order of 100 kHz. Both AOMs and LC-SLMs can impress in the order of 1,000 independent features onto the spectrum and are suitable for amplitude and phase modulation. Programmable polarization shaping has been demonstrated so far only with LC-SLMs.

The pulse shaping techniques described up to now allow control of the temporal profile of an output waveform in phase, amplitude, and polarization. This can be thought of as control over one spatial dimension, the direction of propagation, and the "temporal-only" pulse shaping is thus one dimensional. Automated two dimensional phase-only pulse shaping employing an optically addressed reflective two-dimensional SLM with negligible interpixel gaps allows real-space pulse shaping in which a sample or device is irradiated with different temporally shaped waveforms at different locations [38]. The pulse shaping arrangement in [38] is

similar to conventional $4f$ spectral filtering arrangements, with the difference that the incoming beam is expanded in one dimension and the SLM is employed in reflection geometry.

5.2.6 Optimization Strategies

Combining pulse shaping techniques with feedback learning loops (closed-loop approach) to optimize light-induced processes, a new class of experiments emerged [39–42]. As indicated in Fig. 5.7, the pulse control unit is connected to an experimental device quantifying the laser action. Then, a given pulse shape is evaluated in order to produce an improved pulse form which enhances the feedback signal. The experimental output requires real-time monitoring techniques for in-situ process control. The loops are usually driven by deterministic or non-deterministic optimization algorithms, or specific pulse shapes are designed using intuitive phase masks or predictive phase-retrieval approaches (e.g., Gerchberg–Saxton). These techniques have an impact on an increasing number of developments in physics, chemistry, biology, and engineering due to the fact that primary light-induced processes can be studied and actively controlled via adaptive femtosecond (fs) pulse shaping.

Often evolutionary algorithms [43] are applied, ranging from simple implementations used, for example, in initial automated pulse compression experiments [40] to sophisticated Covariance Matrix adaption techniques [44]. Usually, a set of arbitrary phase patterns is initially applied on the optical modulator which evolves through genetic propagators towards an optimal solution. In [44], a theoretical survey of modern evolutionary approaches to the problem of molecular alignment has been performed, concluding that it pays off to use more elaborate optimization schemes

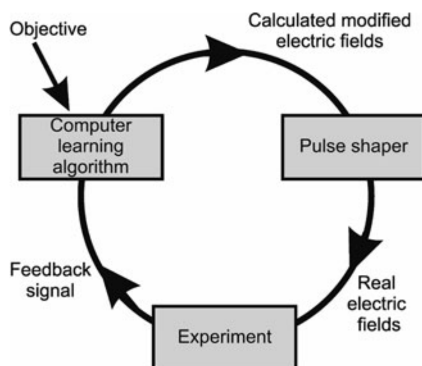

Fig. 5.7 Schematic presentation of adaptive fs pulse shaping: Generated specific electric fields via a pulse shaper are tested in an experiment. A learning algorithm calculates modified electric fields based on the information from the experimental feedback signal and the user defined control objective. Cycling the loop results in iteratively optimized laser pulse shapes that finally approach the objective(s)

for such a high-dimensional optimization problem. It was also demonstrated that a covariance matrix adaptation evolutionary strategy (CMA-ES) performs better than a traditional evolutionary strategy for high-dimensional search landscapes [45].

If the optimization of a light-induced process is based on some physical insight, then it is often useful to use analytical phase functions (see Sec. 5.2.2) and optimize the parameters, either systematically or via evolutionary approaches. Open loops may be followed by *post mortem* analysis. An intuitive solution landscape may be built, allowing to extract useful physical information about the processes in question.

5.3 Material Interaction with Temporally Shaped Pulses

Upon the impact of an ultrashort laser pulse on a solid material [46, 47], electromagnetic energy is first converted into electronic excitation and then, by specific electron–lattice interactions, transformed into thermal, chemical, and mechanical forms. During the whole process, the molecular structure and the macroscopic properties of the material are changed in various ways, culminating with permanent alterations, optical damage, and ablation. All these processes occur on various timescales accompanied by variations of the optical properties. This suggests that the light packets interacting with the material on these timescales may accommodate the changes and create specific synergies between light and material. Optimality is then defined as the ability to achieve a user defined evolution. This section reviews possible control mechanisms of laser-induced excitation and discusses their relevant timescales.

5.3.1 Control of Laser-Induced Primary Excitation Events

Laser interaction with wide band-gap materials leads to the development of an electron–hole plasma. Depending on intensity, multiphoton processes (MPI) or tunneling ionization (TI) [48] is followed by inverse bremsstrahlung and, subsequently, by seeded collisional carrier multiplication (or avalanche ionization AI) [49–51]. The transient free carrier density plays a fundamental role in determining the optical properties, in addition to various propagation and relaxation mechanisms. Optical damage thresholds were used as experimental evidence for exceeding a certain critical electron density after the laser interaction and the regulatory effect of pulse duration was investigated [49, 52, 53]. Studies of transient electron densities range from intensities below [54, 55] up to well above the breakdown threshold [56, 57]. The temporal evolution of the free-electron population and the role of the fundamental ionization processes are strongly depending on timely energy feedthrough, as well as on the instantaneous frequency [50, 58–60].

The excitation acquired in the two sequential steps, photoionization and free carrier absorption, offers the possibility of regulating the amount of energy coupled to the material and the outcome in terms of possible transformation paths. The absorption efficiency is controlled via the photoionization cross-section and by the timescale of electronic collisions, thus a competition between direct and collisional processes becomes possible. Each of these factors may be tuned via peak intensity, polarization state, and temporal envelope of the pulse. The direct photoionization rate in both MPI and TI regimes is mainly determined by the pulse intensity and depends on the direction of the electric field [55]. For longer temporal envelopes, a highly efficient free electron heating process develops, resulting in enhanced rates of electronic multiplication. Additionally, the electronic density may suffer fast relaxation phenomena due to, for example, carrier trapping in self-induced deformation potentials [54]. The resulting electronic density has consequences on the onset of catastrophic optical damage in band-gap dielectrics or on the structural mechanical stability. This suggests that the pulse temporal form can develop into a dominant control knob to manipulate primary excitation events and to channel possible relaxation paths in wide band-gap materials.

A situation where reduced exfoliation is displayed by structures induced in CaF_2 irradiated by modulated pulses [61] is presented in Fig. 5.8 (also see Chap. 1). The improvements can be related to a transient change in the material properties as a consequence of swift excitation and charge trapping. The sequential energy delivery induces a preparation of the surface (i.e., defined electron density and lattice deformations) and an associated material softening during the initial steps of excitation, thus changing the energy coupling for the subsequent steps. This leads to lower stress and improved structures. Especially for brittle materials with strong electron–phonon coupling, carrier trapping, lattice deformations, and associated softening can be advantageous since they provide the means for relaxation of the induced stress, with a reduction of cracking and fracture phenomena. Similar behavior was also noticed during burst micromachining using multipeak sequences on MHz scales [62].

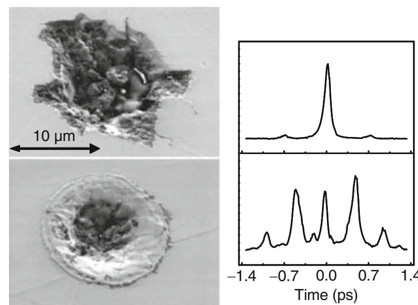

Fig. 5.8 Laser-induced structures on CaF_2 surfaces with single ultrashort pulse of 90 fs (*upper part*) and triple-pulse sequences (*bottom part*) with 0.5 ps separation. The results show improvements for the structures generated by temporally modulated excitation. The number of pulses used to form the structures was $N = 5$ and the laser fluence was 7 J/cm^2, respectively 12 J/cm^2 [61]

At the same time, manipulation of pulse frequencies indicated sensible variations in the damage threshold [59]. Multiple pulse sequences were used to influence the occurrence of optical damage, the profile, and the size of the induced structures in various dielectrics (a-SiO_2, Al_2O_3) [9, 61, 63], leading to changes in the ablation morphology. For fused silica, the temporal control on the spatial crater profile is facilitated by the synchronization with the electron trapping dynamics. The spatio-temporal coupling provided by the material nonlinearities opens the possibility to design spatial excitation features which map in space the temporal modulation of the laser pulse.

Cubic chirped pulses (with asymmetric intensity envelopes) have shown surprising reduction in the damaged area, below the diffraction limit [64, 65]. The balance between photoionization and collisional ionization mediates the localized formation of a hot electron population, taking into account the different process dependencies on intensity. This results in different thresholds for material modification in fused silica and reproducible nanoscale surface structures as documented in Fig. 5.9a. As theoretical simulations based on a multiple rate equation (MRE) model [58] show, the timing of an intense photoionizing sub-pulse can turn on or off AI as illustrated in Fig. 5.9b. Different final electron densities can be achieved depending on the temporal profile since the ionization processes may be addressed in a different fashion. The proposed scenario [64] involves the interplay of MPI creating free electrons in a spatially confined region followed by AI. This further restricts the area of reaching the critical electron density that may eventually lead to the nanoscale structures seen for positive and negative TOD pulses with characteristic sizes well below the diffraction limit (Fig. 5.9c). This strategy opens the route to develop tailored pulse shapes for controlled nanoscale material processing of dielectrics. Note that smaller structures have been reported at the backside surface of dielectric samples by using high numerical aperture immersion objectives [66].

To the other end, in metals as well, the efficiency of laser absorption depends on the electronic collision frequency, which, in the solid phase, is a sensitive function of temperature [67]. The dynamics of the electron temperature may thus influence the rate at which laser photons are absorbed. Apart from the regulating factor of electronic collisions via temperature at nonequilibrium electron–ion conditions, the resulting transient optical properties, heat transport, and energy conversion factors may also intervene. The subsequent thermodynamic behaviour can be mastered using controlled energy feedthrough, which is a prerequisite for tailoring the laser ablation outcome, structure, and plume kinetics. An overview of possible control paths for nontransparent materials is given in the following section.

5.3.2 Engineered Thermodynamic Phase-Space Trajectories

Subsequent to primary excitation, the electronic energy is relaxed to the material matrix via electronic to vibrational coupling which locally heats the material, via bond softening caused by electronic perturbations, or is released by a

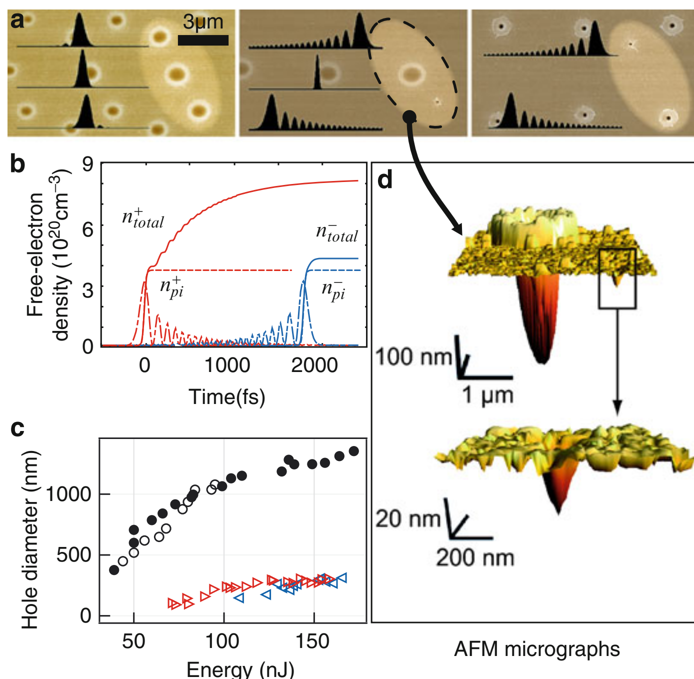

Fig. 5.9 (**a**) SEM images of laser-induced structures in fused silica. For a specific energy and focusing conditions (NA = 0.5, 35 fs), a triplet of applied laser pulses (negative, zero and positive TOD) is highlighted by the ellipse. Normalized temporal intensity profiles are sketched for comparison between different TODs. *Left*: low TOD results in negligible differences between created structures. *Middle*: high positive TOD results in a change of structure size and threshold energy. *Right*: the threshold energy for ablation with high negative TOD is reached at $E = 110$ nJ. (**b**) Transient free-electron density $n^{\pm}_{\text{total}}$ (*solid lines*) as calculated with the help of the MRE model, together with the density of electrons provided by photoionization $n^{\pm}_{\text{pi}}$ (*dashed lines*) and the corresponding transient intensities (*dashed-dotted lines*) of the pulse with positive TOD (index +) and negative TOD (index −), respectively. (**c**) Diameters of ablation structures as a function of pulse energy for unshaped pulses (different circles indicate two independent measurements), for (+) shaped pulses (*triangles pointing right*) and for (−) shaped pulses (*triangles pointing left*). Structures below 300 nm are obtained over a considerable energy range thus providing a large process window for the creation of nanostructures. The smallest structures are about 100 nm in diameter. (**d**) Blow-up of laser-induced structures; atomic force microscope micrographs

pressure-induced mechanical activity. The possibility to temporally design pulses enhances the flexibility to manipulate transformation pathways using nonlinear and non-thermally initiated phase transitions, and minimally-diffusive energy input. A high degree of electronic excitation in solid materials triggers lattice instabilities and, consequently, mixed electronic, mechanical and thermal alterations of the material structure. These structural transformations occur on fast scales, and a certain control on their competition may be established. This may potentially lead to the creation of metastable states around critical points or transitions to energy states

hardly attainable by other means. These effects are important for surface treatment and patterning or in applications related to optical switching [68].

For semiconductor samples, improvements were seen in the structuring quality by using multipulse sequences [69–71]. Synchronizing the laser temporal irradiation profile with the solid-to-liquid phase transition time and the associated augmentation in the absorption efficiency, conditions can be found to evaporate the resultant liquid layer, avoiding its gradual cooling and return to the surface as recast. Additionally, the energy delivery can control the resulting self-organization of nanotexturing in the irradiated zone [72].

Enhancement and kinetic tunability of ions were observed during temporally tailored laser irradiation of silicon. The approach has illustrated a versatile possibility to optimize the kinetic properties of the Si^+ ions by controlling the development of the electron–hole plasma on sub-ps scales [73] or by taking advantage of a fast succession of structural transitions on ps scales [74]. The latter results is shown in Fig. 5.10. The optimal irradiation sequence was obtained using a mass-resolved ion-detection optimization loop guided by an adaptive strategy and is represented by a fast peak followed by a ps tail of energy distribution. The ion acceleration mechanism was connected to an improved energy coupling related to the formation of a highly absorptive transient liquid state right at the beginning of the irradiations sequence. Most of the energy is then coupled to the absorptive state and determines significant temperatures. Highly energetic and volatile thermodynamic states are thus produced with minimal energy expenses [74].

If for the low band-gap material presented above the main factor of improving energy deposition is related to a fast change to an absorptive state, other materials show no significant differences in the dielectric function between the solid and the liquid phase at the photon energy of 1.5 eV and, therefore, no specific absorption enhancement apart from the regular temperature-induced collisional effects. This is the case of metallic aluminum. The relevant question is then related to the factors that may improve the energy coupling in this case. Commonly for metals, electronic excitation determines a high temperature and pressure phase so that the evolution control factors involve hydrodynamic advance. This has consequences on the transient optical properties and, equally important, on the heat transport characteristics. Feedback-based ion emission was used as a probe of the efficiency of energy deposition into the material. An ion acceleration effect was observed, similar to the Si case, and explained by a laser pulse regulated balance between the

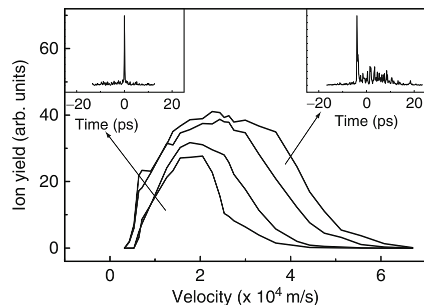

Fig. 5.10 Velocity distributions of energetically tunable Si^+ ion beams generated by laser ablation of silicon with ultrashort and adaptively generated optimal temporal pulse shapes. Irradiation conditions: initial pulse duration 170 fs, input fluence 0.8 J/cm^2 [74]

mechanical and thermal energy of the ablation products. If ultrafast radiation favours the accumulation of mechanical energy due to fast pressure release [75], the optimal ps tailored envelope determines a preferential heating of the ablation products which induces variations in the ionization degree, while still keeping the losses by heat conduction at a minimal level. This indicates to possibility of regulating thermal effects and designing thermodynamic trajectories and has consequences for the processing accuracy and composition of ablation products, or for other quality criteria, such ablation efficiency, smoothness, or aspect ratios. On the other hand, it constitutes a description of thermal manipulation for interactions commonly considered as athermal. It has to be noted that phonon control via pulse shaping has gathered attention for regulating heat transport in laser irradiated materials [76].

In parallel to ion acceleration, a strong decrease in nanoparticle emission was observed from metallic targets irradiated with temporally shaped laser radiation. The effect, simulated by hydrodynamic codes, is illustrated in Fig. 5.11 for Al exposed to ultrashort and to the previously determined optimal pulse. Ultrafast irradiation is associated with an initial isochoric increase of pressure due to electronic excitation. The pressure release determines a fast expansion into the two-phase region and ejection of nanodroplets from the liquid phase as visible in Fig. 5.11a. This is related to the trapping of expanding layers at the liquid-gas border undergoing further expansion under gas confinement, alongside with a recondensation mechanism. The tailored pulse favours instead the heating of the expanding material, reducing the trapping time of the confined liquid layers and determines a dominant transition to a gaseous phase (Fig. 5.11b) with low particulate content [75, 77]. This aspect has consequences for the rate and the dimensions of the produced nanoparticles. The validity of the adapted approach was extended for other materials for generating nanoparticles of controllable sizes [72]. The sequential energy transformation into mechanical and thermal forms builds the premises for particular phase transformations. Despite the reduced sensitivity for intensity effects in linear materials, the overall absorption efficiency can be elevated if the proper conditions for density and temperature are met for the expanding layers, with implications, as discussed before, for the ablation yield. Changing the composition of ablation products is a

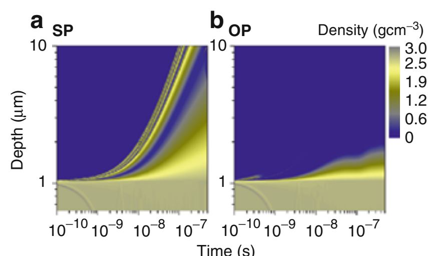

Fig. 5.11 Transient density phases and material ejection under laser excitation for (**a**) short and (**b**) optimal pulses. The onset of liquid nanolayers is observable for ultrashort pulses. The liquid layers expand under confinement between gas layers. Optimal pulses generate a preferential transition to the gas phase [77]

prime objective in the field of ultrafast laser-induced breakdown spectroscopy, that combines spatial resolution with spectrochemical sensitivity [78] as well as in techniques of material transfer [79].

5.3.3 Refractive Index Engineering by Temporally Tailored Pulses

In that concerns bulk transparent materials, the ability to locally design the dielectric function is based on the potential balance of electronic and structural transformations associated with the refractive index change (see, e.g., [80]). Chapter 9 reviews the interplay of several modification factors, including generation of defects, altering the local structure, or accumulating stress. Their relative importance can assist in engineering particular index changes in the conditions where the transformation sequence is jointly determined by the material response and the spatio-temporal character of excitation [81].

Current photoinscription techniques (for a brief review see [47, 80, 82–86] and the references therein) aim at producing positive refractive index in optical glasses, for example, for waveguiding applications. However, the material response to optical excitation is given by the relaxation properties of the glass. The irradiation outcome determines a complex dielectric design and electronic and structural alterations associated with either increasing or decreasing the refractive index under light exposure. In many glassy materials, the standard ultrafast radiation induces merely a decrease of the refractive index, detrimental for waveguiding. Speculatively, this is related to a strong volumetric expansion and subsequent rarefaction. Guiding regions may be restricted to stressed region around the excitation area. The possibility to reverse the natural tendency to rarefaction towards compaction carries then fundamental and technological significance. The follow-up idea is to design a type of irradiation able to overturn the unsatisfactory standard material response, with the purpose of, for example, producing positive refractive index changes in materials where the regular response is rarefaction. The temporal beam modulation techniques and subsequent control on energy delivery are natural candidates for this task due to their influence on the physical behaviour of the interaction process.

The temporal shaping approach integrated in a phase-contrast microscopy loop indicated the possibility to flip the refractive index in borosilicate crown BK7 [87] from the standard negative change to a significant region of index increase (Fig. 5.12a, b). This particular glass, used here as a model material with high expansion coefficient and low softening point, usually shows a decrease of the refractive index under standard tightly-focused ultrafast laser excitation. This behaviour is associated with the formation of a hot region, where, due to rapid thermal expansion, the material is quenched in a low-density phase, rich in oxygen centres. The control mechanism is related to the design of the resultant heat source which influence the subsequent stress-induced plasticity driving axial compaction. The optimal ps sequence allows higher energy concentration and the achievement of an elevated temperature due to a less efficient plasma generation and light defo-

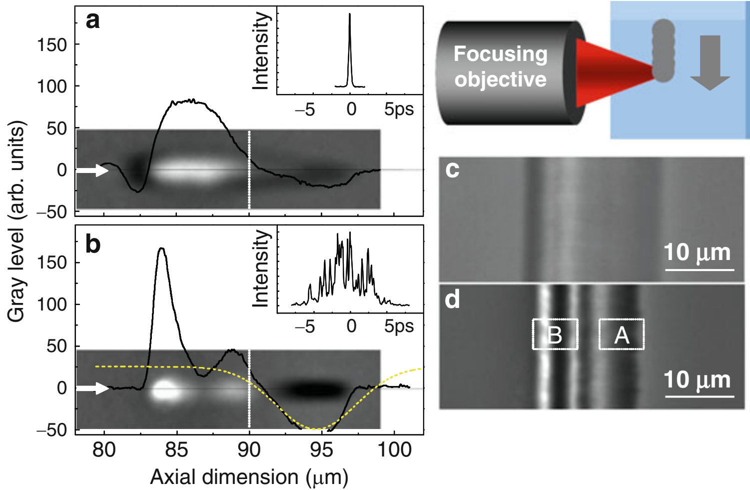

Fig. 5.12 Refractive index flip in borosilicate crown BK7 under multipulse (**a**) short (150 fs) and (**b**) optimally tailored irradiation (4.5 ps). Pulse energy 0.17 μJ, irradiation dose 10^5 pulses at 100 kHz. Phase contrast microscopy images of refractive index changes (*white* and *black* colours represent negative and positive refractive index changes, respectively). The onset of a significant compression zone is visible under optimal conditions. Transverse trace written by (**c**) short pulses and (**d**) optimal laser pulses at a scan velocity of 50 μm/s and pulse energy of 1.1 μJ. Two regions of positive refractive index changes are indicated by the labels A and B

cusing. This leads to plastic deformations accompanied by partial healing of the lateral stress due to preferential heat flow. As a result, a transition from a radial expansion regime to directional compaction was observed. The matter momentum relaxation conducts to axial densification and to a positive refractive index change. The adaptive technique was then able to determine an excitation sequence which induces a thermo-mechanical path leading to compaction. This is particularly interesting for laser repetition rates on the timescale of mechanical relaxation (100 kHz) and shows the importance of the heating and relaxation rates for defining proper processing windows. The influence one can exercise on the refractive index distributions indicates the possibility to create waveguide structures (see the development in Figs. 5.12c, d) and symmetric guiding conditions in materials that do not easily allow it in standard ultrafast irradiation conditions.

Adaptive control of pulse temporal forms was recently used to regulate filamentary propagation in nonlinear environments [89, 90]. The location and the spectral properties of the ionization region were shown to be modulative. The key factor is the intensity feedthrough which determines the competition between self-focusing and ionization. Breakdown probability was equally observed to be controllable via temporal envelopes [91]. All these observations indicate flexibility in manipulating propagation, ionization, and energy gain events generated by ultrashort laser pulses in nonlinear environments using judicious intensity adjustments. The nonlinear control has consequently proven its capability to induce energy confinement

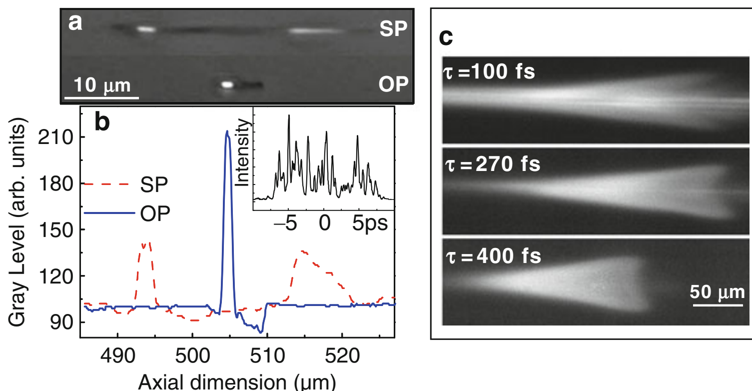

Fig. 5.13 (**a**) Short pulse (SP) and optimal pulse (OP) induced structures at a depth of 500 μm and 1 μJ input energy indicating the spatial confinement of the OP structure in the presence of aberrations. (**b**) The corresponding axial cross-sections. The inset shows the optimal pulse shape [87]. (**c**) Control of spatial distribution of excitation using the pulse duration [88]. Plasma emission images recorded in waveguide writing conditions in phosphate glass using different laser pulse durations and a slit shaping technique. Beam filamentation and prefocal energy depletion are minimized for circular polarization and increasing pulse durations

even in the presence of wavefront distortions [92]. When aberrations occur, the length of the laser-induced structure augments, which is detrimental to the photoinscription precision. The focal elongation influences the nonlinear energy deposition, and modulation of the refractive index appears in the exposed region. If usually spatial corrections are applied to correct wavefront distortions, it was indicated that the energy can as well be confined using adaptive temporal pulse shaping, delivering in addition desired changes of the refractive index (Fig. 5.13a, b). The decreased nonlinearity and the lower ionization efficiency of the optimal pulse assist the energy confinement, regulating the structuring precision in the presence of wavefront distortions [92]. Furthermore, control of pulse duration was recently implemented [88] in photoinscription techniques complementary to spatial beam modulation [83, 84, 86, 88, 93] resulting in a uniform irradiation region (Fig. 5.13c) suitable for waveguide writing in phosphate glasses.

5.4 Conclusion and Perspectives

The present review has illustrated that control of laser-induced effects in processing materials is possible, and energy coupling can be optimized. The outcome is an improved laser structuring approach with additional flexibility, accuracy and a higher degree of process control. This has relevance for upgrading current laser processing technologies and offers a better understanding of the laser-induced physical processes, the nature of material modification, including the ability to identify

competitive relaxation processes. The control factors were identified in the absorption phase, in the degree of non-equilibrium or nonlinearity of propagation, and in the succession of phase transitions. Consequently, using temporal pulse forming, control may be achieved on the chemical composition and the kinetic properties of the ablation products, as well as on the structural changes of the irradiated material and energy confinement on smallest spatial scales. The potential spectrum of applications ranges from quality structuring for increased functionality to integration in analytical methods sensitive to particle emission; however, designing material removal characteristics can be appealing for a broader range of applications. The results have also documented the possibility to attain desired structural modifications in bulk transparent materials. Using these tools, it was, for example, possible to achieve refractive index changes in glasses which are otherwise difficult to process. Novel properties and functions are attached in this way to the material, laying a groundwork for adaptive optimization in material processing.

References

1. J.C. Diels, W. Rudolph, *Ultrashort Laser Pulse Phenomenon: Fundamentals,Techniques, and Applications on a Femtosecond Time Scale*, 2nd edn. (Academic, London, 2006)
2. C.E. Rullière, *Femtosecond Laser Pulses. Principles and Experiments* (Springer, Berlin, 2004)
3. M. Wollenhaupt, A. Assion, T. Baumert, in *Springer Handbook of Lasers and Optics*, ed. by F. Träger (Springer Science + Business Media, New York, 2007)
4. I.V. Hertel, C.P. Schulz, *Atome, Moleküle und Optische Physik*, vol. 1 (Springer, Berlin, 2008)
5. A.M. Weiner, Prog. Quantum Electron. **19**, 161 (1995)
6. A. Präkelt, M. Wollenhaupt, C. Sarpe-Tudoran, T. Baumert, Phys. Rev. A **70**, 063407 (2004)
7. M. Wollenhaupt, A. Präkelt, C. Sarpe-Tudoran, D. Liese, T. Baumert, Appl. Phys. B Laser Opt. **82**, 183 (2006)
8. J.D. McMullen, J. Opt. Soc. Am. **67**, 1575 (1977)
9. R. Stoian, M. Boyle, A. Thoss, A. Rosenfeld, G. Korn, I.V. Hertel, Appl. Phys. A: Mat. Sci. Process. **77**, 265 (2003)
10. M. Renard, R. Chaux, B. Lavorel, O. Faucher, Opt. Exp. **12**, 473 (2004)
11. A.M. Weiner, D.E. Leaird, G.P. Wiederrecht, K.A. Nelson, Science **247**, 1317 (1990)
12. D. Meshulach, Y. Silberberg, Nature **396**, 239 (1998)
13. R.M. Koehl, K.A. Nelson, Chem. Phys. **267**, 151 (2001)
14. J.L. Herek, W. Wohlleben, R. Cogdell, D. Zeidler, M. Motzkus, Nature **417**, 533 (2002)
15. M. Wollenhaupt, A. Präkelt, C. Sarpe-Tudoran, D. Liese, T. Bayer, T. Baumert, Phys. Rev. A **73**, 063409 (2006)
16. D. Meshulach, Y. Silberberg, Phys. Rev. A **60**, 1287 (1999)
17. P. Panek, A. Becker, Phys. Rev. A **74**, 023408 (2006)
18. A.M. Weiner, Rev. Sci. Instrum. **71**, 1929 (2000)
19. M.M. Wefers, K.A. Nelson, J. Opt. Soc. Am. B **12**, 1343 (1995)
20. T. Tanabe, F. Kannari, F. Korte, J. Koch, B. Chichkov, Appl. Opt. **44**, 1092 (2005)
21. G. Vogt, P. Nuernberger, R. Selle, F. Dimler, T. Brixner, G. Gerber, Phys. Rev. A **74**, 033413 (2006)
22. T. Bayer, M. Wollenhaupt, T. Baumert, J. Phys. B At. Mol. Phys. **41**, 074007 (2008)
23. A. Galler, T. Feurer, Appl. Phys. B Laser Opt. **90**, 427 (2008)
24. B. von Vacano, T. Buckup, M. Motzkus, J. Opt. Soc. Am. B **24**, 1091 (2007)
25. M. Hacker, G. Stobrawa, T. Feurer, Opt. Exp. **9**, 191 (2001)
26. A. Rundquist, A. Efimov, D.H. Reitze, J. Opt. Soc. Am. B **19**, 2468 (2002)

27. T. Brixner, G. Gerber, Opt. Lett. **26**, 557 (2001)
28. T. Brixner, G. Krampert, T. Pfeifer, R. Selle, G. Gerber, M. Wollenhaupt, O. Graefe, C. Horn, T. Baumert, Phys. Rev. Lett. **92**, 208301 (2004)
29. A.M. Weiner, J.P. Heritage, E.M. Kirschner, J. Opt. Soc. Am. B **5**, 1563 (1988)
30. M.M. Wefers, K.A. Nelson, Opt. Lett. **93**, 2032 (1993)
31. E. Zeek, K. Maginnis, S. Backus, U. Russek, M.M. Murnane, G. Mourou, H.C. Kapteyn, Opt. Lett. **24**, 493 (1999)
32. M. Hacker, G. Stobrawa, R.A. Sauerbrey, T. Buckup, M. Motzkus, M. Wildenhain, A. Gehner, Appl. Phys. B Laser Opt. **76**, 711 (2003)
33. S.H. Shim, D.B. Strasfeld, E.C. Fulmer, M.T. Zanni, Opt. Lett. **31**, 838 (2006)
34. J.X. Tull, M.A. Dugan, W.S. Warren, in *Advances in Magnetic and Optical Resonance*, ed. by W.S. Warren (Academic, New York, 1997)
35. D. Goswami, Phys. Rep. **374**, 385 (2003)
36. P. Tournois, Opt. Commun. **140**, 245 (1997)
37. F. Verluise, V. Laude, Z. Cheng, C. Spielmann, P. Tournois, Opt. Lett. **25**, 575 (2000)
38. J.C. Vaughan, T. Feurer, K.A. Nelson, J. Opt. Soc. Am. B **19**, 2489 (2002)
39. R.S. Judson, H. Rabitz, Phys. Rev. Lett. **68**, 1500 (1992)
40. T. Baumert, T. Brixner, V. Seyfried, M. Strehle, G. Gerber, Appl. Phys. B Laser Opt. **65**, 779 (1997)
41. C.J. Bardeen, V.V. Yakolev, K.R. Wilson, S.D. Carpenter, P.M. Weber, W.S. Warren, Chem. Phys. Lett. **280**, 151 (1997)
42. D. Yelin, D. Meshulach, Y. Silberberg, Opt. Lett. **22**, 1793 (1997)
43. T. Back, *Evolutionary Algorithms in Theory and Practice* (University Press, New York, 1996)
44. C. Siedschlag, O.M. Shir, T. Back, M.J.J. Vrakking, Opt. Commun. **264**, 511 (2006)
45. J.W. Wilson, P. Schlup, M. Lunacek, D. Whitley, R.A. Bartels, Rev. Sci. Instrum. **79**, 033103 (2008)
46. F. Dausinger, F. Lichtner, H. Lubatschowski (eds.), *Femtosecond Technology for Technical and Medical Application* (Springer, Berlin, 2004)
47. H. Misawa, S. Juodkazis (eds.), *3D Laser Microfabrication: Principles and Applications* (Wiley, Weinheim, 2006)
48. L.V. Keldysh, Sov. Phys. JETP **20**, 1307 (1965)
49. B.C. Stuart, M.D. Feit, A.M. Rubenchik, B.W. Shore, M.D. Perry, Phys. Rev. Lett. **74**, 2248 (1995)
50. A. Kaiser, B. Rethfeld, M. Vicanek, G. Simon, Phys. Rev. B **61**, 11437 (2000)
51. V.E. Gruzdev, Phys. Rev. B **75**, 205106 (2007)
52. A.C. Tien, S. Backus, H.C. Kapteyn, M.M. Murnane, G. Mourou, Phys. Rev. Lett. **82**, 3883 (1999)
53. M. Lenzner, J. Krüger, S. Sartania, Z. Cheng, C. Spielmann, G. Mourou, W. Kautek, F. Krausz, Phys. Rev. Lett. **80**, 4076 (1989)
54. S.S. Mao, F. Quéré, S. Guizard, X. Mao, R.E. Russo, G. Petite, P. Martin, Appl. Phys. A Mat. Sci. Process. **79**, 1695 (2004)
55. V.V. Temnov, K. Sokolowski-Tinten, P. Zhou, A. El-Khamhawy, D. von der Linde, Phys. Rev. Lett. **97**, 237403 (2006)
56. I.H. Chowdhury, X. Xu, A.M. Weiner, Appl. Phys. Lett. **86**, 151110 (2005)
57. C. Sarpe-Tudoran, A. Assion, M. Wollenhaupt, M. Winter, T. Baumert, Appl. Phys. Lett. **88**, 261109 (2006)
58. B. Rethfeld, Phys. Rev. Lett. **92**, 187401 (2004)
59. E. Louzon, Z. Henis, S. Pecker, Y. Ehrlich, D. Fisher, M. Fraenkel, A. Zigler, Appl. Phys. Lett. **87**, 241903 (2005)
60. X. Zhu, T.C. Gunaratne, V.V. Lozovoy, M. Dantus, Opt. Express **15**, 16061 (2007)
61. R. Stoian, M. Boyle, A. Thoss, A. Rosenfeld, G. Korn, I.V. Hertel, E.E.B. Campbell, Appl. Phys. Lett. **80**, 353 (2002)
62. P.R. Herman, R.S. Marjoribanks, A. Oettl, K. Chen, I. Konovalov, S. Ness, Appl. Surf. Sci. **154**, 577 (2000)

63. I.M. Burakov, N.M. Bulgakova, R. Stoian, A. Rosenfeld, I.V. Hertel, Appl. Phys. A Mat. Sci. Process. **81**, 1639 (2005)
64. L. Englert, B. Rethfeld, L. Haag, M. Wollenhaupt, C. Sarpe-Tudoran, T. Baumert, Opt. Exp. **15**, 17855 (2007)
65. L. Englert, M. Wollenhaupt, L. Haag, C. Sarpe-Tudoran, B. Rethfeld, T. Baumert, Appl. Phys. A Mat. Sci. Process. **92**, 749 (2008)
66. M. Merano, G. Boyer, A. Trisorio, G. Chériaux, G. Mourou, Opt. Lett. **32**, 2239 (2007)
67. K. Eidmann, J. Meyer-ter Vehn, T. Schlegel, S. Hüller, Phys. Rev. E **62**, 1202 (2000)
68. J. Solis, C.N. Afonso, J.F. Trull, M.C. Morilla, J. Appl. Phys. **75**, 7788 (1994)
69. M. Spyridaki, E. Koudoumas, P. Tzanetakis, C. Fotakis, R. Stoian, A. Rosenfeld, I.V. Hertel, Appl. Phys. Lett. **83**, 1474 (2003)
70. I.H. Chowdhury, X. Xu, A.M. Weiner, in *Commercial and biomedical applications of ultrafast lasers III*, *Proceedings of SPIE*, vol. 4978, eds. by J. Neev, A. Ostendorf, C.B. Schaffer (SPIE, Bellingham, 2003), p. 138
71. Y. Prior, K.Y. Zhang, V. Batenkov, Y. Paskover, J.H. Klein-Wiele, P. Simon, in *High-Power Laser Ablation V*, *Proceedings of SPIE*, vol. 5448, ed. by C.R. Phipps (SPIE, Bellingham, 2004), p. 1049
72. R. Hergenröder, M. Miclea, V. Hommes, Nanotechnology **17**, 4065 (2006)
73. H. Dachraoui, W. Husinsky, Phys. Rev. Lett. **97**, 107601 (2006)
74. R. Stoian, A. Mermillod-Blondin, N.M. Bulgakova, A. Rosenfeld, I.V. Hertel, M. Spyridaki, E. Koudoumas, P. Tzanetakis, C. Fotakis, Appl. Phys. Lett. **87**, 124105 (2005)
75. J.P. Colombier, P. Combis, A. Rosenfeld, I.V. Hertel, E. Audouard, R. Stoian, Phys. Rev. B **74**, 224106 (2006)
76. A.Q. Wu, X. Xu, Appl. Phys. Lett. **90**, 251111 (2007)
77. J.P. Colombier, E. Audouard, P. Combis, A. Rosenfeld, I.V. Hertel, R. Stoian, Appl. Surf. Sci. **255**, 9597 (2009)
78. A. Assion, M. Wollenhaupt, L. Haag, F. Maiorov, C. Sarpe-Tudoran, M. Winter, U. Kutschera, T. Baumert, Appl. Phys. B Laser Opt. **77**, 391 (2003)
79. A. Klini, P.A. Loukakos, D. Gray, A. Manousaki, C. Fotakis, Opt. Express **16**, 11300 (2008)
80. K. Itoh, W. Watanabe, S. Nolte, C. Schaffer, MRS Bull. **31**, 620 (2006)
81. I.M. Burakov, N.M. Bulgakova, R. Stoian, A. Mermillod-Blondin, E. Audouard, A. Rosenfeld, A. Husakou, I.V. Hertel, J. Appl. Phys. **101**, 043506 (2007)
82. R.R. Gattass, E. Mazur, Nat. Photonics **2**, 219 (2008)
83. G. Cerullo, R. Osellame, S. Taccheo, M. Marangoni, D. Polli, R. Ramponi, P. Laporta, S. De Silvestri, Opt. Lett. **27**, 1938 (2002)
84. Y. Cheng, K. Sugioka, K. Midorikawa, M. Masuda, K. Toyoda, K. Kawachi, K. Shihoyama, Opt. Lett. **28**, 55 (2003)
85. S. Nolte, M. Will, J. Burghoff, A. Tünnermann, Appl. Phys. A Mat. Sci. Process. **77**, 109 (2003)
86. R.R. Thomson, A.S. Bockelt, E. Ramsey, S. Beecher, A.H. Greenway, A.K. Kar, D.T. Reid, Opt. Express **16**, 12786 (2008)
87. A. Mermillod-Blondin, I.M. Burakov, Y.P. Meshcheryakov, N.M. Bulgakova, E. Audouard, A. Rosenfeld, A. Husakou, I.V. Hertel, Phys. Rev. B **77**, 104205 (2008)
88. W. Gawelda, D. Puerto, J. Siegel, A. Ferrer, A. Ruiz de la Cruz, H. Fernandez, J. Solis, Appl. Phys. Lett. **93**, 121109 (2008)
89. G. Heck, J. Sloss, R.J. Levis, Opt. Commun. **259**, 216 (2006)
90. R. Ackermann, E. Salmon, N. Lascoux, J. Kasparian, P. Rohwetter, K. Stelmaszczyk, S. Li, A. Lindinger, L. Wöste, P. Béjot, L. Bonacina, Appl. Phys. Lett. **89**, 171117 (2006)
91. M.Y. Shverdin, S.N. Goda, G.Y. Yin, S.E. Harris, Opt. Lett. **31**, 1331 (2006)
92. A. Mermillod-Blondin, C. Mauclair, A. Rosenfeld, J. Bonse, I.V. Hertel, E. Audouard, R. Stoian, Appl. Phys. Lett. **93**, 021921 (2008)
93. M. Ams, G.D. Marshall, D.J. Spence, M.J. Withford, Opt. Express **13**, 5676 (2005)

Chapter 6
Laser Nanosurgery, Manipulation, and Transportation of Cells and Tissues

Wataru Watanabe

Abstract Noninvasive manipulation and processing of cells and tissues is important for biological and medical applications. Lasers can be used to noninvasively image, manipulate, and process intracellular objects, cells, and tissues. In this chapter, laser nanosurgery including dissection, removal, disruption, and transfection are reviewed. The manipulation and transportation of cells and tissues using lasers are described.

6.1 Introduction

Lasers allow high-precision imaging, manipulation, and processing for biological and medical applications with minimal invasiveness [1–3]. Laser processing and manipulation techniques in biophotonics include the optical trapping, sorting, dissection, ablation, transient permeabilization, transport of cells, and laser-based preparation of biomolecules.

In order to achieve precise manipulation and processing of intracellular objects such as organelles and protein complex, and of cells and tissues, two regimes can be employed: direct method and laser-assisted method. In the direct method, a laser beam is tightly focused to manipulate and modify cells. For example, focused laser beams with shorter wavelengths can achieve precise manipulation. Lasers in the ultraviolet (UV) and visible regions present some disadvantages, namely, low light penetration depth, collateral damage outside the focal volume, and the possibility of photodamage to living cells. In contrast, lasers in the near-infrared region offer attractive advantages including deep penetration into thick biological samples and reduced photon-induced damage owing to the lack of an endogenous absorber. The trapping and manipulation of intracellular objects, cells, and tissues are best

W. Watanabe (✉)
Photonics Research Institute, National Institute of Advanced Science and Technology (AIST), Higashi 1-1-1, Tsukuba, Ibaraki, 305-8565 Japan
e-mail: wataru.watanabe@aist.go.jp

K. Sugioka et al. (eds.), *Laser Precision Microfabrication*,
Springer Series in Materials Science 135, DOI 10.1007/978-3-642-10523-4_6,

© Springer-Verlag Berlin Heidelberg 2010

performed by near-infrared lasers. In addition, near-infrared femtosecond (fs) lasers can be used to image and process cells and tissues. A salient feature of focusing femtosecond laser pulses is the limited interaction region in three-dimensional space. The laser-assisted method employs a laser beam that is not directly focused on a target structure; in fact, processing and manipulation can be performed by targeting specific biological media and absorbing nanoparticles or fluorophores. In addition, focusing laser pulses on solids or liquids generates a shockwave, and this laser-induced shockwave technique can be employed in transfection and cell manipulation. This chapter highlights laser nanosurgery, manipulation, and the transportation of cells and tissues.

6.2 Laser Direct Surgery

6.2.1 Nanosurgery with a Focused Laser Beam in the Ultraviolet and Visible Region

Performing highly targeted manipulation and surgery is an important area of research for cell biology. An intense beam – either in the UV region or the visible region – that is tightly focused through high numerical aperture (NA) objectives results in the intensity of the focal volume becoming sufficiently high to induce plasma formation. The material in the cell's focal volume could be damaged and even ablated in the submicron size regime, allowing site-specific dissection, removal, or disruption of organelles (Fig. 6.1). The dissection and inactivation of subcellular organelles in plant and animal cells were demonstrated with submicron spatial resolution [4–12]. CW lasers and long-pulse laser pulses (nanosecond (ns) regime) were employed in micro/nanosurgery. The disadvantages of UV lasers include low light penetration depth, the risk of collateral damage outside the focal volume, the risk of photo-damage to living cells due to absorption, and the possible induction of oxidative stress leading to apoptosis. A focused ns pulse laser beam causes thermal damage and denaturation of the protein molecules around the laser focus.

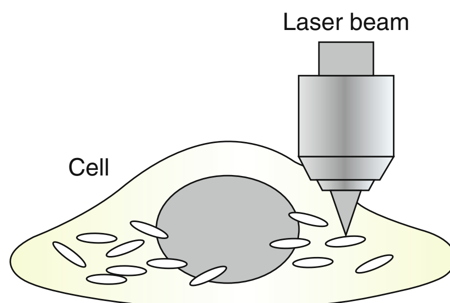

Fig. 6.1 Schematic for laser surgery by focusing a visible or UV laser beam

6.2.2 Femtosecond Laser Surgery

Focused near-infrared femtosecond lasers can be employed as highly precise nanosurgical tools for tissues, cells, and intracellular structures [2]. König et al. proposed a novel nanosurgery tool using near-infrared femtosecond lasers to perform the dissection of chromosomes [13, 14]. The limited heat generation enables precise control of cell modification, thus avoiding peripheral thermal damage.

6.2.2.1 Chromosome Dissection Using Femtosecond Nanosurgery

König et al. first proposed nanosurgery with femtosecond lasers in 1999 [13]. They demonstrated the dissection of human chromosomes using tightly focused, high-repetition-rate (80 MHz) femtosecond laser pulses [14]. Measurements with an atomic force microscope revealed chromosome dissection with a cut size of below 300 nm. In addition, the removal of chromosome material with a precision of 110 nm was achieved (Fig. 6.2). The cells remained alive and completed cell division after laser surgery. The limited heat generation enables the precise control of chromosome modifications, thereby avoiding peripheral thermal damage.

König et al. also cut chromosomes within a living cell. Here too, the cells remained alive and completed cell division after laser surgery [2]. This femtosecond

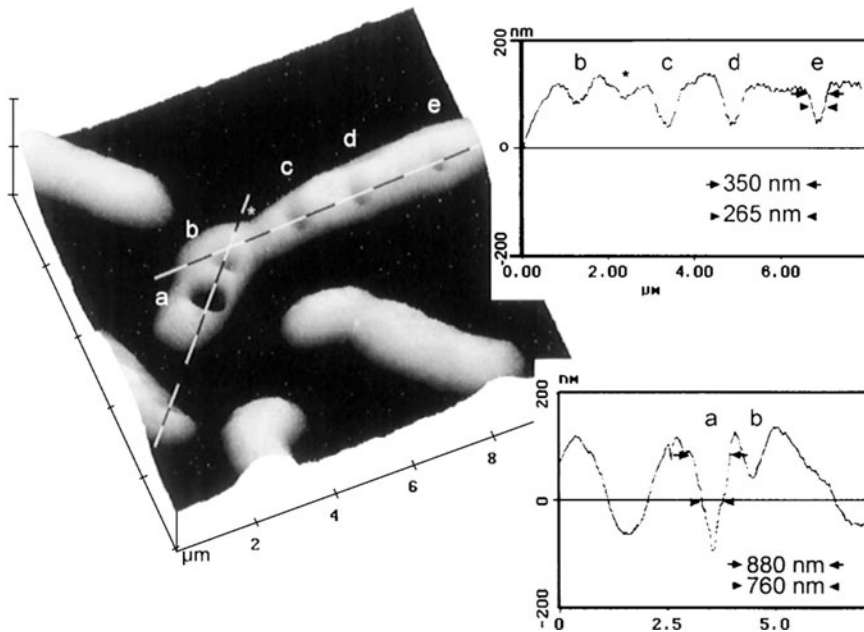

Fig. 6.2 Nanoablation of DNA with 800 nm femtosecond laser pulses. Reprinted with permission from [14]

laser processing was also used to produce spatially defined regions of DNA damage in live rat kangaroo cells (PtK1) and human cystic fibrosis pancreatic adenoma carcinoma cells (CFPAC-1) [15]. Spatially defined alterations in the cell nucleus as a result of this femtosecond laser technique are useful for studying DNA damage and repair.

6.2.2.2 Nanosurgery of Intracellular Organelles

Femtosecond laser pulses can be employed for nanosurgery of targeted organelles within a living cell with high spatial resolution [2]. For instance, nanosurgery could remove or replace certain sections of a damaged gene inside a chromosome, sever axons to study the growth of nerve cells, or destroy an individual cell without affecting the neighboring cells. A single organelle (cytoskeleton, mitochondrion, etc.) is completely disrupted or dissected without disturbing surface layers and affecting the adjacent organelles or the viability of both plant cells [16] and animal cells [2]. Femtosecond lasers were used for nanosurgery of organelles and structures within yeast mitotic spindles [17–30]. Figure 6.3 illustrates nanosurgery performed on a targeted

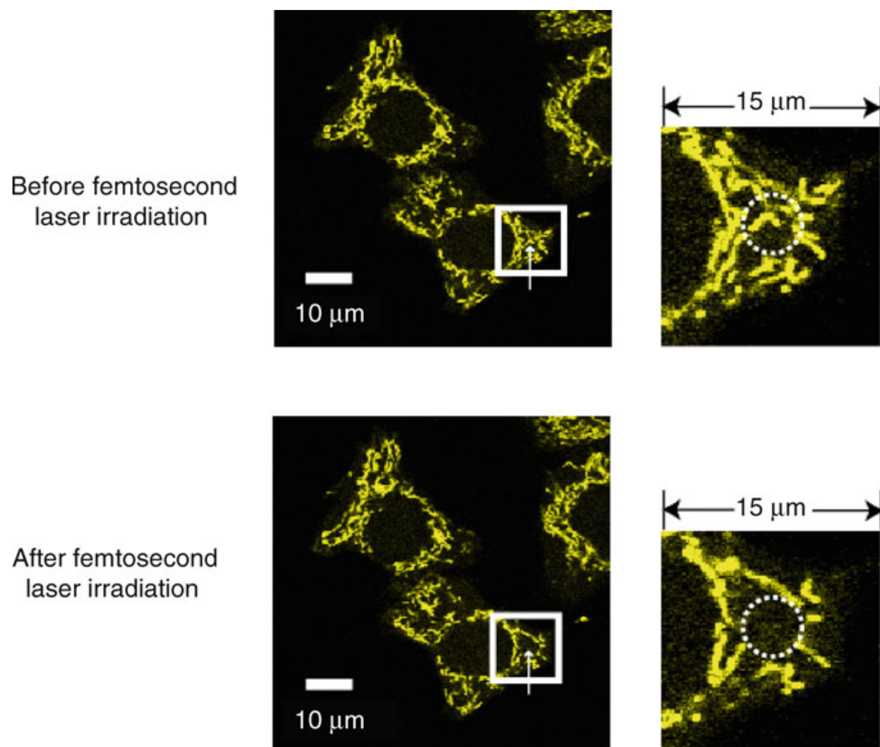

Fig. 6.3 Nanosurgery of a single mitochondrion in a living HeLa cell. Target mitochondrion (marked by *arrow*). Fluorescence has yellow color which shows mitochondria visualized by EYFP. Reprinted with permission from [27]

mitochondrion in a HeLa cell before and after irradiation with 800-nm femtosecond laser pulses at a repetition rate of 1 kHz and energy of 3 nJ/pulse [27].

Mazur et al. demonstrated that on a scale of a few hundred nanometers, by using femtosecond laser pulses with energies of a few nanojoules at a repetition rate of 1 kHz, a single mitochondrion could be separated from a living cell without disturbing the rest of the cell [22–26]. They also demonstrated the dissection of an individual actin filament and investigated the tension in actin stress fibers in living endothelial cells (Fig. 6.4) [26].

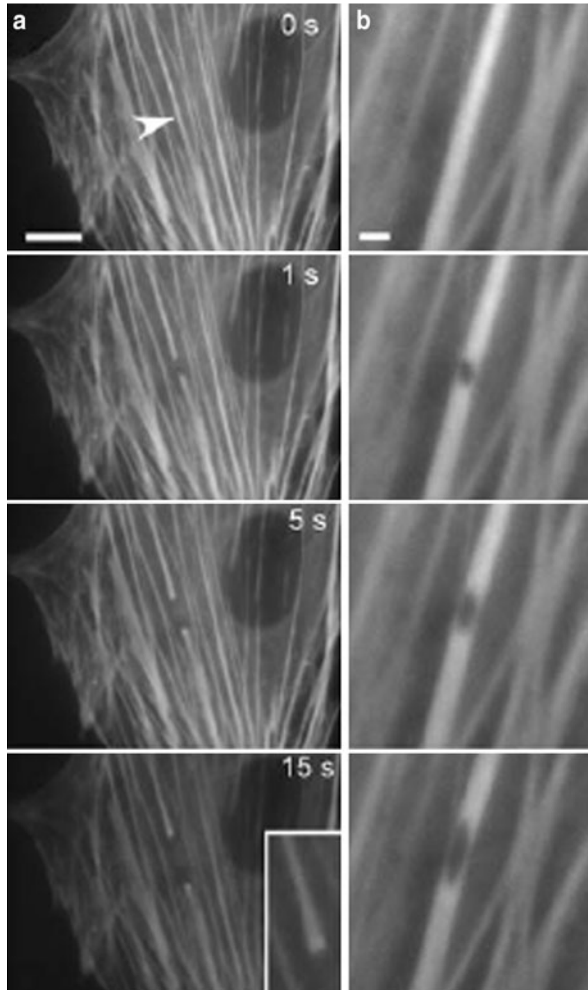

Fig. 6.4 Dissection of stress fibers in living cells by focusing femtosecond laser pulses. (**a**) Severing and retraction of a single stress fiber bundle in an endothelial cell expressing EYFP-actin. Scale bar, 10 μm. (**b**) Strain relaxation of a single stress fiber bundle after a 300-nm hole was ablated in the fiber. Scale bar, 2 μm. Reprinted with permission from [26]

Supatto et al. described the application of femtosecond laser nanosurgery in developmental biology [20]. They used femtosecond laser pulses to perform three-dimensional microdissections inside live Drosophila embryos in order to locally modify their structural integrity. By tracking the outcome of the microdissections by nonlinear microscopy using the same laser source, it was found that local nanosurgery can be used to modulate remote morphogenetic movements. Kohli et al. also demonstrated nanosurgery on living embryonic cells of zebrafish [30].

Kohli et al. demonstrated cell isolation by nanosurgical ablation of focal adhesions adjoining epithelial cells [30]. Uchugonova et al. proposed optical cleaning of selected cells [31] by knocking out some living single stem cells within a 3D microenvironment without causing any collateral damage. Neighbor cells can be optically destroyed while keeping the cell of interest alive. This novel method provides the possibility of controlling the development of stem cells in three dimensions, of destroying undesired cells, and of isolating stem cells of interest.

6.2.2.3 Femtosecond Laser Nanoaxotomy

Femtosecond laser nanosurgery can also be used to dissect neurons within living tissues or animals [32–34]. By only cutting a few nanoscale nerve connections (axons) inside a *Caenorhabditis elegans* (*C. elegans*), the backward crawl of the nematode was greatly hindered [32]. Femtosecond laser nanosurgery can control neural regrowth and allow the investigation of important biochemical and genetic pathways that are responsible for neuronal regeneration and axotomy study.

Femtosecond laser axotomy is now a versatile tool in regeneration studies when combined with micro-fluidic chips [35–37]. Ben-Yakar et al. demonstrated that the two-layer miocrofluidic trap allows both the immobilization of *C. elegans* and the performance of nanosurgery to sever axons and study nerve regeneration [35]. Using the nanoaxotomy chip, they discovered that axonal regeneration occurs much faster than previously described; surprisingly, the distal fragment of the severed axon regrows in the absence of anesthetics.

Yanik et al. demonstrated on-chip in vivo small-animal genetic and drug screening technologies in high-throughput neural degeneration and regeneration studies [36–38]. The high-throughput microfluidic platform allows the real-time immobilization of animals without the use of anesthesia and facilitates the sub-cellular resolution multi-photon imaging on physiologically active animals. Using femtosecond laser nanosurgery and pattern recognition algorithms, sub-cellular precision neurosurgery can be performed in microfluidic chips on awake but immobilized animals with minimal collateral damage (Figs. 6.5 and 6.6) [38]. The ability to perform precise nanosurgery provides the potential for rapidly screening drugs and for discovering new biomolecules that affect regeneration and degeneration.

6.2.2.4 Optoperforation and Transfection

Transfection is the introduction of membrane impermeable substances such as foreign DNA into a cell and is an indispensable method for investigating and

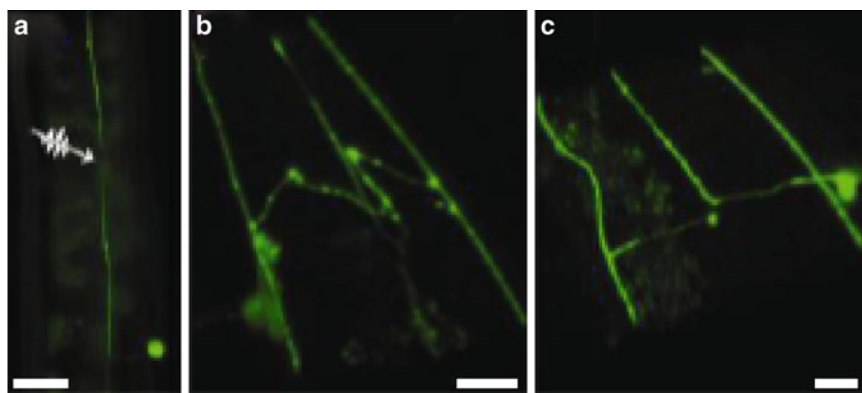

Fig. 6.5 Microfluidic immobilization enables sub-cellular manipulation and three-dimensional imaging of live, awake animals. (**a**) Severing of the axons. Arrow indicates the focus of femtosecond laser pulses and the axotomized region. (**b**), (**c**) Volume reconstruction of images captured using two-photon microscopy. Scale bars, 20 μm. Reprinted with permission from [38]

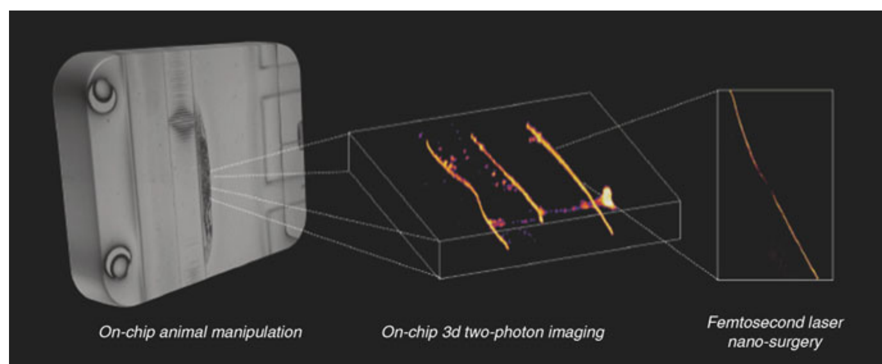

Fig. 6.6 Microfluidic immobilization of living and unanesthetized animals by three-dimensional two-photon imaging and femtosecond laser nanosurgery. Reprinted with permission from [38]

controlling the individual functions of living cells. Various types of gene injection techniques have been developed, such as lipofection, electroporation, sonoporation, virus vector, and particle gun injection. Laser optoperforation of individual targeted cells can be employed by directly focusing a laser beam. When an ultraviolet laser was used for targeted gene transfection, it was determined that laser irradiation disrupted cellular integrity [1]. König et al. reported the targeted transportation of plasmid DNA vector pEGFP-N1 encoding enhanced green fluorescent protein (EGFP) into Chinese hamster ovarian (CHO) cells [39] by focusing femtosecond laser pulses. Femtosecond laser transfection was also applied to kidney epithelial (PtK2) cells of rat kangaroo [40], canina mammary cells MTH53a [41,42] and stem cells [43]. Kohli and Elezzabi used femtosecond laser pulses to perform nanosurgery on living zebrafish embryos to introduce exogenous material into the embryonic cells [44–46].

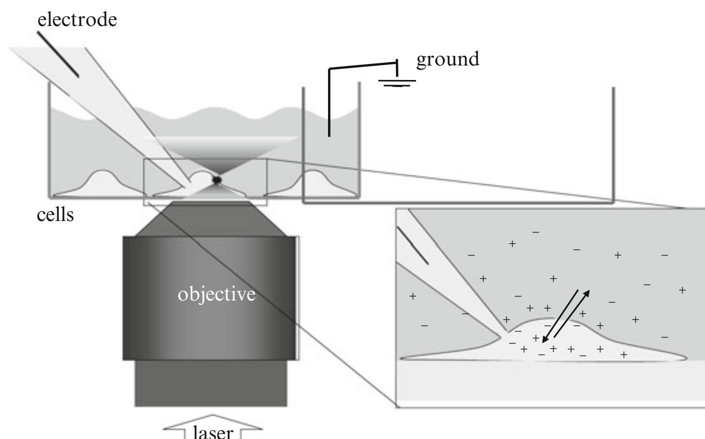

Fig. 6.7 Schematic of simultaneous patchclamp and optoperforation of a living cell. Induced transient pore allows diffusion of molecules through the membrane. Reprinted with permission from [42]

Baumgart et al. combined an femtosecond laser with the patchclamp technique on GFSHR17 granulosa cells to obtain more insight into the mechanisms of optoperforation [41, 42]. The measurement of membrane potential variations allows the estimation of the volume exchanged between the extracellular and the intracellular space (see Fig. 6.7) during perforation, relative to the cell volume (dilution factor) and provides an idea of the maximal life of the induced transient pore. Using this technique, Baumgart et al. optoperforated MTH53a and transfected them with a GFP vector or a vector coding for a GFP fusion protein with the architectural transcription factor HMGB1 (GFPHMGB1).

Dholakia used a nondiffracting light mode, such as a Bessel beam, for multiphoton cell transfection. This approach allows transfection in the cell monolayer samples over large axial distances, because beam focusing is less critical [47, 48].

6.2.2.5 Nanosurgery of Tissue

Femtosecond lasers can also be used to perform surgery or to modify the structure of biological tissues [49, 50]. Femtosecond lasers have an important application in the laser-assisted in situ leratomileusis (LASIK) technique, where they have been shown to provide better visual outcomes and to reduce higher order aberrations, glare, and haloes when compared with traditional microkeratomes [51–57].

Schaffer et al. used femtosecond lasers to visualize and induce single-vessel occlusions and hemorrhages in the cortex of live, anesthetized rodents as a means to provide a comprehensive animal model of small-scale strokes [58, 59]. A tightly focused femtosecond laser pulse is used to deposit laser energy into the endothelial cells that line a specifically targeted vessel; this causes an injury that triggers

clotting or causes hemorrhage, but only in the targeted vessel. This technique allows any blood vessel, including individual arterioles, capillaries, and venules, in the top 0.5 mm of the cortex of a rodent to be selectively lesioned.

6.2.2.6 Mechanisms for Femtosecond Laser Surgery

Femtosecond laser surgery has been demonstrated using both low-repetition-rate (1–250 kHz) amplified laser systems and high-repetition-rate oscillators (∼80 MHz). Vogel et al. proposed mechanisms for femtosecond laser nanosurgery [60, 61]. Nanosurgery at a repetition rate of 80 MHz is performed in the low-density plasma regime at pulse energies well below the optical breakdown threshold. It is mediated by free-electron-induced chemical decomposition (bond breaking) in conjunction with multiphoton-induced chemistry and is not related to heating or thermo-elastic stresses. An increase in the energy gives rise to long-lasting bubbles by accumulative heating and leads to unwanted dissociation of tissue into volatile fragments. In contrast, dissection at repetition rate of 1 kHz is performed using larger (tenfold) pulse energies and relies on thermoelastically induced formation of minute transient cavities with a lifespan of <100 ns.

Vogel et al. examined femtosecond laser-induced bubble formations in water through real-time monitoring. At the threshold, the bubbles produced by fs optical breakdown in water are smaller than the diffraction-limited focus diameter [62, 63].

In order to simulate the interaction of ultrashort laser pulses with transparent materials at high NA focusing, a comprehensive numerical model was introduced, taking into account nonlinear propagation, plasma generation, as well as the pulse's interaction with the generated plasma [64, 65].

6.3 Nanoparticles and Chromophore-Assisted Manipulation and Processing

6.3.1 Chromophore-Assisted Laser Inactivation

Chromophore-assisted laser inactivation (CALI) is a technique that selectively inactivates proteins of interest to elucidate their in vivo functions. Specific proteins are targeted by means of antibodies attached to metallic nanoparticles or chromophores [66–68]. When the antibody–absorber conjugates are bound to the target proteins, the entire cell or group of cells is exposed to a short-pulsed laser beam. Protein inactivation occurs through linear absorption of the laser irradiation in the nanoparticles or chromophores, resulting in thermomechanical or photochemical destruction of the target proteins, regardless of their localization within the cell. By application of multiphoton excitation to CALI, Tanabe et al. showed that enhanced green fluorescent protein (EGFP) is an effective chromophore for inactivation of a protein's function without nonspecific photodamage in living mammalian cells [69].

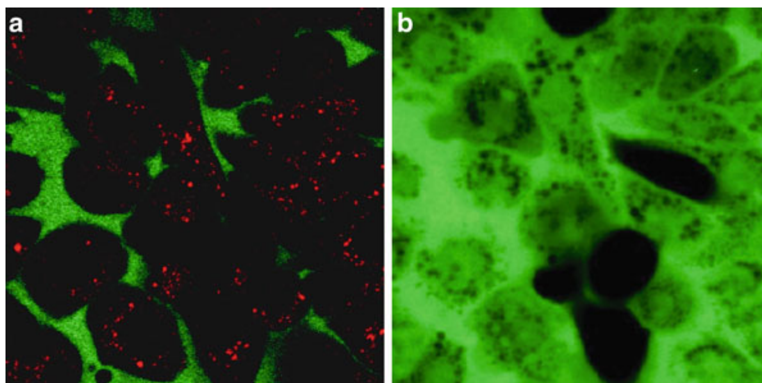

Fig. 6.8 Plasmonic laser nanoablation of cancer cells (MDA-MB-468) labeled with 80 nm gold nanoparticles functionalized with anti-EGFR antibodies. (**a**) Nanoparticles in red, imaged at a 850 nm wavelength through multiphoton luminescence, and cell membrane-impermeable dye (10 kDa FITC-Dextran) in green, imaged at a 760 nm wavelength; (**b**) Fluorescence images show reduced membrane integrity, as seen by the intake of FITC-Dex, after the application of 80 MHz laser pulses of 18 mJ/cm^2 for 10 s [72]

6.3.2 Plasmonic Nanosurgery

Local field enhancement in the near-field region of metal nanoparticles irradiated with laser pulses is a promising technique [70–72] that involves light intensity enhancement of plasmon in metal nanoparticles or fluorophores. Ben-Yakar et al. investigated plasmonic laser nanoablation of biological materials [72]. Plasmonic laser nanoablation takes advantage of the enhanced plasmonic scattering of femtosecond laser pulses in the near-field region of gold nanoparticles to vaporize various materials with a nanoscale resolution. While the use of femtosecond laser pulses ensures non-thermal tissue ablation, the use of nanoparticles improves the precision and selectivity of the ablation/surgery process. Eversole et al. showed that the technique using femtosecond laser pulses can be used to reduce the ablation threshold of cancer cell membranes labeled with anti-EGFR-coated gold nanoparticles by 7–8 times the original value (Fig. 6.8).

6.4 Laser Manipulation and Transport of Cells and Tissues

6.4.1 Optical Tweezers

Optical tweezers using infrared lasers have allowed us to manipulate cells, organelles, and subcellular particles [1, 73]. Tightly focused near-infrared laser beams generate a gradient force, which confines particles and biological objects in the vicinity of the laser focus. By scanning the beam, three-dimensional optical trap-

ping and manipulation can be performed. Cells and organelles can be confined in the focal volume of an object by radiation pressure. Optical tweezers can be used for optical manipulation, cell sorting, force measurement, Kinesin molecular movement, drug screening, cell sorting, and investigation of DNA mechanics. Shelby et al. demonstrated the optical extraction of intracellular organelles from living cells in combination with optical tweezers and laser surgery [74]. A pulsed N_2 laser was used to disrupt the cell membrane and remove it. A CW Nd:YAG laser was used for the optical trapping of a single intracellular organelle. An optical vortex Laguerre–Gaussian beam with a helical phase distribution at its wavefront was applied in the laser manipulation. Chiu et al. took advantage of polarization effects to fashion vortex traps for particles with different sizes, while minimizing photodamage to the trapped particles and subcellular organelles [75]. The ability to optically manipulate submicrometer subcellular structures while minimizing photodamage has several practical applications. In combination with laser surgery, polarization-shaped optical vortex traps allow the unambiguous extraction of specific fluorescent subcellular organelles.

6.4.2 Laser Transport of Cells

The isolation and capture of homogeneous cells or a group of cells aids the understanding of the molecular mechanisms involved in cell growth and differentiation. The laser can also be used to eject microdissected samples from the object plane. Laser microdissection of samples of interest followed by laser-induced transportation (laser catapulting) provides high-resolution control of sample composition by allowing us to select and reject individual cells.

Vogel et al. investigated the dynamics of laser microdissection and laser catapulting using focused and defocused laser pulses (wavelength 337 nm, pulse duration 3 ns) by means of time-resolved photography [76–78]. The working mechanism for the microdissection of histologic specimens was found to be plasma-mediated ablation initiated by linear absorption.

6.5 Application of Laser-Induced ShockWaves and Mechanical Waves

6.5.1 Targeted Gene Transfection by Laser-Induced Mechanical Waves

Stress waves can be generated by focusing nanosecond laser pulses on a black rubber sheet covering a tissue, allowing a DNA plasmid placed between the tissue and the rubber sheet to permeate the tissue (Fig. 6.9). Laser microinjection has been demonstrated for tissues and organs through application of laser-induced stress

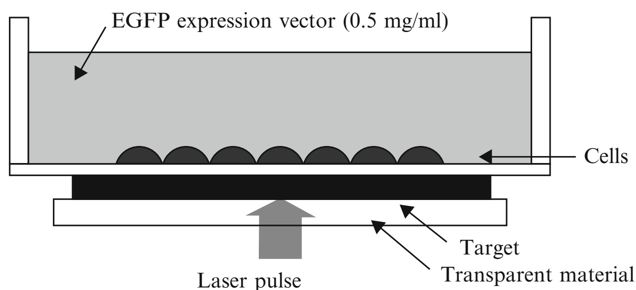

Fig. 6.9 Experimental configuration for gene transfection using a laser-induced mechanical wave. Reprinted with permission from [79]

waves. This method has been reported to result in effective gene expression in tissues and organs. Sato et al. demonstrated that genes can be delivered into cells and tissues by using laser induced stress waves [79–81]. The second harmonics of a Q switch Nd:YAG laser (wavelength 532 nm, pulse duration 6 ns) were used to irradiate a solid material placed on the targeted cultured cells or tissue. A laser-induced plasma was formed on the target, and its expansion created a stress wave and induced deformation in the cellular membranes. This deformation allowed exogenous macromolecules to enter the cytoplasm.

6.5.2 Femtosecond Laser-Induced ShockWave in Liquid

6.5.2.1 Femtosecond Laser-Induced Crystallization of Proteins and Molecules

When a femtosecond laser beam was focused on water, a shockwave and cavitation bubbles were created [82]. Masuhara and Hosokawa used this phenomena with an 800 nm femtosecond laser to induce efficient protein crystallization, such as lysozyme, glucose isomerase, Ribonuclease H, trypanosome brussei, and others egg-white lysozyme and 4-(dimethylamino)-*N*-methyl-4-stilbazolium tosylate (DAST) [83].

6.5.2.2 Patterning of Protein Cubes and Cells by Femtosecond Laser Induced Impulsive Force

Accurate placement of individual and groups of cells is an important requirement in the development of engineered tissues and other pattern-forming biological systems. A variety of laser-based printing methods have been shown to enable the accurate placement of robust cells and other resilient biomaterials. A functional DNA microarray was prepared by the laser-induced forward transfer (LIFT) technique [84] (see Chap. 11). The patterning of protein cubes and cells was performed using an

1.

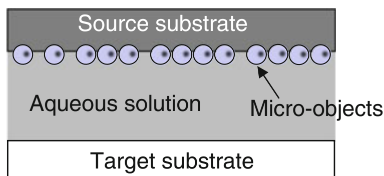

2. Micro-objects such as protein cubes or cells are transferred by a femtosecond laser induced impulsive force.

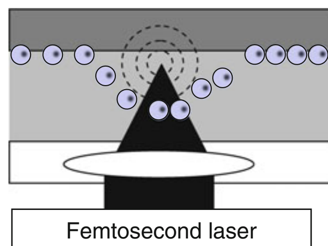

3.

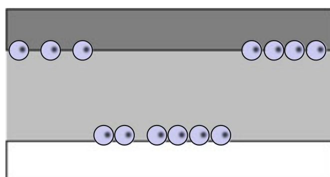

4. After removal of the source substrate

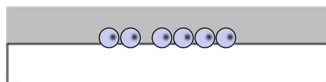

Fig. 6.10 Schematic illustration of micro-patterning of protein cubes by focused femtosecond laser irradiation in the water medium. (Courtesy of Y. Hosokawa)

femtosecond laser-induced impulsive force (Fig. 6.10). Shockwave and cavitation bubbles were created by focusing femtosecond laser pulses on water, resulting in convection and micrometer-sized objects being pushed in the solution without any damage. This technique can be used as an impulsive mechanical force for patterning various micrometer-sized materials such as protein cubes and biological cells [84, 85].

6.5.2.3 Femtosecond Laser-Induced Injection of Nanoparticles into Cell

The impulsive mechanical force generated by formation of the femtosecond laser-induced shockwave and bubbles has been applied to inject nanoparticles into single cells (Fig. 6.11) [86]. The laser pulse was focused on water to prevent hitting the mouse fibroblast NIH3T3 cell itself. The observations were fluorescent, suggesting that the particles were injected into the cell as a result of shockwave and bubble formation.

6.6 Laser-Induced Stimulation

Near-infrared ultrashort pulsed laser irradiation has been used for cellular stimulation [87–91]. Smith et al. demonstrated that the localized irradiation effects in living cells can lead to photo-induced intracellular Ca^{2+} waves [88], which can trigger

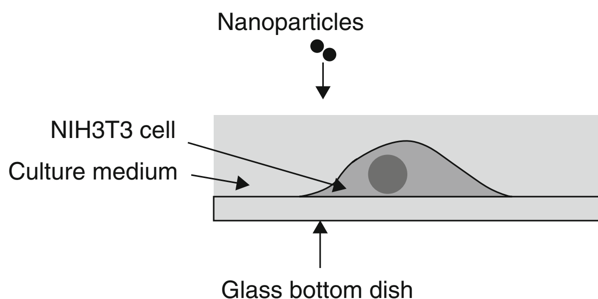

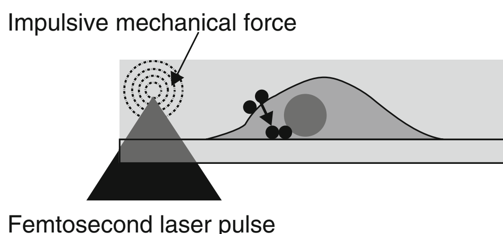

Fig. 6.11 Schematic illustration for the femtosecond laser-induced injection of nanoparticles into a single animal cell. (Courtesy of Y. Hosokawa)

contraction in individual heart muscle cells. By adapting the periodic application of laser light, this approach could be used in an optical pacemaker. This laser technique allows a driving stimulus and may possibly be able to penetrate substantial depths of heart muscle tissue due to multiphoton absorption.

By exciting the low-frequency vibrational modes of the viral capsid through impulsive stimulated Raman scattering to a high-energy state, Tsen et al. successfully inactivated viruses such as bacteriophage M13 using a visible femtosecond laser [92, 93]. This method is highly selective and is applicable to any viral or bacterial system.

6.7 Fabrication of Microfluidic Channels and Scaffolds

Microfabrication technology is an attractive tool for developing tissue-engineering systems. Microfluidic channels and chips can also be fabricated by laser technology (see Chap. 9). The cell–substrate interaction is dependent on substrate chemistry and

topography because both factors strongly influence how well cells grow and live. Several lasers including femtosecond lasers can be used for texturing and nanostructuring biopolymers and biomaterials such as collagen and gelatine, thus creating nanoporous structures (Chap. 4). Researchers investigated the use of structures, fabricated by two-photon polymerization, in three-dimensional mechanical implants or cell scaffolds that may be useful for cultivating artificial skin for treating wounds and ulcers [94–97]. Tiny mechanical parts such as microscale needles for drug delivery and tiny fluidic valves were also successfully fabricated [98, 99].

6.8 Summary and Conclusions

Recent advances in laser nanosurgery, manipulation, and the transportation of cells and tissues were reviewed. Laser manipulation can be employed as a highly precise tool for manipulation and nanosurgery of tissues, cells, and intracellular compartments without collateral damage. It is anticipated that the manipulation and transportation of cells without compromising cell viability will offer versatile and feasible tools for use in applications related to the fields of cell biology and medicine. Lasers are widely used for processing biocompatible materials. Nanoparticle and nanomaterial synthesis using lasers is an important area of research in biophotonics and is described in Chap. 7.

References

1. M. Berns, K. Greulich, in *Laser manipulation of cells and tissues*. (Academic, Elsevier, San Diego, 2007)
2. K. König, Histochem. Cell. Biol. **114**, 79 (2000)
3. A. Ashkin, J.M. Dziedzic, T. Yamane, Nature **330**, 769 (1987)
4. R.L. Amy, R. Storb, Science **150**, 756 (1965)
5. M.W. Berns et al., Science **213**, 505 (1981)
6. M.W. Berns, W.H. Write, R.W. Steubing, Int. Rev. Cytol. **129**, 1 (1991)
7. K.O. Greulich, in *Micromanipulation by light in biology and medicine*. (Birkhauser, Basel, Switzerland, 1999)
8. V. Venygopalan, A. Guerra III, K. Hahen et al. Phys. Rev. Lett. **88**, 078103 (2002)
9. J. Colombelli, S.W. Grill, E.H.K. Stelzer, Rev. Sci. Instrum. **75**, 4728 (2004)
10. J. Colombelli, E.G. Reynaud, J. Rietdorf, R. Pepperkok, E.H.K. Stelzer, Traffic **6**, 1093 (2005)
11. A. Khodjakov, R.W. Cole, C.L. Rieder, Cell. Motil. Cytoskel. **38**, 311 (1997)
12. E.L. Botvinick, V. Venugopalan, J.V. Shah et al., Biophys. J. **87**, 4203 (2004)
13. K. König, I. Riemann, P. Fischer et al., Cell. Mol. Biol. **45**, 195 (1999)
14. K. König, I. Riemann, W. Fritzsche, Opt. Lett. **26**, 819 (2001)
15. V. Gomez-Godinez, N.M. Wakida, A.S. Dvornikov et al., J. Biomed. Opt. **12**, 020505 (2007)
16. U.K. Tirlapur, K. König, Planta **214**, 1 (2001)
17. U.K. Tirlapur, K. König, Plant. J. **31**, 365 (2002)
18. K. König, I. Riemann, F. Stracke et al., Med. Laser. Appl. **20**, 169 (2005)
19. T. Shimada, W. Watanabe, S. Matsunaga et al., Opt. Express **13**, 9869 (2005)
20. W. Supatto, D. Débarre, B. Moulia et al., Proc. Natl. Acad. Sci. U S A **102**, 1047 (2005)

21. L. Sacconi, I.M. Tolić-Nørrelykke, R. Antolini et al., J. Biomed. Opt. **10**, 014002 (2005)
22. N. Shen, D. Datta, C.B. Schaffer et al., Mech. Chem. Biosyst. **2**, 17 (2005)
23. I. Maxwell, C. Chung, E. Mazur, Med. Laser. Appl. **20**, 193 (2005)
24. E. Mazur, in *LAMP2006—The 4th International Congress on Laser Advanced Materials Processing*, *#Tu1-1*, 2006
25. A. Heisterkamp, I.Z. Maxwell, E. Mazur et al., Opt. Express **13**, 3690 (2005)
26. S. Kumar, I.Z. Maxwell, A. Heisterkamp et al., Biophysical. J. **90**, 3762 (2006)
27. W. Watanabe, N. Arakawa, S. Matsunaga et al., Opt. Express **12**, 4203 (2004)
28. W. Watanabe, S. Matsunaga, T. Shimada et al., Med. Laser Appl. **20**, 185 (2005)
29. N.M. Wakida, C.S. Lee, E.T. Botvinick et al., J. Biomed. Opt. **12**, 024022 (2007)
30. V. Kohli, J.P. Acker, A.Y. Elezzabi, Laser Surg. Med. **37**, 2270 (2005)
31. A. Uchugonova, A. Isemann, E. Gorjup et al., J. Biophoton. **1**, 463 (2008)
32. M.F. Yanik, H. Cinar, H.N. Cinar et al., Nature **432**, 822 (2004)
33. M.F. Yanik, H. Cinar, H.N. Cinar et al., IEEE J. Sel. Top. Quant. **12**, 1283 (2006)
34. F. Bourgeois, A. Ben-Yakar, Opt. Express **15**, 8521 (2007)
35. S.X. Guo, F. Bourgeois, T. Chokshi et al., Nature Method **5**, 531 (2008)
36. C.B. Rohde, F. Zeng, R. Gonzalez-Rubio et al., Proc. Natl. Acad. Sci. U S A **104**, 13891 (2007)
37. F. Zeng, C.B. Rohde, M.F. Yanik, Lab. Chip. **8**, 653 (2008)
38. C. Rohde, F. Zeng, C. Gilleland et al., in *Proceedings of LPM2008—The 9th International Symposium on Laser Precision Microfabrication, Tu-A-1210*, 2008
39. U.K. Tirlapur, K. König, Nature **418**, 290 (2002)
40. D. Stevenson, B. Agate, X. Tsampoula et al., Opt. Express **14**, 7125 (2006)
41. J. Baumgart, W. Bintig, A. Ngezahayo et al., Opt. Express **16**, 3021 (2008)
42. J. Baumgart, W. Bintig, A. Ngezahayo et al., in *Proceedings of LPM2008—The 9th International Symposium on Laser Precision Microfabrication, Tu-A-1130*, 2008
43. A. Uchugonova, K. König, R. Bueckle et al., Opt. Express **16**, 9357 (2008)
44. V. Kohli, A.Y. Elezzabi, BMC Biotechnol. **8**, 7 (2008)
45. V. Kohli, J.P. Acker, A.Y. Elezzabi, Biotechnol. Bioeng. **92**, 889 (2005)
46. V. Kohli, V. Robles, M.L. Cancela et al., Biotechnol. Bioeng. **98**, 1230 (2007)
47. X. Tsampoula, V. Garces-Chavez, M. Comrie et al., Appl. Phys. Lett. **91**, 053902 (2007)
48. K. Dholakia, in *LPM2008—The 9th International Symposium on Laser Precision Microfabrication, Tu-A-950*, (2008)
49. B.M. Kim, M.D. Feit, A.M. Rubenchik et al., J. Biomed. Opt. **6**, 332 (2001)
50. P.S. Tsai, B. Friedman, A.I. Ifarraguerri et al., Neuron **39**, 27 (2003)
51. K. König, O. Krauss, I. Riemann, Opt. Express **10**, 171 (2002)
52. T. Juhasz, H. Frieder, R.M. Kurtz et al., IEEE J. Sel. Top. Quant. **5**, 902 (1999)
53. H. Lubatschowski, G. Maatz, A. Heisterkamp et al., Graf. Arch. Clin. Exp. **238**, 33 (2000)
54. K.S. Frederickson, W.E. White, R.G. Wheeland et al., Arch. Dermatol. **129**, 989 (1993)
55. W. Kautek, S. Mitterer, J. Kruger et al., Appl. Phys. A **58**, 513 (1994)
56. R.M. Kurtz, X.B. Liu, V.M. Elner et al., J. Refract. Surg. **13**, 653 (1997)
57. R.M. Kurtz, C. Horvath, H.H. Liu et al., J. Refract. Surg. **14**, 541 (1998)
58. N. Nishimura, C.B. Schaffer, B. Friedman et al., Nature Method **3**, 99 (2006)
59. N. Nishimura, J. Nguyen, N.L. Rosidi et al., in *LPM2008—The 9th International Symposium on Laser Precision Microfabrication, Tu-A-1400*, 2008
60. A. Vogel, J. Noack, G. Hüttman et al., Appl. Phys. B **81**, 1015 (2005)
61. A. Vogel, J. Noack, G. Hüttman et al., in *Proc. 4th Int. Congress on Laser Advanced Materials Processing (LAMP2006)*, 2006
62. A. Vogel, N. Linz, S. Freidank et al., Phys. Rev. Lett. **100**, 038102 (2008)
63. A. Vogel, N. Linz, S. Freidank et al., in *LPM 2008—The 9th International Symposium on Laser Precision Microfabrication (LPM 2008), Tu-A-1050*, 2008
64. C.L. Arnold, A. Heisterkamp, W. Ertmer et al., Opt. Express **15**, 10303 (2007)
65. C.L. Arnold, A. Heisterkamp, H. Lubatschowski, in *Proceedings of LPM2008—The 9th International Symposium on Laser Precision Microfabrication*, 2008
66. D.G. Jay, Proc. Natl. Acad. Sci. U S A **85**, 5454 (1988)
67. J.C. Liao et al., Proc. Natl. Acad. Sci. U S A **91**, 2659 (1994)

68. Z. Rajfur et al., Nat. Cell. Biol. **4**, 286 (2002)
69. T. Tanabe, M. Oyamada, K. Fujita et al., Nature Method **2**, 5038 (2005)
70. F. Garwe, A. Csaki, G. Maubach et al., Med. Laser Appl. **20**, 201 (2005)
71. A. Csaki, F. Garwe, A. Steinbruec et al., Nano Lett. **7**, 247 (2007)
72. A. Ben-Yakar, D. Eversole, O. Ekici et al., in *Metallic nanomaterials for life sciences*, vol. 1, ed. by Challa, (2008), pp. 493–539
73. A. Ashkin, Phys. Rev. Lett. **24**, 156 (1970)
74. J.P. Shelby, J.S. Edgar, D.T. Chiu, Photochem. Photobiol. **81**, 994 (2007)
75. G.D.M. Jeffries, J.S. Edgar, Y. Zhao et al., Nano Lett. **7**, 415 (2007)
76. A. Vogel, K. Lorenz, V. Horneffer et al., Biophys. J. **93**, 4481 (2007)
77. V. Horneffer, N. Linz, A. Vogel, J. Biomed. Opt. **12**, 054016 (2007)
78. A. Vogel, K. Lorenz, V. Horneffer et al., in *LPM2008, TU-A-1430*, 2008
79. M. Terakawa, S. Sato, H. Ashida et al., J. Biomed. Opt. **11**, 014026 (2006)
80. M. Terakawa, M. Ogura, S. Makoto et al., Opt. Lett. **29**, 1227 (2004)
81. S. Sato, M. Terakawa, M. Obara, in *LAMP2006, #Fr1–5*, 2006
82. T. Juhasz, G.A. Kastis, C. Suarez et al., Laser Surg. Med. **19**, 23 (1996)
83. T. Kaji, S. Ito, H. Miyasaka et al., Appl. Phys. Lett. **91**, 023904 (2007)
84. H.Y. Yoshikawa, Y. Hosokawa, K. Suzuki et al., Jpn. J. Appl. Phys. **45**, 323 (2006)
85. Y. Hosokawa, S. Matsumura, H. Masuhara et al., J. Appl. Phys. **96**, 2945 (2004)
86. A. Yamaguchi, Y. Hosokawa, G. Louit et al., Appl. Phys. A **93**, 39 (2008)
87. A.B. Uzdensky, V.V. Savransky, J. Photochem. Photobiol. B Biology **39**, 224 (1997)
88. N.I. Smith, K. Fujita, T. Kaneko et al., Appl. Phys. Lett. **79**, 1208 (2001)
89. H. Hirase, V. Nikolenko, J.H. Goldberg et al., J. Neurobiol. **51**, 237 (2002)
90. N.I. Smith, Y. Kumamoto, S. Iwanaga et al., Opt. Express **16**, 8604 (2008)
91. Y. Zhao, Y. Zhang, X.I. Liu et al., Opt. Express **17**, 1291 (2009)
92. K.T. Tsen, S.W.D. Tsen, C.L. Chang et al., Virol. J. **4**, 50 (2007)
93. K.T. Tsen, S.W.D. Tsen, C.L. Chang et al., J. Phys. Condens Matter **19**, 322102 (2007)
94. R.J. Narayan, C.M. Jin, A. Doraiswamy et al., Adv. Eng. Mat. **7**, 1083 (2005)
95. A. Ovsianikov, S. Schlie, A. Ngezahayo et al., J. Tissue Eng. Regen. Med. **1**, 443 (2007)
96. S. Schlie, A. Ngezahayo, A. Ovsianikov et al., J. Biomed. App. **22**, 275 (2007)
97. F. Claeyssens, E.A. Hasan, A. Gaidukeviciute et al., Langmuir **25**, 3219 (2009)
98. C. Reinhardt, A. Ovsianikov, S. Passinger et al., Proc. SPIE **6466**, M4660 (2007)
99. S. Maruo, H. Inoue, App. Phys. Lett. **89**, 44101 (2006)

Chapter 7
Laser Synthesis of Nanomaterials

Sébastien Besner and Michel Meunier

Abstract We present an overview of the basic principles and applications of laser-based synthesis of nanomaterials. Pulsed laser ablation (PLA) of a bulk solid leads to the formation of nanoparticles having essentially the target composition. When performed in vacuum or in a gas, the ejected clusters may accumulate on a subtrate, thus producing a nanostructured thin film. In liquids, it produces a colloidal solution. Laser interaction with micro/nanomaterials that are embedded in a solid or suspended in either a liquid or a gas is capable to melt and/or fragment the materials and/or induce the formation of new nanostructures and alloys. For these approaches, a detailed description of the mechanisms of laser ablation and nanoparticles growth is given.

7.1 Introduction

There is a growing interest in the fabrication of nanomaterials and in their applications in various fields such as electronics, health care, energy generation, and storage. Nanomaterials, defined as materials having typical dimensions less than 100 nm, present very special physical and chemical properties that strongly depend on their size and shape. Nanostructures having various shapes including a sphere (e.g., nanoparticles, quantum dots) or a cylinder (e.g., nanorods, nanotubes, nanowires) have been investigated. To further tailor their properties, multilayered nanomaterials are also produced to form, for instance, core-shell nanostructures. According to the BCC Research [1], the global market for nanoparticles in biomedical, pharmaceutical, and cosmetic applications has an estimated worth of $204.6 million in 2007. This is expected to increase to over $684.4 million by 2012, corresponding to a compound average annual growth rate (CAGR) of 27.3%.

S. Besner and M. Meunier (✉)
Laser Processing Laboratory, Canada Research Chair in Laser Micro/nano-Engineering of Materials, Department of Engineering Physics, École Polytechnique de Montréal, CP6079, Succ. Centre-ville, Montréal, QC, H3C 3A7, Canada
e-mail: sebastien.besner@polymtl.ca; michel.meunier@polymtl.ca

K. Sugioka et al. (eds.), *Laser Precision Microfabrication*,
Springer Series in Materials Science 135, DOI 10.1007/978-3-642-10523-4_7,

© Springer-Verlag Berlin Heidelberg 2010

Pulsed laser ablation (PLA) of material was first introduced in the 1960s with the apparition of the ruby laser [2]. Since then, PLA has never stopped to attract the attention, and was driven by numerous technological achievements giving rise to new wavelength bands, higher average and peak output power and shorter pulse duration, for example, picosecond (ps), femtosecond (fs), and attosecond laser source. This technique was naturally adopted for material processing as light does not induce any contamination, and is not subject to wear or tear. PLA can bring the material to a very high pressure and temperature state where unique chemistry can take place, giving rise, for instance, to the formation of various oxide, carbide, and nitride compounds. The very high quenching rate resulting from the rapid plasma plume expansion also enables the production of metastable nanomaterials unachievable by any other means. PLA has a very long history in cutting, micro-structuring, and patterning of materials [3, 4], as well as in the production of thin films [5, 6]. It is now being integrated in various biological applications such as dentistry, ophthalmology, and cell treatment [7–9]. During the last decades, numerous papers have been devoted to the production of nanomaterials by PLA in liquids or gases [10–12]. This technique is now translating from an esoteric method to a viable alternative route to the traditional chemical reduction synthesis of nanomaterials in the close-field of colloidal chemistry [13–15].

A comprehensive study of the various laser–matter interactions and the physics of excitation, energy transfer, and relaxation based on numerical simulations has already been given in Chap. 2 of this book. Here, we present an overview of the basic principles and applications of laser-based synthesis of nanomaterials. Section 7.2 reviews the different mechanisms of laser ablation for nanosecond (ns) and ultrafast laser pulses. The thermodynamic properties of the ejected species define the initial conditions for nanoparticles generation. Nucleation and condensation dynamics is the scope of Sect. 7.3. In Sect. 7.4, the formation of thin films and aerosols by laser ablation of a bulk solid in vacuum or gases is described. The formation of colloidal solutions by PLA in a liquid environment is detailed in Sect. 7.5. Finally, we discuss the interaction of the laser with micro/nanomaterials that are embedded in a solid or suspended in a gas or a liquid. In this case, the laser can melt and/or fragment the materials and/or induce the formation of new nanostructures and alloys. This process is described in Sect. 7.6.

7.2 General Principles of Laser Based Synthesis of Nanomaterials

Although the application of PLA is conceptually very simple, this apparent simplicity hides a wealth of complicated material removal mechanisms extending over several orders of magnitude in time. When focused on a solid target, the incoming photons are initially absorbed by the electrons which eventually transfer their energy to the lattice by emission of phonons. Such energy absorption results in either non-thermal (mostly in dielectrics and small nanoclusters) or thermal activated

processes (metals and semiconductors). In this section, we mainly focus on experimental evidences of the laser ablation and plasma formation for absorbing materials, and relate those phenomena to nanomaterial synthesis. The laser ablation mechanisms and the characteristics of the ejected species strongly depend on the radiation parameters (wavelength, pulse duration, and laser fluence). Laser–matter interaction is discussed here for ns and ultrafast (ps and fs) laser pulses.

7.2.1 Nanosecond Pulsed Laser Ablation

In the case of ns laser ablation, material ejection, and nanoparticles (NPs) generation are likely dominated by photothermal processes, which are summarized in Fig. 7.1. The energy deposition is considered to be slow enough to couple with both the electronic and vibrational modes of the target and results in the material heating, melting, and vaporization in the timescale of tens to hundreds of ps. For relatively low laser irradiances ($I < 0.3$–$1\,\mathrm{GW/cm^2}$), the thickness of the ablated layer per pulse is regulated by the thermal diffusion inside the solid, $l \approx 2(D\tau_l)^{1/2}$, where D is the heat diffusion constant and τ_l is the laser pulse duration [3]. In this regime, the ablated mass is mostly ejected in the form of atomic-sized vapor though desorption or thermal evaporation [17].

The vapor plume then expands perpendicularly to the surface and gets further ionized by the incoming radiation. At fluences near the ablation threshold, ionization is normally attributed to the direct heating and can be calculated by the well-known Saha equation [18]. When the laser intensity is higher than the gas ionization threshold, the ion generation is dominated by the optical breakdown phenomenon, and Boltzmann equations are required to estimate the degree of ionization [18, 19]. Ionization greatly influences the condensation dynamic of the plume [16]. It also plays an important role in the plasma absorption through

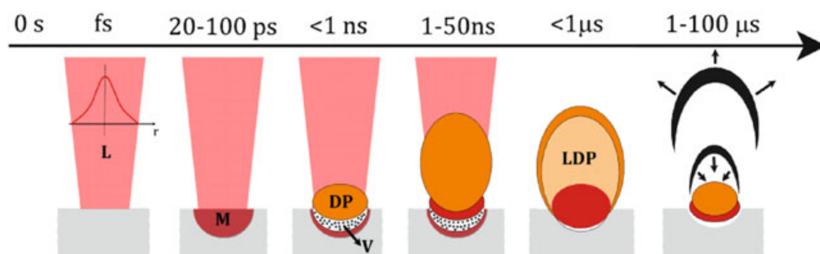

Fig. 7.1 Plasma expansion dynamic during ns PLA in gas (L: laser, M: melt, V: vapor, DP: dense plasma, LDP: low density plasma). In chronological order, this includes photon absorption (occurring over a fs scale during the entire pulse width of the laser), phase change and mass expulsion in both liquid and vapor states (20–100 ps), plasma formation leading to partial absorption in the plume (<1 ns), explosive phase change and plasma heat transfer to the target (1–50 ns), adiabatic expansion, plume splitting followed by rapid condensation (<1 μs), and finally plume detachment and collapse onto the surface (1–100 μs) [16]

the inverse electron-ions Bremsstrahlung mechanism [20]. The plasma shielding is normally much stronger for IR pumping radiation, since this radiation is strongly absorbed through such mechanism. For shorter wavelengths, electron-neutral inverse Bremsstrahlung and photo-ionization also impact the energy absorption by the plasma [21]. It is also shown to increase significantly with the increase of the laser irradiance and with the pulse duration under constant irradiance conditions [21–23]. In vacuum, plasma shielding leads to a saturation of the ablation rate for laser irradiance above 0.5–1 GW/cm^2 [23]. In gas environment, portion of the absorbed energy by the plasma can be transferred to the target due to the air confinement. Such energy transfer induces vaporization of the target material, albeit at a slower rate in comparison to direct laser ablation mechanism [24]. Similar secondary plasma-related and cavitation-related ablation mechanisms are also found during PLA in liquids and are attributed to the strong enhancement of the ablation rate in comparison to air or vacuum ablation [25–27]. However, in this case the ablation rate is found to decrease at fluences above a certain threshold due to the optical breakdown of the water layer surrounding the target [28].

Increase of the laser irradiance above $\sim 10^{11}\,\text{W/cm}^2$ leads to remarkable increase in mass removal, suggesting a major change in the ejection mechanism itself [17, 23, 29–33]. Miotello and Kelly [30–32] have proposed that when the surface temperature approaches the thermodynamic critical point, $T \sim 0.9T_c$, transition to phase-explosion occurs. Phase explosion is a rapid boiling process where the matter undergoes a rapid transition from an overheated liquid to a mixture of vapor and liquid droplets due to great density and entropy fluctuation. However, this interpretation was recently questioned by Lorazo et al. [34], where it is proposed that for ns pulse, the ablation is rather due to a second-order phase transition at the critical point. Whatever the explanation, it is observed experimentally that the mass removal in this regime occurs as a mixture of vapor and large micrometer-size particulates [23, 33]. Other ejection mechanisms such as hydrodynamic sputtering, and exfoliation are also found to be responsible for the production of large droplets and solid flakes during ns PLA [11, 35, 36].

At the end of the laser pulse, a dense plasma with very large temperature and pressure is created due the inertia of confinement. The energetic neutral atoms, ions, particulates, and molten droplets then expand at supersonic velocity due to very large pressures. The later plasma transformation and condensation result in the production of thin films in vacuum and NPs in gas or in water environment. Such processes are discussed in Sect. 7.3.

7.2.2 Ultrafast Laser Ablation

In comparison to ns and longer laser pulses, ultrafast laser ablation provides two major advantages: (1) a net decrease of the ablation threshold for identical laser wavelength and focusing conditions [37] and (2) an important decrease of the heat affected zone leading to much sharper ablated contour [38]. Such characteristics are due to the rapid energy deposition inside the target material. Experimentally,

it is shown that the thermal equilibrium of the electron distribution after excitation with a femtosecond laser pulse takes few hundred fs up to few ps [39, 40]. Thermalization between the electron subsystem and the lattice is usually much longer and is of the order of 1–100 ps, depending on the electron–phonon coupling strength [41, 42]. Thus, ultrafast laser excitation generates an hot electron gas which is highly not in equilibrium with the lattice. Typically, the electron–phonon coupling is also much faster than the heat diffusion. Hence, the melting or ablation depth is be determined by the maximum of the optical and ballistic electron heat penetration depth [43, 44]. For femtosecond laser pulses, the energy deposition is also much shorter than the mechanical relaxation time defined as $\tau_M \sim (L_p + L_e)/C_M$, where L_p is the optical penetration depth, L_e is the electron energy transfer depth and C_M is the speed of the rarefaction wave in the solid target [45]. In other words, the pulse duration is shorter than the time needed to initiate a collective motion of the atoms within the absorbed volume. This results in a very fast heating of the near surface region of the target that can reach a very high temperature at constant density. This sets multiple (T_0, ρ_0) initial conditions as a function of the depth, and the following adiabatic expansion leads in different ablation mechanisms [34, 46]. This dependence is schematically illustrated in Fig. 7.2. In the top layer of the solid, the energy absorption is so high that vaporization occurs. Here, vaporization should not be seen as a thermal desorption process (like in the ns laser case) but, rather, as a rapid "atomization" following the rupture of the atomic cohesion in the solid due to extreme absorbed energy [34]. Such process leads to the expansion of a plume composed of atoms and ions along the normal of the target with very low angular aperture and with velocities ranging

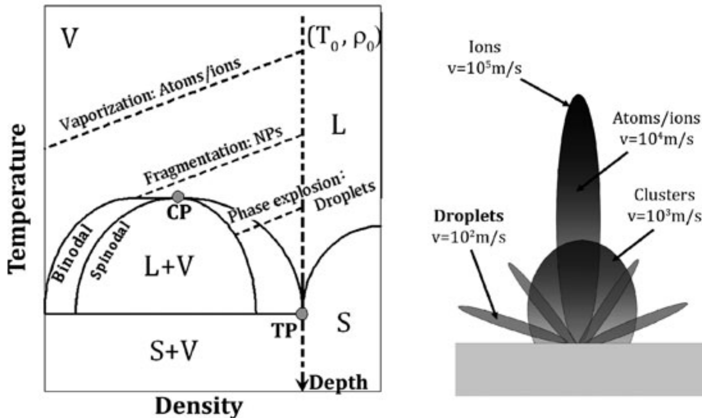

Fig. 7.2 Schematic temperature vs density diagram of the various domain boundaries (S: solid, L: liquid, V: vapor). The binodal defines the liquid–gas mixture domain from a gas or from a liquid. The spinodal defines the boundary of the mechanically unstable region where voids (*bubble*) grow as highly localized perturbations. All different curves represent an adiabatic expansion from (T_0, ρ_0) initial conditions leading to different pathways of the fs laser ablation above threshold. Right image sketches the involved ablated species with their respective angular distributions and velocities. Adapted from [47]

between 10^4 and 10^5 m/s [47–50]. However, vaporization only accounts for a relatively small portion of the total ablated material for laser fluences above the ablation threshold [51]. This first plume is observed whatever the nature of the target and only small variations in the species velocity are obtained [47]. According to molecular dynamic and hydrodynamic simulations, the major part of the ablated species results from fragmentation [52–54]. This process leads to the direct emission of clusters having very distinct propagation and spectroscopic signature. In comparison to the initial fast atomic plume, clusters emission is delayed by few microseconds (μs) and expands with significantly higher angular aperture and reduced velocity ($\sim 10^2$–10^3 m/s) [47, 50, 51]. Furthermore, the structureless continuum emission of this secondary plume observed by optical emission spectroscopy (OES) could be accounted by the Plank's blackbody-like curve for small spherical particles, evidencing the direct NPs ejection [48, 50, 52]. In contrast, OES of the first plume is characterized by strong emission lines of atoms and ions of the target [48, 50, 52]. Interestingly, the NP ejection for femtosecond laser pulse is seen for all laser fluences, while the characteristic OES emission of atoms and ions ejection is only observed when the $F \geq 1.5\ F_{\text{th}}$ [48]. Furthermore, NPs formation during femtosecond laser ablation occurs for all materials, even in vacuum condition where gas phase condensation and coalescence are inhibited [55]. Post-mortem size characterizations have shown that the NPs distribution ranges from few nanometers to 100 nm [47–49, 51, 52, 55, 56]. Deeper into the solid, the initial temperature, T_0, is much smaller and the adiabatic expansion pathway cross the binodal below the critical point. For layers relaxing near the critical point, $T \sim 0.7T_c$, the material removal is dominated by phase-explosion and large droplets are produced. For the deepest layer, tensile stresses can overcome the dynamic strength of the target material and lead to mechanical separation and ejection of material [57]. This phenomenon is also called spallation and should only occur in metals, since ultrafast laser ablation of semiconductors always lead to the formation of a liquid phase [54]. Both processes should give rise to the ejection of larger micrometer-size molten droplets. This third population is observed at much longer time delays (few tens of μs) and is recognized by its very slow expansion speeds ($\sim 10^2$m/s) [47].

As a final result, the femtosecond laser ablation in vacuum leads to three different species (atom/ions, NPs and droplets) that are separated both in time and space and that follow their own transformation and condensation phases. However, in gas or water environments, the smallest species are significantly slowed down due to the collision with the background and all three species eventually overlap in space, giving rise to much stronger interactions.

7.3 Synthesis of Nanomaterials Based on Laser Ablation of a Bulk Target

In a broad picture, the production of nanomaterials by PLA arises from direct ejection of clusters as described previously, as well as from gas-to-particle condensation. The current evidence found in the literature reveals that the final size of the

condensates may vary over four orders of magnitude, extending from a nanometer to few tens of micrometers. Such production strongly depends on laser parameters (which impact the material ejection mechanisms and the initial dynamic of the plume), as well as on the environmental conditions (which significantly influence the thermodynamic and kinetic properties of the plume). Numerous models were proposed for clusters formation in vacuum or low pressure conditions [16, 58–61], atmospheric conditions [62, 63], or water confinement [28, 64]. In comparison to the expansion in vacuum, the interaction of the plume with an ambient gas is far more complex and involves deceleration, attenuation, and thermalization of the ablated species, as well as interpenetration, recombination, formation of shock waves, and clustering [16, 63]. In water, the shock wave generated by the expansion of the laser-induced plasma under liquid confinement pushes the laser-induced plasma into a thermodynamic state characterized by a higher temperature, higher pressure and higher density than that of the initially generated plasma [65,66]. However, independently of the environment, the formation of nanomaterial follows a series of steps which are summarized in Fig. 7.3.

Vaporization (ns pulses) and atomization (fs pulses) of the surface layer account for the major part of atoms and ions ejection. In addition to atoms emission, phase explosion, fragmentation, mechanical exfoliation/spallation, and hydrodynamic sputtering lead to the direct ejection of clusters of various sizes (see Sect. 7.2). The high temperature and density of the ejected material near the target surface lead to a pressure exceeding by many orders of magnitude the background pressure, creating a driving force for vapor expansion. During the following adiabatic expansion, the thermal energy is converted in kinetic energy and the plasma cools down very rapidly. In vacuum, this expansion is roughly linear with time and cooling rates as high as 10^{10-11} K/s and 10^{12-18} K/s can be reached for nanosecond [58, 67, 68] and femtosecond [69, 70] laser pulses, respectively. In confined environments, the plume expansion may be characterized by a free-flight regime (collision-less) until the mass of the plume is comparable to the mass of the external shock wave [71].

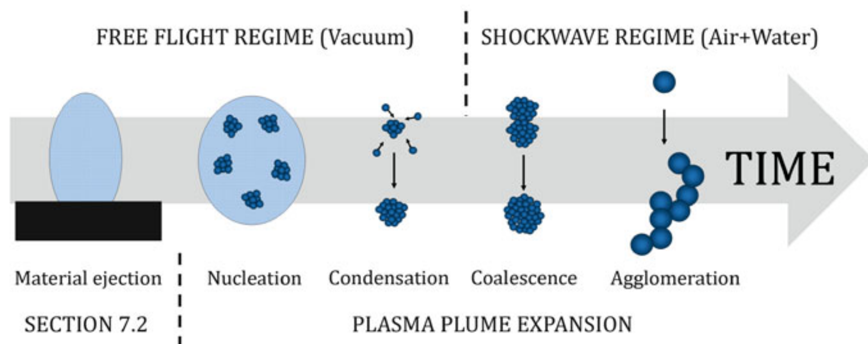

Fig. 7.3 General steps involved in the gas to particles formation during PLA of solid. In a first approximation, the growth mechanisms appear subsequently and separately during the plume expansion. Growth by coalescence and agglomeration is only seen for confined environment, where particle–particle collisions are enhanced

In low-pressure gas, initiation of the drag forces by the background gas starts about 100 ns after the plasma generation [67,72]. The cooling rates then drop to $\sim 10^6$ K/s due to the restricted expansion of the plume [67, 73, 74]. In any case, the extremely fast cooling drives the plasma into a strong oversaturation regime where nucleation is becoming energetically favored.

According to the classical nucleation theory [75], the nucleation barrier to form a spherical condensed cluster of radius r is given by

$$W(r) = -\frac{4}{3}\pi r^3 (n\Delta\mu) + 4\pi r^2\sigma + \left(1 - \frac{1}{\varepsilon_c}\right)\left(\frac{Q^2}{8\pi\varepsilon_0}\right)\left(\frac{1}{r} - \frac{1}{r_a}\right) \qquad (7.1)$$

where $\Delta\mu = kT \ln S$ is the difference in chemical potential between the condensed and uncondensed atoms, S is the saturation ratio, σ is the surface tension, n is the atom density, ε_c is the dielectric constant of the cluster, Q is the ionic charge, and r_a is the radius of the jacketed ions. It accounts for the cohesive forces between atoms in the liquid phase, the energy barrier due to surface tension and the plasma ionization. In a dielectric material, the electric field induced by the ions leads to its polarization. Hence, the charged ions tend to be jacketed by the surrounding polarized vapor atoms. As a result, the nucleation energy barrier is lowered, leading to a higher nucleation rate and a smaller critical radius [16]. This effect is of significant importance as the degree of ionization of the laser-induced plasma, n_i/n_o, can be greater than 10% in typical experimental conditions for pulsed laser deposition or NPs synthesis [16, 76]. The critical radius upon which monotonous growth happens is defined by the maximum of $W(r)$, that is, by $\partial W(r)/\partial r = 0$ and is normally composed of few atoms to few tens of atoms [16, 62]. Such process is called homogeneous nucleation as clusters are formed directly from the vapor atoms. In contrast, if clusters are already present in the vapor plume during the expansion, heterogeneous condensation must be considered. In this case, the already formed nuclei act as condensation center and their role in the later condensation stage becomes dominant. This process is of significant importance, especially for femtosecond laser ablation where most of the matter is ejected in the form of clusters.

Once nuclei are created, the state of matter within the plume is characterized by a two-phase liquid–vapor system. The degree of condensation is governed by the degree of supersaturation and increases with both the formation of new nuclei and the growth of pre-existing clusters. In the condensation regime, the growth of clusters is kinetically controlled and stops when the collisions between the clusters and the vapor atoms become negligible in the expanding vapor plume. In vacuum, the condensation stops in less than 1 μs and results in the production of nanoclusters smaller than 1 nm [62]. In this case, additional growth by coalescence is normally quenched due to the rapid expansion, leading to a fast decrease of the cluster density. However, in gas or water environments, the condensed clusters are confined at the front part of the plasma plume and interact for a much longer time. Particles collisions and coalescence lead to a reduction of the total number of particles and to an increase of the average size. Coalescence in a vapor–liquid system occurs spontaneously as

the reduction of the total surface area during this process corresponds to a reduction of the Gibbs free energy. Hence, under the assumption that the nanodroplets and the plasma follow the same temperature, coalescence continues until the plasma temperature reaches the melting threshold of the material. This time occurs few ms after the end of the laser pulse [77]. The solid NPs then aggregate due to the Van der Waals interaction and electrostatic forces, to form larger agglomerates composed of much smaller, round, primary particles. The formation of aggregates is a characteristic feature of the laser synthesis of NPs in gases or in liquids if no stabilizing agent (SA) is added to the environment [10, 11].

7.4 Laser Ablation in Vacuum/Gas Environment

The use of PLA in vacuum or low background gas as a direct source for film growth has been explored since the discovery of the laser in the 1960s [5]. However, the popularization of this method occurred only in the late 1980s with the successful production of in situ epitaxial high-temperature superconducting oxide thin films [6]. Pulsed laser deposition (PLD) is now established as one of the simplest, cheapest, and more versatile methods of depositing thin films of a very wide range of material, including insulators, semiconductors, metals, polymers, and "soft" biological materials. It has also been the subject of many books and reviews [5, 6, 76]. The growth of the film generally requires the delivery of a growth flux with adequate stoichiometry in a background gas which is favorable to the desired phase formation. The introduction of reactive gases (e.g., O_2 and N_2) also enables the generation of very complex oxides or nitrides thin films. In this area, great effort has been made to increase the film quality by reducing the droplet density [6, 78–81] and subsurface damage [82, 83]. PLD of epitaxial smooth films is, however, outside the scope of this chapter and we refer the reader to the above-mentioned books for more details.

At sufficiently large background pressure (typically $>10^{-1}$ Torr), the homogeneous nucleation in the ablated plume results in the production of nanoclusters. The onset of NPs formation after the laser pulse is visualized using laser-induced fluorescence imaging and Rayleigh scattering [84]. Ex-situ transmission electron microscopy (TEM) or atomic force microscopy (AFM) of the NPs formed during the laser ablation process also provide key information. Investigation of semiconducting nanostructures such as SiO_x, ZnO_x, and the study of their photoluminescence as a function of the nanoclusters size and oxidation state are reported in the literature [84–87]. Synthesis of nanostructured metallic film is also investigated [88–90]. Most of these studies reveal a monotonous increase in the cluster size and film porosity with the increase of the ambient gas pressure [83, 86], although more complex pressure and target distance dependence is also noted [91, 92]. The flow pattern, the spatial cluster distribution and the cluster size distribution also depend on the mass of gas-phase atoms [84, 93]. At constant pressure, the clusters size typically increases using heavier gas atoms or molecules. Different authors have also reported

efficient size control by changing the laser fluence. An increase in the laser energy normally gives rise to higher average grain size, packing density, and cluster size [58, 94]. Theoretical and experimental comparison has also shown that the initial density profile of the ablated plume profoundly modifies the final size distribution of the NPs [59].

Nanosecond and femtosecond pulsed-laser ablation in gas or vacuum also possess very distinctive characteristics. Multiple diagnostic methods such as Langmuir probe, optical emission spectroscopy, and fast time-resolved imaging revealed significant difference in the ejected species and plasma properties [70, 82, 95–101]. Under the same film growth rate, nanosecond laser pulse produces a greater concentration of neutral and low energetic species in comparison to femtosecond laser pulses [101]. The ablated plasma plume is also much narrower for femtosecond laser pulses [82, 95]. Furthermore, experimental results show that the generation of NPs is a characteristic feature of the ultrashort laser pulses ablation even in high vacuum [55]. Decrease of the pulse duration from 500 ps to ~25ps results in the increase of the nanoclusters size from 1.5 to 7.5 nm [102]. Further decrease of the pulse duration has only small effect in the cluster formation [103]. However, the increase of the pulse energy results in the increase of the cluster size. Size is varying in the range of few nanometers to few tens of nanometers as the intensity increases from 10^{11} to 10^{13} W/cm^2 [103]. Multiple pulses experiments result in much larger particles, indicating a strong coalescence of the impacting particles on the substrate [47]. Hence, for the majority of materials, the films produced by ultrafast laser ablation consist of random stacking of NPs in the size range of 1–100 nm. Fs PLD is now applied as an efficient route for the synthesis of semiconducting, metallic, as well as insulating nanostructured films [6,47]. The production of atomically flat thin films using ultrafast spatially shaped pulses and/or use of low energetic short-pulses at MHz repetition rate has also been demonstrated [6, 104].

PLA under atmospheric conditions is primary used for analytical detection techniques such as laser-induced breakdown spectroscopy (LIBS) or laser ablation inductively coupled plasma mass spectrometry (LA-ICP-MS). Under ICP laser ablating conditions (few J/cm^2 to few tens of J/cm^2), NPs distribution is usually bimodal. The mean diameter of the smaller portion is around some 10 nm and the largest part has a mean diameter of few microns. Furthermore, the NPs usually form larger aggregates, as no repulsion mechanism is provided to limit particles collision in the gas environment. Hence, significant efforts are currently made for the development of efficient flow cell to separate the NPs of different sizes and to limit the aggregation of the aerosol. A very interesting review on LIBS and LA-ICP-MS can be found in the literature [11]. Few articles on the synthesis and characterization of NPs produced under such conditions have also been published [10, 105]. However, the use of laser ablation under atmospheric conditions is of limited interest for nanomaterial synthesis due to the poor control of the NPs size produced and their complicated collection. For such application, PLA in liquids has proven to be much more efficient and is the scope of the next section.

7.5 Laser Ablation in Liquids: Formation of Colloidal Nanoparticles

Colloidal solutions are usually produced by a wet-chemical technique where some precursors (e.g., metal salts, metal carbonyls, molecular precursor, etc.) are reduced or decomposed to produce solvated atoms which then nucleate and grow to form NPs inside the solution. Such techniques use various chemical steps involving most of the time non-biocompatible chemical products. While the chemical approach has been quite successful for producing a large variety of nanomaterials, there are some limitations in terms of composition, crystalline state and surface contamination [13]. Laser based techniques offer alternative approaches to produce nanomaterials in a clean environment and biocompatible chemistry [106–108]. Furthermore, the laser matter interaction offers the advantage to produce unique nanomaterials and nanostructures of composition difficult to synthesize by conventional chemical means [12]. A variety of metallic NPs including Au [106–119], Ag [106, 120–129], Cu [106], Pt [106, 130–133], Ni [109, 134], Co [134], and semiconducting NPs including Si [135], CdS [136, 137], ZnSe [137], InP [138] have been produced by PLA of the respective target in liquids. Furthermore, various oxides (FeO [139], ZnO [140–142], TiO_2 [143, 144]), nitrides (C_3N_4 [145], BN [146]), and chlorides $AuCl_3$ [147] can be synthesized through chemical reactions between the energetic plasma plume and the solvent.

7.5.1 Ablation Mechanisms

Despite the fact that NPs fabrication and collection is relatively straightforward in practice, the technique involves many complex phenomena which are depicted in Fig. 7.4. In all experiments, the radiation is coupled to the target surface by focusing a laser beam through a liquid layer. The wavelength is usually chosen to be transparent to the liquid environment. For transparent liquids, this condition is generally satisfied by using lasers emitting in the visible or near infrared region. However, when the laser power density is sufficiently high, optical breakdown of the liquid layer occurs and the resulting plasma absorbs and scatters a portion of the incoming light. The energy balance of the optical breakdown in water reveals that the energy loss is at least one order of magnitude larger for nanosecond laser pulses in comparison to ultrashort (ps and fs) pulses [27]. This energy loss is also found to increase as the pulse energy and the focusing angle increase [27]. The presence of such breakdown plasma during typical nanosecond laser ablation in water is evidenced by ns time-resolved shadowgraphs and is shown in Fig. 7.4b [148]. Furthermore, the ablation rate is found to increase significantly with the use of slightly defocused radiation [106, 111, 112]. In such conditions, the sound emitted during the ablation and the plasma intensity on the target surface are at their maximum, indicating a much better coupling of the radiation energy to the surface. Hence, optical

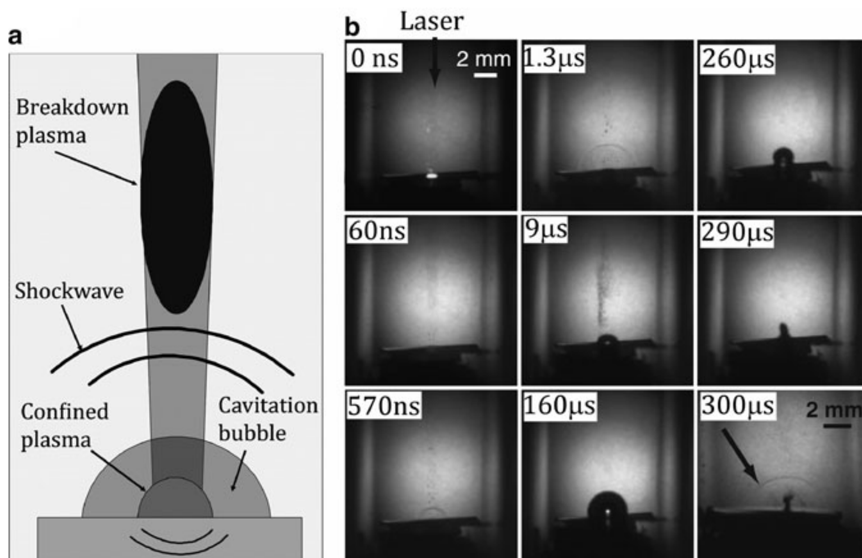

Fig. 7.4 (**a**) Schematic representation of the phenomenon involved during PLA in liquids. (**b**) Time-resolved shadowgraph images of the laser ablation process for a silver plate in water. From Tsuji et al. [148], used with permission from The Japan Society of Applied Physics

breakdown directly competes with the material ablation and must not be disregarded in pulsed laser ablation in liquid (PLAL). Secondary absorption and scattering by the NPs in solution also decreases the efficiency of the PLAL [28, 113, 121]. Laser interaction with the colloids also induces significant changes in the size, shape and chemical composition of the NPs and will be the scope of the Sect. 7.6.

The remaining part of the laser energy then interacts with the target and induces an ablated plasma plume. This plasma adiabatically expands at a supersonic velocity and creates a shockwave under the confinement of the liquid [66, 149, 150]. Then, the shockwave produces an extra pressure and temperature increase in the plasma plume. The plasma pressure involved in typical ns PLAL ranges from 1 to 10 GPa for pulse duration between 1 and 10 ns and laser irradiance between 1 and 10 GW/cm^2 [149, 150]. Literature on laser-induced shockwave in water is vast due to the great potential of laser shock peening to improve fatigue and corrosion properties of metals [151]. The plasma pressure and related shockwave are shown to vary with the laser irradiance [66], the laser wavelength [149], the thickness of the water layer [26], and on the focusing condition [111]. Unfortunately, laser shock peening applications focus on the structural modification of the target and thermodynamic properties of the ablated part are normally not measured. No data is yet available for the plasma properties generated by ultrafast pulses and only limited studies were dedicated to the measurement of the plasma temperature and density for nanosecond laser pulses. The initial plasma temperature is estimated to $\sim 10^4$ K during nanosecond pulse laser ablation in water and n-hexane [152, 153]. The temperature then drops to $\sim$3,600 K within 1 μs [152]. Plasma expansion is also much

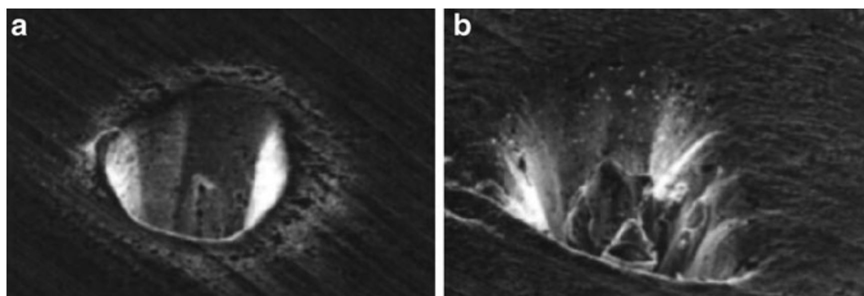

Fig. 7.5 Typical craters formed (**a**) at low and (**b**) high laser fluence during femtosecond laser ablation in water. High fluence ablation is characterized by strong coupling of the plasma with the target surface. From Kabashin et al. [114], used with permission from the Journal of Applied Physics

smaller in comparison to the expansion in air or vacuum [154]. Time-resolved images of the plasma plume indicates that the thickness of the plasma above the target surface ranged between 50 and 70 μm for pulse durations between 20 and 150 ns [155]. Such confinement results in an extremely high density which is typically of the order of 10^{19}–10^{21} cm^{-3} [152, 153]. Furthermore, in comparison to the laser ablation in air, the plasma lifetime is 10 times shorter in water for similar irradiating conditions [153]. Hence, the rapid quenching time of the plasma plume would limit the growth of the particles.

The plasma formation is found to profoundly impact the ablation rate, as well as the NP size for both nanosecond [26, 122] and femtosecond laser pulses [111, 112, 114]. As shown in Fig. 7.5, the craters formed during femtosecond laser ablation of gold significantly differ at low and high laser fluences. When a low laser fluence (<60 J/cm^2) is used, the plasma formation is inhibited and craters with sharp edges are formed. In contrast, at higher laser fluences (>150 J/cm^2), the confined plasma plume and the plasma generated by the optical breakdown produce severe thermal damage of the target surface. In the case of ns PLAL, plasma-induced thermal damage always occurs since the plasma is excited to much higher energetic states by inverse Bremsstrahlung absorption of the end part of the pulse [123]. Hence, heat transfer of the plasma to the target surface should be responsible for additional material removal. This secondary plasma etching should occur only during the first 100 ns, since the plasma pressure abruptly decreases after this time [66, 148].

In addition, the plasma expansion in liquid is accompanied by the production of bubbles, formed as a result of the liquid vaporization on contacting with the hot plasma. These bubbles quickly merge to form a single larger bubble, known as the cavitation bubble. Its radius and lifetime are found to be dependant of the laser energy, beam waist, target thickness, and on the solvent density [124, 148, 156]. For example, when a low energy radiation ($E = 20$ mJ, $\lambda = 1,064$ nm, $\tau = 8$ ns) is focused on the target surface ($\omega_0 = 200$ μm), the cavitation bubble collapses after ∼250 μs after reaching a maximum radius of 2 mm [148]. In contrast, by using a much more energetic pulse ($E = 200$ mJ, $\lambda = 532$ nm, $\tau = 7$ ns) with a larger spot size ($\omega_0 = 1.1$ mm), the cavitation bubble reaches a maximum radius of 5 mm and

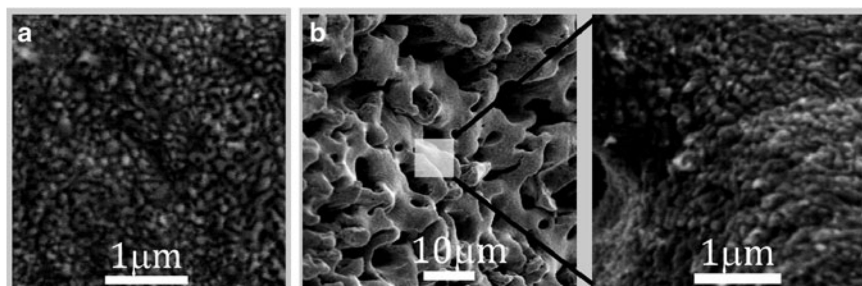

Fig. 7.6 Surface morphology of the gold surface after fs PLAL. (**a**) One surface scan (∼5 pulses/spot) and (**b**) 10 surface scans (∼50 pulses/spot). In both cases, electron microscopy indicates the presence of nanostructures in the range of 60–150 nm which may be ejected due to the secondary shockwave

collapses only after 800 μs [156]. The same studies also reveal that a secondary shockwave is generated upon the collapse of the cavitation bubble [148, 156]. The generation of a second shockwave indicates that impulsive high pressure is induced on the target surface and may result in a third round of material ejection. A careful analysis of the target surface after the 800 nm fs PLAL shows that the process leads to a rapid surface nanotexturation followed by the formation of micron size peaks and valleys (Fig. 7.6). In the two structural regimes, a close analysis of the peaks by electron microscopy reveals the presence of nanostructures in the range of 60–150 nm which may be ejected by the secondary shockwave caused by the cavitation bubble collapse. Similar surface corrugation is also noted for nanosecond laser pulses and would lead to the same shockwave etching process [123, 133]. However, the contribution of this third material ejection should be small in comparison to the direct laser ablation and secondary plasma etching. Indeed, the pressure involved during the collapse of the cavitation bubble is 3–4 orders of magnitude smaller than the pressure involved during the initial plasma expansion. A complete mass analysis (in contrast to the traditional TEM particles size frequency analysis) would however be necessary to estimate the real importance of this third process.

7.5.2 Effect of Laser Parameters

The size of particles produced by PLAL usually varies between few nm and few hundreds of nm. The full prediction of the NP size would require the complete determination of the plasma density, pressure and temperature, as well as the full particle–particle interaction during the later cavitation phenomena. However, the liquid confinement in PLAL makes direct diagnostics of such thermodynamic properties very challenging. Furthermore, the strong interaction of the ejected species in the liquid eliminates evidence of the primary ejection mechanism and only secondary processes are generally observed. Nevertheless, the general trends in

the NP formation mechanisms may be concluded through the large collection of experimental data. First, an increase of the mean size of the particles is encountered with the increase of the laser fluence for most materials [111, 114]. Similar increase in NP size is found when defocused radiation (i.e., larger beam size) is used [111, 112, 122]. In fact, those parameters greatly influence the thermodynamic properties of the plasma and cavitation bubble. Increase of the laser fluence and beam size increase the production rate of the NPs [28, 108, 111, 112, 125, 130, 132]. Thus, the local concentration of ablated species increases sharply with such parameters due to the liquid confinement. The plasma intensity and the intensity of the acoustic wave are also enhanced in such conditions and relate to a higher plasma temperature and pressure. Moreover, the longer duration of the cavitation bubble at higher pulse energy and larger beam waist would promote the formation of bigger particles by coalescence [148, 156]. Further growth by diffusion and coalescence in the liquid solution may also increase the mean size of the particles, but at a much lower rate [130]. Hence, this process cannot contribute significantly to the strong modification of the NPs size with the variation of the laser parameters. Thus, we reason that most of the growth occurs inside the cavitation bubble during the first 0.1–1 ms following the end of the pulse.

The same arguments would also explain the smaller size usually achieved by using an ultrafast laser [107, 114, 123]. Indeed, the number of ejected species per pulse is much lower for fs laser pulses in comparison to ns pulses. Typically, the number of ejected atoms per pulse with the use of nanosecond laser is of the order of 10^{14}–10^{15} [28, 122, 153], while for femtosecond laser pulses, it ranges between 10^{12} and 10^{13} as the laser energy is increased from 100 to 500 μJ [108, 111]. The overall production rate is however compensated with the higher repetition rate of the laser source (1 kHz vs. 10 Hz). Furthermore, the fs pulse ends long before the beginning of the plasma expansion, leading presumably to a reduced plume and cavitation bubble lifetime. Thus, the growth of nuclei becomes accordingly shorter, yielding to the production of smaller particles. Similar decrease in size is also encountered with the use of lasers having shorter wavelengths [126, 132]. This observation may be explained by two reasons. First, the reduction of the laser wavelength decreases the absorption of the plasma through inverse Bremsstrahlung [21]. Hence, the plasma and associated cavitation bubble lifetime should be shorter and the NP growth period would be accordingly shorter. Furthermore, the secondary interaction between the laser and the produced NPs increases with the decrease of the laser wavelength. This secondary interaction results in the size reduction of the colloid through laser induced fragmentation, a phenomenon discussed in details later [121, 126].

7.5.3 Effect of Stabilizing Agents

The growth scheme radically changes when stabilizing agents are added to the liquid environment. Introduction of salts [115, 127], surfactants [28, 110, 124, 128, 130, 134], and various biocompatible molecules [107, 108, 112, 115–119] prior to the ablation process is found to profoundly alter the final size distribution of the

NPs for fixed laser parameters. In all cases, the increase of the SA concentration leads to a decrease of the mean size of the particles. For example, the addition of 0.01 M of sodium dodecyl sulfate to a water solution results in the narrowing of the size distribution from 2–50 nm to 1–12 nm during ns PLAL [113]. The same effect is also noted during fs PLAL where the addition of 10 mM of β-cyclodextrin led to a decrease of the mean size from ∼55 to 2 nm [107]. Furthermore, all experiments evidence a saturation of the size reduction for highly concentrated SA solutions. In those conditions, the size of the NPs ranges between 2 and 10 nm and does not change significantly with laser parameters (wavelength, fluence, pulse duration, and focusing conditions). Typical size distributions achieved during femtosecond laser ablation in various concentration of SA aqueous solution are given in Fig. 7.7. From a chemical point-of-view, the interaction between the SA and the species in the plasma is improbable, since the high temperature and pressure would degrade the chemical compound. However, no degradation product is found during the nanosecond laser ablation of silver in phtalazine solution [129], neither during femtosecond laser ablation of gold in β-cyclodextrin solution [107]. The presence of organic SA inside the plasma would also form carbides through chemical interaction with the ejected species. Again, such compounds are not witnessed by X-ray photoelectron spectroscopy characterization of the NPs, for example, unpublished results for dextran, polyethylene glycol, and α, ω-dithiol poly(N-isopropylacrylamide) aqueous solutions. See also [135]. The influence of the SA would, therefore, only start when the plasma has sufficiently cooled down, quenching only the later growth by coalescence of the particles.

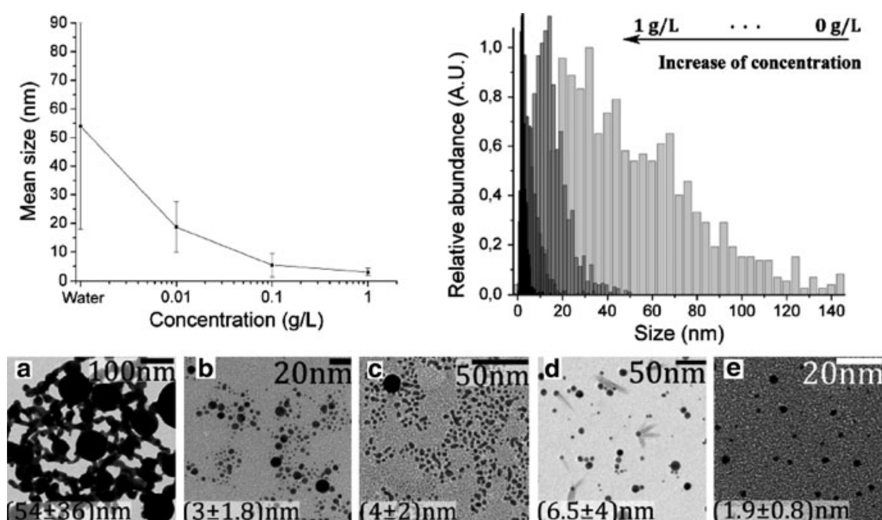

Fig. 7.7 *Top panel*. TEM histograms and mean size variation of gold produced in various concentration of dextran solution. The error bars represent the standard deviation of the NPs population. *Bottom panel*. TEM images of gold NPs produced in (**a**) water, (**b**) 1 g/L dextran (MW = 40 kDa) (**c**) 5 mM β-cyclodextrin (**d**) 1 g/L chitosan (MW = 10 kDa), (**e**) 1 g/L α, ω-dithiol poly(N-isopropylacrylamide) (MW = 10 kDa)

7.5.4 Process Model

The NP formation process may be considered as an ensemble of distinct and subsequent steps which are summarized in Fig. 7.8. First, the laser energy is deposited at the interface between the target and the confining medium and generates a plasma. The plasma induces two shock waves which propagate inside the solid and the liquid medium. These waves open an interface between the solid and the liquid and most of the material is subsequently ejected in a region depleted in liquid atoms. This phenomenon is confirmed by molecular dynamic simulations of femtosecond laser ablation of a wet solid [157]. The highly excited ejected species forming the plasma stay in close proximity of the target surface due to the liquid confinement [155]. During the first hundred of ns, the energy transfer to the target should be strongly enhanced due to the extremely high plasma pressure involved and should lead to a secondary plasma-related ablation. The material ejected by direct laser ablation and by the secondary plasma etching are essentially indistinguishable and should follow the same growth mechanisms. Both processes should lead to the ejection of atoms or very small clusters (<1 nm). Indeed, molecular dynamic simulation reveals that the presence of the surrounding liquid inhibits phase explosion, which is the main cause of large cluster ejection [157]. Furthermore, no significant change is observed in the final size distribution of the particles produced at low and high laser fluence when SA is added to the solution. The laser and plasma ablated species are then experiencing a fast decrease of their temperature due to their expansion and to the thermal contact with the solvent. The confined vapor enters in a strong supersaturation regime and homogeneous nucleation starts. Nucleation and growth through condensation is expected to occur for approximately 1 μs, time at which the plasma temperature reaches ~2 times the material melting point [152, 158]. At the end of this period, most of the material is compressed in a thin shell at the plasma–liquid interface. It is in this region that coalescence of the initial nuclei should arise. As in ablation in air, strong temperature gradient should be seen in this layer, leading to different solidification times and widened size distribution. Note also that the two first growth phases (i.e., nucleation/condensation and coalescence) are accompanied by the vaporization of the liquid layer which is contacting with the hot plasma. Hence, most of the growth by coalescence should occur inside the cavitation bubble and be enhanced by the strong pressure involved in this cavity.

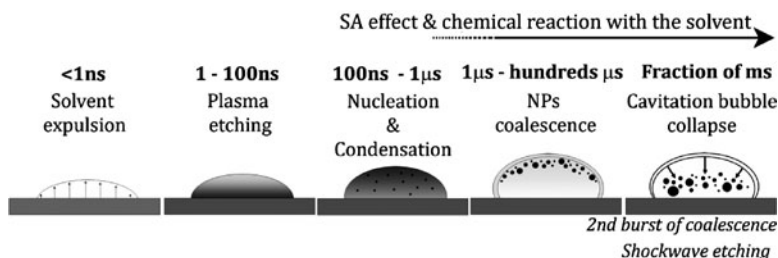

Fig. 7.8 NPs formation steps involved in PLAL. See text for full description

The first growth by coalescence, up to the melting point of the particles, would be the same for the laser ablation in either pure solutions or in solutions containing SA. However, once NPs resolidify, the SA action takes place and competes with the NP growth. The surface coverage by the SA should happen very quickly after the resolidification process as the smallest particles achieved by laser ablation in liquid are in the range of 2–4 nm (∼200–2,000 atoms) [107, 113, 130]. This would also mean that the initial growth steps by nucleation and condensation result in the production of very small clusters. This is in contradiction with the kinetic model proposed by Yang which predicts the formation of 40–200 nm NPs from the nucleation and condensation processes [64].

In pure solution, the growth by coalescence and aggregation continues for the complete duration of the cavitation bubble. It would also be amended due to an increase of the cluster temperature and density during the collapse of the cavitation bubble. Actually, the violent collapse of the cavitation bubble created hot spots of thousands of Kelvin within the bubble in ultrasonic cavitation [159]. Similar increase in the temperature would also occur for laser-induced cavitation, leading to a second burst of nucleation by coalescence. Then, the secondary shockwave associated with the collapse will (1) expel the NPs from the surface region and (2) cause a third round of material ejection by pressure etching. Finally, growth in solution and from plume to plume interaction could also result in the size increase of the NPs, especially in low volume and stagnant solution. Chemical interactions between the ejected species and the solvent can also result in the production of new compounds such as oxides, carbides, and halides [139–146]. In such cases the addition of a surfactant, such as sodium dodecyl sulfate, was able to slow down or stop the oxidation of Zn particles in water [140]. Hence, both capping action and chemical reaction should mainly happen during the late stage of the plasma condensation at the solvent–plasma interface and during the later growth in the cavitation bubble as the action of surfactant on NPs growth is very improbable in the initial plasma expansion step.

7.6 Synthesis of Nanomaterials Based on Laser Interaction with Micro/Nanomaterials

The laser interaction with micro/nanoparticle changes profoundly the characteristics of the particles incorporated in a solid or suspended in a gas, or in a liquid environments. In solids, most of the studies are related to the interaction of the laser light with plasmonic noble metals. In such treatment, the laser light excites the plasmon of the particles which results in the formation of NPs with specific size [160, 161] and shape [162] by choosing appropriate laser fluences and wavelengths. In gases, the laser ablation of microparticles (LAM) significantly increases the production rate of nanoscale aerosol in comparison to the direct laser ablation. Nichols et al. [163] have demonstrated that a production rate as high as 20 g/h could be achieved using this approach. Formation of alloys [164, 165] and core-shell NPs [166] have also

been reported by the irradiation of a mixture of aerosol. Furthermore, by impacting the NPs produced by the LAM process onto a substrate, nanostructured thin films can be produced [94]. In this section, we mostly discuss the interaction of the laser radiation with micro/nanoparticles in liquids (i.e., colloids), as the investigation is much more mature in this area. However, the mechanisms should be valid for the other media, keeping in mind the different thermal diffusivity and NP mobility.

As in the case of gases, laser-induced microparticles fragmentation has also been reported for colloidal solutions. Again, this process leads to an increase in the production rate in comparison to the laser ablation but to a lesser extent due to the finite solubility of NPs in various solvents [167–171]. Laser interaction with NPs has also been studied thoroughly. Laser-induced fragmentation [172–179], growth [119, 180, 181], and reshaping [182–184] can be achieved by tuning the laser parameters properly. The formation of alloys [169, 185–188] and core-shell structure [168] is also achievable by irradiating a mixture of colloidal solution. In general, the produced NPs after a secondary irradiation treatment exhibit a much narrower size distribution in comparison to the initial product made by the direct laser ablation process. As shown in Fig. 7.9, fs supercontinuum laser-induced fragmentation (LIF) enables the production of NPs with size ranging between few nanometers to few tens of nanometers with a coefficient of variation of the order of 15–20% [108, 175, 177]. In LIF, the laser brings the NPs to a temperature much greater than their vaporization threshold. For identical laser parameters and chemical environment, the mean size of the gold NP increases with the gold concentration. It also increases with the decrease of SA concentration for similar laser parameters and gold concentration. Hence, the final size of the NPs in the LIF process is mainly determined by the equilibrium between the fragmentation rate governed by the laser parameters and the coalescence rate controlled by the gold and SA concentrations. In laser-induced growth (LIG) process, the laser irradiance is normally much smaller

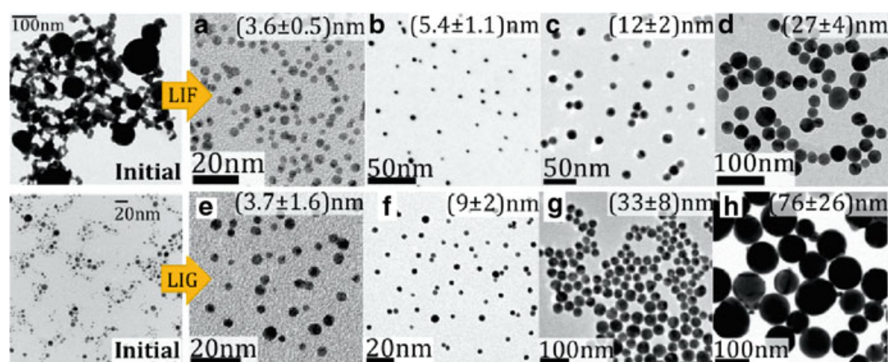

Fig. 7.9 *Top panel*. Fs white-light supercontinuum LIF ($F = 25\,\mathrm{J/cm^2}$) of gold NPs in aqueous dextran (D) solutions (**a**) [Au] = 0.08 g/L; [D] = 1 g/L, (**b**) [Au] = 0.12 g/L; [D] = 1 g/L, (**c**) [Au] = 0.17 g/L; [D] = 1 g/L, (**d**) [Au] = 0.2 g/L; [D] = 0.1 g/L. Bottom panel. Fs white-light supercontinuum LIG ($F = 1.2\,\mathrm{J/cm^2}$) of gold NPs at various dextran to gold molar ratio (R) (**e**) $R = 0.16$, (**f**) $R = 7 \times 10^{-3}$, (**g**) $R = 2 \times 10^{-3}$, (**h**) $R = 2 \times 10^{-4}$. From Besner et al. [119], used with permission from the Journal of Physical Chemistry C

in comparison to the one used in LIF processes. As shown in Fig. 7.9, fs white-light supercontinuum LIG of small seeds allows the formation of 4–80 nm NPs when lower pulse energy and smaller numerical aperture are used [119]. Here, the final size is found to depend exclusively on the gold to SA molar ratio when the laser brings the NPs to a temperature between their melting and vaporization thresholds.

In the literature, such laser-induced NPs modifications are associated either with thermal or non-thermal mechanisms. Takami et al. [173] propose a heating–melting–evaporation model to explain the reshaping and size decrease observed in unfocused nanosecond laser irradiation of gold nanocolloids. This model is corroborated by numerous groups using nanosecond [184], picosecond [174] and femtosecond laser pulses [119]. Nichols et al. [189] also demonstrate that the vaporization process is accompanied by a secondary breakdown-induced shockwave NPs formation for particles much larger than the laser skin depth. This contribution is found to significantly increase with the laser fluence, leading to the fractionation of microscale aerosol into very small NPs (3–6 nm). In contrast, Kamat et al. [172] conclude from ps photo-absorption spectroscopy that the size reduction observed with 355 nm unfocused ns irradiation is due to the Coulomb explosion of the photoionized Ag NPs. Later, Mafuné et al. [178] show from the transient absorbance of the solvated electron that the nascent charged state of 8 nm gold NPs irradiated by focused 355 nm ns radiation could be as high as 710, confirming the possible existence of Coulomb explosion. In fact, the two mechanisms should occur in different regimes. The use of a high irradiance and short wavelength favor the NP fragmentation through the Coulomb explosion, while a milder laser irradiation contributes to photothermal pathways. The observed processes are also greatly dependent on the size of the particles. Hence, in laser-micro/nanoparticle interaction, the analysis should be done in terms of number of photon per atoms (or electron), instead of laser fluence [184, 190]. If the transmitted photon energy during the electron dephasing time (photoionization) or during the electron–phonon coupling time (thermionic emission) is much smaller than the electron work function of the material, then photothermal pathways should be responsible of the NPs fragmentation [184]. In the other case, Coulomb explosion must be considered. For gold NPs, theory predicts a dominant electron ejection by thermionic emission [191]. The size of the resulting fragments is also found to decrease with the increase of the charged state [179]. However, independently of the laser-induced NPs modification mechanisms, the final size distribution reflects the equilibrium between the fragmentation rate and growth rate of the NPs in solution. Such rates are controlled by the modification of the laser parameters and the addition of SA and enable the production of much narrower NPs size distribution in comparison to direct laser ablation.

7.7 Conclusions and Perspective

Laser synthesis of nanomaterials has been the subject of intensive research during the last 20 years. The low selectivity of the laser ablation enables the production of a variety of complex materials. In such process, the key for obtaining NPs

with specific size, shape, and composition is to control the plasma thermodynamic properties which govern the nucleation and condensation, as well as the later growth of the particles through coalescence and agglomeration mechanisms. This control is provided by choosing appropriate laser parameters and chemical environment. The large collection of theoretical and experimental data now available allows the prediction of the final NP characteristics. Furthermore, in comparison to the other chemical synthesis techniques, the NPs can be produced in a clean, well controlled environment. The generation of ultrapure and size-controlled NPs will have significant impact in biological applications, as well as in catalysis. The main goal is now to produce larger gram scale quantities of nanomaterials with the same control achieved in the lab scale production. This challenge would surely be accomplished by the further development of the ablation of micro/nanoparticles in gas or water environment.

Acknowledgments The authors would like to thank collaborators who have contributed in our research efforts in this field, in particular Dr. Andrei V. Kabashin and Dr. Jean-Philippe Sylvestre from École Polytechnique de Montréal (EPM). We also thank David Rioux, Paul Boyer, and Etienne Boulais from EPM for fruitful discussions. This work was supported by Canada Research Chair on Laser micro/nanoengineering of materials and the NSERC (Natural Science and Engineering Research Council) of Canada.

References

1. BCC Research, *Nanostructured Materials for the Biomedical, Pharmaceutical, & Cosmetic Markets*, **NAN017D** (2007)
2. T.H. Maiman, Nature **187**, 493 (1960)
3. D. Bäuerle, *Laser processing and chemistry*, 3rd edn. (Springer, Berlin, 2000)
4. J.F. Ready, D.F. Farson (eds.), *LIA handbook of laser materials processing*, 1st edn. (Laser Institute of America; Magnolia Publishing, Orlando, FL, 2001)
5. D.B. Chrisey, G.K. Hubler (eds.), *Pulsed laser deposition of thin films*, 1st edn. (Wiley, New York, Toronto, 1994)
6. R. Eason, *Pulsed laser deposition of thin films: applications-led growth of functional materials*, 1st edn. (Wiley, Hoboken, NJ, 2007)
7. M.H. Niemz, *Laser-tissue interactions: fundamentals and applications*, 2nd rev. edn. (Springer, Berlin, 2002)
8. M. Braun, P. Gilch, W. Zinth, *Ultrashort Laser Pulses in Biology and Medicine*, 1st edn. (Springer, Berlin, 2008)
9. P.N. Prasad, *Introduction to biophotonics*, 1st edn. (Wiley, Hoboken, NJ, 2003)
10. A.V. Kabashin, M. Meunier, in *Recent advances in laser processing of materials*, ed. by J. Perrière, É. Millon, É. Fogarassy (European Materials Research Society: Elsevier, Amsterdam, 2006), p. 1
11. R. Hergenroder, Spectrochim. Acta B **61**, 284 (2006)
12. G.W. Yang, Prog. Mater. Sci. **52**, 648 (2007)
13. O. Masala, R. Seshadri, Ann. Rev. Mater. Res. **34**, 41 (2004)
14. Z.Y. Zhong, K.B. Male, J.H.T. Luong, Anal. Lett. **36**, 3097 (2003)
15. J.A. Dahl, B.L.S. Maddux, J.E. Hutchison, Chem. Rev. **107**, 2228 (2007)
16. M.S. Tillack, D.W. Blair, S.S. Harilal, Nanotechnology **15**, 390 (2004)
17. J.H. Yoo, O.V. Borisov, X.L. Mao, R.E. Russo, Anal. Chem. **73**, 2288 (2001)
18. G. Bekefi, *Principles of Laser Plasmas*, 1st edn. (Wiley, New York, 1976)

19. A. Takahashi, K. Nishijima, Jpn. J. Appl. Phys. **37**(1), 313 (1998)
20. Y.B. Zeldovich, Y.P. Raizer, *Physics of shock waves and high-temperature hydrodynamic phenomena*, 1st edn. (Academic, New York, 1967)
21. A. Bogaerts, Z.Y. Chen, Spectrochim. Acta B **60**, 1280 (2005)
22. J.G. Lunney, R. Jordan, Appl. Surf. Sci. **127**, 941 (1998)
23. N.M. Bulgakova, A.V. Bulgakov, Appl. Phys. A-Mater **73**, 199 (2001)
24. M.A. Shannon, et al., Anal. Chem. **67**, 4522 (1995)
25. A. Dupont, P. Caminat, P. Bournot, J.P. Gauchon, J. Appl. Phys. **78**, 2022 (1995)
26. S. Zhu, Y.F. Lu, M.H. Hong, Appl. Phys. Lett. **79**, 1396 (2001)
27. A. Vogel, et al., Appl. Phys. B-Lasers O. **68**, 271 (1999)
28. F. Mafune, et al., J. Phys. Chem. B **104**, 9111 (2000)
29. C. Porneala, D.A. Willis, Appl. Phys. Lett. **89**, 3 (2006)
30. A. Miotello, R. Kelly, Appl. Phys. Lett. **67**, 3535 (1995)
31. A. Miotello, R. Kelly, Appl. Phys. A-Mater **69**, S67 (1999)
32. R. Kelly, A. Miotello, Nucl. Instrum. Meth B **122**, 374 (1997)
33. J.H. Yoo, et al., Appl. Phys. Lett. **76**, 783 (2000)
34. P. Lorazo, L.J. Lewis, M. Meunier, Phys. Rev. B **73**, 22 (2006)
35. C. Korner, R. Mayerhofer, M. Hartmann, H.W. Bergmann, Appl. Phys. A-Mater **63**, 123 (1996)
36. S.H. Jeong, et al., Anal. Chem. **71**, 5123 (1999)
37. B.C. Stuart, et al., J. Opt. Soc. Am. B **13**, 459 (1996)
38. B.N. Chichkov, et al., Appl. Phys. A-Mater **63**, 109 (1996)
39. W.S. Fann, R. Storz, H.W.K. Tom, J. Bokor, Phys. Rev. B **46**, 13592 (1992)
40. C.K. Sun, et al., Phys. Rev. B **50**, 15337 (1994)
41. S.S. Wellershoff, J. Hohlfeld, J. Gudde, E. Matthias, Appl. Phys. A-Mater **69**, S99 (1999)
42. J. Hohlfeld, et al., Chem. Phys. **251**, 237 (2000)
43. S. Nolte, et al., J. Opt. Soc. Am. B **14**, 2716 (1997)
44. N.N. Nedialkov, S.E. Imamova, P.A. Atanasov, J. Phys. D Appl. Phys. **37**, 638 (2004)
45. J. Yang, et al., Phys. Rev. B **76**, 165430 (2007)
46. P. Lorazo, L.J. Lewis, M. Meunier, Phys. Rev. Lett. **91**, 225502 (2003)
47. J. Perriere, C. Boulmer-Leborgne, R. Benzerga, S. Tricot, J. Phys. D Appl. Phys. **40**, 7069 (2007)
48. S. Amoruso, et al., Appl. Phys. Lett. **84**, 4502 (2004)
49. S. Amoruso, et al., J. Phys. B-At. Mol. Opt. **38**, L329 (2005)
50. S. Noel, J. Hermann, T. Itina, Appl. Surf. Sci. **253**, 6310 (2007)
51. S. Amoruso, R. Bruzzese, X. Wang, J. Xia, Appl. Phys. Lett. **92**, 3 (2008)
52. S. Amoruso, et al., J. Phys. D Appl. Phys. **40**, 331 (2007)
53. M.E. Povarnitsyn, et al., Phys. Rev. B **75**, 235414 (2007)
54. L.J. Lewis, D. Perez, Appl. Surf. Sci. (in press) DOI:10.1016/j.apsusc.2008.07.116
55. S. Amoruso, et al., Phys. Rev. B **71**, 4 (2005)
56. E. Millon, et al., Appl. Phys. A-Mater **77**, 73 (2003)
57. E. Leveugle, D.S. Ivanov, L.V. Zhigilei, Appl. Phys. A-Mater **79**, 1643 (2004)
58. B.S. Luk'yanchuk, W. Marine, S.I. Anisimov, G.A. Simakina, Proc. SPIE **3618**, 434 (1999)
59. M. Kuwata, B. Luk'Yanchuk, T. Yabe, Jpn. J. Appl. Phys. 1 **40**, 4262 (2001)
60. T.E. Itina, M. Sentis, W. Marine, Appl. Surf. Sci. **252**, 4433 (2006)
61. T.E. Itina, et al., Appl. Surf. Sci. **253**, 7656 (2007)
62. R. Hergenroder, J. Anal, Atom. Spectrom. **21**, 1016 (2006)
63. A. Bailini, P.M. Ossi, A. Rivolta, Appl. Surf. Sci. **253**, 7682 (2007)
64. C.X. Wang, P. Liu, H. Cui, G.W. Yang, Appl. Phys. Lett. **87**, 201913 (2005)
65. R. Fabbro, et al., J. Appl. Phys. **68**, 775 (1990)
66. L. Berthe, et al., J. Appl. Phys. **82**, 2826 (1997)
67. H.R. Pakhal, R.P. Lucht, N.M. Laurendeau, Appl. Phys. B-Lasers O. **90**, 15 (2008)
68. R.E. Russo, et al., Appl. Phys. A-Mater **A69**, 887 (1999)
69. T.E. Glover, J. Opt, Soc. Am. B **20**, 125 (2003)
70. X. Zeng, X.L. Mao, R. Greif, R.E. Russo, Appl. Phys. A-Mater **80**, 237 (2005)

71. N. Arnold, J. Gruber, J. Heitz, Appl. Phys. A-Mater **A69**, 87 (1999)
72. S.S. Harilal, et al., J. Appl. Phys. **93**, 2380 (2003)
73. S.B. Wen, X.L. Mao, R. Greif, R.F. Russo, J. Appl. Phys. **100**, 14 (2006)
74. H.S. Park, S.H. Nam, S.M. Park, J. Appl. Phys. **97**, 5 (2005)
75. D. Kashchiev, *Nucleation: Basic Theory with Applications*, 1st edn. (Butterworth-Heinemann, Oxford, 2000)
76. M.N.R. Ashfold, F. Claeyssens, G.M. Fuge, S.J. Henley, Chem. Soc. Rev. **33**, 23 (2004)
77. S.B. Wen, X.L. Mao, R. Greif, R.E. Russo, J. Appl. Phys. **101**, 15 (2007)
78. T. Yoshitake, G. Shiraishi, K. Nagayama, Appl. Surf. Sci. **197**, 379 (2002)
79. E.V. Pechen, et al., Appl. Phys. Lett. **66**, 2292 (1995)
80. E. Agostinelli, S. Kaciulis, M. Vittori-Antisari, Appl. Surf. Sci. **156**, 143 (2000)
81. Z. Trajanovic, S. Choopun, R.P. Sharma, T. Venkatesan, Appl. Phys. Lett. **70**, 3461 (1997)
82. J. Perriere, et al., J. Appl. Phys. **91**, 690 (2002)
83. D.P. Norton, et al., Appl. Phys. Lett. **74**, 2134 (1999)
84. D.B. Geohegan, A.A. Puretzky, G. Duscher, S.J. Pennycook, Appl. Phys. Lett. **72**, 2987 (1998)
85. A.V. Kabashin, J.P. Sylvestre, S. Patskovsky, M. Meunier, J. Appl. Phys. **91**, 3248 (2002)
86. X.Y. Chen, et al., J. Appl. Phys. **93**, 6311 (2003)
87. U. Ozgur, et al., J. Appl. Phys. **98**, 103 (2005)
88. J. Roder, J. Faupel, H.U. Krebs, Appl. Phys. A-Mater **93**, 863 (2008)
89. N. Benchikh, et al., Surf. Coat. Tech. **200**, 6272 (2006)
90. S. Bouhtiyya, L. Roue, Int. J. Hydrogen. Energ. **33**, 2912 (2008)
91. D.H. Lowndes, et al., Appl. Surf. Sci. **127**, 355 (1998)
92. D.H. Lowndes, et al., J. Mater. Res. **14**, 359 (1999)
93. J. Koch, A. von Bohlen, R. Hergenroder, K. Niemax, J. Anal. Atom. Spectrom. **19**, 267 (2004)
94. C. Huang, et al., J. Appl. Phys. **101**, 11 (2007)
95. O. Albert, et al., Appl. Phys. A-Mater **76**, 319 (2003)
96. G.M. Fuge, M.N.R. Ashfold, S.J. Henley, J. Appl. Phys. **99**, 12 (2006)
97. X.L. Tong, D.S. Jiang, L. Liu, H. Dai, J. Vac. Sci. Technol. B **26**, 1398 (2008)
98. A. De Giacomo, M. Dell'Aglio, A. Santagata, R. Teghil, Spectrochim. Acta B **60**, 935 (2005)
99. A. Giardini, et al., Appl. Surf. Sci. **252**, 4632 (2006)
100. J. Koch, et al., Spectrochim. Acta B **62**, 20 (2007)
101. Z. Zhang, P.A. VanRompay, J.A. Nees, P.P. Pronko, J. Appl. Phys. **92**, 2867 (2002)
102. T.W. Trelenberg, et al., Appl. Surf. Sci. **221**, 364 (2004)
103. S. Amoruso, et al., Appl. Surf. Sci. **252**, 4863 (2006)
104. E.G. Gamaly, et al., J. Appl. Phys. **95**, 2250 (2004)
105. S. Barcikowski, A. Hahn, A.V. Kabashin, B.N. Chichkov, Appl. Phys. A-Mater **87**, 47 (2007)
106. J. Neddersen, G. Chumanov, T.M. Cotton, Appl. Spectrosc. **47**, 1959 (1993)
107. A.V. Kabashin, M. Meunier, C. Kingston, J.H.T. Luong, J. Phys. Chem. B **107**, 4527 (2003)
108. S. Besner, A.V. Kabashin, F.M. Winnik, M. Meunier, Appl. Phys. A-Mater **93**, 955 (2008)
109. A. Fojtik, A. Henglein, Berich. Bunsen Phys. Chem. **97**, 252 (1993)
110. F. Mafune, J.y. Kohno, Y. Takeda, T. Kondow, J. Phys. Chem. B **106**, 7575 (2002)
111. J.P. Sylvestre, A.V. Kabashin, E. Sacher, M. Meunier, Appl. Phys. A-Mater **80**, 753 (2005)
112. S. Petersen, J. Jakobi, S. Barcikowski, Appl. Surf. Sci. (In press) DOI:10.1016/j.apsusc.2008.08.064
113. F. Mafune, et al., J. Phys. Chem. B **105**, 5114 (2001)
114. A.V. Kabashin, M. Meunier, J. Appl. Phys. **94**, 7941 (2003)
115. J.P. Sylvestre, et al., J. Phys. Chem. B **108**, 16864 (2004)
116. J.P. Sylvestre, et al., J. Am. Chem. Soc. **126**, 7176 (2004)
117. A.V. Kabashin, M. Meunier, J. Phys. Conf. Ser. **59**, 354 (2007)
118. A.V. Kabashin, M. Meunier, J. Photoch. Photobio. A **182**, 330 (2006)
119. S. Besner, A.V. Kabashin, F.M. Winnik, M. Meunier, J. Phys. Chem. C **113**, 9526 (2009)
120. F. Mafune, et al., J. Phys. Chem. B **104**, 8333 (2000)
121. G.A. Shafeev, E. Freysz, F. Bozon-Verduraz, Appl. Phys. A-Mater **A78**, 307 (2004)
122. A. Pyatenko, et al., Appl. Phys. A-Mater **79**, 803 (2004)

123. T. Tsuji, T. Kakita, M. Tsuji, Appl. Surf. Sci. **206**, 314 (2003)
124. T. Tsuji, et al., Appl. Surf. Sci. **254**, 5224 (2008)
125. J.S. Jeon, C.S. Yeh, J. Chin. Chem. Soc.-Taip **45**, 721 (1998)
126. T. Tsuji, K. Iryo, N. Watanabe, M. Tsuji, Appl. Surf. Sci. **202**, 80 (2002)
127. M. Prochazka, et al., Anal. Chem. **69**, 5103 (1997)
128. Y.H. Chen, C.S. Yeh, Colloid Surf. A **197**, 133 (2002)
129. M. Prochazka, et al., J. Mol. Struc. **410**, 213 (1997)
130. F. Mafune, J.y. Kohno, Y. Takeda, T. Kondow, J. Phys. Chem. B **107**, 4218 (2003)
131. W.T. Nichols, T. Sasaki, N. Koshizaki, J. Appl. Phys. **100**, 114913 (2006)
132. W.T. Nichols, T. Sasaki, N. Koshizaki, J. Appl. Phys. **100**, 114912 (2006)
133. W.T. Nichols, T. Sasaki, N. Koshizaki, J. Appl. Phys. **100**, 114911 (2006)
134. Z. Jin, C.Q. Lan, Mater. Lett. **62**, 1521 (2008)
135. S.K. Yang, W.P. Cai, H.B. Zeng, Z.G. Li, J. Appl. Phys. **104**, 5 (2008)
136. W. Gong, et al., J. Appl. Phys. **102**, 064304 (2007)
137. K.V. Anikin, et al., Chem. Phys. Lett. **366**, 357 (2002)
138. O.R. Musaev, et al., Physica E **40**, 3147 (2008)
139. P.S. Liu, W.P. Cai, H.B. Zeng, J. Phys. Chem. C **112**, 3261 (2008)
140. Z. Haibo, et al., J. Phys. Chem. B **109**, 18260 (2005)
141. S.C. Singh, R. Gopal, J. Phys. Chem. C **112**, 2812 (2008)
142. C. He, et al., J. Photoch. Photobio. A **191**, 66 (2007)
143. T. Sasaki, et al., Appl. Phys. A-Mater **79**, 1489 (2004)
144. C.H. Liang, Y. Shimizu, T. Sasaki, N. Koshizaki, Appl. Phys. A-Mater **80**, 819 (2005)
145. L. Yang, et al., J. Nanopart. Res. **9**, 1181 (2007)
146. Q.X. Liu, C.X. Wang, G.W. Yang, Phys. Rev. B **71**, 155422 (2005)
147. G. Compagnini, A.A. Scalisi, O. Puglisi, Phys. Chem. Chem. Phys. **4**, 2787 (2002)
148. T. Tsuji, Y. Okazaki, Y. Tsuboi, M. Tsuji, Jpn. J. Appl. Phys. 1 **46**, 1533 (2007)
149. L. Berthe, R. Fabbro, P. Peyre, E. Bartnicki, J. Appl. Phys. **85**, 7552 (1999)
150. L. Berthe, et al., J. Phys. D Appl. Phys. **33**, 2142 (2000)
151. B.X. Wu, Y.C. Shin, J. Appl. Phys. **101**, 103514 (2007)
152. T. Sakka, et al., J. Chem. Phys. **112**, 8645 (2000)
153. K. Saito, K. Takatani, T. Sakka, Y.H. Ogata, Appl. Surf. Sci. **197**, 56 (2002)
154. B.X. Wu, Appl. Phys. Lett. **93**, 3 (2008)
155. H. Oguchi, T. Sakka, Y.H. Ogata, J. Appl. Phys. **102**, 23306 (2007)
156. A. Sasoh, K. Watanabe, Y. Sano, N. Mukai, Appl. Phys. A-Mater **80**, 1497 (2005)
157. D. Perez, et al., Phys. Rev. B **77**, 014108 (2008)
158. H. Ushida, N. Takada, K. Sasaki, J. Phys. Conf. Ser. **59**, 563 (2007)
159. Y.T. Didenko, W.B. McNamara III, K.S. Suslick, J. Am. Chem. Soc. **121**, 5817 (1999)
160. J. Bosbach, et al., Appl. Phys. Lett. **74**, 2605 (1999)
161. D.Q. Yang, M. Meunier, E. Sacher, J. Appl. Phys. **95**, 5023 (2004)
162. H. Ouacha, C. Hendrich, F. Hubenthal, F. Trager, Appl. Phys. B-Lasers O. **81**, 663 (2005)
163. W.T. Nichols, et al., Appl. Phys. Lett. **78**, 1128 (2001)
164. J. Lee, et al., IEEE T. Magn. **32**, 4484 (1996)
165. G. Malyavantham, et al., J. Nanopart. Res. **6**, 661 (2004)
166. I. Gallardo, K. Hoffmann, J.W. Keto, Appl. Phys. A-Mater **94**, 65 (2009)
167. M.S. Yeh, et al., J. Phys. Chem. B **103**, 6851 (1999)
168. J. Zhang, et al., J. Phys. Chem. B **110**, 7122 (2006)
169. J. Zhang, et al., J. Phys. Chem. B **107**, 6920 (2003)
170. M. Kawasaki, K. Masuda, J. Phys. Chem. B **109**, 9379 (2005)
171. M. Kawasaki, N. Nishimura, Appl. Surf. Sci. **253**, 2208 (2006)
172. P.V. Kamat, M. Flumiani, G.V. Hartland, J. Phys. Chem. B **102**, 3123 (1998)
173. A. Takami, H. Kurita, S. Koda, J. Phys. Chem. B **103**, 1226 (1999)
174. S. Inasawa, M. Sugiyama, Y. Yamaguchi, J. Phys. Chem. B **109**, 9404 (2005)
175. S. Besner, A.V. Kabashin, M. Meunier, Appl. Phys. Lett. **89**, 233122 (2006)
176. K. Yamada, Y. Tokumoto, T. Nagata, F. Mafune, J. Phys. Chem. B **110**, 11751 (2006)
177. S. Besner, A.V. Kabashin, M. Meunier, Appl. Phys. A-Mater **88**, 269 (2007)

178. K. Yamada, K. Miyajima, F. Mafune, J. Phys. Chem. C **111**, 11246 (2007)
179. H. Muto, K. Miyajima, F. Mafune, J. Phys. Chem. C **112**, 5810 (2008)
180. X.L. Zheng, et al., J. Phys. Chem. C **111**, 14962 (2007)
181. R.C. Jin, et al., Nature **425**, 487 (2003)
182. C.M. Aguirre, C.E. Moran, J.F. Young, N.J. Halas, J. Phys. Chem. B **108**, 7040 (2004)
183. S. Link, et al., Phys. Rev. B **61**, 6086 (2000)
184. A. Pyatenko, M. Yamaguchi, M. Suzuki, J. Phys. Chem. C **111**, 7910 (2007)
185. G. Compagnini, E. Messina, O. Puglisi, V. Nicolosi, Appl. Surf. Sci. **254**, 1007 (2007)
186. U. Pal, et al., Appl. Phys. A-Mater **79**, 79 (2004)
187. Y.H. Chen, Y.H. Tseng, C.C. Yeh, J. Mater. Chem. **12**, 1419 (2002)
188. S.H. Tsai, Y.H. Liu, P.L. Wu, C.S. Yeh, J. Mater. Chem. **13**, 978 (2003)
189. W.T. Nichols, et al., J. Nanopart. Res. **4**, 423 (2002)
190. C.B. Stipe, et al., J. Nanopart. Res. **6**, 467 (2004)
191. P. Grua, et al., Phys. Rev. B **68**, 12 (2003)

Chapter 8
Ultrafast Laser Micro- and Nanostructuring

Wolfgang Kautek and Magdalena Forster

Abstract Near-threshold non-linear nanoscale processing phenomena generated by sub-100fs laser pulses are reviewed. Coupled with high NA focusing optics, high power oscillators demonstrated a high-repetition rate approach for the precise laser machining of dielectrics on a submicrometer scale. A new field of nanostructuring proposed on the basis of apertureless scanning near-field optical nanomachining and examples of femtosecond nanosurgery are discussed.

List of Abbreviations

a	Absorbed fraction of incident laser light
α	Absorptivity
d_0	Beam diameter
w_0	Beam radius
ρ	Density
Γ	Electron–phonon coupling constant
$\tau_{e\text{-}p}$	Electron–phonon relaxation time
δ	Film thickness
F	Fluence
$C_{e,l}$	Heat capacity (electron, lattice)
$\kappa_{e,l}$	Heat conductivity (electron, lattice)
$\beta(I)$	Impact ionisation rate
ξ	Incubation factor
I	Intensity
Q	Laser source term
d_0	Mean distance between two defects

W. Kautek (✉) and M. Forster
Department of Physical Chemistry, University of Vienna, Währinger Strasse 42,
A-H1090 Vienna, Austria
e-mail: wolfgang.kautek@univie.ac.at

K. Sugioka et al. (eds.), *Laser Precision Microfabrication*,
Springer Series in Materials Science 135, DOI 10.1007/978-3-642-10523-4_8,
© Springer-Verlag Berlin Heidelberg 2010

N	Number of applied pulses
n_k	Number of electrons above a critical energy
k	Number of photons required to reach this energy
n_{mpi}	Number of(multi)photon induced electrons
N	Number of excited electrons
$1/\alpha$	Penetration depth
p	Pressure
P	Probability
τ	Pulse length
ν_{rep}	Repetition rate
d	Structure diameter
$T_{\mathrm{e,l}}$	Temperature (the electrons, lattice)
F_{th}	Threshold fluence
t	Time
V	Volume

8.1 Introduction

Femtosecond (fs) excitation provided the promising perspective that laser radiation interaction with the evolving plasma is minimized and that heat affected zones are reduced into the nanoscale range in contrast to picosecond (ps) and nanosecond (ns) laser processing. This triggered intensive investigations in the sub-ps regime which was technically accessible in the early 1990s [1–6]. Near-infrared ultrashort laser pulses down to durations of 5 fs yielded unexpected machining qualities characterized by high precision and deterministic features [5, 7–9]. Self-organization of solid surfaces by femtosecond laser treatment led to so-called ripples with sub-micrometer periodicity not only on inorganic dielectrics [10–14], but also on silicon [15–21], indium phosphide [22,23], titanium nitride [22–24] and polymers [6]. This chapter focuses on ultra-short laser pulse interaction with matter with pulse durations below 100 fs down to the physical limit.

8.2 Theoretical Background

The dynamics of laser–matter interaction starts with the electronic excitation and relaxation (Fig. 8.1) (also see Chaps. 2 and 4). Sub-100fs ultra high intensity laser irradiation interacts only with the electronic system. For weak electric fields, ionisation of an atom is considered possible when the incoming photon energy exceeds the binding energy of the valence electron. Thus, in wide band gap materials, in contrast to metals, no electrons are excited directly into the conduction band.

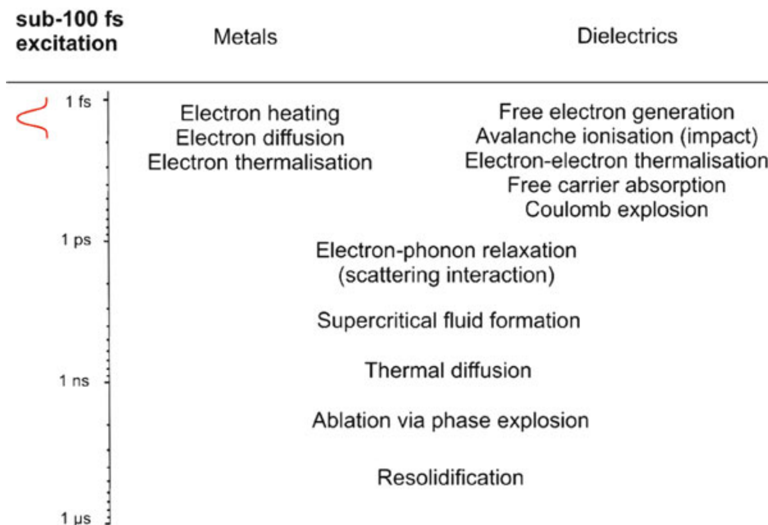

Fig. 8.1 Fundamental differences in material responses on fs-excitation in metals and dielectrics

8.2.1 Dielectrics

In the case of a dielectric, the initial generation of free electrons can occur via strong-field ionisation [25]. Such strong fields can be generated with sub-100fs ultra high intensity excitation. Multiphoton absorption is strongly dependent on the laser intensity. It can occur either from initially present morphological or structural defect states or by direct interband transitions (Fig. 8.2). When the electric field strength approaches the atomic unit it becomes sufficiently strong to perturb the Coulomb potential that is binding the electron to the nucleus. In this case, the electron can tunnel through the suppressed barrier and ionisation can occur [26]. When the field becomes even stronger the potential barrier can be reduced to such an extent that the electron directly escapes into the continuum without tunneling through a barrier called "over-the-barrier ionisation". The dashed lines in Fig. 8.2 represent the unperturbed Coulomb potential, the dotted lines are the electric field from the laser, and the resulting solid lines are the effective potentials experienced by the electrons.

Once the generation of free electrons is initiated, electron–electron collision processes occur and multiplication can take place due to inverse Bremsstrahlung (impact or avalanche ionisation). With free electrons present, absorption of the remaining part of the light pulse can take place, which leads to further heating of the excited electrons. Thus, the dielectric starts to behave as a metal. The abrupt change from an insulator to a material where a significant amount of the electrons are excited to the conduction band introduces changes in the refractive index. Further strong ionisation and electron emission from the solid surface may subsequently occur. Thus, the remaining atomic cores charge the near surface region positively. If this charge is not compensated quickly enough, as would be the case for a metallic

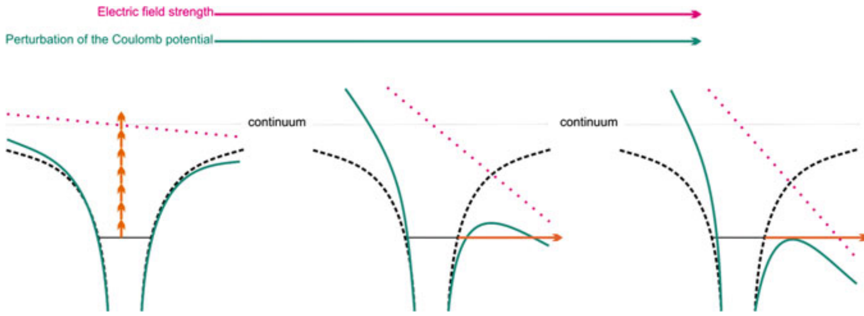

Fig. 8.2 The three regimes of strong field ionisation: multiphoton ionisation (*left*), tunnelling regime (*middle*), and over-the-barrier regime (*right*)

conductor or semiconductor, positive ion emission by so-called Coulomb explosion (CE) with high kinetic energies takes place within several tens of fs [27, 28]. Dielectrics show a metal-like behavior in a narrow surface layer only. CE often referred to as a gentle ablation regime releases fast ions with a narrow velocity distribution indicating a non-thermal process leaving behind an atomically smooth surface. This is in contrast to the strong ablation regime, where phase explosion dominates [29]. After the electron–phonon relaxation time, the hot carriers are thermalised and reach thermal equilibrium with the lattice. The following thermal processes are similar for metals and dielectrics and are described in a thermodynamic approach (Sect. 8.2.3).

For modeling the ablation threshold of dielectrics one has to take into account the strong field ionisation and the impact ionisation. A simple approach [30] describes the generation rate, i.e., the change of the number of excited electrons $\partial n_{\text{total}}/\partial t$ by:

$$\frac{\partial n_{\text{total}}}{\partial t} = \dot{n}_{mpi}(I) + \beta(I)n. \tag{8.1}$$

Here, $\dot{n}_{mpi} = \mathrm{d}n_{mpi}/\mathrm{d}t$ is the intensity-dependent strong field ionisation term (mainly the density of multiphoton-induced (*mpi*) excited electrons) and $\beta(I)$ is an intensity-dependent impact ionisation rate. Another more sophisticated model involves, e.g., the excitation process [31] but needs in turn, due to its complexity, a high amount of calculation time. This complicated model was simplified by proposing a multiple rate equation (MRE) which included the most dominant effects of the previous model [32]. In the MRE model, electrons are initially excited from the valence to the conduction band by strong field ionisation. This is then followed by one photon excitation leading to an increased energy of the conduction band electrons. When the energy of an electron in the conduction band is sufficiently high, impact ionisation can occur with a rate β and two electrons with lower kinetic energy are generated. In the MRE model, this has been described by introducing discrete levels in the conduction band spaced with the photon energy of the incident light. The total generation rate is then given by (8.1) replacing n by n_k which takes into account, that only electrons in the conduction band with sufficient energy can undergo impact

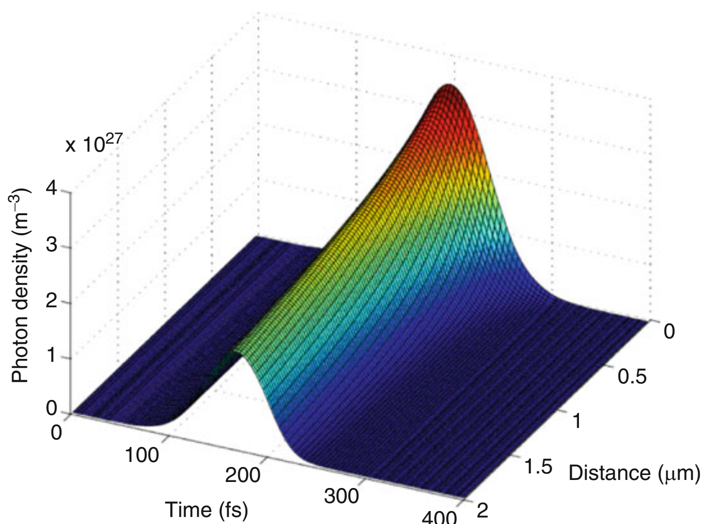

Fig. 8.3 The photon density as a function of space and time for a 100-fs pulse [33]

ionisation [32]. The second term describes the impact ionisation, which depends now on the number of electrons above a critical energy. The index k stands for the number of photons required to reach this energy.

According to this, the space–time evolution of the density of photons in a 5-eV bandgap solid delivered from a 100-fs pulse centered at 800 nm (fluence of 5.5 J/cm^2) has been calculated recently (Fig. 8.3) [33]. At the onset of the photon pulse, the penetration depth is high due to the low absorptivity before any of the mentioned processes such as multiphoton absorption, impact ionisation, and free carrier absorption can take place. In the later part of the pulse, hardly any light propagates significantly into the sample due to these various absorption processes. This result demonstrates the complexity of light–matter interaction in the fs time domain. The details of the space–time relationship of the photon density are strongly dependent on the wavelength, the bandgap and the fluence as is discussed below.

Shorter wavelengths lead to lower ablation thresholds and reduced ablation depths (Fig. 8.4a). The lower thresholds can be explained by the facilitation of multiphoton absorption due to higher photon energies. The ablation depth simply correlates to the penetration depth $1/\alpha$ which is proportional to the wavelength in analogy to metals. The ablation depth dependence on the bandgap comes out in analogy to the parameter wavelength (Fig. 8.4b).

The calculation for pulse durations between 30 and 800 fs demonstrated that the longer pulses lead to higher ablation thresholds as the maximum intensity at constant fluence is reduced and thereby few electrons are generated by multiphoton processes. The ablation rate, respectively the ablation (penetration) depth peaks at intermediate duration around 100 fs. Below, penetration depth is reduced due to efficient non-linear coupling leading, e.g., to free electron absorption. Above, less intensity causes less coupling and thus reduced ablation rates.

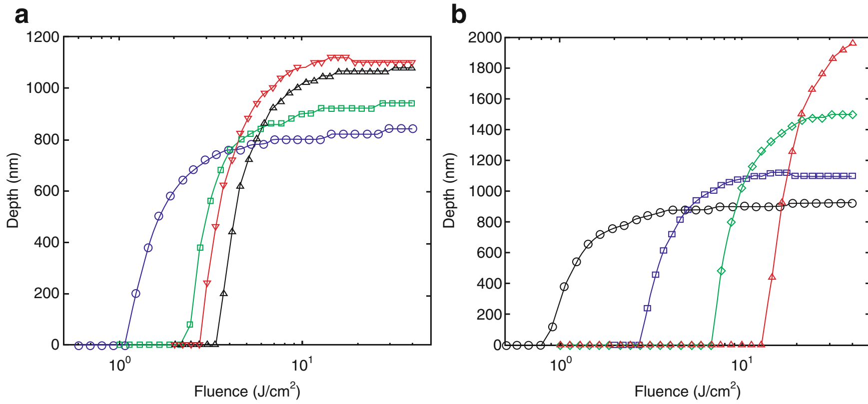

Fig. 8.4 (**a**) Ablation depth vs. fluence for varying wavelengths. Pulse duration 100 fs, bandgap 5 eV. Circles 400 nm, squares 530 nm, triangles 800 nm, up-pointing triangles 1060 nm. (**b**) Ablation depth vs. fluence for varying bandgaps. Bandgaps: circles 3 eV, squares 5 eV, diamonds 7 eV, triangles 9 eV [33]

8.2.2 Metals

In metals, the optical absorption is usually dominated by free carrier absorption, i.e., electrons in the conduction band absorb photons and gain higher energy. Thermalisation within the electronic system by electron-electron collision occurs also on a fs-timescale. This results in different temperatures of the electron system (T_e) and the atomic cores (T_l). As long as there is no thermal equilibrium between electrons and phonons [34–37] there is a diffusive energy transport by hot electrons. The resulting electron thermal diffusion length is the decisive quantity for femtosecond laser material processing, determining both, the damage threshold and the structure sharpness. The range of electronic thermal diffusion is determined by the electron–phonon coupling strength [37]. The diffusion of the hot electrons presupposes the thermal equilibrium of the electrons which depends on the excitation energy and density of states (DOS) at the Fermi level. This explains different diffusion lengths for different metals under identical excitation conditions.

The energy transfer from hot electrons to the initially cold lattice is usually described by the two-temperature model [38]. The model is valid for fs-pulses only since electron–phonon scattering occurs on a ps-timescale. For ns-pulses the electron–lattice equilibrium is reached within the pulse duration. The two temperatures of lattice and electrons are functions of space and time, and their development is governed by two coupled differential equations:

$$C_e \frac{\partial T_e}{\partial t} = \nabla \cdot \{\kappa_e \nabla T_e\} - \Gamma\{T_e - T_l\} + Q, \tag{8.2}$$

$$C_l \frac{\partial T_l}{\partial t} = \nabla \cdot \{\kappa_l \nabla T_l\} + \Gamma\{T_e - T_l\}. \tag{8.3}$$

Here, C_e and C_l are the heat capacities and κ_e and κ_l the heat conductivities for the electron and lattice systems, respectively. Q is the laser source term that is often assumed to be a Gaussian pulse in space with an exponential decay in the sample. The Γ parameter accounts for the coupling between the electron and lattice systems and is normally considered to be constant. For single crystalline materials studies demonstrated an increase in the electron–phonon coupling term with electron temperature [39]. In recent numerical calculations [40], a linear dependence of the electron lattice coupling strength on temperature, also for amorphous materials, was assumed. Simulated ablation rates yielded better agreement with experimental results than when using a temperature independent Γ [33].

8.2.3 Thermodynamic Approach

Thermal processes occur after the electron–phonon relaxation time, when the system has reached a state of local equilibrium. There are basically four thermal processes to be considered [41]. (a) Normal vaporization can operate at basically every pulse length. The Hertz–Knudsen equation describes the surface recession. (b) Normal boiling takes place when sufficiently long pulse lengths yield heterogeneous nucleation. In this context, the boiling zone extends from the surface to a depth related to the absorption length. (c) Phase explosion (explosive boiling) requires sufficiently high laser intensity so that the target can reach temperatures about 10% below the critical value ($\sim 0.9T_c$) and leads to the characteristic homogeneous bubble formation. The target makes a rapid transition from a superheated liquid to a mixture of vapor and liquid droplets. (d) Subsurface heating is caused by the fact that normal vaporization leads to a loss of heat carried away by the gas. The target exhibits a modified temperature profile with a peak in the subsurface bulk because of the surface cooling effect due to the vaporization.

The theory of real gases in equilibrium with their condensed phases can be described in a 3D-graph with the axes pressure (p), volume (V), or density (ρ) and temperature (T) (Fig. 8.5). Laser physical literature uses 2D-representations in the p–T plane, the V–T plane or in the p–$V(\rho)$ plane which is very popular in the chemical community. The 3D diagram shows single phase areas as well as domains where two phases are simultaneously present. The line which separates the two mixed phase domains (gas–liquid, gas–solid) is the triple line. In the 2D p–T projection, there is only one point where the three phases are simultaneously present, i.e., the triple point.

In the schematic p–V phase diagram in Fig. 8.6, the line A–P_c is known as the boiling line, A–P_c–D is the binodal line and B–P_c–C is the spinodal line where P_c is the critical point. Above the critical temperature no thermodynamic distinction between liquid and vapor phases can be made. The binodal line is the equilibrium curve for liquid and vapor, in the region A–P_c–B a mixture of liquid and vapor, as well as a superheated liquid state can exist. The spinodal line B–P_c is the boundary of thermodynamic stability of a superheated metastable liquid. Using high heating

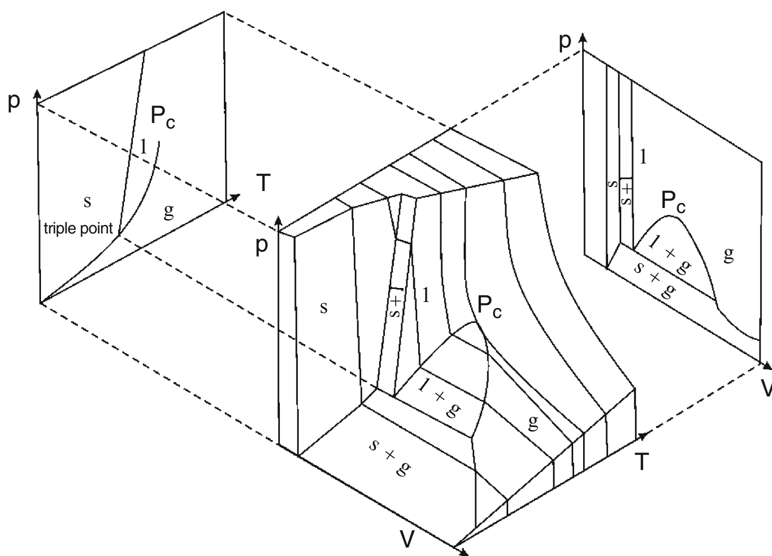

Fig. 8.5 Schematic p–V–T phase diagram with projections in 2D planes

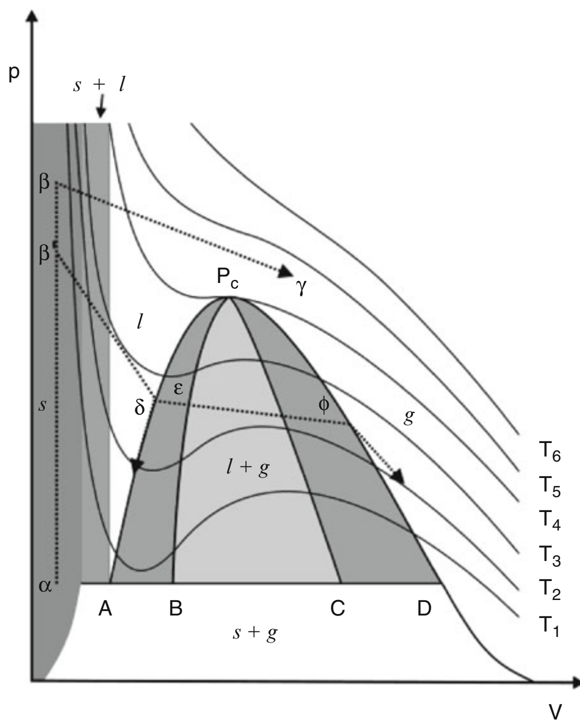

Fig. 8.6 Schematic phase diagram in the p–V plane showing fs-excitation mechanisms

rates liquid metals can be superheated up to the spinodal line. Near the spinodal line volume fluctuations begin with the sudden growth of vapor nuclei in the superheated liquid. The area within B–P_c–C is unstable and therefore a 'jump' into the region C–P_c–D, the so called phase explosion, with a large increase of volume, will occur. This powerful expansion produces a shock wave in the surrounding medium. At the moment of phase explosion the surface temperature starts to decrease due to the cooling of the liquid phase, as it loses the more energetic atoms to the vapor phase.

With fs-irradiation isochoric heating with drastic pressure increase is possible which pulls the system away from the metastable region. The rate at which expansion proceeds determines the ablation process and is accompanied by a cooling process far away from thermal equilibrium [42]. At high energies, the resulting rapid expansion causes the breakup of the supercritical fluid through fragmentation (Fig. 8.6 $\alpha-\beta-\gamma$) [43]. A nonequilibrium transition from a homogeneous supercritical fluid to a heterogeneous, clustered phase upon rapid expansion in vacuum, i.e., "nontrivial" fragmentation, seems to determine the early stages of the ablation process [44]: experimental investigation of silicon nanoparticle generation via femtosecond laser ablation in vacuum supports this scenario [45].

Closer to the threshold energy, however, the expansion is too slow to induce fragmentation. Nevertheless, it is sufficiently rapid to push the system into the metastable regime (near the spinodal limit) before significant thermal diffusion has occurred ($\alpha-\beta'-\delta-\varepsilon$), that means cooling is adiabatic. Homogeneous bubble nucleation then sets in, converting the superheated material into a mixture of liquid and gas ($\varepsilon-\phi$) through phase explosion.

Recent Monte Carlo and molecular-dynamics simulations [44] reveal thermal phase transitions on mesoscopic-lengths and ps-to-ns-time scales. Upon fs irradiation relatively far from the melting threshold, thermal disordering of a mechanically unstable solid in a time period of 10^{-12} s is calculated. Under lower superheating with ps pulses, rapid homogeneous nucleation of liquid in the metastable solid is followed by slower, heterogeneous melting of the crystal. The solidification of the remaining supercooled melt to a crystalline or amorphous solid is a relatively slow process occurring on a 10^{-11}–10^{-9} s time scale, independent of the pulse duration. Under near-threshold irradiation with fs pulses, the subcritical material undergoes rapid adiabatic cooling to the liquid-gas regime where a phase explosion-like process takes place in 10^{-12}–10^{-11} s. Under these conditions there was the consideration that the onset of ablation, determined by the growth of critical nuclei of the stable vapor phase in the metastable liquid phase, is not initiated by large, localized, thermal fluctuations but, rather, by a direct conversion of translational, mechanical energy into surface energy [44].

Conversely, under irradiation with long (ns)-pulses, the material responds to the slow heating with a slow expansion along the binodal likely up to the critical point, where phase separation proceeds via a second-order transition; for $\tau \geq 100$ ns, normal vaporization may also be important [46]. Consequently, there must exist a "critical" pulse duration, ${\tau_L}^c$, beyond which phase explosion is suppressed. Here,

however, expansion occurs in a time of the order of, or greater than, the characteristic time for heat conduction (10^{-11} s [47]). As a result, the system cools along the binodal by thermal diffusion, i.e., it does not enter the metastable region and phase explosion does not take place. In this case, only those regions associated to an expansion above the critical point contribute to the ablated mass.

8.3 Recent Results

Highlights of recent results of ultra-short laser pulse processing with pulse durations below 100 fs are discussed in the next sections.

8.3.1 Top-Down Approaches to Nanostructures

The minimization of the heat affected zones into the nanoscale range in contrast to pico- and nanosecond lasers provides the basis for nanostructuring by femtosecond lasers. Top down precision of laser machining in the far field is limited by the Abbe diffraction limit, i.e., the wavelength. Therefore, a straightforward strategy is the reduction of the wavelength by, e.g., the generation of higher harmonics. Thus, sub-micrometer features could be generated with a femtosecond laser with 267 nm in analogy to UV-excimer lasers [48]. Using infrared fs pulses one can overcome the diffraction limit by choosing the peak laser fluence slightly above the ablation threshold. In this case, only the central part of the beam ablates yielding sub-diffraction structures. Ablation occurs when $F \geq F_{th}$, which, for a Gaussian beam profile, corresponds to $F = F_0 \exp(-d^2/{d_0}^2) \geq F_{th}$, where d is the structure diameter, d_0 is the beam diameter, and F_0 is the peak laser fluence [49, 50]. Therefore, one expects an ablated structure of $d = d_0[\ln(F_0/F_{th})]^{1/2}$. Top down structuring of biomaterials below the 100 nm-scale such as the nanodissection of human chromosomes as well as targeted transfection of cells with DNA [51, 52] has been achieved using 800 nm laser pulses. Even resolutions by orders of magnitude exceeding the diffraction limited spot size, e.g., in glass down to 10 nm, could be demonstrated (Fig. 8.7) [53]. It was speculated that in contrast to the accepted damage theory, multiphoton ionisation would not play a significant role, rejecting the use of the Keldysh parameter in predicting the role of multiphoton effects. A dominant Zener ionisation mechanism followed by a combination of Zener and Zenerseeded avalanche ionisation was proposed. Thus, the minimum feature size ultimately should depend on the valence electron density, which is sufficiently high and uniform, to confer deterministic behavior on the damage threshold even at the nanoscale [53].

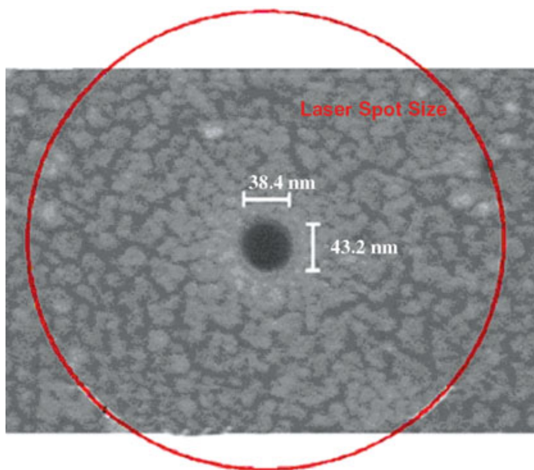

Fig. 8.7 Example of a nanometre-scale hole. The circle indicates the $1/e^2$ focus-spot size [53]

8.3.2 Thin Film Ablation

The heat affected zone controls to a high extent the machining precision. It is quantified by the heat diffusion length $L_{th} = (2\kappa\tau)^{1/2}$ [54], where κ is the thermal diffusivity, and τ the pulse duration. In order to validate this simple relationship, thin film model systems have been used in connection with ns- [55] and fs-pulse [34, 50, 56–58] treatments. It has been shown that the nanosecond-pulse laser ablation threshold fluence F_{th} of thin, thermally conducting films on thermally poor conducting substrates is lowered when the film thickness d becomes less than the heat diffusion length $L_{th}(d < L_{th})$. F_{th} increases linearly with film thickness d for $d < L_{th}$ up to the point where $d = L_{th}$, as, e.g., shown for Ni films processed with 14-ns pulses at 248 nm wavelength [55]. When $d > L_{th}$, F_{th} becomes independent of d and equal to the bulk material value [57]. The pulse length τ should be replaced by $\tau_{e\text{-}p}$ in the L_{th}-formula above [3, 6] when pulses shorter than the electron phonon relaxation time are employed ($\tau < \tau_{e\text{-}p}$). Besides these inorganic model systems organic diamond-like carbon (DLC) layers grown on silicon wafers by Inverse Pulsed Laser Deposition (IPLD) [59] were investigated recently [58]. F_{th} increases linearly with d for thicknesses $d < 60$ nm (Fig. 8.8). When $d > 60$ nm, F_{th} becomes independent of d. The thermal model discussed above and also the emergence length of ballistic hot electrons cannot explain the behavior of diamond-like carbon films. In contrast, the threshold thickness of 60 nm is determined by the optical penetration depth due to two-photon absorption [58]. AFM cross sections show typical ablated and modified surfaces at different fluences F and numbers of pulses N (Fig. 8.9). For high N and F (Fig. 8.9a) deep ablation craters are observed which exceed the thickness of the IPLD layer (here 150 nm). Processing with lower N and F (Fig. 8.9b, c) results in shallower craters with more pronounced rims

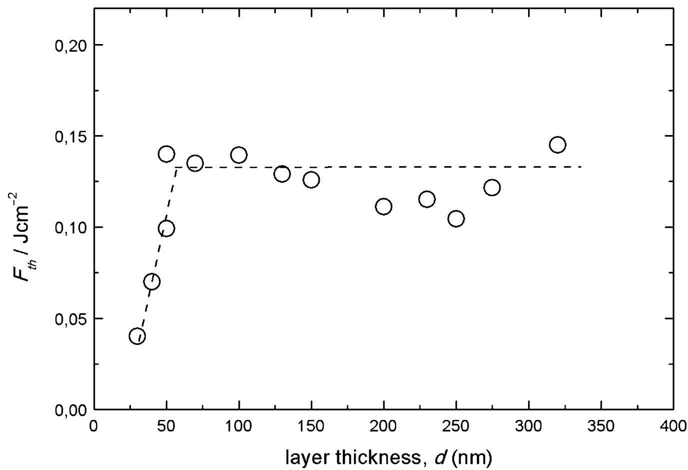

Fig. 8.8 Single pulse DLC modification thresholds as a function of film thickness [58]

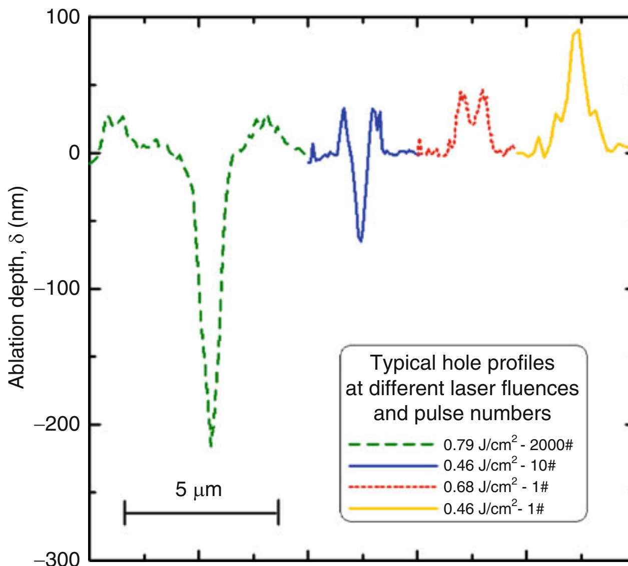

Fig. 8.9 AFM measured ablation and modification topographies of a 150-nm thick IPLD layer [58]

above the surface level. At single shot experiments with low F (Fig. 8.9d), a volume increase probably due to foaming can be observed.

Nanosecond investigations on thin triazene film showed that F_{th} is higher than for the bulk polymer in contrast to all cases discussed above [60]. A conclusive explanation for this behavior could not be given to date. However, this may be due to the fact that the ablation mechanism is not only determined by thermal degradation but also by photochemical and thermally activated photochemical bond breaking.

8.3.3 Incubation Phenomena

Incubation is a general phenomenon in laser processing with repetitive pulses. Even sub-threshold treatments have the potential to irreversibly modify materials chemically and mechanically. That means that after the first pulse a material already has changed into an often undefined condition. Even though this situation is far from satisfactory for physico–chemical investigations, it however reflects the technical condition in every micromachining job in industry. Therefore, the investigations of incubation are of overriding importance at least as a bridge between fundamental studies and applied materials science.

The relation between the single pulse $F_{\mathrm{th}}(1)$ and the multiple pulse threshold $F_{\mathrm{th}}(N)$ can be described by the phenomenological model

$$F_{\mathrm{th}}(N) = F_{\mathrm{th}}(1)N^{\xi-1} \tag{8.4}$$

where the parameter ξ indicates the degree of incubation [6]. A value of $\xi = 1$ is indicative of the absence of incubation. From a plot of $\log[NF_{\mathrm{th}}(N)]$ vs. $\log N$, the incubation factor ξ can be derived from the slope.

Substantial differences in the incubation factor ξ could be found, e.g., between chemically different polymer types. A strong incubation could be found for polycarbonate (PC), polyethylene terephtalate (PET), and polymethyl methacrylate (PMMA) with $\xi \sim 0.7$ – comparable to that of metals [36] – in contrast to the "inert" polymers polyimide (PI) and polytetrafluoroethylene (PTFE). The origin of this difference could be related to the fact that the ester bonds in PET, PC, and PMMA show much less stability towards repeated laser pulsing than, e.g., the CO–N or ether bridges in PI [61].

Defect states can play a major role in incubation phenomena and substantially influence thresholds – both modification and ablation. One important reason for this is that defects facilitate resonant multiphoton transitions in dielectrics and thus reduce ablation thresholds.

Particularly interesting findings related to this may be spot-size dependencies of thresholds. A damage threshold spot-size dependence of NaCl and SiO_2 with 40-ps pulses was explained by a qualitative model of defect dominated laser-induced breakdown involving avalanche breakdown as well as multiphoton ionization of defects levels within the focal volume [62]. For ns-pulses, a spot size dependence of ablation rates at $LiNbO_3$ was explained by ablation plume screening [63]. A spot size dependent ns-pulse laser fluence of single half-wave-thick films of ZrO_2 on glass was correlated to an increased absorption for bigger beam radii thus addressing more point defects on the films surface [64]. A comparable behavior was observed for fs-irradiation on human dentine [65], barium borosilicate (BBS) glass [66], and ion doped glass filter materials [67]. Due to the fs-irradiation the model including the screening by the ablation plume did not hold. A significant decrease of F_{th} on BBS glass by a factor of five was observed for an increasing beam radius between 20 and 400 μm (Fig. 8.10) [66]. The measurements were tried to be fitted using a thermal accumulation model: if the pulse-repetition rate is high enough,

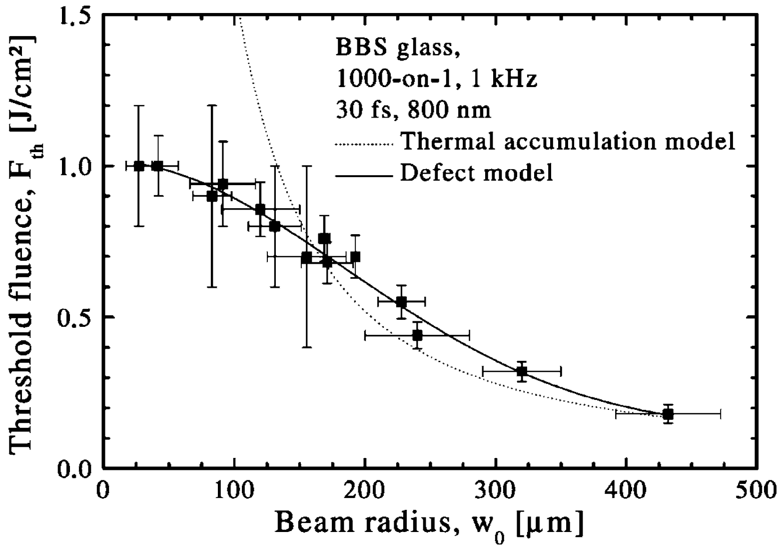

Fig. 8.10 Ablation threshold fluence in dependence of the spot radius [66]. Both described fitting models are shown

heat storage arising from previous pulses increases the temperature within the illuminated area. Ablation takes place when the temperature exceeds a critical value T_c. The dependence of the ablation threshold F_{th} on the beam radius w_0 can be written according to [65]

$$F_{th} = \frac{4CF\delta\kappa T_c}{a\nu_{rep}w_0^2 \ln\left(\frac{3N\kappa}{\nu_{rep}w_0^2}\right)}. \tag{8.5}$$

Here, ν_{rep} denotes the repetition rate, N the number of pulses per site and δ the sample thickness. The absorbed fraction of the incident laser energy is a. The material constants specific heat capacity C, and thermal diffusivity κ are given. For low spot radii, the formula above goes to infinity while the measured thresholds are limited. Therefore, this model was discarded.

A defect-driven mechanism was more successful [64]. There, randomly distributed defect states are responsible for the ablation process. For a spatially Gaussian beam, the probability P of interacting with a defect is

$$P(w_0) = 1 - \exp\left[-\frac{\pi^2}{32}\left(\frac{w_0}{d_0^2}\right)\right] \tag{8.6}$$

where d_0 is the mean distance between two defects. Two limiting cases are possible. (a) The laser beam hits a defect which subsequently causes the ablation of material with a threshold fluence of F_d. (b) No defects are excited within the spot and the ablation threshold is determined by the intrinsic threshold F_i. Taking into

account the probability of the spots overlap with defects, the ablation threshold can be described by [64]

$$F_{\mathrm{th}}(w_0) = P(w_0)F_{\mathrm{d}} + [1 - P(w_0)]F_{\mathrm{i}}. \tag{8.7}$$

The application of this model to the experimental findings results in an excellent fit to the data points (Fig. 8.10). In this special case, a defect distance of $d_0 = (650 \pm 50)\,\mu\mathrm{m}$ was calculated. Although the nature of the defect states remains unclear, this simple model proved high applicability in many cases.

8.3.4 Bottom-Up Approaches to Nanostructures

Besides the top-down approach to manufacture nanostructures by near threshold interactions with solids the bottom-up principle opens up fascinating possibilities when femtosecond laser are employed. Ablation craters and ditches machined by repetitive laser pulsing exhibit ordered surface microstructures, so-called ripples. This classical ripple formation is known since the early days of laser application [68]. Their origin was found in the interference of the incident, reflected or refracted laser radiation with the scattered or diffracted light traveling near the surface. Their periodicity depends on the wavelength, the angle of incidence, and the polarization of the laser beam.

Femtosecond treatment with circular light polarization of highly degradation-resistive polymers such as polyimide (PI) generated radially orientated ripples in cone shape with a period of $\sim 0.8\,\mu\mathrm{m}$ [61], which were topped by nanoscale craters.

Investigations with high-performance ceramics like silicon carbide, aluminum nitride and a composite compound SiC–TiC–TiB_2, revealed that a direct correlation between chemical composition and ripple character exists [69, 70]. Moreover, femtosecond laser interaction with the silicon–water interface showed that also an adjacent condensed phase has a strong physico–chemical influence on these phenomena [71,72]. Sequential fs-irradiation of silicon surfaces immersed in water can lead to high-density regular arrays of 50 nm-scale rods [73]. It was proposed that the surface energy relaxation would be the driving force for self organization on a non-thermally melted surface film [74]. This picture is becoming more detailed by the scanning probe observation of surface potential changes on Si of about 100 mV localized in the nm-scale. This suggests a mechanism related to (a) a segregation-like accumulation of dopant concentration during the self-organized nanostructure formation and (b) a crystal phase transformation of the silicon upon ablation, completely changing the material properties [75, 76]. Nanoscale ablation is obviously preferentially induced on the crest of the ripples where the local field intensity would be enhanced by the high surface curvature along the laser E-field direction, implying that localized nanofields (nanoscale potential changes) play a key role in nanostructuring [77]. The bottom-up nanostructuring by femtosecond lasers may open up a wide field of applications in surface technology, such as the preparation of super water repellent surfaces [78].

8.3.5 Biogenetic Materials

Laser processing of polymers [6, 79, 80] and biomaterials, particularly gelatine [81–83], collagen-based tissues [84–86] such as human cornea [2], human teeth [87], as well as laser cleaning of parchment [88, 89] or leather [90] has attracted vivid attention in recent years. Collagen, e.g., is a major structural protein of the extracellular matrix and an essential component of all connective tissues. Gelatine is the product of denaturation (hydrolysis) of collagen. Femtosecond pulse irradiation of gelatine at 266, 400 and 800 nm leads to foam layers with μm-thicknesses [81] when using amplified femtosecond laser sources. Bubble sizes can be controlled by the wavelength selection. Dynamics of the formation of the foam layer are discussed in [83]. Using a high numerical aperture focused fs-beam at 11 MHz repetition rate instead, large-area foaming does not occur in the way described above. In this case [91], a single layer of bubbles arranged around the central channel of the crater which exhibited a much smaller diameter inside the channel (Fig. 8.11 b) than at the surface (a). The lateral extent of these bubbles is larger than the crater diameter at the surface. The scanning force and environmental scanning electron micrographs reproduce the outer morphology only (Fig. 8.11c, d). With a low number of pulses below the ablation threshold a swelling of the surface takes place (Fig. 8.12a). The volume of the swelled area increases with fluence. Above F_{th}, a crater develops on top of the swelled area (b) and grows further in depth and width as fluence increases (c and d).

The recent results of near-threshold non-linear nanoscale processing phenomena generated by sub-100fs laser pulses can be summarized as follows. The finding that such ultrashort pulses lead to a drastic quality increase of dielectric ablation in the nJ-energy range triggered the development of high power oscillators. Coupled with high numerical aperture focusing optics they demonstrated one of the most promising high-repetition rate approaches for the precision laser machining of dielectrics on a submicrometer scale.

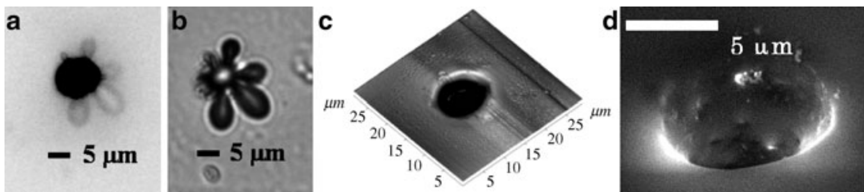

Fig. 8.11 Irradiated zone of a pure gelatine film ($F = 0.286\,\mathrm{J/cm^2}$, $N = 1375000$ pulses). Optical micrographs of the same irradiated zone in (**a**) reflection, (**b**) transmission. Micrographs of the crater formed in the film obtained by (**c**) SFM and (**d**) ESEM [91]

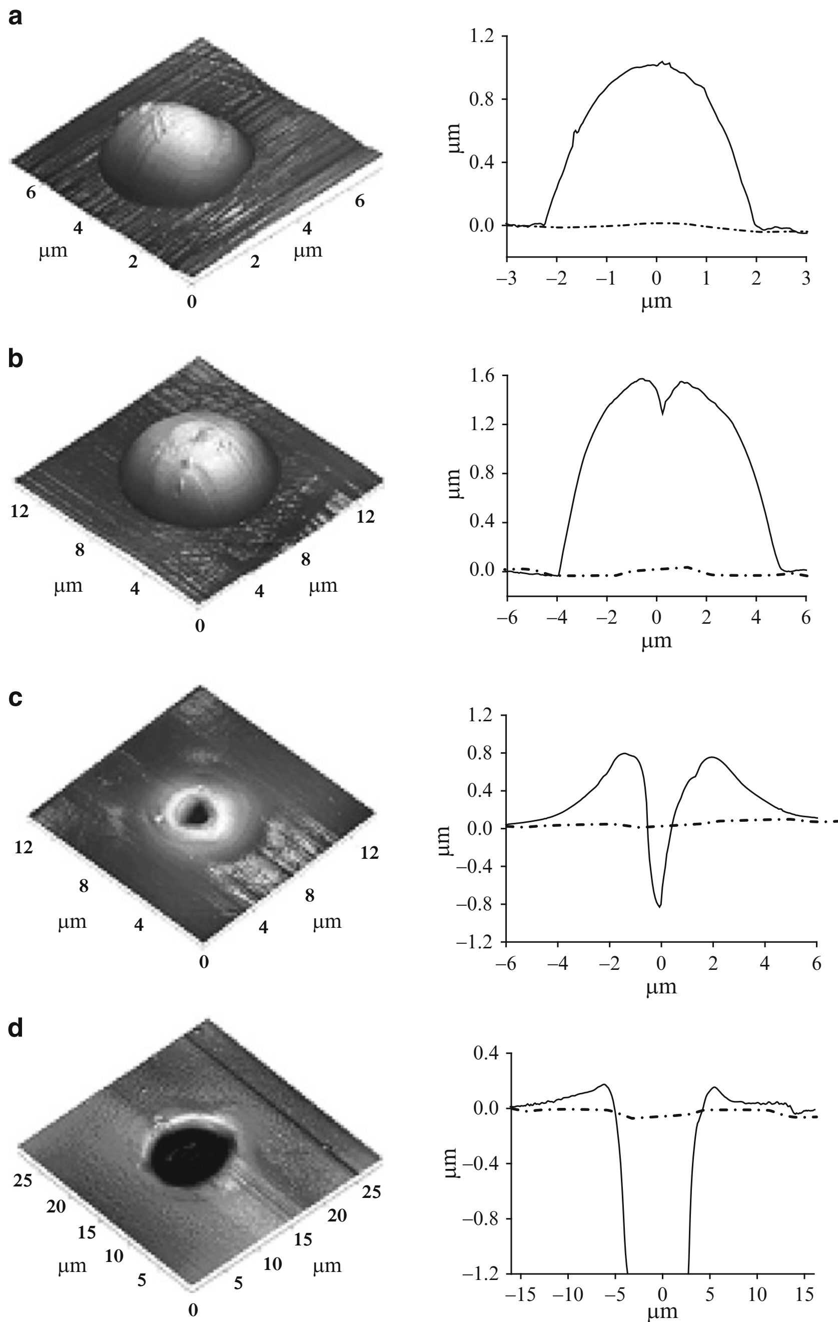

Fig. 8.12 SFM micrographs (*left*) and transversal sections (*right*) of a gelatine film irradiated with (**a**) 0.048 J/cm^2, 44000 pulses, (**b**) 0.151 J/cm^2, 88000 pulses, (**c**) 0.103 J/cm^2, 183333 pulses, (**d**) 0.286 J/cm^2, 1375000 pulses. The dotted line indicates the original surface level [91]

8.4 Outlook

8.4.1 Recent Instrumental Developments

Sub-100fs laser processing of solid materials yields success when near-threshold phenomena are targeted. The application of high energy fs-pulses on the basis of amplified low repetition rate systems (chirped pulse amplifier CPA) may not be purposeful in this context. The finding that sub-100fs pulses lead to a drastic quality increase of dielectric ablation of dielectrics in the nJ-energy range [7, 8, 92] triggered the development of high power oscillators [93]. Femtosecond laser oscillators delivering pulses with energies at the hundred nanojoule level or beyond using high numerical aperture focusing optics are of interest, e.g., for the precision laser machining of dielectrics on a submicrometer scale [94]. These technologies are important for scientific and industrial applications likewise and have so far mainly relied on CPA systems [95–99]. Replacement of these complex and expensive femtosecond laser systems with compact and relatively low-cost sources without compromising their efficiency in machining materials at MHz rates would greatly enhance proliferation of these novel optical technologies. Standard femtosecond laser oscillators deliver pulses with energies of merely a few nanojoules [100], which is insufficient for most machining and modification purposes, such as writing waveguide structures in bulk material which requires pulse energies >10 nJ [101, 102]. On the other hand, CPA systems suffer from low pulse energy stability and correspondingly reduced material processing quality.

The traditional approach of increasing the pulse energy from femtosecond laser oscillators has been cavity dumping [103]. Its complexity and limitations (pulse energies typically below 100 nJ) barred this technique from widespread use. Another, more recent concept is based on a substantial increase of the resonator length [104, 105]. This approach provides room for increasing the pulse energy at constant average power but, in the early demonstrations [104, 105], it was limited in its scalability by instabilities caused by excessive nonlinear effects in the laser medium. A further approach to increase pulse energies is the increase of pump power of the pump source. For Ti:Sapphire these are frequency doubled continuous wave solid state laser at wavelength of 532 nm just recently breaking the barrier of 10 W. Nowadays pump sources up to 20 W are available. Difficulties with this method are thermal side effects in the crystal, like thermal lensing and less efficiency due to thermal population of the lower laser level.

Recently, these limitations were overcome by breaking the 100 nJ barrier in fs-pulse generation from laser oscillators. The first concept stabilizes single fs-pulses by high net negative cavity group-delay dispersion (GDD) and allowed 150 nJ scale pulse generation [106] at the full repetition rate of a mode-locked laser (NDR: negative dispersion regime) [104]. The main advantage of this concept is the generation of chirp-free, near-bandwidth limited fs-pulses directly from the laser oscillator. However, the laws of soliton-like pulse formation imply that the pulse duration must be traded off against the pulse energy.

An alternative technique introduces a net positive cavity GDD [107, 108], which tends to broaden the pulse with increasing pulse energies, thereby permitting scaling to higher pulse energies without the onset of instabilities [109]. In this chirped-pulse mode locking approach, the laser delivers heavily chirped pulses of several ps duration, requiring pulse compression outside the cavity but allows pulse energy scaling without compromising the compressed pulse duration [110, 111] (CPO: chirped pulse oscillator). This type is one of the most promising high-repetition rate approaches with sufficient pulse energy for non-linear nanoscale processing.

The typical average output power of CPA and CPO systems is in the range of 1 W (Fig. 8.13). While CPA sources operate at kilohertz repetition rates, a CPO emits pulses in a megahertz train. For highest precision micro- or nanomachining, the pulse energy must be attenuated to slightly above the damage threshold. Because the CPO already operates in this regime, almost all the average power is available for use. Moreover, for many industrial applications there is an absolute requirement for higher productivity, i.e., higher repetition rates, which can be provided by a CPO [93].

It has been shown that by carefully designing chirped-pulse oscillators, pulse energies of up to 500 nJ at pulse durations of <50 fs can be gained [100], which is much higher than pulse energies achieved in NDR systems. A typical setup is shown in Fig. 8.14a which is in use in the authors' laboratory (Fig. 8.14b) in an analogue configuration. It uses an imaging telescope optics (Herriott multipass cell [112, 113]) to maintain the stability of the cavity by prolonging its length.

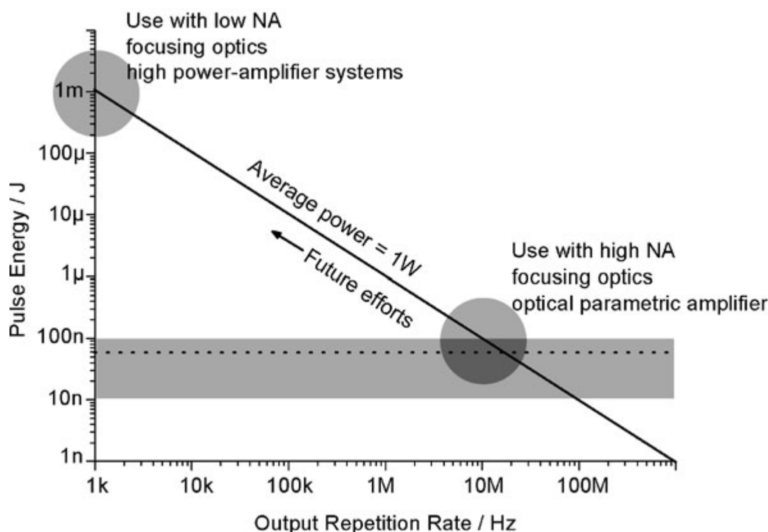

Fig. 8.13 Comparison between amplified laser system (CPA) and high energy oscillators concerning repetition rate and output energy

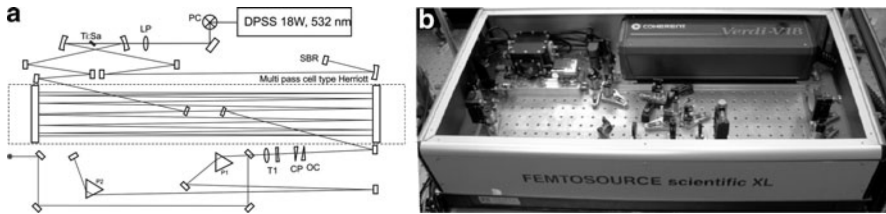

Fig. 8.14 (**a**) Cavity configuration of a 5-MHz 500 nJ CPO. PC: Periscope in the pump beam. L: lens. SBR: Saturable Bragg Reflector. OC: Output coupler. CP: Compensation Plate. T: Telescope. P: Prism. DPSS: Diode Pumped Solid State Laser. (Courtesy: Femtolasers Produktions GmbH). (**b**) Chirped-pulse oscillators (CPO) pumped by a 18-W frequency-doubled Nd:YAG laser (Department of Physical Chemistry, University of Vienna, Austria)

8.4.2 Nanostructuring in the Nearfield

A new field of nanostructuring was proposed on the basis of apertureless scanning near-field optical microscopy (a-SNOM) nanomachining with nanosecond laser illuminated scanning tunneling microscopy tips [114, 115] (also see Chap. 1). A local intensity enhancement of the nanosecond laser radiation close to the sharp STM tip was considered as mechanism [115–118]. STM based nanoprocessing schemes have the restriction to work only with electrically conductive samples and tips. A femtosecond laser STM study [119] suggested that not only ns- but also fs-irradiation of STM tips leads to thermal expansion resulting in scratching of the sample and not to a tunneling current increase due to local field enhancement. Resolution limitations of the technique are the contact of the tip with the sample surface due to thermal expansion [119, 120].

For non-metallic materials an AFM approach to the nearfield enhancement on the tip was developed [121, 122]. Thermal expansion of the tip, the field enhancement factor underneath the tip, and the sample surface heating were estimated. It is proposed that a field-enhancement mechanism is the dominant reason for this nanoprocessing [123]. Even 10 nm-sized structures were observed [124].

Another approach to make use of a local field enhancement on substrates was the deposition of gold nanoantennas [125, 126] (also see Chaps. 1 and 12). An additional field enhancement derives from surface plasmon resonance in contrast to silicon tips in AFM applications.

Femtosecond nanosurgery has been demonstrated well below the breakdown threshold of water. Chemical cell damage, intracellular dissection, and cell transfection can be correlated with increasing local free electron densities between 10^{14} and 10^{18} cm^{-3}, well below densities above 10^{19} cm^{-3} yielding bubble formation [127] (also see Chap. 6).

8.5 Summary

Femtosecond excitation provided the promising perspective that laser radiation interaction with the evolving plasma is minimized and that heat affected zones are reduced into the nanoscale range in contrast to pico- and nanosecond laser processing. This triggered intensive investigations in the sub-ps regime. Near-threshold non-linear nanoscale processing phenomena generated by sub-100fs laser pulses have been reviewed.

A theoretical review covered all kinds of sub-100fs laser irradiation interactions with the electronic systems resulting in ionisation, impact ionisation, strong-field ionisation, multiphoton absorption, and, e.g., so-called over-the-barrier ionisation. An increase in the electron–phonon coupling term with electron temperature is a recent improvement in modeling experiments of metals by the well-established two-temperature model. A detailed review of a thermodynamic approach of thermal processes occurring after the electron–phonon relaxation time covers processes such as normal vaporization, normal boiling, phase explosion, and subsurface heating.

Top-down approaches to nanostructures are based on the minimization of the heat affected zones into the nanoscale range. Top-down precision of laser machining in the far field is limited by the Abbe diffraction limit. Femtosecond pulses can overcome the diffraction limit by choosing the peak laser fluence slightly above the ablation threshold. Even resolutions down to 10 nm were demonstrated. The heat affected zone and heat diffusion length, respectively, could be validated for various thin film systems by monitoring the ablation threshold fluence when the film thickness becomes less than the heat diffusion length. The investigations of incubation are of overriding importance at least as a bridge between fundamental studies and applied materials science. An empirical observable is the incubation factor.

Besides the top-down approach to manufacture nanostructures by near threshold interactions with solids the bottom-up principle opens up fascinating possibilities when femtosecond lasers are employed to generate so-called ripples. Their periodicity depends on the wavelength, the angle of incidence, the fluence and the polarization of the laser beam. A direct correlation exists between chemical composition, fluid contact and ripple character.

Laser processing of biogenetic materials has attracted vivid attention in medicine and also in art conservation. Sub-100fs laser near-threshold processing of solid materials is triggering the development of high power oscillators with the advantage of high-repetition rate approaches with sufficient pulse energy for non-linear nanoscale processing.

References

1. S. Küper, M. Stuke, *Appl. Phys. B-Photophys. Laser Chem.* **44**, 199 (1987)
2. W. Kautek, S. Mitterer, J. Krüger, W. Husinsky, G. Grabner, *Appl. Phys. A-Mater. Sci. Process.* **58**, 513 (1994)

3. J. Krüger, W. Kautek, *Laser Phys.* **9**, 30 (1999)
4. D. Bäuerle, *Laser Processing and Chemistry*, 3rd rev. enlarged ed., (Springer, Berlin, London, 2000)
5. C.R. Phipps, B.S. Lukyan'chuk, *Laser Ablation and Its Applications*, (Springer, New York, 2007)
6. J. Krüger, W. Kautek, *Adv. Polym. Sci.* **168**, 247 (2004)
7. W. Kautek, J. Krüger, M. Lenzner, S. Sartania, C. Spielmann, F. Krausz, *Appl. Phys. Lett.* **69**, 3146 (1996)
8. M. Lenzner, J. Krüger, S. Sartania, Z. Cheng, C. Spielmann, G. Mourou, W. Kautek, F. Krausz, *Phys. Rev. Lett.* **80**, 4076 (1998)
9. M. Lenzner, F. Krausz, J. Krüger, W. Kautek, *Appl. Surf. Sci.* **154**, 11 (2000)
10. J. Krüger, W. Kautek, *Appl. Surf. Sci.* **96–8**, 430 (1996)
11. J. Krüger, P. Meja, M. Autric, W. Kautek, *Appl. Surf. Sci.* **186**, 374 (2002)
12. F. Costache, M. Henyk, J. Reif, *Appl. Surf. Sci.* **186**, 352 (2002)
13. J. Reif, F. Costache, M. Henyk, S.V. Pandelov, *Appl. Surf. Sci.* **197**, 891 (2002)
14. F. Costache, M. Henyk, J. Reif, *Appl. Surf. Sci.* **208**, 486 (2003)
15. J. Bonse, M. Geuss, S. Baudach, H. Sturm, W. Kautek, *Appl. Phys. A-Mater. Sci. Process.* **69**, S399 (1999)
16. J. Bonse, P. Rudolph, J. Krüger, S. Baudach, W. Kautek, *Appl. Surf. Sci.* **154**, 659 (2000)
17. J. Bonse, S. Baudach, J. Krüger, W. Kautek, M. Lenzner, *Appl. Phys. A-Mater. Sci. Process.* **74**, 19 (2002)
18. H.O. Jeschke, M.E. Garcia, M. Lenzner, J. Bonse, J. Krüger, W. Kautek, *Appl. Surf. Sci.* **197**, 839 (2002)
19. J. Bonse, K.W. Brzezinka, A.J. Meixner, *Appl. Surf. Sci.* **221**, 215 (2004)
20. F. Costache, S. Kouteva-Arguirova, J. Reif, *Appl. Phys. A-Mater. Sci. Process.* **79**, 1429 (2004)
21. F. Costache, S. Kouteva-Arguirova, J. Reif, *Gettering Defect Eng. Semiconductor Technol.* **95–96**, 635 (2004)
22. J. Bonse, J.M. Wrobel, J. Krüger, W. Kautek, *Appl. Phys. A-Mater. Sci. Process.* **72**, 89 (2001)
23. J. Bonse, J.M. Wrobel, K.W. Brzezinka, N. Esser, W. Kautek, *Appl. Surf. Sci.* **202**, 272 (2002)
24. J. Bonse, H. Sturm, D. Schmidt, W. Kautek, *Appl. Phys. A-Mater. Sci. Process.* **71**, 657 (2000)
25. L.V. Keldysh, *Soviet Phys. Jetp-Ussr* **20**, 1307 (1965)
26. S. Augst, D. Strickland, D.D. Meyerhofer, S.L. Chin, J.H. Eberly, *Phys. Rev. Lett.* **63**, 2212 (1989)
27. R. Stoian, D. Ashkenasi, A. Rosenfeld, M. Wittmann, R. Kelly, E.E.B. Campbell, *Nucl. Instrum. Methods Phys. Res. B* **166**, 682 (2000)
28. T.E. Dermota, Q. Zhong, A.W. Castleman, *Chem. Rev.* **104**, 1861 (2004)
29. R. Stoian, D. Ashkenasi, A. Rosenfeld, E.E.B. Campbell, *Phys. Rev. B* **62**, 13167 (2000)
30. B.C. Stuart, M.D. Feit, A.M. Rubenchik, B.W. Shore, M.D. Perry, *Phys. Rev. Lett.* **74**, 2248 (1995)
31. A. Kaiser, B. Rethfeld, M. Vicanek, G. Simon, *Phys. Rev. B* **61**, 11437 (2000)
32. B. Rethfeld, *Phys. Rev. Lett.* **92** (2004)
33. B.H. Christensen, Ph.D. thesis, University of Aarhus, (2008)
34. S.S. Wellershoff, J. Hohlfeld, J. Güdde, E. Matthias, *Appl. Phys. A-Mater. Sci. Process.* **69**, S99 (1999)
35. J. Hohlfeld, S.S. Wellershoff, J. Güdde, U. Conrad, V. Jahnke, E. Matthias, *Chem. Phys.* **251**, 237 (2000)
36. J. Güdde, J. Hohlfeld, J.G. Muller, E. Matthias, *Appl. Surf. Sci.* **129**, 40 (1998)
37. P.B. Corkum, F. Brunel, N.K. Sherman, T. Srinivasanrao, *Phys. Rev. Lett.* **61**, 2886 (1988)
38. S.I. Anisimov, B.L. Kapeliov, T.L. Perelman, *Zhurnal Eksperimentalnoi i Teoreticheskoi Fiziki* **66**, 776 (1974)
39. P.B. Allen, *Phys. Rev. Lett.* **59**, 1460 (1987)
40. B.H. Christensen, K. Vestentoft, P. Balling, *Appl. Surf. Sci.* **253**, 6347 (2007)
41. A. Miotello, R. Kelly, *Appl. Phys. Lett.* **67**, 3535 (1995)
42. P. Lorazo, L.J. Lewis, M. Meunier, *Phys. Rev. Lett.* **91** (2003)
43. D. Perez, L.J. Lewis, *Phys. Rev. B* **67** (2003)

44. P. Lorazo, L.J. Lewis, M. Meunier, *Phys. Rev. B* **73** (2006)
45. S. Amoruso, R. Bruzzese, N. Spinelli, R. Velotta, M. Vitiello, X. Wang, G. Ausanio, V. Iannotti, L. Lanotte, *Appl. Phys. Lett*. **84**, 4502 (2004)
46. R. Kelly, A. Miotello, *Phys. Rev. E* **60**, 2616 (1999)
47. D. von der Linde, K. Sokolowski-Tinten, J. Bialkowski, *Appl. Surf. Sci*. **110**, 1 (1997)
48. J.X. Zhao, B. Hüttner, A. Menschig, *Opt. Laser Technol*. **33**, 487 (2001)
49. F. Korte, J. Serbin, J. Koch, A. Egbert, C. Fallnich, A. Ostendorf, B.N. Chichkov, *Appl. Phys. A-Mater. Sci. Process*. **77**, 229 (2003)
50. J. Koch, E. Fadeeva, M. Engelbrecht, C. Ruffert, H.H. Gatzen, A. Ostendorf, B.N. Chichkov, *Appl. Phys. A-Mater. Sci. Process*. **82**, 23 (2006)
51. K. König, I. Riemann, W. Fritzsche, *Opt. Lett*. **26**, 819 (2001)
52. U.K. Tirlapur, K. König, *Nature* **418**, 290 (2002)
53. A.P. Joglekar, H.H. Liu, E. Meyhofer, G. Mourou, A.J. Hunt, *Proc. Natl. Acad. Sci. USA* **101**, 5856 (2004)
54. E. Matthias, M. Reichling, J. Siegel, O.W. Kading, S. Petzoldt, H. Skurk, P. Bizenberger, E. Neske, *Appl. Phys. A-Mater. Sci. Process*. **58**, 129 (1994)
55. E. Matthias, J. Siegel, S. Petzoldt, M. Reichling, H. Skurk, O. Kading, E. Neske, *Thin Solid Films* **254**, 139 (1995)
56. J. Krüger, D. Dufft, R. Koter, A. Hertwig, *Appl. Surf. Sci*. **253**, 7815 (2007)
57. S. Preuss, E. Matthias, M. Stuke, *Appl. Phys. A-Mater. Sci. Process*. **59**, 79 (1994)
58. M. Forster, L. Égerházi, C. Haselberger, C. Huber, T. Szörényi, W. Kautek, submitted (2010)
59. L. Egerhazi, Z. Geretovszky, T. Szörényi, *Appl. Surf. Sci*. **247**, 182 (2005)
60. R. Fardel, M. Nagel, T. Lippert, F. Nuesch, A. Wokaun, B.S. Luk'yanchuk, *Appl. Phys. A-Mater. Sci. Process*. **90**, 661 (2008)
61. S. Baudach, J. Bonse, W. Kautek, *Appl. Phys. A-Mater. Sci. Process*. **69**, S395 (1999)
62. E.W. Vanstryland, M.J. Soileau, A.L. Smirl, W.E. Williams, *Phys. Rev. B* **23**, 2144 (1981)
63. M. Eyett, D. Bäuerle, *Appl. Phys. Lett*. **51**, 2054 (1987)
64. L.G. DeShazer, B.E. Newnam, K.M. Leung, *Appl. Phys. Lett*. **23**, 607 (1973)
65. B.M. Kim, M.D. Feit, A.M. Rubenchik, E.J. Joslin, J. Eichler, P.C. Stoller, L.B. Da Silva, *Appl. Phys. Lett*. **76**, 4001 (2000)
66. S. Martin, A. Hertwig, M. Lenzner, J. Krüger, W. Kautek, *Appl. Phys. A-Mater. Sci. Process*. **77**, 883 (2003)
67. A. Hertwig, S. Martin, J. Krüger, W. Kautek, *Thin Solid Films* **453–54**, 527 (2004)
68. M. Birnbaum, *J. Appl. Phys*. **36**, 3688 (1965)
69. P. Rudolph, K.W. Brzezinka, R. Wäsche, W. Kautek, *Appl. Surf. Sci*. **208**, 285 (2003)
70. P. Rudolph, W. Kautek, *Thin Solid Films* **453–54**, 537 (2004)
71. W. Kautek, P. Rudolph, G. Daminelli, J. Krüger, *Appl. Phys. A-Mater. Sci. Process*. **81**, 65 (2005)
72. G. Daminelli, J. Krüger, W. Kautek, *Thin Solid Films* **467**, 334 (2004)
73. M. Shen, J.E. Carey, C.H. Crouch, M. Kandyla, H.A. Stone, E. Mazur, *Nano Lett*. **8**, 2087 (2008)
74. W. Kautek, *Physical Chemistry of Ultrafast Laser Interaction with Solids*, (Springer, New York, 2007)
75. J. Reif, M. Ratzke, O. Varlamova, F. Costache, *Mater. Sci. Eng. B-Solid State Mater. Adv. Technol*. **134**, 114 (2006)
76. O. Varlamova, F. Costache, M. Ratzke, J. Reif, *Appl. Surf. Sci*. **253**, 7932 (2007)
77. G. Miyaji, K. Miyazaki, *Appl. Phys. Lett*. **91** (2007)
78. M. Groenendijk, *Fabrication of Super Hydrophobic Surfaces by fs Laser Pulses, Vol. 3*, (Wiley, Weinheim, 2008)
79. C.A. Aguilar, Y. Lu, S. Mao, S.C. Chen, *Biomaterials* **26**, 7642 (2005)
80. E. Rebollar, G. Bounos, M. Oujja, C. Domingo, S. Georgiou, M. Castillejo, *J. Phys. Chem. B* **110**, 14215 (2006)
81. S. Gaspard, A. Oujja, R. de Nalda, C. Abrusci, F. Catalina, L. Banares, M. Castillejo, *Appl. Surf. Sci*. **253**, 6420 (2007)

82. S. Gaspard, M. Oujja, R. de Nalda, C. Abrusci, F. Catalina, L. Banares, S. Lazare, M. Castillejo, *Appl. Surf. Sci*. **254**, 1179 (2007)
83. S. Gaspard, M. Oujja, R. de Nalda, M. Castillejo, L. Banares, S. Lazare, R. Bonneau, *Appl. Phys. A-Mater. Sci. Process*. **93**, 209 (2008)
84. Y.M. Liu, S. Sun, S. Singha, M.R. Cho, R.J. Gordon, *Biomaterials* **26**, 4597 (2005)
85. S. Lazare, V. Tokarev, A. Sionkowska, M. Wisniewski, *Appl. Phys. A-Mater. Sci. Process*. **81**, 465 (2005)
86. S. Lazare, V.N. Tokarev, A. Sionkowska, M. Wisniewski, *COLA'05 8th Internatl. Conf. Laser Ablation* **59**, 543 (2007)
87. J. Krüger, W. Kautek, H. Newesely, *Appl. Phys. A-Mater. Sci. Process*. **69**, S403 (1999)
88. W. Kautek, S. Pentzien, P. Rudolph, J. Krüger, E. Künig, *Appl. Surf. Sci*. **129**, 746 (1998)
89. W. Kautek, S. Pentzien, P. Rudolph, J. Krüger, C. Maywald-Pitellos, H. Bansa, H. Grosswang, E. König, *Opt. Lasers Biomed. Cult. Optics Within Life Science (OWLS V)*, Springer-Verlag, Heidelberg, 100 (2000)
90. S. Batishche, A. Kouzmouk, H. Tatur, T. Gorovets, U. Pilipenka, V. Ukhau, W. Kautek, *Lasers Conserv. Artworks Proc*. **116**, 221 (2007)
91. S. Gaspard, M. Forster, C. Huber, C. Zafiu, G. Trettenhahn, W. Kautek, M. Castillejo, *Phys. Chem. Chem. Phys*. **10**, 6174 (2008)
92. M. Lenzner, J. Krüger, W. Kautek, F. Krausz, *Appl. Phys. A-Mater. Sci. Process*. **68**, 369 (1999)
93. A. Fürbach, A. Stingl, M. Essary, *Laser Focus World* **40**, 135 (2004)
94. S. Naumov, A. Fernandez, R. Graf, P. Dombi, F. Krausz, A. Apolonski, *New J. Phys*. **7** (2005)
95. T. Brabec, F. Krausz, *Rev. Modern Phys*. **72**, 545 (2000)
96. A.H. Nejadmalayeri, P.R. Herman, J. Burghoff, M. Will, S. Nolte, A. Tünnermann, *Opt. Lett*. **30**, 964 (2005)
97. N. Takeshima, Y. Narita, S. Tanaka, Y. Kuroiwa, K. Hirao, *Opt. Lett*. **30**, 352 (2005)
98. N. Sanner, N. Huot, E. Audouard, C. Larat, P. Laporte, J.P. Huignard, *Appl. Phys. B-Lasers Opt*. **80**, 27 (2005)
99. F. Dausinger, F. Lichtner, H. Lubatschowski, *Femtosecond Technology for Technical and Medical Applications*, (Springer, Berlin, New York, 2004)
100. Femtolasers Produktions GmbH, Fernkorngasse 10, A-1100 Wien, Austria; www.femtolasers.com
101. A.M. Kowalevicz, V. Sharma, E.P. Ippen, J.G. Fujimoto, K. Minoshima, *Opt. Lett*. **30**, 1060 (2005)
102. R. Osellame, N. Chiodo, V. Maselli, A. Yin, M. Zavelani-Rossi, G. Cerullo, P. Laporta, L. Aiello, S. De Nicola, P. Ferraro, A. Finizio, G. Pierattini, *Opt. Express* **13**, 612 (2005)
103. A. Killi, U. Morgner, M.J. Lederer, D. Kopf, *Opt. Lett*. **29**, 1288 (2004)
104. S.H. Cho, B.E. Bouma, E.P. Ippen, J.G. Fujimoto, *Opt. Lett*. **24**, 417 (1999)
105. A. Apolonski, A. Poppe, G. Tempea, C. Spielmann, T. Udem, R. Holzwarth, T.W. Hansch, F. Krausz, *Phys. Rev. Lett*. **85**, 740 (2000)
106. A.M. Kowalevicz, A.T. Zare, F.X. Kärtner, J.G. Fujimoto, S. Dewald, U. Morgner, V. Scheuer, G. Angelow, *Opt. Lett*. **28**, 1597 (2003)
107. B. Proctor, E. Westwig, F. Wise, *Opt. Lett*. **18**, 1654 (1993)
108. J.M. Dudley, S.F. Boussen, D.M.J. Cameron, J.D. Harvey, *Appl. Opt*. **38**, 3308 (1999)
109. A. Fernandez, T. Fuji, A. Poppe, A. Fürbach, F. Krausz, A. Apolonski, *Opt. Lett*. **29**, 1366 (2004)
110. V.L. Kalashnikov, E. Podivilov, A. Chernykh, S. Naumov, A. Fernandez, R. Graf, A. Apolonski, *New J. Phys*. **7** (2005)
111. A. Fernandez, A. Verhoef, V. Pervak, G. Lermann, F. Krausz, A. Apolonski, *Appl. Phys. B-Lasers Opt*. **87**, 395 (2007)
112. D. Herriott, R. Kompfner, H. Kogelnik, *Appl. Opt*. **3**, 523 (1964)
113. A. Sennaroglu, J.G. Fujimoto, *Opt. Express* **11**, 1106 (2003)
114. A.A. Gorbunov, W. Pompe, *Physica Status Solidi A-Appl. Res*. **145**, 333 (1994)
115. J. Jersch, K. Dickmann, *Appl. Phys. Lett*. **68**, 868 (1996)

116. J. Jersch, F. Demming, J. Hildenhagen, K. Dickmann, *Opt. Laser Technol*. **29**, 433 (1997)
117. J. Jersch, F. Demming, L.J. Hildenhagen, K. Dickmann, *Lasers Mater. Process*. **3097**, 244 (1997)
118. Y.F. Lu, Z.H. Mai, G. Qiu, W.K. Chim, *Appl. Phys. Lett*. **75**, 2359 (1999)
119. J. Boneberg, H.J. Münzer, M. Tresp, M. Ochmann, P. Leiderer, *Appl. Phys. A-Mater. Sci. Process*. **67**, 381 (1998)
120. R. Huber, M. Koch, J. Feldmann, *Appl. Phys. Lett*. **73**, 2521 (1998)
121. K. Dickmann, J. Jersch, F. Demming, *Surf. Interface Anal*. **25**, 500 (1997)
122. Y.F. Lu, B. Hu, Z.H. Mai, W.J. Wang, W.K. Chim, T.C. Chong, *Jpn. J. Appl. Phys. 1-Regular Papers Short Notes Rev. Papers* **40**, 4395 (2001)
123. S.M. Huang, M.H. Hong, Y.F. Lu, B.S. Lukyanchuk, W.D. Song, T.C. Chong, *J. Appl. Phys*. **91**, 3268 (2002)
124. A. Chimmalgi, T.Y. Choi, C.P. Grigoropoulos, K. Komvopoulos, *Appl. Phys. Lett*. **82**, 1146 (2003)
125. P. Leiderer, C. Bartels, J. König-Birk, M. Mosbacher, J. Boneberg, *Appl. Phys. Lett*. **85**, 5370 (2004)
126. J. Boneberg, J. König-Birk, H.J. Münzer, P. Leiderer, L. Shuford, C. Schatz, *Appl. Phys. A-Mater. Sci. Process*. **89**, 299 (2007)
127. A. Vogel, J. Noack, G. Hüttman, G. Paltauf, *Femtosecond Plasma-Mediated Nanosurgery of Cells and Tissues*, (Springer, New York, 2007)

Chapter 9
3D Fabrication of Embedded Microcomponents

Koji Sugioka and Stefan Nolte

Abstract Multiphoton absorption in transparent materials irradiated by a femtosecond (fs) laser can be used for three-dimensional (3D) microstructuring inside the materials. This technique has been widely applied to produce optical microcomponents and microfluidics embedded in glass. In this chapter, the principles of internal modification and fabrication by the laser are introduced, and state-of-the-art techniques are reviewed for applications in 3D photonics devices and integrated microchips for biochemical analysis and medical inspection.

9.1 Introduction

The ultra-short pulse widths and extremely high peak powers of femtosecond (fs) lasers are opening up new avenues for materials processing, and such lasers are becoming common tools for various applications. Their short pulse widths (typically $\sim$100 fs) minimize the formation of heat affected zones in the processed region, allowing for high-quality microstructuring of soft materials such as biological tissues [1] and hard or brittle materials, such as semiconductors and insulators [2]. This suppression of heat diffusion to the surroundings can also improve the spatial resolution of nanoscale processing [3]. The high peak powers of femtosecond lasers can induce strong absorption, even in materials such as glass that are transparent to the laser frequency, due to nonlinear multiphoton absorption. If the femtosecond laser beam is focused inside glass with a moderate pulse energy, multiphoton absorption can be confined to the region near the focal point, so that internal modification of transparent materials can be performed with a high spatial resolution.

K. Sugioka (✉)
Laser Technology Laboratory, RIKEN – Advanced Science Institute, Wako,
Saitama 351-0198, Japan
e-mail: ksugioka@riken.jp

S. Nolte
Institute of Applied Physics, Friedrich-Schiller-University Jena, Max-Wien-Platz 1,
07743 Jena, Germany
e-mail: stefan.nolte@uni-jena.de

K. Sugioka et al. (eds.), *Laser Precision Microfabrication*,
Springer Series in Materials Science 135, DOI 10.1007/978-3-642-10523-4_9,
© Springer-Verlag Berlin Heidelberg 2010

Three-dimensional (3D) microstructures and microcomponents can be embedded inside a material using this scheme. One active research area is the writing of optical waveguides buried in glass by refractive index modification [4, 5]. The internal index modification can be used to fabricate other embedded optical microcomponents including optical couplers and splitters [6], volume Bragg gratings [7], diffractive lenses [8], and waveguide lasers [9]. Another interesting application is the formation of 3D hollow microstructures by ablation [10, 11] or by internal modification followed by selective etching with wet chemicals [12, 13] for microfluidics. Integration of microfluidics with optical microcomponents enables the direct fabrication of 3D microchips for biochemical analysis or medical inspections. An example is the micro-total analysis system (μ-TAS) [14, 15].

In this chapter, the principles of internal modification and machining of transparent materials using an femtosecond laser are explained. Next, state-of-the-art techniques for fabricating optical microcomponents and 3D hollow microstructures, and for integrating these microcomponents in a single glass chip for biophotonic microchips, are reviewed.

9.2 Principles of Internal Processing

One of the most important features in materials processing using a femtosecond laser is nonlinear multiphoton absorption even in materials that are transparent to the frequency of the laser beam. Figure 9.1 depicts single and multiphoton absorption based on the electron excitation process. The normal absorption process is linear single-photon absorption. When light, whose photon energy is larger than the band gap of a specific material, is incident on the material, an electron is excited from the valence band to the conduction band by a single photon resulting in light absorption. On the other hand, light whose photon energy is smaller than the band gap cannot excite electrons, so that no absorption occurs. However, when

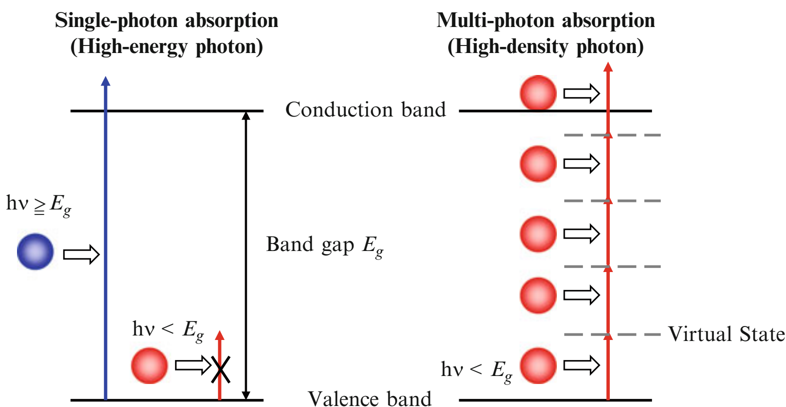

Fig. 9.1 Electron excitation process in materials by single and multiphoton absorption

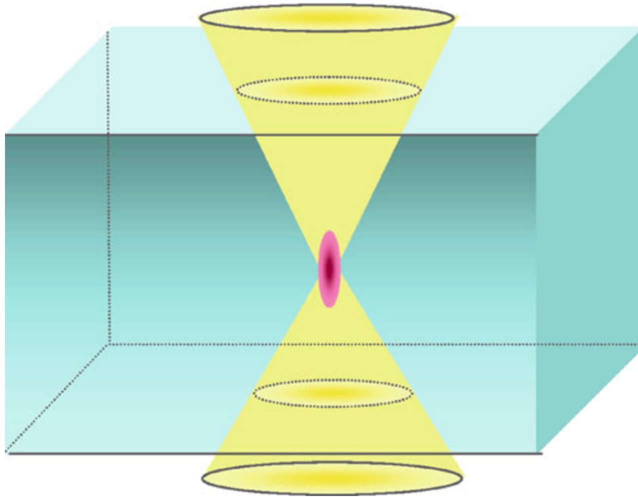

Fig. 9.2 Schematic of internal modification in a material by multiphoton absorption using a femtosecond laser

very high-density of photons, resulting from an extremely high peak power beam, are incident on the material, an electron can be excited by multiple photons even if the photon energy is smaller than the band gap. This phenomenon is referred to as multiphoton absorption. A high density of photons is obtained using femtosecond lasers due to the ultra-short pulse width. Thus, such lasers can induce strong absorption even in transparent materials, thereby enabling high-quality microprocessing of glass materials.

Multiphoton absorption is a nonlinear process and only occurs at intensities above a threshold, which is dependent on both the material and the pulse width. When the femtosecond laser beam is focused inside a transparent material with an adequate pulse energy, as shown in Fig. 9.2, absorption occurs in a region local to the focal point. Thus, internal modification and processing of materials can be performed using femtosecond lasers. This internal processing can be used to write 3D optical waveguides or to fabricate optical microcomponents and microchannels embedded in glass.

9.3 Refractive Index Modification

9.3.1 Advantages of Femtosecond Laser in Photonic Device Fabrication

Modern communication systems are based on integrated optical devices to control the properties of light in all-optical networks. Key elements within these networks

are active and passive waveguides, splitters, connectors, filters, and switches. The optical function of these elements is based on a spatial refractive index modification within the glass matrix, which is typically altered by ionic exchange or diffusion processes. Although these technologies are well established and very successful, their application is in general restricted to the generation of planar (two-dimensional (2D)) elements.

As described in Sect. 9.2, femtosecond lasers have the ability to induce bulk refractive index changes inside transparent materials. Since the energy deposition occurs through nonlinear absorption, the sample is modified only in the focal volume, where the laser intensity is high enough. Other regions including the substrate surface remain unaffected. This enables the direct fabrication of buried optical waveguides and more complex 3D photonic devices with great flexibility in different types of transparent media [16].

9.3.2 Optical Waveguide Writing

For the fabrication of waveguides, the localized, single-point modifications have to be combined into a line by moving the focus through the sample. This can be accomplished using two principally different writing geometries: focus movement parallel or transverse to the axis of the laser beam (see Fig. 9.3). The former tech-

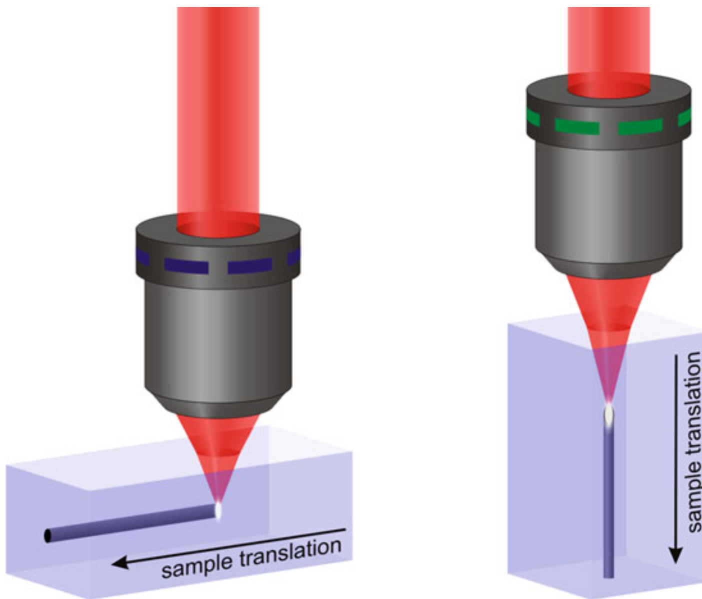

Fig. 9.3 Schematic of the different writing geometries. *Left*: sample movement transverse to writing beam; *Right*: sample movement parallel to writing beam

nique offers the advantage that the waveguides are circular in shape [17]; however, the working distance of the focusing lens and spherical aberrations limit the writing length of the waveguide. Thus, low numerical aperture (NA) objectives with long focal length are required to produce a few centimeter long waveguides. On the other hand, it has been demonstrated that such focusing conditions offer the potential for the generation of beam filamentation and the production of waveguides even without moving the focus [18].

In contrast, the transverse writing geometry is much more flexible. Structures can be fabricated within the bulk material, limited in size only by the positioning system, while the maximum structure depth is determined by the working distance of the focusing objective. The main disadvantage, however, is the asymmetry of the produced structure. Except for very high-NA objectives, the focal radius will always be much smaller than the confocal parameter, resulting in a waveguide with an elliptical cross section [19]. However, beam shaping techniques using an elliptical or rectangular writing beam result, in combination with the focus movement, in the formation of waveguides with a circular cross section [20–23] as discussed in Sect. 9.6. Symmetric waveguides have been recently also demonstrated by employing a multiscan approach, where the waveguide is composed by several overlapping modification lines [24–27].

It is important to note that such beam shaping is not required, if high repetition rate laser systems are used for the inscription. For repetition rates above $\sim$1 MHz, the time interval between successive pulses is shorter than the characteristic time for heat diffusion out of the focal volume, which is on the order of 1 μs. Consequently there is not enough time for the energy deposited by one laser pulse to diffuse out of the focal volume before the next pulse arrives. Over time, the energy from successive pulses accumulates, finally resulting in melting of the sample around the focal volume [28–30]. Note, that this is completely different from other thermal processing since it resembles a point source of heat within the bulk material.

However, despite the different techniques discussed above a localized increase of the refractive index, as required for waveguiding, cannot be obtained in all materials. Whether the refractive index change is positive or negative depends mainly on the material itself [31–35] but also on the processing parameters [36, 37]. These fundamentally different modifications – refractive index increase and decrease – are typically termed type I and II, respectively (Fig. 9.4). In type I modifications, the refractive index increases directly within the focal volume. Thus, the fabrication of a waveguide is straightforward.

Type II modifications are based on a refractive index decrease and/or massive damage of the lattice structure in the focal volume. Outside of this volume, a polarization dependent refractive index increase can be observed due to compression and densification as well as induced stress [5, 37]. While these structures intrinsically have an asymmetry, symmetric waveguiding structures are obtained by overlapping stress fields from different modifications [37, 38] (see Fig. 9.4, right). Since the light is guided in this case in an area which is not directly structured by the femtosecond laser, material properties such as nonlinearity are preserved [39]. This is important when considering devices for frequency conversion or electro-optical modulation (see Sect. 9.3.3).

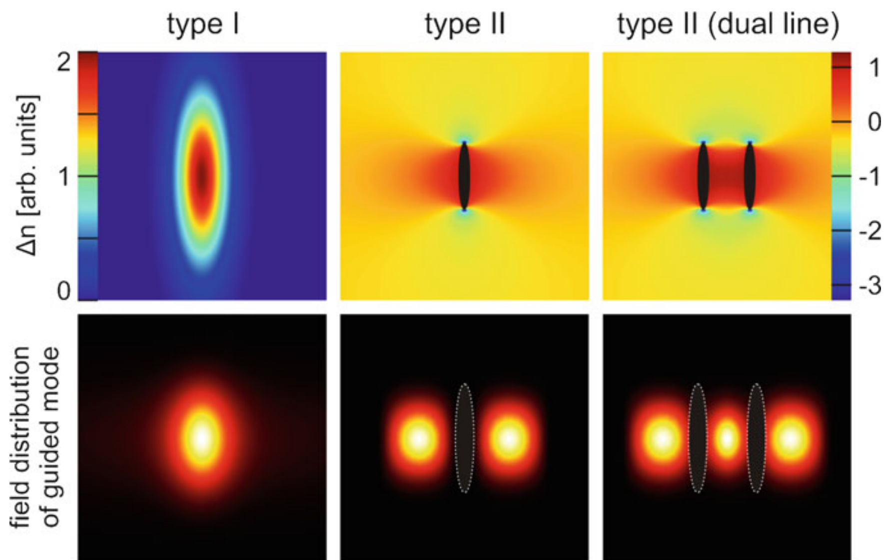

Fig. 9.4 Different types of refractive index modification (*upper row*) and resulting near field intensity distributions of guided light (*lower row*). Type I (*left*): refractive index increase in the focal region, ideally suited for direct waveguide writing. Type II (*middle*): Refractive index decrease/material destruction within focal volume; guiding occurs outside the central region. *Right*: By overlapping two stress fields symmetrical guiding can be obtained in between the modifications; the guiding properties depend on writing parameters and on the distance between modifications. Using appropriate excitation conditions single mode guiding can be obtained in the central region

Using the approaches described above, buried waveguides have been directly written in various glasses [4, 17, 34, 35, 40], actively doped glasses [41–44], crystals [4, 45–47], and polymers [48–51]. The change in refractive index depends on the pulse energy [52] and the writing speed [19] and is typically around 10^{-3}, which is comparable to conventional ion diffusion techniques. This allows the generation of single- as well as multimode waveguides. Transmission losses of <0.4 dB/cm are typically achieved [25, 53], which are suitable for most integrated optics applications. However, also significantly lower losses (0.05 dB/cm) have been realized by thermal annealing following irradiation [54]. While this sequential direct write approach is obviously applicable for prototyping, also small scale mass fabrication can be considered taking into account that writing speeds of up to 10 cm/s have been demonstrated [53].

9.3.3 Fabrication of Photonic Devices

Apart from simple waveguides, even much more complex devices can be fabricated simply by moving the focus along the desired paths. The use of 3D capabilities offers the potential for higher packing density and allows avoiding crossings

quite easily. Therefore, couplers and splitters have been reported not only in 2D [52, 55, 56] but also in 3D [6, 57, 58]. Moreover, the large flexibility in processing allows even to fabricate complex structures such as multimode interference (MMI) couplers [59]. Here, the radiation, which is inserted into a single mode waveguide, is propagating inside the device in a multimode region. Depending on the wavelength, the single mode output ports can have different coupling ratios.

Such a wavelength dependent coupling is also one of the fundamental principles of directional couplers, where the coupling is based on the waveguides being in close proximity. Energy exchange takes place via the evanescent fields of the guided modes. By control of the interaction lengths, the desired wavelength dependent coupling ratios are obtained. Even full 3D devices have been demonstrated [6, 60], showing high integration density as well as the incorporation of resonant structures [58].

The density of optical functions on one chip can be also increased by stacking the waveguides up to an array [61]. While this approach directly makes use of the third dimension, even more interesting devices can be generated when stacking the waveguides so close together that the evanescent fields will be able to couple to adjacent waveguides as in the directional couplers described above. In this case, the structure can no longer be described as a collection of single waveguides but must be treated as a whole. In contrast to the unstructured material, this device no longer shows the standard diffraction behavior when exposed to light but exhibits the peculiar features of discrete diffraction [62, 63]. Due to the discrete nature, there exist many analogies to other discrete systems, for example, in solid state physics [64] or quantum mechanics [65]. However, this optical approach allows to directly visualize [64, 66, 67] a variety of fundamentally interesting effects like the influence of surfaces [68] or of the interface between different arrays [69]. In addition, for very high intensities, when the interaction with the material becomes nonlinear, the formation of stable discrete solitons can be observed [70, 71] which opens the possibility for the realization of new all-optical switching and routing concepts [72, 73]. Note that the realization of such an array of coupled waveguides requires a high homogeneity of the refractive index changes induced in each waveguide, since even small deviations in phase between the waveguides will result in a significantly altered intensity distribution at the exit of the device. Thus, these experiments are an excellent demonstration of the high accuracy that can be obtained by the femtosecond laser direct writing approach.

For real photonic chips, however, active devices also have to be realized. In particular the realization of optical amplifiers is important in order to provide an opportunity for the compensation of device losses. While the first demonstration of gain in a femtosecond written waveguide was done in a Nd-doped silicate glass [41], most of the work concentrated on active devices in Er:Yb-doped phosphate glasses. Here, net gain over the whole C-band of optical communications was demonstrated [74]. The obtained peak internal gain of $\sim$2.5 dB/cm is comparable to state-of-the-art Er:Yb-doped waveguide amplifiers fabricated by ion exchange. Meanwhile, waveguide amplifiers have been demonstrated also in a variety of other glasses and crystals with other dopants [75–82].

When the waveguide amplifiers are combined with wavelength selective reflectors, they can be operated as waveguide lasers. These wavelength selective reflectors can be made of fiber Bragg gratings, which are located inside the fibers used for launching the pump light into the active waveguide amplifier. Using such an approach, fs-written waveguide lasers were demonstrated in Er:Yb-doped glasses [36, 83, 84] as well as Nd-doped YAG and YAG ceramics [76, 81]. Note that also the fiber Bragg gratings can be fabricated by the femtosecond laser direct writing approach (see Sect. 9.3.4). The incorporation of the Bragg grating into the waveguides itself [85–87] allows the fabrication of monolithic waveguide lasers [88] with output powers of more than 100 mW [89]. On the other hand, the waveguide amplifiers can be used in a ring cavity. Even the modelocked operation of such an arrangement has been reported providing pulse durations of few picoseconds (ps) [90].

Magneto-optical and electro-optical switching devices have been demonstrated recently in fs-written samples. The magneto-optical switching waveguides have been produced inside a bulk terbium-doped Faraday glass, where, quite remarkably, the micromachined region shows almost no change in the Verdet constant compared to the non-irradiated material [91]. Electro-optical switching has been demonstrated both in glass as well as in crystals. Since glasses do not exhibit an electro-optical effect due to their inherent symmetry, thermal poling can induce this switching. For the modulator, a 3D Mach–Zehnder interferometer (MZI) was written into bulk fused silica and a thin (20 μm thick) nonlinear layer was induced by thermal poling afterward [92]. The input and output ports of the MZI were written significantly below the surface to avoid surface and edge defects, while the central two arms were written close to the sample surface in order to maximize the overlap with the nonlinear layer, thus making full use of the 3D capability of the process.

In contrast to thermally poled glass, bulk crystals exhibit much higher second order nonlinearity. For example, lithium niobate ($LiNbO_3$) is widely used in integrated optics due to its wide transparency range and its outstanding electrooptic and nonlinear properties. While in most crystals only type II modifications can be realized, $LiNbO_3$ shows both types of modifications depending on processing parameters [93], which can be understood based on the induced lattice defects [37]. At low intensities, only point defects are generated, resulting in a reduction of the spontaneous polarization. This leads to an increase of the extraordinary refractive index in the modified region. In contrast, at high intensities strong material damage is induced, causing stresses in the surrounding materials, leading to a polarization dependent refractive index increase (type II).

Although type I structures are easier to use for the fabrication of waveguides, type II structures show a higher thermal stability [93]. Moreover, the nonlinearity in type I structures is significantly reduced. Since the guiding is occurring outside the directly modified regions in type II waveguides, these structures still show the full nonlinearity. Therefore, efficient modulators have been realized using type II waveguides [93, 94].

In addition to MZI, the waveguides in $LiNbO_3$ can be used for frequency conversion. In contrast to conventional integrated optical waveguides located at the surface, the inherent symmetry of the deeply buried fs-written waveguides results

in a better overlap between fundamental and second harmonic light. Such wavelength converters have been realized in periodically poled $LiNbO_3$ (to ensure quasi phase-matching) by type I as well as type II structures. The nonlinearity in type I structures was almost preserved in this case by choosing special processing parameters [27]. However, since type II structures are much more temperature resistant, these structures can be operated at elevated temperatures avoiding damage due to the photorefractive effect [39].

9.3.4 Fabrication of Fiber Bragg Gratings (FBGs)

The femtosecond laser writing technique has also been successfully applied for the realization of fiber Bragg gratings (FBG). FBGs have become key components for optical telecommunication systems and sensor applications. They exhibit low losses and allow in-line spectral control of the guided light. Application examples include narrow-bandwidth reflectors and the selective coupling of light into other fiber modes. This is achieved by a periodic variation of the refractive index located in the fiber core. The standard fabrication techniques for FBGs are based on the exposure to CW or long pulsed UV laser sources to induce the refractive index changes [95–97]. Since this approach relies on the photosensitivity of the fiber material, prior chemical treatment, such as codoping with germanium or hydrogen loading, is necessary for the inscription of a refractive index modification. However, fibers with a high concentration of rare earth dopants, which are used in state-of-the-art fiber lasers, possess material properties that make photosensitization difficult or impossible. Only recently, such modifications have been demonstrated in a nonphotosensitive fiber using nanosecond (ns) pulses at 193 nm but at the expense of long exposure times [98, 99].

This limitation can be overcome by using ultrashort laser pulses for the grating inscription, since it does not rely on photosensitivity. While the typical UV-inscription techniques based on two beam interference are difficult to adapt for ultrashort pulses due to the short coherence length [100], FBGs have been fabricated with ultrashort pulses mainly using the point-by-point [101, 102] and the phase mask techniques [103–105] (see Fig. 9.5). While the point-by-point technique is very flexible, it requires a high accuracy positioning system. In this case, the fiber is moved from shot to shot by a certain (fixed) amount equal to the Bragg grating period. Since the size of the induced modifications defines a minimum grating period, a tight focusing regime is typically used. By choosing the appropriate laser parameters, even a single shot modification per spot can be strong enough for the grating inscription. Thus, the sample might be translated at constant speed and the Bragg grating period is then determined by the translation speed divided by the repetition rate of the laser [102]. Although the single spot modification is typically much smaller than the fiber core, resulting in a small overlap with the mode field, resonant transmission losses exceeding 50 dB have been obtained in standard telecom fibers [106].

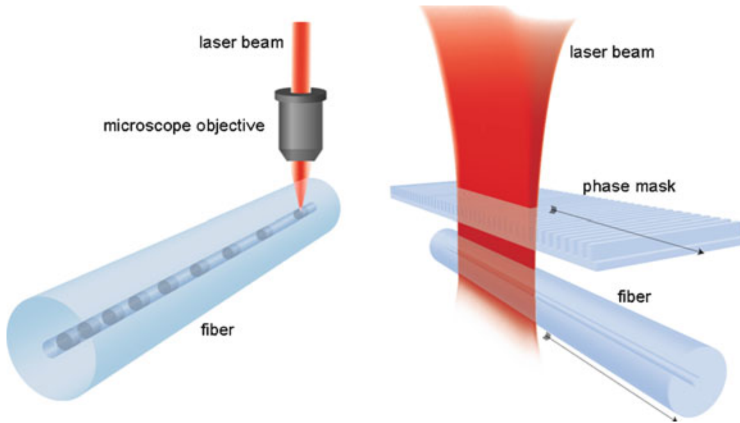

Fig. 9.5 Schematic of the different techniques for the fabrication of fiber Bragg gratings: point-by-point (*left*) and phase mask technique (*right*)

In contrast, when using a phase mask to produce the periodical pattern, the grating homogeneity and quality do not depend on the accuracy of the positioning system used. In this case, the periodic structure is due to the interference of the $+1$st and -1st diffraction orders of the phase mask, yielding a FBG with half the period of the phase mask grating. Thus, all requirements on the accuracy are transferred to the phase mask, which can be produced with high accuracy, for example, by e-beam lithography.

When working with CW or long-pulse lasers, it is important that the energy contained in the 0th diffraction order of the phase mask be reduced to a few percent to avoid the formation of a parasitic periodical structure. In contrast, it is possible to obtain pure two beam interference with ultrashort laser pulses without such high requirements on the phase mask design due to the so-called order walk-off effect [107, 108]. Since the different diffraction orders propagate with different angles, they will arrive at different times in the observation plane (fiber core) [109]. By choosing an appropriate distance between the phase mask and the fiber, the time difference between the 1st diffraction orders and the 0th order will be larger than the short coherence length of the laser. Therefore, the 0th order will be unable to interfere with the 1st orders and a pure two-beam interference pattern is obtained.

Since the grating length is determined by the area where the two interference orders overlap, the laser beam is typically focused in this case only weakly in the direction perpendicular to the fiber axis by a cylindrical lens. In order to produce FBGs of practically arbitrary length, the fiber as well as the phase mask can be translated simultaneously along the fiber axis with respect to the laser beam [109].

Meanwhile, FBGs have been realized using the femtosecond laser direct writing approach in various fibers, including non-photosensitive Er-doped [110], Yb-doped [111], Er:Yb-doped [112, 113], polarization-maintaining [114, 115], large core diameter [116], multimode [117], and photonic crystal fibers [118]. Moreover, it has

been demonstrated that these FBGs, when directly written within the core of the active fiber, are suitable for realizing high power fiber lasers with narrow linewidth and output powers >100 W [119].

9.4 Formation of 3D Hollow Microstructures

9.4.1 Direct Ablation in Water

Irradiating a piece of glass placed in water with a focused femtosecond laser beam can drill 3D holes by ablation. For example, a laser beam with an 800-nm wavelength and a 120-fs pulse width can be focused onto the bottom of a piece of fused silica immersed in water through the front surface of the substrate via a 0.55 (NA) objective lens, as shown in Fig. 9.6 [10] (also see Chap. 12). By scanning the glass substrate through the laser focus, embedded 3D microchannels with a diameter of ∼4 μm having a complicated structure can be easily produced free of debris as

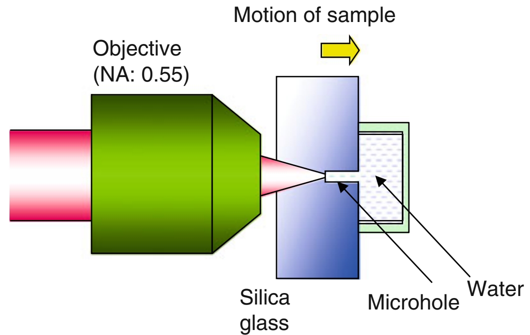

Fig. 9.6 Illustration of a scheme for microchannel fabrication in fused silica by femtosecond laser ablation in water (courtesy of K. Itoh and W. Watanabe)

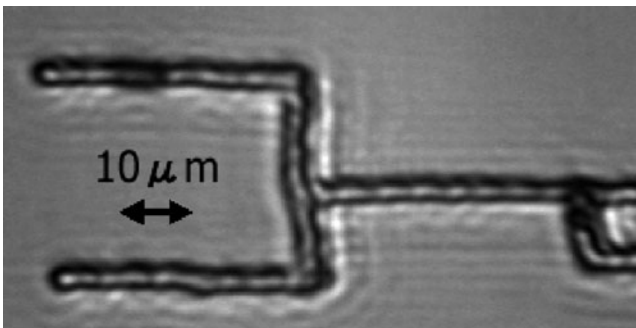

Fig. 9.7 Optical microscopy image of 3D microchannels fabricated in fused silica by femtosecond laser ablation in water by scanning the glass substrate through the laser focus (courtesy of K. Itoh and W. Watanabe)

shown in Fig. 9.7. The water plays an important role in removing ablated materials from the microchannels, resulting in the formation of long, 3D microchannels.

When fs pulses having a shorter wavelength of 527 nm were focused through an objective lens having a higher NA of 1.3, nanochannels with an extremely small diameter (<700 nm) and a relatively long length (>200 μm) could be fabricated in glass [11]. This technique has been applied to rapidly prototype 3D nanofluidic devices for mixing femtoliter fluid volumes.

9.4.2 Internal Modification Followed by Wet Etching

Internal modification of transparent materials by a femtosecond laser induces a change not only in the refractive index but also in the chemical properties of the materials. When treated with a dilute HF acid solution, the modified regions typically have etching rates that are about fifty times higher than those of the unmodified regions. Thus, laser writing followed by chemical wet etching can be used to form 3D hollow microstructures, for example, fused silica, including high aspect ratio 3D channels as narrow as 10 μm in diameter with any angle of interconnection between the channels [12].

By using this two-step technique, ship-in-a-bottle rotators were fabricated in a microcavity in fused silica, whose schematic is shown in Fig. 9.8(a) [120, 121]. The

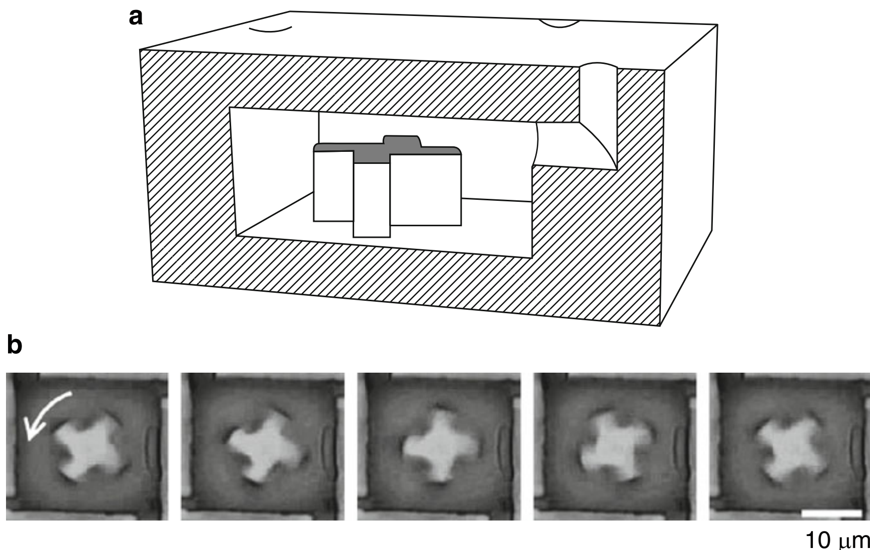

Fig. 9.8 (**a**) Schematic of a ship-in-a-bottle rotator fabricated in a microcavity inside fused silica by femtosecond laser direct writing followed by wet etching in a dilute HF solution. (**b**) Reorientation of the rotator inside the substrate using a laser trapping technique (optical microscope images) (courtesy of S. Matsuo)

cross-shaped rotator is free of the substrate and can be spun using a laser trapping technique, as demonstrated in Fig. 9.8(b). Such a rotator can be used as a micropump and micromixer, offering technical merits for fabrication of a μ-TAS.

The etching selectivity is an important issue to form the microchannel with a high aspect ratio. The etch rate of modified regions strongly depends on the laser polarization, and the linearly polarized beam whose electric vector is perpendicular to the writing direction results in the maximum etching selectivity of ∼280 due to long-range, periodic, polarization-dependent nanostructures formed in the laser-modified regions [122–124].

The two-step technique can be applied to fabricate 3D hollow microstructures in other materials such as borosilicate glass BK7 [124], crystal quartz [125], and sapphire [126, 127]. Meanwhile, photosensitive glass, such as lithium aluminosilicate glass doped with trace amounts of silver and cerium, is an attractive material for the fabrication of 3D hollow microstructures due to its high efficiency and high processing throughput, as well as its much smoother etched surfaces as compared with fused silica and other materials, although a thermal treatment is necessary prior to wet etching [13, 128–133]. Figure 9.9 depicts a schematic of the fabrication procedure consisting of (1) 3D writing of the photosensitive glass by a femtosecond laser (775 nm, 150 fs, 1 kHz), (2) baking to form modified regions in the laser-exposed areas, and (3) wet etching in dilute HF solution to selectively remove the modified regions. After this procedure, the average roughness of the etched surfaces is ∼80 nm, which can be greatly improved to ∼0.8 nm by a post-thermal treatment [134].

Figure 9.10 shows a prototypical microfluidic device fabricated in photosensitive glass [135]. This device contains a microplate detached from the glass matrix that can move in the microfluidic chamber and act as a microvalve to switch the flow direction of liquid samples.

An interesting application of 3D microfluidic structures is the manufacture of microchips designed for dynamic observations of microorganisms, referred to as a *nano-aquarium* [136]. The *nano-aquarium* has several advantages over

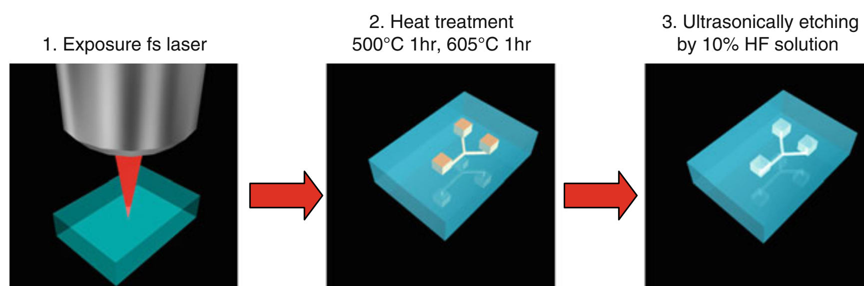

Fig. 9.9 Schematic of the fabrication of 3D hollow microstructures inside photosensitive glass by (1) 3D direct writing of the photosensitive glass by a femtosecond laser (775 nm, 150 fs, 1 kHz), (2) baking to form modified regions in the laser-exposed areas, and (3) selective wet etching in dilute HF solution

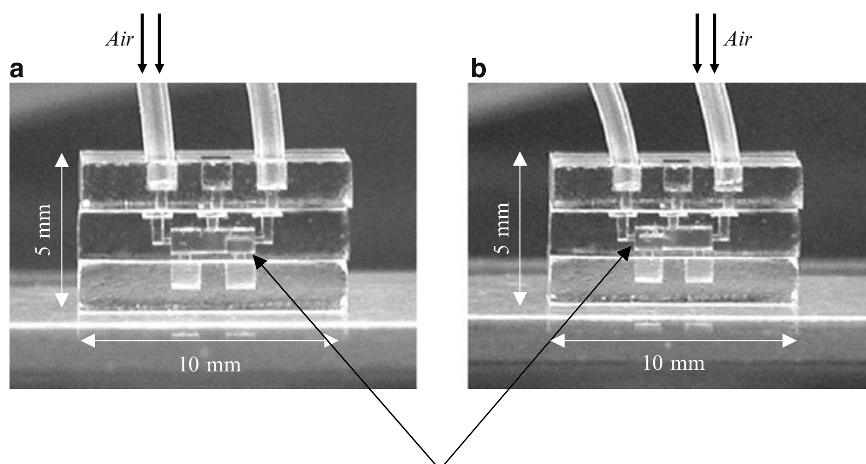

Fig. 9.10 Prototype of a microfluidic device with a freely movable microplate that can switch the flow direction of liquid samples. (**a**) By infusing compressed air from the left opening of the top, the microplate moves to the right side. (**b**) As the compressed air is infused from the right opening of the top part, the microplate slides to the left side

conventional observation methods. It can significantly shorten observation times, and it can be used for 3D observations. In addition, the microorganisms can be easily stimulated using mechanical microcomponents integrated into the microchip.

This technique of fabricating 3D hollow microstructures embedded in photosensitive glass can also be used to fabricate optical microcomponents such as mirrors, beam splitters, and lenses since the surfaces of these microcomponents after post-thermal treatment possess excellent optical quality with an average roughness of only $\sim$0.8 nm [134]. Figure 9.11(a) illustrates an optical microscopy image of a microlens buried in glass [137]. The fabricated hollow structures have openings at either the top or bottom (or both) of the glass chip, and one of the internal sidewalls of the hollow structure has a spherical shape with a radius of curvature of 0.75 mm that serves as a planoconvex lens. The fabricated hollow structure can focus a He–Ne laser beam to a spot of $\sim$30 μm in diameter with a focal length of 1.7 mm, as shown in Fig. 9.11(b).

9.5 3D Integration of Microcomponents

The integration of microfluidics and micro-optics can be used to realize a micro dye laser, which is a tunable light source in the visible range for optical biosensing in a μ-TAS [138].

A microchip in which a microfluidic channel was integrated with three optical waveguides in fused silica glass is shown in Fig. 9.12(a). It was used for

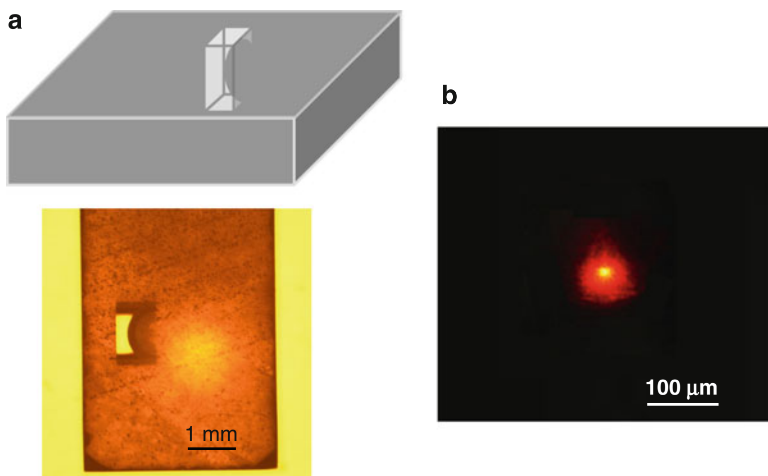

Fig. 9.11 (**a**) Optical microscopy image of a microlens embedded in photosensitive glass. (**b**) Image of a He–Ne laser beam focused by the fabricated structure

site-selective fluorescence measurements of liquid samples [14]. By filling the microfluidic channel with the laser dye rhodamine 6G (Rh6G) and coupling 543 nm light into one of the waveguides, yellow fluorescence was visible in the microfluidic channel. Figure 9.12(c) shows the intensity profile along the y-direction in Fig. 9.12(b). The full width at half maximum of the fluorescence signal corresponds to a waveguide mode diameter of 11 μm. Furthermore, when 543-nm light was individually coupled into each of the three waveguides, a fluorescence signal at three different points in the microfluidic channel was observed, as shown in Fig. 9.12(b). Thus, site-selective excitation can be performed using this microchip, which could be useful for parallel optical biosensing. The integration of microfluidics with the optical waveguide can also be used to perform fluorescence monitoring of labeled DNA molecules in an electrophoresis microchip [139].

Another type of microchip for performing high-sensitivity optical biosensing can be realized by integrating a microfluidic chamber with two microlenses and an optical waveguide [15]. Figure 9.13 shows a schematic illustration of such a 3D integrated microchip, in which one waveguide of 6-mm length was connected to a microchamber of $1.0 \times 1.0 \times 1.0\,\text{mm}^3$ volume, and two microlenses of 0.75-mm radius of curvature were used for fluorescence and absorption measurements. For fluorescence analysis, the microfluidic chamber was filled with Rh6G, and a 532-nm probe beam was coupled into the optical waveguide. Emission from the excited dye was collected by the detector via microlens #I. An emission spectrum with a central wavelength of 566 nm (the peak at 532 nm is due to the pump laser) was observed, as shown in Fig. 9.14. For comparison, the fluorescence measurement was also performed using a microfluidic chamber integrated with the optical waveguide but without microlenses. Eight times higher emission intensity was achieved for the microlens-integrated microchip. Furthermore, optical absorption analysis through

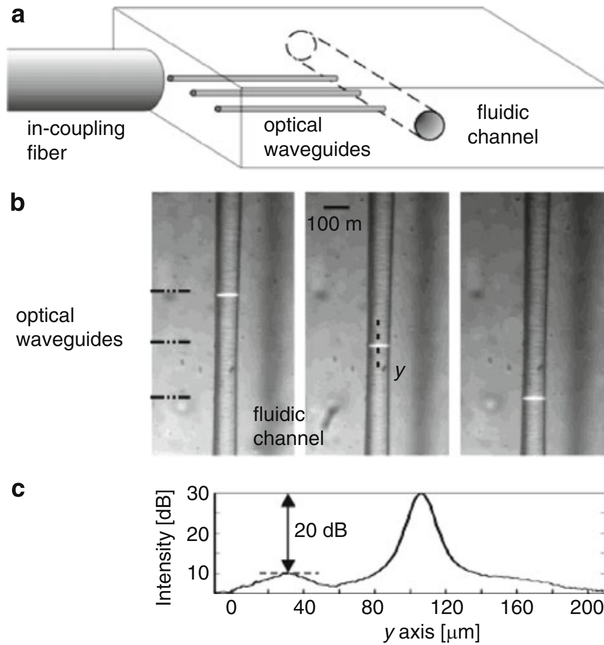

Fig. 9.12 (**a**) Schematic of a microchip in which the microfluidic channel is integrated with three optical waveguides. (**b**) Optical microscopy image of the microfluidic channel with fluorescence excited using each optical waveguide separately. (**c**) Intensity profile acquired in the middle of the microchannel along the y-axis in panel (**b**) (courtesy of R. Osellame)

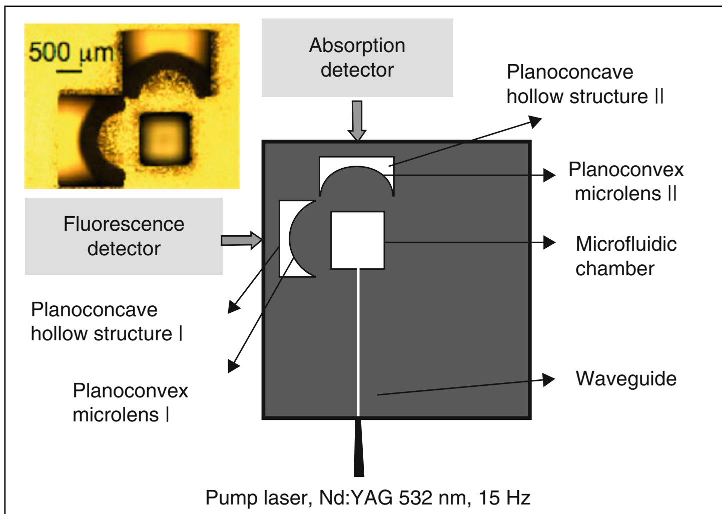

Fig. 9.13 Configuration of optofluidics in which micro-optical planoconvex lenses and an optical waveguide are integrated with a microfluidic chamber in a single glass chip. An optical microscopy image of the fabricated microchip is shown in the upper left corner

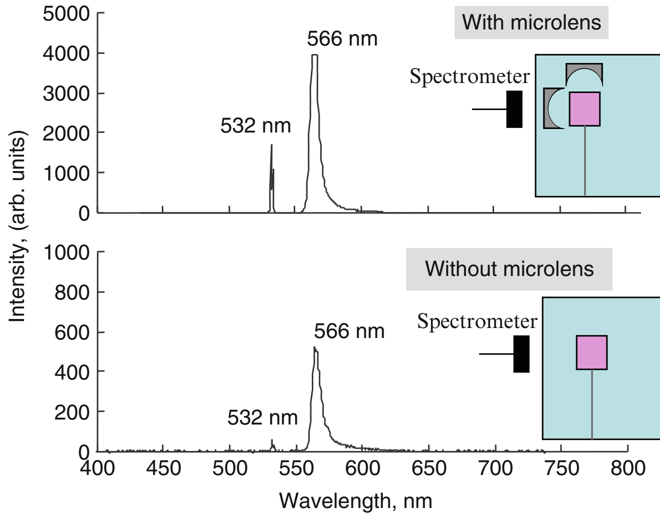

Fig. 9.14 Emission spectra from Rh6G in the microchamber in Fig. 9.13 pumped by 32 mW of second harmonic from a Nd:YAG laser. The images were taken using the microchip integrated with (*top*) and without (*bottom*) microlenses

microlens #II was demonstrated using dilute black ink as a liquid sample and white light as a probe beam. This time, the sensitivity was enhanced by a factor of three for the microlens-integrated microchip.

The integration of micro-optics and micro-mechanics in a monolithic substrate opens new applications for a variety of micro-sensors where optical waves are used as the signal source and information carrier. A displacement micro-sensor was fabricated in fused silica, which has two key elements: a flexure-based micromechanism that accurately guides the motion of the platform along one axis and a waveguide-based element that senses displacement [140].

9.6 Beam Shaping for Fabrication of 3D Microcomponents

A problem in optical waveguide writing and microchannel fabrication using femtosecond lasers is that the cross-sectional shapes of the fabricated structures become longitudinally prolonged even when using a large NA objective lens. This distortion arises from a mismatch between the Rayleigh length and the focal radius when the substrates are scanned perpendicularly to the laser beam axis (in the side-writing technique) [4, 19, 57, 129]. Optical waveguides with asymmetrical shapes result in propagation and coupling losses. In addition, it would be preferable to have fine control over the cross-sectional shapes of the microchannels to provide flexible control of fluid flow for microfluidics.

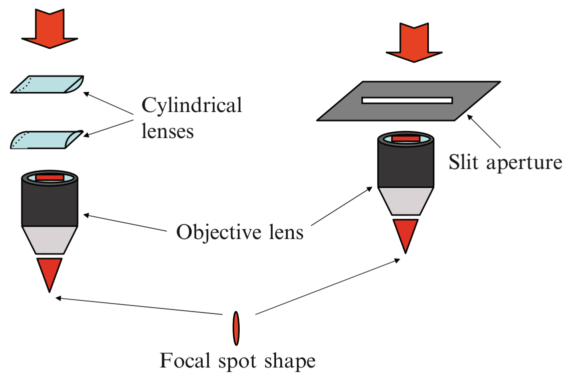

Fig. 9.15 Two kinds of spatial beam shaping techniques to control the cross-sectional profiles of optical waveguides and microchannels embedded in transparent materials

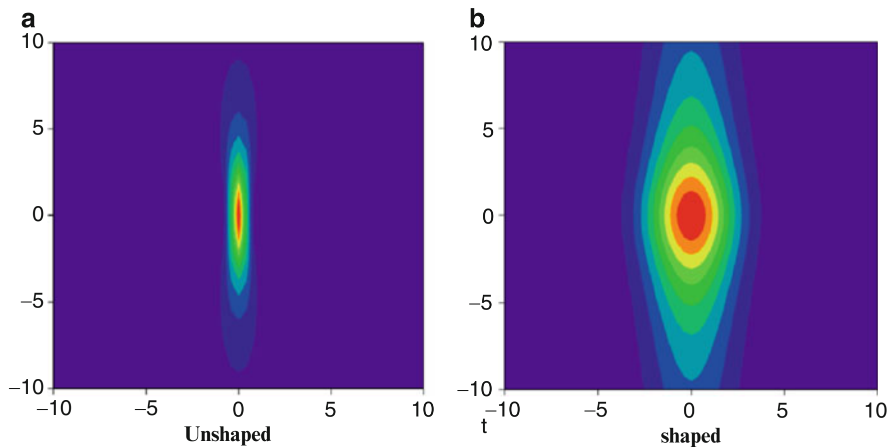

Fig. 9.16 Energy distributions along the beam axis at the focal plane of a 0.46-NA objective lens (**a**) without and (**b**) with beam shaping

Two spatial beam-shaping techniques have been developed to control the cross-sectional shapes of optical waveguides and microchannels [20, 141]. Both techniques are based on astigmatic beam focusing. The femtosecond laser beam shape is made spatially elliptical before it is introduced into the objective lens, as shown in Fig. 9.15. Either a pair of cylindrical lenses or a narrow slit can be used to perform this beam shaping. Figure 9.16 shows the energy distribution along the beam axis at the focal plane of a 0.46-NA objective lens (a) without and (b) with the beam shaping (the aspect ratio of the elliptical beam was fixed at 6). The energy distribution near the laser's focal point is more symmetrical when the beam shaping technique is used. The energy distribution can be accurately controlled by changing the aspect ratio of the elliptical beam.

Microchannels were fabricated by this beam shaping technique using narrow slits [141]. Figure 9.17 shows optical microscopy images of cross sections of the microchannels fabricated by (a) the unshaped beam and (b) the shaped beam with a

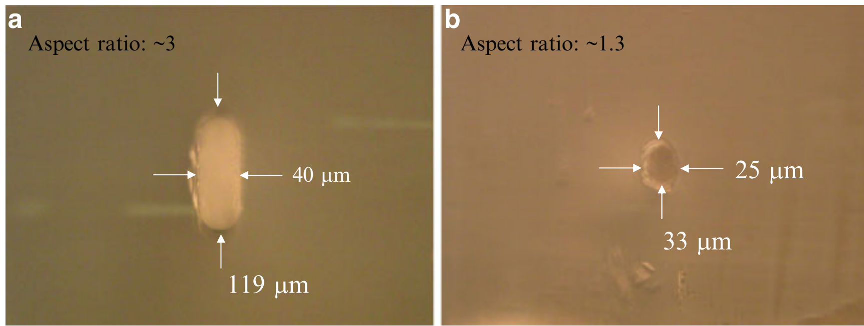

Fig. 9.17 Optical microscopy images of cross sections of fabricated microchannels using (**a**) an unshaped beam and (**b**) a shaped beam with a slit width of 0.2 mm

slit width of 0.2 mm. The aspect ratio of the microchannels improved from $\sim$3 to $\sim$1.3 by the beam shaping. This technique was also applied to optical waveguide writing, resulting in almost circular cross sectional shapes with a great reduction in both the propagation and coupling losses [22].

Recently, symmetric waveguides have been also demonstrated by using a deformable mirror for appropriate beam shaping [23]. A more sophisticated technique for obtaining circular cross-sectional shapes is the crossed-beam irradiation method, in which two focused laser beams are spatiotemporally overlapped inside a material at an angle of 90° [142]. Microfluidic channels with substantially circular cross-sectional shapes were successfully fabricated inside photosensitive glass using this technique. An advantage of this method is that the cross-sectional shapes of the channels can be varied by changing the crossing angle of the two beams.

9.7 Summary

Femtosecond lasers are becoming a common tool for micro- and nano-scale fabrication of various materials given the rapid advance in their performance including their reliability, stability, and output power. High-quality internal fabrication and modification of transparent materials are possible by multiphoton absorption using femtosecond lasers. Refractive index modification inside fused silica and other glass or crystalline materials is an important application of these techniques. One can thereby embed optical waveguides, couplers, splitters, volume Bragg gratings, diffractive lenses, and waveguide lasers inside the bulk glass. Another important application is the formation of 3D hollow microstructures in glass to produce microfluidics and optical microcomponents such as mirrors and spherical lenses. These techniques enable integration of microfluidics, optical waveguides, and optical microcomponents in a single glass chip. Beam shaping techniques are of great use for controlling the cross-sectional shapes of optical waveguides and microchannels, leading to the fabrication of higher performance microcomponents.

Three-dimensional formation of microcomponents embedded in materials by femtosecond lasers is an active area in the fields of femtosecond laser microprocessing. However, a significant fraction of the research work in this area must still be conducted at a fundamental level. At the same time, work towards developing practical applications is steadily progressing. These combined efforts should make possible for 3D integrated photonic devices, optofluidics, and *nano-aquarium* fabricated by these techniques to be ready for practical use soon.

References

1. M.F. Yanik, H. Cinar, H.N. Cinar, A.D. Chisholm, Y.I. Jin, A. Ben-Yakar, Nature, **432**, 822 (2004)
2. N. Barsch, K. Korber, A. Ostendorf, K.H. Tonshoff, Appl. Phys. **A77**, 237 (2003)
3. Y. Nakata, T. Okada, M. Maeda, Appl. Phys. Lett. **81**, 4239 (2002)
4. K.M. Davis, K. Miura, N. Sugimoto, K. Hirao, Opt. Lett. **21**, 1729 (1996)
5. T. Gorelik, M. Will, S. Nolte, A. Tünnermann, U. Glatzel, Appl. Phys. **A76**, 309 (2003)
6. W. Watanabe, T. Asano, K. Yamada, K. Itoh, J. Nishii, Opt. Lett. **28**, 2491 (2003)
7. L. Sudrie, K.A. Winick, J. Lightwave Technol. **21**, 246 (2003)
8. E. Bricchi, J.D. Mills, P.G. Kazansky, B.G. Klappauf, J.J. Baumberg, Opt. Lett. **27**, 2200 (2002)
9. G.D. Valle, S. Taccheo, R. Osellame, A. Festa, G. Cerullo, P. Laporta, Opt. Express **84**, 3190 (2007)
10. Y. Li, K. Itoh, W. Watanabe, K. Yamada, D. Kuroda, J. Nishii, Y. Jiang, Opt. Lett. **26**, 1912 (2001)
11. K. Ke, E.F. Hasselbrink, A.J. Hunt, Anal. Chem. **77**, 5083 (2005)
12. A. Marcinkevicius, S. Juodkazis, M. Watanabe, M. Miwa, S. Matsuo, H. Misawa, Opt. Lett **26**, 277 (2001)
13. K. Sugioka, Y. Cheng, K. Midorikawa, Appl. Phys. **A81**, 1 (2005)
14. R. Osellame, V. Maselli, R.M. Vazquez, R. Ramponi, G. Cerullo, Appl. Phys. Lett. **90**, 231118 (2007)
15. Z. Wang, K. Sugioka, K. Midorikawa, Appl. Phys. **A93**, 225 (2008)
16. K. Itoh, W. Watanabe, S. Nolte, C.B. Schaffer, MRS Bulletin **31**, 620 (2006)
17. K. Miura, J. Qiu, H. Inouye, T. Mitsuyu, K. Hirao, Appl. Phys. Lett. **71**, 3329 (1997)
18. K. Yamada, W. Watanabe, T. Toma, K. Itoh, J. Nishii, Opt. Lett. **26**, 19 (2001)
19. M. Will, S. Nolte, B.N. Chichkov, A. Tünnermann, Appl. Opt. **41**, 4360 (2002)
20. G. Cerullo, R. Osellame, S. Taccheo, M. Marangoni, D. Polli, R. Ramponi, P. Laporta, S. De Silvestri, Opt. Lett. **27**, 1938 (2002)
21. R. Osellame, S. Taccheo, M. Marangoni, R. Ramponi, P. Laporta, D. Polli, S. De Silvestri, G. Cerullo, J. Opt. Soc. Am. **B20**, 1559 (2003)
22. M. Ams, G.D. Marshall, D.J. Spence, M.J. Withford, Opt. Express **13**, 5676 (2005)
23. R.R. Thomson, A.S. Bockelt, E. Ramsay, S. Beecher, A.H. Greenaway, A.K. Kar, D.T. Reid, Opt. Express **16**, 12786 (2008)
24. J. Liu, Z. Zhang, C. Flueraru, X. Liu, S. Chang, C.P. Grover, IEEE J. Sel. Top. Quantum Electron. **10**, 169 (2004)
25. Y. Nasu, M. Kohtoku, Y. Hibino, Opt. Lett. **30**, 723 (2005)
26. R.R. Thomson, H.T. Bookey, N. Psaila, S. Campbell, D.T. Reid, S. Shen, A. Jha, A.K. Kar, IEEE Photonics Technol. Lett. **18**, 1515 (2006)
27. R. Osellame, M. Lobino, N. Chiodo, M. Marangoni, G. Cerullo, R. Ramponi, H.T. Bookey, R.R. Thomson, N.D. Psaila, A.K. Kar, Appl. Phys. Lett. **90**, 241107 (2007)
28. C.B. Schaffer, A. Brodeur, J.F. Garcia, E. Mazur, Opt. Lett. **26**, 93 (2001)

29. C.B. Schaffer, J.F. Garcia, E. Mazur, Appl. Phys. A **76**, 351 (2003)
30. S.M. Eaton, H. Zhang, P.R. Herman, F. Yoshino, L. Shah, J. Bovatsek, A.Y. Arai, Opt. Express **13**, 4708 (2005)
31. J.W. Chan, T. Huser, S. Risbud, D.M. Krol, Opt. Lett. **26**, 1726 (2001)
32. J.W. Chan, T.R. Huser, S.H. Risbud, J.S. Hayden, D.M. Krol, Appl. Phys. Lett. **82**, 2371 (2003)
33. J.W. Chan, T.R. Huser, S.H. Risbud, D.M. Krol, Appl. Phys. A **76**, 367 (2003)
34. D. Ehrt, T. Kittel, M. Will, S. Nolte, A. Tünnermann, J. Non-Cryst. Solids **345/346**, 332 (2004)
35. V.R. Bhardwaj, E. Simova, P.B. Corkum, D.M. Rayner, C. Hnatovsky, R.S. Taylor, B. Schreder, M. Kluge, J. Zimmer, J. Appl. Phys. 97, **083102** (2005)
36. R. Osellame, N. Chiodo, G. Della Valle, G. Cerullo, R. Ramponi, P. Laporta, A. Killi, U. Morgner, O. Svelto, IEEE J. Sel. Top. Quantum Electron. **12**, 277 (2006)
37. J. Burghoff, S. Nolte, A. Tünnermann, Appl. Phys. **A89**, 127 (2007)
38. J. Burghoff, C. Grebing, S. Nolte, A. Tünnermann, Appl. Phys. Lett. **89**, 081108 (2006)
39. J. Thomas, M. Heinrich, J. Burghoff, S. Nolte, A. Ancona, A. Tünnermann, Appl. Phys. Lett. **91**, 151108 (2007)
40. M. Hughes, W. Yang, D. Hewak, Appl. Phys. Lett. 90, **131113** (2007)
41. Y. Sikorski, A.A. Said, P. Bado, R. Maynard, C. Florea, K.A. Winick, Electron. Lett. **36**, 226 (2000)
42. R. Osellame, S. Taccheo, G. Cerullo, M. Marangoni, D. Polli, R. Ramponi, P. Laporta, S. De Silvestri, Electron. Lett. **38**, 964 (2002)
43. S. Taccheo, G. Della Valle, R. Osellame, G. Cerullo, N. Chiodo, P. Laporta, O. Svelto, A. Killi, U. Morgner, M. Lederer, D. Kopf, Opt. Lett. **29**, 2626 (2004)
44. R. Osellame, N. Chiodo, G. Della Valle, S. Taccheo, R. Ramponi, G. Cerullo, A. Killi, U. Morgner, M. Lederer, D. Kopf, Opt. Lett. **29**, 1900 (2004)
45. L. Gui, B. Xu, T.C. Chong, IEEE Photon. Technol. Lett. **16**, 1337 (2004)
46. V. Apostolopoulos, L. Laversenne, T. Colomb, C. Depeursinge, R.P. Salathé, M. Pollnau, R. Osellame, G. Cerullo, P. Laporta, Appl. Phys. Lett. **85**, 1122 (2004)
47. A.H. Nejadmalayeri, P.R. Herman, J. Burghoff, M. Will, S. Nolte, A. Tünnermann, Opt. Lett. **30**, 964 (2005)
48. A. Zoubir, M. Richardson, C. Rivero, A. Schulte, C. Lopez, K. Richardson, N. Hô, R. Valle, Opt. Lett. **29**, 748 (2004)
49. S. Sowa, W. Watanabe, J. Nishii, K. Itoh, Opt. Express **14**, 291 (2006)
50. A. Baum, P.J. Scully, M. Basanta, C.L. Paul Thomas, P.R. Fielden, N.J. Goddard, W. Perrie, P.R. Chalker, Opt. Lett. **32**, 190 (2007)
51. C.R. Mendonca, L.R. Cerami, T. Shih, R.W. Tilghman, T. Baldacchini, E. Mazur, Opt. Express **16**, 200 (2008)
52. D. Homoelle, S. Wielandy, A.L. Gaeta, N.F. Borrelli, C. Smith, Opt. Lett. **24**, 1311 (1999)
53. S. Nolte, M. Will, J. Burghoff, A. Tünnermann, J. Mod. Opt. **51**, 2533 (2004)
54. T. Fukuda, S. Ishikawa, T. Fujii, K. Sakuma, H. Hosoya, Proc. SPIE **5339**, 524 (2004)
55. A.M. Streltsov, N.F. Borrelli, Opt. Lett. **26**, 42 (2001)
56. K. Minoshima, A.M. Kowalevicz, E.P. Ippen, J.G. Fujimoto, Opt. Express **10**, 645 (2002)
57. S. Nolte, M. Will, J. Burghoff, A. Tuennermann, Appl. Phys. **A77**, 109 (2003)
58. A.M. Kowalevicz, V. Sharma, E.P. Ippen, J.G. Fujimoto, K. Minoshima, Opt. Lett. **30**, 1060 (2005)
59. W. Watanabe, Y. Note, K. Itoh, Opt. Lett. **30**, 2888 (2005)
60. K. Suzuki, V. Sharma, J.G. Fujimoto, E.P. Ippen, Y. Nasu, Opt. Express **14**, 2335 (2006)
61. K. Minoshima, A.M. Kowalevicz, I. Hartl, E.P. Ippen, J.G. Fujimoto, Opt. Lett. **26**, 1516 (2001)
62. T. Pertsch, U. Peschel, F. Lederer, J. Burghoff, M. Will, S. Nolte, A. Tünnermann, Opt. Lett. **29**, 468 (2004)
63. A. Szameit, D. Blömer, J. Burghoff, T. Pertsch, S. Nolte, A. Tünnermann, Appl. Phys. **B82**, 507 (2006)

64. N. Chiodo, G. Della Valle, R. Osellame, S. Longhi, G. Cerullo, R. Ramponi, P. Laporta, U. Morgner, Opt. Lett. **31**, 1651 (2006)
65. F. Dreisow, A. Szameit, M. Heinrich, T. Pertsch, S. Nolte, A. Tünnermann, S. Longhi, Phys. Rev. Lett. **101**, 143602 (2008)
66. A. Szameit, F. Dreisow, H. Hartung, S. Nolte, A. Tünnermann, F. Lederer, Appl. Phys. Lett. **90**, 241113 (2007)
67. F. Dreisow, M. Heinrich, A. Szameit, S. Döring, S. Nolte, A. Tünnermann, S. Fahr, F. Lederer, Opt. Express **16**, 3474 (2008)
68. A. Szameit, I.L. Garanovich, M. Heinrich, A.A. Sukhorukov, F. Dreisow, T. Pertsch, S. Nolte, A. Tünnermann, Y.S. Kivshar, Phys. Rev. Lett. **101**, 203902 (2008)
69. A. Szameit, H. Trompeter, M. Heinrich, F. Dreisow, U. Peschel, T. Pertsch, S. Nolte, F. Lederer, A. Tünnermann, New J. Phys. **10**, 103020 (2008)
70. A. Szameit, J. Burghoff, T. Pertsch, S. Nolte, A. Tünnermann, F. Lederer, Opt. Express **14**, 6055 (2006)
71. A. Szameit, H. Trompeter, M. Heinrich, F. Dreisow, U. Peschel, T. Pertsch, S. Nolte, F. Lederer, A. Tünnermann, New J. Phys. **10**, 103020 (2008)
72. D.N. Christodoulides, E.D. Eugenieva, Phys. Rev. Lett. **87**, 233901 (2001)
73. E.D. Eugenieva, N.K. Efremidis, D.N. Christodoulides, Opt. Lett. **26**, 1978 (2001)
74. G. Della Valle, R. Osellame, N. Chiodo, S. Taccheo, G. Cerullo, P. Laporta, A. Killi, U. Morgner, M. Lederer, D. Kopf, Opt. Express **13**, 5976 (2005)
75. K. Kawamura, M. Hirano, T. Kurobori, D. Takamizu, T. Kamiya, H. Hosono, Appl. Phys. Lett. **84**, 311 (2004)
76. A.G. Okhrimchuk, A.V. Shestakov, I. Khrushchev, J. Mitchell, Opt. Lett. **30**, 2248 (2005)
77. P. Nandi, G. Jose, C. Jayakrishnan, S. Debbarma, K. Chalapathi, K. Alti, A.K. Dharmadhikari, J.A. Dharmadhikari, D. Mathur, Opt. Express **14**, 12145 (2006)
78. N.D. Psaila, R.R. Thomson, H.T. Bookey, A.K. Kar, N. Chiodo, R. Osellame, G. Cerullo, G. Brown, A. Jha, S. Shen, Opt. Express **14**, 10452 (2006)
79. N.D. Psaila, R.R. Thomson, H.T. Bookey, A.K. Kar, N. Chiodo, R. Osellame, G. Cerullo, A. Jha, S. Shen, Appl. Phys. Lett. 90, **131102** (2007)
80. T.T. Fernandez, G. Della Valle, R. Osellame, G. Jose, N. Chiodo, A. Jha, P. Laporta, Opt. Express **16**, 15198 (2008)
81. G.A. Torchia, A. Rodenas, A. Benayas, E. Cantelar, L. Roso, D. Jaque, Appl. Phys. Lett. **92**, 111103 (2008)
82. G. Della Valle, R. Osellame, P. Laporta, J. Opt. A: Pure Appl. Opt. **11**, 013001 (2009)
83. G. Della Valle, S. Taccheo, R. Osellame, A. Festa, G. Cerullo, P. Laporta, Opt. Express **15**, 3190 (2007)
84. N.D. Psaila, R.R. Thomson, H.T. Bookey, N. Chiodo, S. Shen, R. Osellame, G. Cerullo, A. Jha, A.K. Kar, IEEE Photon. Technol. Lett. **20**, 126 (2008)
85. H.B. Zhang, S.M. Eaton, P.R. Herman, Opt. Lett. **32**, 2559 (2007)
86. G.D. Marshall, M. Ams, M.J. Withford, Opt. Lett. **31**, 2690 (2006)
87. H.B. Zhang, S.M. Eaton, P.R. Herman, Opt. Lett. **32**, 2559 (2007)
88. G.D. Marshall, P. Dekker, M. Ams, J.A. Piper, M.J. Withford, Opt. Lett. **33**, 956 (2008)
89. M. Ams, P. Dekker, G.D. Marshall, M.J. Withford, arXiv:0809.4550v1 [physics.optics]
90. G. Della Valle, R. Osellame, G. Galzerano, N. Chiodo, G. Cerullo, P. Laporta, O. Svelto, U. Morgner, A.G. Rozhin, V. Scardaci, A.C. Ferrari, Appl. Phys. Lett. **89**, 231115 (2006)
91. T. Shih, R.R. Gattass, C.R. Mendonca, E. Mazur, Opt. Express **15**, 5809 (2007)
92. G. Li, K.A. Winick, A.A. Said, M. Dugan, P. Bado, Opt. Lett. **31**, 739 (2006)
93. J. Burghoff, H. Hartung, S. Nolte, A. Tünnermann, Appl. Phys. **A86**, 165 (2007)
94. Y. Liao, J. Xu, Y. Cheng, Z. Zhou, F. He, H. Sun, J. Song, X. Wang, Z. Xu, K. Sugioka, K. Midorikawa, Opt. Lett. **33**, 2281 (2008)
95. G. Meltz, W.W. Morey, W.H. Glenn, Opt. Lett. **14**, 823 (1989)
96. K.O. Hill, B. Malo, F. Bilodeau, D.C. Johnson, J. Albert, Appl. Phys. Lett. **62**, 1035 (1993)
97. R. Kashyap, in *Fiber Bragg Gratings* (Academic, New York, 1990)
98. J. Albert, M. Fokine, W. Margulis, Opt. Lett. **27**, 809 (2002)

99. N. Groothoff, J. Canning, E. Buckley, K. Lyttikainen, J. Zagari, Opt. Lett. **28**, 233 (2003)
100. M. Becker, J. Bergmann, S. Brückner, M. Franke, E. Lindner, M.W. Rothhardt, H. Bartelt, Opt. Express **16**, 19169 (2008)
101. E. Wikszak, J. Burghoff, M. Will, S. Nolte, A. Tünnermann, T. Gabler, "Recording of fiber Bragg gratings with femtosecond pulses using a point by point technique," in Conference on Lasers and Electro-Optics, 2004
102. A. Martinez, M. Dubov, I. Khrushchev, I. Bennion, Electr. Lett. **40**, 1170 (2004)
103. A. Dragomir, D.N. Nikogosyan, Opt. Lett. **28**, 2171 (2003)
104. S.J. Mihailov, C.W. Smelser, D. Grobnic, R.B. Walker, P. Lu, H. Ding, J. Unruh, J. Lightw. Techn. **22**, 94 (2004)
105. S.T. Slattery, D.N. Nikogosyan, G. Brambilla, J. Opt. Soc. Am B **22**, 354 (2005)
106. A. Martinez, I.Y. Khrushchev, I. Bennion, Opt. Lett. **31**, 1603 (2006)
107. C.W. Smelser, D. Grobnic, S.J. Mihailov, Opt. Lett. **29**, 1730 (2004)
108. C.W. Smelser, S.J. Mihailov, D. Grobnic, P. Lu, R.B. Walker, H. Ding, X. Dai, Opt. Lett. **29**, 1458 (2004)
109. J. Thomas, E. Wikszak, T. Clausnitzer, U. Fuchs, U. Zeitner, S. Nolte, A. Tünnermann, Appl. Phys. A **86**, 153 (2007)
110. E. Wikszak, J. Thomas, J. Burghoff, B. Ortac, J. Limpert, S. Nolte, U. Fuchs, A. Tünnermann, Opt. Lett. **31**, 2390 (2006)
111. N. Jovanovic, A. Fuerbach, G.D. Marshall, M.J. Withford, S.D. Jackson, Opt. Lett. **32**, 1486 (2007)
112. Y. Lai, A. Martinez, I. Khrushchev, I. Bennion, Opt. Lett. **31**, 1672 (2006)
113. D. Grobnic, S.J. Mihailov, R.B. Walker, C.W. Smelser, C. Lafond, A. Croteau, IEEE Phot. Technol. Lett. **19**, 943 (2007)
114. E. Wikszak, J. Thomas, S. Klingebiel, B. Ortac, J. Limpert, S. Nolte, A. Tünnermann, Opt. Lett. **32**, 2756 (2007)
115. N. Jovanovic, G.D. Marshall, A. Fuerbach, G.E. Town, S. Bennetts, D.G. Lancaster, M.J. Withford, IEEE Phot. Technol. Lett. **20**, 809 (2008)
116. J. Thomas, E. Wikszak, C. Voigtländer, S. Nolte, A. Tünnermann, in *Conference on Lasers and Electro-Optics and Photonic Applications Systems Technologies (CLEO/PHAST)* (Optical Society of America, 2007), paper CJ6–1-THU
117. D. Grobnic, S.J. Mihailov, C.W. Smelser, IEEE Phot. Technol. Lett. **18**, 2686 (2006)
118. S.J. Mihailov, D. Grobnic, H. Ding, C.W. Smelser, J. Broeng, IEEE Phot. Technol. Lett. **18**, 1837 (2006)
119. N. Jovanovic, M. Aslund, A. Fuerbach, S.D. Jackson, G.D. Marshall, M.J. Withford, Opt. Lett. **32**, 2804 (2007)
120. S. Matsuo, S. Kiyama, Y. Shichijo, T. Tomita, S. Hashimoto, Y. Hosokawa, H. Masuhara, App. Phys. Lett. **93**, 051107 (2008)
121. S. Kiyama, T. Tomita, S. Matsuo, S. Hashimoto, J. Laser Micro/Nanoengin. 4, 18 (2009)
122. C. Hnatovsky, R.S. Taylor, E. Simova, V.R. Bhardwaj, D.M. Rayner, P.B. Corkum, Opt. Lett. **30**, 1867 (2005)
123. V.R. Bhardwaj, E. Simova, P.P. Rajeev, C. Hnatovsky, R.S. Taylor, D.M. Rayner, P.B. Corkum, Phys. Rev. Lett. 96, **057404** (2006)
124. C. Hnatovsky, R.S. Taylor, E. Simova, P.P. Rajeev, D.M. Rayner, V.R. Bhardwaj, P.B. Corkum, Appl. Phys. **A84** 47 (2006).
125. S. Matsuo, Y. Tabuchi, T. Okada, S. Juodkazis, H. Misawa, Appl. Phys. **A84**, 99 (2006)
126. S. Juodkazis, K. Nishimura, H. Misawa, T. Ebisui, R. Waki, S. Matsuo, T. Okada, Adv. Mater. **18**, 1361 (2006)
127. S. Juodkazis, Y. Nishi, H. Misawa, Physica Status Solidi – Rapid Res. Lett. **2**, 275 (2008)
128. Y. Kondo, J. Qiu, T. Mitsuyu, K. Hirao, T. Yoko, Jpn. J. Appl. Phys. **38**, L1146 (1999)
129. M. Masuda, K. Sugioka, Y. Cheng, N. Aoki, M. Kawachi, K. Shihoyama, K. Toyoda H. Helvajian, K. Midorikawa, Appl. Phys. **A76**, 857 (2003)
130. T. Hongo, K. Sugioka, H. Niino, Y. Cheng, M. Masuda, I. Miyamoto, H. Takai, K. Midorikawa, J. Appl. Phys. **97**, 063517 (2005)

131. J. Kim, H. Berberoglu, X.F. Xu, J. Microlitho. Microfab. Microsys. **3**, 478 (2004).
132. B. Fisette, M. Meunier, J. Laser Micro/Nanoengin. **1**, 7 (2005)
133. B. Fisette, F. Busque, J.Y. Degorce, M. Meunier, Appl. Phys Lett. **88**, 091104 (2006)
134. Y. Cheng, K. Sugioka, K. Midorikawa, M. Masuda, K. Toyoda, M. Kawachi, K. Shihoyama, Opt. Lett. **28**, 1144 (2003)
135. M. Masuda, K. Sugioka, Y. Cheng, T. Hongo, K. Shihoyama, H. Takai, I. Miyamoto, K. Midorikawa, Appl. Phys. **A78**, 1029 (2004)
136. Y. Hanada, K. Sugioka, H. Kawano, I.S. Ishikawa, A. Miyawaki, K. Midorikawa, Biomed. Microdevices **10**, 403 (2008)
137. Z. Wang, K. Sugioka, K. Midorikawa, Appl. Phys. **A89**, 951 (2007)
138. Y. Cheng, K. Sugioka, K. Midorikawa, Opt. Lett. **29**, 2007 (2004)
139. C. Dongre, R. Dekker, H.J.W.M. Hoekstra, M. Pollnau, R. Martinez-Vazquez, R. Osellame, G. Cerullo, R. Ramponi, R. van Weeghel, G.A.J. Besselink, H.H. van den Vlekkert, Opt. Lett. **33**, 2503 (2008)
140. Y. Bellouard, A.A. Said, P. Bado, Opt. Express **13**, 6635 (2005)
141. Y. Cheng, K. Sugioka, K. Midorikawa, M. Masuda, K. Toyoda, M. Kawachi, K. Shihoyama, Opt. Lett. **28**, 55 (2003)
142. K. Sugioka, Y. Cheng, K. Midorikawa, F. Takase, H. Takai, Opt. Lett. **31**, 208 (2006)

Chapter 10
Micromachining and Patterning

Jürgen Ihlemann

Abstract Laser micromachining and patterning by laser ablation is used for the fabrication of micro-fluidic and micro-optic components. Irradiation configurations comprise direct spot writing, mask projection, and multiple beam interference. The fabrication of grooves, micro channels, micro lenses, dielectric masks, gratings, and diffractive elements is described. Special attention is paid to layer ablation in order to create planar optical structures.

10.1 Introduction

Laser micromachining and patterning comprises the utilization of lasers for creating a specific surface relief by pulsed ablation of material. Materials treated are polymers, glass, ceramics, metals, and composite materials. To create a predefined pattern, either a mask containing this pattern is projected onto the sample, or the intensity pattern is formed by two- or multiple beam interference, or a direct write process is accomplished by focus scanning. The mask can contain a fixed pattern (stencil mask or Cr on quartz mask), it can be a variable aperture (variable slit, hole), it can contain only fully transparent and opaque areas, or even gray levels. Multiple beam interference is usually applied for the generation of periodic patterns. The beams are generated by reflective or diffractive beam splitters and recombined on the sample. Combinations of mask imaging and interference of selected beams are possible. Periods ranging from about 300 nm to some μm are made this way.

Applications (except drilling, cutting, marking, which are treated in Chap. 13) are mainly in the fields of micro fluidics and micro optics. Micro fluidic applications comprise the fabrication of grooves, micro channels or channel systems, and the fabrication of periodically patterned surfaces with increased or diminished hydrophilicity or tribology. Micro optical elements, which can be fabricated by ablative micro fabrication, comprise planar optics (e.g., masks, gratings, diffractive elements, planar waveguides), where the binary or multilevel or continuous

J. Ihlemann (✉)
Laser-Laboratory Goettingen, Germany
e-mail: juergen.ihlemann@llg-ev.de

K. Sugioka et al. (eds.), *Laser Precision Microfabrication*,
Springer Series in Materials Science 135, DOI 10.1007/978-3-642-10523-4_10,
© Springer-Verlag Berlin Heidelberg 2010

(e.g., sinusoidal) profile is either produced on the surface of a substrate, or it is generated by patterning of a coating on the substrate. In addition, 3D micro optics, for example, micro lenses, are made by using variable masks or processes providing the desired smooth relief profile. Complex functionalities are obtained by, for example, creating a micro lens on a fiber tip.

Whereas in the case of metal micro machining, often femtosecond (fs) lasers are applied to minimize heat affected zones (HAZs) (see Chaps. 2 and 4), for micro machining of polymers, glasses and ceramics, UV-lasers are mainly used enabling sufficient (linear) absorption even of weakly absorbing materials. Whereas Nd:YAG lasers are typically used in a scanning spot mode, for complex shaping using mask technology, excimer lasers are best suited delivering high pulse energy with nearly flat top beam profiles [1]. This chapter addresses micromachining with (nanosecond (ns)) pulsed lasers utilizing ablation of bulk or layered material and surface patterning by mask projection or direct writing.

10.2 Direct Writing

A laser process is called a direct write process, if the laser beam is delivered to the work piece on a predefined line in a continuous or quasicontinuous way. This can be accomplished with a focused beam by scanning the beam or by moving the work piece. In contrast, the simultaneous irradiation of multiple lines or spots or extended areas is termed mask projection. The term *laser direct writing* is often used for additive processing such as deposition of metallic lines by laser induced decomposition of metal organic compounds or by laser induced printing or forward transfer (Chap. 11). Also the material modification by femtosecond laser induced alteration of the refractive index is often accomplished in a direct write mode (Chap. 9). All these processes are not treated in this chapter; we concentrate on *ablative direct writing*, where material is removed in a sequential mode.

Using *scanning ablation*, one has to consider that the morphology of the line or channel made by this method can look different from that observed in the case of *static ablation*. For the fabrication of channels in stretched polyethylene-terephthalate (PET) by ArF-laser ablation, it has been observed that the structure on the ground of the channel depends on the ramp angle produced when starting the process [2]. This ramp angle in turn depends on the combination of mask size, fluence, laser repetition rate, and scanning velocity. Furthermore, for precise machining by direct writing, the ablation behavior at varying angle of incidence of the laser beam on the surface has to be taken into account. For focused 266 nm-ablation of Ormocer- and SU8-material, it has been shown that the dependence of the angle of incidence is significant at high fluences, but can be negligible in a certain low fluence regime [3].

Even below the material ablation threshold, significant changes in the surface morphology are possible. For instance, laser direct writing on polyimide with a continuous wave argon ion laser at 351 nm leads to melted lines which influence the alignment of organic liquid crystals [4].

Direct write ablation of thin films is a promising technique to be applied in the production of flat panel displays. For example, the patterning of indium tin oxide (ITO) thin films by writing electrically isolating lines is of great interest. Basically, this process is possible with laser wavelengths from the IR to the UV, but it has been shown that only the absorption of the UV-light by the glass substrate (demonstrated for 262 nm) leads to residue free removal of the ITO film, whereas at longer wavelengths a ripple-like morphology due to incomplete material removal has been observed [5]. However, due to the economically more favorable fundamental wavelength of a Nd:YAG laser, beam delivery has been optimized to achieve satisfactory results also at 1,064 nm [6].

Many applications of direct write ablation deal with the fabrication of microfluidic systems, using mainly UV-lasers [7], but also visible and IR lasers [8, 9]. An example is the fabrication of planar micromixers on polymethylmethacrylate (PMMA) by KrF-excimer laser ablation [10]. With the same laser, the hydrophilicity of the PMMA-surface (e.g., in the channel) can be modified [11]. Below the ablation threshold, the irradiation at 248 nm leads to an increase of the hydrophilicity without any significant change in the surface topography. Irradiation above the ablation threshold leads to a contact angle that is inversely proportional to the obtained surface roughness.

10.3 Micro Fluidics

Though hole drilling or via drilling is one of the most widespread applications of laser precision micro fabrication (treated in Chap. 13), there are a lot of activities to extend the machining techniques to achieve more complex patterns like, for example, the terraced multilevel pit shown in Fig. 10.1. The main processes to form microfluidic devices are channel fabrication and surface texturing. Using ArF-excimer lasers, channels or channel systems with typical dimensions of 10–50 μm in depth and width have been made in polymers [12, 13] and borosilicate glass [14].

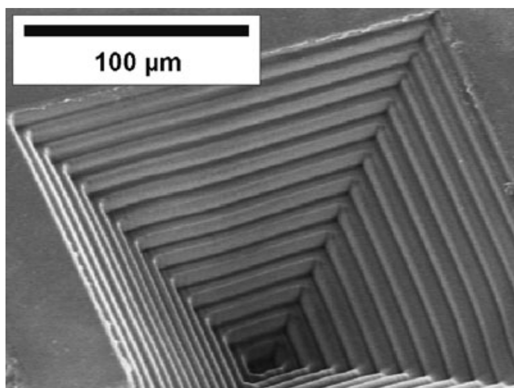

Fig. 10.1 Multilevel pattern in polyethersulfone fabricated by XeCl-excimer laser ablation (308 nm) (Laser-Laboratorium Goettingen)

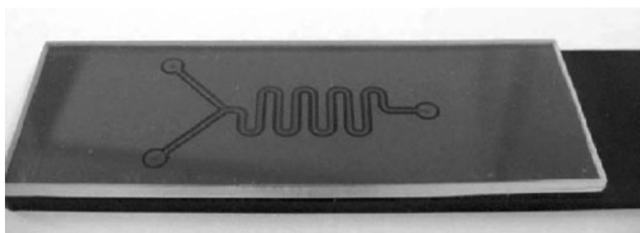

Fig. 10.2 Diffusion mixer on a 25 × 50 mm plastic chip [12]

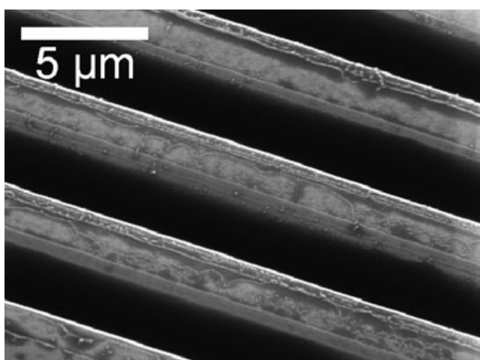

Fig. 10.3 Micro channels made in fused silica by ArF-excimer laser ablation [15]

Figure 10.2 displays such a channel system operating as a mixer. Even in fused silica, micro channels could be fabricated using a laser wavelength of 193 nm [15] (Fig. 10.3). Though with a Nd:YAG laser at 355 nm smooth channels in glass without cracks could be obtained under well controlled conditions [16], and even at 532 nm, the cutting of borosilicate glasses is possible [17], for the fabrication of precise grooves in weakly absorbing glasses, the use of an F_2-laser seems to be more appropriate [18]. Micro features produced in N-BK7-glass using an F_2-laser have been replicated by polydimethylsiloxane (PDMS) moulding [19]. The obtained stamps have been used then to print arrays of fluorescent molecules with sub-micron fidelity. Hole arrays ablated in BK7 have been used to fabricate microneedle arrays by micromolding [20]. Such needle arrays are used in biomedical applications such as gene and drug delivery.

Microchannels with uniform size and shape in stainless steel have been obtained by a laser etching technique utilizing a frequency doubled YAG-laser in combination with a phosphoric acid solution [21]. The fiber guided laser induces a thermochemical reaction between the workpiece and the etchant which is delivered through a coaxial nozzle arrangement that houses the optical fiber. Grooves that were made by direct 355 nm-laser machining of steel have been successfully replicated in PMMA by hot embossing [22]. As this laser micro machining offers complementary advantages compared with micro milling, a hybrid combination of both processes is suggested [22].

Mesa-like microstructures have been fabricated from PMMA with an F_2-laser using a fluid mask [23]. Mask and substrate are ablated simultaneously, and local variations of the thickness of the mask are transferred into a 3D surface profile on the substrate.

10.4 Gratings

The fabrication of optical grating structures by laser ablation has been a subject of study for a long time. This work aimed either at the demonstration of high resolution capability of the ablation process or at the fabrication of real gratings to be used, for example, as coupling gratings for planar waveguides.

Various methods are applied to generate an intensity distribution with high spatial frequency necessary to produce high resolution gratings. The laser beam is split into two (or more) beams using a reflective or diffractive beam splitter, and these beams are recombined on the workpiece, for example using a Talbot interferometer [24, 25]. The requirements concerning the coherence parameters of the used laser can be significantly reduced, if a projection set-up is used, that is, if the plane of the beam splitter is imaged onto the surface of the work piece [26]. Reflective objectives of the Schwarzschild-type are well suited for the required high resolution projection. However, in an on-axis arrangement, the Schwarzschild-objective does not transmit the complete zero order beam due to its inherent obstruction on the optical axis (Fig. 10.4). To obtain high quality interference patterns with high fluence, therefore either phase-mask-beam-splitters with good zero order suppression [27] or an off-axis configuration utilizing interference of the zero order beam and only *one* first order beam have to be applied [28]. Using this method, a surface relief grating with 400 nm period on fused silica could be obtained (Fig. 10.5).

Even the proximity method, where the beam splitting phase mask is in close proximity to the workpiece, has been applied [29], though this method does not

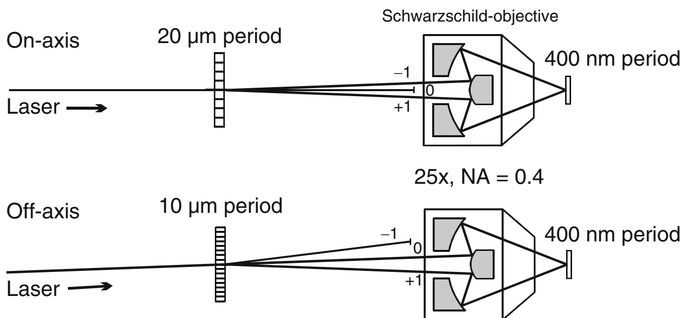

Fig. 10.4 Grating projection using a Schwarzschild-objective: on axis projection leads to obstruction of the zero order beam; off-axis projection utilizes interference of the zero order beam with the +1st order beam

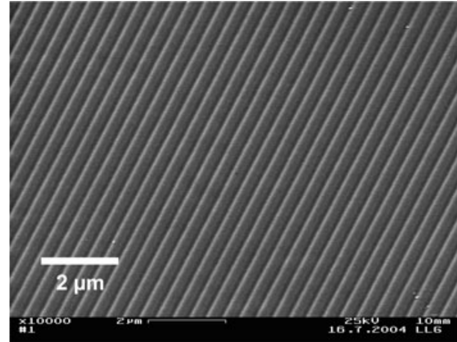

Fig. 10.5 Surface relief grating in fused silica made by 193-nm-ablation, 3.9 J/cm^2, 2 pulses [28]

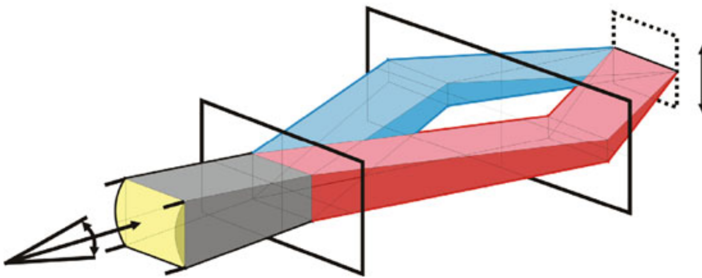

Fig. 10.6 Two grating interferometer for the ablation of large area line patterns [31]

allow high fluences and may easily cause damage or contamination of the phase mask. To avoid these drawbacks, another approach based on a two-grating interferometer was applied. A pair of phase gratings was illuminated with non-collimated (convergent) laser beams to generate a periodic intensity distribution with high energy density and high contrast on the sample surface [30]. Large line numbers without phase distortions were reached by applying cylindrical focusing perpendicular to the grating lines. Scanning the illuminating laser beam in the direction parallel to the grooves enabled the fabrication of cm-scale grating sizes with multiple pulse ablation, while keeping the whole line structure in phase (Fig. 10.6). Experimental results demonstrate the capability of the method to generate laser ablated grating structures with submicron periods down to ~300 nm [31] (Fig. 10.7).

Such grating designs are used in several micro-optic applications such as grating demultiplexers for telecommunication components, light couplers for planar optical waveguides, Bragg reflectors, and alignment grooves for liquid crystals [32, 33]. Sub-micron periodic structures, which are required for ultraviolet, visible, and near-infrared spectral applications, have been structured by UV-laser ablation with ns duration pulses on polymers [34–37] and borosilicate glass [38] surfaces. F_2-lasers were applied for the treatment of weakly absorbing materials such as fused silica [39]. For the application of planar waveguides, it is of great importance to provide gratings for coupling light into the waveguide layer.

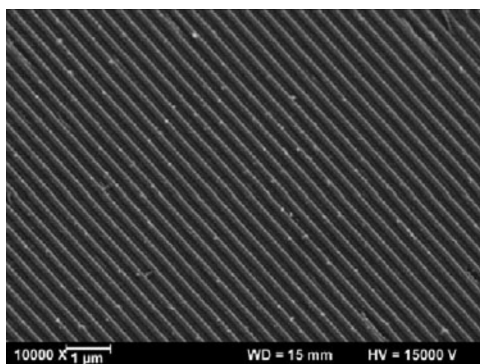

Fig. 10.7 Grating pattern with a period of 331 nm in polyimide made by 248-nm-ablation in combination with the two grating interferometer shown in Fig. 10.6 [31]. The total size of the irradiated area is 6 × 5 mm. The complete area was irradiated with a total of 1,250 pulses, scanning a beam stripe of 400 µm × 6 mm over the sample at an average fluence of 50 mJ/cm^2. Each location of the sample was irradiated "on the fly" with 100 pulses on average, at a repetition rate of 80 Hz

Such gratings were made by excimer ablation in Ta_2O_5- and Nb_2O_5-waveguides [40, 41]. The difficulties in achieving grating structures with high resolution and high modulation depth in these metal oxides are obviously caused by the ns pulse duration, which leads to nonnegligible thermal diffusion smearing out the grating lines. Therefore, for high contrast patterning of materials such as Ta_2O_5 or $LiNbO_3$, the use of ultrashort pulse (excimer) lasers is favorable [42, 43], for pure metals it is even essential [44].

10.5 Diffractive Optical Elements

Diffractive optical elements (DOE) make use of the diffraction at small structures. They open a wide range of new beam shaping applications [45] (see Chap. 3). Specifically, diffractive phase elements (DPE) enable the generation of complex irradiation patterns without substantial optical system energy losses. In many cases, a computer generated two dimensional phase function is transferred into an optically effective phase controlling element by fabricating a surface relief on a transparent substrate.

These elements can be applied for beam homogenization or fiber coupling, for correction of lens systems, or for the generation of arbitrary irradiation patterns such as ring-shaped structures or spot arrays. In laser materials processing, they offer efficient mask illumination or even provide for direct maskless processing. In addition, DOEs enable laser micro machining with ultrashort pulses without vacuum, whereas geometrical imaging leads to air breakdown in the focus at high intensities. DPEs allow for a reduction of the number of optical elements without loss of functionality.

Diffractive optical elements can be characterized as amplitude or phase elements. Phase elements, sometimes called kinoforms, can have a binary or a multilevel

structure. The simplest element to be used at a wavelength λ is a binary surface relief structure on a material of refractive index n with a depth modulation of $d = \lambda/2(n-1)$. Lateral structure dimensions are of the order of 5 to some 10λ, depending on the optical configuration and the coherence parameters of the light for which the DOE is designed. For a DOE made of a polymer material, to be used in the visible spectral range, surface structures with a depth of about 0.5 μm and lateral dimensions of 5 μm are required. These dimensions are easily accessible by excimer laser ablation. Some attempts have been made to fabricate DOEs by laser ablation, either on the basis of pixel by pixel irradiation [46,47] or image based using chrome masks [48]. Multilevel DOEs could be produced in polymers by excimer laser ablation using a half tone mask [49]. Dielectric masks were used for fabricating DOEs that can be used for UV laser applications, requiring the processing of fused silica or other materials with high UV transmission [50]. The ablative shaping of diamond for IR-DOEs was also demonstrated [51].

The minimum pixel size that can be obtained by laser ablation in an accurate shape is about 3×3 μm. The fabrication of a four level DOE with 256×256 pixels will last about 30 min, if the laser and the positioning system allow an average repetition rate of 50 Hz. This is rather long for mass production, but the advantage of laser ablation is, that nearly any material can be patterned this way. The conventional fabrication method of laser- or electron beam lithography with pattern transfer by reactive ion etching is capable of higher resolution but requires a more complex processing scheme. Reactive ion etching works quite well with fused silica, but not all types of glass can be treated as well by this process. For the mass fabrication of plastic DOE replication techniques are available, and only the master has to be made either by ablation or by etching.

Though fused silica is only very weakly absorbing at 193 nm, this wavelength was applied to fabricate diffractive phase elements from this material [52]. Due to a plasma mediated ablation process, controlled and reproducible material removal is only possible choosing a limited number of high fluence laser pulses per position. As the possibilities of precise adjustment of the ablation depth are therefore limited, the adjustment of the phase delay for the specific application of a phase element fabricated this way is therefore assisted by tuning the refractive index of the environment (immersion liquid).

More flexibility concerning the ablation of fused silica is provided by F_2-lasers. Due to the better ablation depth control, diffractive phase elements with four or more levels of good quality could be obtained [53,54] (Fig. 10.8).

10.6 Micro Lenses/Lens Arrays

Besides the use of lithographic methods to fabricate micro lens arrays, for example, laser interference lithography [55], it is very attractive to fabricate micro lenses directly by laser ablation. If the basic problems of creating a smooth, three-dimensional surface in an optical material are solved, a great variety of lens shapes

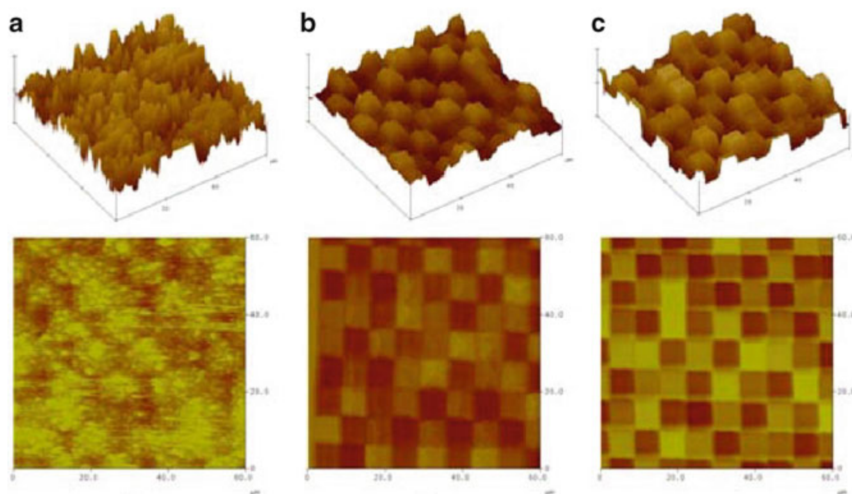

Fig. 10.8 AFM images of DOE fabricated with F_2 laser (**a**) before cleaning, (**b**) after acetone bath, and (**c**) after EtOH bath. Probe area is $60 \times 60\,\mu$m. Top shows 3-D profile of the $7 \times 7\,\mu$m pixels [54]

should be possible (aspheric etc). The processing of cylindrical lenses is rather straightforward, if a mask technology utilizing variable blades is applied [15]. In the case of processing glass, the ablation debris is one of the major problems, which can be solved by ablating in a vacuum or applying appropriate cleaning processes. For the generation of spherical polymer lenses, there are basically two approaches. The first one is based on a single laser exposure per micro lens causing the lens directly or by post processing. Microlens arrays from amorphous Teflon were made this way by excising small pads out of a doped Teflon film using ArF-laser ablation, removing the dopant, and shaping the pads into lenses by a thermal reflow process [56]. Multipulse KrF-laser irradiation of PMMA below the ablation threshold with successive exposition to styrene vapor leads to surface swelling and micro lens formation [57]. Single pulse micro lens formation is possible when using PMMA doped with a UV-sensitive and photoreactive absorber such as diphenyltriazene [58]. In this case, the volume expansion by photochemically produced molecular nitrogen leads to the formation of lens-like elevations. Negative lenses made by 248 nm-irradiation of PMMA have been used as a mould for the replication of PDMS micro lenses [59].

Another approach is based on direct writing with a circular laser spot. By scanning a polymer surface with an excimer beam along well-chosen multiple concentric contours, micro lenses of arbitrary shape can be realized [60,61]. Smoothing and removal of debris are accomplished by large beam irradiation of the raw lens. Densely packed micro lens arrays have been obtained using synchronized-image-scanning (SIS) in combination with half tone masks [62] (Fig. 10.9). In the SIS-process, the work piece movement and laser pulsing are synchronized in a way that for each pulse the mask (or the arrangement of multiple partial masks) is imaged on

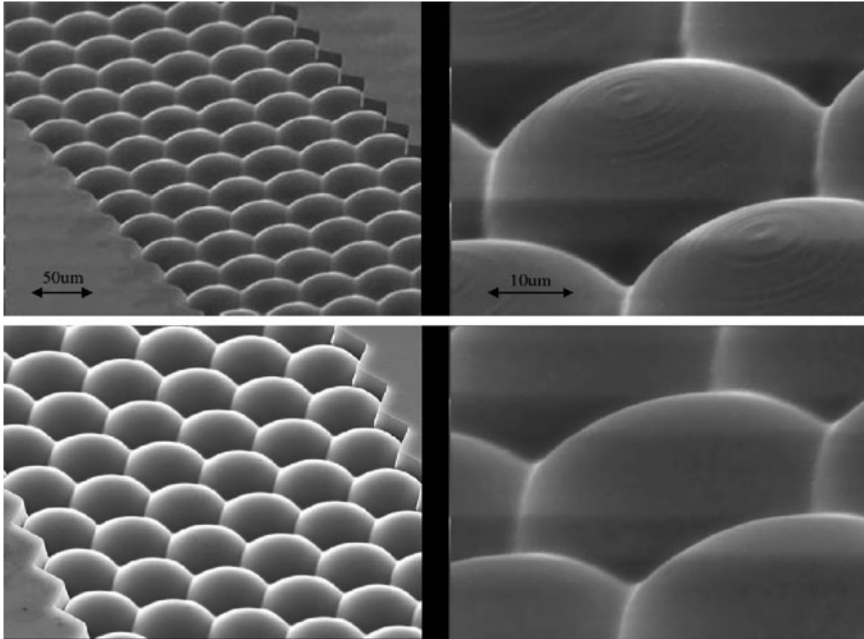

Fig. 10.9 Micro lenses made by synchronized-image-scanning (SIS) in polycarbonate. The residual roughness obtained with standard SIS (*top*) can be minimized by combining SIS with halftone mask processing (*bottom*) [62]

a predefined work piece area. If for instance a single convex micro lens can be fabricated by a set of ring shaped masks with varying diameter of the opaque area, which are inserted one after the other into the beam of the ablating laser, an array of such lenses is made by a mask that contains all these partial masks arranged in a row. By moving the work piece after each laser exposure to a position corresponding to the next partial mask, a number of micro lenses are fabricated simultaneously without need of exchanging the whole mask. Of course, this composition of a 3D-surface profile from a limited number of contour masks leads to a step like profile, which has to be smoothed by a post processing by laser polishing. Alternatively, the ring masks with sharply defined contours can be replaced by halftone masks to reduce the surface roughness.

Several attempts have been made to micro machine optical fibers. CO_2-laser cleaving of fibers was shown to lead to as good results as mechanical cleaving concerning insertion loss performance [63]. In order to fabricate an integrated lens at the tip of a fiber, various laser types have been applied. Using a CO_2-laser, the processing is more or less based on a defined melting process [64]. For precise shaping of silica fiber tips, a VUV-laser emitting at 157 nm is the optimum choice. Two different techniques for the fabrication of micro-lenses directly on the end face of multimode silica fibers have been demonstrated using an F_2-laser processing station [65] (Fig. 10.10). The first method is based on a mask projection arrangement

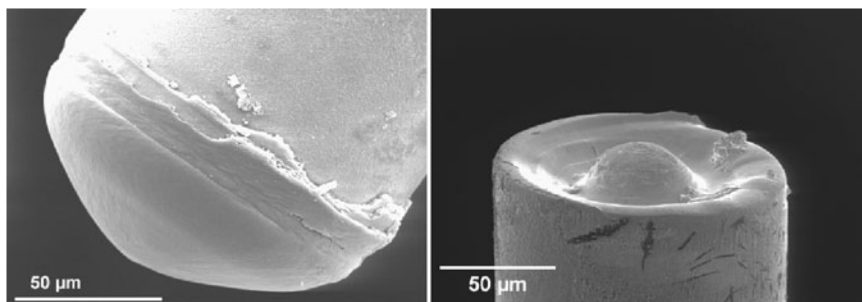

Fig. 10.10 *Left*: Micro-lens with lens radius 60 µm on the end facet of a 50/125 µm silica fiber made by 157-nm-ablation with irradiation perpendicular to the fiber axis. *Right*: Parabolic micro-lens at the end face of a 50/125 µm silica fiber. The radius of curvature in the center is 25 µm. 157-nm-ablation with irradiation parallel to the fiber axis [65]

perpendicular to the fiber axis. The fiber is rotated axially while the laser cuts through the fiber, yielding a spherically shaped tip with radius defined by the mask dimensions. For the second technique, a uniform ablation spot is projected onto the fiber end face in axial direction and steered along a trajectory of overlapping concentric circles. The lens profile is controlled by the spot size, the number of circles in the trajectory, and the scanning speed. Strong 157 nm absorption by the silica glass facilitates precise structuring without micro-crack formation in both cases. The surface quality of the fiber-lenses is characterized by AFM and SEM and reveals ~40 nm rms roughness with good control of the surface profile. Optical beam profiling indicates the possibility for creating spot sizes of 1/5 the core diameter at the fiber output. Good results have been obtained also for processing single mode fibers [66].

For the integration of optical components in micro systems, besides refractive micro lenses, also diffractive patterns are increasingly applied. They feature extremely flat architecture, high design flexibility and strong dispersion. For instance, they can be used for chromatic confocal distance sensors. For the fabrication of the diffractive lenses, a mask with a number of specially designed apertures, one for each zone, was applied. Keeping the mask in a fixed position and rotating the target, a combination of laser fluence, repetition rate, and rotation speed leads to the desired profile of the zones [67]. Figure 10.11 shows such a diffractive lens made by F_2-laser processing of fused silica.

10.7 Patterning of Layers

The patterning of layers by laser ablation has been studied for many years. Mostly, ablation of organic films has been investigated, and this technique is still investigated in order to enable new applications, for example, the pentacene patterning for the

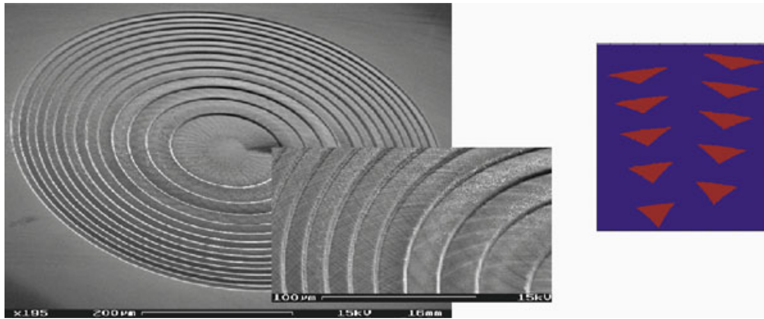

Fig. 10.11 *Left*: 157nm-laser fabricated diffractive micro lens (fused silica); diameter: 600 μm, focal length: 5 mm at 633 nm; profile depth: 1.38 μm; min. zone width: 10 μm *Right*: part of the corresponding mask design [67]

fabrication of organic thin film transistors [68]. For a number of optical applications, inorganic layers are better suited due to their chemical and thermal stability and of course also due to their optical performance, for example, if high refractive index is required. For example, the ablation of ITO films to be used for flat panel displays is accomplished by using a 266 nm-YAG-laser [69]. Rib waveguides can be fabricated in that way, that first a coating with a thickness corresponding to the desired waveguide thickness is deposited on a substrate, and then the coating is ablated in a way that a stripe of the desired waveguide width remains on the substrate. This way a waveguide was made from GeO_2-doped silica on silica glass by F_2-laser ablation [70].

Inorganic optical coatings have a variety of applications. Especially design, fabrication, and applications of dielectric optical interference coatings are subject of numerous studies [71]. For the classical use as mirror, beam splitter, or anti reflection coating, extended areas have to be homogeneously coated. Therefore, the production of dielectric coatings has been optimized to obtain such high quality coatings nearly without defects on large substrates. But there are other applications, where the coating is needed in locally well defined areas, for example, masks or waveguides. Coating technology is not well developed in this direction. Deposition through stencil masks is possible but not with high spatial resolution. In this case, the coatings have to be processed following the deposition process in order to generate spatially well defined patterns. Usually, lithographic processes are applied, but they have limited applicability, because the required etching processes are complicated and not sufficiently developed for all used materials. Therefore laser ablation seems to be a versatile alternative process for the patterning of optical coatings. In contrast to the treatment of bulk materials, where many laser pulses are required to, for example, drill a material to a certain depth, in the case of thin layers very few or even a single pulse are sufficient to generate the desired ablation pattern. Regarding the capability of simultaneous processing of large areas by mask projection, which is enabled by the flat top beam profile of excimer lasers, there seems to be a huge potential of patterning thin films by this method.

There are several advantages of layer ablation compared to bulk ablation. Because under certain conditions the layer-layer or layer-substrate boundaries act as predetermined breaking points, the ablated depth profile is not directly correlated with the (sometimes, inhomogeneous) beam profile. Whereas in the case of bulk material ablation, spatial variations of the beam intensity will lead to a correspondingly irregular surface profile, this will not necessarily be the case for layer ablation, because there is a certain process window concerning the fluence for complete layer ablation [72]. Thus even with some spatial variations of the irradiation fluence, a very flat surface can be achieved.

Patterning of optical layers is useful for the fabrication of optical components such as waveguides, coupling gratings, refractive, reflective, or diffractive structures. In most cases, transparent films with high transmission in the operation wavelength range are required. For applications in the visible or infrared spectral ranges, often polymeric materials can be applied, though their mechanical and thermal stability are limited. For example, the laser-patterning of layers for fabricating (diffractive) optical elements has been performed with polyimide films [46]. For UV-applications, the control of processing UV-transparent materials, especially inorganic oxide materials, is necessary.

Excimer lasers are optimally suited for a number of tasks concerning ablation of optical coatings. The emitted UV-light is readily absorbed by most of the relevant coating materials. However, due to the specific band edge of each material, different laser wavelengths are required. Whereas TiO_2 absorbs already in the near UV, for efficient absorption of, for example, Ta_2O_5 a wavelength of 248 nm and for HfO_2 even 193 nm are required. Excimer lasers emit powerful pulses with a flat top beam profile enabling large area processing, for example, by mask projection. Even the pulse duration of 10 or 20 ns seems to be quite optimal for the ablation of optical layers. The thermal diffusion length L of around 50–500 nm, which is related to the laser pulse length τ by $L \sim \tau^{1/2}$ and characterizes the HAZ, is short enough to minimize lateral damage, but sufficiently long to provide heat flow within the typical layer thickness, which promotes the lift-off of a complete layer with a single pulse [73, 74]. However, when structure details in the sub-micron range have to be fabricated, for example, gratings with a period of several 100 nm, this thermal diffusion length is too large, so that shorter laser pulses are required.

Excimer laser processing is usually carried out in a mask projection configuration. In principle, there are two different methods to induce ablative removal of a film from a substrate (Fig. 10.12): Either the beam is directed head-on toward the film leading to "front side ablation", or the beam hits the film from the other side after passing through the substrate ("rear side ablation"). Rear side ablation is possible, if the substrate is sufficiently transparent at the laser wavelength. For standard excimer laser wavelengths, this is the case, for example, for UV grade fused silica.

In the case of front side ablation, depending on laser fluence, film thickness, and absorption properties of film and substrate, the whole film or part of it can be ablated. If the film consists of a layer stack, it is even possible to ablate layer after layer by successive laser pulses [75]. In the case of rear side irradiation with sufficient fluence, the whole film or layer stack is ablated with a single laser pulse. The advantage of this method is that due to the forward transfer of the material

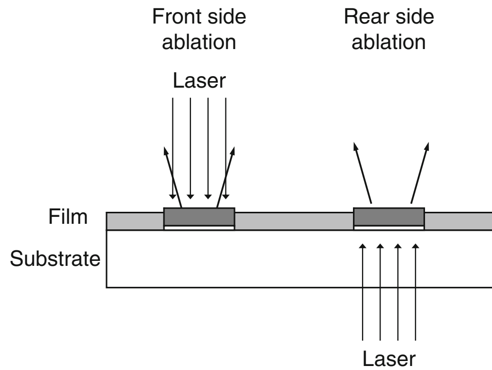

Fig. 10.12 Definition of front side- and rear side ablation of layers

in the direction of the laser beam, there is no possibility for the interaction of the laser radiation with already ablated fragments. In the case of front side ablation, this interaction can lead to considerable debris formation around the ablated area, if no countermeasures are applied. Furthermore, the required laser fluence for complete ablation is much higher, and the edge quality is lower for front side ablation.

The materials of the coatings studied are mainly transparent metal oxides such as Al_2O_3, HfO_2, Ta_2O_5, and Nb_2O_5 with absorption edges somewhere in the UV. As a sufficiently high absorption is a prerequisite for precise ablation, special care has to be taken when selecting the laser wavelength. The applied laser wavelength should be below the absorption edge of the material. Ta_2O_5 and Nb_2O_5 are transparent above about 300 nm, so for ablation 248 nm is required. HfO_2 is transparent down to about 220 nm, so that 193 nm should be used for ablation. Al_2O_3 and SiO_2 are transparent even at 193 nm, so the use of 157 nm-radiation is necessary.

As an example for the patterning of a transparent film on a transparent substrate, the fabrication of a binary DPE is demonstrated [76]. DPE are very attractive for beam shaping because of their basically lossless operation. The ablation process can be performed pixel by pixel according to the calculated DPE design or by creating the whole structure at the same time using a mask. For applications of the DPE in the near UV, Ta_2O_5 is an adequate material. Ta_2O_5 absorbs at 248 nm sufficiently, to be patterned by ablation, but is transparent at 308 nm. This means that a DPE for use at 308 nm can be fabricated using 248 nm [76].

10.8 Dielectric Masks

A typical application for the patterning of multilayers for optical applications is the fabrication of dielectric optical masks. Such multilayer stacks, for example, of alternating HfO_2- (high refractive index) and SiO_2-layers (low refractive index) can be ablated by an ArF-excimer laser, because HfO_2 is absorbing at 193 nm. Although the thickness of the film is more than 1 μm, under certain conditions, sub-μm edge definition is achieved in the case of rear side ablation [72].

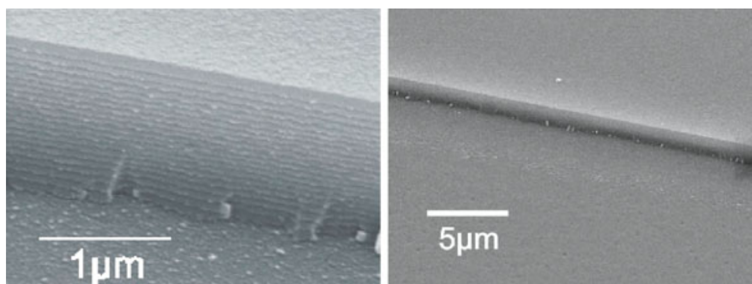

Fig. 10.13 Ablation edge of a HR dielectric layer stack ($HfO_2 + Al_2O_3/SiO_2$), ablation parameters: 193 nm, 350 mJ/cm^2, 1 pulse, rear-side ablation [78]

If both materials of the dielectric layer stack are transparent at 193 nm, the ablation of these systems has to be performed either at even shorter wavelengths (Vacuum-UV) [77] or with an absorbing subsidiary layer. Thus, dielectric mirrors with high reflectivity at 193 nm consisting of a stack of alternating SiO_2- and Al_2O_3-layers were patterned by depositing a 193 nm-absorbing HfO_2- or SiO-layer between substrate and HR-stack and ablating in a rear side configuration [78]. Figure 10.13 shows such an ablation edge, where the multilayer-structure of the stack can be clearly resolved.

Dielectric masks fabricated by this method can be applied for high intensity laser applications, where metal masks (Cr on quartz) would be easily damaged [79]. It is even possible to fabricate grey level masks by ablating only a defined number of single layers instead of the whole stack [75]. As this process works only by front side ablation, the edge definition of the ablated structures is limited.

10.9 Two Step Processing of Layers: Ablation + Oxidation

SiO_2 is one of the most important inorganic layer materials. As shown before, its transparency makes laser processing difficult. An alternative approach to direct ablation is the following: instead of a SiO_2-coating, a layer of silicon monoxide (SiO) or at least a substoichiometric silicon oxide (SiO_x, $x < 2$) is deposited. These materials are UV-absorbing and can therefore be easily processed using 193 nm or 248 nm excimer lasers [80]. After patterning, the remaining SiO_x is oxidized to SiO_2 by heating it in air to obtain the desired functionality (e.g., phase mask) of the patterned coating [81] (Fig. 10.14).

Figure 10.15 shows the results of rear side ablation of a single silicon monoxide layer. Clean ablation with sharp edges and nearly without redeposition of debris is observed. The measured ablation depth as a function of the laser fluence for a 171 nm thick and a 285 nm thick SiO-layer on fused silica is displayed in Fig. 10.16. Within a fluence range of about 200–600 mJ/cm^2, the complete layer is ablated with a single laser pulse (the ablation depth is constant and corresponds to the film thickness). Above this process window, at about 1 J/cm^2 the fused silica substrate is

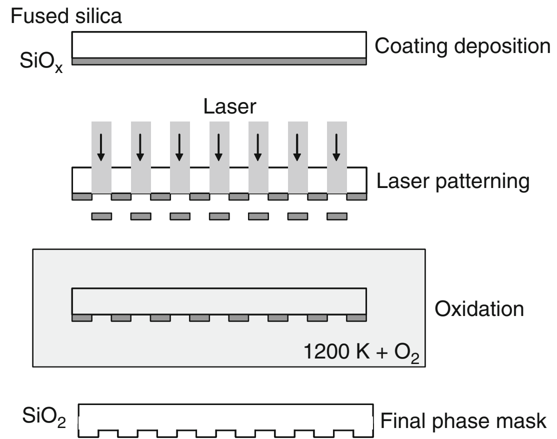

Fig. 10.14 Scheme of two step processing. After laser ablation patterning of the UV-absorbing SiO-layer the remaining material is thermally oxidized to SiO_2 [81]

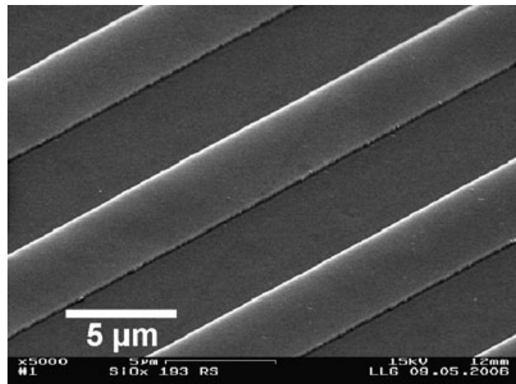

Fig. 10.15 Pattern of 5 µm lines and spaces made by rear side ablation in SiO on fused silica, laser: 193 nm, 20 ns, 540 mJ/cm^2, 1 pulse [82]

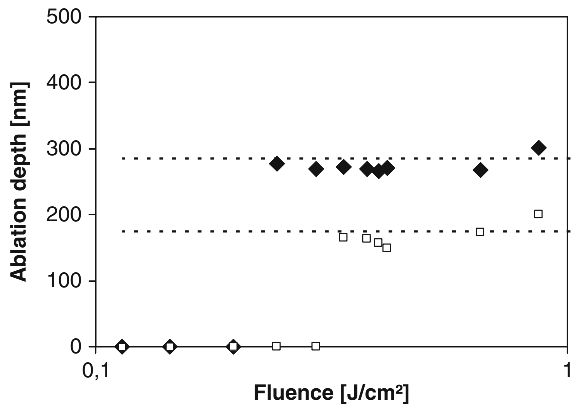

Fig. 10.16 Single pulse 193 nm laser ablation depth of SiO on fused silica measured with a Dektak profilometer; (*black diamond*) 285 nm thick SiO-layer; (*white square*) 171 nm thick SiO-layer [82]

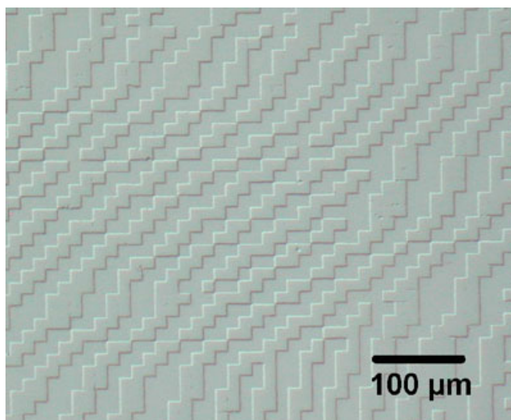

Fig. 10.17 Diffractive phase element (SiO_2) made by two step processing (laser patterning + oxidation) [81]

ablated, too. These observations can be explained by treating the layer-substrate boundary as predetermined end points, so that precise depth control and a very smooth surface can be achieved, even if the laser beam is somewhat inhomogeneous within the limits given by the process window. The two step processing (patterning of SiO, oxidation to SiO_2) has been applied for fabricating a phase element to operate in the deep UV, for example, at 193 nm [81] (Fig. 10.17).

10.10 Summary and Outlook

The strength of ablative laser micro machining lies in the large flexibility concerning material that can be processed, shapes and surface morphologies that can be obtained, and applications that can be addressed. Especially, UV-wavelengths provide strong material interaction needed for precise patterning and the potential of high structure resolution. Various processing methods (direct spot writing, mask projection, or interference patterning) lead to a variety of possible patterns ranging from simple hole arrays and line gratings to complex aspheric micro lens arrays. The ability to ablate glass and other transparent materials by deep UV- or VUV-lasers makes laser micro machining to an ideal tool for the production or prototyping of optical elements. In the future, especially, those micro fabrication processes which cannot be accomplished by other methods such as etching or replication due to the specialty of the material or the required precision in combination with a non-flat geometry will be performed by laser based micro machining. In particular, the combination of several different laser processes to fabricate micro-systems will become more important. For example, the fabrication of channel systems by ablation may be combined with subsequent laser welding to produce closed devices. But also combination and integration of laser processes (e.g., ablation) with non-laser process (e.g., plasma activation) are of great interest.

References

1. A.S. Holmes, Proc. SPIE **4274**, 297 (2001)
2. F. Wagner, P. Hoffmann, Appl. Phys. A **69**, S841 (1999)
3. D.S. George, A. Onischenko, A.S. Holmes, Appl. Phys. Lett. **84**, 1680 (2004)
4. D.J. Versteeg, C.W.M. Bastiaansen, D.J. Broer, J. Appl. Phys. **91**, 4191 (2002)
5. O. Yavas, M. Takai, J. Appl. Phys. **85**, 4207 (1999)
6. M. Henry, P.M. Harrison, J. Wendland, Proceedings of the 4th International Congress on Laser Advanced Materials Processing (2006)
7. C.G.K. Malek, Anal. Bioanal. Chem. **385**, 1351 (2006)
8. C.G.K. Malek, Anal. Bioanal. Chem. **385**, 1362 (2006)
9. D. Yuan, S. Das, J. Appl. Phys. **101**, 024901 (2007)
10. H. Qi, Y. Liu, X. Wang, F. Shen, Y. Yu, T. Chen, T. Zuo, Microsyst. Technol. **15**, 297 (2009)
11. H. Qi, T. Chen, L. Yao, T. Zuo, Microfluid Nanofluid **5**, 139 (2008)
12. M. Wehner, P. Jacobs, R. Poprawe, Proc. SPIE **6459**, 645908 (2007)
13. W. Pfleging, R. Adamietz, H.J. Brückner, M. Bruns, A. Welle, Proc. SPIE **6459**, 645907 (2007)
14. B. Keiper, R. Ebert, R. Böhme, H. Exner, Proc. SPIE **5116**, 20 (2003)
15. J. Ihlemann, B. Wolff-Rottke, Appl. Surf. Sci. **106**, 282 (1996)
16. S. Nikumb, Q. Chen, C. Li, H. Reshef, H.Y. Zheng, H. Qiu, D. Low, Thin Solid Films **477**, 216 (2005)
17. D. Ashkenasi, M. Schwagmeier, Proc. SPIE **6458**–14 (2007)
18. P.R. Herman, A. Yick, J. Li, N.R. Munce, L. Lilge, E. Jervis, S. Krylov, CLEO Tech. Digest CLF5 (2003)
19. P.E. Dyer, S.M. Maswadi, C.D. Walton, M. Ersoz, P.D.I. Fletcher, V.N. Paunov, Appl. Phys. A **77**, 391 (2003)
20. A.A. Tseng, Y.T. Chen, C.L. Chao, K.J. Ma, T.P. Chen, Opt. Lasers Eng. **45**, 975 (2007)
21. H.D. Im, K.H. Oh, H.T. Lim, S.G. Kim, S.H. Jeong, Proceedings of LPM2008, paper #08–20 (2008)
22. E. Bordatchev, S. Nikumb, Proceedings of LPM2008, paper #08–25 (2008)
23. M. Lapczyna, M. Stuke, Appl. Phys. A **66**, 473 (1998)
24. H.M. Phillips, R.A. Sauerbrey, Opt. Eng. **32**, 2424 (1993)
25. P.E. Dyer, R.J. Farley, R. Giedl, D.M. Karnakis, Appl. Surf. Sci. **96–98**, 537 (1996)
26. O. Apel, F. Beinhorn, J. Ihlemann, J.H. Klein-Wiele, G. Marowsky, P. Simon, Zeitschrift für physikalische Chemie **214**, 1233 (2000)
27. J. Ihlemann, R. Weichenhain-Schriever, Proceedings of LPM2008, paper #08–23 (2008)
28. J. Ihlemann, M. Schulz-Ruhtenberg, T. Fricke-Begemann, J. Phys. Conf. Ser. **59**, 206 (2007)
29. P.E. Dyer, R.J. Farley, R. Giedl, C. Ragdale, D. Reid, Appl. Phys. Lett. **64**, 3389 (1994)
30. J. Bekesi, J. Meinertz, J. Ihlemann, P. Simon, J. Laser Micro/Nanoengineering **2**, 221 (2007)
31. J. Bekesi, J. Meinertz, J. Ihlemann, P. Simon, Appl. Phys. A **93**, 27 (2008)
32. C.J. Newsome, M. O'Neill, R.J. Farley, G.P. Bryan-Brown, Appl. Phys. Lett. **72**, 2078 (1998)
33. M. Behdani, S.H. Keshmiri, S. Soria, M.A. Bader, J. Ihlemann, G. Marowsky, T.h. Rasing, Appl. Phys. Lett. **82**, 2553 (2003)
34. K.J. Ilcisin, R. Fedosejevs, Appl. Opt. **26**, 396 (1987)
35. H.M. Phillips, D.L. Callahan, R. Sauerbrey, Appl. Phys. Lett. **58**, 2761 (1991)
36. T. Lippert, T. Gerber, A. Wokaun, D.J. Funk, H. Fukumura, M. Goto, Appl. Phys. Lett. **75**, 1018 (1999)
37. K. Rubahn, J. Ihlemann, G. Jakopic, A.C. Simonsen, H.G. Rubahn, Appl. Phys. A **79**, 1715 (2004)
38. S. Pissadakis, L. Reekie, M. Hempstead, M.N. Zervas, J.S. Wilkinson, Appl. Phys. A **69**, S739 (1999)
39. J. Ihlemann, S. Müller, S. Puschmann, D. Schäfer, M. Wei, J. Li, P.R. Herman, Appl. Phys. A **76**, 751 (2003)
40. S. Pissadakis, M.N. Zervas, L. Reekie, J.S. Wilkinson, Appl. Phys. A **79**, 1093 (2004)

41. M.A. Bader, C. Kappel, A. Selle, J. Ihlemann, M.L. Ng, P.R. Herman, Appl. Opt. **45**, 6586 (2006)
42. F. Beinhorn, J. Ihlemann, P. Simon, G. Marowsky, B. Maisenhölder, J. Edlinger, D. Neuschäfer, D. Anselmetti, Appl. Surf. Sci. **138–139**, 107 (1999)
43. K. Chen, J. Ihlemann, P. Simon, I. Baumann, W. Sohler, Appl. Phys. A **65**, 517 (1997)
44. P. Simon, J. Ihlemann, Appl. Phys. A **63**, 505 (1996)
45. J. Turunen, F. Wyrowski (eds.), *Diffractive Optics for Industrial and Commercial Applications* (Akademie, Berlin, 1997)
46. G.P. Behrmann, M.T. Duignan, Appl. Opt. **36** 4666 (1997)
47. N.A. Vainos, S. Mailis, S. Pissadakis, L. Boutsikaris, P.J.M. Parmiter, P. Dainty, T.J. Hall, Appl. Opt. **35** 6304 (1996).
48. X. Wang, J.R. Leger, R.H. Rediker, Appl. Opt. **36** 4660 (1997)
49. F. Quentel, J. Fieret, A.S. Holmes, S. Paineau, Proc. SPIE **4274**, 421 (2001)
50. J. Ihlemann, D. Schäfer, Appl. Surf. Sci. **197–198**, 856 (2002)
51. V.V. Kononenko, V.I. Konov, S.M. Pimenov, A.M. Prokhorov, V.S. Pavelyev, V.A. Soifer, B. Lüdge, M. Duparré, Proc. SPIE **4426**, 128 (2002)
52. J. Bekesi, D. Schäfer, J. Ihlemann, P. Simon, Proc. SPIE **4977A**, 235 (2003)
53. M. Schulz-Ruhtenberg, J. Ihlemann, G. Marowsky, A.H. Nejadmalayeri, M.L. Ng, J. Li, P.R. Herman, Proc. SPIE **5063**, 113 (2003)
54. M.L. Ng, P.R. Herman, A.H. Nejadmalayeri, J. Li, J. Phys, Conf. Ser. **59**, 696 (2007)
55. M.H. Hong, F. Ma, C.S. Lim, Y. Lin, Z.Q. Huang, L.S. Tan, L.P. Shi, T.C. Chong, Proceedings of LPM2007, paper #07–20 (2007)
56. S. Mihailov, S. Lazare, Appl. Opt. **32**, 6211 (1993)
57. S. Lazare, J. Lopez, J.M. Turlet, M. Kufner, S. Kufner, P. Chavel, Appl. Opt. **35**, 4471 (1996)
58. F. Beinhorn, J. Ihlemann, K. Luther, J. Troe, Appl. Phys. A **68**, 709 (1999)
59. M.F. Jensen, U. Krühne, L.H. Christensen, O. Geschke, J. Micromech. Microeng. **15**, 91 (2005)
60. K. Naessens, P. Van Daele, R. Baets, Proc. SPIE **4941**, 133 (2003)
61. K. Naessens, H. Ottevaere, R. Baets, P. van Daele, H. Thienpont, Appl. Opt. **42**, 6349 (2003)
62. J.E.A. Pedder, A.S. Holmes, R. Allott, K. Boehlen, Proc. SPIE **6462**, (2007)
63. M. Levesque, R. Beaulieu, E. Weynant, M. Bergeron, N. Tovmasyan, Proceedings of LPM2008, paper #08–26 (2008)
64. H.M. Presby, A.F. Benner, C.A. Edwards, Appl. Opt. **29**, 2692 (1990)
65. T. Fricke-Begemann, J. Li, J. Dou, J. Ihlemann, P.R. Herman, G. Marowsky, Proceedings of the Third International WLT-Conference Lasers in Manufacturing, LIM 2005, p. 733
66. J. Dou, J. Li, P.R. Herman, J.S. Aitchison, T. Fricke-Begemann, J. Ihlemann, G. Marowsky, Appl. Phys. A **91**, 591 (2008)
67. T. Fricke-Begemann, J. Meinertz, J. Ihlemann, Proceedings of the EOS Topical Meeting on Micro-Optics, Diffractive Optics and Optical MEMS (17 – 19 October 2006, Paris, France), p. 114 (2006)
68. K.Y. Baek, D.Y. Kim, J.Y. An, J.W. Kim, H.S. Kang, S.K. Hong, J.H. Son, J.W. Chang, S.E. Lee, Proceedings of LPM2007, paper #07–90 (2007)
69. N. Fukuda, K. Kunishio, S. Nakayama, Proceedings of LPM2007, paper #07–44 (2007)
70. P.R. Herman, J. Yang, K. Kurosawa, T. Yamanishi, Proc. SPIE **2991**, 170 (1997)
71. N. Kaiser, H.K. Pulker (eds.), *Optical Interference Coatings* (Springer, Berlin 2003)
72. J. Ihlemann, K. Rubahn, Appl. Surf. Sci. **154–155**, 587 (2000)
73. E. Matthias, M. Reichling, J. Siegel, O. Käding, S. Petzoldt, H. Skurk, P. Bizenberger, E. Neske, Appl. Phys. A **58**, 129 (1994)
74. J. Ihlemann, B. Wolff-Rottke, Appl. Surf. Sci. **86**, 228 (1995)
75. K. Rubahn, J. Ihlemann, Appl. Surf. Sci. **127–129**, 881 (1998)
76. J. Ihlemann, D. Schäfer, Appl. Surf. Sci. **197–198**, 856 (2002)
77. D. Schäfer, J. Ihlemann, G. Marowsky, P.R. Herman, Appl. Phys. A **72**, 377 (2001)
78. J. Ihlemann, K. Rubahn, R. Thielsch, Proc. SPIE **4426**, 437 (2002)
79. J.R. Lankard, G. Wolbold, Appl. Phys. A **54**, 355 (1992)
80. C. Fiori, R.A.B. Devine, Appl. Phys. Lett. **47**, 361 (1985)
81. M. Schulz-Ruhtenberg, J. Ihlemann, J. Heber, Appl. Surf. Sci. **248**, 190 (2005)
82. J. Ihlemann, J.H. Klein-Wiele, J. Békési, P. Simon, Proc. SPIE **6462**, 646216 (2007)

Chapter 11
Laser Transfer Techniques for Digital Microfabrication

Alberto Piqué

Abstract Laser transfer techniques are becoming widely used for digital microfabrication applications. These non-lithographic processes are ideally suited for generating high-resolution patterns of complex materials without negatively affecting their properties. This chapter reviews the fundamentals of the laser forward transfer process, describes its evolution from its origins over 20 years ago, its numerous variations, and presents some of its most successful applications. It concludes discussion on the future of laser-based digital microfabrication techniques.

11.1 Introduction

Since the initial reports of laser transferred copper metal patterns by Bohandy et al. over 20 years ago [1], the use and development of laser forward transfer techniques has grown steadily. These simple yet powerful techniques employ a pulsed laser to locally transfer material from a source film onto a substrate in close proximity or in contact with the film, thus achieving the non-lithographic processing or laser direct-write of patterns on a given surface. The source is typically a coated laser-transparent substrate, referred to as the target, donor, or ribbon. Laser pulses propagate through the transparent ribbon and are absorbed by the film. Above an incident laser energy threshold, material is ejected from the film and propelled toward the acceptor or receiving substrate. Translation of the source and receiving substrate, or scanning and modulation of the laser beam, enables complex pattern formation in three dimensions with velocities typically limited by the laser repetition rate. Commercially available, computer-controlled translation stages and/or galvanometric scanning mirrors enable rapid motion and high-resolution patterns

A. Piqué (✉)
Materials Science and Technolgy Division, US Naval Research Laboratory,
Washington, DC 20375, USA
e-mail: pique@nrl.navy.mil

K. Sugioka et al. (eds.), *Laser Precision Microfabrication*,
Springer Series in Materials Science 135, DOI 10.1007/978-3-642-10523-4_11,
© Springer-Verlag Berlin Heidelberg 2010

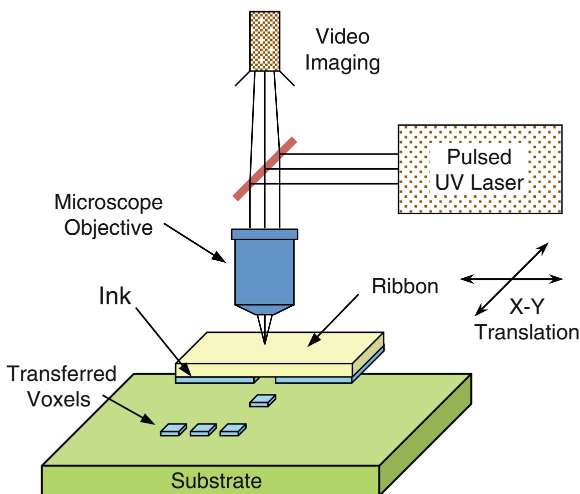

Fig. 11.1 Schematic diagram showing the basic components of a laser direct-write system

from the individually written 3-D volumetric pixels (or voxels) that result from the laser transfer process. A schematic showing the basic components of a laser direct-write system is shown in Fig. 11.1. The fact that the laser transfer process does not require the use of vacuum or cleanroom equipment greatly contributes to its great simplicity and compatibility with virtually any type of material and substrate.

These laser transfer techniques, known as laser direct-write or LDW, belong to a class of processes capable of generating high-resolution patterns without the need for lithographic processes afterwards [2, 3] (see Chap. 10 for a discussion on laser micromachining or subtractive LDW). Other examples of laser direct-write techniques include pyrolitic or photolytic decomposition of gas- or liquid-phase precursors, also known as laser CVD, LCVD, or laser-assisted deposition [4, 5]. This chapter, however, will not cover these techniques because they are non-forward transfer in nature. To better understand the applicability and potential new uses of laser direct-write and associated laser transfer techniques for digital microfabrication, its useful to compare/contrast them with other well-established digital microfabrication processes such as ink-jet. Like ink-jet, laser transfer techniques are capable of precisely depositing or direct-writing many types of functional materials (or their precursors) over virtually any type of surface or substrate in a conformal fashion. Unlike ink-jet, laser transfer techniques are not constrained to deliver the material through a nozzle (thus impervious to clogging problems) and can deposit fluid materials ranging from very low viscosity inks to high viscosity pastes (making them immune to ink-surface wetting issues), as well as solids. Furthermore, laser transfer techniques offer the added benefit of laser processing, such as micromachining, for material removal (not possible with ink-jet) and laser materials modification, for in-situ annealing, curing or sintering, all with the same tool.

This chapter provides a review of the laser forward transfer and laser direct-write literature, describing the technique's numerous variations, range of materials, structures, and applications. Particular emphasis will be given to the applications of laser transfer for electronic materials, micropower sources, and embedded micro-electronics. This chapter then concludes with a discussion of the role that the laser transfer techniques may play in the future of microelectronic manufacturing and other applications.

11.2 Lasers in Digital Microfabrication

The advent of computer aided manufacture (CAM) techniques and tools made possible the fabrication of mechanical parts in digital fashion, i.e., from computer design to final product without the need for intermediate steps to verify the compatibility and fit of a part relative to the rest of the design. In general, the term digital fabrication describes any process that allows the generation of patterns or structures from their design directly under computer control. Digital fabrication using CAM tools, although revolutionary on its own, was far from ideal since it could only be used to remove material through machining steps. Additive digital fabrication had to wait until the development of solid freeform fabrication techniques such as selective laser sintering and laser stereolithography. These processes, although capable of digitally generating three-dimensional prototypes accurate in form from computer designs, are still limited to the early design stages within the manufacture cycle, given the lack of functionality of the generated parts. Over the last decade, however, new applications in areas beyond large-scale manufacture of mechanical parts have surfaced, where the rapid prototyping of designs comprising multiple types of materials and feature sizes down to a few microns is required. These applications, mainly in the electronics, optoelectronics, sensor, and biomedical industries are in need of novel microfabrication techniques beyond lithography and other traditional semiconductor manufacturing processes. Non-lithographic techniques such as digital microfabrication offer great promise for applications requiring processing on plastic or flexible substrates, production of small batch sizes, and customization or prototype redesign. Gao and Sonin were the first to use the concept of digital microfabrication for fabricating three-dimensional structures by precisely dispensing microdrops of molten wax, with each microdrop serving as a 3-D pixel or voxel of the final three-dimensional design [6]. The use of a rapid solidifying wax allowed the printing of 3-D microstructures in a digital fashion. However, as a material, wax had limited functionality and offered little if no practical application.

Of the direct-write techniques mentioned already, LDW is ideally suited for digital microfabrication applications. As mentioned in the Introduction, LDW systems are capable of operating in various modes from additive (laser forward transfer), subtractive (laser micromachining), and modifying (laser sintering, laser annealing, etc.) [7]. What makes LDW unique is its ability to laser transfer such a wide range of materials with relatively high resolution conformal to the surface. As will be

described later in this chapter, the laser transfer process does not have a deleterious effect on the electrical, chemical, and even biological properties of the voxels of material forming the digital pattern. The ability of LDW to laser transfer functional materials and then process them or modify them in order to achieve the required properties and behavior is unique and offers the best opportunity to realize the advantages that digital microfabrication has to offer.

11.3 Origins of Laser Forward Transfer

Lasers are uniquely suited for digital microfabrication processes requiring the forward transfer of functional materials given that their energy output is monochromatic and can be controlled in time. The monochromatic light generated by lasers allows for the direct-write process to be carried out via a specific excitation path characteristic of a given wavelength while minimizing or eliminating other reaction channels. Meanwhile, the ability to generate very short pulses ($<10^{-8}$ s) of laser radiation allows the interaction of the laser pulse with the functional material to take place with minimal thermal effects. By directing single wavelength, very short laser pulses of sufficient intensity through a transparent substrate coated at the opposite end with a thin layer of material, discrete (or digital) material transfer in the forward laser direction can be achieved. The transferred material can be collected on a separate substrate facing the thin layer. The straightforwardness of this approach led to many groups to try it with different types of materials as the following sections will show. Despite its inherent simplicity, laser forward transfer exists in many different variations, is compatible with virtually any type of material, and takes place under ambient atmospheric conditions, thus making it one of the most versatile digital microfabrication techniques developed to date.

11.3.1 Early Work in Laser-Induced Forward Transfer

The earliest report of laser-induced transfer of material across an air gap can be found in the work performed by Levene et al. back in 1970 [8]. The material transferred consisted of black ink from a polyethylene backed typewriter ribbon and colored dies from a Mylar substrate across gaps up to 100 μm wide using a Nd:YAG laser ($\lambda = 1.06$ μm). Although the authors motivation was to develop a laser-based printing or marking process (the authors referred to it as recording), their work was prescient in highlighting the simplicity and high writing speed of the technique, while proposing a simple model based on the melting and vaporization of the transferred material as a function of the laser pulse energy. Unfortunately, the authors did not apply their technique to any other types of materials, and their work went unnoticed until the late 1990s when their article began being cited within the printing and image science community. Fifteen years later, the laser forward transfer process was

rediscovered, this time with metals. In 1986 Bohandy et al. reported the deposition of copper metal patterns via laser forward transfer inside a vacuum chamber [1]. Excimer laser pulses ($\lambda = 193$ nm, 15 ns) were focused with a cylindrical lens to a 25 mm long by 50 μm wide line on a source substrate containing a thin copper film. The Cu was transferred onto silicon and fused silica substrates, where further examination revealed resistivities ranging between 3 and 50 times the value for bulk copper with adhesion behavior that passed simple tape tests. Bohandy's group coined the term laser-induced forward transfer (LIFT) to denote the process and proposed a model more detailed but similar to Levene's to describe the process. According to this model; (1) the laser pulse heats the interface of the film at the source substrate; (2) a resulting melt front propagates through the film until it reaches the free surface; (3) at about this time, the material at the interface is superheated beyond its boiling point until, (4) the resulting vapor induced pressure at the interface propels the molten film forward toward the acceptor substrate [9]. Figure 11.2 shows a schematic illustrating the phases of this model. The same group then demonstrated that this process could be carried out in air, i.e., under atmospheric conditions, without the need for a vacuum [10].

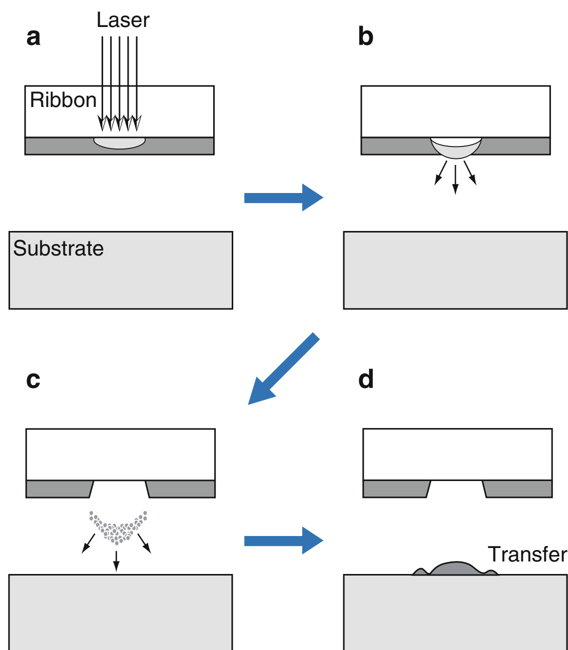

Fig. 11.2 Schematic representation of the Laser-induced forward transfer (LIFT) process. (**a**) The laser pulse is absorbed and heats the thin solid film at the ribbon interface. (**b**) The melted film is pushed away from the ribbon by the confined superheated vapor. (**c**) Both melted and vaporized film are ejected away from the donor substrate toward the receiving substrate. (**d**) The ejected material is collected on the receiving substrate

11.3.2 Transferring Metals and Other Materials with LIFT

The LIFT technique gained acceptance in a short time and was used successfully for a wide variety of single element materials, mainly metals such as copper [10], vanadium [11], gold [10, 12], aluminum [13], tungsten [14, 15], chromium [16], nickel [17], and Ge/Se thin film structures [18]. Reports of LIFT for oxide compounds such as Al_2O_3 [19], In_2O_3 [16], V_2O_5, [20] and $YBa_2Cu_3O_7$ high temperature superconductors [21] are worth mentioning, although the quality of the transferred ceramics was not as good as those deposited by traditional film growth techniques. In a variation to the basic process, polycrystalline silicon films can be deposited using a hydrogen assisted LIFT technique [22]. More recent examples include transfers of TiO_2-Au nanocomposite films [23], carbon nanotubes for field emitter applications [24, 25], conducting polymers such as Poly(3,4-ethylenedioxythiophene) (PEDOT) [26], and semiconducting β-$FeSi_2$ crystalline phases [27]. Repetitive transfers from the ribbon over the same area can be used to increase the thickness of the transferred film on the acceptor substrate. In a similar way, by changing the type of ribbon material, multilayer structures can be generated.

In general, to achieve uniform transfers with good morphology and spatial resolution on the acceptor substrate with the basic LIFT technique the following conditions need to be satisfied: (1) the thickness of the film on the ribbon should not exceed 100 nm; (2) the ribbon film should strongly absorb the laser wavelength in use; (3) the ribbon should be in contact or very close ($\approx$10's of micrometers) to the acceptor substrate; and (4) the laser fluence should barely exceed the threshold fluence for removal of the film from the ribbon. This last parameter is very important in order to control the quality of the films, since too high fluences tend to cause excessive vaporization of the film resulting in an explosive-like transfer affecting the morphology and resolution of the deposited material, while fluences below or at threshold result in incomplete transfers.

A later variation on the LIFT process employed an organic precursor compound (palladium acetate) rather than a pure metal for transfer [28]. This is significant as it demonstrated that the laser forward transfer process can take advantage of the photoinduced decomposition of a precursor at the ribbon/coating interface to propel the reminder of the film forward and create a metal pattern. By irradiating the transferred mixture with additional laser pulses, a very thin ($<$100 nm) but grainy palladium coating was produced, on which a thicker metal layer could be grown by means of electroless plating. In their paper, the authors consider the laser transfer and subsequent electroless metal plating as a two-step process enabling the selective deposition of metal patterns. However, their key contribution was to show that the LIFT process can be used to deposit a metal-organic precursor of the desired material, which once transferred can then be decomposed or processed into its final form.

11.3.3 Fundamental Limitations of the Basic LIFT Approach

Despite its successful application to the deposition of thin metal layers, the actual uses of the LIFT process are limited due to several shortcomings. In LIFT, metal films are required to be deposited on the ribbon by conventional thin film techniques that require vacuum deposition and other expensive processes. Since these metal films tend to be very thin (a few hundred nanometers), the individual layers deposited by LIFT are similarly thin, thus limiting its application to lithographic mask repair and other niche areas. During LIFT, the melting and solidification of the transferred material results in the formation of interfaces between adjacent voxels, which can have deleterious effects in the electrical transport properties of the patterned structure being fabricated. Furthermore, the melting of the transferred material becomes a serious issue when LIFT is performed under atmospheric conditions, because most metals are easily oxidized when melted in air. Moreover, the rapid quenching of the metal voxels can result in high intrinsic stresses between the transferred metal and the substrate, ultimately leading to poor adhesion and delamination of the transferred layers. Finally, LIFT is not suited for the transfer of ceramics and other inorganic phases given the irreversible phase changes and decomposition that these materials tend to experience upon melting and solidification.

The main source of the above-mentioned limitations derives from the reliance of the basic LIFT technique on phase transformations of the material undergoing laser transfer. Obviously, it is very difficult, if not impossible, for these transformations to take place with no changes to the material once the transfer is completed. Clearly, for the LIFT process to be truly compatible with the widest possible range of materials, it is necessary that the laser induced forward transfer takes place with minimal or no change or modification of the starting material to be deposited from the donor substrate. This is very critical since many types of materials, in particular complex multicomponent and multiphase systems will undergo irreversible changes upon melting or vaporization, which will degrade their desirable properties such as composition, phase, structure, homogeneity, electrical behavior, or chemical and biological activity.

11.4 Evolution of Laser Forward Transfer Techniques

The above limitations explain why LIFT is not suitable for the laser transfer of complex, sensitive materials such as those found in electronic and power generation devices. In fact, this realization is underscored by the decline in the number of publications reporting on LIFT of metals and other types of materials that followed for a few years afterward. However, for some applications, the original LIFT process works very well. For example, LIFT of Cr patterns has been shown to be useful for the repair of photolithography masks where pinholes or voids in the chrome film on the mask can easily be filled by LIFT. In this case, slight oxidation of the

laser-transferred chrome is not an issue, as long as the resulting chrome layer is continuous and opaque to the UV light used for exposure of the pattern on the mask. On the other hand, the success of any digital microfabrication technique depends on its ability to direct-write a wide variety of materials over many different types of surfaces. It is the ability to precisely control the intensity and nature of the interaction of the laser pulse at the interface between the laser transparent substrate and the coating in the donor substrate or ribbon that gives LIFT its unique advantages. This interaction can be modified in many different ways allowing many variations of the basic laser forward transfer technique, some of which are compatible with a wide range of materials. Obviously, one way to achieve these variations is by changing laser parameters such as wavelength and pulse length. In particular the use of very short laser pulses has been shown to enhance the quality of the laser transferred material and allow resolutions below the diffraction limit, imposed by the laser wavelength used. On the other hand, most of the variations of the basic LIFT technique have resulted from taking advantage of the unique role that the donor substrate plays in this process.

11.4.1 The Role of the Donor Substrate

To certain extent, the donor substrate is the key to the successful application of the laser forward transfer process. The ribbon of a typewriter provides a good analogy to the role of the donor substrate in this process. The resulting transfer of material from the donor to the acceptor substrate upon illumination with a laser pulse reminds us of a typewriter key striking the ribbon and transferring ink onto a piece of paper. Furthermore, the ability to transfer different materials from different donor substrates is comparable to printing different colors by changing the pigment of the ink in the ribbon. Clearly without the ribbon, the typewriter is useless and similarly without the appropriate donor substrates, LIFT will not work. It is with this in mind that some groups refer to the donor substrate as the ribbon. Throughout this chapter, the terms donor substrate and ribbon will be used to denote the same.

The main benefits provided by the ribbon to the LIFT process reside in the fact that the ribbon is both independent of the source of transfer energy and the target, i.e. the laser and the receiving substrate. As such, it can easily be modified without requiring complex adjustments to the basic setup and components, and it can be adapted to a specific material or application. Furthermore, since it is a totally independent part of the process, issues such as minimizing cross-contamination with the acceptor substrate, change of transferred material and removal of the donor substrate to allow direct interaction of the laser with the surface of the acceptor substrate are all easily achieved. Finally, since the type and form of the material in the ribbon can easily be changed, ranging from heterogenous multilayers, through composites, to liquid dispersions and complex fluids, the nature of the laser interaction with the material from the ribbon can be adjusted almost endlessly. It is this wide range of adaptation in the properties of the material present in the donor substrate that gives

rise to the numerous variations that have been proposed so far to the laser transfer process. Some of the most successful of these variations will be discussed in the remaining sections of this chapter.

11.4.2 Development of Multilayered Ribbons and Dynamic Release Layers

One early variation designed to overcome some of LIFT's limitations employed multilayered films. This variation on the LIFT process was originally intended for high speed laser color printing applications and was called laser ablation transfer or LAT [29]. The multilayers can be formed by depositing a thin laser-absorbing layer on the transparent support, followed by a second layer comprising of the material to be transferred. The thin absorbing layer is referred to as the dynamic release layer or DRL. DRL's can be made from vacuum deposited 20–100 nm thick thin film metal layers or from spin coated polymer layers up to 1 μm in thickness depending on the type of polymer used. With metallic DRL's laser energies above the ablation threshold result in melting and vaporization of the metal in a similar manner as in LIFT. While in the case of polymeric DRL's, the laser pulse tends to cause both photochemical and photothermal decomposition of the organic molecules into vapor byproducts. Under the right conditions, it is possible for the transferred material to avoid exposure to the incident laser pulse and experience minimum heating from the DRL. Therefore, materials exhibiting weak absorption to the laser radiation or materials that can be damaged by their interaction with the laser pulse can be transferred by this approach. The type of DRL, its thickness, the thickness of the second layer, the incident laser energy, and pulse shape need all to be optimized in order for the transfer to be successful with minimum effects of the incident laser on the transferred materials. A schematic of the DRL-mediated laser forward transfer process is shown in Fig. 11.3. Transfers of solid materials with this approach rely on van der Waals forces for adhesion to the receiving substrate, which are not practical for device applications, while in the case of liquids, wetting effects between the fluid and the surface of the receiving substrate must be taken into consideration.

The use of Teflon AF and poly(methacryolonitrile) as DRL's for the transfer of gold and aluminum thin films was shown to take place at lower laser energies than those required for transferring the metal films by themselves [30]. However, the use of DRL-mediated laser transfers of solid films is not useful for practical applications given the resulting poor adhesion between the transferred metal film voxel and the receiving substrate and also between adjacent voxels, i.e., only van der Waals forces. More recently, the use of metallic DRL's was applied to LDW aqueous suspensions of materials extremely sensitive to laser irradiation such as protein and DNA biomolecules using a 50–60 nm thick titanium DRL [31, 32], and fungi (*Trichoderma conidia*) using a 50 nm thick silver DRL [33]. The ability to precisely control the laser transfer with the use of a DRL was later shown with the preparation of fully functional biomolecule microarrays containing 40 μm droplets

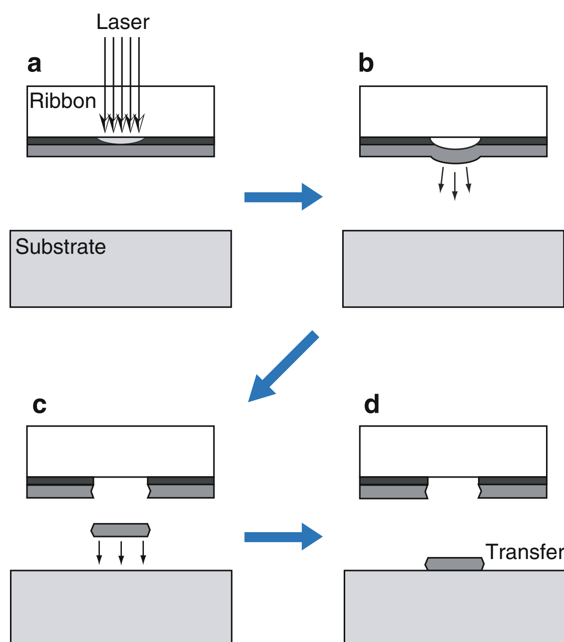

Fig. 11.3 Schematic showing the steps laser transfer with a dynamic release layer in the donor substrate. (**a**) The laser pulse is absorbed by the dynamic release layer. (**b**) The dynamic release layer is vaporized pushing the second layer forward. (**c**) A section of the second layer is sheared from the donor substrate and directed toward the receiving substrate. (**d**) The released layer reaches the receiving substrate

of viable human gene cDNA solutions [34, 35]. Studies of the transfer process of a 50/50 by volume water and glycerol fluid mediated by a 60 nm titanium DRL layer have shown that for laser energies slightly above the transfer threshold energy, circular liquid droplets can be deposited uniformly and reproducibly [36]. Furthermore, at energies just over the transfer threshold energy, the smallest diameter ($\approx$30 μm) and most uniform droplets were obtained without removal or ablation of the DRL. This work showed that the volume of the transferred fluid exhibits a linear dependence with the laser pulse energy with no loss of fluid due to vaporization during the transfer process. Despite these successes, the use of a metal DRL is complicated by the potential for the transferred material to be contaminated by the volatilized DRL and degraded due to thermal exposure and mechanical shock damage induced by the laser pulse.

An alternative is provided by the use of a polymer DRL tailored to absorb and fully decompose into vapor species during its interaction with the laser pulse, as has been shown with the deposition of mammalian cell cultures [37]. The key to this approach is the use of an aryltriazene polymer, which upon irradiation from the laser pulses generated by an XeCl excimer laser (308 nm) photodecomposes into small gaseous fragments at a low fluence ($\approx$25 mJ/cm^2). More complex

multilayer structures comprising of this DRL polymer and a bilayer have also been demonstrated. These bilayers, formed from a thin metal film and an active material such as quantum dots like CdSe(CdS) nanocrystals [38], or an electroluminescent polymer like poly[2-methoxy-5-(2-ethylhexyloxy)-1,4-phenylenevinylene] or MEH-PPV [39], were laser transferred intact with most of the aryltriazene polymer decomposing. The intact laser transfers of 0.5×0.5 mm voxels 80–100 nm thick of various materials such as aluminum, dyed gelatin, and methylcellulose were demonstrated using aryltriazene DRL's ranging in thickness from 90 to 350 nm [40]. It is worth noting that for aryltriazene DRL thicknesses below 50 nm, heat diffusion into the transparent donor substrate results in a dramatic increase in the laser ablation threshold, thus the thermal properties of the donor substrate need to be taken into consideration in these cases [41]. The aryltriazene DRL has also been tested for transfers of 150 nm thick amorphous GdGaO films using single pulses from a femtosecond (fs) Ti:sapphire laser (800 nm, $\approx$130 fs) resulting in the deposition of 10 μm diameter discs without shattering of the transparent oxide layer [42].

The use of very thick (>2μm) polymer absorbing layers provides one more recent variation to the DRL-mediated LIFT approach. By relying in a DRL layer significantly thicker than the laser absorption depth, it is possible to bring about the transfer of a fluid layer covering the polymer through plastic deformation of the polymer without its total vaporization and removal. Thick (4 μm) polyimide layers were used for this purpose insulating the laser transfer (λ=355 nm, 15 ns) of mouse embryonic stem cells cultures from thermal and mechanical shocks [43].

11.4.3 LIFT with Ultra-Short Laser Pulses

The work by Tolbert using LIFT with a dynamic release layer showed for the first time that the pulse duration has an effect on the transfer process. Their experiments indicated that picosecond (ps) laser pulses are more efficient in ablating the multilayered films than nanosecond (ns) pulses, with transfer laser fluence thresholds an order of magnitude smaller [44]. Various groups later demonstrated laser forward transfers without the use of DRLs with sub-picosecond laser pulses. For example, chromium metal and indium oxide microstructures were laser transferred using 500 fs KrF excimer (248 nm) laser pulses in a low vacuum environment (0.1 Torr) [16, 45, 46]. In this work the authors showed the transfer of highly reproducible, well-adhered structures of submicron size to demonstrate the fabrication of binary-amplitude and multilevel optical structures. Bähnisch et al. used similar ultrashort-laser pulses to transfer Au/Sn (80/20 wt%) discs for soldering pad applications using a Ti:sapphire laser (775 nm, 0.1–8 ps) [47]. Shortly thereafter, Tien et al. reported the transfer of simple arrays of aluminum circular discs with diameters down to 800 nm on glass substrates using 1 ps pulses from a 1.06 μm Nd:glass chirped-pulse amplified laser under atmospheric pressure [48].

The use of fs-LIFT at atmospheric pressures was later reported for generating gold patterns for selective surface texturing [49], copper microdroplets on quartz

substrates [50], chromium droplets of micron [51] and submicron [52] diameters, and micron-sized aluminum droplets [53]. In all these works, the use of ultrashort laser pulses (<100 ps) allowed higher precision on the transfer of material, since the melt zone generated by lateral heat diffusion on the donor substrate can be limited to widths smaller than the spatial extent of the impinging laser pulse.

Imaging studies of the ejected material resulting from ultra-short laser pulses have been carried out to better understand the nature of the transfer process. Shadowgraphy and time-integrating imaging for edge velocity measurements with 2–3 ps laser pulses ($\lambda = 1{,}053$ nm) showed that the velocity of the transferred material is limited by the onset of laser induced damage to the donor substrate carrier [54]. More recently, studies of fs-LIFT using ultrafast shadowgraphy [55] and stroboscopic Schlieren imaging [56] indicate that the high spatial resolution fs-LIFT is due to the highly directional nature of the transfer with narrow angular divergence. It is also possible to take advantage of the highly localized interaction of the femtosecond laser pulse with the material in the donor substrate to transfer extremely delicate materials such as biomaterials. Given the very short time-scales involved, limited heat diffusion prior to ejection allows for most of the biomaterial to be transferred mostly intact [57, 58]. Further examples of fs-LIFT for biological materials will be provided in the Applications section (Sect. 11.5).

Two recent variations of fs-LIFT are worth mentioning. In one approach, multiple femtosecond laser pulses with energies below the fluence threshold for LIFT are used to achieve the transfer of Cr films without causing their melting. The initial pulses, cause delamination of the Cr film from the donor substrate, while the later pulses overcome the shear forces still maintaining the Cr layer attached to the donor film resulting in a gentler lift-off process [59]. However, this process is difficult to implement since the number of pulses required to complete the transfer varies from one transfer to the next, while the adhesion of the transferred material to the acceptor substrate was not evaluated. In the second approach, an ultra-thin (25 μm thick) quartz substrate is used as the support for the donor substrate. The support substrate side facing the acceptor substrate is coated with a 40–400 nm thick layer of metals such as Cr, Ti, Ti/Cr, and Ti/Au, while the opposite side is coated with a monolayer of close-packed polystyrene microbeads ($\approx$100–150 μm in diameter). Each of the microbeads serve as individual focusing lenses resulting in the transfer of metal features with micron to sub-micron dimensions [60]. However, the difficulties in fabricating and handling such a complex donor substrate and the fact that the transfer distribution is restricted to hexagonal patterns greatly limit the application of this technique.

11.4.4 Laser Transfer of Composite or Matrix-Based Materials

Another variation of the basic LIFT process relies on the transfer of materials in powder form mixed with an organic binder. Such mixtures or matrices are then applied as a uniform coating on the transparent donor substrate to form a ribbon.

The advantage of this approach resides in the fact that the transfer of thicker films from the ribbon can be achieved at lower laser fluences than with LIFT of homogenous films. Furthermore, the composite film is transferred in its solid phase, thus avoiding the melting and re-condensation steps that take place in traditional LIFT. This modified LIFT approach has been used for the LDW of diamond nanopowders [61], ferroelectric ($BaTiO_3$ and $SrTiO_3$) and ferrite ($Y_3Fe_5O_{12}$) micron sized powders [62, 63], phosphor powders [64], and carbon composite polymers for gas sensing elements [65]. Despite the materials versatility of this approach, the adhesion of the transferred layers can be poor and the organic binder remains after the transfer, thus high temperature calcination steps are necessary to remove the binder and achieve some degree of densification. However, the resulting properties of the deposited films are adequate for many applications where dense layers are not required.

The use of LIFT with ribbons containing organic binders can be applied to the direct transfer of many complex material formulations such as rheological systems [66, 67]. The realization that pastes, inks, suspensions, sol-gel solutions, and even cell cultures (see Sect. 11.5.3) could be deposited in patterns via LIFT without physical or chemical modification during their transfer meant that a wider range of materials and formulations for many applications were laser printable. Originally, this wet laser forward transfer technique was named matrix-assisted pulsed laser evaporation direct-write (MAPLE-DW), in reference to the transfer of a loosely defined matrix comprising of powders or particles dispersed in a liquid. However, since the transfer process does not necessarily involve the evaporation of a matrix, this terminology should be discarded in favor of the less confusing laser direct-write or LDW.

11.4.5 Laser Transfer of Rheological Systems

The use of LDW for the deposition of high quality electronic materials requires the generation of structures comprising of multiple voxels, adjacent or on top of each other, that readily merge to form a single, continuous pattern. Electrical interconnects provide a perfect example of this requirement as heterogeneous interfaces between voxels can degrade the overall conductivity. By enabling the transferred material to remain fluid, adjacent voxels on the receiving substrate will merge into one continuous segment. Figure 11.4 shows a simple schematic illustrating the basic steps on the laser direct-write of rheological systems.

In reality, the LDW process is very different from prior LIFT experiments as functional materials are deposited without direct vaporization, which could affect their desirable physical or chemical properties such as electrical conductivity, dielectric properties, or electrochemical activity. As shown schematically in Fig. 11.4, a small region of the laser absorbing ink interacts with a low fluence ($<100\,mJ/cm^2$) laser pulse causing a small amount of the ink to evaporate. As the resulting vapor expands, it generates shear forces that result in the ejection of a droplet from the

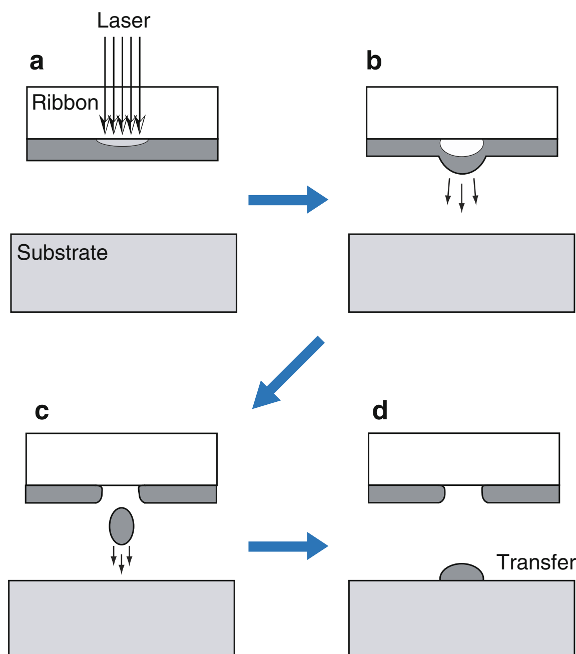

Fig. 11.4 Schematic representation of the steps involved in the forward transfer of viscous rheological systems during the LDW process. (**a**) The laser pulse is absorbed by the paste or ink layer at the interface. (**b**) The absorption of the laser pulse heats and vaporizes a small fraction of the ink. (**c**) A droplet or voxel of ink is ejected away from the donor substrate toward the receiving substrate. (**d**) The ejected material is collected on the receiving substrate with little or no surrounding debris

film toward the receiving substrate, where it is deposited with its original rheological properties intact. The results obtained with transfers of extremely laser sensitive systems, such as buffer solutions containing biomaterials, proteins and living cells [68], or electrochemically sensitive materials [69] confirm that most if not all of the transferred fluid does not interact with the laser pulse.

The uniqueness of the laser transfer of rheological systems resides in the fact that it represents a totally new approach to LIFT based on the non-phase transforming forward transfer of complex suspensions, inks, or pastes. This is made possible by the reduced shear forces required to dislodge and release the portion of the coating in the donor substrate illuminated by a laser pulse, which allows the use of lower laser energy fluences, thus resulting in virtually no ablation of the transferred material. Given the diverse nature and large number of parameters affecting the laser transfer process for rheological systems, a simple description as the one provided in the previous paragraph cannot be expected to completely explain its behavior. For instance, it is known that laser parameters such as fluence, pulse duration and wavelength, laser beam dimensions and gap or distance between donor and acceptor substrates play an important role in the laser transfer of complex fluids or inks.

Additionally, parameters such as the composition of the ink in the ribbon, its thickness, viscosity, solids content, solids particle size, and the surface chemistry and morphology of the receiving substrate greatly affect the ability to transfer a particular fluid and the resulting morphology of the transferred voxels. The use of fast imaging techniques in order to be able to determine the timing and shape of the transfer front can provide a better understanding of the laser transfer of rheological systems.

11.4.6 Jetting Effects

The wide parameter space available during LDW of rheological fluids leads to greater versatility in materials choice than is available with any other direct-write technique. Analyzing the images obtained through time-resolved optical microscopy of the laser transfer of various types of complex fluids and modeling the behavior of fluids under such extreme conditions has yielded relevant insight in the nature of the transfer process of complex fluids and the role of various key parameters such as laser fluence and ink properties.

The various studies conducted to date underscore the differences between traditional LIFT and LDW of rheological fluids and demonstrate the fluid nature of the transfers responsible for the coalescence of the individual voxels into continuous, pinhole-free layers on the surface of the receiving substrate. Early works measured the effect of various laser fluences on the transfer of medium viscosity inks comprised of barium-zirconium titanate (BZT) [70] or barium titanate ($BaTiO_3$, BTO) [71] nanopowders (150 nm dia.) suspended in α-terpineol. These studies revealed the existence of three distinct regimes as a function of laser fluence. In order of increasing laser fluence, these regimes were labeled sub-threshold, jetting, and plume. Molecular dynamics simulations of laser-induced processes on fluids in similarly spatially confined systems reveal three distinct and very similar regimes to those observed in this experiments, i.e., no ejection below a laser energy threshold, cluster formation for intermediate energies and explosive boiling at higher energies [72].

Later studies have shown that depending on the thickness and properties of the complex fluid in the ribbon, laser transfer of material can occur at what were originally considered to be energies below the sub-threshold for transfers. The definition of sub-threshold was based in the failure to separate and eject the fluid from the ribbon. This definition did not take into consideration the generation of bubbles, which would retract and collapse back, since not enough laser energy had been provided for their severance from the ribbon. In fact, it is possible to achieve material transfer from the contact of these bubbles with the receiving substrate. This behavior, observed with the transfers of high viscosity fluids or pastes has been labeled the bubble regime [73].

In a different study, reproducible transfers of uniformly sized droplets from low viscosity fluids using a DRL were shown under the jetting regime [74]. The same group had previously demonstrated that under certain conditions the size of

the transfered droplets is independent of the gap between the ribbon and acceptor substrate[75]. Their work showed why at low laser fluences no transfers are observed as the gap is increased. Operating under the jetting regime is key in order to achieve well-defined and repeatable transfers of aqueous solutions with uniform spatial resolutions determined by the laser spot size on the ribbon. Furthermore, the jetting transfer regime avoids the excessive spreading of material and formation of satellite droplets and debris on the receiving substrate, resulting in higher quality transfers with the smallest possible feature size for a given laser spot and ink layer thickness.

11.4.7 Laser Transfer of Entire Devices

The use of LIFT processes for the transfer and placement of prefabricated parts or components onto a receiving substrate was first reported by Holmes et al. [76]. In their work, the authors describe the laser-driven release of Si-based microstructures from a UV-transparent substrate with an intermediate polymer sacrificial layer. Upon irradiation with an excimer laser pulse, a thin fraction of the sacrificial layer is vaporized, releasing the microstructure. This technique was later used to demonstrate the laser-assisted assembly of microelectromechanical devices from parts fabricated on separate substrates [77]. These initial results showed how to use the laser transfer process as an alternative to conventional pick-and-place approaches for the placement of electronic components such as passives and semiconductor bare dies. The basic concept is a derivation of the DRL approach. In essence, it requires a sacrificial layer such as the polymer layer used by Holmes to attach the individual components to a UV-transparent support. A laser pulse then ablates the sacrificial layer generating gases that release and propel the component toward a receiving substrate placed in close proximity. This laser device-transfer process is contact-less and thus allows the transfer of very small and very thin components, which could easily be damaged by pick-and-place tools.

Recently, this concept has been applied to the laser transfer of semiconductor bare dies. Karlitskaya and coworkers have developed a simple model that predicts the fluence threshold for the release of $200\times200\,\mu m^2$ by $150\,\mu m$ thick Si dies held with a polyvinyl chloride (PVC) sacrificial layer [78, 79]. The model shows that the release threshold is below the thermal damage threshold for the reverse side of the die (<673 K) based on heat diffusion of the absorbed laser pulse through the Si substrate. In this case, the authors applied the laser transfer process to devices with the active region facing opposite to the laser pulse. This configuration is not very practical since in order to establish the electrical connections between the pads on the transferred die and the acceptor substrate, extremely precise alignment is required. A better solution is to transfer the die with its active surface facing up enabling wire bonding tools or direct-write approaches to interconnect the device with the acceptor substrate. The challenge, however, is to be able to illuminate the active region of the die with the transfer laser pulse without damaging it.

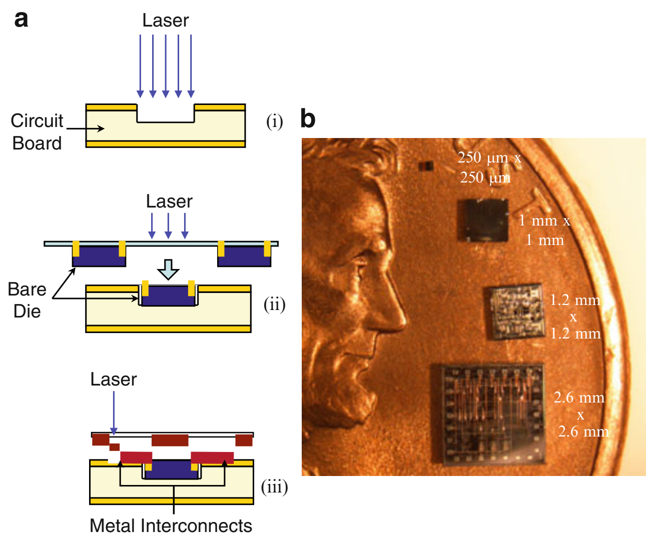

Fig. 11.5 (**a**) Schematic diagram showing the steps required to embed electronic components inside a substrate using laser digital microfabrication: (*i*) laser micromachine the pocket on the substrate; (*ii*) transfer of the device using lase-and-place; (*iii*) LDW of the interconnects to complete the circuit. (**b**) Photograph showing various sizes of bare-die integrated circuits (ICs) transferred using lase-and-place

At the U.S. Naval Research Laboratory, this capability was demonstrated for the laser forward transfer of individual InGaN LED semiconductor substrates ($250 \times 350\,\mu m^2$) in bare die form, i.e., unpackaged, using a series of low fluence ($\approx$150–200 mJ/cm^2) 10 ns pulses from either excimer (248 nm) or YAG (355 nm) lasers [80]. Once laser transferred, the LEDs were electrically tested and their operation verified. This laser-driven pick-and-place of electronic devices has been named lase-and-place, and it is shown schematically in Fig. 11.5a. The fact that the devices are not damaged upon laser illumination of their active surface and subsequent transfer demonstrates that a uniquely versatile laser-based component placement and interconnecting process can be developed by combining lase-and-place with LDW.

The lase-and-place technique has been used successfully to laser transfer a wide variety of components such as surface mount devices (SMDs) and semiconductor integrated circuits (ICs) ranging in size from 0.1 to over 6 mm^2 in area [81]. The range in size of semiconductor bare die substrates transferrable with this method can be seen in Fig. 11.5b. This technique has also been shown to be compatible with the transfer of extremely thin ($\approx$10 μm) silicon substrates, which despite their fragility can be deposited by lase-and-place with extreme precision on the surface of an acceptor substrate without being damaged or fractured [82, 83].

11.4.8 Recent Variations of the Basic LIFT Process

One of the greatest constraints of the basic LIFT technique is the fact that diffraction effects limit the minimum feature size that can be transferred. One way to achieve resolutions beyond the diffraction limit experienced with conventional optics is by using a donor substrate covered with a monolayer of self-assembled microspheres and subsequently illuminating this surface with a laser pulse. This approach makes it possible to take advantage of the resulting near-field effects to achieve subwavelength nanopatterning [84]. LIFT of 900 nm gold dots forming a hexagonal lattice has been demonstrated by using a two-dimensional array of microspheres coated with a 50–100 nm thick gold film and illuminated with a 20 mJ/cm^2 excimer laser pulse ($\lambda = 248$ nm, 28 ns) [85]. Similar results have also been shown using femtosecond lasers [60]. However, the fabrication and handling of the complex donor substrate, as mentioned earlier, combined with the fact that only hexagonal close-packed arrays with spacing features no smaller than the radius of the microspheres can be achieved have limited the use of this approach. An interesting new method to achieve subwavelength nanopatterning is to use Bessel beam laser trapping of microspheres near the surface of a substrate to enable near-field direct-write [86]. This novel approach allows the relative position of the microsphere, which serves as the focusing element for the laser beam and the substrate underneath, to be adjusted with accuracies of the order of 10 nm. Using 355 nm pulses from a DPSS laser, patterning of 100 nm features on polyimide surfaces has been demonstrated. By combining this setup with an array of optical traps, a high-throughput probe-based method for patterning surfaces with subwavelength features becomes feasible. It remains to be seen, however, if this technique can be adapted to transfer material onto a surface to truly achieve a digital nano-fabrication capability.

Another shortcoming of the LIFT process is the generation of satellite droplets during transfer that result in debris formation on the donor substrate with deleterious effects to the achievable resolution. The use of ribbons thinly coated ($\leq 1\,\mu$m) with high viscosity ($>$10,000 cps) nanoinks or nanopastes has been shown to mitigate this problem [87]. This process, which has been termed laser decal transfer, offers the possibility for the laser transfer of patterns with feature fidelity and thickness uniformity comparable to lithographically patterned thin films [88]. This new approach represents a significant advance in LIFT-based direct-write processes given the improved spatial resolution (down to 2 μm), increased thickness uniformity (within 50 nm), sharper edge features, and minimal surrounding debris compared to previous laser transfer processes. Figure 11.6 shows some examples of the types of features generated by laser decal transfer. As the AFM image in Fig. 11.6b shows, the edges of the transferred voxels are well defined, their surface matches the area of the transfer laser pulse, and their thickness is extremely uniform. This capability to faithfully reproduce the size and shape of the laser spot by the laser-transferred nano-suspension is unique to laser decal transfer. The key to laser decal transfer is the use of thin and highly viscous nanoink layers in the ribbon, which can be sheared away from the transparent donor substrate with very low laser fluences, usually below 200 mJ/cm^2, without deforming or breaking apart the shape of the thin layer.

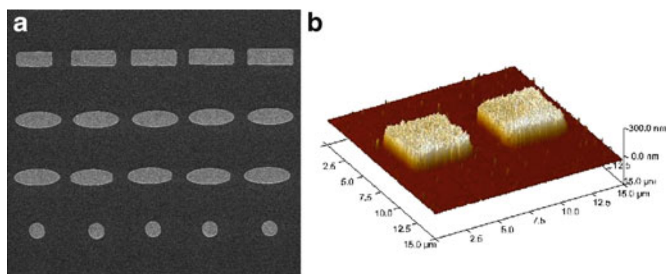

Fig. 11.6 Types of patterns and structures deposited using laser decal transfer of a silver nanopaste. (**a**) SEM image showing rows of patterns generated with different laser apertures. (**b**) AFM image showing detail of two square voxels transferred on an Si substrate

The laser decal transfer process has great potential since it can minimize the time it takes for the digital microfabrication of a pattern or design by allowing the size and profile of the transferred voxel to be varied without loss in resolution. This means that with laser decal transfer it should be possible to generate the patterns required to digitally microfabricate interconnects, transmission lines, circuit repairs, and even complete devices in considerably fewer steps [89]. This is possible since the shape and size of each "bit" , i.e., voxel, required for the digital microfabrication of a pattern or design, can be changed at will without loss of resolution during the laser decal transfer process. Such capability is unique among other digital microfabrication processes and might lead to the development of novel applications and new types of structures, as shown later in this chapter (Sect. 11.6.1).

11.5 Applications

The continuing evolution of the laser transfer process, as demonstrated by the numerous variants to the basic LIFT approach described in the previous sections, has been driven by the wide range of applications ready to benefit from the use of direct-write processes. In fact, in most cases, a specific application has caused the development of a new LIFT technique derived from the original approach. In the following sections, selected examples in application areas ranging from electronic devices to biosensor arrays are presented to illustrate the versatility and great potential of these laser-based digital microfabrication techniques.

11.5.1 Microelectronics

The capability offered by the LDW technique to conformally transfer viscous fluids, pastes, or inks has been used with great success for the fabrication of metal interconnects, vias, and antenna structures [90, 91]. In fact, LDW has been used to

deposit metallic screen printable inks over complex 3-D surfaces, which has always been extremely difficult if not impossible using traditional lithographic processes. Typically, a commercially available screen printable silver paste is used for the ink. The laser spot size is adjusted depending on the required line-width of the metal lines. Once the transfers are completed, the acceptor substrate (usually printed circuit board) is baked at 100–150°C to obtain the final metallic silver patterns. The electrical resistivity of these patterns ranges between 3 and 50 times higher than that of bulk silver depending on the silver ink used and the baking temperature. The adhesion and mechanical properties of patterns made by LDW are very good, as indicated by tape and flexing tests. Overall, the ability to deposit conformal metal patterns on substrates at low temperatures allows for the fabrication of novel types of electronic designs such as conformal GPS antennas [92] on polymer radomes and miniature electrode contacts for DC potential drop fatigue studies from arrays of defects on metal samples [69]. More recently, LDW has been used to print the interconnects for individual components, including unpackaged semiconductor devices, placed under the surface of a substrate in order to fabricate fully functional embedded circuits. This important application of LDW technologies will be discussed in a later section dedicated to embedded microelectronics (Sect. 11.5.4).

Similarly, LDW of thick film polymer or ceramic pastes has been used to fabricate passive electronic components such as resistors [93] and interdigitated capacitors [94]. The use of LDW to fabricate simple electronic circuits comprising of several passive components and their interconnects has been demonstrated as in the case of a simple chemoselective gas sensor circuit [95–98] and RF filter test structures [99].

11.5.2 Sensor and Micropower Generation Devices

The use of LDW for the digital microfabrication of sensors offers one of the earliest examples for applications of these non-lithographic techniques. The first type of sensor device made by LDW was a chemical vapor sensor based on the ability of a chemoselective polymer loaded with graphite particles to reversibly change volume when exposed to solvent vapors [62,63]. Upon exposure, the chemoselective polymer (polyepichlrohydrin or PECH) expands increasing the average distance between the graphite particles and thus exhibiting an increase in its electrical resistance. Figure 11.7a shows a photograph of the chemiresistor sensor element (black portion) across a set of silver interdigitated electrodes entirely fabricated by LDW [97]. Figure 11.7b shows an image of a fully operational chemiresistor sensor circuit with a chemiresistor sensor element, Ag metal interconnects and polymer thick film (PTF) resistors all made by LDW [98]. The 4-Quad comparator device chip and the surface mount LED components were soldered to the silver interconnects and power to the circuit was provided by an external battery. In the presence of organic vapors, the resistance change across the chemiresistor sensor caused the 4-Quad comparator to sequentially light up individual LED's depending on the magnitude of the change in resistance across the sensor, proportional to the vapor concentration.

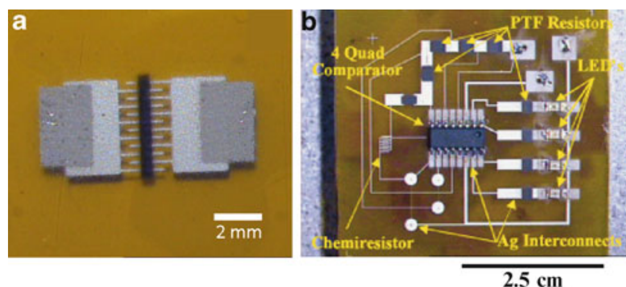

Fig. 11.7 Examples of devices fabricated using LDW. (**a**) Chemiresistor sensor element. (**b**) Fully functional gas sensor circuit with chemiresistor sensing element

LDW techniques have been used to fabricate other types of small size sensor devices such as temperature [95] and strain sensors on polyimide substrates [98], and simple electrochemical biosensors for the detection of small concentrations of dopamine on aqueous solutions [95, 100] at the U.S. Naval Research Laboratory (NRL). Other groups have used LIFT techniques for depositing micro patterns of tin oxide layers with various oxygen ratios, which have potential application as gas sensors [101]. More recently, a capacitive chemical sensor array was produced using LIFT by laser transferring three different types of polymer materials sensitive to organic solvent vapors. Droplets of each polymer in solution were deposited onto an array of thin silicon membranes to demonstrate a micromechanical capacitive vapor sensor [102].

At NRL, LDW has been used with great success for laser printing materials for the fabrication of electrochemical micropower sources, such as ultracapacitors, batteries, and die sensitized solar cells [103–106]. These micropower sources require the use of materials with a large degree of structural complexity, such as nanocomposites, solid-state polymers, liquids, or mesoporous mixtures of electrochemically active materials. Any technique designed for the fabrication of electrochemical micropower sources must be able to deposit the above types of materials while maintaining their electrochemical activity and structural integrity in a confined space subject to the processing limitations, such as temperature and pressure, imposed by the microdevices, their substrates, and packaging.

One of the important attributes of LDW in the context of electrochemical systems is that it allows for the deposition of highly porous, multicomponent materials without modifying their properties. In all cases, the technique results in uniform transfer of the structurally complex materials with a porous structure that allows for good electrolyte penetration. Another key advantage of LDW in constructing electrochemical cells is the flexibility in the design of operating geometries. The two main approaches include placing the anode and cathode adjacent to each other in the same plane (planar), or layering the anode and cathode on top of one another (stacked). For instance, in the case of stacked geometries, one can obtain higher area densities and lower resistances owing to the relatively thin separator layer, but this layer must be structurally stable enough to support the anode/cathode/current

collectors. Furthermore, by combining LDW with laser ablation to micromachine the substrates, it is possible to reduce packaging difficulties by embedding the electrochemical components directly within a substrate, further reducing the packaged size of an entire microdevice while allowing its geometry to be adapted to fit virtually any form factor.

Planar alkaline microbatteries can be constructed with electrodes formed from different materials such as Zn for the anode and Ag_2O_3 for the cathode [107, 108]. The LDW transfer process can include the KOH electrolyte in the inks and generate various planar geometries such as parallel, interdigitated, or ring structures. Afterwards, laser micromachined can be used to maintain electronic isolation and sharp interface structures. In this manner, 1.5 V microbatteries with an energy density of more 0.6 mW h/cm^2 and specific energy of more than 160 mW h/g have been demonstrated [109].

Although planar structures are relatively easy to construct, stacking the electrodes can provide a greater interface area for the microbattery structures and reduced contact resistance. One approach taken is to LDW the electrodes on separate current collectors and then manually assemble the layers [110]. A better approach is to LDW a nanocomposite solid polymer ionic liquid between the electrodes to directly generate stacked structures that are rigid enough to support the upper layers without compromising their electrochemical performance. The nanocomposite polymer ionic system serves as the separator and solid electrolyte simultaneously, since this material has high ionic conductivity yet it is chemically and structurally stable [111, 112]. LDW has been used to deposit sequential layers of the cathode material ($LiCoO_2$ or $LiMnO_4$), nanocomposite polymer, and the anode (carbon) into a laser-micromachined pocket on a thin polyimide substrate for a Li-ion microbattery. This layered structure is significantly thicker (30–50 μm) than a typical thin-film microbattery structure (1–5 μm) yet thin enough to remain entirely embedded in the substrate. These batteries are shown to be rechargeable for more than 100 cycles with an energy density of more than 1.3 mW h/cm^2 (or 0.4 mW h/cm^3 based on volume) [113]. Figure 11.8a shows a photograph of two packaged Li-ion thick film microbatteries made by LDW designed to be embedded inside the laser

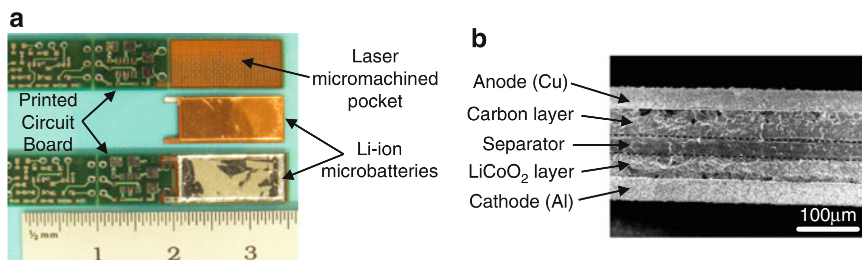

Fig. 11.8 (**a**) Optical micrograph showing two sealed Li-ion microbatteries made by LDW, with the bottom microbattery shown embedded inside the printed circuit board. (**b**) Cross-section SEM image clearly showing each layer from one such microbattery

machined pockets on the printed circuit boards shown above and below them. The microbattery on the top shows the copper current collector corresponding to the anode side (–), while the bottom microbattery is shown embedded with the aluminum current collector, i.e., cathode (+) side, facing up. An SEM cross section from one of these microbatteries, showing each of the above described layers, can be seen in Fig. 11.8b.

Li-ion microbatteries made by LDW with thicker cathodes and anodes (each over 100 μm thick) have been demonstrated at NRL [114]. The high porosity of the laser transferred active electrode layers allowed their thickness to be increased without sacrificing their performance. State-of-the-art sputter-deposited thin-film Li-ion microbatteries cannot be made thicker than a few microns before losses due to their very high internal resistance compromise their performance. $LiCoO_2$ cathodes up to 115 μm and carbon anodes up to 130 μm in thickness were laser transferred to demonstrate Li-ion microbatteries with maximum power densities of near 40 mW/cm^2 at current densities of 10 mA/cm^2 [114]. For lower current densities (100 $\mu A/cm^2$), discharge capacities in excess of 2,500 $\mu Ah/cm^2$ have also been demonstrated with these thick-film microbatteries [114]. These discharge capacities are over an order of magnitude higher than what has been achieved with sputter-deposited Li-ion microbatteries ($\approx$160 $\mu Ah/cm^2$) [115].

The final components required for the development of a fully integrated micropower system are devices capable of harvesting energy from the environment to replenish the limited power stored in the microbatteries and ultracapacitors. Combining a micropower generator capable of harvesting solar energy with the various microbatteries and ultracapacitors previously described would allow the development of truly autonomous microsystems which could operate without interruption and the need of service or maintenance schedules. Toward this end, LDW has been used at NRL to digitally microfabricate prototype nanoparticle TiO_2-based die sensitized solar cells with greater than 4% conversion efficiencies [106]. The use of local laser sintering for the TiO_2 nanoparticles has also been investigated to develop the ability to process the entire die sensitized solar cell at low-substrate temperatures to enable a large carrier lifetime without destroying the high-surface-area mesoporous structure [116].

11.5.3 Biomaterials

The successful transfer of very small volume droplets (as low as 10 fL) from liquid solutions has led to the use of LDW with water-based solutions of protein and single cell suspensions for the patterning of biological materials. Round shaped and uniform micron sized droplets of controlled diameters can be obtained through the appropriate choice of both laser pulse energy and beam focusing conditions. The high degree of spatial and volumetric resolution achievable with biomaterials makes LDW highly competitive against other direct-write techniques such as inkjet printing. Furthermore, the fact that the amount of transferred material per laser pulse can

be controlled through the characteristics of the laser beam (energy and spot dimensions) renders the use of nozzles unnecessary, thus avoiding potential clogging and contamination problems.

An important issue specific to LDW of biological solutions is their absorption properties with respect to the laser wavelength. Most biomaterials are dissolved in water based solvents, making these solutions transparent to a wide range of common laser wavelengths, for instance, the second and third harmonics of a Nd:YAG laser, preventing laser transfer. If shorter wavelengths are used, then the risk of damaging the functionality of the biomaterial through photochemical reactions becomes an issue. It is also important to minimize thermal effects that can result in denaturing of the biomolecules. One way to achieve this is by using femtosecond laser pulses as described previously. This approach has been demonstrated for the laser transfer of lambda bacteriophage DNA, bovine serum albumin, and glutathione *S-Transferase* using 500 fs pulses from an excimer laser at 248 nm [58]. The functionality of the transferred biomolecules was demonstrated by hybridization reactions for the DNA and binding of the proteins with their specific fluorescent-labeled antibodies.

A different approach utilizes a culture media with the biomaterial of interest, which is highly absorbent to the laser radiation to mediate the laser transfer. This matrix assisted LDW has been used with pulses from an ArF (193 nm, 10 ns) excimer laser to transfer active proteins [117], viable *Escherichia coli (E. coli)* bacteria [118], and mammalian Chinese hamster ovarian cells [68], with a high fraction of the bacteria and cells remaining viable after the transfer as determined by live/dead assays.

A better approach to reduce or eliminate the risk of damage to the biomaterial during the laser transfer is to use a biocompatible dynamic release layer or DRL. The application of DRL-mediated laser transfers for biomaterials has received a variety of names in the literature, such as biological laser printing (BioLP^{TM}) [119] or absorbing-film-assisted LIFT (AFA-LIFT) [120]. Fundamentally, all these approaches work on the same DRL principle previously described in Sect. 11.4.2. The work performed by Serra et al. at the University of Barcelona has demonstrated the versatility of using a donor substrate with DRL's made of 50–60 nm thick titanium films for the laser transfer of biomolecule bioarrays. Since titanium is biocompatible, any titanium transferred alongside the biomolecules does not present a serious issue. Thus, using a Nd:YAG laser (355 nm, 10 ns pulse), the University of Barcelona group has shown the deposition of functional *Treponema pallidum* protein antigen [32], and undamaged double stranded DNA from salmon sperm on poly-*L-lysine*-treated glass [31]. More recent results by other groups have employed polymer-based absorbing DRL's that decompose upon laser irradiation, thereby preventing contamination of the transferred solution [37].

The ability to accurately place undamaged biomaterials onto solid substrates through LDW transfers makes this technique an exciting tool for cutting-edge applications such as manufacturing of miniaturized biosensors for parallel multi-analyte detection in vivo, implantable drug delivery systems, tissue engineering studies and

other applications where a controlled amount of solution and placement of cells with high spatial resolution is required. For instance, the University of Barcelona group has tested the applicability of laser printing for biosensor preparation through the fabrication of a simple biosensor consisting of a DNA microarray capable of discriminating between two different DNA strands [34]. The microarray is prepared by depositing onto poly-*L-lysine*-treated glass droplets of three different solutions, two of them containing single DNA strands of a different human gene each and the other containing the control solvent. Fluorescence analyses after hybridization with the complementary base sequences, each tagged with a different fluorochrome, reveal that the microarray is fully functional and selective for biomolecule detection [35]. The same group has also shown the ability to laser transfer microarrays of other proteins such as bovine serum albumin [75] and rabbit antibody immunoglobulin G (IgG) [121].

11.5.4 Embedded Electronic Circuits

The development of embedded SMDs, semiconductor bare die ICs, interconnects, and power source elements offers the ability to achieve levels of miniaturization beyond the capabilities of current manufacturing techniques. Given an arbitrary circuit design, significant reductions in volume and overall weight can be achieved by using embedded components. Furthermore, embedded circuits exhibit higher device density and improved electrical performance, resulting in enhanced functionality within a given form factor.

The use of LDW techniques for the fabrication of embedded microbatteries and electronic circuits has been demonstrated at NRL [91, 107, 122]. For example, a simple blinker circuit comprised of six passive SMD components (4 resistors and 2 capacitors), two SMD LEDs, and one unpackaged IC (LM555 chipset in bare die form) was embedded in a thermoplastic polyetherimide substrate using LDW. Laser micromachining was used to generate the pockets in the substrate wherein each component was buried. Once in place, the components were planarized with a layer of polyimide. The interconnects required by the circuit were made by laser micromachining blind vias to expose the contact pads on each device. The metal interconnects were then generated by laser printing a conductive silver ink. The resulting embedded circuit occupied a footprint smaller than a single packaged LM555 chip as shown in Fig. 11.9a. Figure 11.9b shows a close up of the LM555 chip with its laser printed silver interconnects. It is estimated that these LDW embedded circuits can occupy footprints of about 1/4 or less and require less than 1/10 of the thickness of a printed circuit board design, resulting in an overall circuit volume reduction of near two orders of magnitude. This shows that by using LDW processes it is possible to fabricate functional electronic circuits buried under the surface, with the surface or substrate serving both as circuit board and enclosure.

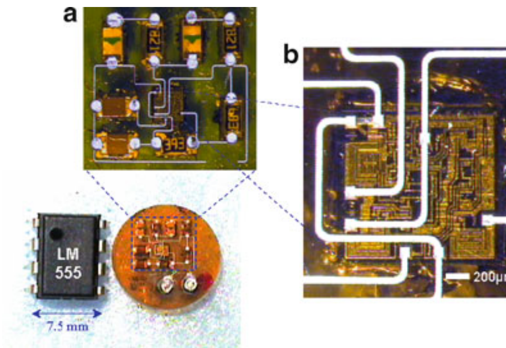

Fig. 11.9 Embedded circuit made by LDW. (**a**) Optical micrograph of the embedded circuit with a LM555 timing bare-die semiconductor chip at the center and shown to scale next to a packaged LM555 chip for size comparison. (**b**) Higher magnification micrograph showing the laser printed interconnects over the LM555 chip

11.6 The Future of Laser-Based Digital Microfabrication

For commercial, aerospace, and military applications, miniaturization and functionality are key aspects where the driving force is the need to achieve enhanced capabilities within any given form factor. Many times, traditional lithographic fabrication techniques cannot deliver the required solution due to cost, time constraints, or process limitations. Digital microfabrication techniques such as laser direct-write can offer a viable alternative in such situations.

The benefits of laser direct-write are numerous, particularly in cost reduction for prototyping, customization and production, reduction in processing steps, and greater design freedom due to its geometrical and material versatility. As the previous sections have shown, laser-based transfer techniques offer a wide range of applications with the potential to expand into large volume production. Clearly, LDW is still an emerging technology with developmental challenges remaining to be solved. However, the opportunities for LDW and other digital microfabrication processes are real, and how the technique evolves and where it is applied might determine its future success. Given that LDW is a laser-based materials processing technique which takes advantage of the unique properties offered by the laser radiation that serves as its source of energy, its applications in the field of digital microfabrication should grow and evolve with time. Some of these properties, such as wavelength, intensity, and spatial profile of the laser beam combined with control of the time length and temporal profile of the laser pulse give LDW a clear advantage over other more popular digital microfabrication techniques such as ink-jet.

11.6.1 Laser Forward Transfer vs. Other Digital Microfabrication Processes

The application of digital microfabrication technologies and processes span a wide range of industries including microelectronics, opto-electronics, aerospace, military, pharmaceutical, biomedical, and medical. This is in part due to the ability of digital microfabrication techniques to process virtually any type of material over a wide range of dimensions ranging from the mm to the submicron scale. One of the best established direct-write process which offers a great potential for digital microfabrication is ink-jet. However, despite the great progress achieved with ink-jet and the substantial R&D investment made by commercial and academic entities to develop the technology, ink-jet is limited to only additive processes. Furthermore, with ink-jet, the constraints imposed by the narrow nozzles required to achieve finer features limit its applicability to very low viscosity inks. Such inks might not be available for many types of materials, such as those required for the microfabrication of batteries and solar cells; while for other applications, such as electrical interconnects and electrodes, thicker patterns generated from inks or pastes with a heavy solids content might be more effective. For example, high quality gate and source/drain electrodes for organic thin film transistors (OTFTs) made from laser printed silver nano-inks have been demonstrated [123]. When the source and drain electrodes were laser printed on top of the pentacene organic semiconductive layer, the resulting top-contact OTFTs exhibited reduced contact resistance and improved device performance when compared with similar bottom-contact devices. Top-contact OTFTs are very difficult to fabricate by ink-jet because the organic solvents present in the low viscosity metallic inks tend to dissolve or etch the organic layer as soon as they come in contact with it.

These are some examples of applications where laser direct-write offers the most opportunities given its capability to remove material, by ablative processes, and through laser forward transfer, to deposit complex solutions or suspensions of a wide range of viscosities, particle size, and solids loading. In fact, laser forward transfer remains a leader in the field of digital microfabrication given its great versatility with materials and surfaces. An example of the novel types of structures that can only be fabricated by LDW is the ability to deposit free standing MEMS-like structures by laser decal transfer (not possible with other digital microfabrication techniques without using additional steps requiring sacrificial layers and their removal). Figure 11.10 provides an example of a 8 μm long microbridge made of silver nanoparticles over a trench on a silicon substrate at NRL fabricated after one single laser pulse resulted in the decal transfer of the structure shown.

The benefits of LDW are plentiful, particularly in cost reduction for prototyping and production, manufacture simplification (through the reduction of production steps), and greater design freedom due to its geometrical versatility. As the material is only deposited on-demand, little material is wasted and greater efficiencies and lower environmental impact can be achieved. LDW offers a very wide window

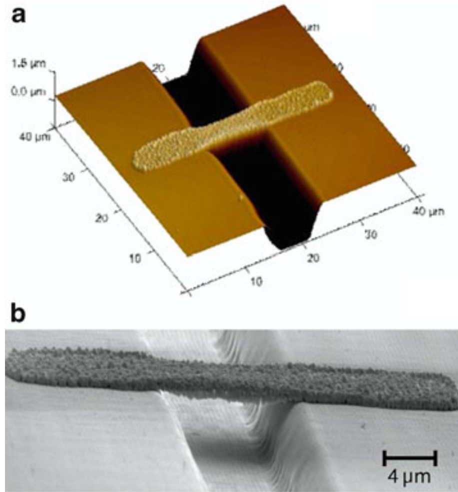

Fig. 11.10 (**a**) AFM and (**b**) SEM images from a silver microbridge made by laser decal transfer across a 8 µm wide gap on a silicon substrate. No other direct-write technique is capable of printing free standing structures without using sacrificial layers and etching steps

of applications ranging from R&D and prototyping to high-throughput production. Many applications have already been identified with many more awaiting development.

Key challenges for LDW are the establishment of design rules, process modeling and optimization, integration of the devices and systems fabricated, metrology and evaluation of the performance of the patterns and devices generated, and long term reliability of the LDW-made parts. Solving these challenges will require a considerable investment in funds, effort and time, but as commercial applications begin to grow, industry should embrace laser-based digital microfabrication process and these issues will be addressed. With increasing development and opportunities in micro- and nano-systems combining electronics, optical, fluidics, and bioactivity, LDW will play a significant role in the new paradigm offered by digital microfabrication.

11.7 Summary

This chapter has described how the original laser-induced forward transfer or LIFT concept has evolved into different LDW techniques and found use in many applications in the past 20 years. The ability to laser direct-write many types of materials over virtually any surface at room temperature and without the need of a special environment or vacuum conditions represents a paradigm shift in microfabrication processes. These LDW techniques are ideally suited for digital microfabrication

applications and offer opportunities for the generation of patterns, structures, and devices not possible with traditional photolithographic tools. Because they are non-lithographic digital microfabrication processes, laser transfer techniques can be used for rapid prototyping applications, allowing the design, fabrication, and testing of a given structure to be completed quickly. As this chapter has shown, LDW techniques can be used for many different types of applications. Some examples of the applications described include metal patterns for interconnects, antennae, and circuits, as well as various types of chemical and biological sensors. LDW processes have been used with great success for the fabrication of micropower devices such as microbatteries for energy storage, as well as prototype electrochemical solar cells for power generation. Examples of applications of LDW for organic and other biomaterials were also presented. In each case, the ability to transfer complex inks or pastes from a ribbon to an acceptor substrate at room temperature without changing their physical, chemical, or biological properties is one of several unique attributes of the LDW process.

The recent application of LDW techniques for the transfer of preformed devices such as semiconductor bare dies, and for embedding microbatteries and simple electronic circuits, opens the door for the development of a unique laser-based microelectronics fabrication tool. Such a tool would be capable of fabricating and embedding electronic circuits with the required power storage and power harvesting components within the same substrate. The resulting fully integrated systems could easily be reconfigured to fit within a desired form factor, thus allowing the placement of electronic systems in places that seem inconceivable today. In fact, the functionality of these digitally microfabricated circuits can be customized for a particular application by choosing the appropriate electronic modules or building blocks from a circuit library available in the LDW tool. Such a laser-based digital microfabrication system does not yet exist, but it is just a matter of time before the various processes described in this chapter are combined into a single machine capable of making this vision a reality.

Acknowledgments The author would like to thank all the members of the laser direct-write group at NRL. Special thanks to Heungsoo Kim, Ray Auyeung, and Scott Mathews. This work was sponsored by the U.S. Office of Naval Research.

References

1. J. Bohandy, B. Kim, F.J. Adrian, J. Appl. Phys. **60**, 1538 (1986)
2. A. Piqué, D.B. Chrisey (eds.), *Direct-write Technologies for Rapid Prototyping Applications: Sensors, Electronics and Integrated Power Sources*. (Academic, San Diego, 2002)
3. C.B. Arnold, A. Piqué, MRS Bull. **32**, 9 (2007)
4. R.M. Osgood, T.F. Deutsch, Science **227**, 709 (1985)
5. I.P. Herman, Chem. Rev. **89**, 1323 (1989)
6. F. Gao, A.A. Sonin, Proc. R. Soc. Lond. A **444**, 533 (1994)
7. C.B. Arnold, P. Serra, A. Piqué, MRS Bull. **32**, 23 (2007)
8. M.L. Levene, R.D. Scott, B.W. Siryj, Appl. Opt. **9**, 2260 (1970)

9. F.J. Adrian, J. Bohandy, B.F. Kim, A.N. Jette, P. Thompson, J. Vac. Sci. Technol. B **5**, 1490 (1987)
10. J. Bohandy, B. Kim, F.J. Adrian, A.N. Jette, J. Appl. Phys. **63**, 1158 (1988)
11. P. Mogyorósi, T. Szörényi, K. Bali, Z. Tóth, I. Hevesi, Appl. Surf. Sci. **36**, 157 (1989)
12. R.J. Baseman, N.M. Froberg, J.C. Andreshak, Z. Schlesinger, Appl. Phys. Lett. **56**, 1412 (1990)
13. V. Schultze, M. Wagner, Appl. Surf. Sci. **52**, 303 (1991)
14. Z. Tóth, T. Szörényi, A.L. Tóth, Appl. Surf. Sci. **69**, 317 (1993)
15. Z. Kántor, Z. Tóth, T. Szörényi, A.L. Tóth, Appl. Phys. Lett. **64**, 3506 (1994)
16. I. Zergioti, S. Mailis, N.A. Vainos, P. Papakonstantinou, C. Kalpouzos, C.P. Grigoropoulos, C. Fotakis: Appl. Phys. A **66**, 579 (1998)
17. T. Sano, H. Yamada, T. Nakayama, I. Miyamoto, Appl. Surf. Sci. **186**, 221 (2002)
18. Z. Tóth, T. Szörényi, Appl. Phys. A Solids Surf. **52**, 273 (1991)
19. J.A. Greer, T.E. Parker, in *SPIE Proceedings*, vol. 998, 1988, pp. 113–125
20. S. Chakraborty, H. Sakata, E. Yokoyama, M. Wakaki, D. Chakravorty, Appl. Surf. Sci. **254**, 638 (2007)
21. E. Fogarassy, C. Fuchs, F. Kerherve, G. Hauchecorne, J. Perriere, J. Appl. Phys. **66**, 457 (1989)
22. D. Toet, M.O. Thompson, P.M. Smith, T.W. Sigmon, Appl. Phys. Lett. **74**, 2170 (1999)
23. H. Sakata, S. Chakraborty, E. Yokoyama, M. Wakaki, D. Chakravorty, Appl. Phys. Lett. **86**, 114104 (2005)
24. S.K. Chang-Jian, J.R. Ho, J.W.J. Cheng, C.K. Sung, Nanotechnology **17**, 1184 (2006)
25. C.W. Cheng, S.C. Liao, H.T. Chen, J.R. Ho, J.W.J. Cheng, H.Y. Liao, L.E. Chou, in *SPIE Proceedings*, vol. 6459, 2007, p. 645910
26. B. Thomas, A.P. Alloncle, P. Delaporte, M. Sentis, S. Sanaur, M. Barret, P. Collot, Appl. Surf. Sci. **254**, 1206 (2007)
27. A. Narazaki, T. sato, R. Kurosaki, Y. Kawaguchi, H. Niino: Appl. Phys. Express **1**, 057001 (2008)
28. H. Esrom, J.-Y. Zhang, U. Kogelschatz, A.J. Pedraza, Appl. Surf. Sci. **86**, 202 (1995)
29. W.A. Tolbert, I.Y.S. Lee, M.M. Doxtader, E.W. Ellis, D.D. Dlott, J. Imaging Sci. Technol. **37**, 411 (1993)
30. S. Lätsch, H. Hiraoka, W. Nieveen, J. Bargon, Appl. Surf. Sci. **81**, 183 (1994)
31. J.M. Fernández-Pradas, M. Colina, P. Serra, J. Domínguez, J.L. Morenza, Thin Solid Films **453–454**, 27 (2004)
32. P. Serra, J.M. Fernández-Pradas, F.X. Berthet, M. Colina, J. Elvira, J.L. Morenza, Appl. Phys. A Mater. Sci. Process. **79**, 949 (2004)
33. B. Hopp, T. Smausz, Z. Antal, N. Kresz, Z. Bor, D. Chrisey, J. Appl. Phy. **96**, 3478 (2004)
34. P. Serra, M. Colina, J.M. Fernández-Pradas, L. Sevilla, J.L. Morenza, Appl. Phys. Lett. **85**, 1639 (2004)
35. M. Colina, P. Serra, J.M. Fernández-Pradas, L. Sevilla, J.L. Morenza, Biosens. Bioelectron. **20**, 1638 (2005)
36. M. Colina, M. Duocastella, J.M. Fernández-Pradas, P. Serra, J.L. Morenza, J. Appl. Phys. **99**, 84909 (2006)
37. A. Doraiswamy, R.J. Narayan, T. Lippert, L. Urech, A. Wokaun, M. Nagel, B. Hopp, M. Dinescu, R. Modi, R.C.Y. Auyeung, D.B. Chrisey, Appl. Surf. Sci. **252**, 4743 (2006)
38. J. Xu, J. Liu, D. Cui, M. Gerhold, A.Y. Wang, M. Nagel, T.K. Lippert, Nanotechnology **18**, 25403 (2007)
39. R. Fardel, M. Nagel, F. Nüesch, T. Lippert, A. Wokaun, Appl. Phys. Lett. **91**, 61103 (2007)
40. R. Fardel, M. Nagel, F. Nüesch, T. Lippert, A. Wokaun, Appl. Surf. Sci. **254**, 1322 (2007)
41. R. Fardel, M. Nagel, T. Lippert, F. Nüesch, A. Wokaun, B.S. Luk'Yanchuk, Appl. Phys. A Mater. Sci. Process. **90**, 661 (2008)
42. D.P. Banks, K. Kaur, R. Gazia, R. Fardel, M. Nagel, T. Lippert, R.W. Eason, Europhys. Lett. **83**, 38003 (2008)

43. N.T. Kattamis, P.E. Purnick, R. Weiss, C.B. Arnold, Appl. Phys. Lett. **91**, 171120 (2007)
44. W.A. Tolbert, I.Y.S. Lee, X. Wen, D.D. Dlott, M.M. Doxtader, E.W. Ellis, J. Imaging Sci. Technol. **37**, 485 (1993)
45. I. Zergioti, S. Mailis, N.A. Vainos, C. Fotakis, S. Chen, C.P. Grigoropoulos, Appl. Surf. Sci. **127–129**, 601 (1998)
46. P. Papakonstantinou, N.A. Vainos, C. Fotakis, Appl. Surf. Sci. **151**, 159 (1999)
47. R. Bähnisch, W. Gros, A. Menschig, Microelectron. Eng. **50**, 541 (2000)
48. A.C. Tien, Z.S. Sacks, F.J. Mayer, Microelectron. Eng. **56**, 273 (2001)
49. B. Tan, K. Venkatakrishnan, K.G. Tok, Appl. Surf. Sci. **207**, 365 (2003)
50. L. Yang, C.Y. Wang, X.C. Ni, Z.J. Wang, W. Jia, L. Chai, Appl. Phys. Lett. **89**, 161110 (2006)
51. A.P. Alloncle, R. Bouffaron, J. Hermann, M. Sentis, in *SPIE Proceedings*, vol. 6263, 2006, p. 62630R
52. D.P. Banks, C. Grivas, J.D. Mills, R.W. Eason, I. Zergioti, Appl. Phys. Lett. **89**, 193107 (2006)
53. S. Bera, A.J. Sabbah, J.M. Yarbrough, C.G. Allen, B. Winters, C.G. Durfee, J.A. Squier, Appl. Opt. **46**, 4650 (2007)
54. A.B. Bullock, P.R. Bolton, J. Appl. Phys. **85**, 460 (1999)
55. D.G. Papazoglou, A. Karaiskou, I. Zergioti, C. Fotakis, Appl. Phys. Lett. **81**, 1594 (2002)
56. I. Zergioti, D.G. Papazoglou, A. Karaiskou, C. Fotakis, E. Gamaly, A. Rode, Appl. Surf. Sci. **208–209**, 177 (2003)
57. A. Karaiskou, I. Zergioti, C. Fotakis, M. Kapsetaki, D. Kafetzopoulos, Appl. Surf. Sci. **208–209**, 245 (2003)
58. I. Zergioti, A. Karaiskou, D.G. Papazoglou, C. Fotakis, M. Kapsetaki, D. Kafetzopoulos, Appl. Phys. Lett. **86**, 163902 (2005)
59. D.P. Banks, C. Grivas, I. Zergioti, R.W. Eason, Opt. Express **16**, 3249 (2008)
60. C.M. Othon, A. Laracuente, H.D. Ladouceur, B.R. Ringeisen, Appl. Surf. Sci. **255**, 3407 (2008)
61. S.M. Pimenov, G.A. Shafeev, A.A. Smolin, V.I. Konov, B.K. Vodolaga, Appl. Surf. Sci. **86**, 208 (1995)
62. A. Piqué, D.B. Chrisey, R.C.Y. Auyeung, S. Lakeou, R. Chung, R.A. McGill, P.K. Wu, M. Duignan, J. Fitz-Gerald, H.D. Wu, in *SPIE Proceedings*, vol. 3618, 1999, pp. 330–339
63. A. Piqué, D.B. Chrisey, R.C.Y. Auyeung, J. Fitz-Gerald, H.D. Wu, R.A. McGill, S. Lakeou, P.K. Wu, V. Nguyen, M. Duignan, Appl. Phys. A Mater. Sci. Process. **69**, S279 (1999)
64. J.M. Fitz-Gerald, A. Piqué, D.B. Chrisey, P.D. Rack, M. Zeleznik, R.C.Y. Auyeung, S. Lakeou, Appl. Phys. Lett. **76**, 1386 (2000)
65. A. Piqué, D.B. Chrisey, J.M. Fitz-Gerald, R.A. McGill, R.C.Y. Auyeung, H.D. Wu, S. Lakeou, V. Nguyen, R. Chung, M. Duignan, J. Mater. Res. **15**, 1872 (2000)
66. A. Piqué, J. Fitz-Gerald, D.B. Chrisey, R.C.Y. Auyeung, H.D. Wu, S. Lakeou, R.A. McGill, in *SPIE Proceedings*, vol. 3933, 2000, pp. 105–112
67. R.C.Y. Auyeung, H.D. Wu, R. Modi, A. Piqué, J.M. Fitz-gerald, H.D. Young, S. Lakeou, R. Chung, D.B. Chrisey, in *SPIE Proceedings*, vol. 4088, 2000, pp. 393–396
68. P.K. Wu, B.R. Ringeisen, J. Callahan, M. Brooks, D.M. Bubb, H.D. Wu, A. Piqué, B. Spargo, R.A. McGill, D.B. Chrisey, Thin Solid Films **398–399**, 607 (2001)
69. C.B. Arnold, T.E. Sutto, H. Kim, A. Piqué, Laser Focus World **40**, S9 (2004)
70. D. Young, R.C.Y. Auyeung, A. Piqué, D.B. Chrisey, D.D. Dlott, Appl. Phys. Lett. **78**, 3169 (2001)
71. D. Young, R.C.Y. Auyeung, A. Piqué, D.B. Chrisey, D.D. Dlott, Appl. Surf. Sci. **197–198**, 181 (2002)
72. M. Goto, L.V. Zhigilei, J. Hobley, M. Kishimoto, B.J. Garrison, H. Fukumura, J. Appl. Phys. **90**, 4755 (2001)
73. B.R. Lewis, E.C. Kinzel, N.M. Laurendeau, R.P. Lucht, X. Xu, J. Appl. Phys. **100**, 33107 (2006)
74. M. Duocastella, J.M. Fernández-Pradas, P. Serra, J.L. Morenza, Appl. Phys. A Mater. Sci. Process. **93**, 453 (2008)
75. M. Duocastella, M. Colina, J.M. Fernández-Pradas, P. Serra, J.L. Morenza, Appl. Surf. Sci. **253**, 7855 (2007)

76. A.S. Holmes, S.M. Saidam, J. Microelectromech. Syst. **7**, 416 (1989)
77. A.S. Holmes, in *SPIE Proceedings*, vol. 4426, 2002, pp. 203–209
78. N.S. Karlitskaya, D.F.D. Lange, R. Sanders, J. Meijer, in *SPIE Proceedings*, vol. 5448, 2004, pp. 935–943
79. N.S. Karlitskaya, J. Meijer, D.F.D. Lange, H. Kettelarij, in *SPIE Proceedings*, vol. 6261, 2006, p. 62612P
80. S.A. Mathews, R.C.Y. Auyeung, A. Piqué, J. Laser Micro/Nanoeng. **2**, 103 (2007)
81. A. Piqué, N.A. Charipar, H. Kim, R.C.Y. Auyeung, S.A. Mathews, in *SPIE Proceedings*, vol. 6606, 2007, p. 66060R
82. A. Piqué, N.A. Charipar, R.C.Y. Auyeung, H. Kim, S.A. Mathews, in *SPIE Proceedings*, vol. 6458, 2007, p. 645802
83. S.A. Mathews, N.A. Charipar, K. Metkus, A. Piqué, Photonics Spectra **41**, 70 (2007)
84. K. Piglmayer, R. Denk, D. Bäurle, Appl. Phys. Lett. **80**, 4693 (2002)
85. L. Landström, J. Klimstein, G. Schrems, K. Piglmayer, D. Bäurle, Appl. Phys. A Mater. Sci. Process. **78**, 537 (2004)
86. E. McLeod, C.B. Arnold, Nat. Nanotechnol. **3**, 413 (2008)
87. R.C.Y. Auyeung, H. Kim, S.A. Mathews, A. Piqué, J. Laser Micro/Nanoeng. **2**, 21 (2007)
88. A. Piqué, R.C.Y. Auyeung, K.M. Metkus, H. Kim, S. Mathews, T. Bailey, X. Chen, L.J. Young, in *SPIE Proceedings*, vol. 6879, 2008, p. 687911
89. A. Piqué, R.C.Y. Auyeung, H. Kim, K.M. Metkus, S.A. Mathews, J. Laser Micro/Nanoeng. **3**, 163 (2008)
90. A. Piqué, C.B. Arnold, B. Pratap, R.C.Y. Auyeung, H.S. Kim, D.W. Weir, in *SPIE Proceedings*, vol. 4977, 2003, pp. 602–608
91. A. Piqué, B. Pratap, S.A. Mathews, B.J. Karns, R.C. Auyeung, M. Kasser, M. Ollinger, H. Kim, S. Lakeou, C.B. Arnold, in *SPIE Proceedings*, vol. 5713, 2005, pp. 223–230
92. R.C.Y. Auyeung, M.W. Nurnberger, D.J. Wendland, A. Piqué, C.B. Arnold, A.R. Abbott, L.C. Schuette, in *SPIE Proceedings*, vol. 5339, 2004, pp. 292–297
93. R. Modi, H.D. Wu, R.C.Y. Auyeung, C.M. Gilmore, D.B. Chrisey, J. Mater. Res. **16**, 3214 (2001)
94. D. Young, H.D. Wu, R.C.Y. Auyeung, R. Modi, J. Fitz-Gerald, A. Piqué, D.B. Chrisey, P. Atanassova, T. Kodas, J. Mater. Res. **16**, 1720 (2001)
95. A. Piqué, D.W. Weir, P.K. Wu, B. Pratap, C.B. Arnold, B.R. Ringeisen, R.A. McGill, R.C.Y. Auyeung, R.A. Kant, D.B. Chrisey, in *SPIE Proceedings*, vol. 4637, 2002, pp. 361–368
96. A. Piqué, C.B. Arnold, R.C. Wartena, D.W. Weir, B. Pratap, K.E. Swider-Lyons, R.A. Kant, D.B. Chrisey, in *SPIE Proceedings*, vol. 4830, 2002, pp. 182–188
97. A. Piqué, R.C.Y. Auyeung, J.L. Stepnowski, D.W. Weir, C.B. Arnold, R.A. McGill, D.B. Chrisey, Surf. Coatings Technol. **163–164**, 293 (2003)
98. A. Piqué, C.B. Arnold, R.C. Wartena, B. Pratap, B. Shashishekar, K.E. Swider-Lyons, D.W. Weir, R.A. Kant, in *RIKEN Reviews* vol. 50 (2002), pp. 57–62
99. I. Zhang, D. Liu, S.A. Mathews, J. Graves, T.M. Schaefer, B.K. Gilbert, R. Modi, H.D. Wu, D.B. Chrisey, Microelectron. Eng. **70**, 41 (2003)
100. P.K. Wu, B.R. Ringeisen, D.B. Krizman, C.G. Frondoza, M. Brooks, D.M. Bubb, R.C.Y. Auyeung, A. Piqué, B. Spargo, R.A. McGill, D.B. Chrisey, Rev. Sci. Instrum. **74**, 2546 (2003)
101. K. Komorita, T. Sano, H. Yamada, I. Miyamoto, in *SPIE Proceedings*, vol. 4830, 2003, pp. 20–24
102. C. Boutopoulos, V. Tsouti, D. Goustouridis, S. Chatzandroulis, I. Zergioti, Appl. Phys. Lett. **93**, 191109 (2008)
103. C.B. Arnold, R.C. Wartena, B. Pratap, K.E. Swider-Lyons, A. Piqué, in *MRS Proceedings*, vol. 689, 2002, pp. 275–280
104. C.B. Arnold, R.C. Wartena, K.E. Swider-Lyons, A. Piqué, J. Electrochem. Soc. **150**, (2003) A571
105. C.B. Arnold, R.C. Wartena, B. Pratap, K.E. Swider-Lyons, A. Piqué, in *SPIE Proceedings*, vol. 4637, 2002, pp. 353–360

106. H. Kim, G.P. Kushto, C.B. Arnold, Z.H. Kafafi, A. Piqué, Appl. Phys. Lett. **85**, 464 (2004)
107. A. Piqué, S.A. Mathews, R.C. Auyeung, M. Ollinger, H. Kim, B. Pratap, C.B. Arnold, T.E. Sutto, in *SPIE Proceedings*, vol. 5662, 2004, pp. 564–569
108. A. Piqué, C.B. Arnold, H. Kim, M. Ollinger, T.E. Sutto, Appl. Phys. A Mater. Sci. Process. **79**, 783 (2004)
109. C.B. Arnold, H. Kim, A. Piqué, Appl. Phys. A Mater. Sci. Process. **79**, 417 (2004)
110. R. Wartena, A.E. Curtright, C.B. Arnold, A. Piqué, K.E. Swider-Lyons, J. Power Sources **126**, 193 (2004)
111. M. Ollinger, H. Kim, T.E. Sutto, T.E. Martin, A. Piqué, J. Laser Micro/Nanoeng. **1**, 102 (2006)
112. M. Ollinger, H. Kim, T. Sutto, A. Piqué, Appl. Surf. Sci. **252**, 8212 (2006)
113. T.E. Sutto, M. Ollinger, H. Kim, C.B. Arnold, A. Piqué, Electrochem. Solid State Lett. **9**, A69 (2006)
114. H. Kim, R.C.Y. Auyeung, A. Piqué: J. Power Sources **165**, 413 (2007)
115. J.B. Bates, N.J. Dudney, B. Neudecker, A. Ueda, C.D. Evans, Solid State Ionics **135**, 33 (2000)
116. H. Kim, R.C.Y. Auyeung, M. Ollinger, G.P. Kushto, Z.H. Kafafi, A. Piqué, Appl. Phys. A Mater. Sci. Process. **83**, 73 (2006)
117. B.R. Ringeisen, D.B. Chrisey, A. Piqué, D. Krizman, M. Brooks, B. Spargo, R. Auyeng, P. Wu, Am. Biotechnol. Lab. **19**, 42 (2001)
118. B.R. Ringeisen, D.B. Chrisey, A. Piqué, H.D. Young, R. Modi, M. Bucaro, J. Jones-Meehan, B.J. Spargo, Biomaterials **23**, 161 (2002)
119. J.A. Barron, B.R. Ringeisen, H. Kim, B.J. Spargo, D.B. Chrisey, Thin Solid Films **453–454**, 383 (2004)
120. B. Hopp, T. Smausz, N. Kresz, N. Barna, Z. Bor, L. Kolozsvári, D.B. Chrisey, A. Szabó, A. Nógrádi, Tissue Eng. **11**, 1817 (2005)
121. M. Duocastella, J.M. Fernández-Pradas, J. Domínguez, P. Serra, J.L. Morenza, Appl. Phys. A Mater. Sci. Process. **93**, 941 (2008)
122. A. Piqué, S.A. Mathews, B. Pratap, R.C.Y. Auyeung, B.J. Karns, S. Lakeou, Microelectron. Eng. **83**, 2527 (2006)
123. H. Kim, R.C.Y. Auyeung, S.H. Lee, A.L. Huston, A. Piqué, Appl. Phys. A Mater. Sci. Process. **96**, 441 (2009)

Chapter 12
Hybrid Laser Processing of Transparent Materials

Hiroyuki Niino

Abstract The following chapter is an overview of processing fused silica and other transparent materials by pulsed-laser irradiation: (1) Direct excitation of materials with multi-wavelength excitation processes, and (2) Media-assisted process with a conventional pulsed laser. A method to etch transparent materials by using laser-induced plasma-assisted ablation (LIPAA), or laser-induced backside wet etching (LIBWE), has been described in detail.

12.1 Introduction

The high precision surface micro-structuring of the optical transparent materials such as a silica glass, silicate glass, and sapphire is one of the key technologies of optics and optical devises. However, these materials are hard and brittle, and precision surface microfabrication is very difficult. Laser-induced micro-fabrication of various materials has served as an important technique in surface structuring for optics and optoelectronic devices [1]. In particular, significant attention has been given toward the micro-fabrication of silica glass, since, in spite of the difficulty involved, silica is a commonly used material. The use of pulsed lasers can involve several approaches, such as conventional UV laser ablation [2], vacuum UV (VUV) laser processing [3], femtosecond (fs)-pulsed laser micromachining [2, 4]. Figure 12.1 shows the absorption spectrum of synthetic silica glass in UV and VUV region. As the linear absorption of the glass is negligible in UV region, it is characterized by high transmission from the UV to the visible region. Therefore, the laser ablation of the glass by nanosecond (ns)-pulsed UV laser irradiation requires a high intensity of laser beam onto the target. The threshold fluence of silica glass ablation with a ns-pulsed KrF excimer laser ($\lambda = 248$ nm, pulse duration = 28 ns (FWHM)) was

H. Niino (✉)
National Institute of Advanced Industrial Science and Technology (AIST),
Tsukuba, Ibaraki 305-8565 Japan
e-mail: niino.hiro@aist.go.jp

K. Sugioka et al. (eds.), *Laser Precision Microfabrication*,
Springer Series in Materials Science 135, DOI 10.1007/978-3-642-10523-4_12,
© Springer-Verlag Berlin Heidelberg 2010

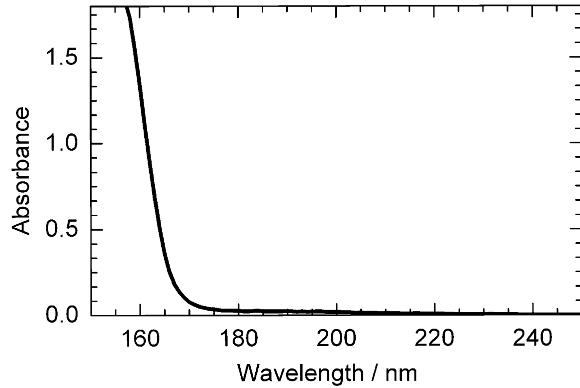

Fig. 12.1 UV and vacuum UV absorption spectrum of a synthetic silica glass plate (thickness: 0.57 mm)

estimated to be ca. 10 J cm^{-2} pulse^{-1} [2], thus the ablation needed the laser beam to be tightly focused. Hybrid laser processes by simultaneous laser irradiation with multi-wavelength beams are effective to improve the ablation quality and modification efficiency for the materials. Hybrid laser processes also embrace a plasma-assisted laser process, ion-beam-assisted laser process, e-beam assisted laser process, and media-assisted process. Media-assisted processes by using external photo-absorbers on laser irradiation especially lead to effective etching for the reduction of laser fluence on precise patterning processes.

In this chapter, high-quality and high-efficiency microfabrication of the optical transparent materials has been reviewed by laser hybrid and media-assisted processes. The laser-induced fabrication techniques by these processes have great potential for precision micromachining of the materials for practical applications.

12.2 Multiwavelength Excitation Process

12.2.1 Principle of Multiwavelength Excitation Process

When the substrate has a sufficient absorption at the wavelength of incident laser, conventional ablation takes place on the front surface of the substrate, as shown in Fig. 12.2a. F_2 laser at the wavelength of 157 nm is a useful tool for the ablation of silica glass because direct excitation process of the glass with a high efficiency is induced by the laser irradiation. Femtosecond laser is also an attractive instrument. Multiphoton process of the glass is readily achieved by focusing the femtosecond laser beam. While the unfocused laser beam is not absorbed by transparent materials and only a limited region with focused laser irradiation is selectively processed with femtosecond laser (see e.g., Chap. 9), VUV–UV multiwavelength excitation process as a laser hybrid process is a unique approach to the precision microfabrication of

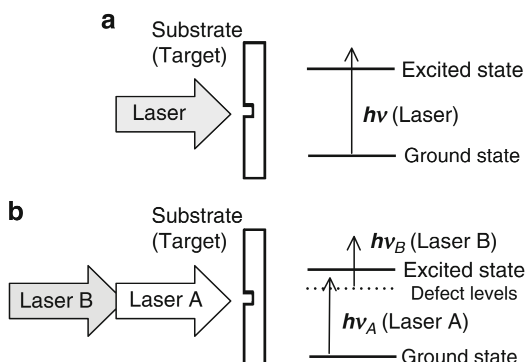

Fig. 12.2 Scheme of the hybrid laser process, (**a**) conventional laser process with a single laser, (**b**) hybrid laser processes by simultaneous laser irradiation with multi-wavelength beams. The front surface of the substrate was ablated by the process

hard materials (Fig. 12.2b). The energy density of the VUV laser is as small as a few hundred mJ cm^{-2} $pulse^{-1}$, which is one orders of magnitude lower than that of single F_2 laser ablation. The energy density of the simultaneously irradiated UV laser beam is of the order of J cm^{-2} $pulse^{-1}$. For micropatterning of solid surfaces by this method, the unpatterned VUV beams were irradiated on the substrate, and only the UV laser irradiation area would be etched on the surface.

12.2.2 Microfabrication of Transparent Materials by Multiwavelength Excitation Process

Simultaneous irradiation with a ns-pulsed UV laser and VUV laser was achieved to fabricate a micropattern on optical transparent materials [5–18] (also see Chap. 1). The VUV laser beam (Laser A in Fig. 12.3) trapped electrons at the defect levels thus promoting etching by the intense absorption of the UV laser beam (Laser B). A KrF laser ($\lambda_B = 248$ nm) or a fourth harmonic generation (FHG) of a Q-switched Nd:YAG laser ($\lambda_B = 266$ nm) was used as the UV laser, and an F_2 laser ($\lambda_A = 157$ nm) or a VUV Raman laser ($\lambda_A = 133$, 141, 150, 160, 171, or 184 nm (multi-lines)) as the VUV laser. The throughput and etching quality were much improved compared to etching with only the UV laser alone. Micropatterning was also possible by using a photomask for the UV laser beam. By adjusting the laser fluences, refractive index modification and synthesis of a waveguide were also achieved on the fused silica plate with the simultaneous double sources irradiation technique [17].

Figure 12.4 shows AFM images of fused silica ablated by (a) the multiwavelength excitation process and (b) only the KrF excimer laser. The AFM image in Fig. 12.4a shows a well-defined pattern with a sharp edge and flat sidewall. A periodic ripple structure is formed on the bottom of the ablated area due to the diffraction of the KrF excimer laser through the contact mask, indicating little thermal influence. The AFM image in Fig. 12.4b shows irregular roughness at the bottom and

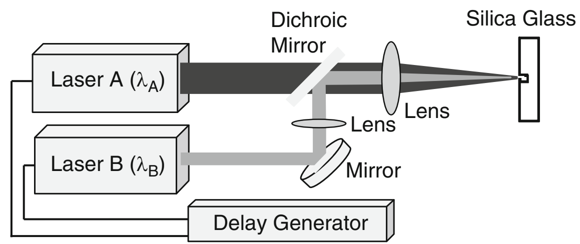

Fig. 12.3 Experimental setup for etching silica glass by collinear irradiation system with two laser beams at the different wavelength of VUV laser (λ_A) and UV laser (λ_B)

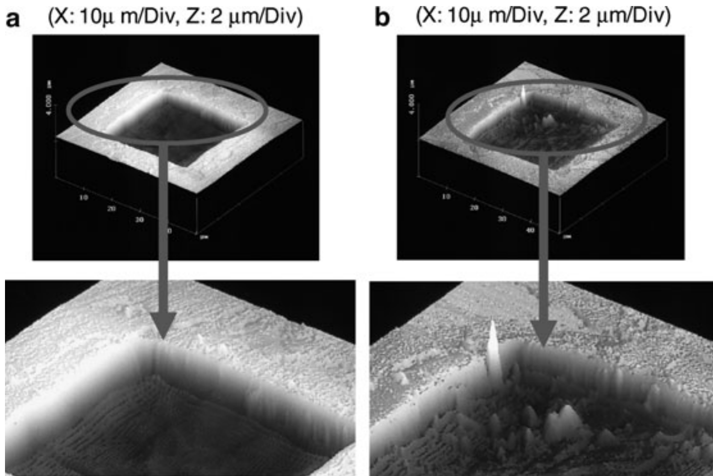

Fig. 12.4 AFM images of ablated fused silica, (**a**) multiwavelength excitation process by F_2–KrF excimer lasers (KrF: 4.0 J cm^{-2} pulse^{-1}, F_2: 0.23 J cm^{-2} pulse^{-1}), (**b**) KrF excimer laser ablation (KrF: 4.0 J cm^{-2} pulse^{-1}). (courtesy of K. Sugioka)

swelling at the edges. It is clear that the multiwavelength excitation process significantly improved the ablation quality of fused silica. The VUV irradiation excited electrons to the defect levels, allowing strong absorption of UV photon. Hybrid laser processing of fused silica, crystal quartz, sapphire, GaN, Lithium niobate, Si, SiC, polyethylene, and polymethyl-methacrylate (PMMA) was achieved with high efficiency (Table 12.1.).

The ablation rate strongly depended on the irradiation timing of each laser beam [12, 19–21]. In the case of nanosecond lasers, an extremely high ablation rate of over 30 nm pulse^{-1} in fused quartz was obtained within the delay time of $\pm$10 ns [14]. The ablation rate of the simultaneously irradiated sample showed a linear increase with the logarithm of the UV excimer laser fluence, which suggested single-photon absorption of the UV excimer laser beam by electrons excited by VUV laser irradiation.

Table 12.1 Microfabrication of transparent materials by laser hybrid processes

Materials	Laser A	Laser B	Reference
Synthetic fused quartz	VUV Raman laser[1]	4th YAG laser[2] ($\tau = 8$ ns)	[5]
	VUV Raman laser[3]	4th YAG laser[2]	[6–8]
	VUV Raman laser[4]	YAG lasers[5]	[9, 12]
	F_2 laser[6]	KrF excimer laser[7]	[13–18]
	Laser plasma soft x rays	4th YAG laser[2]	[19]
SiC	VUV Raman laser[4]	4th YAG laser[2]	[10]
Crystal quartz	VUV Raman laser[1]	4th YAG laser[2]	[11]
Sapphire	VUV Raman laser[1]	4th YAG laser[2]	[11]
	F_2 laser[6]	KrF excimer laser[7]	[15]
Lithium niobate	VUV Raman laser[1]	4th YAG laser[2]	[11]
GaN	F_2 laser[6]	KrF excimer laser[7]	[15]
Si	ps laser[8]	ps laser[9] ($\tau = 10$ ps)	[20, 21]
Polyethylene	ArF excimer laser[10] (23 ns)	fs laser[11] ($\tau = 130$ fs)	[22]
	Fs laser[12] ($\tau = 130$ fs)	fs laser[11] ($\tau = 130$ fs)	[23]
PMMA[15]	KrF excimer laser[7]	XeCl excimer laser[13]	[24]
	ArF excimer laser[10]	XeCl excimer laser[13]	[25]
PMMA with dopant[16]	XeCl excimer laser[13]	Dye laser[14]	[26, 27]

Laser wavelength: [1]133–594 nm (multi-lines), [2]266 nm, [3]171 nm or 160 nm, [4]133, 141, 150, 160, 171, and 184 nm (multi-lines), [5]1,064,532 or 266 nm, [6]157 nm, [7]248 nm, [8]532 nm, [9]1,064 nm, [10]193 nm, [11]790 nm, [12]390 nm, [13]308 nm, [14]580 nm, Materials: [15]Polymethylmethacrylate, [16]Spyropyran (Photo-chromic dopant)

12.3 Media Assisted Process

12.3.1 Classification of Media Assisted Processes

The surface fabrication by indirect excitation process that is based on the deposition of laser energy onto a thin photo-absorber placed on the "rear" surface of the substrate is a unique method where laser ablation of another material is used to excite a transparent substrate (Fig. 12.5). Assuming negligible absorption by the substrate, the incident laser beam passes through the substrate plate resulting in the excitation of the thin layer as an external photon absorber. When the external photon absorber close to the rear surface becomes ablated using laser irradiation with sufficient fluence, etching on the rear surface of the substrate is achieved. Metal plates and dye solutions are suitable for the external photon absorber by UV and visible laser irradiation. These media were activated to produce high reactive species such as plasma and radicals with high temperature and high pressure in the ablation. One is by laser ablation of a metal target in laser-induced plasma-assisted ablation (LIPAA) [17, 18, 28–39], or by laser ablation of an organic dye solution in laser-induced backside wet etching (LIBWE) [40–109]. LIPAA and LIBWE of transparent substrates are detailed in the section of 12.3.2. and 12.3.3., respectively.

In addition, the surface fabrication under liquid such as solution and water provides better tolerances and smaller heat affected zone widths and avoid the

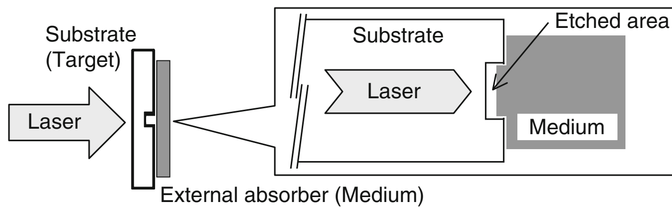

Fig. 12.5 Scheme of the media-assisted processes. External medium as a photon absorber of incident laser is activated by "Laser" irradiation. The rear surface of the substrate was etched by the laser irradiation through indirect excitation process

re-deposition of debris [110–112]. In the case of femtosecond laser pulses, high-aspect-ratio microchannels are fabricated on the rear surface of silica glass that is in contact with water [113–117] (also see Chap. 9). When distilled water was introduced into a hole drilled from the rear surface of the glass, the effects of blocking and redeposition of ablated material were greatly reduced, and the aspect ratio of the depth of the hole was increased. Straight holes of 4-μm diameter were more than 200 μm deep. Three-dimensional channels such as a square-wave-shaped hole inside silica glass can be micromachined inside transparent materials by use of this method [111]. The morphology of the debris ejected from the amorphous synthesized silica was analyzed by scanning electron microscopy, and the chemical structures are investigated by X-ray diffraction analysis and Fourier transform infrared spectroscopy [115]. Rapid fabrication of submicrometer-diameter pores was performed with femtosecond laser in borosilicate glass [116]. Synova S.A. has developed the water-jet-guided laser (Laser Microjet®) by use of water to cool the material and remove molten material [117–119]. The basic principle of the water-jet-guided laser implies that a laser beam is focused into a nozzle while passing through a pressurized water chamber [117]. The water jet emitted from the nozzle guides the laser beam by means of total internal reflection that takes place at the water-air interface, in a manner similar to conventional glass fibers. The long cylindrical water jet avoids the need of focus control. The water jet carries the laser beam down to the bottom of the cutting kerf and allows us to dice semiconductor wafers with a high width/depth aspect ratio [118, 119].

Nano-sized modification of metal (Au), semiconductor (Si), dielectric (SiO_2 or soda lime glass), or poly(methyl acrylate) substrates using near-electromagnetic field enhancement in the vicinity of gold nanoparticles are reported [120–124] (also see Chaps. 1 and 8). The particles are placed on the substrate in the case of a single isolated particle and 2D nanoparticle array [120]. Theoretical simulation shows that the electromagnetic field in the near-field zone of gold nanoparticles excited by an 800 nm ultrashort laser pulse is enhanced as the magnitude of the field intensity depends on the substrate material and the interparticle distance for 2D array [122, 123]. For closely arrayed nanoparticles on the gold substrate, the maximal field intensity is more than two times lower than that of a single particle. With the increase of the distance between 200 nm diameter gold particles, the value of the field intensity increases up to a distance of about 800 nm [122].

The laser etching of surfaces was possible by use of a thin layer adsorbed onto the back side of a transparent material that absorbs the laser photon [125–136]. The adsorbed layer causes the etching of the material surface. Laser etching at a surface adsorbed layer (LESAL) [125–130] and laser induced backside dry etching (LIBDE) [131–135] allow precision etching of fused silica at low laser fluences with small etch rates. The thin layer of SiO [136], silver [130, 133, 135], aluminum [132, 133], copper [133, 137], tin [134], carbon [129], and toluene [126–128, 130] was effective for the etching. Laser-induced etching of sapphire and glass by quasi-CW radiation from a copper vapor laser, where an absorbing liquid such as a hydrocarbon solution or an aqueous solution of CrO_3 or $KMnO_4$, was employed to reduce the required laser fluence [138–143].

12.3.2 LIPAA Process

When a single conventional laser at UV, visible, or IR region would be utilized for microfabrication of transparent materials such as silica glass and related glass materials, greater advantages of cost-effective processes are provided for practical applications. Laser-induced plasma-assisted ablation (LIPAA) is a media-assisted laser processing method to etch the surface of the materials [17, 18, 28–39]. The important feature of LIPAA is that single ns-pulsed lasers lead to effective ablation of the materials by coupling the laser beam to plasma that is generated from a metal target by the same laser. Figure 12.6 shows a schematic diagram of the LIPAA process. A ns-pulsed UV laser beam was passed through a phase mask, focused with a lens, and irradiated a metal target through a transparent substrate. The laser-induced plasma was generated from the metal target and attacked the rear surface of the transparent substrate together with the laser pulse resulting in the etching of the substrate with high efficiency. A well-defined surface grating on the fused quartz with a period of 1.06 μm and a depth of 200 nm was fabricated by irradiation with 40 pulses of a KrF excimer laser at a fluence of 1.3 J cm^{-2} $pulse^{-1}$ through a phase mask in a vacuum chamber, where the distance between the Fe metal target and the fused silica quartz was 200 μm [28]. The ablation rates was able to be controlled

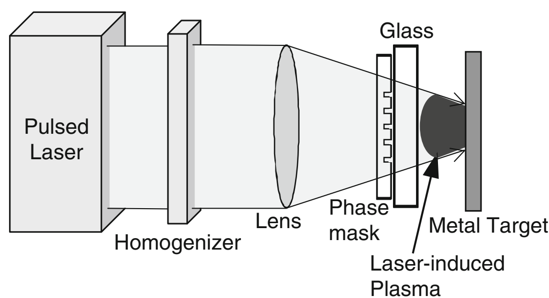

Fig. 12.6 Schematic diagram of microfabrication of glass with laser-induced plasma-assisted ablation (LIPAA)

Table 12.2 Microfabrication and marking of transparent materials by LIPAA

Materials	Lasers	Metals	Topics	Reference
Fused quartz	KrF excimer laser[1]	Fe[7]	Etching property	[28]
	2nd YAG laser[2] ($\tau = 6$ ns)	Fe[7]	Etching property	[29]
	4th YAG laser[3] ($\tau = 6$ ns)	Fe[7]	Etching property	[30]
	YAG lasers[4] ($\tau = 6$ ns)	Ag	Etching property	[31]
	KrF excimer laser[1]	Ag	Etching property	[32, 33]
Pyrex glass	2nd YAG laser[2]	Fe[7]	Etching property	[29]
	2nd YAG laser[2]	Ag	Etching property	[31]
Borosilicate glass	2nd YAG laser[2]	Ag, Cu[8], Si	Color marking	[33, 34, 39]
	2nd YAG laser[2]	Pb[9]	Color marking	[39]
	2nd YAG laser[2]	Cu, SiC	Color marking	[17, 18]
	2nd YAG laser[2]	Cr[10], Al, SiC	Marking, Metallization	[34, 39]
	2nd YAG laser[2]	Cu	Marking, Metallization	[35]
	KrF excimer laser[1]	Ag	Optical emission	[33]
	fs-laser[5] ($\tau = 180$ fs)	Cu	Mechanism	[36]
	2nd YAG laser[2]	Cu	Mechanism	[38]
Polyimide	YAG laser[6] ($\tau = 6$ ns)	Au	Etching property,	[37]
			Cu-Plating	[37]

Laser wavelength: [1]248 nm, [2]532 nm, [3]266 nm, [4]1,064, 532, or 266 nm, [5]775 nm (double pulse), [6]1,064 nm, Materials: [7]Stainless steel 304, [8]Cu or $Cu(C_{32}H_{15}ClN_8)$, [9]Pb_3O_4, [10]Cr or Cr_2O_3

from several nm pulse^{-1} to several hundred nm pulse^{-1} by adjusting laser fluence and the substrate-to-target distance. The ablation threshold of the LIPAA process depends on the wavelength of the laser beam used. Upon irradiation with a ns-pulsed YAG laser (pulse duration: 6 ns), the ablation thresholds for 266, 532, and 1,064 nm were estimated to be 0.7, 1.5, and 3.7 J cm^{-2} pulse^{-1}, respectively [17]. Metals and Si were selected as the target materials, as shown in Table 12.2.

LIPAA can be performed even in air. In the LIPAA process, the etch rate strongly depends on the pressure of the surrounding gas. When the surrounding N_2 pressure was increased from 10^{-2} to 760 Torr, the etch rate decreased by about 90% [30]. This was due to the confinement and deactivation of the laser-induced plasma by the surrounding N_2 gas.

The action of the laser-induced plasma of the metals caused transient absorption of the glass substrate at the laser wavelength. The origin of the transient absorption is electron excitation by ions with kinetic energy more than approximately 10 eV in the plasma. The excitation was revealed with a transient electric polarization change in the glass substrate by plasma conductivity measurement that was applied with a high external pulsed electric field during LIPAA process [38]. This interpretation is also supported by double-pulse irradiation using a near-IR femtosecond laser [36]. The ablation depth of the glass was dependent on the delay time between the first and the second laser pulse. The first pulse generated the laser-induced plasma from the metals, but did not induce ablation of the glass. The second pulse induced the high-efficiency ablation of the substrate at a delay time within several ns.

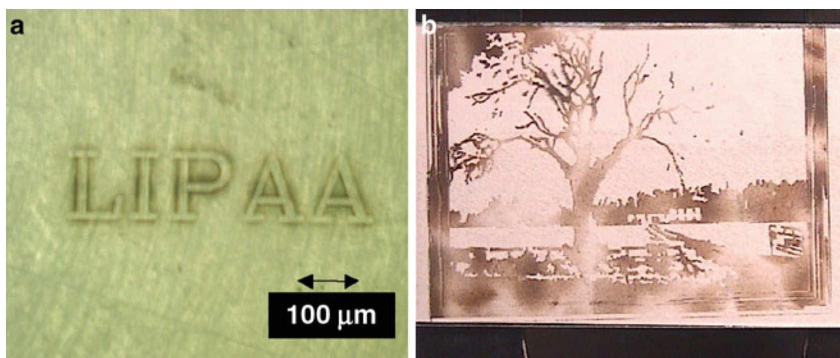

Fig. 12.7 Microstructuring of glass performed by LIPAA (Cu target, *red color*) using a 532-nm diode-pumped solid state laser, (**a**) glass surface marking, (**b**) picture drawing on glass. (courtesy of K. Sugioka)

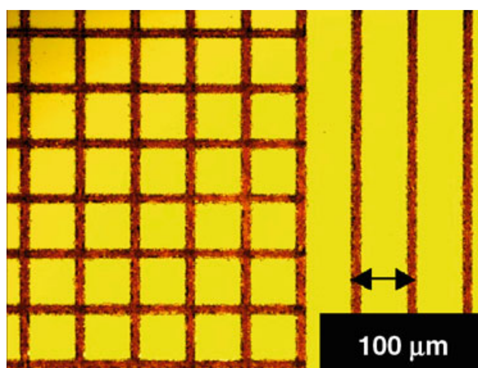

Fig. 12.8 Optical microscope images of microstructured glass substrate. LIPAA (532-nm laser, Cu target) followed by electroless Cu plating. (courtesy of K. Sugioka)

As high-visibility thin metal films were deposited on the ablated glass surface just after the LIPAA process by optimizing the process parameters of laser fluence and the substrate-to-target distance, color marking and printing were achieved on the glass surface [33–35, 39]. Figure 12.7 shows surface marking of glass performed by LIPAA with a 532-nm diode-pumped solid state laser [17, 18]. Copper deposition along the marking path gives the reddish color of the word and excellent contrast on the transparent glass background. It took about 5 min to finish the printing of a picture with a size of 50×50 mm, where laser beam was scanned beam on the target surface with a galvanometer (Fig. 12.7b). RGB color marking of glass by LIPAA was achieved by using various metal-containing targets. Targets were SiC for dark black color, Pb_3O_4 for red, Cr_2O_3 for green, and $[Cu(C_{32}H_{15}ClN_8)]$ for blue color marking [39].

The feature of metal thin film deposition on the surface is also useful for selective metallization and metal interconnection on the materials [17, 35, 37]. The LIPAA processing followed by metal plating realized selective deposition of metal films with good electric conductivity. Figure 12.8 shows an optical microscope image of

the glass ablated by using the objective lens with a distance between the Cu target and the glass substrate of 10 μm, the laser fluence of 1.4 J cm^{-2} pulse^{-1} and the laser scanning speed of 3 mm min^{-1} [35]. It is clear that well-defined grid and line & space structures were fabricated without any damage. The ablated linewidth and the ablation depth were measured to be 25 μm and 7 μm, respectively. The Cu metal film with a thickness of 5.9 μm were selectively deposited by electroless Cu plating on the LIPAA processed area. The resistivity of the plated Cu film was estimated to be 3.0 $\mu\Omega$ cm, which almost coincide with that of bulk Cu of 2.7 $\mu\Omega$ cm. By increasing the target–substrate distance, the influence of the plasma became weak so that only a center part of the laser beam with high intensity induced ablation, resulting in a narrower linewidth. The spatial resolution of 2 μm at a minimum was performed at the target-substrate distance of 400 μm.

12.3.3 LIBWE Process

Laser-induced backside wet etching (LIBWE) in terms of micro-pattern fabrications on transparent materials was described in this section [40–109]. The LIBWE method is based on the deposition of laser energy onto a thin layer at the glass-liquid interface during the ablation of a liquid substance. The indirect excitation of the glass that caused etching on a surface layer of the glass was performed by the ablation of a dye or organic solution. The nonradiative relaxation of the excited dye molecules would generate a temperature jump, which resulted in softening of the glass. The rear surface layer of the glass was removed in the next step after softening/melting of glass. An excimer laser mask projection system and a galvanometer based point scanning system of a single-mode laser beam from a diode-pumped solid state (DPSS) laser were employed for LIBWE, as shown in Fig. 12.9. Projection with a diffractive gray tone phase mask [93, 95], two-beam interference method with a phase mask [86], demagnifying Schwarzschild objective [67], and beam splitter [100–103] were also effective for the surface micro-/nano-structuring of LIBWE.

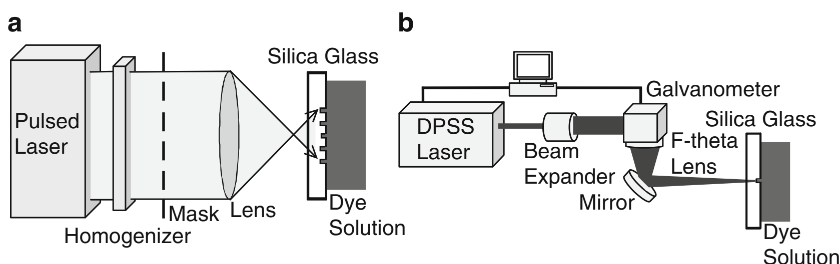

Fig. 12.9 Experimental setup for LIBWE method; (**a**) excimer laser mask projection system and (**b**) DPSS laser beam point scanning system

Table 12.3 Micro-fabrications of various transparent materials by LIBWE

Materials	Reference
Silica glass	[40, 43–47, 49–68, 70–85, 87–89, 93, 97–103]
Quartz	[41, 66, 69, 90–96, 107]
Sapphire	[48, 66, 86, 91, 104, 105]
Glasses[1]	[67, 106, 107]
Calcium fluoride	[43, 66, 91]
Magnesium fluoride	[66]
Barium fluoride	[69, 91, 93]
Fluorocarbon resin[2]	[42]
ITO[3]	[108, 109]

[1]Pyrex, borosilicate glass, soda lime glass
[2]Poly(tetrafluoroethylene-co-hexafluoropropylene) (FEP)
[3]Indium tin oxide (ITO) coated on glass

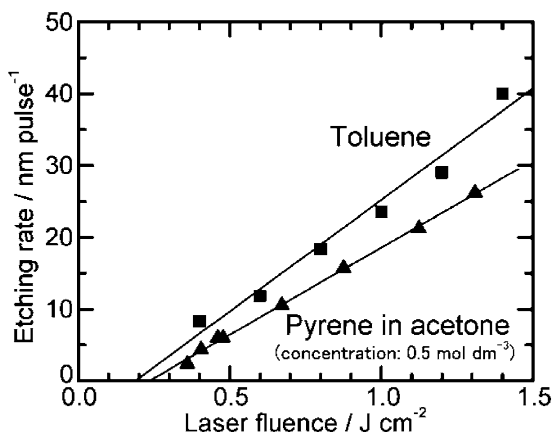

Fig. 12.10 Etching rate of silica glass by LIBWE of KrF excimer laser and organic solutions

By the analyses of time-resolved shadowgraph imaging [46, 47, 51], reflectivity measurements [74], and transient pressure measurements [53, 54, 56, 57, 63, 65], the dynamics of liquid ablation was monitored to estimate the initial pressure and propagation rate of vapor bubbles.

The micro-pattern etching by LIBWE is possible on various materials (Table 12.3). The depth of the etch increases linearly with the number of laser shots (Fig. 12.10). Typical etching rates of the material were 0.1–40 nm pulse^{-1}, depending on irradiation conditions, such as laser wavelength, laser fluence, and dye concentrations. At an extensive fluence regime, the etching rate and roughness were reported [90]. A moderate fluence range of 1–2 J cm^{-2} pulse^{-1} was suitable for a well-defined etching without a damage. Furthermore, dye solutions (dye/solvent), such as pyrene/acetone [40, 41, 43, 44, 48–50, 55, 62, 90–93, 96, 99, 106], pyrene/tetrahydrofuran [42, 92–95], pyrene/tetrachloroethylene [66, 67, 69, 70, 72, 73], pyrene/cyclohexane [66], pyrene/toluene [67–73, 77, 78, 80, 83, 85, 87, 88], pyrene/halogenated aromatics [77, 81, 85], pyranine/water [45], naphthalenesulfonic

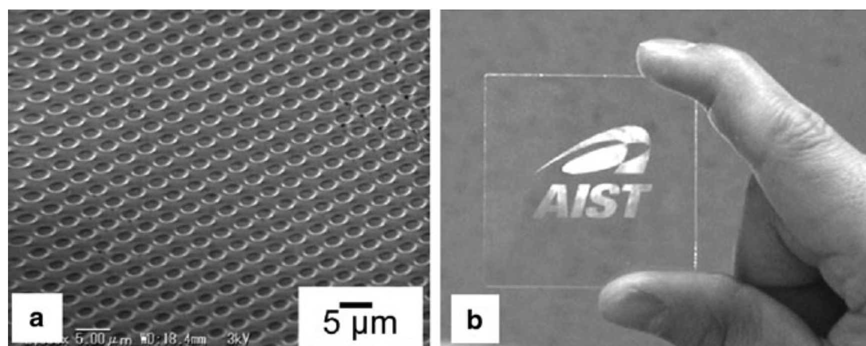

Fig. 12.11 Surface micro-structures on silica glass by LIBWE; (**a**) pits-array with KrF excimer laser mask projection and (**b**) patterned grating with DPSS laser beam scanning system

acid/water [46,51], naphthalene/methyl methacrylate [97–103], phenolphthalein/*N*-methyl-2-pyrrolidone [104, 105], chlorobenzene [86], mercury [82, 89], liquid gallium [75, 79, 81, 84, 88], and pure toluene [47, 52–54, 56–58, 61, 63, 74, 85], have been used in conjunction with irradiation with UV or visible laser.

Figure 12.11 shows well-defined etching structures on silica glass, which were free of debris and microcracks around the area. The array of 2 μmϕ pits structure in Fig. 12.11a was fabricated with the excimer laser mask projection system. The organic solution for a laser absorber was an aqueous naphthalene solution (dye concentration: 0.4 mol dm^{-3}) [52]. A well-defined 1 μm-scale grid pattern and grating as narrow as 0.75 μm-sized was fabricated via fine adjustments to the mask projection system [51].

Figure 12.11b shows that well-defined patterned gratings of the “AIST” logo mark was formed upon the irradiation of DPSS laser at 266 nm with a Galvanometer scanner. Pure toluene was used as an organic solution. The etching grooves with ca. 5–15 μm in width, which was free of debris and microcracks around the area, were fabricated by UV laser irradiation using a single-mode laser beam [60, 61, 63, 65]. The laser irradiation was carried out at laser power of 1–10 μJ $pulse^{-1}$ with the repetition rate of 5–100 kHz. The laser beam was scanned on the sample surface at the rate of 50–100 mm s^{-1}. Upon the scanning irradiation accumulated up to tens scans at the same positions to make a deep groove structure on the surface, the etch depth was increased as increase with the number of scanning times. As the laser beam of DPSS UV laser at a high repetition rate up to 5–100 kHz is scanned on the sample surface with the galvanometer controlled by a computer for flexible operations, galvanometer-based point scanning system is suitable for a rapid prototyping process according to electronic design data in the computer as mask-less exposure system in a conventional atmospheric environment.

Figure 12.12 shows that a unique feature of LIBWE is to fabricate a fine deep micro-trench about 7 μm wide and 420 μm deep on silica glass with a maximum aspect ratio of 60 by LIBWE with a KrF laser [55, 58, 62]. As the projection lens has

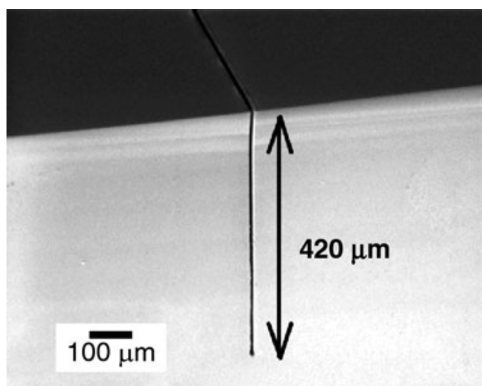

Fig. 12.12 Cross sectional SEM images of deep trenches on silica glass fabricated by the LIBWE method: 25,000 pulses at 80 Hz for a trench about 7 μm wide. A saturated pyrene/acetone solution (0.4 mol dm^{-3}) was in contact with the silica glass plate, and a KrF excimer laser beam was irradiated at $F = 1.0\,J\,cm^{-2}\,pulse^{-1}$. Before SEM observation, the silica plates were cut perpendicular to the deep trenches

Table 12.4 The application of micro-fabrication by LIBWE

Applications	Reference
Optics	
Random-phase-plates	[90]
Fresnel lenses	[90, 91, 93]
Beam-homogenizers (plano-convex microlens array)	[92–95]
Convex cylinder lens arrays	[72]
Surface relief gratings	[67, 86, 100–103]
Patterned grating	[56, 57]
Semiconductors	
Patterned sapphire (Growth of AlN)	[104, 105]
Molding	
Imprinting templates	[52, 58]
Bio-chemical application	
Microarrays of polymer-microbeads	[50, 59, 60, 64]
Microfluidic channels	[65, 106–109]
SAM[1] patterning on glass	[49, 50]

[1] Self-assembled monolayer

a limited depth of focus, the silica plate was moved further from the projection lens after irradiation of every 1,000 pulses in order to adjust the position of the interface between the silica plate and the solution to the imaging area of the projection lens.

The application of micro-fabrication by LIBWE is progressed to optics, semiconductors, and bio-chemical applications (Table 12.4). A lens array on the optical materials was fabricated with the excimer laser with a diffractive gray tone phase

mask [93, 95]. Two-beam interferometric laser irradiation of LIBWE was applied into making silica glass gratings with a 104 nm period. The spatially filtered fourth harmonic of Nd:YAG laser ($\lambda = 266$ nm, $\tau = 8$ ns) pulses were split into two parts which then interfered at the backside of the fused silica target in contact with a liquid absorber [102].

LIBWE can be applied for fabricating microfluidic devices used as "Lab on a Chip" or micro-total analysis system (μ-TAS). In such devices, various functions are integrated onto one chip [59, 60, 64, 65, 106–109]. Microstructure with 1 μm resolution fabricated within microfluidic channels can afford additional functions to the chip. Color-encoded microbeads with surface functional groups randomly arranged in the microstructure can be used for bioarray analyses. A novel microfluidic device incorporating two-dimensional array of microbeads with 10 μm diameter was fabricated [59, 60, 64].

12.4 Conclusions

This chapter has presented a review of the current and potential development of hybrid laser and media-assisted processes and their applications. It has revealed that laser-induced microfabrication techniques by these processes is an important technique for precision micromachining of optical transparent materials for practical usages as industrial tools. Well-defined micropattern without any crack or debris formation on the materials was fabricated by multiwavelength excitation, LIPAA, and LIBWE processes. The capability of these processes to use a variety of conventional laser sources with optimized processing conditions, that was based on indirect excitation process, has led to the microfabrication of new and advanced optical materials. The technical challenges are particularly great in this region, but recent developments in LIPAA and LIBWE have made the new frontiers both alluring and reachable. These methods are mature and versatile techniques that present some key benefits over other more-established microfabrication techniques.

As the microstructures on the materials are possible to be fabricated by laser-induced direct writing (pattering) methods, a flexible rapid manufacturing without a photolithographic process will be available mainly because of cost and reliability considerations as a practical efficient tool. The techniques are particularly well suited for rapid prototyping, optimizing concepts and during production-development stage of a functional device and chip to reduce development time. This offer also possesses the potential to be scaled up for large area or mass production. It is especially utilized for rapid fabrication of small and medium lot sizes in a beginning stage of specific application. The manufacturing systems can be compact, will fit on an optical bench with a small foot-print, and will be suitable for individual practical use.

References

1. D. Bäuerle, *Laser Processing and Chemistry*, 3rd edn. (Springer, Berlin, Heidelberg, 2000)
2. J. Ihlemann, B. Wolff, P. Simon, Appl. Phys. **A54**(4), 363 (1992)
3. P.R. Herman, R.S. Marjoribanks, A. Oettl, K. Chen, I. Konovalov, S. Ness, Appl. Surf. Sci. **154–155**, 577 (2000)
4. H. Varel, D. Ashkenasi, A. Rosenfeld, M. Wähmer, E.E.B. Campbell, Appl. Phys. **A65**(4–5), 367 (1997)
5. K. Sugioka, S. Wada, A. Tsunemi, T. Sakai, H. Takai, H. Moriwaki, A. Nakamura, H. Tashiro, K. Toyoda, Jpn. J. Appl. Phys. **32**(12B), 6185 (1993)
6. K. Sugioka, S. Wada, H. Tashiro, K. Toyoda, A. Nakamura, Appl. Phys. Lett. **65**(12), 1510 (1994)
7. K. Sugioka, S. Wada, H. Tashiro, K. Toyoda, Y. Ohnuma, A. Nakamura, Appl. Phys. Lett. **67**(19), 2789 (1995)
8. K. Sugioka, S. Wada, Y. Ohnuma, A. Nakamura, H. Tashiro, K. Toyoda, Appl. Surf. Sci. **96–98**, 347 (1996)
9. J. Zhang, K. Sugioka, S. Wada, H. Tashiro, K. Toyoda, Jpn. J. Appl. Phys. **35**(11A), L1422 (1996)
10. J. Zhang, K. Sugioka, S. Wada, H. Tashiro, K. Toyoda, Appl. Phys. **A64**(5), 477 (1997)
11. K. Sugioka, S. Wada, H. Tashiro, K. Toyoda, Appl. Surf. Sci. **109–110**, 179 (1997)
12. K. Sugioka, J. Zhang, S. Wada, H. Tashiro, K. Toyoda, Nanotechnology **9**(2), 99 (1998)
13. J. Zhang, K. Sugioka, T. Takahashi, K. Toyoda, K. Midorikawa, Appl. Phys. **A71**(1), 23 (2000)
14. K. Obata, K. Sugioka, T. Akane, N. Aoki, K. Toyoda, K. Midorikawa, Appl. Phys. **A73**(6), 755 (2001)
15. K. Sugioka, T. Akane, K. Obata, K. Toyoda, K. Midorikawa, Appl. Surf. Sci. **197–198**, 814 (2002)
16. K. Obata, K. Sugioka, T. Akane, N. Aoki, K. Midorikawa, N. Aoki, K. Toyoda, Opt. Lett. **27**(5), 330 (2002)
17. K. Sugioka, K. Obata, M.H. Hong, D.J. Wu, L.L. Wong, Y.F. Lu, T.C. Chong, K. Midorikawa, Appl. Phys. **A77**(2), 251 (2003)
18. K. Sugioka, K. Obata, K. Midorikawa, M.H. Hong, D.J. Wu, L.L. Wong, Y.F. Lu, T.C. Chong, J. Photochem, Photobiol. A Chem. **158**(2–3), 171 (2003)
19. T. Makimura, S. Mitani, Y. Kenmotsu, K. Murakami, M. Mori, K. Kondo, Appl. Phys. Lett. **85**(7), 1274 (2004)
20. S. Zoppel, R. Merz, J. Zehetner, G.A. Reider, Appl. Phys. **A81**(4), 847 (2005)
21. S. Zoppel, J. Zehetner, G.A. Reider, Appl. Surf. Sci. **253**(19), 7692 (2007)
22. M. Okoshi, N. Inoue, J. Jpn, Appl. Phys. **42**(9A), 5642 (2003)
23. M. Okoshi, N. Inoue, Appl. Phys. **A79**(4–6), 841 (2004)
24. S. Preuss, H.C. Langowski, T. Damm, M. Stuke, Appl. Phys. **A54**(4), 360 (1992)
25. R. Srinivasan, B. Braren, J. Appl. Phys. **68**(4), 1837 (1990)
26. S. Preuss, M. Stuke, Appl. Surf. Sci. **69**(1–4), 253 (1993)
27. S. Preuss, M. Stuke, Ber. Bunsenges. Phys. Chem. **97**(12), 1674 (1993)
28. J. Zhang, K. Sugioka, K. Midorikawa, Opt. Lett. **23**(18), 1486 (1998)
29. J. Zhang, K. Sugioka, K. Midorikawa, Appl. Phys. **A67**(4), 499 (1998)
30. J. Zhang, K. Sugioka, K. Midorikawa, Appl. Phys. **A67**(5), 545 (1998)
31. J. Zhang, K. Sugioka, K. Midorikawa, Appl. Phys. **A69**, S879 (1999)
32. M.H. Hong, K. Sugioka, Y.F. Lu, K. Midorikawa, T.C. Chong, Proc. SPIE **4088**, 359 (2000)
33. M.H. Hong, K. Sugioka, Y.F. Lu, K. Midorikawa, T.C. Chong, Appl. Surf. Sci. **186**(1–4), 556 (2002)
34. M.H. Hong, K. Sugioka, D.J. Wu, L.L. Wong, Y.F. Lu, K. Midorikawa, T.C. Chong, Proc. SPIE **4637**, 270 (2002)
35. Y. Hanada, K. Sugioka, Y. Gomi, H. Yamaoka, O. Otsuki, I. Miyamoto, K. Midorikawa, Appl. Phys. **A79**(4–6), 1001 (2004)

36. Y. Hanada, K. Sugioka, I. Miyamoto, K. Midorikawa, Appl. Surf. Sci. **248**(1–4), 276 (2005)
37. Y. Hanada, K. Sugioka, H. Takase, H. Takai, I. Miyamoto, K. Midorikawa, Appl. Phys. **A80**(1), 111 (2005)
38. Y. Hanada, K. Sugioka, K. Obata, S.V. Gamov, I. Miyamoto, K. Midorikawa, J. Appl. Phys. **99**(4), 043301 (2006)
39. Y. Hanada, K. Sugioka, I. Miyamoto, K. Midorikawa, J. Phys Conf. Ser. **59**, 687 (2008)
40. J. Wang, H. Niino, A. Yabe, Appl. Phys. **A68**(1), 111 (1999)
41. J. Wang, H. Niino, A. Yabe, Appl. Phys. **A69**(Supplement 1), S271 (1999)
42. J. Wang, H. Niino, A. Yabe, Jpn. J. Appl. Phys. **38**(2A), L761 (1999)
43. J. Wang, H. Niino, A. Yabe, Appl. Surf. Sci. **154–155**, 571 (2000)
44. Y. Yasui, H. Niino, Y. Kawaguchi, A. Yabe, Appl. Surf. Sci. **186**(1–5), 552 (2002)
45. X. Ding, Y. Yasui, H. Niino, Y. Kawaguchi, A. Yabe, Appl. Phys. **A75**(3), 437 (2002)
46. X. Ding, Y. Kawaguchi, H. Niino, A. Yabe, Appl. Phys. **A75**(6), 641 (2002)
47. H. Niino, Y. Yasui, X. Ding, A. Narazaki, T. Sato, Y. Kawaguchi, A. Yabe, J. Photochem. Photobiol. A Chem. **158**(2–3), 179 (2003)
48. X. Ding, T. Sato, Y. Kawaguchi, H. Niino, Jpn. J. Appl. Phys. **42**(2B), L176 (2003)
49. X. Ding, Y. Kawaguchi, T. Sato, A. Narazaki, H. Niino, Chem. Commun. **2003**(17), 2168 (2003)
50. X. Ding, Y. Kawaguchi, T. Sato, A. Narazaki, H. Niino, Langmuir **20**(22), 9769 (2004)
51. X. Ding, Y. Kawaguchi, T. Sato, A. Narazaki, R. Kurosaki, H. Niino, J. Photochem. Photobiol. A Chem. **166**(1–3), 129 (2004)
52. H. Niino, X. Ding, R. Kurosaki, A. Narazaki, T. Sato, Y. Kawaguchi, Appl. Phys. **A79**(4–6), 827 (2004)
53. Y. Kawaguchi, X. Ding, A. Narazaki, T. Sato, H. Niino, Appl. Phys. **A80**(2), 275 (2005)
54. Y. Kawaguchi, X. Ding, A. Narazaki, T. Sato, H. Niino, Appl. Phys. **A79**(4–6), 883 (2004)
55. Y. Kawaguchi, T. Sato, A. Narazaki, R. Kurosaki, H. Niino, Jpn. J. Appl. Phys. **44**(1–7), L176 (2005)
56. H. Niino, Y. Kawaguchi, T. Sato, A. Narazaki, T. Gumpenberger, R. Kurosaki, Appl. Surf. Sci. **252**(13), 4387 (2006)
57. H. Niino, Y. Kawaguchi, T. Sato, A. Narazaki, T. Gumpenberger, R. Kurosaki, J. Laser Micro/Nanoeng. **1**(1), 39 (2006)
58. Y. Kawaguchi, T. Sato, A. Narazaki, R. Kurosaki, H. Niino, J. Photochem. Photobiol. A Chem. **182**(3), 319 (2006)
59. T. Gumpenberger, T. Sato, R. Kurosaki, A. Narazaki, Y. Kawaguchi, H. Niino, Chem. Lett. **35**(2), 218 (2006)
60. T. Gumpenberger, T. Sato, R. Kurosaki, A. Narazaki, Y. Kawaguchi, H. Niino, J. Laser Micro/Nanoeng. **1**(3), 201 (2006)
61. H. Niino, Y. Kawaguchi, T. Sato, A. Narazaki, R. Kurosaki, Appl. Surf. Sci. **253**(19), 8287 (2007)
62. Y. Kawaguchi, H. Niino, T. Sato, A. Narazaki, R. Kurosaki, J. Phys. Conf. Ser. 59, 380 (2007)
63. H. Niino, Y. Kawaguchi, T. Sato, A. Narazaki, T. Gumpenberger, R. Kurosaki, J. Phys. Conf. Ser. **59**, 539 (2007)
64. T. Sato, R. Kurosaki, A. Narazaki, Y. Kawaguchi, H. Niino, Proc. SPIE **6458**, 64580B (2007)
65. H. Niino, Y. Kawaguchi, T. Sato, A. Narazaki, R. Kurosaki, Proc. SPIE **6879**, 68790C (2008)
66. R. Böhme, A. Braun, K. Zimmer, Appl. Surf. Sci. **186**(1–4), 276 (2002)
67. K. Zimmer, R. Böhme, A. Braun, B. Rauschenbach, F. Bigl, Appl. Phys. **A74**(4), 453 (2002)
68. K. Zimmer, A. Braun, R. Böhme, Appl. Surf. Sci. **208–209**, 199 (2003)
69. R. Böhme, D. Spemann, K. Zimmer, Thin Solid Films **453–454**, 127 (2004)
70. R. Böhme, J. ZaJadacz, K. Zimmer, B. Rauschenbach, Appl. Phys. **A80**(2), 433 (2005)
71. K. Zimmer, R. Böhme, Appl. Surf. Sci. **243**(1–4), 415 (2005)
72. K. Zimmer, R. Böhme, Opt. Lasers Eng. **43**(12), 1349 (2005)
73. R. Böhme, K. Zimmer, Appl. Surf. Sci. **247**(1–4), 256 (2005)
74. R. Böhme, T. Otto, K. Zimmer, Appl. Surf. Sci. **252**(13), 4392 (2006)
75. K. Zimmer, R. Böhme, S. Pissadakis, L. Hartwig, G. Reisse, B. Rauschenbach, Appl. Surf. Sci. **253**(5), 2796 (2006)

76. R. Böhme, K. Zimmer, B. Rauschenbach, Appl. Phys. **A82**(2), 325 (2006)
77. R. Böhme, K. Zimmer, Appl. Phys. **A83**(1), 9 (2006)
78. R. Böhme, S. Pissadakis, M. Ehrhardt, D. Ruthe, K. Zimmer, J. Phys. D Appl. Phys. **39**(21), 1398 (2006)
79. K. Zimmer, R. Böhme, D. Ruthe, B. Rauschenbach, Appl. Phys. **A84**(4), 455 (2006)
80. R. Böhme, S. Pissadakis, D. Ruthe, K. Zimmer, Appl. Phys. **A85**(1), 75 (2006)
81. K. Zimmer, R. Böhme, B. Rauschenbach, J. Laser Micro/Nanoeng. **1**(3), 292 (2006)
82. K. Zimmer, R. Böhme, D. Hirsch, B. Rauschenbach, J. Phys. D Appl. Phys. **39**(7), 4651 (2006)
83. R. Böhme, K. Zimmer, J. Phys. D Appl. Phys. **40**(10), 3060 (2007)
84. K. Zimmer, R. Böhme, B. Rauschenbach, Appl. Phys. **A86**(3), 409 (2007)
85. R. Böhme, S. Pissadakis, M. Ehrhardt, T. Rudolph, D. Ruthe, K. Zimmer, J. Phys. Conf. Ser. **59**, 173 (2007)
86. S. Pissadakis, R. Böhme, K. Zimmer, Opt. Express **15**(4), 1428 (2007)
87. K. Zimmer, R. Böhme, D. Ruhte, B. Rauschenbach, Appl. Surf. Sci. **253**(15), 6588 (2007)
88. R. Böhme, K. Zimmer, Appl. Surf. Sci. **253**(19), 8091 (2007)
89. R. Böhme, K. Zimmer, J. Laser Micro/Nanoeng. **2**(3), 178 (2007)
90. G. Kopitkovas, T. Lippert, C. David, A. Wokaun, J. Gobrecht, Microelectron. Eng. **67–68**, 438 (2003)
91. G. Kopitkovas, T. Lippert, C. David, A. Wokaun, J. Gobrecht, Thin Solid Films **453–454**, 31 (2004)
92. G. Kopitkovas, T. Lippert, C. David, S. Canulescu, A. Wokaun, J. Gobrecht, J. Photochem. Photobiol. A Chem. **166**(1–3), 135 (2004)
93. G. Kopitkovas, T. Lippert, C. David, S. Canulescu, A. Wokaun, J. Gobrecht, J. Laser Micro/Nanoeng. **1**(1), 23 (2006)
94. G. Kopitkovas, T. Lippert, J. Venturini, C. David, A. Wokaun, J. Phys. Conf. Ser. **59**, 526 (2007)
95. G. Kopitkovas, T. Lippert, N. Murazawa, C. David, A. Wokaun, J. Gobrecht, R. Winfield, Appl. Surf. Sci. **254**(4), 1073 (2007)
96. G. Kopitkovas, V. Deckert, T. Lippert, F. Raimondi, C.W. Scheider, A. Wokaun, Phys. Chem. Chem. Phys. **10**(22), 3195 (2008)
97. C.S. Vass, B. Hopp, T. Smausz, F. Ignacz, Thin Solid Films **453–454**, 121 (2004)
98. C.S. Vass, T. Smausz, B. Hopp, J. Phys. D Appl. Phys. **37**(17), 2449 (2004)
99. C.S. Vass, D. Sebok, B. Hopp, Appl. Surf. Sci. **252**(13), 4768 (2006)
100. C.S. Vass, K. Osvaya, M. Csete, B. Hopp, Appl. Surf. Sci. **253**(19), 8059 (2007)
101. C.S. Vass, K. Osvay, Opt. Express **14**(18), 8354 (2006)
102. C.S. Vass, K. Osvay, B. Hopp, Z. Bor, Appl. Phys. **A87**(4), 611 (2007)
103. C.S. Vass, K. Osvay, T. Veso, B. Hopp, Z. Bor, Appl. Phys. **A93**(1), 69 (2008)
104. X. Fujito, T.Hashimoto, K. Samonji, J.S. Speck, S. Nakamura, J. Cryst. Growth **272**(1–4), 370 (2004)
105. T. Hashimoto, K. Fujito, K. Samonji, J.S. Speck, S. Nakamura, Jpn. J. Appl. Phys. **44**(2), 869 (2005)
106. J.Y. Cheng, M.H. Yen, C.W. Wei, Y.C. Chuang, T.H. Young, J. Micromech. Microeng. **15**(6), 1147 (2005)
107. J.Y. Cheng, M.H. Yen, T.H. Young, J. Micromech. Microeng. **16**(11), 2420 (2006)
108. J.Y. Cheng, M.H. Yen, W.C. Hsu, J.H. Jhang, T.H. Young, J. Micromech. Microeng. **17**(11), 2316 (2007)
109. J.Y. Cheng, M.H. Yen, C.T. Kuo, T.H. Young, Biomicrofluidics **2**(2), 024105 (2008)
110. A. Kruusing, Opt. Lasers Eng. **41**(2), 307 (2004)
111. A. Kruusing, Opt. Lasers Eng. **41**(2), 329 (2004)
112. A.A. Tseng, Phys. Stat. Sol. A Appl. Mater. Sci **204**(3), 709 (2007)
113. Y. Li, K. Itoh, W. Watanabe, K. Yamada, D. Kuroda, J. Nishii, Y. Jiang, Opt. Lett. **26**(23), 1912 (2001)
114. Y. Iga, T. Ishizuka, W. Watanabe, K. Itoh, Y. Li, J. Nishii, Jpn. J. Appl. Phys. **43**(7A), 4207 (2004)

115. Y. Iga, W. Watanabe, Y. Li, Y. Li, J. Nishii, K. Itoh, Jpn. J. Appl. Phys. **44**(11), 8013 (2005)
116. R. An, J.D. Uram, E.C. Yusko, K. Ke, M. Mayer, A.J. Hunt, Opt. Lett. **33**(10), 1153 (2008)
117. F.R. Wagner, A. Spiegel, N. Vago, B. Richerzhagen, Proc. SPIE **4637**, 479 (2002)
118. O. Sibailly, B. Richerzhagen, Proc. SPIE **5339**,394 (2004)
119. T.A. Mai, B. Richerzhagena, P.C. Snowdon, D. Wood, P.G. Maropoulos, Proc. SPIE **6459**, 64590P-1 (2007)
120. P.A. Atanasov, H. Takada, N.N. Nedyalkova, M. Obara, Appl. Surf. Sci. **253**(19), 8304 (2007)
121. N.N. Nedyalkova, T. Miyanishi, M. Obara, Appl. Surf. Sci. **253**(19), 6558 (2007)
122. N.N. Nedyalkova, P.A. Atanasov, M. Obara, Nanotechnology **18**(30), 305703 (2007)
123. P.A. Atanasov, N.N. Nedyalkova, T. Sakai, M. Obara, Appl. Surf. Sci. **254**(4), 794 (2007)
124. K. Yamada, T. Itoh, Y. Tsuboi, Appl. Phys. Express **1**(8), 087001 (2008)
125. R. Böhme, K. Zimmer, Appl. Surf. Sci. **239**(1), 109 (2004)
126. K. Zimmer, R. Böhme, B. Rauschenbach, Appl. Phys. **A79**(8), 1883 (2004)
127. K. Zimmer, R. Böhme, B. Rauschenbach, Microelectron. Eng. **78–79**, 324 (2005)
128. R. Böhme, K. Zimmer, B. Rauschenbach, Appl. Phys. **A82**(2), 325 (2006)
129. R. Böhme, D. Hirsch, K. Zimmer, Appl. Surf. Sci. **252**(13), 4763 (2006)
130. K. Zimmer, R. Böhme, B. Rauschenbach, J. Laser Micro/Nanoeng. **1**(3), 190 (2006)
131. B. Hopp, C.S. Vass, T. Smausz, Appl. Surf. Sci. **253**(19), 7922 (2007)
132. B. Hopp, T. Smausz, M. Bereznai, Appl. Phys. **A87**(1), 77 (2007)
133. T. Smausz, T. Csizmadia, N. Kresz, C.S. Vass, Z.S. Márton, B. Hopp, Appl. Surf. Sci. **254**(4), 1091 (2007)
134. B. Hopp, T. Smausz, T. Csizmadia, J. Budai, A. Oszkó, G. Szabó, J. Phys. D Appl. Phys. **41**(17), 175501 (2008)
135. T. Smausz, Z. Zalatnai, B. Papdi, T. Csako, Z.S. Bor, B. Hopp, Appl. Surf. Sci. (2008) in press
136. J. Ihlemann, Appl. Phys. **A93**(1), 65 (2008)
137. Z.Q. Huang, M.H. Hong, T.B.M. Do, Q.Y. Lin, Appl. Phys. **A93**(1), 159 (2008)
138. S.I. Dolgaev, A.A. Lyalin, A.V. Simakin, G.A. Shafeev, Quantum Electron. **26**(1), 65 (1996)
139. S.I. Dolgaev, A.A. Lyalin, A.V. Simakin, V.V. Voronov, G.A. Shafeev, Appl. Surf. Sci. **109–110**, 201 (1997)
140. A. Blatter, M. Maillat, S.M. Pimenov, G.A. Shafeev, A.V. Simakin, E.N. Loubnin, Wear **232**(2), 226 (1999)
141. A.A. Lyalin, E.N. Loubnin, A.V. Simakin, G.A. Shafeev, Thin Solid Films **357**(2), 144. (1999)
142. A.V. Simakin, E.N. Loubnin, G.A. Shafeev, Appl. Phys. **A69**(Supplement 1), S267 (1999)
143. A.V. Simakin, E.N. Loubnin, G.A. Shafeev, Quantum Electron. **30**(3), 263 (2000)

Chapter 13
Drilling, Cutting, Welding, Marking and Microforming

Oliver Suttmann, Anas Moalem, Rainer Kling, and Andreas Ostendorf

Abstract The following chapter provides an overview on laser based microprocessing in different industrial applications. Depending on the used parameter regime, the systems technology and optics and the laser source applications like drilling, precise cutting, marking, or microjoining can be realized. Besides describing the specific laser material interaction and their influence by the laser parameters the main industrial applications will be highlighted.

13.1 Parameter Regimes

All laser processes can be described by a set of interacting sub-processes which are influenced by the process parameters in a complex manner. For laser micro processing, one essential process parameter is the laser power density, i.e., power over a focal spot area. With the beam parameter product

$$\theta w_0 = \frac{\lambda}{\pi} M^2, \tag{13.1}$$

A. Ostendorf (✉)
Lehrstuhl für Laseranwendungstechnik und Meßsysteme, Ruhr-Universität Bochum, Germany
e-mail: Andreas.Ostendorf@ruhr-uni-bochum.de

O. Suttmann
Laser Zentrum Hannover e.V, Germany
e-mail: o.suttmann@lzh.de

A. Moalem
Laser Zentrum Hannover e.V, Germany
e-mail: a.moalem@lzh.de

R. Kling
Laser Zentrum Hannover e.V, Germany
e-mail: r.kling@lzh.de

K. Sugioka et al. (eds.), *Laser Precision Microfabrication*,
Springer Series in Materials Science 135, DOI 10.1007/978-3-642-10523-4_13,
© Springer-Verlag Berlin Heidelberg 2010

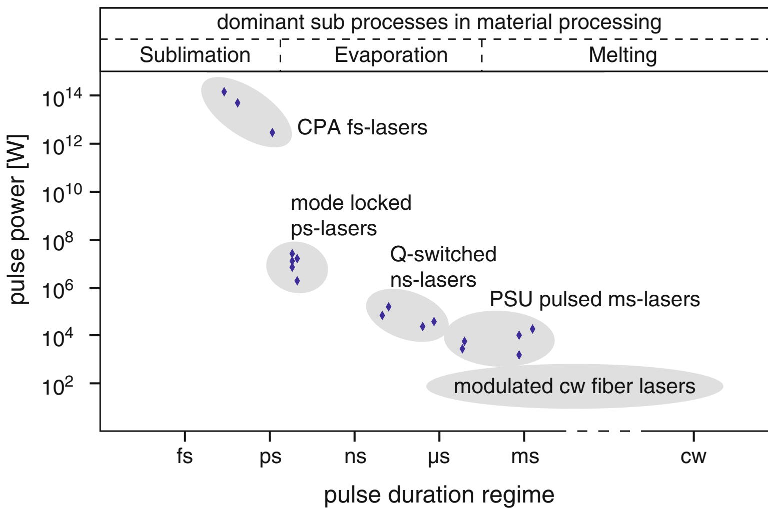

Fig. 13.1 Pulse power and pulse duration of state-of-the-art laser systems for micro processing and dominant sub processes

it is obvious, that for achieving a small focal radius w_0 and thereby a small focal spot area, different methods can be applied: Of course, a laser system with a good beam quality can be chosen (small M^2), but also a short wavelength λ or a small focal distance (i.e., larger divergence angle θ) will in principle enable small focal spots, too. Based on this relation, recent developments of laser sources with excellent beam qualities are especially useful for remote processing, where a large focal distance and a small spot size are present together. Besides the spatial concentration of power using beam parameters, also time resolved measures can be taken to influence the intensity of the laser radiation: Using pulsed lasers, the average laser power is optically accumulated, and the pulses can reach multiple orders higher peak powers. The pulse duration can range from femtoseconds (fs) to the milliseconds (ms), depending on the laser systems and on the required physical interaction when using the laser pulses for machining. In Fig. 13.1, a survey is given, where state-of-the-art laser systems are depicted according to their pulse power, pulse duration, and the physical sub-processes that dominate during machining.

13.1.1 Pulse Duration

The pulse duration is a parameter that ranges currently over 13 orders of magnitude (250 ms to 35 fs). This can be compared to the ratio of one heartbeat (1 s) to the age of our species (homo sapiens, 300,000 years). A brief overview regarding the energy transitions in the range of fs and picoseconds (ps) is given to illustrate the temporal effect of the duration of light material interaction taking the example of

metals (see Chaps. 2 and 8). The light is absorbed within approximately 10 fs. The transition of the excited energy into thermal energy of the electron system takes typically 100 fs (electron–electron relaxation). The heat transfer from the electrons to the lattice typically starts after 1–10 ps (electron–phonon relaxation). The ablation process itself also starts within this time frame. Thermal conduction begins within the range of 100 ps (phonon–phonon relaxation) [1]. So it is obvious, that there are different interaction mechanisms of light and matter when applying laser pulses of different timescales.

13.1.1.1 Continuous Wave and Long Laser Pulses

Continuous wave (CW) lasers emit laser radiation with a power that continuously depends on the pump power (see Chap. 3). CW lasers are used for applications which require a thermal impact, e.g. welding or melt cutting. Currently, available laser sources used for laser precision microfabrication deliver powers in the range of 200 W. Pulsed systems with long laser pulses ($\sim$1 ms) are used when higher power densities are required on short timescales, e.g. for micro welding. Long laser pulses are realized through pulsed pumping with appropriate power supply units (Chap. 3).

The recent transition from lamp pumping to diode pumping leads to laser systems with a significant increase in long term stability and less maintenance efforts. Another development with high impact is the fiber laser technology. Fiber lasers allow a significant improvement of beam quality, much smaller installation size, and much better degree of efficiency.

13.1.1.2 Short Laser Pulses

The motivation for using short laser pulses (pulse duration 1 ns to 1 μs) is a reduction of thermal impact on the material. Material removal requires an energy density above the ablation threshold. A short laser pulse with an energy density above the ablation threshold is absorbed by the material and a part of this material is transformed into an expanding plasma plume within several picoseconds. Short pulses interact on the later stages with the expanding plasma plume and are partially absorbed. A part of the energy deposited in the plasma can be transferred to the solid or molten material and still contribute to material processing. The molten material is moved out of the ablation zone by the pressure gradient caused by the expanding plasma plume. The thermal penetration depth into the material can be described by the equation

$$d \approx \sqrt{4k\tau}, \tag{13.2}$$

with the thermal diffusivity k of the material and the pulse duration τ. For a pulse duration of 25 ns, the thermal penetration depth in aluminium ($k = 98.8 \times 10^{-6}$ m/s^2) is approximately 3 μm, and the thermal penetration depth for a pulse duration of 1 μs is 20 μm, respectively.

Short laser pulses are generated through resonator q-switching. Due to the high peak power, q-switched solid state lasers allow for efficient frequency conversion and therefore they can deliver visible- or UV-wavelengths.

13.1.1.3 Ultrashort Laser Pulses

Laser pulses with pulse durations below 10 ps are defined as ultrashort. Similar to short laser pulses, the energy density has to be above the ablation threshold. In contradiction to short laser pulses, the energy is deposited in a time period shorter than the relaxation time between the electron system and the lattice. Hence, the electron system exhibits a higher temperature than the lattice. This state and the energy transfer from the electron system into the lattice are described by the *two temperature model* (Chaps. 2 and 8). The vaporization and plasma formation take place much faster than heat conduction occurs. This leads to a decrease in thermal impact and allows material processing without thermally affecting the sourrounding material when processing at moderate fluences [1]. Processing at higher fluences can lead to thermal manipulation of the surrounding material. Therefore, ablation processes based on the *two temperature model* can be differentiated into a non-thermal (gentle) and a thermal (strong) fluence regime. Ultrashort laser pulses do not interact with the expanding plasma plume because ablation and plasma formation start after the pulse has passed [2,3]. Another characteristic of ultrashort laser pulses is the non-linear absorption, due to the very high power densitiy (Fig. 13.1). This enables the processing of materials which normally are optically transparent for the used wavelengths (Chap. 9).

Although femtosecond laser ablation results in better qualities compared to ablation with picosecond lasers, laser ablation using pulse durations around 10 ps recently has also gained importance [4–6]. One reason is the less complex design of picosecond laser sources. Over the last years, mode-locked ps sources have obtained industrial relevance. Another benefit of mode-locked systems is the much higher pulse repetition rate enhancing the processing speed.

13.1.2 Wavelength

To understand the motivation for converting infrared lasers to green or even UV operation, in Fig. 13.2, the spectral absorption of different metals is shown. For example, when machining copper, the absorption at 532 nm, compared to 1,064 nm, is increased from 2 to 40%. In other words, the percentage of absorbed radiation is 20 times higher with 532 nm radiation compared to 1,064 nm radiation. Therefore, the same result can be achieved with much less laser power when using green radiation instead of IR radiation. Even after taking the conversion efficiency into account, the energy balance is still superior for converted laser systems. However, due to the complexity of the conversion technology, cost efficiency plays an important role in determining the required wavelength.

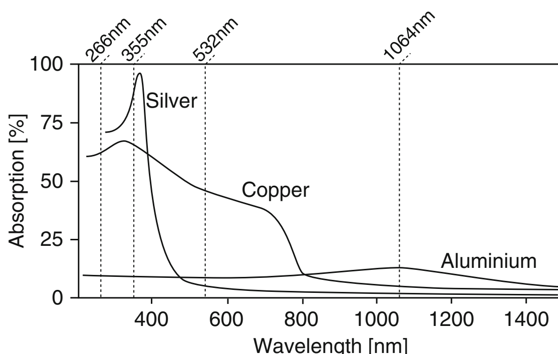

Fig. 13.2 Spectral absorptivity of high reflectivity metals. With frequency conversion, common solid state lasers deliver radiation with wavelengths of $\lambda = 532$ nm, $\lambda = 355$ nm, and $\lambda = 266$ nm

13.1.3 Beam Quality

The spatial intensity distribution of laser radiation mainly depends on the laser source. Depending on the design of the resonator, different transverse modes can be emitted. The most common intensity distribution is the gaussian beam or TEM_{00} mode, which corresponds to $M^2 = 1$ (see 13.1).

As described above, high beam quality is desired to decrease the spot size as well as to increase the working distance. An additional motivation for high beam quality is its well defined intensity distribution in the focal plane for using beam shaping elements. Thereby, various intensity distributions, e.g., flat-tops or multi-spots for thin-film scribing can be generated. Today, disc and fiber lasers can deliver beam qualities with $M^2 \leq 1.1$.

13.1.4 Output Power

Cost efficient processing requires a certain output power. For pulsed systems, the specified average power is not sufficient to estimate if a laser allows fast machining. Assessing pulsed lasers requires the knowledge of pulse duration, pulse peak power, pulse energy, and pulse repetition rate.

Scaling the power of CW lasers generally leads to a better process performance, e.g., faster cutting or deeper welding seams.

Scaling the output power of pulsed systems can be realized by two approaches. These are pulse energy or pulse peak power respectively and repetition rate. The first approach, increasing the energy or peak power of a pulse influences the amount of affected material. An increase of pulse energy will lead to quality losses due to thermal effects. This limitation can be avoided by splitting the laser radiation into multiple spots and a parallel processing strategy. The second approach for scaling the output power of pulsed systems is the repetition rate. The repetition rate is

limited due to residual thermal effects and interaction with the plasma of preceding pulses. The plasma plume life time increases with the pulse energy. This can lead to a laser power shielding, affecting subsequent pulses [7,8]. Hence, a trade-off between energy per pulse and pulse repetition rate has to be found.

13.2 Drilling

Drilling has been one of the first applications in laser machining. A traditional method to determine the laser power is one Gillette. One Gillette measures how many razor blades can be drilled through by one laser pulse. As the methods for measuring the energy per pulse evolved, the drilling processes did as well [1,7,9].

Today, laser drilling is an established application for lasers in the field of microfabrication. Application examples are broad and vary in quality, processing time, costs, and other conditions. Each application has its own and specific demands. Two application examples are briefly introduced to show the different requirements on the drilling process.

Drilled holes for *particle filters* have low requirements on the hole geometry, such as diameter, conicity, circularity, and other quality parameters. Crucial points of this application are cost and processing time for each hole. A filter element can consist of several thousands of holes. The costs for each hole should therefore be in the range of a fraction of a cent. The processing time should be in a fraction of a second.

Holes for *injection nozzles* have very high demands regarding the geometry and overall-quality. In contrast to filter elements, diameter, conicity, and circularity have to be in a tolerance of a few µm. The amount and costs of the holes are still demanding, although the processing time and the costs are allowed to be much higher than for filtering applications.

It is obvious, that each of these applications requires an adapted approach according to the demands in a cost effective production. Therefore, different drilling strategies are explained in the following. Fig. 13.3 shows a classification of laser drilling processes and depicts the fundamental principles.

13.2.1 Laser Drilling Without Relative Movement Between Laser Spot and Workpiece

Drilling processes described here are characterized by the absence or neglectability of a relative movement between laser spot and workpiece during the drilling process. Therefore, the hole diameter strongly corresponds to the focal diameter and the applied pulse energy. This simplifies the process but also decreases the flexibility when changing the diameter of the drilled hole.

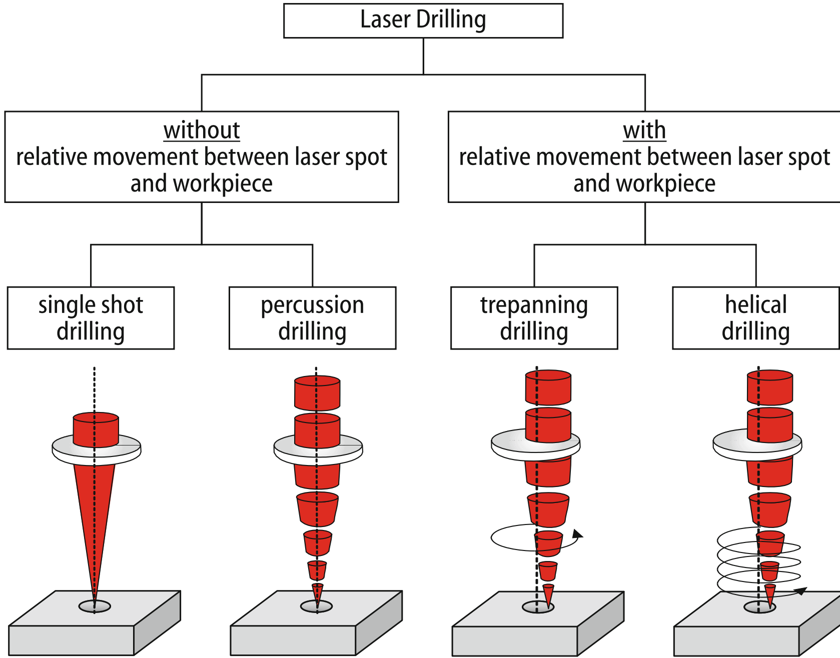

Fig. 13.3 Overview of drilling methods

13.2.1.1 Single Pulse Drilling

Single pulse drilling is the least complex process strategy. Only one laser pulse hits the target and generates the complete drilling [10]. Therefore, very high pulse energies are required. Single pulse drilling is mostly performed with pulsed solid-state lasers. The pulse duration is usually in the range of several hundred μs [11]. Due to the pulse duration, the material removal is based on melt ejection. Drilled holes often show recast inside the holes and on the entrance of the drilling as well as a pronounced heat affected zone. Single pulse drilling is often carried out with reactive processing gas to improve the drilling rate by enthalpy gains.

A typical material thickness for single pulse drilling is about one mm in steel materials. The achievable aspect ratio is approximately 1:10 [11]. Holes drilled with single pulse drilling often show a decrease in diameter on the backside of the workpiece.

Deformation of the focal spot and fluctuations of energy per pulse lead to relatively low reproduceability and deviations of circularity. A typical application for single pulse drilling is the production of filter elements. Single pulse drilling is a fast and low cost drilling process.

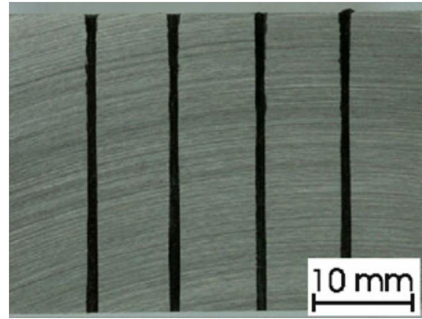

Fig. 13.4 Holes drilled by percussion drilling in hard metal, depth 30 mm, diameter 1 mm, drilling time 2 min

13.2.1.2 Percussion Drilling

Percussion drilling makes use of multiple laser pulses at the same position on the workpiece to generate the hole [10]. There are two reasons to apply percussion drilling instead of single pulse drilling. On the one hand, it can be used to improve the accuracy of the hole by ablating smaller volumes with each laser pulse. On the other hand, percussion drilling can be used to increase the depth of the drilled hole up to several mm depth [10]. Generally, similar beam sources and pulse durations are used as for single pulse drilling. Typical applications are cooling holes on blades for turbo engines. Drilling depths up to 30 mm with an aspect ratio of up to 30 have recently been realized (Fig. 13.4).

Today, beam sources with shorter wavelength and pulse duration are used to further improve the quality of the drilled holes. A typical application for percussion drilling with short pulses is drilling of metal-polymer multi-layer material for electronic packaging. Drilling by percussion techniques requires longer processing times than single shot drilling but still can be regarded as low cost drilling.

A further increase in drilling quality can be achieved by drilling “on-the-fly". Drilling “on-the-fly" describes a technique with a fast movement between the laser and the workpiece. Consecutive pulses hit the workpiece on the different positions to be drilled. In a later loop, the pulses hit exactly the same positions as before, and the loops repeat until the hole is finally drilled. This technique requires in most cases a machining setup with galvo-scanners and decreases the thermal stress put into the workpiece.

13.2.2 Laser Drilling with Relative Movement Between Laser Spot and Workpiece

Drilling techniques that are characterized by relative movement between the laser spot and the workpiece are described in the following. The movement can be performed by the methods of CNC-axes and galvo-scanners. A further method is using

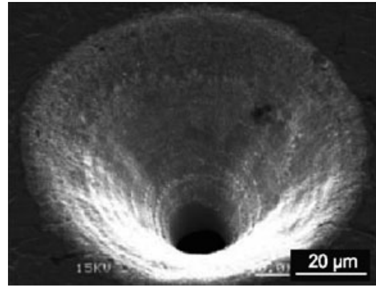

Fig. 13.5 Inkjet nozzle drilled in stainless steel with a picosecond laser[12]

trepanning optics. The fundamental principle and design of trepanning optics is described below. Trepanning and helical drilling have similarities to laser cutting processes and the transition from drilling to cutting is floating.

Trepanning and helical drilling generally provide higher precision as well as higher costs compared to single pulse and percussion drilling. The diameter of the drilled hole correlates with the spot diameter and the laser spot path. Thus, distortions of the laser spot have smaller influence on the geometry of the hole. Holes performed with relative movement between laser spot and workpiece are not limited to circular shapes. Even the entrance and the exit of the hole might show different geometries, assuming that the handling system allows the appropriate relative movement between laser radiation and workpiece (Fig. 13.5).

The concepts of trepanning and helical drilling are often used inconsistently in literature. Therefore, special care has to be taken while working with these concepts. We refer to the most common definitions for both concepts.

13.2.2.1 Trepanning

Trepanning describes a drilling process that can be subdivided into two phases. The first is the percussion drilling of a through hole. The second is effectively a cutting movement along a closed path which creates the contour of a bigger through hole. Trepanning is often performed with long pulsed lasers. The fields of application are similar to percussion drilling, e.g., drilling of turbo engine blades [13].

13.2.2.2 Helical Drilling

Helical drilling is the drilling technique that enables the best quality (Fig. 13.6). In contrast to trepanning, the hole is drilled with more than one revolution of the laser spot and can be understood as multi pass trepanning. With each pass, the ablation front moves downward on a helical path. The amount of material ablated with each pulse is smaller compared to trepanning. This leads to an increase in contour accuracy and a decrease in thermal load of the workpiece. Aspect ratios reach values up to 70. Typical diameters are in the range from 15 μm to several hundred μm.

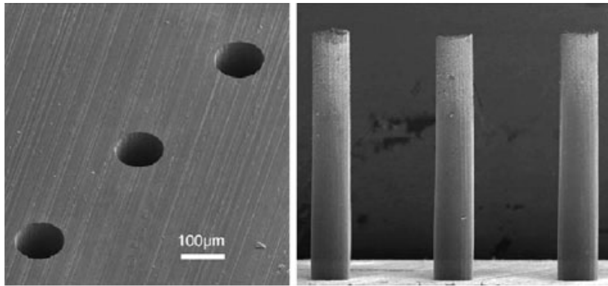

Fig. 13.6 Holes drilled in a 1 mm thick stainless steel by femtosecond laser pulses and their replicas [14]

Helical drilling is generally performed with short and ultrashort pulsed laser sources, hence, it is the laser drilling process with the highest costs. Some time ago, drilling a hole with 150 μm diameter and 500 μm depth was a question of several seconds. Today's high power picosecond lasers drill such holes in less than 1 s [8].

13.2.3 Trepanning Head

Trepanning heads only allow a circular movement of the laser spot. Trepanning heads are often based on rotating wedged plates to deflect the beam. The diameter of the beam path can be adjusted on the trepanning head. An important feature of trepanning heads is the possibility of adjusting the angle of incidence of the laser beam. This angle can be used to control the conicity of the drilled hole. Trepanning heads allow the manufacturing of positively or negatively conical holes without moving the workpiece [15].

13.2.4 Further Trends and Outlook

The polarization state of the laser radiation is a factor which can lead to geometrical distortions of the drilled hole, especially on the backside of the drilled hole. These distortions are caused by polarization dependent multiple reflections and absorption inside the hole. A simple possibility to overcome this problem is the integration of rotating half wave plates, fixed quarter wave plates, or a combination of fixed and rotating quarter wave plates [16]. These components can easily be integrated into the beam path.

Distortions of the beam might also lead to deviation of the circularity even when applying trepanning or helical drilling techniques. Machining heads with rotating dove tail prisms have been developed, which allow the rotation of the beam with up

to 20.000 revolutions per minute [15]. Using this technique, the circularity can be significantly improved.

Approaches of decreasing the amount of redeposites without negatively effecting the processing speed is using processing chambers with lower ambient pressure [17, 18], use of special processing nozzles and the use of sacrificial layers.

Despite all technical developments in drilling and related components, laser micro-drilling often lacks processing speed compared to other drilling techniques such as mechanical drilling or electrical discharge machining (EDM). Recent trends to increase speed are the improvement of efficiency through double or multiple-pulse ablation [19–22] and development of novel ultrashort pulsed beam sources [8].

13.3 Cutting

Laser cutting techniques can be subdivided into two groups considering the mechanisms responsible for material ejection at the cutting front.

The first group, melt cutting, contains processes where the laser provides the energy to heat and melt the material but does not deliver the energy to remove the material from the processing zone. Here, the material is driven out by a coaxial high-pressure gas jet. Melt cutting can be supported by a chemical reaction with additionally supplied oxygen gas.

The second group is laser ablation cutting. Using pulsed laser radiation or high brilliance CW lasers leads to vaporization and eventually plasma formation at the laser material interaction zone. The resulting pressure gradient at the gas melt interface is responsible for melt ejection. Hence these processes do not require an external gas jet to remove the material which is molten or vaporized. Laser ablation cutting can be classified with respect to the pulse duration into short pulsed and ultrashort pulsed laser cutting.

Besides these main groups, other cutting techniques have recently gained importance: In laser scribing, a groove or a pattern of blind holes is generated on the workpiece which can be used as initiator for a following mechanical breaking process or for electrical insulation of solar cells. Another promising technique which is applied to brittle materials such as silicon or glass is the Laser Induced Stress (LIS) cutting.

13.3.1 Melt Cutting

In melt cutting, the laser induced melt is removed by a coaxial cutting gas jet that is applied by a gas nozzle close to the laser material interaction zone.

Therefore, the laser optics and the gas nozzle usually form a unit, that is moved over the workpiece surface, along the cutting path (Fig. 13.7). In the steady state cutting process, a part of the laser radiation is absorbed at the solid workpiece sur-

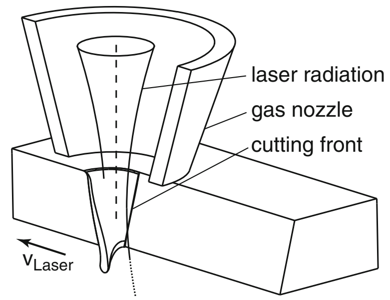

Fig. 13.7 Half section sketch of the melt cutting interaction zone

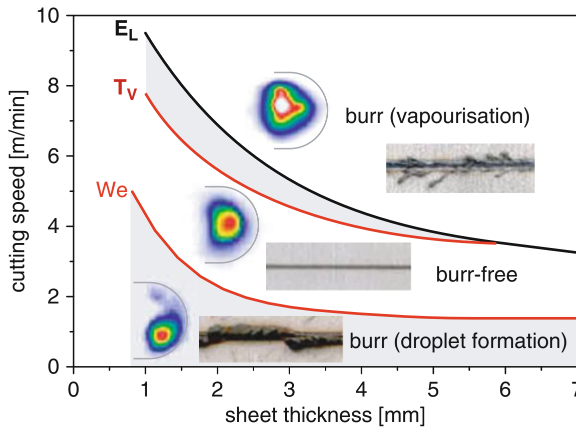

Fig. 13.8 Weber number We and boiling temperature T_V as process boundaries for burr-free melt cutting, corresponding coaxial thermal images of the cutting front and photographs of the cutting kerf lower side [23]

face resulting in pre-heating. Another part of the laser radiation is absorbed at the liquid cutting front, where heat diffusion and advection transport the heat to the solid liquid interface, i.e., the melting front.

Besides the straightness of the cutting ridge, a very important quality feature is the absence of burr at the lower cutting edge. In Fig. 13.8, the process boundaries for burr-free melt cutting are shown [23].

The dominant driving force responsible for melt removal is usually the gas jet friction force at the gas liquid interface. In this case, if the melt flow is high enough, the melt is ejected at the center of the lower edge cutting front. With increasing cutting speed, also more laser power is required, which results in higher demand of laser intensities and melt temperature. The cutting front can locally reach boiling temperature. Secondary order cutting burr can form if the resulting vapor pressure gradient on the melt surface applies a significant driving force on the melt. It might accelerate the melt sideways or azimuthal, which reaches the lower cutting edge off centered where it cools down and partially resides as secondary order cutting burr.

In contrast, if the cutting speed is too low, formation of primary order cutting burr, is possible: According to mass conservation, the melt film thickness at the cutting front is small. With the small melt film thickness, the surface tension of the melt becomes significant and causes the disposition of droplets at the kerf edge, where they cool down and eventually solidify forming burr. A stronger gas jet and thereby a higher melt velocity can counteract the effect of the surface tension, reducing burr. The balance between melt flow pressure ρv_m^2 and curvature pressure $\frac{\sigma}{d_m}$ from surface tension can be described by the dimensionless Weber number

$$We = \frac{\rho v_m^2 d_m}{\sigma}, \tag{13.3}$$

where v_m is the melt velocity at the lower edge, d_m is the melt film thickness which corresponds to the curvature diameter of the ejected melt and σ the surface tension [23]. A small Weber number ($We \ll 1$) indicates primary order burr formation, while a large Weber number ($We \gg 1$) can indicate burr-free cutting or, at high speeds secondary order burr formation.

13.3.2 Laser Ablation Cutting

Pulsed lasers with high peak intensities are used for laser ablation cutting, resulting in melting, vaporization, and plasma ignition (Fig. 13.9). While the plasma plume expands, pressure gradients at the gas liquid interface lead to the ejection of molten and vaporized material out of the cutting zone. Therefore, no gas nozzle is necessary which enables the use of highly dynamic laser scanners. Laser ablation cutting is mostly performed with high pulse energies (≥10 μJ) and repetition rates in the kHz regime. The choice of the laser system in terms of pulse duration regimes has to consider the desired cut quality and economical aspects such as cutting speed, investment costs, and operating expenses.

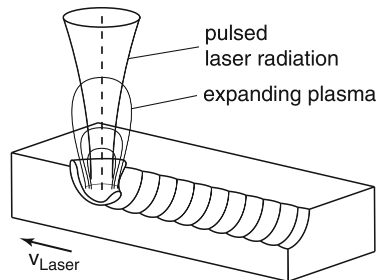

Fig. 13.9 Half section sketch of the ablation cutting and scribing interaction zone

13.3.2.1 Short Pulse Laser Cutting

Cutting metals with short laser pulses always leads to the appearance of molten material. Therefore, the kerf is covered with resolidified material and the surface of the workpiece can show burr formation. Nevertheless, the thermal load is much smaller compared to machining with long pulses. While metals can be cut with fundamental wavelength of solid state lasers, cutting of polymers often requires shorter wavelengths. However, with the UV-wavelength provided by frequency converted solid-state lasers and excimer lasers, almost any material sufficiently absorbs the laser radiation.

Short pulse laser cutting is a relatively slow process compared to melt cutting. Although ablation using short laser pulses exhibits reduced heat input, it is more common for cutting of non-metals. This is due to the appearance of a resolidified burr while machining metals. Short laser pulses are often used to machine silicon [24]. Recently achieved cutting speeds are in the range of 8 mm/s for 220 μm silicon wafers (Fig. 13.10 [25]).

13.3.2.2 Ultra-Short Pulse Laser Cutting

Due to the very high peak intensities of ultra-short pulses, nonlinear effects dominate the absorption of the laser radiation. Therefore, almost every material can be cut regardless of the used wavelength. Ultrashort pulse laser cutting is considered to be without thermal impact on the workpiece. Although cutting without thermal impact is possible, some process conditions must be fulfilled, e.g., moderate fluence. An important field for cutting with ultra-short laser pulses is the manufacturing of medical devices. Stents are mainly cut by melt cutting. However, some materials which are promising for biodegradable stents and cannot be machined by melt cutting, e.g., magnesium, can be cut by ultra-short laser pulses [26]. Another field of application is separation of silicon chips. Recently achieved cutting speeds are in the range of 0.6 mm/s for 220 μm wafers of silicon with a picosecond laser [25].

13.3.2.3 Process Parameters

Compared to conventional melt cutting, laser ablation cutting removes the material layer by layer until the cut is finished after multiple cycles. Besides the laser source, which determines the pulse duration and wavelength, and optical components which define the focal diameter, also the fluence, pulse overlap, and repetition rate are essential and genuine to the laser ablation processes.

Fluence

The fluence is the most important parameter affecting the ablation result, using short and ultrashort laser pulses. The fluence is defined as the energy density on

the workpiece. The fluence determines the ablation diameter and depth as well as the thermal impact. The ablation depth and the square of the ablation diameter are proportional to the logarithm of the fluence.

Using ultrashort laser pulses, a gentle and a strong regime (Sect. 13.2) can be identified. Highest precision and the absence of burr can only be achieved by working in the optical regime. The threshold from gentle to strong ablation can easily be determined by ablating spots with increasing fluence. Plotting the square of the diameter or the depth of the ablated spot versus the logarithm of the fluence will lead to the threshold fluence for the used combination of laser system and material [27]. The easiest way to change the fluence on the workpiece is by setting the energy per pulse.

Pulse Overlap

The pulse overlap is another important parameter for cutting with ultrashort laser pulses. The pulse overlap describes the spatial overlap between two subsequent laser pulses. It is defined by

$$P_0 = 1 - \frac{v_{\mathrm{rel}}}{2w_0 f_{\mathrm{pulse}}}, \tag{13.4}$$

with the relative speed between laser spot and workpiece v_{rel}, the pulse repetition rate f_{pulse} and the focal radius w_0. In experimental studies, a pulse overlap of around 75% has been determined to be appropriate. Higher pulse overlap often shows a significant decrease of quality due to thermal effects [28].

Assuming common values for the laser spot radius in the order of $w_0 = 10\,\mu\mathrm{m}$ and the repetition rate of $f_{\mathrm{pulse}} = 200\,\mathrm{kHz}$, a pulse overlap of 75 percent will lead to a relative speed between laser spot and workpiece of $v_{\mathrm{rel}} = 1\,\mathrm{m/s}$. Such fast movements of the laser spot on the workpiece can be realized by galvo-scanners.

Repetition Rate

The repetition rate defines the number of pulses per second used for machining. The cutting speed can be scaled by the repetition rate. Thermal impact occurs by increasing the repetition rate even for ultrashort laser pulses.

The thermal impact is caused by two different factors. The first is heat accumulation. Increasing the repetition rate leads to a reduction of time for heat diffusion into the workpiece. With higher repetition rates, the heat put into the material cannot be transferred out of the interaction zone. Hence, the temperature of the workpiece rises. This effect leads to a formation of molten material also when applying ultrashort laser pulses. The second cause of thermal impact is particle shielding. Due to the short time interval between two subsequent pulses, ablated airborne particles are located in the region of the laser radiation. The subsequent laser pulse interacts with these particles and leads to plasma ignition above the workpiece. The plasma forms an additional heat source close to the workpiece surface.

The impact of these two effects strongly depends on the laser fluence, the thermal conductivity of the processed material as well as the size and geometry of the ablated structures. Both effects appear at repetition rates above 100 kHz for metals [8].

13.3.3 Laser Scribing

Laser scribing is a process for separating material and is mainly used in two different applications. Compared to laser cutting, laser scribing creates only superficial grooves and does not generate a complete through cut. Due to the lower required ablation depth, laser scribing can also be performed with low pulse energies ($\leq 1\ \mu$J) and very high repetition rates ($\approx$50 MHz).

The first application is the fabrication of a geometry that works as an initiator for a controlled mechanical breaking process on brittle material. Therefore, a groove or a line of blind holes is machined on the surface. Because the ablated volume is smaller compared to a complete through cut, less energy is necessary, and the process is more cost efficient and faster. Another advantage is a reduced amount of redeposites and thermally induced stress. Scribing is performed with short and ultra-short laser pulses, depending on the material [29, 30].

The second meaning of laser scribing is selective ablation of layer systems such as in thin-film solar cells [31]. Thin-film solar cells consist of several layers of metal, semi-conductors and insulating material with different optical properties and ablation thresholds. Layer thicknesses are in the nm and μm range. In the production process, some of these layers have to be patterned without delamination or damage of other layers. Although some layers can be scribed by short laser pulses with sufficient quality, the trend is clearly toward ablation using ultrashort pulses.

13.3.4 Laser Induced Stress Cutting

Besides the traditional cutting technologies which are based on material removal, also a material loss-free technology is established for cutting brittle material, e.g. glass or silicon. The laser radiation is moved across the workpiece and heats up the material. During the following cooling period localized, temporary thermo-mechanical stresses occur that can be used to control and guide the expansion of an initial crack through the material. This practically leads to a cut with a zero kerf width and a perfectly clean and smooth cutting edge. The complete absence of contamination and edge damages supersedes cleaning or edge smoothing processes. Recently achieved cutting speeds are five to ten times faster than with ablation based cutting technologies [25].

In Fig. 13.10, SEM pictures of silicon wafer cutting edges are shown. Using pulsed laser sources, the quality of the cutting edge decreases with longer pulse duration regimes and also with higher cutting speed. However, with laser induced stress (LIS) cutting, the best quality and the fastest cut is achieved.

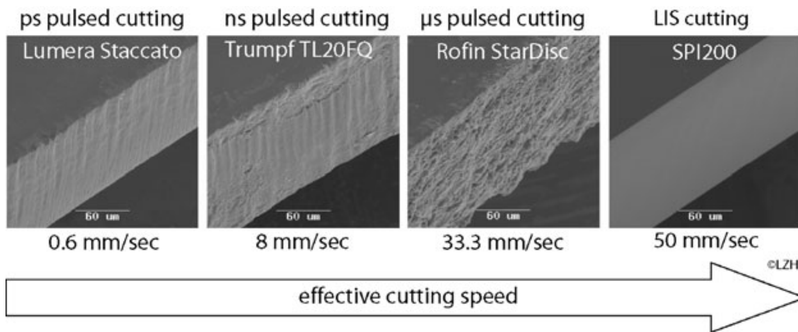

Fig. 13.10 SEM pictures of silicon wafer cut edges using various pulsed cutting systems and novel laser induced stress (LIS) cutting technology [25]

13.4 Microjoining

13.4.1 Welding

Welding is a well established technology of joining. Joining is understood to be the permanent connection of several individual workpieces (joining partners) that are in a geometrically defined, solid state. In welding processes, a phase change of all joining partners is required. They are temporarily molten in the welding zone. Resolidification of the melt mixture leads to a material connection. The connections in micro joining usually have to fulfil at least one of the following requirements:

- Permanently isolate material masses (e.g., gas or liquid containers)
- Carry mechanical load (e.g., clockwork shaft to collar connections)
- Conduct electrical current (e.g., printed circuit board assemblies)

In laser micro welding, the energy for melting the material is supplied by laser radiation. The laser radiation is absorbed by the workpiece and transformed into heat.

In case of metals, the absorption length for most laser wavelengths is small compared to heat diffusion lengths. The absorbed laser radiation can be considered as a surface heat source. However, taking heat transport mechanisms into account, the surrounding volume is heated, leading to a phase change and the formation of a weld zone. In spot welding, the process starts with a heating phase, where the laser power is absorbed in the solid volume of the workpiece. The heat is absorbed near the surface and conducted further into the volume. Advective heat transport is additionally present if melt or vapor flow occurs.

The energy balance includes the absorbed laser energy, heating energy in the solid and in the liquid phase, phase transformation energy between solid and liquid as well as between liquid and vapor (latent heat) and also kinetic acceleration energy and advective heat transport in the melt and vapor. Two welding domains can be distinguished, that mainly depend on the absorbed laser power density I_{abs}:

- *Conduction mode welding* ($I_{abs} < 10^6 W/cm^2$): the absorbed energy is transferred into the material by heat conduction.
- *keyhole mode welding*, also referred to as *deep welding* ($I_{abs} > 10^6 W/cm^2$): The vapor pressure gradient at the melt surface is a significant melt driving force that can lead to keyhole formation, and a weld with a high aspect ratio (Fig. 13.11).

Besides the laser intensity, for different workpiece and material properties, also different process technologies have been established (Fig. 13.12, Table 13.1). Typical welding applications are shown in Fig. 13.13.

Spot Welding

An established application area of spot welding is micro electronics. Because of the material properties of the copper alloys, usually pulsed laser sources are used. The size of spot welds ranges between 50 µm and 200 µm in diameter and corresponds to the laser spot size. With pulse shaping, a fast laser power control during the

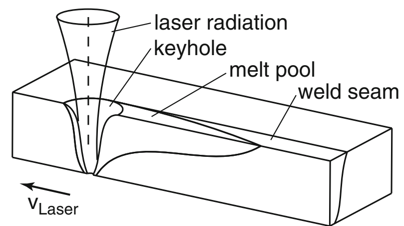

Fig. 13.11 Half section sketch of the deep welding interaction zone

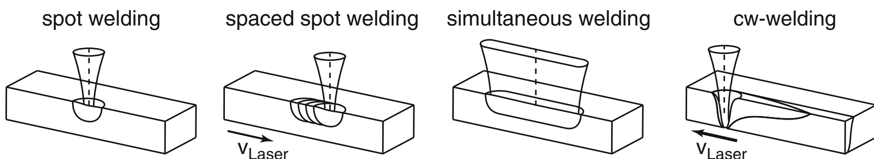

Fig. 13.12 Half section sketches of the interaction zone in different welding technologies

Table 13.1 Characterization of laser welding technologies

Technology	Applications	Advantages	Risks
Spot welding	μ-electronics	Small heat input	Sensitive to disturbances
Simultaneous welding	Plastic housings	Fast	Fixed weld geometry
Spaced spot welding	Sealed packaging, heterogeneous material combinations	Small heat input, reliability, copper alloys	Slow
cw-welding	Wide range	Fast, both shallow and deep welds possible (aspect ratio)	Sensitive to disturbances and positioning tolerances

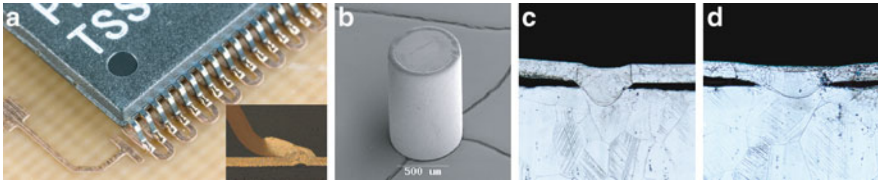

Fig. 13.13 Typical micro welding examples: (**a**) pulsed laser weld of IC to PCB (copper alloy), (**b**) fiber laser weld of tube to cap for sealing of a medical implant (radio seed therapy), wall thickness 50 μm, tube diameter 0.8 mm (titanium), (**c**) cross section of fiber laser weld and (**d**) cross section of pulsed laser weld of membrane welding for sealing in a sensor application, membrane thickness 20 μm (high-grade steel)

laser pulse offers increased reliability when welding of demanding materials such as copper. One possibility to optimize the process stability in spot welding is through closed-loop controls that take into account the starting conditions, like the varying absorptivity of copper surfaces [32]. Another measure for process stability in copper welding is by using frequency converted laser radiation. In Fig. 13.13a, an IC is shown that has been welded to a circuit board by using single laser pulses. Here, due to the increased absorptivity (see Fig. 13.2), the use of a frequency-doubled solid-state laser, operating at a wavelength of 532 nm has been proven to be advantageous also in terms of process stability [33].

Simultaneous Welding

In this welding technology, the laser radiation hits the workpiece with an intensity distribution, that already represents the geometry of the welding seam. This can be achieved by beam manipulating elements (e.g., DOE/ROE/fibers). For example, a gaussian intensity profile can be converted into a ring profile which can be used for single pulse shaft to collar welding. Also, by arranging multiple laser sources to form the desired intensity distribution, a single shot process with more complex welding geometries can be achieved. One example is transmission welding of plastic housings, where multiple diode lasers are arranged in various shapes [34]. In mass production, the poor geometry flexibility is often accepted, given the enormous benefit in processing speed and a lower number of kinematic axes. An alternative is quasi simultaneous welding, where laser scanners are used to perform a high speed multiple movement of the laser radiation along the weld geometry.

Spaced Spot Welding

By subsequently arranging multiple spot welds with a certain overlap next to each other, welding seams can be produced benefiting from the advantages of spot welding, e.g., welding of high reflectivity metals. Also for gas tight welding of sealed housings, the overlapping of single spots offers advantages compared to CW-welding: Due to

the spot overlaps, a weld error caused by a process disturbance at one weld spot can be healed by the next spot weld without additional process control.

Because the speed in spaced spot welding can be chosen slow, the thermal load on the surrounding material can be reduced compared to CW welding. This can be a significant advantage when welding titanium alloys, which at high temperatures require extensive protection from ambient nitrogen and oxygen [35].

CW-Welding

During CW-welding, a relative movement between laser radiation and workpiece takes place along a desired welding path. The available laser systems allow high welding speeds (up to the order of 500 mm/s). Currently, CW-welding offers the best welding results considering the aspect ratio, i.e., large weld depth compared to width. However, CW-welding is a quasi-stationary process that can be disturbed e.g., by material or positioning irregularities. Even after passing a disturbance, returning to the steady state needs a certain time, in which welding errors, such as insufficient welding depths, pores, spatter, etc., can occur. Examples for micro welding with CW laser radiation include welding of high grade steel membranes (Fig. 13.13c) in sensor and battery applications. In micro scale, CW-welding is mostly performed with fiber lasers [36] (preferably single mode), and recent developments also include high brilliance diode lasers [37]. Pulsed lasers suitable for spot welding can also be used for CW-welding: In the SHADOW® process, a fast relative movement between long pulsed laser radiation and work piece is performed, so that during a single laser pulse the weld seam is generated [38].

13.4.2 Soldering

In soldering, diffusion processes are dominantly responsible for the connection. The solid joining partners are wetted by a liquid solder. By material diffusion between the base material of the joining partners and the solder and a subsequent solidification of the solder, a material connection is achieved (Fig. 13.14). Because

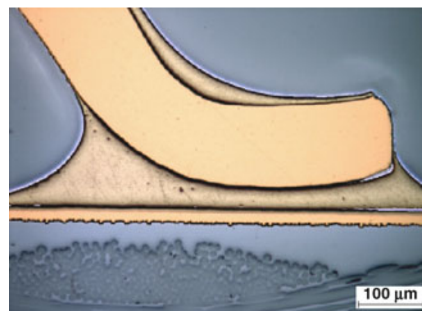

Fig. 13.14 Cross section of soldered IC pin

the solder melt temperature is lower than the base material's, the temperature stability of the joint is lower compared to welding. Also, the diffusion process in soldering requires a one order of magnitude longer processing time compared to welding (several 100 ms, instead of several 10 ms per joint). In order to enable or enhance solder flow, base material wetting and diffusion, fluxing agents are in most cases mandatory. One advantage of soldering compared to welding is a lower process temperature; however, the total energy input and heated volume are in most cases larger. However, for some metal alloys, that are difficult to weld (e.g., high yield aluminium alloys), or in case of heterogeneous joining partners (e.g., aluminium with copper or steel), soldering is a good alternative.

13.5 Marking

Laser marking is a well established industrial application of laser micro-machining and the most obvious in everyday end-user products. Laser markings can be found in car displays, as expiration dates on groceries and as letters on laser marked computer keyboards.

The mechanisms for marking can be divided in two main groups considering the marking mechanisms: Laser marking can take place by material removal/addition or by material modification (Fig. 13.15) [39].

13.5.1 Laser Marking by Material Removal or Addition

Laser marking with material removal can be laser engraving. Engraving may lead to burr or redeposites and therefore can not be recommended where redeposites and cleaning processes are not desired. Laser engraving enables a good resolution but might lead to thermal impact.

Besides engraving, two techniques are used which require a coating, e.g., ink, on the surface of the material to be marked. Bonding is a process that uses the laser to heat and melt the layer and the workpiece to be marked. In a second process step,

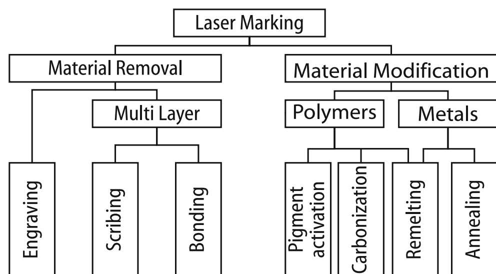

Fig. 13.15 Overview Laser Marking mechanisms

the coating is removed and only the heated areas remain on the workpiece. Scribing is a process described in Sect. 13.3.3, and the marking effect is the result of ablating individual layers.

13.5.2 Laser Marking by Material Modification

The second group of laser marking techniques is based on material modification. The principles are annealing, remelting, pigment activation, and carbonization.

Annealing is a marking technique which can be applied mainly for metals. The material heated by laser radiation reacts with ambient gases and leads to a colorization. Resolution and contrast are quite low, but no change of the surface geometry takes place. Remelting can be performed on both polymers and metals. The scribed structures are defined by the different surface morphologies of the resolidified material that leads to a good visibility. Remelting of polymers often leads to gas emission due to chemical processes in the bulk polymer. During resolidification the emitted gas is trapped and forms pores. These pores lead to a diffuse reflection and scattering of light. Markings created by polymer remelting can also lead to a modification of chemical properties. The resolution is low compared to carbonization and pigment activation.

Pigment activation is a marking process for specifically prepared polymers. The polymer to be marked requires an additive that can be chemically excited by laser radiation. Pigment activation leads to a good contrast and resolution but suffers from the necessity of the additive material. A big advantage of pigment activation is the low thermal impact due to the absence of melting and vaporization.

Carbonization is also a marking process to be applied on polymers. It is based on a chemical reaction below the polymer surface induced by laser radiation. Wavelength and polymer have to be matched for a proper marking. Carbonization can be applied without any change of the physical or chemical properties of the surface. Therefore, this processes is highly interesting for medical applications. Both processes, polymer activation and carbonization, are characterized by a low thermal impact and are therefore suitable for IC-marking (Fig. 13.16).

Fig. 13.16 Typical laser marked die [40]

13.6 Microforming

In microforming, the shape of solid workpieces is changed permanently by plastic deformation. Laser microforming is used for fine adjustment of micro-optical or micro-mechanical devices (MOEMS, MEMS), e.g., laser optics of compact disc drives or sliding heads of hard disc drives, during product assembly. Often, the adjustment relies on selective bending of positioning parts. The bending process can be achieved by taking advantage of the parts' internal mechanical stress, or by applying an external bending force. Common laser microforming technologies include [41, 42]:

- Temperature Gradient Mechanism (TGM) adjustment. The laser radiation forms a thermal load on the workpiece, and the induced thermo mechanical stress results in a work-piece bending.
- Non-Thermal Impact Laser Adjustment (NOTILA). In an upstream process, the part is loaded with internal mechanical stress by thermal or mechanical means. After assembling the part, a fine adjustment is accomplished by laser ablation of material at the surface. Thereby, the part relaxes into a new state of mechanical equilibrium and bends accordingly.
- Micro shock wave forming. Using the recoil pressure of ultra short laser pulse-induced plasma on positioning parts, shock waves can be generated locally that lead to a local plastic yield and part bending.

13.7 Summary

Today, laser micromachining is used in many industrial processes such as drilling, cutting, welding, marking, and microforming. Accordingly, these processes can be found in different industrial sectors ranging from semiconductor fabrications, medical device manufacturers, solar cell industry, and many others. Depending on the specific application, the parameter regimes regarding pulse duration, wavelength, beam quality, and output power can range over several orders of magnitude. Therefore, attention has to be paid on the appropriate set of parameters. They have to be chosen not only with respect to the process. The required quality and throughput define the appropriate process parameters. Cutting, as an example, is an application which can be realized through several parameter regimes: While melt cutting with high precision can be performed using CW or long pulsed lasers, laser ablation cutting is performed by short or ultrashort laser pulses. It has to be taken into account, that laser ablation cutting allows higher precision and enables the processing of materials such as magnesium which cannot processed with melt cutting but will result in higher production costs.

In the near future, laser precision microfabrication will probably be guided by two main trends. On the one hand, the trend toward further precision and quality will be continued toward the machining of micron and even submicron structures in

industrial scale. On the other hand, the throughput in manufacturing will become more important. Whereas the former aspect is driven by new laser sources with higher stability and better beam quality, the latter is motivated by the market which requires a significant reduction in processing time in order to compete with alternative processes. Additionally, this trend is driven by the ever increasing output power of the laser systems, which will also require new solutions in beam guiding and forming. To summarize, laser precision microfabrication has already penetrated many industrial applications. Due to the recent developments regarding the laser sources, novel applications will not only replace conventional manufacturing processes but also enable the development of new products tailored for laser based machining.

References

1. B.N. Chichkov, C. Momma, S. Nolte, F. von Alvensleben, A. Tünnermann, Appl. Phys. A **63**, 109 (1996)
2. D. Bäuerle, *Laser Processing and Chemistry*. (Springer, Berlin, 2000)
3. A. Ruf, *Modellierung des Perkussionsbohrens von Metallen mit kurz- und ultrakurzgepulsten Lasern* Ph.D. thesis, Universitaet Stuttgart, 2004
4. F. Siegel, U. Klug, R. Kling, A. Ostendorf, in *Proceedings of LPM2008-the 9th Symposium on Laser Precision Microfabrication*, 2008
5. S. Sommer, F. Dausinger, in *Proceedings of LPM2008-the 9th International Symposium on Laser Precision Microfabrication*, 2008
6. D. Breitling, A. Ruf, F. Dausinger: in *Proceedings of SPIE*, vol. 5339 (2004)
7. T.V. Kononenko, S.M. Klimentov, V.I. Konov, F. Dausinger, Proc. SPIE **6161**, 1 (2005)
8. A. Ancona, F. Röser, K. Rademaker, J. Limpert, S. Nolte, A. Tünnermann, Opt. Express **16**(12), 8958 (2008)
9. M. von Allmen, J. Appl. Phys. **47**, 5460 (1976)
10. M. Geiger, H. Hügel, E. Tönshoff (eds.), *Präzisionsabtragen mit Lasern*: VDI-Technologiezentrum Physikalische Technologien (2000)
11. L. Trippe, J.Willach, E.W. Kreutz, W. Schultz, J. Petereit, S. Kaierle, R. Proprawe, Proc. SPIE **5662**, 609 (2004)
12. X. Liu, Proc. SPIE **5713** (2006)
13. E.W. Kreutz, L. Trippe, K. Walther, R. Poprawe, Proceedings of the 4th International Congress on laser advanced materials Processing, LAMP 2006 by Japanese Laser Processing Society, pp. 1–5
14. G. Kamlage, T. Bauer, A. Ostendorf, B. Chichkov, Appl. Phys. A **77**, 307–310 (2003)
15. C. Föhl, F. Dausinger, in *International symposium on laser precision microfabrication No. 4, Munich , Germany*, 2003
16. S. Nolte, C. Momma, G. Kamlage, A. Ostendorf, C. Fallnich, F. von Alvensleben, H. Welling, J. Appl. Phys. A **68**, 563 (1999)
17. T. Kononenko, S. Garnov, S. Klimentov, V. Kononov, E. Loubnin, F. Dausinger, A. Raiber, C. Taut, Appl. Surf. Sci. **109/110**, 48 (1997)
18. E. Akman, L. Candan, T. Canel, A. Demir, E. Kacar, LPM, 2008, pp. 1–4
19. C. Hartmann, A. Gillner, in *ICALEO Conrgress Proceedings* (2007)
20. R. Le Harzic, D. Breitling, S. Sommer, C. Föhl, F. Dausinger, E. Audouard, Appl. Phys. A Mater. Sci. Process. **81**, 1121 (2005)
21. B. Campbell, T. Lehecka, V. Semak, J. Thomas, in *ICALEO 2007 Congress Proceedings* (2007)
22. O. Suttmann, B. Wojakowski, U. Klug, R. Kling, A. Ostendorf, in *ICALEO 2008 Congress Proceedings* (2008)

23. W. Schulz, C. Hertzler, Cutting: Modeling and data, in Landolt-Börnstein New Series VIII/1C
24. X. Wang, J.D. Shephard, F.C. Dear, D.P. Hand, in *Proceeedings of the 4th International Congress on Laser Advanced Materials Processing*, LAMP 2006 by the Japanese Laser Processing Society
25. O. Haupt, F. Siegel, A. Schoonderbeek, L. Richter, R. Kling, A. Ostendorf, in *Proceedings of LPM2008 – the 9th International Symposium on Laser Precision Microfabrication* (2008)
26. C. Momma, U. Knop, S. Nolte, Progress in Biomedical Research, 39 (1999)
27. J.M. Liu, Opt. Lett. **7**(5), 196 (1982)
28. U. Klug, B. Kamlage-Rahn, J. Koch, R. Knappe, U. Stute, B. Chichkov, in *ICALEO Congress Proceedings* (2006)
29. H. Niino, Y. Kawaguchi, T. Sato, A. Narazaki, R. Kurasaki, in *Proceedings of LPM2008-the 9th International Symposium on Laser Precision Microfabrication* (2008)
30. K. Yamamoto, N. Hasaka, H. Morita, E. Ohmura, in *Proceedings of LPM2008-the 9th International Symposium on Laser Precision Microfabrication* (2008)
31. P. Engelhart, S. Hermann, T. Neubert, H. Plagwitz, R. Grischke, R. Meyer, U. Klug, A. Schoonderbeek, U. Stute, R. Brendel, Prog. Photovolt. Res. Appl. **15**(6), 521 (2007)
32. S. Amorosi, T. Sidler, R.P. Salathé, H.P. Schwob, J. Hertzberg, J. Laser Appl. **16**, 134 (2004)
33. F. Otte, A. Ostendorf, U. Stute, T. Stehr, in *Proceedings of SPIE*, vol. 6458Ű645804-1, San Jose, California, USA, 2007
34. F. Bachmann, U. Russek, **5121**, Proceedings of SPIE vol. 5121, p. 385–398, 2003
35. K. Richter, U. Reisgen, W. Behr, R. Holtz, J. Laser Appl. **19**, 116 (2007)
36. R. T. Brown, J. Laser Appl. **20**, 201 (2008)
37. N. Abe, Y. Funada, T. Imanaka, M. Tsukamoto, Trans. JWRI **34**, 19 (2005)
38. A. Gillner, A. Olowinsky, K. Klages, J. Gedicke, F. Sari, *International Conference on Lasers, Applications, and Technologies 2005: Laser-Assisted Micro- and Nanotechnologies*, vol. 6161, 2006, p. 616102
39. F. Olsen, A. Kaplan, *Laser cutting and marking*. EuroLaser Academy (1997)
40. B. Gu, R. Schramm, J. Gillespie, G. Mezack, A. Cunningham, in *IMAPS* (2003)
41. J. Ocańa, M. Morales, C. Molpeceres, O. García, J. Porro, J. García-Ballesteros, Appl. Surf. Sci. vol. 254, No. 4, p. 997–1001 (2007)
42. M. Schmidt, M. Dirscherl, M. Rank, M. Zimmermann, J. Laser Appl. **19**, 124 (2007)

Index

3D Hollow microstructures, 216, 225–228, 233
3D Integrated microchip, 229
3D Microchannels, 225
3D Microfluidic structures, 227
3D Photonic devices, 218
3D fabrication, 1

Abbe diffraction limit, 198
Ablation, *see* laser ablation
Ablation cutting, 321, 323
Ablation threshold, 40, 313
Absorption spectrum, 293
Acousto optic modulator, 131
Acousto-optic Q-switching, 70
Alignment grooves, 244
Analytical phase functions, 127–129
  combinations of phase functions, 129
  iterative Fourier, 129
  periodic spectral phase functions, 128
  polynomial phase functions, 127
  Pulse sequences, 128, 129
  spectral phase jumps, 128
  V-shaped function, 128
Anamorphic, 79
Annealing, 332
Antireflection coating, 105
Apertureless scanning near-field optical microscopy, 208
Aqueous suspensions, 267
ArF, 64
Atomization, 167
Azimuthally-Polarized Laser Beams, 77

Basic beam delivery optics, 77
Beam characterization, 84
Beam homogenizers, 78
Beam interference, 239
Beam parameter product, 84
Beam propagation ratios, 84
Beam quality, 315
Beam shaping, 78, 219, 231–233
Beer–Lambert law, 41, 93, 99
Bessel beams, 19
Binodal, 39, 41, 47, 49
Binodal line, 39, 41, 47, 49, 195
Biological implants, 110–116
Biomaterials, 110, 281
Black silicon, 106, 108–110
Boiling, 195
Bonding, 331
Borosilicate glass, 242
Bottom-up, 203
Breathing-sphere model, 43, 50
Burr formation, 323, 324

CAD/CAM
  manufacturing, 2
  software, 2
Carbonization, 332
Cavitation, 38
Cavitation bubble, 156, 157, 175
Cavity dumping, 70
Ceramic lasers, 69
Chirped pulse amplifier, 206
Chirped pulse oscillator, 207
Chirped-pulse amplification (CPA), 73
Chirped-pulse mode locking, 207
Chromophore-assisted laser inactivation, 153
CO_2 lasers, 66
Coalescence, 47
Coherent beam combining, 13
Color marking, 301
Computer simulation, 35, 41
Conduction mode welding, 328
Continuous wave, 313
Copper deposition, 301
Coulomb explosion, 182, 192

Couplers, 216, 221, 233
Cubic chirped pulses, 135
Cutting, 321
Cutting speed, 323
CW-welding, 330

Damages, 55
Deep micro-trench, 304
Deep welding, 328
Defect states, 201
Dielectric mask, 252
DIET
  ESD, 27
  plasmon, 27
  PSD, 27
  pulsed laser desoprtion, 27
  surface defects, 27
Diffraction, 18
Diffractive lens, 249
Diffractive optical element (DOE), 80, 245
Diffusion process, 331
Digital fabrication, 261
Digital microfabrication, 260, 261
Diode-pumped, 68
Diode-pumped solid state (DPSS) laser, 302
Direct writing, 240
Direct-write micromachining, 107
Direct-write patterning
  3DVEP, 24
  laser CVD, 24
  LIBWE, 24
  LIFT, 24
  LIPAA, 24
Dislocations, 58
Disruption, 146
Dissection, 146, 147, 149, 150, 153, 155
Donor substrate, 259, 266
Double-clad fiber structure, 70
Downchirped-pulse amplification (DPA), 73
Drilling, 316
Drilling strategies, 316
Drude-like dynamics, 42
Dynamic release layer (DRL), 267
  biocompatible, 282
  metal, 267
  polymer, 267, 268
  schematic, 267

Electro-optic Q-Switching, 71
Electron energy transfer depth, 167
Electron thermalization, 167
Electron–phonon coupling, 194
Electron–phonon relaxation time, 192
Engraving, 331
Equation of state, 43
Evaporation, 45, 312
Excimer lasers, 64
  Bragg grattings, 3
  holography, 3
  index changes, 3
  Xe, Xe2, 2
Explosive boiling, 38, 40

F_2-laser, 244, 246
Fabricating, 1
Femtosecond laser, 215–219, 225, 227, 231, 233, 234, 314
Fiber Bragg gratings, 222–224
Fiber chirped amplification systems, 76
Fiber chirped pulse amplifier (FCPA), 77
Fiber lasers, 68
Fiber-lens, 249
Field mapping, 78
Fine adjustment, 333
Flat-top beam, 79
Fluence, 324
Foaming, 204
Focus scanning, 239
Fourier shaping, 130
Fragmentation, 36, 38, 42, 47–49, 52, 54–56, 168
Free carrier absorption, 194
Frequency-resolved optical gating (FROG), 85
Fresnel reflection, 93, 105
Front side ablation, 251
Frontier technologies
  China, 2
Fused silica, 244, 249

G-Code toolpath, 21
Galvanometer, 81
Galvanometer scanner, 304
Gas-to-particle condensation, 168
Gaussian profile, 79
Gaussian profile to tophat profile conversion, 79
Glass, 215–218, 220, 222, 225, 227–230, 233, 326
Gold nanoparticles, 298
Government sponsored research
  BMFT, 2
  CNRS, 2
  Department of Industry, 2
  MITI, 2
  NRC, 2

Graded index (GRIN), 105
Gratings, 243
Group delay dispersion, GDD, 124, 127
Growth, 47

Half tone mask, 247
Harmonic generation, 83
HAZ, *see* heat affected zone
Heat accumulation, 325
Heat affected zone, HAZ, 36, 55, 97, 100, 198, 215
Heat diffusion length, 199
Heat equation, 96
Helical drilling, 319, 320
Herriott multipass cell, 207
Heterogeneous joining partners, 331
HfO_2, 251
Hole drilling, 241
Homogeneous nucleation, 38, 47, 52
Homogenous boiling, 39
Hydrophilicity, 239

Impact ionisation, 192
Incubation, 201
Index of refraction, 93
Indium tin oxide, 241
Inductively coupled plasma mass spectrometry, 172
Industrial applications, 1, 311
Industrial laser sales
    microfabrication, 4
Inertial confinement, 50, 52, 53
Ink-jet, 260, 285
Integration of microcomponents, 228
Interfering beams, 17
Intermetallic alloys, 26
Inverse bremsstrahlung, 95

Jetting effects, 273
Joining, 327

Kerr lens, 72
Keyhole mode welding, 328
KrF, 64

Lase-and-place, 275
    schematic, 275
Laser
    diode pumped fiber, 3
    diode pumped solid state, 3
    FEL, 11
    fiber lasers, 2
    MASER, 10
    solid state, 2
    THz, 10
Laser ablation, 35, 99
    ablation plume, 100
    ablation threshold, 99
    Coulomb explosion, 100
    ejection mechanisms, 166
    in liquids, 173
    in vacuum/gas, 171
    mechanisms, 165, 167, 173
    micro/nanoparticles, 180
    nanosecond pulses, 165
    phase explosion, 99
    ultrafast pulses, 166
Laser-assisted in situ leratomileusis, 152
Laser beam shaping, 93
Laser catapulting, 155
Laser decal transfer, 276
    MEMS structures, 285
Laser direct-write (LDW), 259–261
    bacteria, 282
    biosensors, 282
    cells, 282
    chemical sensors, 278
    die sensitized solar cells, 281
    embedded electronics, 283
    key challenges, 286
    LED bare die, 275
    Li-ion microbatteries, 280
    metal interconnects, 277
    micropower sources, 279
    passive components, 278
    planar alkaline microbatteries, 280
    proteins, 282
    semiconductor bare die, 274
    Si-based microstructures, 274
    system schematic, 260
Laser dose
    chemical assisted etching, 13, 14
Laser etching at a surface adsorbed layer (LESAL), 299
Laser forward transfer, 259
    origins, 262
Laser induced backside dry etching (LIBDE), 299
Laser-induced backside wet etching (LIBWE), 297, 302
Laser-induced forward transfer (LIFT), 156, 262, 263
    ceramics, 264
    composites, 270
    conditions for uniform transfer, 264

debris, 276
evolution, 265
fast imaging techniques, 273
fs laser pulses, 269, 282
fundamental limitations, 265
imaging studies, 270
metals, 264, 265
non-phase transformative, 272
organic precursors, 264
phase transformative, 265
ps laser pulses, 269
rheological systems, 271
schematic, 263
Laser-induced periodic surface structures (LIPSS), 107, 108
Laser-induced plasma-assisted ablation (LIPAA), 297, 299
Laser induced stress (LIS) cutting, 326
Laser interference metallurgy, 26
Laser material modification, 98
Laser material processing, 92, 101
excimer laser annealing (ELA), 102
laser cladding, 102
laser cleaning, 102
laser surface heat treatment, 101, 112, 115
laser surface texturing, 103, 107–110, 113–116
non-melt laser annealing (NLA), 102
Laser material processing techniques
laser material processing, *see* laser processing
Laser polarization
control, 21
Laser processing, 133–141
annealing, 5
biological media, 6
bulk modifications, 139–141
excitation events, 133
holding, 5
imaging, 5
irradiating, 5
joining, 5
micromachining, 5
phase transitions, 135–139
photodynamic therapy, 5
rapid prototyping, 5
refractive index engineering, 139–141
repair, 5
scribing, 5
separating, 5
shaping, 5
surface texturing, 134–135
texturing, 5
thermal, 6
thermodynamic trajectories, 137–139
Laser processing of materials, 164
Laser processing parameters
beam character, 7
dose, 4
laser pulse train, 7
pattern generation, 7
power, 4
wavelength, 4
Laser sales, 1
Laser scribing, 321, 326
Laser surface melting, 98
Laser technology
photosensitive cladding, 3
LDW of rheological systems, 271
biomaterials, 272
complex fluids, 272
regimes, 273
schematic, 271
sub-threshold transfers, 273
Lennard–Jones, 41
Lennard–Jones model, 36
LiB_3O_5 (LBO), 83
Light absorption, 93, 94
Light-matter interactions, 36
$LiNbO_3$, 245
Liquid crystal spatial light modulator, LC-SLM, 82, 130, 131
Liquid-solid interface, 53
Liquid-vapor coexistence, 39, 52
Liquid-vapor metastability, 49

Mach-Zehnder interferometer (MZI), 222
MAPLE-DW, 271
Marangoni effect, 99
Marking, 331
Marking and engraving, 1
Maskless processing, 245
Mechanical ablation, 180
Media-assisted processes, 294
Melt cutting, 321–323
Melting, 312
Membrane welding, 329
Metal plating, 301
Metastable zone, 46
Micro lens array, 246
Micro-machining, 55
Microelectronics, 277
Microfluidic chips, 150
Microfluidic devices, 227, 228, 241
Microforming, 333

Microjoining, 327
Micromixers, 241
Microprocessing, 311
Micropulses, 15
Miotello–Kelly, 36, 39
Miotello–Kelly model, 50
MITI, 2
Mode locking, 72
MOEMS, MEMS, 333
Molecular self-assembly, 25
Molecular solids, 50
Molecular-dynamics (MD), 41
Moth-eye effect, *see* subwavelength structures (SWS)
Multilayer stack, 252
Multilayered ribbons, 267
Multiphoton absorption, 94, 191, 215–217, 233
Multiple rate equation, 192
Multiscale surface modification, 91, 104–106, 111, 113–116
Multiwavelength excitation process, 295
Multiwavelength laser processing
  ablation, 8
  chirp pulse processing, 9
  soliton laser, 9

N-BK7-glass, 242
Nanoantennas, 208
Nanoaxotomy, 150
Nanochannels, 226
Nanodissection, 198
Nanomaterials synthesis, 164, 168
Nanometer scale, 1
Nanoparticle, 53, 54, 146, 153, 154, 157, 158
Nanoparticles synthesis
  aggregation, 171
  coalescence, 170, 179
  colloids, 173
  laser fluence, 176
  laser-induced fragmentation, 181
  laser-induced growth, 181
  process model, 179
  pulse width, 177
  stabilizing agents, 177
Nanostructures, 136
Nanosurgery, 146, 148, 150, 153
Nd ion, 68
Nd:$GdVO_4$, 75
Nd:YAG, 66
Nd:YLF, 68
Nd:YVO_4, 66
Near-electromagnetic field enhancement, 298
Newton rings, 41, 45
Nucleation, 39, 47, 51
Nucleation barrier, 170

OCMOCER, 25
OCT (Optical coherence tomography), 86
On-the-fly, 318
Optical absorption depth, 94
Optical breakdown, 38, 94, 100, 153, 173
Optical coherent tomography (OCT)
  opthalmology, 4
Optical emission spectroscopy, 168
Optical layer, 251
Optical microcomponents, 215–217, 228, 233
Optical penetration depth, *see* optical absorption depth, 167
Optical Scanners, 81
Optical tweezers, 154, 155
Optical waveguides, 216, 218, 222, 228, 230, 231, 233
Optimal pulse, 138, 141
Optimization, 132–142
  adaptive, 135–142
  feedback loops, 132, 137–141
  filamentation, 141
  ion acceleration, 137
  ion detection, 137
  nanoparticles, 138
  phase-contrast microscopy, 139
  refractive index flip, 139
  strategies, 132–133
  wavefront distortions, 141
Optoperforation, 151, 152
ORMOCER, 25, 240
Osseointegration, 111
Osteolysis, 110
Output power, 315, 316
Over-the-barrier ionisation, 191
Overview, 1

Parallel processing, 80
Parameter regime, 311
Particle shielding, 325
Pattern generation
  dynamic mask, 23
  holographic exposure, 23
  lithography, 23
  mask dragging, 23
Patterning of layers, 249
Percussion drilling, 318

Phase diagram, 39, 49
Phase element, 245
Phase explosion, 38, 39, 42, 46, 48, 49, 51, 52, 55–57, 166, 168, 195
Phase mask, 302
Phase matching (PM), 83
Phase separation, 38, 47
Phase transformation, 28
  $BaTiO_3$, 28
  chalcogenide GeSb, 28
  $LiNbO_3$, 28
  photostructurable glass ceramic, 28
  vanadium dioxide, 28
Phonons, 37
Photo-decomposition, *see* photochemical
Photochemical, 95
Photolytic, *see* photochemical
Photonic crystal fiber (PCF), 76
Photonic devices, 220, 234
Photophysical, 95
Photothermal, 95, 96, 98
Photothermal processes, 165
Picosecond lasers, 314
Pigment activation, 332
Planar optical waveguides, 244
Plasma
  adiabatic expansion, 169
  expansion dynamic, 165
  free-flight regime, 169
  liquid confinement, 174
  model, 169
  properties, 174
  secondary etching, 166, 175
  shockwave regime, 170
Plasma frequency, 95
Plasma plume, 313, 323
Plasmon, 19, 95, 154
Pockels cell, 71
Polarization, 320
Polarization shaping, 129
Polydimethylsiloxane, 242
Polyethersulfone, 241
Polyethylene-terephthalate, 240
Polymers
  IBM Corp, 3
  microvia fabrication, 3
  photoetching, 3
  Siemens Corp, 3
Polymethylmethacrylate, 241, 242
Pressure waves, 38, 45
Process control, 1
Process monitoring, 85
Processes and techniques, 1
Protean material, 29
Proximity method, 243
Pulse delivery control systems, 12
  pulse amplitude, 12
  pulse length, 13
Pulse duration, 312
Pulse energy, 315
Pulse overlap, 324, 325
Pulse peak power, 315
Pulse power, 312
Pulse shaping, 19, 123–132
  basic layout, 130
  experimental implementation, 130–132
  frequency domain manipulation, 123–127
  fundamentals, 123–127
  mathematical formalism, 123–127
Pulse slicing, 71
Pulse trains, 20
  incubation effects, 20
Pulsed laser deposition, 171
Pump-probe experiments, 45
Pyrolytic, *see* photothermal

Q-switching, 70, 314

Radially-polarized laser beam, 78
Rapid prototyping, 261, 287
Rear side ablation, 251
Receiving substrate, 259
Reflectivity, 93
Refractive index modification, 216, 217, 220, 223, 233
Regenerative amplifiers, 73
Remelting, 332
Repetition rate, 315, 324, 325
Ribbon, 259, 264, 266
Ripples, 203
Rotation of the beam, 320

Saturable absorbers, 72
Scaffold, 158, 159
Scanning ablation, 240
Schwarzschild-objective, 243, 302
Scribing, 323, 332
Second harmonic generation, 83
Second-order phase transition, 166
Self organisation, 203
Self-focusing, 94
Semiconductor diode laser, 64
SESAM, 73

Shadowgraphy, 174
Shockwave, 157
Short laser pulses, 313, 314
Silicon, 326
Silicon monoxide, 253
Silicon wafer, 327
Simultaneous welding, 328, 329
Single pulse drilling, 317
SiO_x, 253
SNOM, 18
Soldering, 330
Solid-liquid coexistence, 51
Solid-State lasers, 65
Spaced spot welding, 329
Spallation, 38, 48, 168
Spatial light modulator (SLM), 82
Spatial pulse shaping, 130
Spatial-temporal control
  causality, 22
  coherent control, 22
Spectral absorptivity, 315
Spectral-phase for direct electric-field reconstruction (SPIDER), 85
Spinodal, 39, 47
Spinodal decomposition, 38, 47, 51
Spinodal line, 195
Splitters, 216, 218, 221, 228, 233
Spot welding, 328, 329
Stainless steel, 242
Static ablation, 240
Stillinger–Weber, 41
Stillinger–Weber model, 36
Strategic tool
  lasers, 2
Stress waves, 155
Strong-field ionisation, 191, 192
Structures, 1
SU8, 240
Sublimation, 312
Submicron period, 244
Subsidiary layer, 253
Subsurface heating, 195
Subwavelength structures (SWS), 105
superhydrophobic surfaces, 103
Supersaturation, 170
Surface plasmon resonance, 208
Surface texturing, 241
Surgery, 145–148, 150–155, 159
Synchronized-image-scanning, 247

Ta_2O_5, 245, 251
Tailor materials
  triazenopolymers, 29
Talbot interferometer, 243
Temperature-density diagram, 167
Temporal pulse tailoring, 142
Thermal diffusivity, 97
Thermal impact, 325
Thermal lensing effects, 67
Thermal penetration depth, 313
Thermal processes, 195
Thermal regime, 39, 42
Thermalization time, 95
Thermally activated processes, 98
Thermocapillarity, *see* Marangoni effect
Thermodynamic evolution, 39
Thermodynamic pathways, 42
Thermodynamic trajectories, 46, 50
Thermodynamics, 37
Thin film, 171
  gas pressure, 171
  nanostructured, 171, 181
  pulse width, 172
Thin-disk laser, 69
Third harmonic generation (THG), 83
Third order dispersion, TOD, 127, 135, 136
Three-dimensional (3D) microstructures, 216
Threshold fluence, 325
Ti:sapphire, Ti:Al_2O_3
  chirp pulse amplification, 3
  laser medium, 3
TiO_2, 251
Top-down approaches, 198
Total-microanalysis system (μ-TAS), 228, 306
Transfection, 150, 198
Transform-limited pulses, 73
Transparent materials, 215–218, 226, 232, 233
Trepanning, 319
Trepanning head, 320
Tribology, 239
Trivial fragmentation, 49, 57
Two step processing, 253
Two temperature model, 194, 314
Two-beam interferometric laser irradiation, 306
Two-grating interferometer, 244

Ultrafast pulsed laser oscillators and amplifiers, 72
Ultrashort laser pulses, 123, 314

Vaporization, 38, 47, 195
Via drilling, 241

Voxel, 260, 261
  multiple, 271
  variable, 277
VUV laser, 295
VUV laser irradiation, 296

Water-jet-guided laser, 298
Waveguide CO_2 lasers, 66
Waveguide lasers, 216, 222, 233
Wavelength, 314
Weber number, 323
Welding, 327
World wide publications
  laser material processing, 2

XeCl, 64
XeF, 64

Yb ion, 68
Yb:YAG, 66